ASME
SETTING THE STANDARD

Editor, **DAVID C. WISLER (2008)**
Assistant to the Editor: **ELIZABETH WISLER**
Associate Editors
Gas Turbine (Review Chair)
K. MILLSAPS, JR. (2007)
Aeromechanics
M. MONTGOMERY (2008)
A. SINHA (2008)
Boundary Layers and Turbulence
G. WALKER (2008)
Computational Fluid Dynamics
J. ADAMCZYK (2008)
M. CASEY (2008)
Experimental Methods
W.-F. NG (2008)
Heat Transfer
R. BUNKER (2009)
J.-C. HAN (2008)
K. A. THOLE (2007)
Radial Turbomachinery
R. VAN DEN BRAEMBUSSCHE (2008)
Turbomachinery Aero
S. GALLIMORE (2008)
D. PRASAD (2008)
A. R. WADIA (2009)

PUBLICATIONS COMMITTEE
Chair, **BAHRAM RAVANI**

OFFICERS OF THE ASME
President, **SAM Y. ZAMRIK**
Executive Director, **VIRGIL R. CARTER**
Treasurer, **T. PESTORIUS**

PUBLISHING STAFF
Managing Director, Publishing
PHILIP DI VIETRO
Manager, Journals
COLIN MCATEER
Production Coordinator
JUDITH SIERANT

Transactions of the ASME, Journal of Turbomachinery (ISSN 0889-504X) is published quarterly (Jan., Apr., July, Oct.) by The American Society of Mechanical Engineers, Three Park Avenue, New York, NY 10016. Periodicals postage paid at New York, NY and additional mailing offices.
POSTMASTER: Send address changes to Transactions of the ASME, Journal of Turbomachinery, c/o THE AMERICAN SOCIETY OF MECHANICAL ENGINEERS, 22 Law Drive, Box 2300, Fairfield, NJ 07007-2300.
CHANGES OF ADDRESS must be received at Society headquarters seven weeks before they are to be effective. Please send old label and new address.
STATEMENT from By-Laws. The Society shall not be responsible for statements or opinions advanced in papers or ... printed in its publications (B7.1, Par. 3).
COPYRIGHT © 2008 by the American Society of Mechanical Engineers. For authorization to photocopy material for internal or personal use under those circumstances not falling within the fair use provisions of the Copyright Act, contact the Copyright Clearance Center (CCC), 222 Rosewood Drive, Danvers, MA 01923, tel: 978-750-8400, www.copyright.com. Request for special permission or bulk copying should be addressed to Reprints/Permission Department.
Canadian Goods & Services Tax Registration #126148048

Journal of Turbomachinery

Published Quarterly by ASME

VOLUME 130 • NUMBER 1 • JANUARY 2008

RESEARCH PAPERS

011001 **PIV Maps of Tip Leakage and Secondary Flow Fields on a Low-Speed Turbine Blade Cascade With Moving End Wall**
P. Palafox, M. L. G. Oldfield, J. E. LaGraff, and T. V. Jones

011002 **On Nonlinear Forced Vibration of Shrouded Turbine Blades**
J. Szwedowicz, R. Visser, W. Sextro, and P. A. Masserey

011003 **Heat Transfer and Pressure Investigation of Dimple Impingement**
K. Kanokjaruvijit and R. F. Martinez-Botas

011004 **Control of Three-Dimensional Separations in Axial Compressors by Tailored Boundary Layer Suction**
Semiu A. Gbadebo, Nicholas A. Cumpsty, and Tom P. Hynes

011005 **Large Eddy Simulation of Flow and Heat Transfer in the Developing Flow Region of a Rotating Gas Turbine Blade Internal Cooling Duct With Coriolis and Buoyancy Forces**
Evan A. Sewall and Danesh K. Tafti

011006 **Stability Increase of Aerodynamically Unstable Rotors Using Intentional Mistuning**
Carlos Martel, Roque Corral, and José Miguel Llorens

011007 **Fully Automated Model-Based Performance Analysis Procedure for On-Line and Off-Line Applications**
Michael Bauer and Stephan Staudacher

011008 **Three-Component LDV Measurements in the Wake of a Compressor Cascade With Flow Separation**
G. V. Hobson, T. M. Caruso, and J. R. Carlson

011009 **The Influence of Compressor Blade Row Interaction Modeling on Performance Estimates From Time-Accurate, Multistage, Navier–Stokes Simulations**
Dale Van Zante, Jenping Chen, Michael Hathaway, and Randall Chriss

011010 **Numerical Investigation of a Transonic Centrifugal Compressor**
Michele Marconcini, Filippo Rubechini, Andrea Arnone, and Seiichi Ibaraki

011011 **Minimizing Maximum Modal Force in Mistuned Bladed Disk Forced Response**
Keith W. Jones

011012 **Combustion Instability and Emission Control by Pulsating Fuel Injection**
Christian Oliver Paschereit and Ephraim Gutmark

011013 **Vibratory Parameters of Blades From Coordinate Measurement Machine Data**
Alok Sinha, Benjamin Hall, Brice Cassenti, and Gary Hilbert

011014 **Improved Diffuser/Volute Combinations for Centrifugal Compressors**
T. Steglich, J. Kitzinger, J. R. Seume, R. A. Van den Braembussche, and J. Prinsier

011015 **Numerical Investigation of End Wall Boundary Layer Removal on Highly Loaded Axial Compressor Blade Rows**
V. Gümmer, M. Goller, and M. Swoboda

011016 **Correlative Analysis of Effusion Cooling Systems**
Lorenzo Arcangeli, Bruno Facchini, Marco Surace, and Lorenzo Tarchi

(**Contents continued on inside back cover**)

This journal is printed on acid-free paper, which exceeds the ANSI Z39.48-1992 specification for permanence of paper and library materials. ♾™
♻ 85% recycled content, including 10% post-consumer fibers.

Downloaded 30 May 2010 to 128.113.26.88. Redistribution subject to ASME license or copyright; see http://www.asme.org/terms/Terms_Use.cfm

Journal of Turbomachinery Volume 130, Number 1 JANUARY 2008

011017 Passive Shroud Cooling Concepts for HP Turbines: Experimental Investigations
Vasudevan Kanjirakkad, Richard Thomas, Howard Hodson, Erik Janke, Frank Haselbach, and Chris Whitney

011018 Time-Resolved Heat Transfer Measurements on the Tip Wall of a Ribbed Channel Using a Novel Heat Flux Sensor—Part I: Sensor and Benchmarks
Tim Roediger, Helmut Knauss, Uwe Gaisbauer, Ewald Kraemer, Sean Jenkins, and Jens von Wolfersdorf

011019 Time-Resolved Heat Transfer Measurements on the Tip Wall of a Ribbed Channel Using a Novel Heat Flux Sensor—Part II: Heat Transfer Results
Sean Jenkins, Jens von Wolfersdorf, Bernhard Weigand, Tim Roediger, Helmut Knauss, and Ewald Kraemer

011020 Vaneless Diffuser Advanced Model
Oleg Dubitsky and David Japikse

011021 Investigation of Three-Dimensional Unsteady Flows in a Two-Stage Shrouded Axial Turbine Using Stereoscopic PIV—Kinematics of Shroud Cavity Flow
Yong Il Yun, Luca Porreca, Anestis I. Kalfas, Seung Jin Song, and Reza S. Abhari

011022 Experimental Validation of Quasisteady Assumption in Modeling of Unsteady Film-Cooling
Stefan Bernsdorf, Martin G. Rose, and Reza S. Abhari

011023 Criteria for Spike Initiated Rotating Stall
Huu Duc Vo, Choon S. Tan, and Edward M. Greitzer

011024 Rain Ingestion in Axial Flow Compressors at Part Speed
Ivor Day, John Williams, and Christopher Freeman

DISCUSSIONS

015501 Discussion: "Criteria for Spike Initiated Rotating Stall" (Vo, H. D., Tan, C. S., Greitzer, E. M., 2008, ASME J. Turbomach., 130, p. 011023)
A. Deppe, H. Saathoff, and U. Stark

The ASME Journal of Turbomachinery is abstracted and indexed in the following:

Aluminum Industry Abstracts, Aquatic Science and Fisheries Abstracts, Ceramics Abstracts, Chemical Abstracts, Civil Engineering Abstracts, Compendex (The electronic equivalent of Engineering Index), Corrosion Abstracts, Current Contents, Ei EncompassLit, Electronics & Communications Abstracts, Energy Information Abstracts, Engineered Materials Abstracts, Engineering Index, Environmental Science and Pollution Management, Excerpta Medica, Fluidex, Fuel and Energy Abstracts, INSPEC, Index to Scientific Reviews, Materials Science Citation Index, Mechanical & Transportation Engineering Abstracts, Mechanical Engineering Abstracts, METADEX (The electronic equivalent of Metals Abstracts and Alloys Index), Metals Abstracts, Oceanic Abstracts, Pollution Abstracts, Referativnyi Zhurnal, Shock & Vibration Digest, Steels Alert

Downloaded 30 May 2010 to 128.113.26.88. Redistribution subject to ASME license or copyright; see http://www.asme.org/terms/Terms_Use.cfm

P. Palafox
e-mail: pepe.palafox@eng.ox.ac.uk

M. L. G. Oldfield
e-mail: martin.oldfield@eng.ox.ac.uk

Department of Engineering Science,
University of Oxford,
Oxford, OX1 3PJ, United Kingdom

J. E. LaGraff
Department of Mechanical, Aerospace Engineering,
Syracuse University,
Syracuse, NY 13244
e-mail: jlagraff@mame.syr.edu

T. V. Jones
Department of Engineering Science,
University of Oxford,
Oxford, OX1 3PJ, United Kingdom
e-mail: terry.jones@eng.ox.ac.uk

PIV Maps of Tip Leakage and Secondary Flow Fields on a Low-Speed Turbine Blade Cascade With Moving End Wall

New, detailed flow field measurements are presented for a very large low-speed cascade representative of a high-pressure turbine rotor blade with turning of 110 deg *and blade chord of* 1.0 m. *Data were obtained for tip leakage and passage secondary flow at a Reynolds number of* 4.0×10^5, *based on exit velocity and blade axial chord. Tip clearance levels ranged from 0% to 1.68% of blade span (0% to 3% of blade chord). Particle image velocimetry was used to obtain flow field maps of several planes parallel to the tip surface within the tip gap, and adjacent passage flow. Vector maps were also obtained for planes normal to the tip surface in the direction of the tip leakage flow. Secondary flow was measured at planes normal to the blade exit angle at locations upstream and downstream of the trailing edge. The interaction between the tip leakage vortex and passage vortex is clearly defined, revealing the dominant effect of the tip leakage flow on the tip end-wall secondary flow. The relative motion between the casing and the blade tip was simulated using a motor-driven moving belt system. A reduction in the magnitude of the undertip flow near the end wall due to the moving wall is observed and the effect on the tip leakage vortex examined.* [DOI: 10.1115/1.2437218]

Introduction

In unshrouded axial flow turbines, there is necessarily a clearance between the rotating blade tips and the surrounding stationary casing, which is the cause of significant efficiency and heat transfer penalties. This gap allows passage fluid to flow from the pressure to the suction side of the blades, driven by the pressure difference across the blade. This tip leakage flow is accelerated through the gap, reducing the work done on the blade, generating losses in the gap and eventually exiting on the suction side where it mixes with oncoming passage flow as it rolls up into the tip leakage vortex. An estimated 1–2% loss in turbine efficiency has been associated with a 1%Span of gap [1]. Highly loaded turbine rotors are especially affected by this leakage flow, where in addition to efficiency losses, the high-temperature exhaust gases from the combustor and elevated heat transfer rates in the vicinity of the tip lead to the reduction of the blade's life. The casing has also been found to become more affected by these heat transfer loads over the blade tip. As pressure ratios and turbine inlet temperatures are raised in the quest for reduced fuel consumption and increased specific power, the understanding of tip flows in unshrouded turbines becomes ever more crucial. Over the past couple of decades, several studies have contributed to the general understanding of the phenomena taking place in turbines. Linear cascades have been used extensively and have been successful in providing a better understanding of the physics involved [2]. While matching the blade loading, Reynolds number, and other key parameters, linear cascades have simplified the problem and allowed for larger-scale cascades to provide greater detailed measurements in the many regions of the turbine. The relative motion between the blades casing end wall is probably the most significant effect not simulated in most cascade experiments.

Early studies by Moore and Tilton [3] showed the acceleration of the flow into the tip gap and the formation of the vena contracta on the tip surface next to the pressure side. The flow subsequently experienced significant diffusion and mixing prior to exiting the gap on the suction side. In contrast to Moore and Tilton's model, where the tip leakage flow mixed fully prior to exiting the gap, Heyes and Hodson [4] put forward a model comprised of an isentropic jet and a separation bubble wake, which took into account the effect of mixing in their thinner-blade cascades. Increasing the amount of total mixing inside the tip gap increased the discharge coefficient. Also, the effect of boundary layer growth over the blade tip revealed a possible reduction effect of 5% on the discharge coefficient, thereby reducing the overall leakage loss. With a microtapping technique, Bindon [5] studied, in more detail, the pressure distribution in the tip region as affected by the tip-gap height. He noted a very low-pressure coefficient on the suction side of his blade, which was reduced as the clearance gap was increased. He found the lowest pressure, 2.8 times smaller than cascade outlet pressure, to occur on the pressure corner. He also found the lowest pressures to occur at 60%Chord and the pressures on the tip and end-wall surfaces to increase with increasing tip-gap height. In another study, Bindon [6] quantified, for the first time, the contributions by mixing (48%), internal gap shear (39%), and end-wall/secondary flow (13%) to the overall tip clearance loss for 2.5%C tip clearance gap. Yaras and Sjolander [7], using more slender blades with lower turning angle and higher gap clearance, found that a much lower loss was generated in the gap.

Yaras and Sjolander [8] and Yaras et al. [9] also studied the effects of the end-wall relative motion on tip-gap flow, downstream flow field and blade loading by employing a motor-driven belt with thin-blade, low turning angle cascade. For a gap clearance of 3.8%C and a $\mathrm{Re}=1.4\times10^5$, they found that although the shearing affect of the moving wall on the gap flow was quite small, it led to a decrease in the pressure difference across the gap and, thus, a reduction in the acceleration of the tip flow. The moving wall strengthened and drew the passage vortex toward the gap flow outlet (suction side), creating a throttling affect on the gap flow, which resulted in a 50% reduction of the mass flow rate

Contributed by the International Gas Turbine Institute of ASME for publication in the JOURNAL OF TURBOMACHINERY. Manuscript received March 30, 2006; final manuscript received April 4, 2006; published online December 14, 2007. Review conducted by David Wisler. Paper presented at the ASME Turbo Expo 2005: Land, Sea and Air, (GT 2005), June 6–9, 2005, Reno, NV. Paper No. GT2005-68189.

 Copyright © 2008 by ASME

Downloaded 30 May 2010 to 128.113.26.88. Redistribution subject to ASME license or copyright; see http://www.asme.org/terms/Terms_Use.cfm

through the gap. Measurements of the flow field, taken downstream of the trailing edge (TE), revealed enhancement of the passage vortex and weakening of the leakage vortex with increasing belt speed. A reduction in blade loading due to the moving wall effect was only noticeable at locations very near the tip.

Yamamoto [10] looked at the interaction of the leakage flow with the passage vortex at a plane 24% C_{ax} downstream. He observed an insignificant interaction between the two vortices for a low tip clearance of $t/h=1.3\%$, but noted stronger interaction with increasing clearance. The stronger leakage vortex pushed the passage vortex, which became weaker, toward the pressure side of the passage. In a later paper [11], detailed velocity vectors and streaklines on a blade-to-blade plane between the end wall and tip surface as well as total pressure contours on a downstream plane were presented. These effectively showed the relationship between the tip leakage and end-wall flow and cascade loss generation.

In an early heat transfer study, Mayle and Metzger [12] looked at the effect of the relative blade-casing motion on the tip heat transfer using a simple rectangular profiled stationary model with concave surface adjacent to a motor-driven rotating disk. The effect on the heat transfer due to the relative motion was found to be negligible over a range of parameters tested. In a later study, Chyu et al. [13] also found that the relative motion had a negligible effect for their simple grooved tip model. In a more recent study by Srinivasan and Goldstein [14], the heat transfer on the tip was studied in a linear cascade incorporating a moving wall apparatus with the use of the naphthalene sublimation technique. Very little effect of the moving wall was found in the region near the trailing edge. However, a 9% reduction on the heat transfer was found to occur at midchord locations for a gap of $t/C=0.6\%$. It was speculated that the tip leakage vortex moving closer to the suction surface was the cause of this reduction. Interestingly, an increase in their measured Sherwood number was found in some regions in the upstream half of the blade. A slight increase was also found in the region near the TE for a gap of $t/C=0.86\%$ with the introduction of the moving wall. No effect due to relative motion was seen at larger clearance gaps. Other tip heat transfer studies, where no relative motion has been simulated, includes that of Bunker et al. [15] and Azad et al. [16], where detailed heat transfer coefficient (HTC) maps on the tip surface have been provided for a range of tip clearances and two turbulence intensities. Increase in the overall heat transfer was found in both cases for increasing gap clearances and increasing turbulence intensities.

Some recent studies have also focused on studying the effect of the tip flow on the heat transfer of the adjoining casing wall. Chana and Jones [17] used thin-film gages to measure the heat transfer on the casing wall and flow adiabatic wall temperature in the gap of their QinetiQ Isentropic Light Piston Facility (ILPF) with correct nondimensional engine conditions. The casing was shown to suffer the highest heat transfer as the rotor blades pass under it; the high heat transfer rates were attributed to the tip leakage flow. In a two-part paper presented by Thorpe et al. [18,19], detailed heat transfer and pressure measurements were provided for the overtip casing wall of their isentropic light piston tunnel, which operates at engine representative conditions. These confirmed the general results of Chana and Jones [17] that the casing heat transfer peaks as the tip passes the casing. Given the previous research studies, there is still a need for further aerodynamic studies, with higher spatial resolution, in order to better understand the behavior of flow in the tip region and how this flow is related to heat transfer. These studies are especially important in cascades that are representative of high-pressure turbines with relative motion simulation, where data are very scarce or nonexistent.

In the present paper, the recent work being conducted at Oxford University with the use of a large-scale linear cascade with a moving belt is introduced. Details concerning the use of particle image velocimetry (PIV) to provide detailed measurements in the restricted region of the tip gap are given. Initial detailed results are presented for the gap region and adjacent passage flow for the largest gap clearance studied.

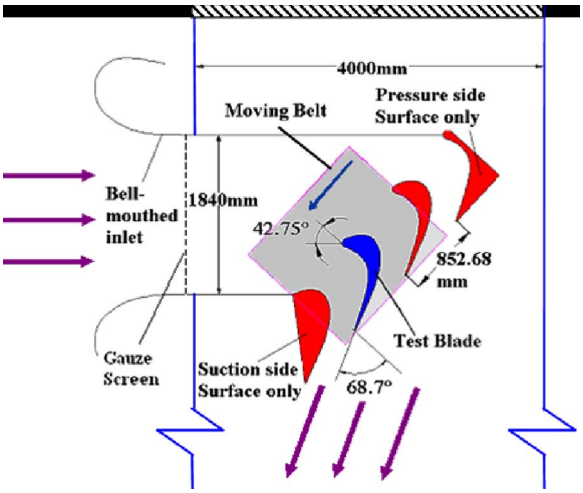

Fig. 1 Cascade Geometry. The cascade was mounted in an existing large wind tunnel.

Experimental Apparatus and Procedures

Test Cascade and Test Section. In order to study the tip leakage flow in great detail, the geometry of the cascade design used in this investigation was scaled up to a blade chord length of 1 m. In doing so, it allows for measurements to be conducted in clearance gaps of up to 30 mm in height, which is equivalent to a 1.68%Span or 3%Chord. Figure 1 and Table 1 summarize the cascade geometry and test conditions used in the present study. As illustrated in Fig. 1, the cascade arrangement was set up inside an existing 2 m×4 m suction-type wind tunnel. In order to achieve the design turning angle, part of the wind tunnel's left wall was removed and a new bell-mouthed inlet, which provides the inlet flow to the cascade, was set up there. The previously existing inlet to the wind tunnel was blocked off.

The blade profile and cascade geometry used was an ERCOFTAC test case comprehensively tested at Durham University by Gregory-Smith and Cleak [20] for research mainly in secondary flow without tip gap. The profile of the blade is that of a high-pressure turbine with a high turning angle of 111.45 deg. It should be noted that actual blade span was chosen to be nearly half of the design span after smoke visualization tests revealed no interaction between the hub end-wall and the tip end-wall secondary flows at a 1 m span. Two fully profiled and two semi-profiled blade models compose the three-passage linear cascade. Passage flow measurements were conducted in the center passage, and tip-leakage flow measurements were conducted on the blade labeled test blade. The blades were made from flexible plywood, which were wrapped around profiled spars. The test blade differs

Table 1 Blade properties and flow conditions

Blade chord, C (mm)	1000
Blade axial Chord, C_{ax} (mm)	808
Blade thickness, t_{max} (mm)	243
Blade pitch, s (mm)	853
Design span, h (mm)	1785.6
Actual span (mm)	1000
Inlet flow angle (deg)	42.75
Blade exit angle (deg)	68.7
Reynolds No. (based on V_{ex} and C_{ax})	4.0×10^5

Downloaded 30 May 2010 to 128.113.26.88. Redistribution subject to ASME license or copyright; see http://www.asme.org/terms/Terms_Use.cfm

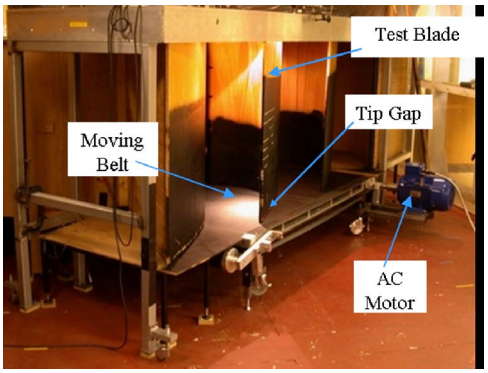

Fig. 2 Cascade test section and moving belt

from the other models in that it is mostly hollow throughout, which is an important part of the design, as will be seen in later sections, when measuring the tip flow without any interference.

The arrangement of the cascade inside the 2 m×4 m wind tunnel, used to generate the appropriate conditions, is illustrated in Fig. 2. As shown, the blade models were secured to a frame, which was fixed to the tunnel floor, and under the suspended blades sits a motor-driven belt system. The moving belt system and wooden boards that make up the end wall were set up on individual frames with height adjusting feet, which allow for the changing of the tip-gap clearance.

The moving belt, designed to simulate the relative motion between the rotor blades and casing wall, completely covers the area under the test blade and center passage where measurements are taken. The belt extends over half an axial chord length upstream of the leading edge of the blade in order to produce a representative skewed inlet boundary layer in tests simulating the relative motion. The belt was made of a top layer of polyurethane (facing the flow) and a lower layer of polyester with a total thickness of 2 mm. The belt sits on a perforated plate, which is the cover of a suction box, and is tensioned by a pair of aluminum rollers at the ends. A 7.5 kW AC motor with a variable speed controller drives one of the rollers and thus drives the belt across the cascade at a constant velocity. Vertical displacements of the belt have been measured to be less than ±0.05 mm, due to proper tensioning and suction applied by the vacuum box. The belt speed is calculated from velocity triangles and defined as 1.34 times the inlet velocity.

The blade loading was measured at a distance of 10%C from the tip end wall with no gap and was compared to Durham's results (Fig. 3). The profiles overlap almost perfectly, ensuring the flow conditions around the test blade are correct. Static pressures measured at the blade leading edge also agreed with the expected stagnation pressures.

Instrumentation and Data Acquisition. PIV was used to measure the flow inside and around the gap region, as well as secondary flow, with and without tip gap. The components of this PIV system were water-based glycerin particles (introduced into the upstream flow by atomizers); the Nd:YAG laser, which was used to illuminate the flow; the CCD camera, which captured successive pairs of particle maps at a rate of 15 Hz; the PIV 1100 processor, used to correlate vector maps from the pairs of particle images; and the FLOWMAP software (on the PC), which allows user interface and postprocessing of data. For each test, a total of 150 pairs of instantaneous vector maps were generated and these 10 s worth of data were averaged to give the mean flow results presented in this paper. Except for the four maps at the end, the instantaneous, unsteady flow results will be presented in a future paper.

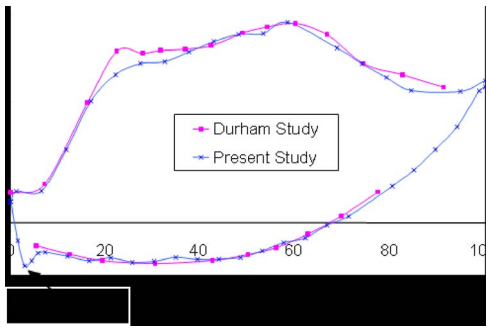

Fig. 3 Blade pressure profile

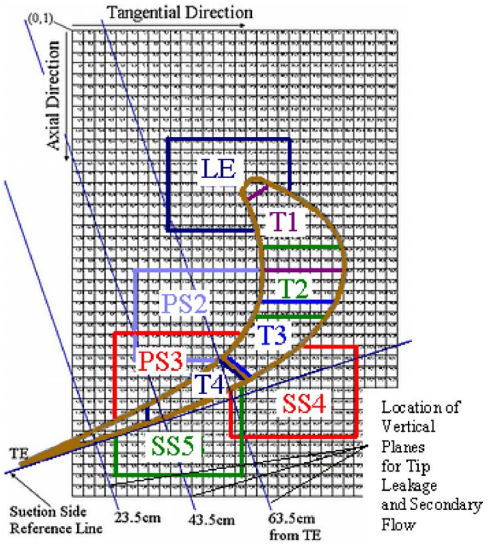

Fig. 4 Grid for mapping tip leakage and secondary flow; note the blade material is shaded in brown (gray)

PIV [21] measures fluid flow fields by tracking the movement of particles seeded into the fluid. The flow is seeded with particles, and pairs of laser pulses separated in time illuminate a thin plane in the flow. A camera, placed at right angles to the sheet, captures frozen images of particles at two closely spaced instants in time. Each pair of successive images is then cross-correlated to obtain the displacement of the particles. With the time interval between successive pulses known, velocities for each particle are computed, thus, generating vector maps. It is important to know that each vector generated pertains to an area of pixels, known as an interrogation area, from which the average displacement of the particles tracked in that area is measured. Typical interrogation areas are 16×16 pixels, 32×32 pixels, 64×64 pixels, and 128×128 pixels.

Given the scale of the geometry, a large gird, which extends 900 mm in the tangential direction and 1290 mm in the axial direction, was used to map out the flow measured in specific planes (Fig. 4). The grid allows for the alignment and placement of the PIV laser sheet and CCD camera in defined locations with reference to the test blade, as well as providing a scale factor needed for the calculation of velocities of particles.

There were essentially two types of measurement planes in these experiments, horizontal planes, which were parallel to the tip and end-wall surface, and vertical planes, which were normal to the tip and end-wall surface. The main objective of this study is to provide detailed three-dimensional flow field maps of the flow within and in the vicinity of the tip gap. This is accomplished by setting up the PIV laser sheet parallel to the tip surface (Fig. 5(a)) and taking measurements at several distances from the end-wall surface. As shown in Fig. 5(a), the CCD camera can be positioned either inside the blade or on top of the blade, at right angle to the

Downloaded 30 May 2010 to 128.113.26.88. Redistribution subject to ASME license or copyright; see http://www.asme.org/terms/Terms_Use.cfm

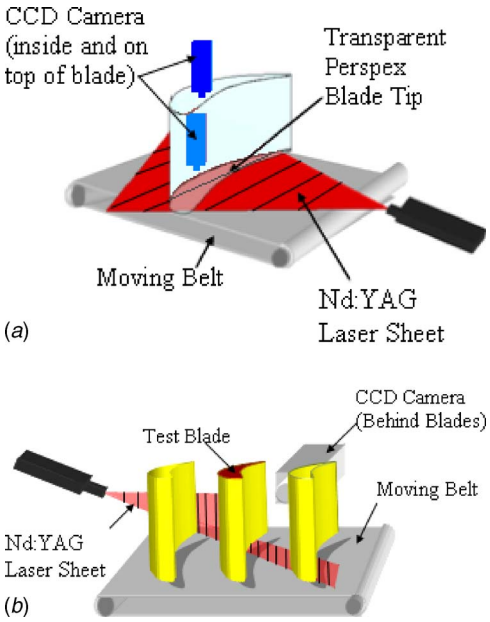

Fig. 5 PIV instrumentation setup

laser sheet. For the current measurements, the camera has been positioned on top of the blade, where it sits on a thick Perspex sheet, which supports the test blade and acts as the hub end wall. Measurements were taken at a range of distances from 3 mm to 27 mm from the end wall with increments of 3 mm, i.e., 3 mm, 6 mm, 9 mm, etc. Thus, the planes located at 3 mm are the closest to the end-wall surface and planes at 27 mm are the closest to the tip surface. As mentioned previously, due to the scale of the cascade, the parallel planes are broken up into smaller planes, which include a leading-edge (LE) plane, 5 pressure-side (PS) planes, 5 suction-side (SS) planes, and 4 tip planes (Fig. 4). Eventually, all the individual flow fields were amalgamated into single planes at a known distance from the end wall. Note that in plane T4 (plane in the aft part of the blade) in Fig. 4 that the flow field near the trailing edge of the blade cannot be measured as the blade structure obscures the view. Also, since the area near the trailing edge is narrower, the smaller area of flow field seen by the camera produces weaker correlations, which are not included in the results presented here.

Measurements in the vertical planes, as shown in Fig. 5(*b*), were taken by having the laser sheet aimed at the suction side of the blade, illuminating a slice of the passage flow and a slice of the tip leakage flow, and the CCD camera looking at the flow illuminated by the laser sheet at a location downstream of the cascade. As shown on the grid map in Fig. 4, these planes are at three locations normal to the suction reference line, which is a line extending from the straight part of the suction surface near the TE, and specified distances from the TE. These planes are the same for both tip leakage flow measurements and secondary flow measurement for the purpose of seeing the development of the flow as it passes through the tip gap and emerges into the passage flow. The location of these planes is essentially in the aft part of the blade, mainly because of the physical obstruction of the adjacent blade on the laser sheet in the case of planes further upstream. However, it is known that the flow in the aft part of the blade that is of most interest.

Experimental Results

Smoke Visualization. Smoke visualization was carried out in order to get a general idea of the behavior of the flow in this arrangement. Initial smoke-visualization experiments were done with zero gap clearance and no moving wall, where the tip end-wall surface was essentially made up of wooden boards. In these experiments, the formation of the horseshoe vortex at the blade leading edge and the passage vortex, as well as the separation of the flow on the blade suction surface were clearly seen in Table 2.

Table 2 Boundary layer properties 1 chord length upstream of LE

99% Boundary layer thickness, δ(mm)	40.0
Displacement thickness, δ^*(mm)	6.53
Momentum thickness, θ(mm)	4.14
Shape factor, H	1.57
Turbulence intensity, Tu %	1.2

Smoke visualization tests were then conducted with a tip gap of 0.58%Span (or 1%Chord). These tests revealed where and to what extent the passage flow near the gap on the pressure side was sucked into the gap. This gave a good indication of favorable locations of where to seed particles for the PIV experiments, which followed. More interestingly, clear visualizations of the tip leakage and passage vortex interaction were obtained (Fig. 6). The superior strength of the tip leakage vortex (TLV) is clearly noticeable.

When compared to the images obtained with no tip gap, it was clearly seen that tip leakage vortex reduces the size of the passage vortex (PV) and shifts it closer to the suction side. These tests also revealed no interaction between the hub end-wall and tip end-wall secondary flows, as seen from the figure that the passage vortex on the tip end-wall side of the blade does not even reach the height of 40% actual span.

Secondary Flow Measurements. Secondary flow measurements were taken at three locations and for three scenarios: (i) no tip gap, (ii) with tip gap but no relative end-wall motion, and (iii) with tip gap and with relative end-wall motion. Results are displayed in the form of vector maps overlapped with a color map of scalar magnitudes, which are divided by the cascade exit velocity, in order to see the strength of the flow. The reader should be aware that since the camera sees the flow on the plane normal to the suction-side reference line from a position downstream of the

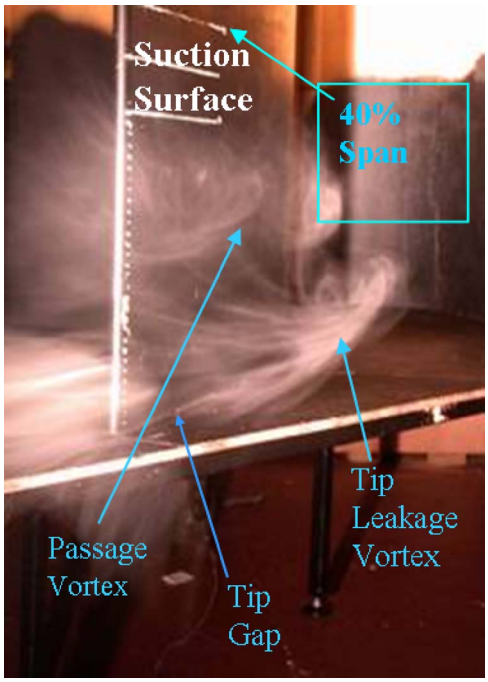

Fig. 6 Smoke visualization of tip leakage vortex and passage vortex interaction for t/h=0.58%, no moving belt

Downloaded 30 May 2010 to 128.113.26.88. Redistribution subject to ASME license or copyright; see http://www.asme.org/terms/Terms_Use.cfm

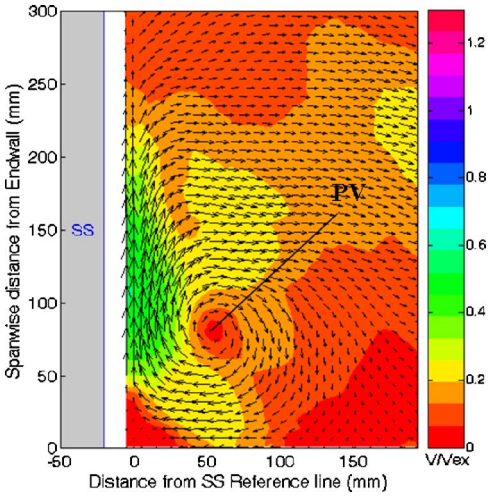

Fig. 7 Secondary flow at 63.5 cm from TE for t/h=0%

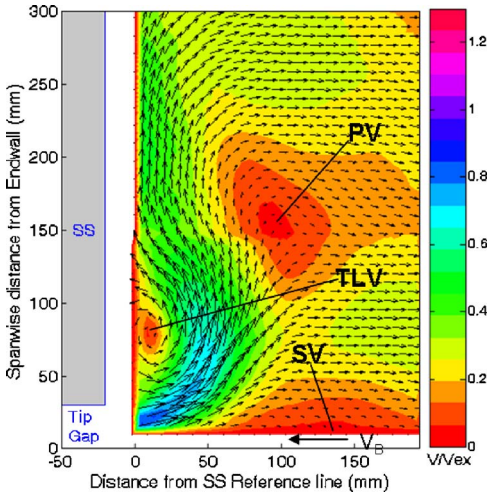

Fig. 9 Secondary flow at 63.5 cm upstream from TE for t/h =1.68%, moving belt on

cascade, flow near the suction side is not seen by the camera because the curvature of the blade produces an obstruction, especially at planes further upstream (refer to Fig. 4). These blank regions are presented as white areas with no vectors. Only the results obtained at the plane 63.5 cm from the TE are presented in this paper.

Secondary flow measurements were conducted with no tip gap in order to see how the flow changes with the introduction of a gap clearance and moving end-wall surface. The measured passage vortex is displayed in Fig. 7. As expected, the pressure gradients in the passage create a cross-flow going from the pressure side of one blade to the suction side of the adjacent blade. As the cross-flow encounters the suction side surface, it rolls up into the passage vortex.

Figure 8 displays the secondary flow for a clearance gap of 1.68%Span with no relative end-wall motion. The reader is advised that the flow up to 10 mm from the end wall is not presented because it cannot be measured due to laser reflections on the end-wall surface. Nevertheless, the jet of high velocity emerging from the tip gap is clearly seen in the lower part of the TLV. The high-velocity jet extends as far as 125 mm from the suction-side reference line before it is turned in the vertical direction and magnitude of the velocity decreases slightly to become the outer region of constant velocity, which goes around the core of the vortex. In comparison to the case of no tip gap, the effect of the TLV on the PV is clear. The TLV shifts the core of the PV upward by about twice the original distance from the end wall. In contrast to the case of no gap, where the PV has a definite circular, vortical shape, the presence of the TLV distorts its shape and weakens it. In the gap case, it is clear that the TLV is significantly stronger than the PV, confirming the importance of the TLV on the passage flow.

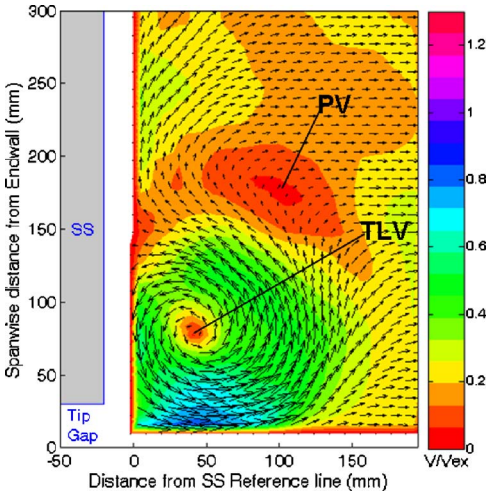

Fig. 8 Secondary flow at 63.5 cm upstream from TE for t/h =1.68%, moving belt off

With relative end-wall motion, as was observed by Yaras and Sjolander [9], the TLV moves toward the suction sides of the passage (Fig. 9), partly blocking the tip gap exit. Interestingly, the jet velocity seems to have the same magnitude as in the case of no relative end-wall motion. However, the belt boundary layer forces itself under the leakage jet and diverts the flow in the vertical direction. Rather than extending further into the passage in the horizontal direction, the high-magnitude flow extends further in the vertical direction. Since the TLV has been dragged closer toward the suction surface of the blade, the leakage jet that had become into the outer region of the vortex now continues vertically upward and becomes part of the outer region of the PV. Similar to the results by Rao and Cengiz [22] in a rotating rig, the PV was located above and slightly to the right of the TLV. Also, the tip leakage jet and opposing flow dragged by the moving belt generates a small vortex (SV) to the right of the TLV. This vortex has been observed in a rotating rig experiment by McCarter et al. [23] and was labeled the scraping vortex. In their study, they also measured the highest loses in the TLV.

Although not presented in this paper, measurements in the two planes further downstream, 43.5 cm and 23.5 cm upstream from the TE, have been carried out. As the flow progresses further downstream, for both cases of endwall motion on and off, the TLV moves further away from the suction surface. For the case of no relative motion, the TLV progressively becomes more elliptical from the near circular shape seen at plane 63.5 cm.

Tip Flow Normal to Tip Surface. The tip leakage flow was measured in planes vertical to the tip surface at three locations in the aft part of blade, in-line with the planes used for the secondary flow measurements. The behavior of the flow in the gap and its development into the tip leakage vortex may thus be seen. Figure 10 presents the measurements, with and without relative motion, at plane 63.5 cm upstream from the TE for a gap of 1.68%Span. Measurements have also been taken at planes 43.5 cm and 23.5 cm from the TE, but due to space limitations are not presented in this paper. As in the case of the secondary flow measurements, small areas of the flow near the end wall and tip sur-

Downloaded 30 May 2010 to 128.113.26.88. Redistribution subject to ASME license or copyright; see http://www.asme.org/terms/Terms_Use.cfm

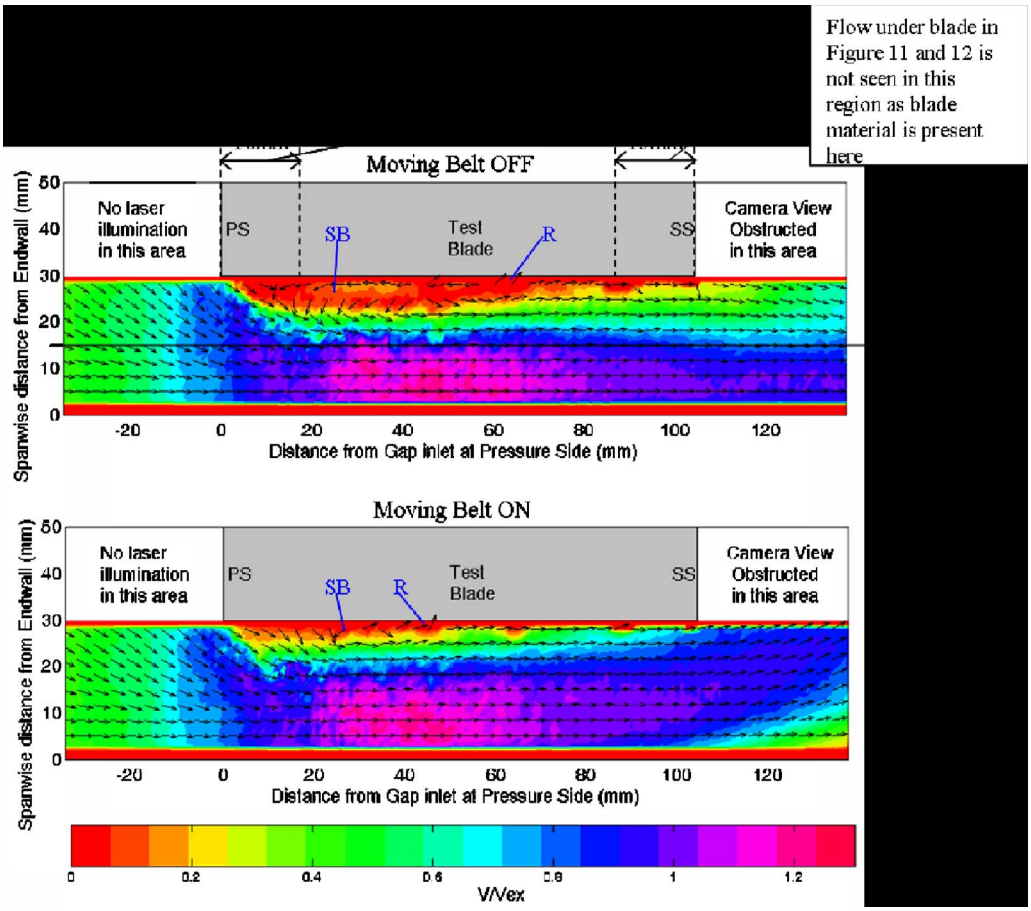

Fig. 10 Tip leakage flow at 63.5 cm from TE for t/h=1.68%

face are not visible due laser reflections, but these are <3 mm from the end wall and <1 mm from the tip surface. Also, flow measurements were not possible in the area above the tip gap adjacent to the pressure and suction sides of the blade, due to illumination or viewing difficulties. Unlike the secondary flow measurements, the velocity vectors are all of the same size and are overlapped with the scalar map of the velocity magnitudes. It was decided to use same-size vectors in order to be able see the smaller velocities in the separation bubble.

From the scalar maps presented in Fig. 10, for the plane located at 63.5 cm upstream from the TE, the acceleration of the leakage flow is clearly displayed. In both cases, the flow accelerates to a maximum velocity that is 20% stronger than the cascade exit velocity. For the no-relative-end-wall-motion case, the separation bubble is clearly defined and the flow appears to reattach at ~65 mm from the gap inlet. The presence of the end-wall motion appears to reduce the height of the separation bubble by as much as half, and reattachment seems to occur much closer to the gap inlet. Interestingly, the gap flow is not weakened by end-wall surface moving in the opposite direction at this location in the blade. It can be seen that the effect of the moving end wall is to force its boundary layer under the leakage flow at the gap exit, pushing the high-speed leakage jet vertically. The development of this flow was seen earlier in the secondary flow measurements. The end-wall boundary layer does not, however, have much effect on the flow in the gap, at this location in the blade.

It should not be assumed that the results presented in Fig. 10 for that particular location in the blade are representative of the flow's behavior at other locations throughout the blade. At locations further downstream, the separation bubble was measured to be more similar in size for both cases of end-wall motion on and off. In the planes further downstream, the flow was actually seen to be slightly strengthened by the opposing moving end wall. In locations very far downstream, where the blade thickness is smallest, the flow was seen not to reattach to the tip surface. Measurements were only carried out in locations in the aft part of the blade near the TE, but it is expected that the end-wall motion has a more significant effect on the tip leakage flow at some locations in the upstream part of the blade where smaller velocities will be present.

Tip Flow Parallel to Tip Surface. Although the tip leakage flow measurements in the vertical planes have provided good insight into the behavior of the flow in the gap, the flow's behavior varies along the blade and it is important to have a complete picture of the entire flow in the gap. Although several studies have provided a great wealth of information concerning the flow in the tip gap, a complete three-dimensional picture of the flow in the gap has never been presented. Although the ideal would be to achieve a volumetric flow field with three-component vectors, the PIV technique used in this study only generates planar flow fields. However, by having a physically large gap and measuring planar flow fields at several locations within the tip gap, it has been possible to provide a more complete and detailed picture of the flow's behavior in the gap.

As stated previously, measurements were taken at several planes parallel to the tip surface within the 30 mm gap. These planar flow fields within the tip gap are measured at regions T1, T2, T3, and T4 on the grid map (as shown in Fig. 4). A portion of the flow field between T3 and T4 is missing due to camera view obstruction by pieces of the wooden spars of the blade located there. As was stated in the previous section, measurements were

Downloaded 30 May 2010 to 128.113.26.88. Redistribution subject to ASME license or copyright; see http://www.asme.org/terms/Terms_Use.cfm

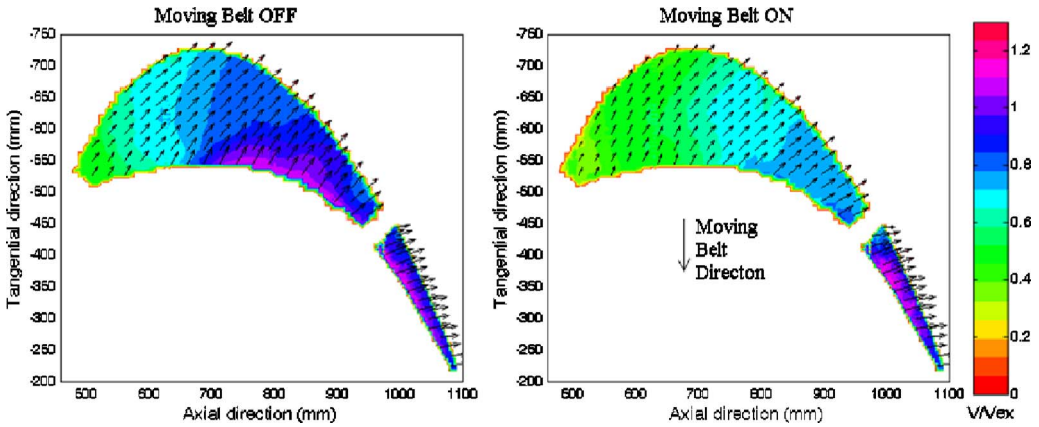

Fig. 11 Flow field in plane 15 mm from the end wall for 30 mm gap (t/h=1.68%); note that the field of view does not extend to the outer blade surface (see Fig. 4)

taken at planes in increments of 3 mm for the range of 3–27 mm. However, for the purpose of clarity, the planar flow fields presented here are in increments of 6 mm. As well, it should be noted that the original vector maps were processed to omit every certain pair of vectors in order to present vector maps that are not too crowded and can be clearly displayed. From Fig. 4, it can be seen that the nose of the blade, which is not be confused with the leading edge, is located at 435 mm in the axial direction. Measurements presented here are located between 485 mm and 1100 mm. Thus, the measurements are from $6.1\%C_{ax}$ to $81.1\%C_{ax}$. Thus, the flow located in the last $20\%C_{ax}$ of the blade is not captured. Likewise, the flow in the $6\%C_{ax}$ from the leading edge is not captured. As stated previously, this is due to camera view obstructions and insufficient flow field area in narrow flow field regions under the blade, which produced weak correlations.

Figure 11 presents the flow field at the center of the gap (15 mm from the end wall and tip surface). For relative end-wall motion ON case, an arrow has been drawn denoting the direction of the moving belt relative the blade, but it is not to scale. Looking first at the case for no relative end-wall motion, the flow is seen to come into the gap at the LE at an angle close to that of the inlet flow angle and a progressive increase in velocity is seen in an axial direction up to $\sim 30\%C_{ax}$ of the blade. After $30\%C_{ax}$, regions of high velocity begin to appear very close to the pressure side of the blade and the flow takes a direction near perpendicular to the blade camber line. The high-velocity regions near the pressure side of the blade vary along the blade depending on the blade loading. These high-velocity regions near the pressure side remain present until about $\sim 75\%C_{ax}$ in the blade.

In relative motion ON case, the flow enters the gap at the leading edge at a slightly steeper angle than that of the inlet flow angle. Similar to the case with no end-wall motion, a progressive increase in velocity is seen to occur in the axial direction. However, this increase occurs at a much slower rate than in the non-moving wall case and seems to carry through until much further downstream in the blade. As shown in the plot, the flow still crosses over from the pressure to the suction side of the blade in a near-perpendicular direction to the camber line, but the flow generally remains of the same magnitude as it crosses the gap. At $\sim 60\%C_{ax}$, a region of higher velocity appears at the gap inlet on the pressure side. In fact, the flow in the aft part of the blade seems to be unaffected by the moving end wall and behaves very similar as in the case of no endwall motion. With the exception of the flow in the aft part of the blade near the trailing edge, a reduction in the magnitude of the velocities in the gap is observed.

Stacked planar flow fields for a gap clearance of 1.68%Span are presented in Fig. 12 for both cases, with and with out endwall motion. It can be seen in both cases that the highest velocities are, in fact, found in the aft part of the blade, around 1000 mm in the axial direction ($65\%C_{ax}$). The flow separation at the gap inlet on

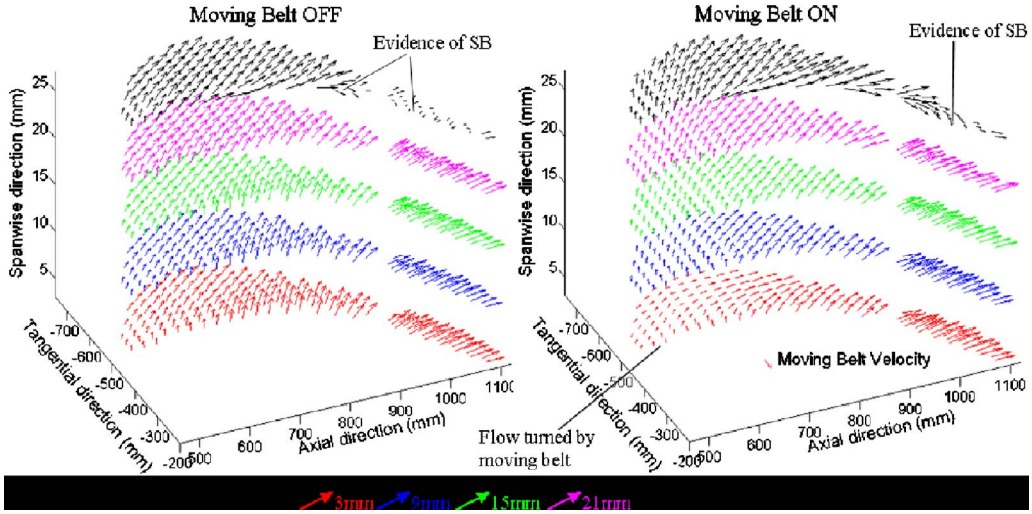

Fig. 12 Plots of two-dimensional flow fields in three-dimensional graphs for t/h=1.68%. At Fig. 11 you can see the planes that are 15 mm from the end wall with magnitudes.

Downloaded 30 May 2010 to 128.113.26.88. Redistribution subject to ASME license or copyright; see http://www.asme.org/terms/Terms_Use.cfm

the pressure side is clearly visible in both cases, as the flow closer to the tip surface tends to turn toward the pressure side of the blade. This is clearly visible at plane 27 mm, where some of the flow is completely directed toward the pressure side, which signifies the presence of the re-circulating flow. Measurements taken along the mean camber line by Yaras and Sjolander [8] also revealed a spanswise variation in the magnitude and direction of the velocities close to the tip. In their slender blade, the presence of the separation bubble was clearly evident after a quarter of the chord length from the LE. In Fig. 11, the presence of separation bubble is seen to commence at $\sim 18.5\% C_{ax}$ from the LE for both cases of moving belt on and off.

In the relative end wall motion OFF case, the flow at plane 27 mm seems to be of very low velocity in the aft part of the blade, which is probably due to the velocity plane being measured in the core area of recirculating flow in the separation bubble. In this area in the plane at 27 mm, the flow seems to split off into two parts, the flow near the pressure side, which is directed toward the PS, and the flow near the suction side, which leaves via the SS. The latter is that part of the flow that has gone over the separation bubble and is trying to reattach as it exits the gap.

With relative end-wall motion, the flow behaves differently at plane 27 mm from the end wall. The flow progressively changes direction, and far downstream closer to the TE the flow is seen to be completely directed toward the pressure side of the blade. The presence of the moving end wall seems to change the flow within the separation bubble. The measuring plane at 27 mm now lies in the top portion of the recirculating flow. Obviously, some of the flow further upstream is not part of the separation bubble as it turns to exit from the SS.

A general reduction in magnitude of the gap flow due to the end-wall motion is observed throughout most of the blade, except for the aft part near the trailing edge. Yaras and Sjolander [8] also reported a global reduction in velocity magnitude due to the relative end-wall motion. As expected, the reduction is most apparent at the planes closest to the moving end wall. For example in plane 3 mm, the vectors are clearly significantly smaller for most of the blade and the direction is more axial. The insignificant effect of the end-wall motion on the flow in the aft part of the blade seen in these flow fields is clearly displayed in the tip flow measurement, previously presented in planes normal to tip surface, where these were carried out at a location in the aft part of the blade.

Flow Unsteadiness. It is well known that the flow in turbines can be unsteady. The results that have been presented here are those averaged over a period of 10 s, captured at 15 frames per second. Figure 13 displays four instantaneous vector maps taken consecutively over a period of 0.20 s at 1/15 s time intervals.

The flow shown is that of the lower part of the secondary flow (Fig. 9) with a 30 mm gap and with the moving belt on. The flow is clearly unsteady, with the vortex core moving significantly. This unsteadiness is the subject of future study, and the examples presented here might warn those researchers who are tempted to treat the averaged flows shown in Figs. 7–12 as steady flows.

Conclusions

A very large-scale linear, three-passage cascade has been developed to produce representative flow conditions around a central blade. This scale has enabled uniquely detailed PIV measurements of overtip leakage flows and associated end-wall flows in the blade passage to be made. This detail was possible due to the large tip gaps (up to 30 mm) employed. The relative motion between the turbine casing and rotor blade has been simulated with a moving belt.

The separation bubble under the tip has been clearly characterized, revealing its significant effect on the leakage flow. The moving end wall had a clear influence on the shape and size of the separation bubble. For example, at the plane examined the bubble was reduced to approximately half of its height from the case

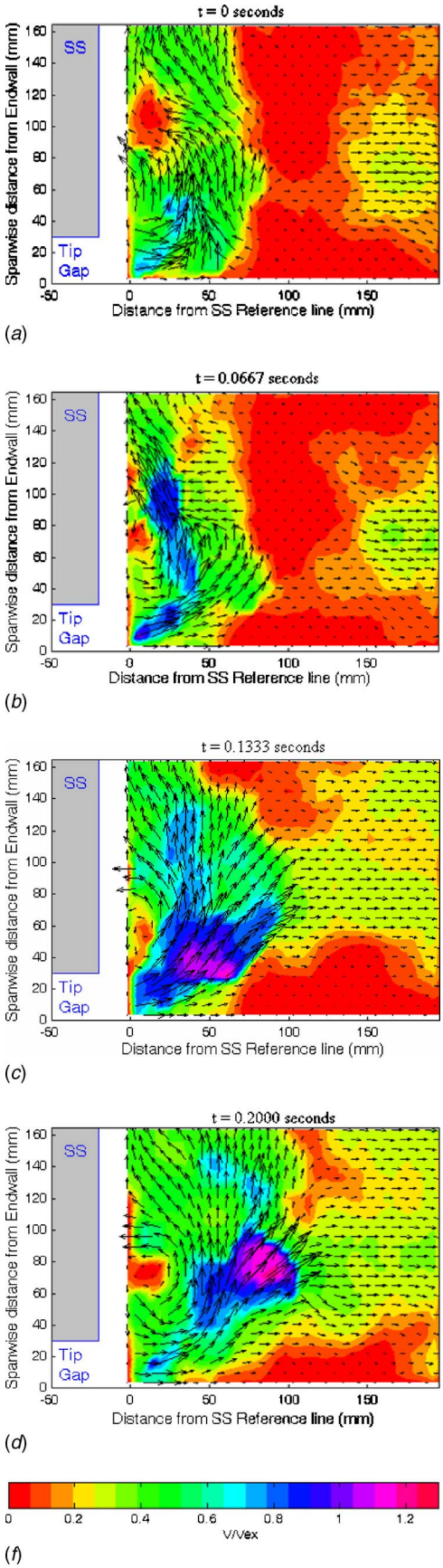

Fig. 13 Instantaneous vector maps at consecutive time intervals of lower part of secondary flow at 63.5 cm from TE for t/h=1.68%, moving belt on, averaged results over 10 s shown

Downloaded 30 May 2010 to 128.113.26.88. Redistribution subject to ASME license or copyright; see http://www.asme.org/terms/Terms_Use.cfm

without end-wall movement. This effect can be attributed to the shifting of the tip leakage vortex closer to the gap exit by the moving end wall, which pushes the exit jet upward and thus decreases the size of the separation bubble.

Dramatic influence of the tip flow on the passage vortex was observed in the secondary flow measurements. The passage vortex was weakened, distorted, and relocated by the presence of the tip leakage vortex.

The relative blade-casing movement had a significant effect on both the tip leakage vortex and the passage vortex. The moving wall distorted the shape of the tip leakage vortex and moved both of the vortices closer to the suction surface. The leakage jet and opposing moving belt generated a third vortex, labeled the scraping vortex in a previous study.

In the upstream portion of the blade, there is a reduction in the magnitude of flow velocity in the gap. Further downstream, near the trailing edge, the velocities are largely unaffected by the blade-casing relative motion.

Although the flow studied here is known to be three-dimensional, it has been investigated using a two-dimensional PIV technique. Great insight into the behavior of the flow in and around the tip region has been provided; however, these results are not complete because they lack a third velocity component. Thus, the results presented should be looked at as planar flow fields and not volumetric flow fields. Further PIV and heat transfer studies for different gap heights and tip geometries, together with the unsteadiness of the overtip flow field, are underway.

Acknowledgment

This work is supported by the Air Force Office of Scientific Research under Grant No. F49620-02-0027, with Thomas Beutner as the technical officer. This support is greatly appreciated. The authors also wish to extend their gratitude to Trevor Godfrey for his useful suggestions and contributions to the design, assembly, and manufacturing of the experimental setup.

Nomenclature

AC = alternating current
C = blade chord
C_{ax} = blade axial chord
CCD = Charge-coupled device
C_P = static pressure coefficient=$(P_\infty - P)/q_\infty$
H = shape factor
h = blade span,
HTC = heat transfer coefficient
k = thermal conductivity
LE = leading edge
L = tip gap length or thickness; characteristic length
$\dot{m}$ = mass flow rate
Nu = Nusselt number
P = static pressure
P_0 = total pressure
PIV = particle image velocimetry
PS = pressure side surface of blade
PV = passage vortex
q = dynamic pressure
R = reattachment location
Re = Reynolds number
SB = separation bubble
s = blade pitch
SS = suction side surface of blade
SV = scraping vortex
T = temperature
t = gap height
TE = trailing edge
TLV = tip leakage vortex
$t_{\max}$ = maximum thickness of the blade
Tu = turbulence intensity
TET = turbine inlet temperature, turbine entry temperature
V = velocity
V_{ex} = cascade exit velocity
V_B = belt velocity
W = work
δ = 99% boundary layer thickness
δ^* = displacement thickness
θ = momentum thickness

Subscripts

s = static conditions
0 = total conditions
1 = cascade inlet conditions
2 = cascade outlet conditions
4 = upstream conditions

References

[1] Booth, T. C., Dodge, P. R., and Hepworth, H. K., 1982, "Rotor-Tip Leakage: Part 1—Basic Methodology," ASME J. Eng. Power, **104**, pp. 154–161.
[2] Sieverding, C. H., 1993, "Modelling Turbomachinery Flows," *Advanced Methods for Cascade Testing*, AGARD-AG-328, The Advisory Group for Aerospace Research and Development of the North Atlantic Treaty Organization, Chap. 1, pp. 1–3.
[3] Moore, J., and Tilton, J. S., 1987, "Tip Leakage Flow in a Linear Turbine Cascade," ASME Paper No. 87-GT-222.
[4] Heyes, F. J. G., and Hodson, H. P., 1991, "The Effect of Blade Tip Geometry on the Tip Leakage Flow in Axial Turbine Cascades," ASME Paper No. 91-GT-135.
[5] Bindon, J. P., 1987, "Pressure Distributions in the Tip Clearance Region of an Unshrouded Axial Turbine as Affecting the Problem of Tip Burnout," ASME Paper No. 87-GT-230.
[6] Bindon, J. P., 1989, "The Measurement and Formation of Tip Clearance Loss," ASME J. Turbomach., **111**, pp. 257–263.
[7] Yaras, M. I., and Sjolander, S. A., 1992, "Prediction of Tip-Leakage Losses in Axial Turbines," ASME J. Turbomach., **114**, pp. 204–210.
[8] Yaras, M. I., and Sjolander, S. A., 1991, "Effects of Simulated Rotation on Tip Leakage in a Planar Cascade of Turbine Blades, Part I: Tip Gap Flow," ASME Paper No. 91-GT-127.
[9] Yaras, M. I., Sjolander, S. A., and Kind, R. J., 1991, "Effects of Simulated Rotation on Tip Leakage in a Planar Cascade of Turbine Blades, Part II: Downstream Flow Field and Blade Loading," ASME Paper No. 91-GT-128.
[10] Yamamoto, A., 1988, "Interaction Mechanisms Between Tip Leakage Flow and the Passage Vortex in a Linear Turbine Rotor Cascade," ASME J. Turbomach., **110**, pp. 329–338.
[11] Yamamoto, A., 1989, "Endwall Flow/Loss Mechanisms in a Linear Turbine Cascade With Blade Tip Clearance," ASME J. Turbomach., **111**, pp. 264–274.
[12] Mayle, R. E., and Metzger, D. E., 1982, "Heat Transfer at the Tip of an Unshrouded Turbine Blade," *Proc. of Seventh Int. Heat Transfer Conference*, Technische Universität, München, Munich, West Germany, Vol. 3, pp. 87–92.
[13] Chyu, M. K., Moon, Moon, H. K., and Metzger, D. E., 1989, "Heat Transfer in the Tip Region of Grooved Turbine Blades," ASME J. Turbomach., **111**. pp. 131–138.
[14] Srinivasan, V., and Goldstein, R. J., 2003, "Effect of Endwall Motion on Blade Tip Heat Transfer," ASME J. Turbomach., **125**, pp. 267–273.
[15] Bunker, R. S., Bailey, J. C., and Ameri, A. A., 2000, "Heat Transfer and Flow on the First-Stage Blade Tip of a Power Generation Gas Turbine: Part 1—Experimental Results," ASME J. Turbomach., **122**, pp. 263–271.
[16] Azad, G. S., Han, J. C., and Teng, S., 2000, "Heat Transfer and Pressure Distributions on a Gas Turbine Blade Tip," ASME Paper No. 2000-GT-194.
[17] Chana, K. S., and Jones, T. V., 2002, "An Investigation On Turbine Tip and Shroud Heat Transfer," ASME Paper No. GT-2002-30554.
[18] Thorpe, S. J., Yoshino, S., Ainsworth, R. W., and Harvey, N. W., 2004, "An Investigation of the Heat Transfer and Static Pressure on the Over-Tip Casing Wall of an Axial Turbine Operating at Engine Representative Flow Conditions (I) Time-Mean Results," Int. J. Heat Fluid Flow, **25**, pp. 933–944.
[19] Thorpe, S. J., Yoshino, S., Ainsworth, R. W., and Harvey, N. W., 2004, "An Investigation of the Heat Transfer and Static Pressure on the Over-Tip Casing Wall of an Axial Turbine Operating at Engine Representative Flow Conditions (II) Time-Resolved Results," Int. J. Heat Fluid Flow, **25**, pp. 945–960.
[20] Gregory-Smith, D. G., and Cleak, J. G. E., 1992, "Secondary Flow Measurements in a Turbine Cascade With High Inlet Turbulence," ASME J. Turbomach., **114**, pp. 173–183.
[21] Keane, R. D., and Adrian, R. J., 1992, "Theory of Cross-Correlation Analysis of PIV Images," Appl. Sci. Res., **49**, pp. 1–27.
[22] Rao, N. M., and Cengiz, C., 2004, "Axial Turbine Tip Desensitization by Injection From a Tip Trench, Part 1: Effect of Injection Mass Flow Rate," ASME Paper No. GT2004-53256.
[23] McCarter, A. A., Xiao, X., and Lakshminarayana, B., 2000, "Tip Clearance Effects in a Turbine Rotor, Part II: Velocity Field and Flow Physics," ASME Paper No. 2000-GT-0477.

Downloaded 30 May 2010 to 128.113.26.88. Redistribution subject to ASME license or copyright; see http://www.asme.org/terms/Terms_Use.cfm

J. Szwedowicz
Thermal Machinery Laboratory,
ABB Turbo Systems Ltd.,
Bruggerstreet 71a,
CH-5401 Baden, Switzerland
e-mail: szwedowicz@ch.abb.com

R. Visser
Faculty of Mechanical Engineering,
University of Twente,
7500 AE Enschede, The Netherlands

W. Sextro
Institute of Mechanics,
Graz University of Technology,
Kopernikusgasse 24/III,
A-8010 Graz, Austria

P. A. Masserey
TSDMH Department,
ALSTOM (Switzerland) Ltd.,
Brown Boveri Street 7,
CH-5401 Baden, Switzerland

On Nonlinear Forced Vibration of Shrouded Turbine Blades

Numerical predictions of the forced vibration of a disk assembly including frictional effects between the shrouds are presented concerning engineering needs for the blade design process. Assuming a tuned disk assembly, numerical static, free, and then forced vibration analyses of a shrouded turbine blade measured in the spin pit are performed systematically. For the excitation forces of an air jet evaluated from the fairly linear behavior of the experimental blade resonance peaks, the reliability of the proposed approach is validated through the very close agreement of the computed and measured resonant peaks. These resonant peaks demonstrate either a fairly linear behavior or a nonlinear one like the jump effect of blade resonance amplitudes, or elastic impacts between the shrouds. Also, the damping performance for different contact configurations between the shrouds is numerically analyzed. These numerical results indicate that the shrouds generate higher frictional damping for small angles (0–30 deg) *between the circumferential direction and the normal vector to the contact surface.*
[DOI: 10.1115/1.2218889]

Introduction

The free vibration of shrouded blades is well understood for grouped or fully coupled turbine stages. In literature, different numerical techniques, such as superelement (e.g., Jacquet-Richardet et al. [1]) or modal synthesis (e.g., Bladh et al. [2]), are well described even for mistuned systems (e.g., Petrov and Ewins [3] or Feiner and Griffin [4]). However, prediction of the forced response of shrouded disk assemblies is still a challenging engineering task because of the unknown excitation loads and friction damping effects. Recently, a remarkable progress in transient flow calculations has allowed the prediction of realistic excitation forces acting on the rotating blades (e.g., Filsinger et al. [5]). Besides the excitation loads, frictional dissipation between the vibrating shrouds has to be included in the computation of the forced response of shrouded blades. A remarkable number of papers about the numerical modeling of the frictional dissipation between the shrouds and on underplatform friction dampers can be found in the literature. Wang et al. [6–9], Petrov and Ewins [10], Sanliturk et al. [11], Sextro [12], Gaul and Nitsche [13], Popp [14], as well as Griffin [15], provide thorough reviews of the available literature and methods solving nonlinear vibrations of mechanical systems with friction. Most of these approaches and numerical tools are only verified on nonrotating experimental setups, which usually use beamlike blade specimens. Very few papers deal with the forced vibration problems of shrouded disks, and only Griffin and Labelle [16] presented a practical procedure for systematic damping analysis of shrouded blades. Their investigations took into account mistuning effects of the real bladed disk and magnitudes of excitation forces in the spin pit environment. By their validation of the numerical results with the experimental data, they found some general difficulties in numerical predictions of strong nonlinear behavior of the measured commercial fan blades by applying the BDAMPER code (Yang and Menq [17]). For designers, Griffin and Labelle [16] propose some practical issues for the effective data presentation of nonlinear vibrations of the shrouded blades, but their work does not give any information about stiffness properties between the shrouds. They assumed a constant friction coefficient of 0.4 for the analyzed titanium shrouds and estimated magnitudes of the normal contact forces from shroud dimensions and acting centrifugal loads. Sextro [12] developed efficient solution methods for calculating the spatial forced vibration of elastic structures with friction contacts including microslip effects and surface roughness.

In this paper, free and forced vibrations of a rotating shrouded blade are systematically investigated with special consideration towards the designer's needs. In the first part of the paper, the theoretical background of the blade dynamics and then contact mechanics are briefly explained and the system equations are derived. This theory has been realized in the HADES software [12] for analyzing the nonlinear forced response of shrouded blades with friction effects. The basis for this software is the calculation of the contact area and the pressure distribution between the shrouds, which are obtained from the cyclic finite element (FE) method. Further contact parameters are the normal and tangential contact stiffness as well as the roughness in the form of a cumulative height distribution of the contact surface. The experimental nodal diameter diagram and different resonance response curves of the real shrouded turbine blade, which has been measured in the spin pit, are compared with the numerical results. The comparison of the calculations with the measurements shows a very close agreement. Finally, the parametric study of the most popular shroud configurations is numerically conducted in order to determine the best damping performance required by blade designers.

The Free Vibration of Shrouded Blades

External excitations acting on the rotating blades induce two traveling waves propagating in opposite circumferential directions within the bladed disk. The superposition of these waves generates a harmonic disk vibration defined by its natural period, which depends on the system mass and stiffness. In reality the bladed disk is a system of N blades, whose geometry slightly differs from each other due to manufacturing tolerances, resulting in the mistuning effect. In the design process, the blade mistuning is not a deterministic quantity. In practice, the tuned system of the coupled

Contributed by the Turbomachinery Division of ASME for publication in the JOURNAL OF TURBOMACHINERY. Manuscript received February 27, 2004; final revision received March 9, 2006; published online December 14, 2007. Review conducted by M. P. Mignolet.

 Copyright © 2008 by ASME

Downloaded 30 May 2010 to 128.113.26.88. Redistribution subject to ASME license or copyright; see http://www.asme.org/terms/Terms_Use.cfm

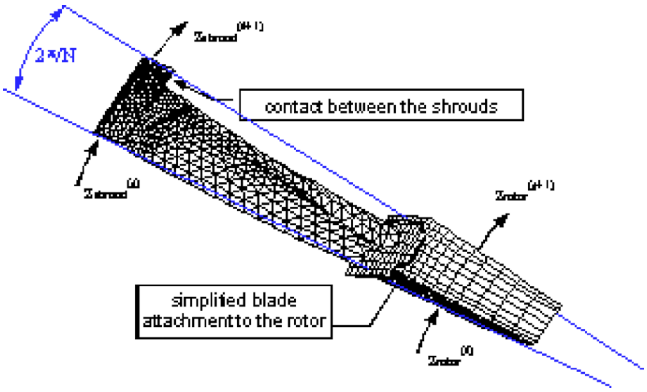

Fig. 1 FE model of the analyzed shrouded turbine blade with the imposed two cyclic constraints, which are separated from the frictional contact kinematic restraints

blades is usually taken into account for the numerical assessment of the static and dynamic behavior of the blade under design.

In this paper, a rotating steam turbine disk assembly containing $N=70$ shrouded blades is considered. The cyclic FE model representing this blade is shown in Fig. 1. The blade is attached to the rotor by a fir tree. Some simplifications are applied to the generated FE model, such as omitted fillet between the airfoil and platform, neglected fir tree and direct attachment of the airfoil shank to the rotor part on a radius referring to the position of the upper shoulder of the fir tree. In the cyclic ABAQUS [18] FE model, an interface between the shrouds is modeled using 45 two-dimensional parabolic contact elements.

Considering assembly forces $\{A\}$, centrifugal loads $\{F_F\}$ depending on the rotational speed Ω and flow pressure $\{P_o\}$ acting on the blade, the system equation for quasi-static equilibrium of the shrouded blade is given in general by

$$[K(\Omega,\mu)]\{z\}=\{A\}+\{F_F(\Omega)\}+\{P_o\} \tag{1}$$

in which frictional effects between the shrouds are included in the stiffness matrix $[K(\Omega,\mu)]$ where μ denotes the friction coefficient. By pretwisting each blade, the turbine stage is assembled. Assembly prestresses between the shrouds are induced by a rigid kinematic rotation about the radial direction of the rotor nodes. Additionally, centrifugal forces relating to the nominal rotational speed are imposed on the blade. Thermal stresses are neglected for an ambient temperature of 25°C given in the spin pit measurements. The contact area between the deformed shrouds is obtained from the nonlinear static analysis with the general purpose ABAQUS FE computer system [18] for large deformations.

The vibration of a tuned bladed disk is represented efficiently using a single blade with complex boundary conditions [19]. For the shrouded or snubbered blades, the frictional and cyclic boundary conditions should be separated from each other for computing reliable disk eigenfrequencies, which significantly depend on the effective contact area between the shrouds [20].

As illustrated in Fig. 1, the harmonic deformations at the shroud and the rotor part of the successive cyclic sector $\ell+l$ is determined from

$$z_{\text{shroud}}^{(\ell+1)}=z_{\text{shroud}}^{(\ell)}e^{j2\pi n/N}\quad z_{\text{rotor}}^{(\ell+1)}=z_{\text{rotor}}^{(\ell)}e^{j2\pi n/N} \tag{2}$$

where $j=\sqrt{-1}$. Rewriting Eq. (2) in trigonometric notation, eigenfrequencies of the cyclic FE system can be computed in the real domain. Consequently, the cyclic model has to be represented by two identical FE meshes, whose nodal boundaries on the circumferential sector sides are constrained as shown in Eq. (2). For each mode i and nodal diameter n (besides $n=0$ and $n=N/2$), two identical eigenfrequencies are computed which refer to two possible orthogonal mode shapes $\{\phi_{i,n}\}^{(\ell)}$ of the disk assembly. Neglecting dissipation effects and assuming small deformations, the

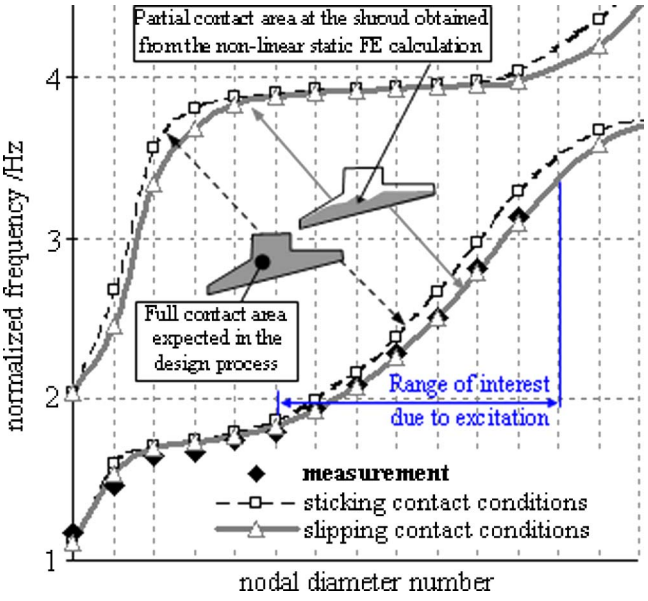

Fig. 2 Numerical and experimental (only the first mode) eigenfrequencies of the shrouded blade for the contact area obtained from the nonlinear static calculations for the sticking ($\mu=\infty$) and slipping ($\mu=0.4$) contact conditions between the shrouds

eigenfrequencies $f_{i,n}=\omega_{i,n}/2\pi$ (where $\omega_{i,n}$ denotes angular eigenfrequency) of the disk assembly are calculated from

$$(\lfloor K(e^{j2\pi n/N},\Omega,\mu=\infty)\rfloor-\omega_{i,n}^2\lfloor M(e^{j2\pi n/N})\rfloor)\{\phi_{i,n}\}^{(\ell)}=0 \tag{3}$$

where the blade complex mass $[M(e^{j2\pi n/N})]$ and stiffness $[K(e^{j2\pi n/N},\Omega,\mu=\infty)]$ matrices depend on nodal diameter number $n=0,1,\ldots,N/2$ for even N or $(N-1)/2$ if N is an odd number of blades, whereby $\mu=\infty$ indicates the stuck (rigid) contact condition on the interface area between the shrouds obtained by solving Eq. (1). Additionally, regarding the rotational speed Ω of the turbine, the stiffening effect is included in the stiffness matrix $[K(\Omega,n,\mu=\infty)]$.

In the FE free-vibration analysis, blade eigenfrequencies are computed for a no-slip contact condition on the contact area obtained from the nonlinear static computation with friction effects between the shrouds. These FE eigenfrequencies are obtained with a very good agreement with the measurement results (see the white triangular symbols in Fig. 2). On the contrary to these satisfactory results, the numerical eigenfrequencies, calculated for the fully designed contact area and the rigidly coupled shrouds, differ remarkably from the measured resonance frequencies in Fig. 2.

Steady-State Dynamic Response

Even for the simplified models of disk assemblies, a time-marching structural FE simulation of the bladed disk response is ineffective because of the need for excessive computational time. Hence, the FE calculations are performed in the frequency domain as mentioned before. In general, forced vibrations of a single coupled blade can be expressed in the time domain by

$$\lfloor M(e^{j2\pi n/N})\rfloor\{\ddot{z}\}+[D]\{\dot{z}\}+\lfloor K(e^{j2\pi n/N},\Omega,\mu=\infty)\rfloor\{z\}=\{P\} \tag{4}$$

where the damping matrix $[D]$ is represented by the Rayleigh dissipation model as a linear combination of the mass and stiffness matrices. The generalized vector $\{P\}$ describes the nonuniform pressure distribution. For a blade rotating with the constant angular speed Ω, the pressure $\{P\}$ is a periodic excitation function with the period $\tau=2\pi/\Omega$. After applying the computed eigenfrequencies $\omega_{i,n}$ and mode shapes $\{\phi_{i,n}\}$ (see Eq. (3)), the steady-state

Downloaded 30 May 2010 to 128.113.26.88. Redistribution subject to ASME license or copyright; see http://www.asme.org/terms/Terms_Use.cfm

response of the disk rotating with the constant angular speed Ω is given for each nodal diameter n in the rotating frame of reference as [5]

$$m_{i,n}\ddot{q}_{i,n} + 2\omega_{i,n}\xi_i\dot{q}_{i,n} + k_{i,n}q_{i,n} = \{\phi\}_{i,n}^T\{P_k\}e^{j(k\varphi_\delta - \rho_k)}e^{jk\Omega t} \quad (5)$$

where $k=1,2,\ldots,\infty$ describes the engine order, $i=1,2,3$ indicates the number of the mode shape, and φ_δ denotes the circumferential position of the excited node of the cyclic FE model. In Eq. (5), $m_{i,n}=\{\phi\}_{i,n}^T[M(n)]\{\phi\}_{i,n}$ and $k_{i,n}=\{\phi\}_{i,n}^T[K(\Omega,n)]\{\phi\}_{i,n}$ are the modal mass and stiffness of the cyclic FE model, respectively, and $\{\phi\}_{i,n}^T$ is the conjugate transposed vector of the disk eigenform $\{\phi\}_{i,n}$. The circumferential position φ_δ is determined from Cartesian coordinates of the excited node δ. The damping ratio ξ_i, given in Eq. (5), should be evaluated from the experimental resonance curves (see Fig. 5) for each engine order corresponding to nodal diameter n.

For the applied two FE meshes of the cyclic model, excitation loads of each engine order k have to be imposed simultaneously on node δ of the "real" and "imaginary" blade as shown by Filsinger et al. [5]

$$F_{\delta,\chi}^{(\text{real_blade})} = P_{k,\chi}[\cos(k\varphi_\delta - \rho_{k,\chi}) + j\sin(k\varphi_\delta - \rho_{k,\chi})] \quad (6)$$

$$F_{\delta,\chi}^{(\text{imag_blade})} = P_{k,\chi}[\sin(k\varphi_\delta - \rho_{k,\chi}) - j\cos(k\varphi_\delta - \rho_{k,\chi})] \quad (7)$$

where χ refers either to the circumferential or the axial direction and ρ denotes the phase delay.

Due to the orthogonality condition between the disk mode $\phi_{i,n}$ and the circumferential pressure distribution P_k in Eq. (5), the resonance occurs only if the excitation order k is equal to $\kappa\cdot N \mp n$ or $\kappa\cdot(N+2) \mp n$ (where $\kappa=0,1,\ldots,\infty$) for the even or odd number N of the blades, respectively. Nodal amplitudes P_k and phase delay ρ_k can be obtained either from the Fourier decomposition of the nonuniform computational fluid dynamics (CFD) pressure [5] or from FE simulation of the measured resonance peaks of the rotating blade (see Fig. 5) by tuning magnitudes of excitation amplitudes P_k in Eq. (5) for the evaluated damping ratio ξ.

Forced Vibrations of the Shrouded Disks With Friction

For the computation of frictional sliding between the shroud or snubber connections, Menq's team in the USA and Popp's group in Europe offer the BDAMPER [17] and HADES [21] codes, respectively. Both codes were developed within industrial-government consortia (GUIde in the USA and FVV[1] in Germany). In addition, Petrov and Ewins [10] have developed their own numerical package for the blade dynamics with friction effects.

Most of the mechanical systems with friction contacts can be reduced to linear elastic bodies with nonlinear contact behavior. To calculate the dynamic response to the forced excitation of the blades with friction contacts, Treyde [23] used the modal description for the elastic components and the theory of Cattaneo [24], Mindlin [25], and Mindlin et al. [26] to describe the contact between adjacent shrouds. To reduce the computational effort, the contact model is linearized by means of the harmonic balance method.

The blade vibration is described in the A-coordinate-system, which is fixed to the root of each blade. The contact deformations are given in the R-reference system (see Fig. 11(a)). The y- and z axis of each R-coordinate-system are parallel to the contact interface of the shroud. The transformation from the A- to the R-coordinate-system is defined by the shroud angle β (Fig. 11(a)).

In most cases the shape of the shroud interfaces can be simplified to rectangular shape (see Fig. 3), with the width b_0 and the height h_0. The origin O of the R-coordinate-system is placed in the center of the contact interface. The point OR denotes the center of the right contact surface of the ℓth blade, while the point OL denotes the center of the left contact surface of the $(\ell+1)$th blade (see Figs. 3 and 6).

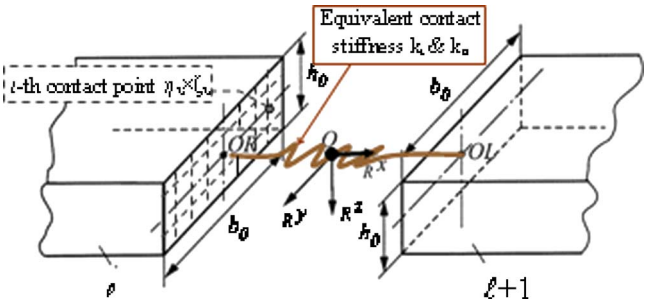

Fig. 3 Geometry of the nominal contact interface in the simulation [19] with the equivalent contact stiffness (k_t, k_n) between points *OR* and *OL* (Fig. 6) and a contact grid $\eta\times\zeta$ (a dashed mesh)

Assuming monofrequency excitation $k\Omega$, the generalized excitation forces, modal and physical responses are given, respectively, by

$$\{f(t)\}_E = \{\hat{f}\}_E e^{jk\Omega t} \quad (8)$$

$$\{q(t)\} = \{\hat{q}\}e^{jk\Omega t} \quad (9)$$

$$\{z(t)\} = \{\hat{z}\}e^{jk\Omega t} \quad (10)$$

Then, the forced vibration of one shrouded blade with one contact interface can be expressed by

$$[\hat{S}]\{\hat{q}\} = [T]_E^T\{\hat{f}\}_E + [T]_O^{TRA}[A]^T\{\hat{f}\}_O \quad (11)$$

with the system matrix for one elastic structure

$$[\hat{S}] = \text{diag}(\omega_{i,n}^2 - (k\Omega)^2 + j2\omega_{i,n}k\Omega\xi_{i,n}) \quad (12)$$

The index i denotes the ith mode, n and k are nodal diameter and engine order numbers, the modal matrix $[T]$, the generalized excitation force vector $\{f\}_E$ defined in the A-coordinate system, the transformation matrix ${}^{AR}\{A\}$, from R into A coordinate system and the generalized contact force vector $\{f\}_O$ with respect to the point O in R-coordinate system (Fig. 3)

$$\{\hat{f}\}_O = [\hat{F}_{x,o}\ \hat{F}_{y,o}\ \hat{F}_{z,o}\ \hat{M}_{x,o}\ \hat{M}_{y,o}\ \hat{M}_{z,o}]_O^T \quad (13)$$

The generalized contact forces are equal to a contact stiffness matrix $[K]_O$ multiplied by the relative motion $\{u\}_O$ between the shrouds, given by

$$\{\hat{f}\}_O = \{\hat{K}\}_O\{\hat{u}\}_O \quad (14)$$

and

$$\{\hat{u}\}_O = \{\hat{u}\}_{OL} - \{\hat{u}\}_{OR} = [\hat{u}_{x,o}\ \hat{u}_{y,o}\ \hat{u}_{z,o}\ \hat{\varphi}_{x,o}\ \hat{\varphi}_{y,o}\ \hat{\varphi}_{z,o}]_O^T \quad (15)$$

where $\hat{u}_{X,0}$, $\hat{u}_{Y,0}$, $\hat{u}_{Z,0}$ indicate three relative translations and $\hat{\varphi}_{X,0}$, $\hat{\varphi}_{Y,0}$, $\hat{\varphi}_{Z,0}$ are relative rotations smaller than 1 deg. The generalized relative displacement vector in the R-coordinate system can be determined by

$$\{\hat{u}\}_O = -{}^{RA}[A][T]_O\{\hat{q}\} \quad (16)$$

assuming that only one shroud interface vibrates. Substituting Eq. (14) and Eq. (15) into Eq. (11), the modal blade vibration is obtained in the form

$$([\hat{S}] + [T]_O^{TRA}[A]^T[\hat{K}]_O{}^{RA}[A][T]_O)\{\hat{q}\} = [T]_E^T\{\hat{f}\}_E \quad (17)$$

After solving a set of linear equations (17), the complex blade response amplitudes are determined by

$$\{\hat{z}\} = [T]\{\hat{q}\} \quad (18)$$

[1]FVV—Forschungsvereinigung Verbrennungskraftmaschinen (Research Association of Combustion Machines) TURBO-04-1037, Szwedowicz et al. [22].

Downloaded 30 May 2010 to 128.113.26.88. Redistribution subject to ASME license or copyright; see http://www.asme.org/terms/Terms_Use.cfm

In general, the same type of equation, as shown in Eq. (17), is obtained for the bladed disk assembly with friction contacts. Then, all matrices and vectors in Eq. (17) have to be adjusted to the number of the investigated blades. For example, for two shrouded blades contacting each other (see, e.g., Fig. 11) the characteristic matrices and vectors in Eq. (17) are given by

$$[\hat{S}] = \begin{bmatrix} [\hat{S}]_1 & 0 \\ 0 & [\hat{S}]_2 \end{bmatrix} \quad [T]_E^T = \begin{bmatrix} [T]_{E1}^T & 0 \\ 0 & [T]_{E2}^T \end{bmatrix}$$

$$\{\hat{q}\} = [\{\hat{q}\}_1^T \{\hat{q}\}_2^T]^T \quad \{\hat{f}\}_E = [\{\hat{f}\}_{E1}^T \{\hat{f}\}_{E2}^T]^T$$

$$[T]_O = [-[T]_{OR1} [T]_{OL2}] \tag{19}$$

A disk with N blades, where the shroud ℓ contacts the shroud $\ell+1$, is defined by

$$\lfloor \hat{S} \rfloor = \mathrm{diag}(\lfloor \hat{S} \rfloor_\ell) \quad \lfloor \hat{K} \rfloor_O = \mathrm{diag}(\lfloor \hat{K} \rfloor_{O\ell})$$

$$^{RA}[A] = \mathrm{diag}(^{RA}[A]_\ell) \quad [T]_E^T = \mathrm{diag}([T]_{E\ell}^T),$$

$$\{\hat{q}\} = [\{\hat{q}\}_1^T \{\hat{q}\}_2^T \cdots \{\hat{q}\}_N^T]^T \quad \{\hat{f}\}_E = [\{\hat{f}\}_{E1}^T \{\hat{f}\}_{E2}^T \cdots \{\hat{f}\}_{EN}^T]^T$$

$$[T]_O = \begin{bmatrix} -[T]_{OR1} & [T]_{OL2} & \cdots & 0 \\ 0 & -[T]_{OR2} & \cdots & 0 \\ \vdots & \vdots & \ddots & [T]_{OLN} \\ [T]_{OL1} & 0 & 0 & -[T]_{ORN} \end{bmatrix} \tag{20}$$

If this system is cut off at the contact $\ell=N$, the corresponding contact stiffness matrix is set to be a null matrix. Then, a multiblade system is modeled. If a cyclic system is investigated, cyclic boundary conditions (see Eq. (2)) are used to reduce the system equations and therefore the computation time is significantly decreased.

Due to the nonlinearity of the contact behavior and the spatial motion, the contact area $h_o \times b_o$ is discretized by a finite number of $\eta \times \zeta$ contact points (Fig. 3). By applying the multipoint constraints, the local contact stiffness and contact forces at each ιth contact point $\eta_\iota \times \zeta_\iota$ are obtained from the equivalent stiffness (k_n and k_t) and resulting contact forces of *OR* and *OL* representative points. Using the kinematic constraints, the initial spatial motion of each contact point ι is determined from the oscillations of point *OR* and *OL* known from the FE free vibration calculation. Finally, the combination of the modal description of the elastic bodies with the point contact model $\eta_\iota \times \zeta_\iota$ leads to an efficient modeling of dynamical problems with friction.

Besides the main physical parameters like the contact stiffness, the point contact model [12] includes the measured cumulative height distribution, which is used for the representation of rough surfaces. Then, the normal contact force and the tangential contact stiffness are nonlinearly dependent on the relative normal displacements. Both nonlinear effects are verified experimentally. The application of the point contact model with the roughness effect is limited to the first eigenfrequency of the layer and yielding deformations. Also, anisotropy with respect to the contact stiffness is modeled and the possibility of separation of the contact is included in the contact model. The harmonic balance method is used to linearize the normal and tangential contact forces. This leads to a complex stiffness matrix, where the components are nonlinearly dependent on the relative displacements of the contact surfaces. A nonrotating experimental setup with three elastic structures and two non-Hertzian contacts is used to verify the numerical results. The measurements of the spatial motion for bending as well as torsional vibration of the elastic structures show a good agreement with the corresponding calculations. The application of this code with respect to the spin test will be shown in the following.

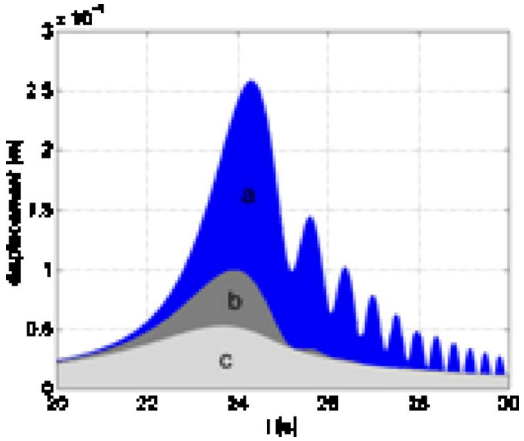

Fig. 4 Results of the transient SDOF responses for damping ratios of (a) ξ=0.02%; (b) ξ=0.1%; (c) ξ=0.2%

Evaluation of Blade Damping Property and Excitation Forces

In the spin pit measurement (vacuum condition), the shrouded blade is excited by an air jet. During the spin pit measurement, the rotational speed Ω is gradually decreased and the excitation frequency f can be related to the rotation speed Ω by $f=k\Omega/(2\pi)$, where k represents the engine order. For this type of the measurement, transient effects are verified by means of the simulated example of a single mass-spring system of one degree of freedom. In the applied MATLAB simulations, the variation of the rotational speed in the time domain is given by $\Omega(t)=\Omega_0+at$ and excitation force $F(\Omega,t)$ is expressed by

$$F(\Omega,t) = P_k \cdot \sin[\Omega(t) \cdot t] \tag{21}$$

where a, P_k, t are the speed parameter, excitation amplitude, and time, respectively.

For the measured constant angular speed deceleration a (see Fig. 9) three MATLAB simulations are performed, each with different damping ratios ξ of 0.02%, 0.1%, and 0.2% (see Fig. 4), respectively. In the case of a modal damping ratio ξ of 0.02% corresponding only to the expected material damping [27,28], significant modulations of the response amplitude of the mass-spring system after encountering its resonance are observed. These undamped vibrations indicate that the rundown speed is too fast in relation to a damping level of 0.02% and transient amplitudes are about 52% smaller than the amplitude obtained from the steady-state response calculation. In the case of a damping ratio ξ of 0.1% the transient effects are much weaker and the transient amplitude is 8% lower than the computed resonance steady-state amplitude. For a damping ratio ξ of 0.2% there is only a negligible difference of 2% between the amplitudes of the transient and steady-state calculations. Also, the magnitude of the "transient resonance frequency" depends on the run-down speed a and is slightly different from the resonance frequency $\omega=\omega^*(1-\xi^2)^{1/2}$ in the frequency domain calculation, where ω is the blade eigenfrequency. These minor frequency fluctuations are not investigated within the scope of this paper.

In general, the shape and resonance amplitude of the transient measurement can be very different from that of a steady-state calculation. Therefore, it is not reliable to estimate the damping value ξ from the transient measured resonance curve by applying the simple formula $\xi=(\omega_2-\omega_1)/(2\omega_r)$ valid only for the steady-state response, as it is illustrated in Fig. 5. In this case, the resonance curve has to be numerically tuned by the mass-spring simulations considering different values of the damping ratio ξ. Since the transient measurement does not show transient effects, the amplitude is about the same magnitude as in the steady-state case.

Downloaded 30 May 2010 to 128.113.26.88. Redistribution subject to ASME license or copyright; see http://www.asme.org/terms/Terms_Use.cfm

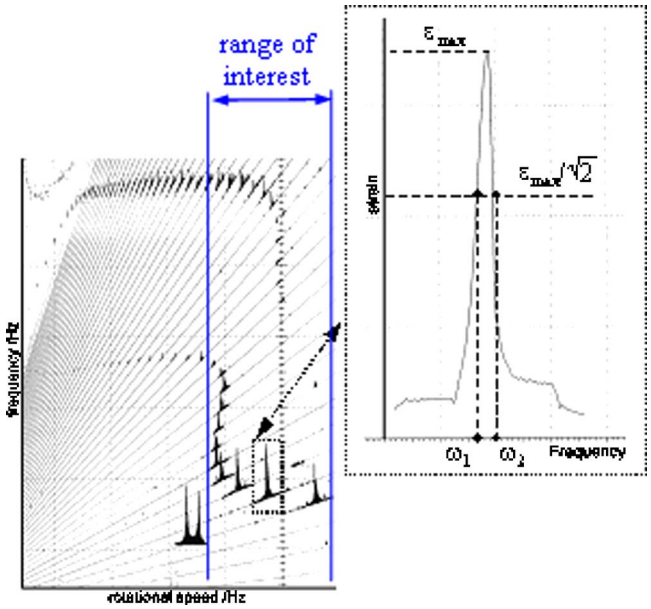

Fig. 5 The Campbell diagram of the shrouded blade (Fig. 6) measured in the spin pit using air jet excitation and zoom of single resonance response curve used for the damping evaluation

Unless the excitation forces are known from CFD simulations [5], their amplitudes can be approximated in a common way, using the stationary gas force and introducing the stimulus, which describes the percentage of the dynamic force amplitudes relative to the stationary gas force. In a similar manner, Griffin and Labelle [16] evaluated forces of air jet excitation acting on the rotating fan blades in the spin pit. Their results showed that this approach was not sufficient for predicting excitation forces for the second mode of the analyzed shrouded blade.

The Campbell diagram of the shrouded blade, measured in the spin pit, is presented in Fig. 5. Reference magnitudes of the excitation forces acting on the blade from the air jet and reference damping ratios are evaluated from the different experimental resonance peaks, which demonstrate a fairly linear behavior as illustrated in Fig. 5. Then, the maximum and minimum values of the experimental damping ratios are obtained between 0.15% and 0.25%, which correspond to both material and frictional damping effects. By computing the steady-state response of the shrouded blades (see Eqs. (4)–(7) for the evaluated damping ratios, the maximum (1.6 N) and minimum (1.1 N) magnitudes of the resulting excitation forces (see Fig. 6) are estimated from the resonance curves, which were not used in the damping evaluation.

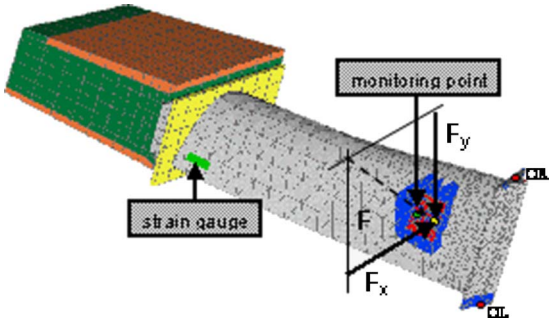

Fig. 6 Equivalent excitation force $F=(F_x^2+F_y^2)^{1/2}$ simulating the air jet excitation in the spin pit measurement

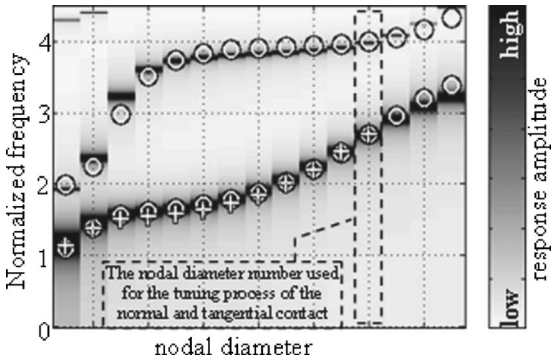

Fig. 7 Dispersion curves calculated for nonlinear (contour plot) and linear contact behavior (circular symbols) which are related to the measured resonance frequencies (crosses)

Regarding the evaluated excitation amplitudes, only small dynamic stresses can be induced in the blade; therefore, the material damping is a minor issue in relation to the damping values found between 0.15% and 0.25%. For the considered rotational speeds close to the nominal speed of the turbine (Fig. 5), relative frictional sliding motions between the blade root and the rotor disk are negligible because of high centrifugal stresses within the tree of the last turbine stage (e.g., Kielb and Abhari [29]). Then, for the analyzed nodal diameter numbers that assure possible relative motion between the shrouds, the damping ratios evaluated from the resonance peaks correspond primarily to the frictional damping effects between the shrouds.

Estimation of Contact Stiffness Between the Shrouds

Nonlinear forced frequency responses of the cyclic shrouded blade are computed for the normal contact pressure distribution, contact area, eigenfrequencies, and mode shapes from the FE calculations. Considering the interface roughness and microfrictional effects due to nonuniform contact pressure distribution, all simulations are done for a constant friction coefficient of 0.4 [22]. In calculations, the normal stiffness of the interface roughness is represented by the Abbott curve.

The equivalent contact stiffness between the shrouds (Fig. 3) is first computed with the FE method neglecting surface roughness (see, e.g., [22]). The resulting FE normal $k_{n,\mathrm{FE}}$ and tangential $k_{t,\mathrm{FE}}$ contact stiffness are applied for computing the nodal diameter diagram of the shrouded turbine blade. The equivalent normal k_n and tangential k_t contact stiffness are calculated for one $\zeta_1 \times \eta_1$ contact point between *OR* and *OL* representative points (see Fig. 3). By comparing the HADES and ABAQUS nodal diameter curves (Fig. 7), the magnitudes of the equivalent tangential k_t and normal k_n contact stiffness are found iteratively for the nodal diagram number of interest. For the analyzed shrouded blade, the normal contact stiffness is about twice as high as the tangential stiffness. However, the normal stiffness can vary in terms of the normal contact deformation due to nonlinear behavior of the surface roughness approximated by the Abbott function.[2] Hence, the relation between the normal and tangential contact stiffness depends on the shroud angle and surface roughness, which is assumed to be equal to 0.32 μm according to the reference experimental results given by Treyde [23].

Once the contact stiffness k_t and k_n have been tuned to the FE eigenfrequencies, a full dispersion diagram is generated for the whole nodal diameter range. In Fig. 7, the circular symbols represent the FE eigenfrequencies calculated for the stuck contact condition, the crosses refer to the spin-pit measurements, and

[2]The Abbott-Firestone curve [30] determines the rough surface as a function of the height distribution, which can be linearized by the five-parameter model [31].

Downloaded 30 May 2010 to 128.113.26.88. Redistribution subject to ASME license or copyright; see http://www.asme.org/terms/Terms_Use.cfm

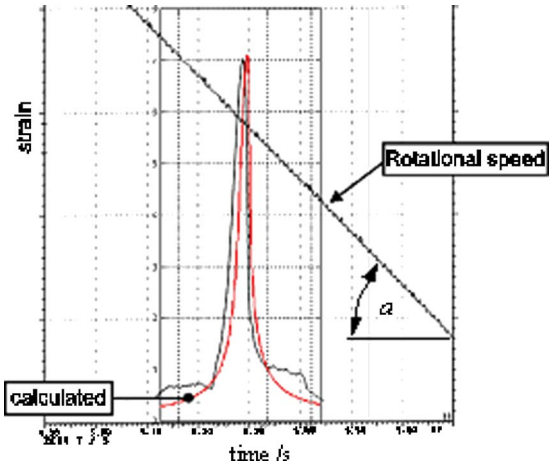

Fig. 8 The measured and computed resonance response curves demonstrating fairly linear behavior of the shrouded turbine blade at a rotational speed of 49^1/s

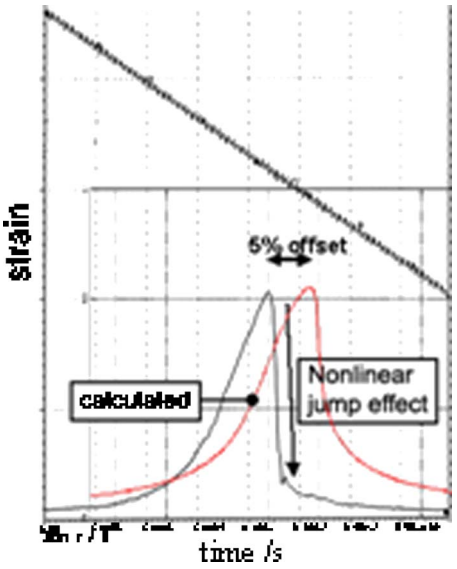

Fig. 9 The measured and computed resonance response curves of the shrouded turbine blade at a rotational speed of 57.1^1/s showing the nonlinear jump effect of the blade amplitude

black shaded strips are the numerical result for the nonlinear contact behavior. The thick or wide black strips (Fig. 7) correspond to the fairly "linear" (e.g., Fig. 8) or nonlinear (e.g., Fig. 10) resonances, respectively. Even when the nonlinear dynamic calculation is tuned for the normal and tangential contact stiffness for only one nodal diameter number (Fig. 7), almost all nodal diameters show a good agreement with the FE calculations and measurements.

Simulations of the Resonance Behavior of the Shrouded Disk in the Spin Pit Tests

For the equivalent normal k_n and tangential k_t contact stiffness between the shrouds, three different experimental resonance peaks of the shrouded blade, measured in the spin pit vacuum conditions, are analyzed numerically. All measurements were transient spin pit experiments performed with a low run-down speed a shown in Fig. 8. In this measurement, negligible transient effects are expected (Fig. 3(*c*)), affecting magnitudes of the measured strain amplitudes. A constant material damping ratio ξ of 0.02%, a surface roughness of 0.32 μm, and an evaluated maximum air jet excitation of 1.6 N are used in the numerical simulations.

The first comparison is done for a fairly "linear" behavior of the resonance response curve measured for a rotational speed of 49^1/s (Fig. 8). By applying the "half-power point" formula $\xi = (\omega_2 - \omega_1)/(2\omega)$ on the measured and computed resonance response functions (Fig. 8), the experimental and numerical damping ratios are equal to 0.12% and 0.10%, respectively. Indeed, instead of the resonance peak, the numerical resonance response function is flat in a very narrow frequency range near the resonance frequency due to the frictional damping. The simulation indicated the microslip frictional dissipation on the contour of the contact area between the shrouds where the normal contact stresses are smaller than the local tangential dynamic stresses.

Next, a more complicated resonance response curve, measured at a rotational speed of 57.1^1/s is analyzed numerically and the comparison between the numerical and experimental results is presented in Fig. 9. Here, the magnitude of the excitation force has to be reduced about 80% to get a good agreement between the measured and computed resonance curves. Also, 5% offset between the numerical and experimental maximum resonance amplitudes is obtained because of some transient effects, which were not included in the simulation. This simulated phenomenon refers to jump effect of blade resonance amplitudes which is caused by nonlinear elastic contact properties between the shrouds, whose contact area is represented by a finite number of contact points $\zeta \times \eta$ (where $\zeta = 16$, $\eta = 6$), including the nonlinear roughness stiffness represented by the Abbott function. Then, no resonance frequency can be found in the well-known form (see Fig. 8), for which the response amplitudes are amplified towards large magnitudes, since damping tends to minimum value. From the resonance response curve, shown in Fig. 9, the damping ratio ξ cannot be evaluated by using the half-power point formula and the blade dissipation properties may be determined numerically only.

Finally, for a turbine speed of 49^1/s, another type of nonlinear behavior of the resonance response function, shown in Fig. 10, is simulated numerically. In this case, the numerical results indicate elastic impacts ("chattering effect") between the shrouds, and therefore the blade resonance becomes very irregular. For the applied roughness value and excitation amplitude, the numerical resonance response function is narrower than the measured one. However, the numerical simulation predicted qualitatively well a strong nonlinear shroud behavior for the analyzed engine order. This qualitative information is a needed feedback for a designer to modify shroud geometry or its configuration regarding the design

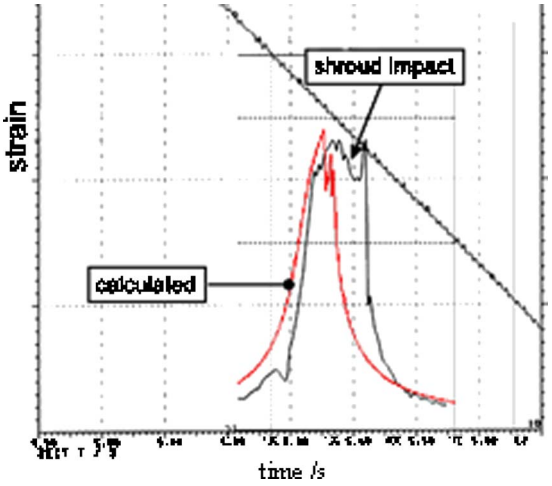

Fig. 10 The numerical and experimental resonance response curves with chattering effects (elastic impacts) between the shrouds at a rotational speed of 49^1/s

Downloaded 30 May 2010 to 128.113.26.88. Redistribution subject to ASME license or copyright; see http://www.asme.org/terms/Terms_Use.cfm

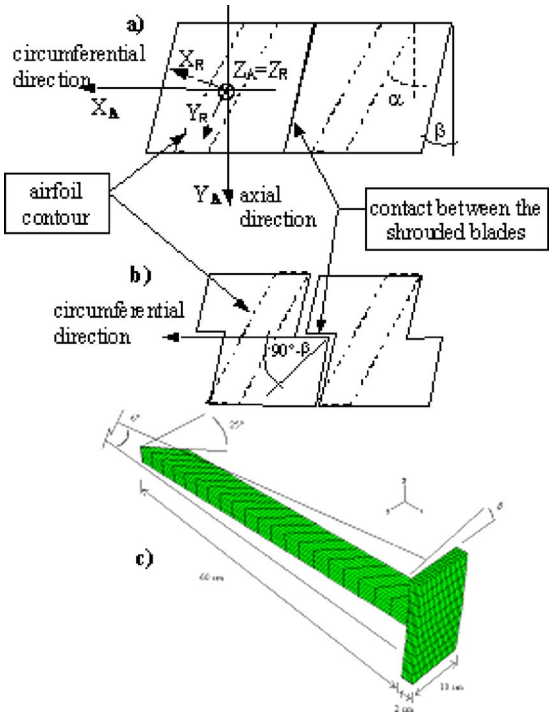

Fig. 11 Analyzed shroud configurations for finding the best damping performance: (a) the slant contact configuration; (b) the zig-zag contact configuration; (c) the FE model of the shrouded blade

HCF restriction. Therefore, further numerical investigations of this type of the resonance response curve were not conducted.

In all cases, the simulations show a good agreement with the experimental resonance response curves given in Figs. 8–10. The obtained differences in the magnitudes of the excitation forces are probably caused by mistuning problems omitted in this study [16]. Moreover, the applied concentrated resulting force (Fig. 6) does not excite the torsion deformation effectively, which is present partly in the mode shapes of the analyzed shrouded blade.

Dynamic Behavior of Different Shroud Configurations

Some typical shroud configurations may be distinguished in the turbine blade design. Two of them, called "further slant" and "zigzag shroud," which couple 60 airfoils (Fig. 11), are analyzed numerically to compare dynamic behavior of the disk assemblies and to find the best damping performance without chattering effects between the shrouds. Both analyzed shrouds are attached to a beamlike blade with a rectangular cross section (see Fig. 11(*c*)). To analyze an influence of centrifugal forces, the stagger angle α of this blade varies from 0 up to 25 deg, whereby the contact orientation angle β between shrouds changes between 0 and 40 deg. Due to the design reasons, the maximum contact area of the zigzag coupling is 60% smaller than the slant one.

For a rotational speed of 50^1/s and a friction coefficient of 0.4 (see also Griffin and Labelle [16]), the nonlinear static FE analyses of these shrouded blades are first performed using the cyclic FE model. For a stagger angle of 0 deg, the resulting normal contact force and effective contact area between these shrouds are compared to each other in Fig. 12. By increasing the contact orientation angle β, from 0 up to 40 deg, reaction forces between the slant shrouds are reduced significantly. For the zigzag shroud configuration the contact normal forces become higher by decreasing the contact orientation angle β from 90 to 50 deg. In terms of the effective contact area, which is nearly always higher for the slant configuration (Fig. 12), the eigenfrequencies of both blades are computed and compared in Fig. 13.

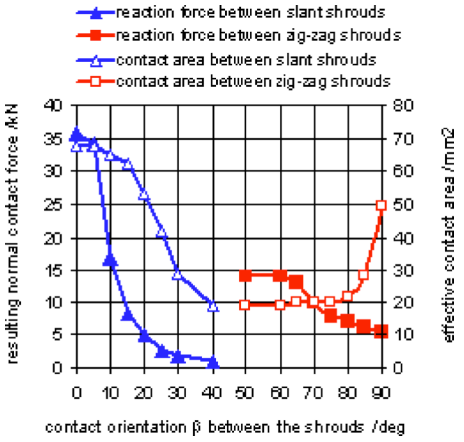

Fig. 12 For a rotational speed of 50^1/s resulting static normal contact forces and effective contact area of both shrouded blades with a stagger angle of 0 deg

Especially for the first disk eigenform, the eigenfrequencies of the slant shrouded blade are more sensitive than the zigzag one with respect to contact configuration β. Also, significant eigenfrequency differences are shown in Fig. 13 between the numerical results for the shroud couplings with the designed (frictionless fully stuck) contact area and with the effective contact area obtained from the cyclic FE analysis with friction.

Finally, by using the nonlinear dynamic contact simulation with an assumed surface roughness of 0.8 μm and a material damping ratio of 0.02% [27], the damping performance of both shroud configurations are compared to each other in Fig. 14 considering the equivalent damping ratio. This damping value is determined as the ratio of the damped resonance response of the shrouded blade

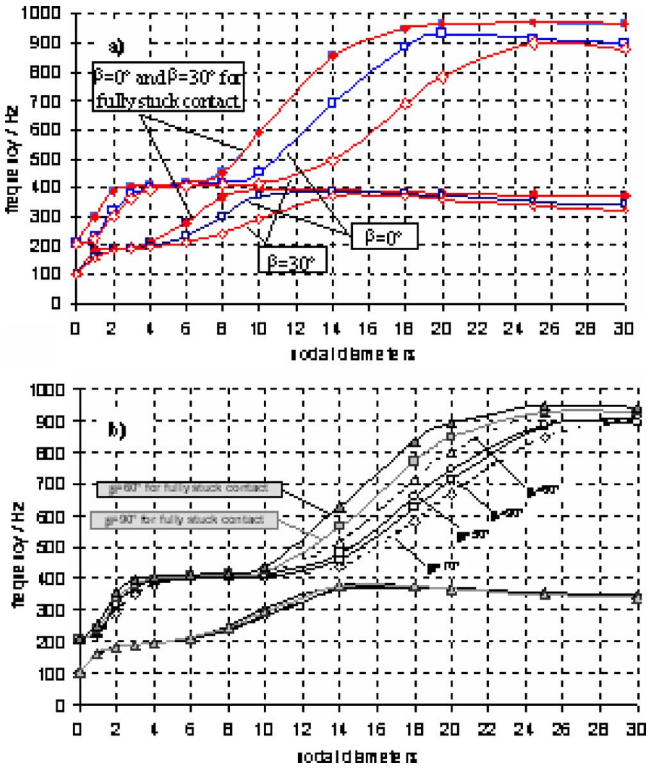

Fig. 13 For a rotational speed of 50^1/s nodal diameter diagrams of 60 blades with a stagger angle of 0 deg coupled by (a) slant shroud and (b) zigzag shroud

Downloaded 30 May 2010 to 128.113.26.88. Redistribution subject to ASME license or copyright; see http://www.asme.org/terms/Terms_Use.cfm

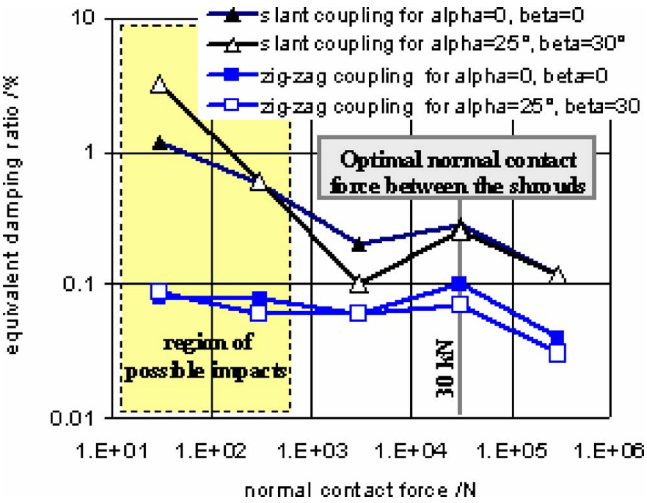

Fig. 14 For an excitation force of 10 N effective damping ratio concerning a friction coefficient of 0.4 and a contact roughness of 0.8 μm

with frictional slip to the steady-state resonance response of the blade for frictionless stuck shroud coupling and a material damping ratio of 0.02% (also called displacement performance by Griffin and Labelle [16]). For all normal static contact forces from 10 N up to 1 MN, the damping performance of the slant shroud configuration is significantly higher than that of the zigzag one. However, for a low normal contact force below 400 N, chattering effects between the shrouds are numerically obtained for both configurations. According to the obtained results, the slant shroud contact generates better frictional damping for vibrating blades than the zigzag one for the assumed constant excitation amplitude of 10 N. For an assumed contact roughness of 0.8 μm, the highest damping performance of both shroud configurations are obtained for a normal contact force of 30 kN (Fig. 14) because of microslip friction effects.

Conclusions

In this paper, free and forced vibrations of a shrouded blade are systematically investigated considering the needs of the designer. In the first part of the paper, the theoretical background of the blade dynamics and contact mechanics are explained briefly and the system of equations is derived. The spin pit measurements of shrouded steam turbine blades are successfully computed for both fairly "linear" and strong "nonlinear" resonance behavior.

For a stagger angle of 0 and 25 deg, the conducted general numerical experiments indicate that the damping of the slant shroud couplings is significantly higher than the zigzag coupling.

The proposed numerical procedure using the harmonic balance method and the general-purpose FE software can be effectively applied in a design process of the real shrouded (or snubbered) blades by providing certain parameters (e.g., surface roughness) that are adjusted through experimental data of the disk assembly measured in the spin pit. Other parameters like the excitation forces acting on the rotating blades can be obtained from unsteady CFD simulations. With respect to temperature, the friction coefficient should be known from the independent experimental setup. For high rotational speeds generating large centrifugal stresses within the blade assembly of the last turbine stage, the frictional damping at the blade root interface has a minor influence on the whole damping value due to negligible relative sliding motions between the blade root and the rotor disk. Therefore, the numerical assessment of the dissipation properties between the shrouds can be successfully determined. The range of the frictional damping at the blade root may be assessed numerically by applying the explicit FE approach, which however, requires a very fine mesh of the blade and extensive computation time that exceed the conventional procedures of the design process.

Acknowledgment

The authors thank the Thermal Machinery Laboratory of ABB Turbo Systems and ALSTOM (Switzerland) Ltd. in Switzerland for support and permitting the publication of this paper.

References

[1] Jacquet-Richardet, G., Moyround, F., and Fransson, T. H., 1997, "An Influence of Shroud Design on the Dynamic and Aeroelastic Behavior of Bladed Disk Assemblies," ASME Paper No. 97-GT-191.
[2] Bladh, R., Castanier, M. P., and Pierre, C., 1999, "Reduced Order Modeling and Vibration Analysis of Mistuned Bladed Disk Assemblies With Shrouds," Trans. ASME: J. Eng. Gas Turbines Power, **121**, pp. 515–522.
[3] Petrov, E. P., and Ewins, D. J., 2001, "Analysis of the Worst Mistuning Patterns in Bladed Disk Assemblies," ASME Paper No. 2001-GT-0292.
[4] Feiner, D. M., and Griffin, J. H., 2002, "A Fundamental Model of Mistuning for a Single Family of Modes," ASME Paper No. GT-2002–30425.
[5] Filsinger, D., Szwedowicz, J., and Schäfer, O., 2002, "Approach to Unidirectional Coupled CFD-FEM Analysis of Axial Turbocharger Turbine Blades," ASME J. Turbomach., **124**, pp. 125–131.
[6] Wang, J. H., and Yau, H. Y., 1990, "Design of Shroud Interface-Angle to Minimize the Forced Vibration of Blades," ASME Paper No. 90-GT-247.
[7] Wang, J. H., and Yau, H. Y., 1990, "Design of Blade-Shroud to Minimize the Sensitivity of Response to Preload Mistuning," Proceedings of the 3rd International Conference on Rotordynamics, Sept. 9–12, Lyon, France.
[8] Wang, J. H., and Shieh, W. L., 1991, "The Influence of Variable Friction Coefficient on the Dynamic Behaviors of Blade with Friction Damper," J. Sound Vib., **149**, pp. 137–145.
[9] Wang, J. H., and Chen, W. K., 1993, "Investigation of a Blade with a Friction Damper by HBM," ASME J. Eng. Gas Turbines Power, **115**, pp. 294–299.
[10] Petrov, E. P., and Ewins, D. J., 2002, "Analysis of Nonlinear Multiharmonic Vibrations of Bladed Disks with Friction and Impacts Dampers," in Proceedings of the 7th National Turbine Engine High Cycle Fatigue (HCF) Conference, May 14–17, Palm Beach Gardens, Florida.
[11] Sanliturk, K. Y., Ewins, D. J., and Stanbridge, A. B., 2001, "Under-platform Dampers for Turbine Blades: Theoretical Modelling, Analysis and Comparison with Experimental Data," ASME J. Eng. Gas Turbines Power, **123**, pp. 919–929.
[12] Sextro, W., 2002, *Dynamical Contact Problems with Friction—Models, Methods, Experiments and Applications*, Habilitationsschrift, Lecture Notes in Applied Mechanics, Vol. 3, Springer-Verlag, Heidelberg.
[13] Gaul, L., and Nitsche, R., 2001, "The Role of Friction in Mechanical Joints," Appl. Mech. Rev., **54**(2), pp. 93–106.
[14] Popp, K., 1994, "Nichtlineare Schwingungen Mechanischer Strukturen mit Füge—oder Kontakt-stellen (Non-linear Vibration of Mechanical Structures with Grooves of Contacts)," Z. Angew. Math. Mech., **74**, pp. 147–165.
[15] Griffin, J. H., 1990, "A Review of Friction Damping of Turbine Blade Vibration," Int. J. Turbo Jet Engines, **7**, pp. 297–307.
[16] Griffin, J. H., and Labelle, R. F., 1996, "A Rational Method for Optimizing Shrouded Damping," ASME Paper No. 96-GT-402.
[17] Yang, B.-D., and Menq, C.-H., Oct. 1997, "Modeling of Friction Contact and Its Application to the Design of Shroud Contact," ASME J. Eng. Gas Turbines Power, **119**, pp. 958–963.
[18] ABAQUS/Standard, 2001, *User's Manual*, Hibbitt, Karlsson & Sorensen, Inc., Pawtucket, Vol. 1–3, Version 6.3.
[19] Thomas, D. L., 1974, "Standing Waves in Rotationally Periodic Structures," J. Sound Vib., **37**, pp. 288–290.
[20] Szwedowicz, J., 1999, "Cyclic Finite Element Modeling of Shrouded Turbine Blades Including Frictional Contact," ASME Paper No. 99-GT-92.
[21] Sextro, W., 2000, "The Calculation of the Forced Response of Shrouded Blades with Friction Contacts and Its Experimental Verification," ASME Paper No. 2000-GT-540.
[22] Szwedowicz, J., Kissel, M., Ravindra, B., and Kellerer, R., 2001, "Estimation of Contact Stiffness and its Role in the Design of a Friction Damper," ASME Paper No. 2001-GT-290, New Orleans.
[23] Treyde, T., 1995, *Modellierung des Kontaktes zwischen den Deckplatten von Turbinen-schaufeln* (Contact Modeling between Shrouds of Turbine Blades), Fortschr.-Ber. VDI-Reihe 11, No. 224, VDI-Verlag, Düsseldorf.
[24] Cattaneo, C., 1938, "Sul Contatto di Due Corpi Elastici: Distribuzione Locale degli Sforzi (On Contact between Elastic Bodies: Local Stress Distribution)," Rend. Accad. Naz. Lincei, **27**(6), pp. 342–348; 1938, Rend. Accad. Naz. Lincei **27**(6), pp. 434–436; 1938, Rend. Accad. Naz. Lincei **27**(6), 474–478.
[25] Mindlin, R. D., 1949, "Compliance of Elastic Bodies in Contact," ASME J. Appl. Mech., **16**, pp. 259–268.

Downloaded 30 May 2010 to 128.113.26.88. Redistribution subject to ASME license or copyright; see http://www.asme.org/terms/Terms_Use.cfm

[26] Mindlin, R. D., Mason, W. P., Osmer, J. F., and Deresiewicz, H., 1952, "Effects of an Oscillating Tangential Force on the Contact Surfaces of Elastic Spheres," in ASME: 1st US National Congress of Applied Mechanics, Chicago, IL, 1951, ASME, New York, pp. 203–208.
[27] Gudmundson, P., and Wuethrich, C., 1986, "Die Werkstoffdämpfung von Stählen bei hohen Dehnungsamplituden (Damping of Steels at High Strain Amplitudes)," Z. Werkstofftech., **17**, pp. 286–292.
[28] Schmidt, R., 1962, "Resonanzverhalten und Schwingungsschierheit der Schaufel von Turbomaschinen (Resonance Behaviour and Vibration Security of Blade from Turbomachinery)," Maschinenbautechnik, **11**(12), pp. 630–637.
[29] Kielb, J. J., and Abhari, R. S., 2003, "Experimental Study of Aerodynamic and Structural Damping in a Full-Scale Rotating Turbine," Trans. ASME: J. Eng. Gas Turbines Power, **125**, pp. 102–112.
[30] Abbott, E. J., and Firestone, F. A., 1933, "Specifying Surface Quality," Mech. Eng. (Am. Soc. Mech. Eng.), **55**, pp. 569–575.
[31] DIN, 1990, "Measurement of Surface Roughness Parameters R_k, R_{pk}, R_{vk}, M_{r1}, M_{r2} for the Description of the Material Position in the Roughness," German Standard, DIN 4776.

Downloaded 30 May 2010 to 128.113.26.88. Redistribution subject to ASME license or copyright; see http://www.asme.org/terms/Terms_Use.cfm

Heat Transfer and Pressure Investigation of Dimple Impingement

K. Kanokjaruvijit
Department of Mechanical Engineering,
Naresuan University,
Muang, Pitsanulok, 65000 Thailand
e-mail: koonlaya@gmail.com

R. F. Martinez-Botas
Department of Mechanical Engineering,
Imperial College London,
London, UK
e-mail: rmbotas@imperial.ac.uk

Heat transfer and pressure results of an inline array of round jets impinging on a staggered array of dimples are reported with the consideration of various geometric and parametric effects; results are normalized against flat plate data. The heat transfer was measured by using transient wideband liquid crystal method. The geometrical configurations considered were crossflow (or spent-air exit) scheme, dimple geometries, and impinging positions. Three crossflow schemes were tested such as one-way, two-way, and free exits. These led to the idea of the coupling effects of impingement and channel flow depending on which one dominated. Hemispherical and cusped elliptical dimple shapes with the same wetted area were considered and found that both dimples showed the similarity in heat transfer results. Impinging positions on dimples and on flat portions adjacent to dimples were examined. Throughout the study, the pitch of the nozzle holes was kept constant at four jet diameters. The investigated parameters were Reynolds number (Re_{Dj}) *ranged from 5000 to 11,500, jet-to-plate spacing* (H/D_j) *varied from 1 to 12 jet diameters, dimple depths* (d/D_d) *of 0.15, 0.25, and 0.29, and dimple curvature* (D_j/D_d) *of 0.25, 0.50, and 1.15. The shallow dimples* ($d/D_d=0.15$) *improved heat transfer significantly by 70% at* $H/D_j=2$ *compared to that of the flat surface, while this value was 30% for the deep ones* ($d/D_d=0.25$). *The improvement also occurred to the moderate and high* D_j/D_d. *The total pressure was a function of* Re_{Dj} *and* H/D_j *when* $H/D_j<2$, *but it was independent of the target plate geometry. The levels of the total pressure loss of the dimpled plates werenot different from those of the flat surface under the same setup conditions. Wall static pressure was measured by using static taps located across each plate.* Re_{Dj} *and* H/D_j *affected the level of the static pressure while the dimple depth influenced the stagnation peaks, and the crossflow scheme affected the shape of the peaks.* [DOI: 10.1115/1.2220048]

1 Introduction

An effective cooling scheme of gas turbine vanes is important because it can improve the gas turbine performance and prolong the lifetime of the materials. Jet impingement is one of the most effective methods in heat transfer augmentation by forming small-scale vortex pairs. It has been used broadly in cooling gas turbine, and the impingement on the flat surface has been well established. There have been numerous attempts to improve the performance of the jet impingement such as applying the protrusions, i.e., rib-rougheners or turbulators, pin-banks or pin fins. However, these also induce excessive pressure loss as well as a different flow field than discretely mounted ribs, which themselves cause massive cooling/heating nonuniformity and thermal stresses [1]. In consequence, the expensive maintenance and manufacturing plus the colossal weight are important concerns for this type of heat transfer enhancer.

Another category of vortex generators is the use of concavity, which is defined as indentation on the surface forming a recess rather than the protrusion. A dimple is one of such concavities and has a drag reduction characteristic in external flows over bodies (i.e., golf balls). In general, dimples can be used to generate organized vortical or swirling flows. Therefore, they can be alternatives to the protruding surface. They require less material and induce less pressure losses, due to the more organized motion, while they help to enhance heat transfer. For instance, Kesarev and Kozlov [2] studied the flow past a single dimple and found 50% enhancement in the overall average heat transfer. Additionally, Chyu et al. [1] stated that the overall heat transfer enhancement caused by dimples was around 2.5 compared to the flat surface, while the pressure losses were about half the values produced by the conventional rib turbulators. Similarly, Moon et al. [3] found the average heat transfer improvement of the flow past a dimpled plate was 2.1 times, and the friction 1.6 to 2 times. On that account, the combination of jet impingement and dimples were thought to have high potential in augmenting heat transfer more than impingement on a conventional flat surface.

The objectives of the current study are to investigate the heat transfer and pressure information for the jets impinging on the dimpled surface. Various geometric and parametric effects are considered such as crossflow scheme, dimple geometry, impinging positions, Reynolds number, jet-to-plate spacing (H/D_j), dimple depth (d/D_d), and ratio of jet diameter to dimple diameter (D_j/D_d). Throughout this research, the pitches of both jets and dimples were kept constant at 4 jet diameters. Note that the influence of crossflow scheme on the heat transfer was primarily examined in order to determine which scheme best suited the application of dimples. Two configurations of dimple arrays were investigated: hemispherical and cusped elliptical dimples; both were designed based on the same equivalent diameter. All results from the dimpled surfaces were also compared to those from the flat surface.

2 Experimental Procedure

2.1 Experimental Apparatus. A plenum chamber of the size 500×500 mm made of Plexiglas was equipped with a honeycomb

Contributed by the International Gas Turbine Institute (IGTI) of ASME for publication in the JOURNAL OF TURBOMACHINERY. Manuscript received October 1, 2004; final manuscript received February 1, 2005 published online December 14, 2007. IGTI Review Chair: K. C. Hall. Paper presented at the ASME Turbo Expo 2005: Land, Sea and Air, Reno, NV, June 6–9, 2005, Paper No. GT2005-68823.

 Copyright © 2008 by ASME

Downloaded 30 May 2010 to 128.113.26.88. Redistribution subject to ASME license or copyright; see http://www.asme.org/terms/Terms_Use.cfm

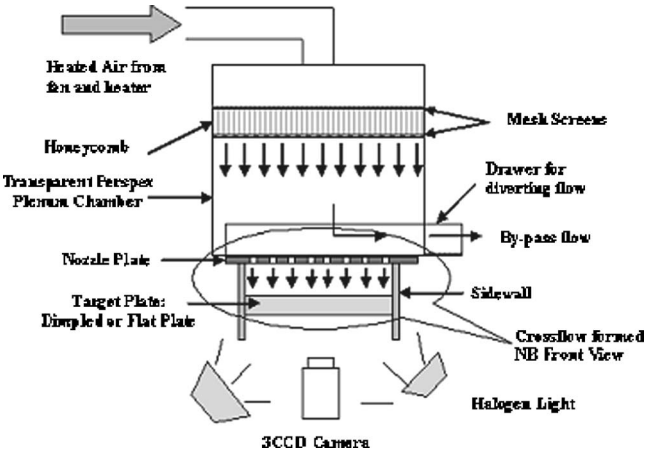

Fig. 1 Experimental apparatus

sandwiched by two mesh screens to straighten the flow before impinging, and had a 320×320 mm hole at the bottom of the chamber, which was attached by a nozzle plate (Fig. 1). Additionally, a drawer was introduced in order to divert the flow and allow it to be settled before discharging through. A target plate was hung by four studs, which allowed the required jet-to-plate spacing to be adjusted. Similarly, sidewalls were also installed or removed by using studs to form a required crossflow scheme as shown in Fig. 2. Table 1 summarizes the various setup configurations as described below. Note also that the pitch of the nozzles was kept constant throughout the investigation at 4 jet diameters.

Phase 1 was experimented on smaller dimples (D_d =17.32 mm) of both dimple shapes: hemispherical and cusped elliptical (Fig. 3) [4,5]; the data inside the dimples was excluded due to the accumulation of the liquid crystal slurry when spraying. Phases 2 and 3 were carried out on bigger dimples (D_d =17.32 mm), and the dimple areas were included. Finally, Phase 4 was done on both the small and big dimples. The impinging positions were exhibited in Fig. 4.

2.2 Heat Transfer Experiments. A transient heat transfer experiment was carried out by heating the air that was generated by a fan with a 9 kW heater. Then, it flowed through the plenum chamber. The flow was diverted by the drawer in order to allow the conditions such as temperature to be set inside the plenum chamber. The thickness of the target plate was designed under the assumption of one-dimensional conduction and from the relation $z=2\sqrt{\alpha t}$ [6]. Liquid crystals in the temperature range of 35–45°C were coated on top of the target plate before spraying black paint for the reflection purpose. A 3 CCD camera was set underneath the plate to view the liquid crystal color transformation as shown in Fig. 1. Since the hue is insensitive to the local light intensity and the illumination angle [7], all the setup was fixed and calibration in situ was achieved in order to make the 1D conduction assumption inside the dimples valid. The liquid crystal calibration of the hue against temperature was carried out with a calculated uncertainty within ±1.5°C. The curve fitting and regression analysis resulted in the fifth-order polynomial temperature-hue relationship. Each camera image was transferred to the personal computer via a firewire lead, which transferred data directly from the camera to the computer without the use of a frame grabber. Each experiment was filmed with the noncompression mode in order to receive the data as complete as possible.

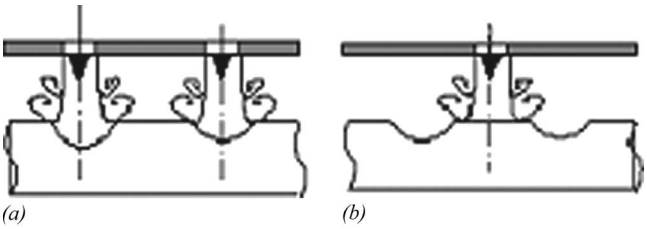

Fig. 3 Dimple geometries: (*a*) Hemispherical dimples and (*b*) Cusped elliptical dimples

The transient method was applied throughout the heat transfer experiments. Hence, the well-known correlation of the one-dimensional unsteady heat conduction was used, $\theta=1-\exp\beta^2\,\mathrm{erfc}\,\beta$, where $\theta=(T_s-T_i)/(T_m-T_i)$ and $\beta=h\sqrt{t}/\sqrt{\rho ck}$. The bulk temperature, T_m, was measured inside the plenum chamber. The experimental uncertainty throughout this study was within ±12.2% based on 95% confidence levels according to Moffat [8]. The highest uncertainty that might happen was the sum of uncertainties of the temperature measured by the liquid crystals, the initial and the bulk flow temperatures measured by thermocouples, the time frame measurement, and the thermal product ($\sqrt{\rho ck}$) for the Plexiglas substrate. Thermocouples used in this study had the uncertainty of ±0.5°C, which made the uncertainties of initial and bulk flow temperatures become ±2.5 and ±1%, respectively. The highest uncertainty of time was ±0.67%. Finally, the uncertainty of the thermal properties of the Perspex substrate was typically ±5% [9].

2.3 Pressure Measurements. Pressure loss measurement was carried out inside the plenum chamber above the nozzle plate by using a 250 mm long Pitot probe connected to a digital manometer, which had a built-in pressure transducer. Surface static pressure measurement was done on each target plate by tapping 7 mm holes from the center of the test plate toward one end. In order to achieve the pressure readings across the plate in both directions, the plate was rotated. Three rows of static taps were drilled:

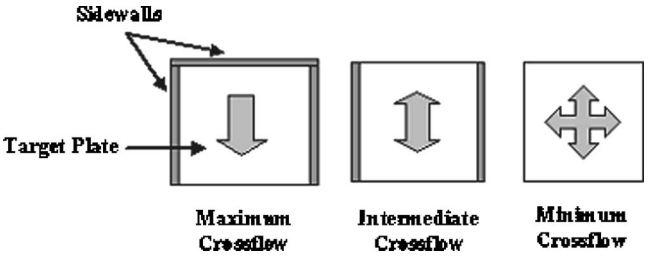

Fig. 2 Crossflow schemes

Table 1 Test parameters

Phase	D_d (mm)	D_j (mm)	Re_{Dj} ($\times10^{-3}$)	H/D_j	Crossflow	d/D_d	Impinging onto
1	17.32	10	11.5	2, 4, 8,12	Min, Int, Max	0.29	Dimples, Flat
2	40	20	5, 8, 11.5	1,2,4,6,8	Max	0.15,0.25	Dimples, Flat
3	40	10	11.5	2,4	Max	0.15,0.25	Dimples, Flat
4	17.32	20	11.5	2,4	Max	0.29	Dimples

Downloaded 30 May 2010 to 128.113.26.88. Redistribution subject to ASME license or copyright; see http://www.asme.org/terms/Terms_Use.cfm

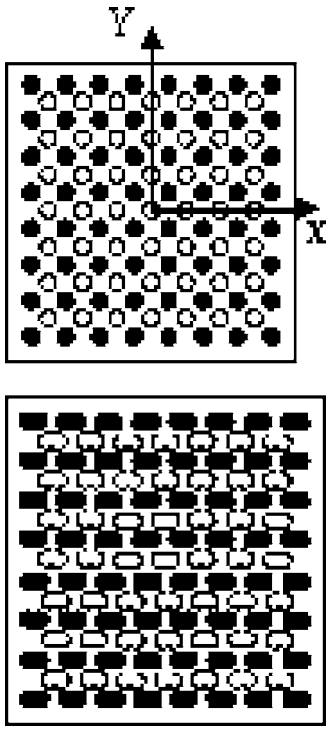

Fig. 4 Impinging positions

through staggered dimples (to the jet holes), inline dimples, and flat portions between the staggered and inline rows as shown in Fig. 5.

3 Results and Discussions

3.1 Heat Transfer Results

3.1.1 Overall Average Heat Transfer of a Flat Surface. Before beginning with the heat transfer results of jet impingement on dimples, a baseline case on a flat surface was examined and compared with the literature such as Andrew and Hussain [10], Obot and Trabold [11], and Huber and Viskanta [12]. Figure 6 [4] shows the overall average results of the flat plate in dimensionless form of Nusselt number at fixed Re_{Dj}=15,000 and various crossflow schemes. As expected, the minimum crossflow scheme led to the highest heat transfer, followed by the intermediate and maximum crossflow schemes, respectively. This was due to the fact that the strong crossflow present in the maximum crossflow scheme caused the heat transfer degradation, especially near the exit region, where the crossflow or spent air affected the most. Note that overall average Nusselt number was defined as the average value over the area of interest. Figure 7 shows the comparison at the same Re_{Dj}, but all the tests were carried out with the maximum crossflow scheme. The comparisons show the agreement.

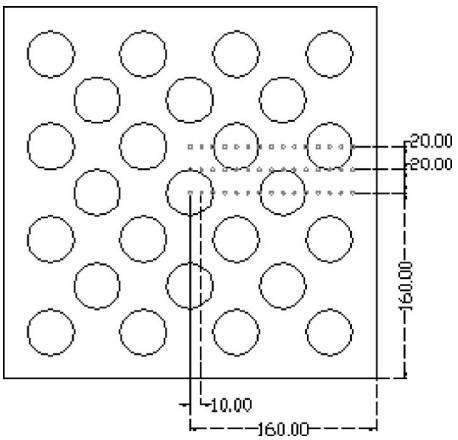

Fig. 5 Static pressure tapping on target plate

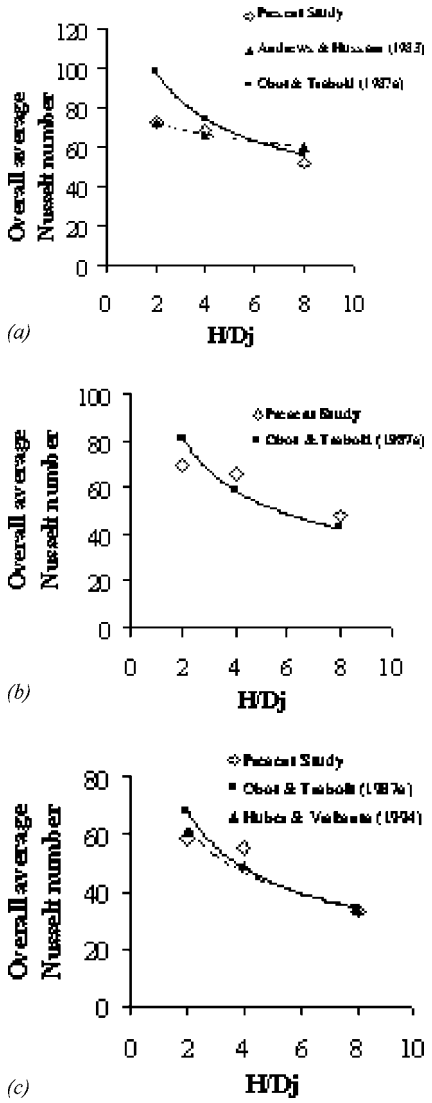

Fig. 6 Comparisons of overall average results of flat plate to literature—consideration of crossflow scheme effect. (*a*) Minimum crossflow. (*b*) Intermediate crossflow. (*c*) Maximum crossflow.

3.1.2 Geometric Effects

3.1.2.1 Effect of crossflow scheme. Impinging jets on dimpled surfaces aimed to use the edges of dimples to detach the boundary layer, and had enhanced the heat transfer on the flat portions adjacent to the dimples. According to Table 1, this effect was done in Phase 1 of the smaller dimples of diameter 17.32 mm, and note that the dimple areas were not taken into account as aforementioned. Dimpled surfaces reacted to the crossflow schemes differently from the flat plate as illustrated in Fig. 7 at H/D_j=2. When the sidewalls were present, the heat transfer was improved significantly, especially with strong crossflow in the maximum crossflow scheme. The coupling effect of impingement and channel flow was proposed, depending on which one dominated.

Downloaded 30 May 2010 to 128.113.26.88. Redistribution subject to ASME license or copyright; see http://www.asme.org/terms/Terms_Use.cfm

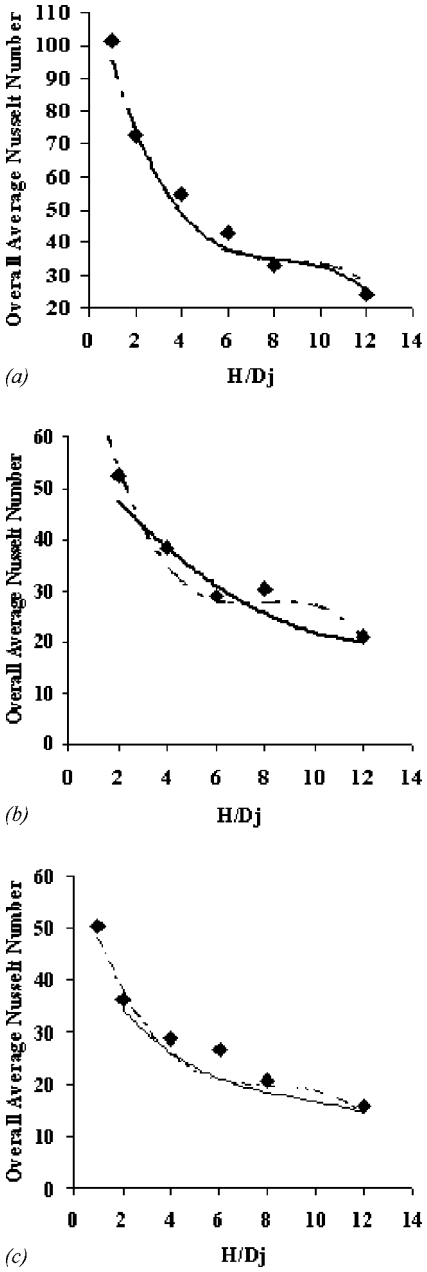

Fig. 7 Comparisons of overall average results of flat plate to literature—results of maximum crossflow scheme at various Re_{Dj} and H/D_j (corresponding to Phase 2, Table 1 ♦ represents data obtained in the present work,—[11,12] (a) Re_{Dj}=11,500. (b) Re_{Dj}=8000. (c) Re_{Dj}=5000.

Figure 8 shows the normalized overall average Nusselt numbers of the hemispherical dimpled plate at different crossflow schemes at H/D_j=2. Figure 9 shows the normalized overall average at various H/D_j values. For the minimum and intermediate crossflow schemes, the application of dimples reduced heat transfer by 8% for both dimple geometries compared to that of the flat plate. Nonetheless, when the strong crossflow was present, the impingement was overwhelmed by channel flow and led to an increase in the heat transfer coefficient by 10% (H/D_j=2). At other H/D_j, the impinging jets on dimples led to the heat transfer improvement, however, the results of the maximum crossflow demonstrated an improvement, compared with those of the flat surface of 28% and 68% for H/D_j=4 and 8, respectively.

3.1.2.2 Effect of dimple geometry. Recalling that both hemi-

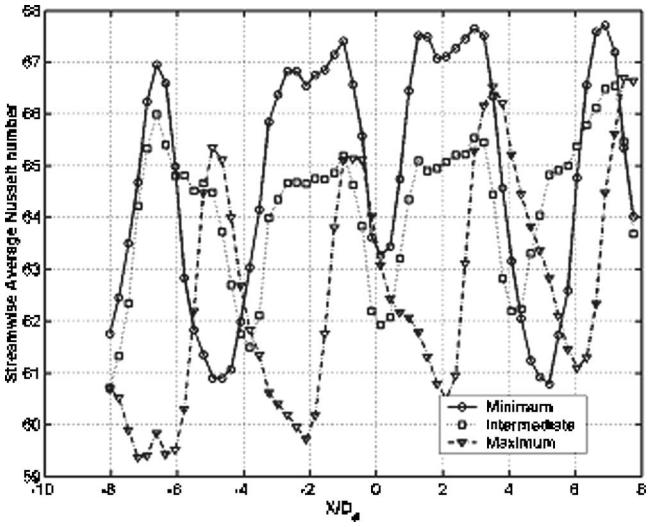

Fig. 8 Streamwise average Nusselt numbers for hemispherical dimples at H/D_j=2, impinging on dimples (Phase 1 in Table 1 [14])

spherical and cusped elliptical shapes were designed based on the same wetted areas, Fig. 10 shows the streamwise average Nusselt number distribution of both shapes compared to that of the flat plate at Re_{Dj}=11,500, H/D_j=4. According to the normalized overall average Nusselt numbers in Fig. 11, the hemispherical

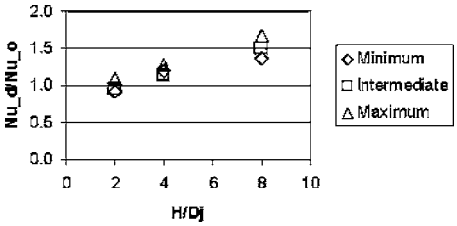

Fig. 9 Normalized overall average Nusselt numbers of hemispherical dimples at different crossflow schemes, impinging on dimples, Re_{Dj}=11,500 (Phase 1 in Table 1)

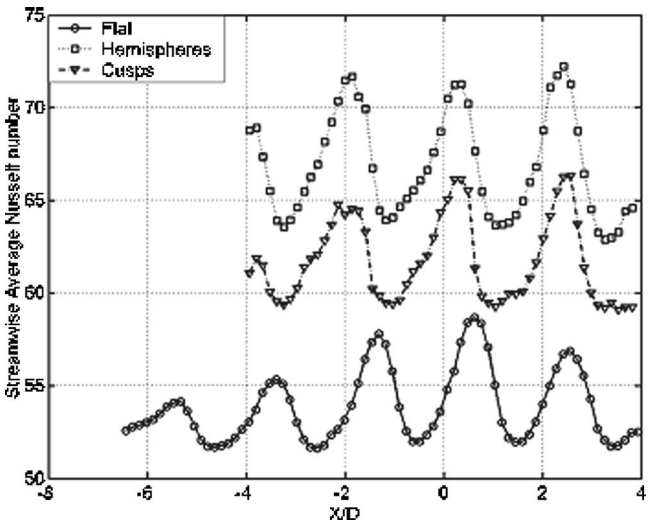

Fig. 10 Streamwise average Nusselt number distribution of different dimple geometries compared to that of the flat surface H/D_j=4, Re_{Dj}=11,500, maximum crossflow, impinging on dimples (Phase 1 in Table 1)

Downloaded 30 May 2010 to 128.113.26.88. Redistribution subject to ASME license or copyright; see http://www.asme.org/terms/Terms_Use.cfm

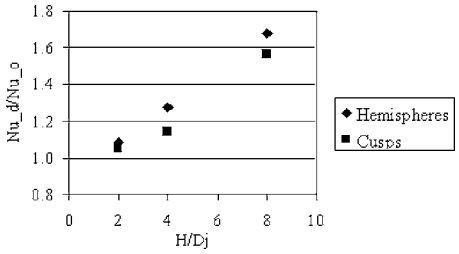

Fig. 11 Normalized average Nusselt numbers of both dimple geometries for maximum crossflow scheme, Re_{Dj}=11,500 (Phase 1 in Table 1)

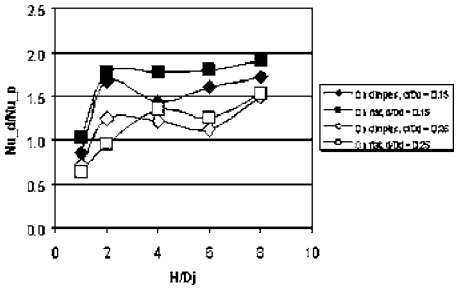

Fig. 13 Normalized overall average Nusselt numbers of dimples with different depths at Re_{Dj}=11,500 (Phase 2, Table 1)

dimples improved the heat transfer by 35%, while the cusped elliptical ones improved it by 26%. This was thought to be due to the double dimples leading to a double rolling-up recirculation, which disturbed the oncoming jets, and thus reduced their temperature as well as momentum

3.1.2.3 Effect of impinging positions. Figure 12 exhibits the comparisons of the streamwise average Nusselt numbers of impinging on dimples and on flat portions at Re_{Dj}=11,500 and H/D_j=2. For the deep dimples (d/D_d=0.25), impinging on dimples (26% improvement on average compared to the result of the flat plate—Fig. 13) led to higher heat transfer results than that on flat portions (no improvement). From the video images, the strong crossflow deflected the jets to impinge on the downstream halves of the upstream rows of the dimples and for the downstream dimple rows on adjacent flat portions. This deflection was thought to function more properly as turbulence promoters. For impinging on flat portions, the oncoming jets were shifted to impinge onto the upstream edges of dimples, which were located downstream of the corresponding flat portions. Additionally, cold regions were found inside the staggered dimples for impinging on flat portions. The jets lost momentum at the upstream edges; hence, the heat transfer was reduced. Notwithstanding, for the shallow dimples (d/D_d=0.15), the results of impinging on flat portions were slightly higher than those of impinging on dimples, because the crossflow could shed the vortices more easily than the deep one. In addition, the distance from the nozzle exit to the stagnation point was narrower, and the jets lost less momentum than impinging on dimples.

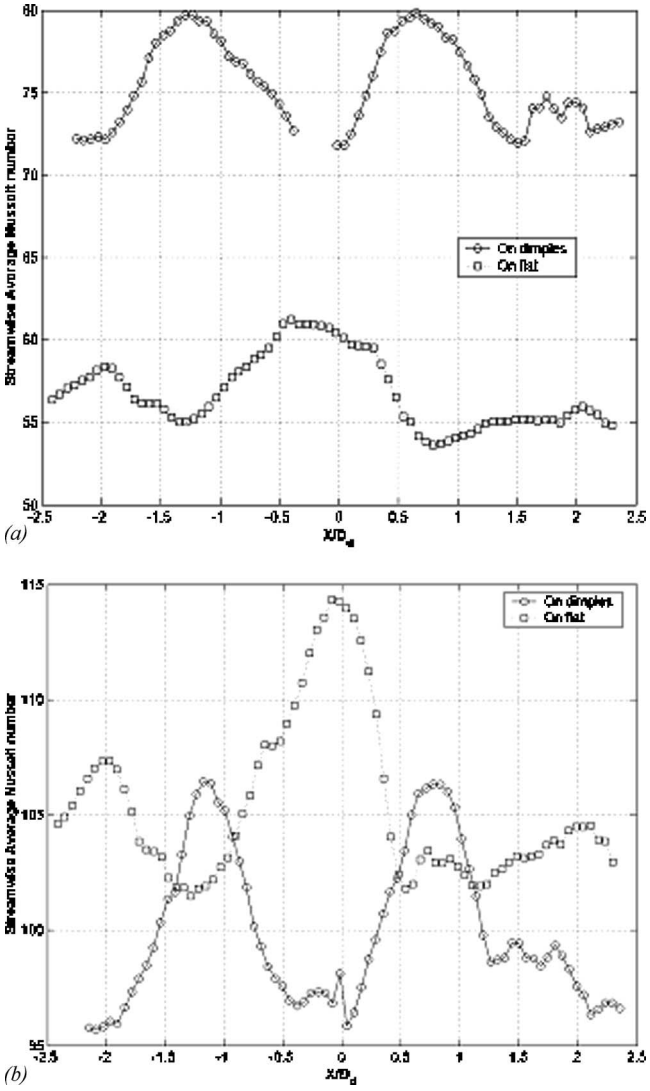

Fig. 12 Streamwise average Nusselt numbers of dimples at H/D_j=2 and Re_{Dj}=11,500 (Phase 2, Table 1). (a) d/D_d=0.25. (b) d/D_d=0.15.

3.1.3 Parametric Effects

3.1.3.1 Effect of Reynolds number. The comparison of the normalized streamwise average Nusselt numbers at H/D_j=8 is shown in Fig. 14. The higher heat transfer improvement was found at Re_{Dj}=11,500, followed by the 8000 and 5000 cases, respectively. In terms of average Nusselt numbers in Fig. 15, the heat transfer at Re_{Dj}=11,500 was 51% higher than that of the flat plate while Re_{Dj} of 8000 and 5000 led to 38% and 22% improvement, respectively. When the jet velocity was increased such as at higher Re_{Dj}, the velocity of the spent air or crossflow was increased, and this allowed the crossflow to deflect the oncoming jets from the intended target positions. This manner led to the heat transfer degradation, especially near the exit. Nevertheless, the

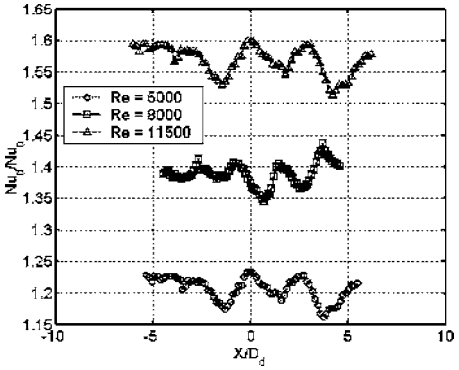

Fig. 14 Normalized streamwise average Nusselt numbers of hemispherical dimples, H/D_j=8 (Phase 1, Table 1 [5])

Downloaded 30 May 2010 to 128.113.26.88. Redistribution subject to ASME license or copyright; see http://www.asme.org/terms/Terms_Use.cfm

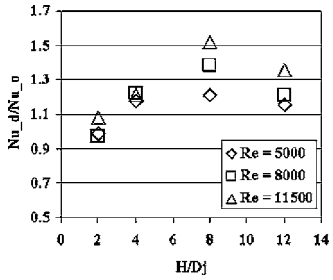

Fig. 15 Effect of Reynolds number on hemispherical dimples, overall average Nusselt numbers at various H/D_j values (Phase 1, Table 1 [5])

presence of dimples assisted the spent-flow to detach in a higher degree than that caused by the flat plate impingement and helped relieve the heat transfer degradation that occurred due to the jet deflection.

3.1.3.2 Effect of jet-to-plate spacing. For the flat plate impingement, the narrow H/D_j led to higher heat transfer. However, the dimple impingement reacted to the effect of H/D_j differently as shown in Fig. 16 that $H/D_j=4$ resulted in higher heat transfer than $H/D_j=2$. This was thought because for the narrow H/D_j, the strong recirculation occurred, and this disturbed the oncoming jets. Hence it caused the heat transfer degradation as seen in Fig. 17 for $H/D_j=2$ that the presence of dimples did not improve the heat transfer compared with that of the flat plate. At wide H/D_j (i.e., $H/D_j=12$), the jets lost momentum to the ambient air during travel towards the target plate.

From the flow visualization of an impinging jet on a concave surface done by Cornaro et al. [13], a potential core occurred at approximately $4.5D_j$, where there was the strong radial oscillation at the stagnation point accelerated and broke down. This ruined the symmetry of the jets, making it dissimilar to impingement on a flat surface. This could explain the heat transfer improvement for moderate jet-to-plate spacings such as $2 \leqslant H/D_j \leqslant 8$.

3.1.3.3 Effect of dimple depth. From the video images, different dimple depths caused different flow propagation from the dimples. However, the trend of heat transfer was similar. Figure 18 shows the streamwise cross section along the inline dimples of $d/D_d=0.15$ and 0.25 at $\mathrm{Re}_{Dj}=11{,}500$ and $H/D_j=4$. The magnitudes of Nusselt numbers of the shallow dimples ($d/D_d=0.15$) are higher than those of the deep ones ($d/D_d=0.25$). The maximum peaks occurred inside the dimples. The overall average quantities in Fig. 19 show that both d/D_d values led to heat transfer improvement compared to the flat surface; the shallow dimples resulted in 48% increase and the deep ones 23.4%.

The shallow dimples conducted higher heat transfer than the deep ones. This was possibly due to the fact that the deep dimples caused higher degree of recirculation while the shallow ones shed

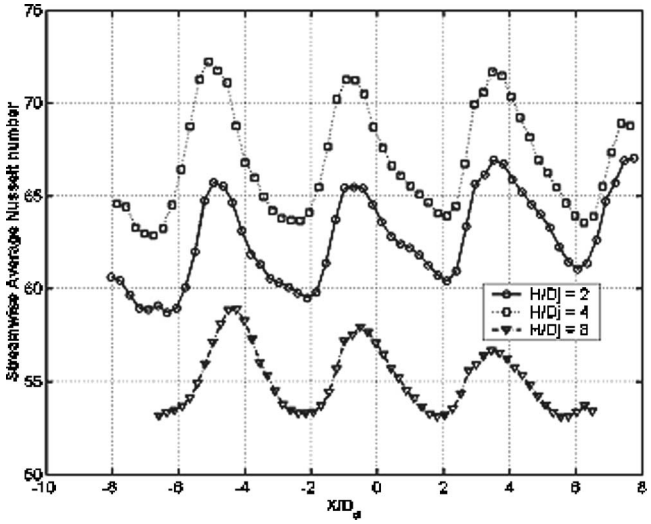

Fig. 16 Streamwise average Nusselt number of hemispherical dimples, maximum crossflow scheme, $\mathrm{Re}_{Dj}=11{,}500$ (Phase 1, Table 1 [4])

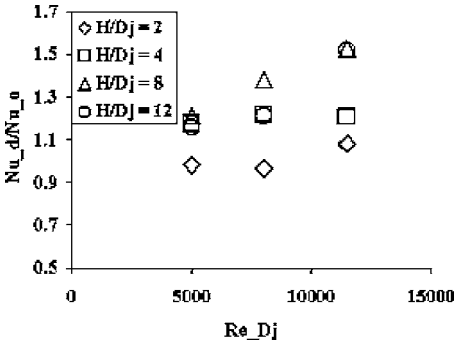

Fig. 17 Normalized overall average Nusselt numbers of hemispherical dimples, maximum crossflow scheme, Re=11,500 (Phase 1, Table 1)

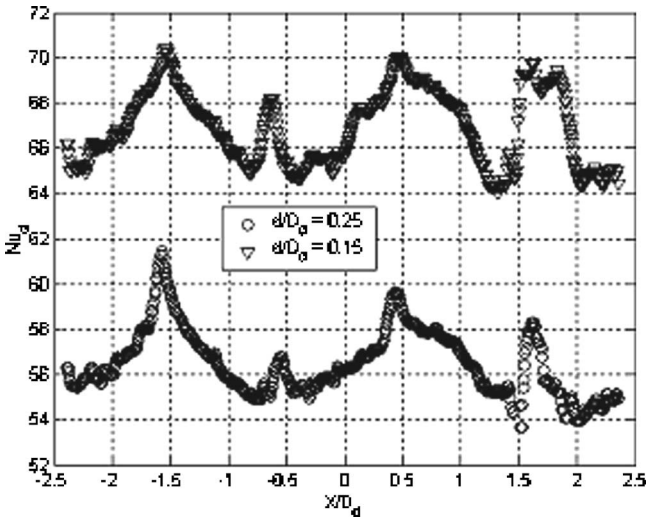

Fig. 18 Cross section along inline dimples (underneath jets) of Nusselt number distribution at $\mathrm{Re}_{Dj}=11{,}500$, $H/D_j=4$ (Phase 2, Table 1 [5])

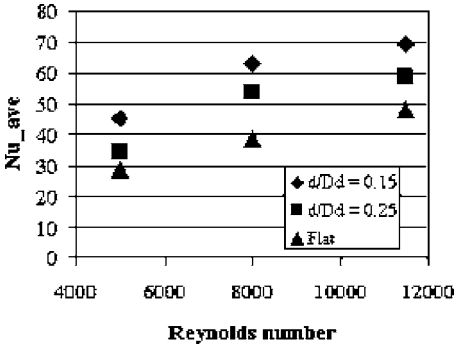

Fig. 19 Overall average Nusselt numbers of dimpled plates of different dimple depths at $H/D_j=4$ (Phase 2, Table 2 [5])

Downloaded 30 May 2010 to 128.113.26.88. Redistribution subject to ASME license or copyright; see http://www.asme.org/terms/Terms_Use.cfm

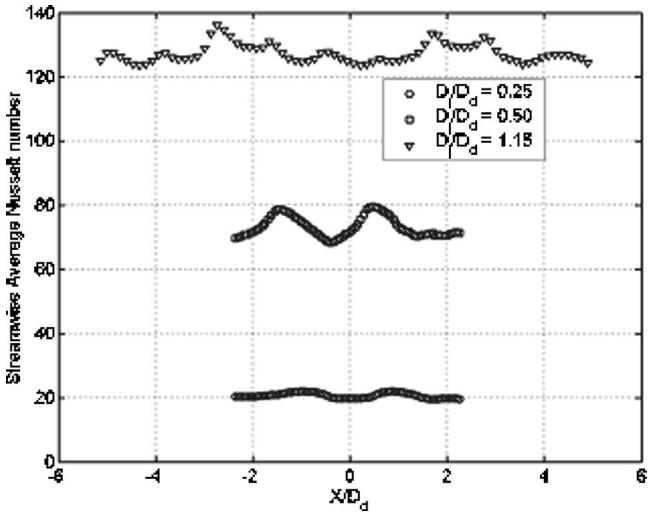

Fig. 20 Streamwise average Nusselt number at $H/D_j=2$, $Re_{Dj}=11,500$, impinging on dimples (see Table 1)

vortices downstream easier and faster. Additionally, the distance from the nozzle exit to the stagnation point for a shallow dimple was narrower than that for a deep one, hence, this led to the higher momentum of the impinging jet.

3.1.3.4 Effect of ratio of jet diameter to dimple diameter. Figure 20 exhibits the streamwise average Nusselt numbers for different D_j/D_d values at $Re_{dj}=11,500$ and $H/D_j=2$. Small $D_j/D_d=0.25$ leads to the lowest heat transfer, and the heat transfer reduction was found compared to the results of the flat plate while the moderate and high D_j/D_d led to heat transfer improvement. The contour plot of the Nusselt numbers for $D_j/D_d=0.25$ suggested that the heat transfer augmentation occurs only inside the inline dimples; after impinging the jets lost their momentum to a large extent. Thereafter, the crossflow was weak. It can be seen from the figure that the low heat transfer occurs everywhere else including the flat portions adjacent to the inline dimples. For the moderate and high D_j/D_d, the heat transfer improvement was found. From the contour plot in Figs. 21(*b*) and 21(*c*), the high heat transfer regions were larger than the $D_j/D_d=0.25$. When the jets traversed towards the dimples, stagnation zones downstream were wider than the dimples themselves. Thus, this allowed the dimple edges to detach and restart the boundary layer on the wall of the plate better. Notwithstanding, the high heat transfer regions for $D_j/D_d=1.25$ were found more than $D_j/D_d=0.50$. This was plausibly due to the fact that there were more dimple peripherals in contact with the jets.

3.2 Pressure Measurements

3.2.1 Pressure Losses. Total pressure was dependent of the crossflow scheme. Figure 22 shows that for the minimum and intermediate crossflow schemes the results show no significant difference. The maximum crossflow led to higher pressure losses especially at $H/D_j=2$ and 4. This was thought to happen because, for the maximum crossflow scheme, the jets lost their symmetry due to the strong crossflow, and at the crossflow exit the areas for $H/D_j=2$ and 4 were less than $H/D_j=8$. From Fig. 23, the total pressure depended on the level of Re_{Dj}, because it is the dimensionless form of the jet velocity, which is changed by the flow rate to the plenum chamber. Hence, the higher Re_{Dj} led to higher pressure loss. When $2 \leqslant H/D_j \leqslant 8$, the total pressure was independent of the jet-to-plate spacing, but it depended on H/D_j at small values such as $H/D_j<2$. Figure 24 exhibits the effect of impinging positions. Impinging on dimples led to higher pressure loss than impinging on flat portions. This could be explained by the

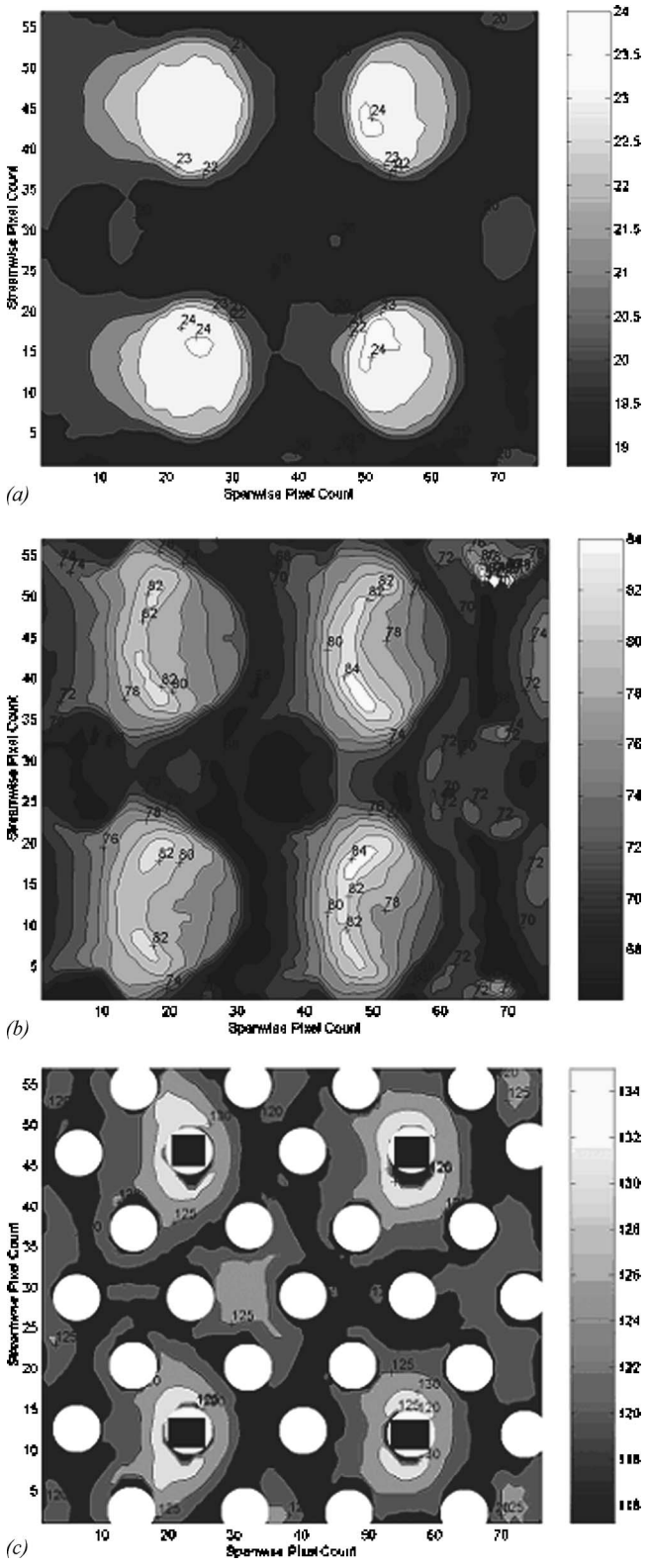

Fig. 21 Contour plots of different D_j/D_d. (a) $D_j/D_d=0.25$ (Phase 3, Table 1). Note that the pitch of the jet plate has become $8D_j$. (b) $D_j/D_d=0.50$ (Phase 2, Table 1). (c) $D_j/D_d=1.15$ (Phase 4, Table 1). Note that the white filled circles represent dimple areas, which are not taken into account, and the filled rectangles are the inline dimples where the jets are impinging.

Downloaded 30 May 2010 to 128.113.26.88. Redistribution subject to ASME license or copyright; see http://www.asme.org/terms/Terms_Use.cfm

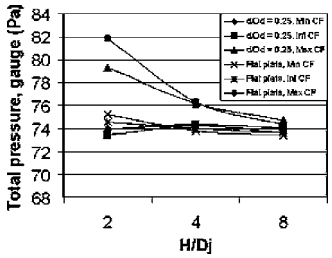

Fig. 22 Effect of crossflow scheme, Re_{Dj}=11,500, impinging on dimples

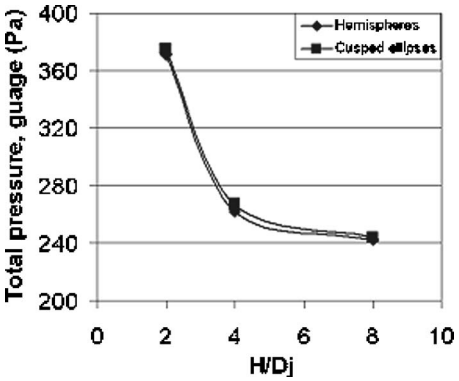

Fig. 25 Effect of dimple geometry

higher degree of the recirculation effect for impinging on dimples. From the same figure, it also shows that the total pressure is insensitive to the dimple depth. Figure 25 shows that the pressure loss is independent of the dimple geometry.

3.2.2 Surface Static Pressure. The labels in Fig. 26 show the position of the data points taken from the target plate, and these were done for the convenience of explaining the results later on. The static tappings were located on three rows: inline dimple row (A), flat portions (B), and staggered dimple row (C). The plate was originally tapped only half of what has been shown in Fig. 26, and, in order to obtain the measurement across the plate, the measurement was done by rotating the plate after finishing measuring half of the plate.

Figure 27 shows the surface static pressure along the inline dimples for various crossflow schemes, Re_{Dj}=11,500 and H/D_j =2. Since symmetry was expected from mid-plate towards the exit for the minimum and intermediate crossflow schemes, the measurement was done for only half the plate. The peaks for these two schemes were symmetric similar to the heat transfer peaks, while for the maximum crossflow scheme where the strong crossflow was present the peaks were shifted downstream—see peaks 3 and 4 representing labels 20 and 28 instead of 19 and 27 like the other two schemes. The strong crossflow also wiped out the peaks downstream. This is analogous to the heat transfer peaks.

Figure 28 exhibits the static pressure along all rows. The maximum peaks along the inline rows are of course higher than those along the flat portions and staggered dimples. However, the minimum peaks of the inline row were lower, especially for the first two peaks. This was thought because after impingement the fluid from the inline dimples was accelerated towards the flat portions adjacent to the corresponding dimples. In addition to being accumulated with the upstream crossflow, the jets lost momentum after impinging, thus, the results along rows B and C were significantly lower than that of row A.

Similar to the heat transfer results on the effect of Reynolds number, higher Re_{Dj} caused higher jet exit velocity. Therefore, increasing Re_{Dj} meant increasing the momentum. The streamwise surface static pressure along the inline dimples for d/D_d=0.15, H/D_j=2, and maximum crossflow is shown in Fig. 29. Re_{Dj} =11,500 led to the highest magnitudes of the peaks. The stagna-

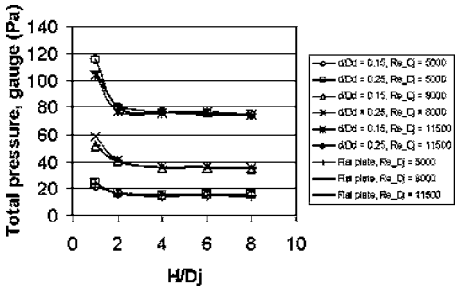

Fig. 23 Total pressure for different setups, impinging on dimples

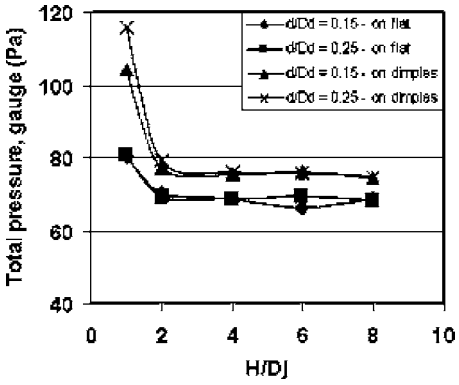

Fig. 24 Effect of impinging positions

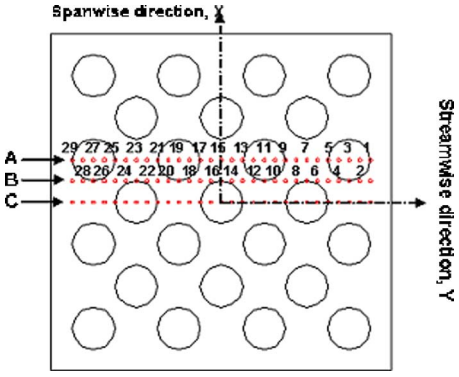

Fig. 26 Dimpled plate with imprinted diameter, D_j=40 mm. Projected view of dimpled plates d/D_d=0.15 and 0.25

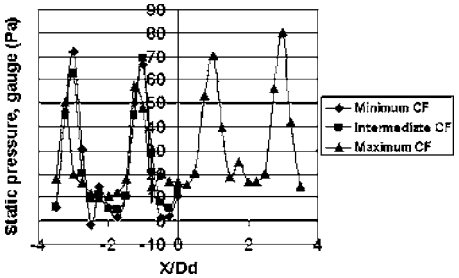

Fig. 27 Crossflow scheme effect on flat plate at Re_{Dj}=11,500, H/D_j=2, streamwise direction

Downloaded 30 May 2010 to 128.113.26.88. Redistribution subject to ASME license or copyright; see http://www.asme.org/terms/Terms_Use.cfm

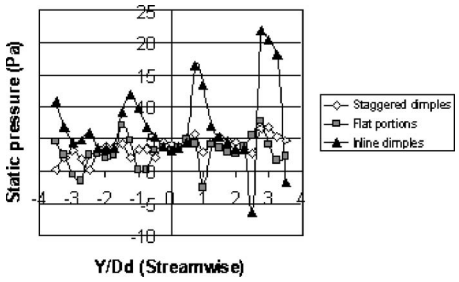

Fig. 28 Surface static pressure measurements across the plate in streamwise direction along all rows at $H/D_j=4$, $Re_{Dj}=8000$, $d/D_d=0.25$, impinging on dimples

tion points of the upstream peaks for all Re_{Dj} values are located on the same position. However, the stagnation point of the second peak for Re_{Dj} was slightly shifted to point 12 instead of 11 like the other two Re_{Dj} values. Due to the crossflow, the stagnation points in downstream were deflected downstream in all cases. Nevertheless, all minimum points appeared at the same position—the downstream edges of the inline dimples—where they accelerated the jet flow towards the flat portions downstream before reaching the next stagnation points. These were analogous to the heat transfer results that the crossflow aided the dimples to function properly as turbulence promoters.

Results for $d/D_d=0.15$ at $Re_{Dj}=11{,}500$ are showed in Fig. 30; the trends are similar for all H/D_j values. However, since impinging the narrow H/D_j contained higher momentum than the wider case, hence the magnitudes of static pressure for narrow H/D_j were then higher. This evidence was analogous to the heat transfer results. The minimum peaks of $H/D_j \geq 1$ are greater than the rest, whose levels were similar. This was thought to occur because at narrow H/D_j, the jets contained higher momentum when impinging onto the dimples and, consequently, the crossflow speed was significantly higher than those of the moderate spacings.

Figure 31 shows the effect of dimple depth at $Re_{Dj}=11{,}500$ and

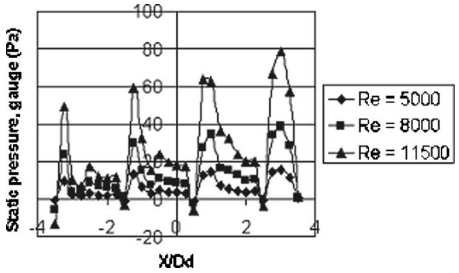

Fig. 29 Surface static pressure along inline dimples at different Reynolds numbers, maximum crossflow, $H/D_j=2$, $d/D_d=0.15$

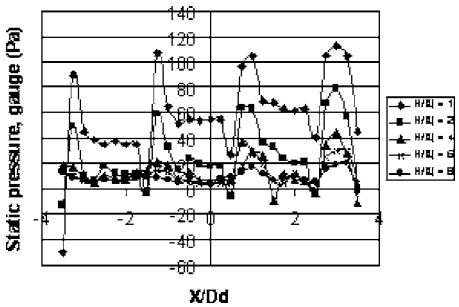

Fig. 30 Surface static pressure along inline dimples at different jet-to-plate spacings, maximum crossflow, $Re_{Dj}=11{,}500$, $d/D_d=0.15$

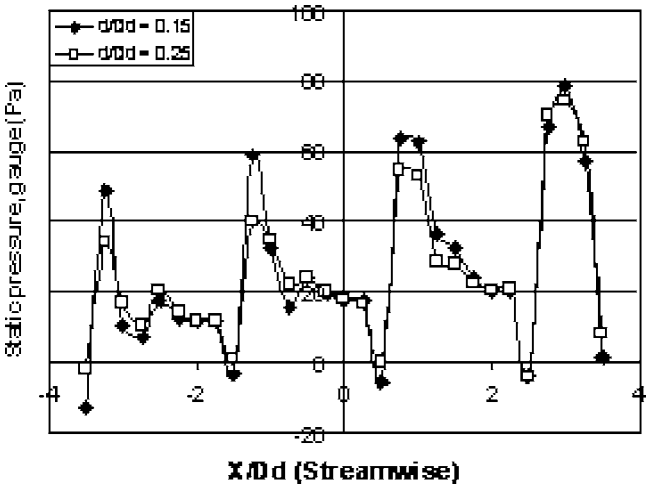

Fig. 31 Surface static pressure along inline dimples at different dimple depths, maximum crossflow, $H/D_j=2$, $Re_{Dj}=11{,}500$

$H/D_j=2$. Both shallow and deep dimples show no significant difference in static pressure on the first peaks upstream. However, further downstream the shallow dimples led to higher static pressure peaks. This was thought to be due to the fact that the oncoming jets mixed with the crossflow, plus the distances from the jet exits to the stagnation points inside the dimples were narrower for the shallow dimples. The impinging jets, therefore, contained higher momentum than the deep ones.

The effect of the ratio of jet diameter to dimple diameter on the surface static pressure is shown in Fig. 32. The small value of $D_j/D_d=0.25$ shows significantly higher stagnation peaks than the moderate and high values, while the static pressure values elsewhere are not significantly different. Since for $D_j/D_d=0.25$ the jets could be assumed entirely impinging within the dimples, according to Ekkad et al. [15], at the same Re_{Dj} the stagnation points contain higher momentum than for $D_j=20$ mm in the other two cases ($D_j/D_d=0.50$ and 1.15), therefore, they were resistant to jet deflection. They were located right underneath the centers of the jet holes even downstream near the exit where the crossflow was expected to be the strongest. The stagnation points of $D_j/D_d=1.15$ also appeared perpendicularly underneath the jet centers. This happened because the stagnation areas covered a wider area than the corresponding dimple. Since the dimples were

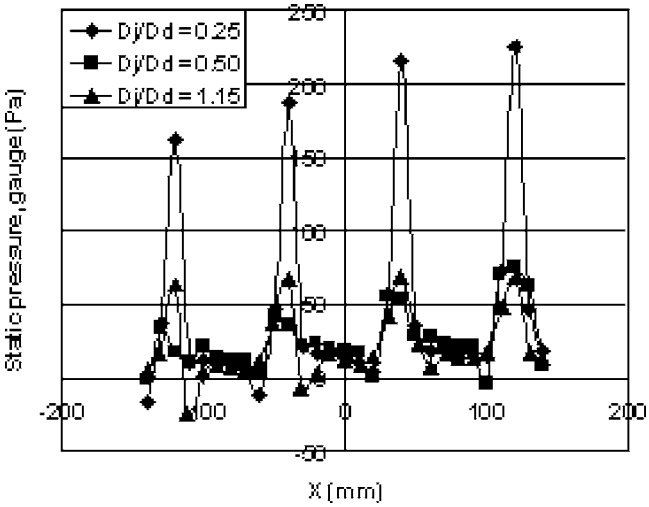

Fig. 32 Surface static pressure along inline dimples at different dimple curvature (D_j/D_d), maximum crossflow, $H/D_j=2$

Downloaded 30 May 2010 to 128.113.26.88. Redistribution subject to ASME license or copyright; see http://www.asme.org/terms/Terms_Use.cfm

denser than the other two cases, dimple edges spontaneously helped detach the boundary layer, and higher turbulence was expected here. Reminiscing the heat transfer results, $D_j/D_d=1.15$ showed the highest heat transfer improvement. Nonetheless, the stagnation points downstream of $D_j/D_d=0.50$ were deflected towards the downstream rims of the dimples. The static pressure in locations other than the stagnation points showed insignificant difference for all cases, possibly due to the crossflow stream containing similar momentum.

The degradation on the stagnation points was not significant for $D_j/D_d=1.15$ compared to the other two cases because the denser dimples stripped the boundary layer better, thus the crossflow did not greatly affect preventing the impinging jets from contacting the target locations. The remarkable degradation in magnitude was found in $D_j/D_d=0.25$ and 0.50.

4 Conclusions

4.1 Heat Transfer and Surface Static Pressure. The tested geometric effects were crossflow scheme, dimple geometries, and impinging positions. The crossflow scheme led to the idea of coupling effect of impingement and channel flow formed by the accumulation of the spent-air flow or crossflow depending on which one dominated. The dimples functioned well as the strong crossflow was present such as for the maximum crossflow scheme, which allowed the dimple edges to detach from the boundary layer. It can be seen from the wall static pressure results that the strong crossflow deflected the jets towards the downstream dimple edges. However, the peaks downstream were wiped out by the crossflow.

Recalling that both dimple geometries, hemispherical and cusped elliptical, were designed based on the same wetted areas, the hemispherical dimples resulted in higher heat transfer. This was thought to be due to the fact that two hemispherical dimples that formed a cusped elliptical dimple caused a higher degree of recirculation than a normal hemispherical dimple.

Different dimple depths led to the different results in the study on the effect of impinging positions; for the shallow dimples, impinging on flat portions resulted in higher heat transfer than impinging on dimples, and vice versa for the deep dimples. This was probably because the shallow dimples shed the vortices formed inside the dimples better, while for the deep dimples the jets lost more momentum.

The experimented parametric effects were Reynolds number, jet-to-plate spacing, dimple depth, and ratio of jet diameter to dimple diameter. As well established by previous researchers, increasing Re_{Dj} means increasing the jet exit velocity, hence, the momentum of the jets at the stagnation zones was higher, and thus the heat transfer was increased. The static pressure also resulted in analogy with the heat transfer.

Jet-to-plate spacing strongly affected the heat transfer. The narrow H/D_j such as $H/D_j<2$ caused vigorous recirculation from the dimple and caused heat transfer degradation compared with the results of the flat plate. However, the wider spacing such as $H/D_j>8$ led to the jets losing the momentum to the ambient air, and the heat transfer decreased. The surface static pressure results show that $H/D_j=1$ and 2 led to significantly higher levels than the rest, while $H/D_j=4$, 6, and 8 resulted in similar levels, especially on the flat portions.

The shallow dimples led to better heat transfer improvement than the deep ones, because they formed less severe recirculation and shed the vortices faster. Additionally, the shallow dimples also resulted in higher surface static pressure downstream than the deep ones.

Impingement occurred entirely inside the dimples for small D_j/D_d such as $D_j/D_d=0.25$. After impinging, the jets lost a great deal of their momentum inside the dimples; hence, the crossflow was not strong enough to allow the dimple edges to detach and restart the boundary layer. This also resulted in significantly high maximum peaks in static pressure at the stagnation points, but the rest were at similar level to the moderate and high D_j/D_d. At $D_j/D_d=1.15$, the stagnation zone covered more dimples than smaller D_j/D_d. This allowed more edges to detach from the boundary layer, and more high heat transfer regions were found than those of the other D_j/D_d values.

4.2 Pressure Losses. Total pressure or total loss was only dependent on the level of Reynolds number and the jet-to-plate spacing less than 2 jet diameters. In addition, it also depended on the crossflow scheme; the maximum crossflow scheme conducted higher pressure loss than the intermediate and minimum ones. It was insensitive to the change of the plate geometry, which includes dimple geometry and dimple depth.

In conclusion, the thermal performance of the dimple impingement was dependent on the heat transfer results rather than the pressure loss. The pressure results over the dimpled plate were not significantly different from those over the flat plate at the same setup condition. This was thought to be due to the fact that the vortices produced from the dimples were organized, hence they helped enhance the heat transfer, whereas, considering this in terms of pressure loss, those vortices did not significantly cause the difference from when the flat plate was employed.

Nomenclature

A_t = total projected area of jet holes
c = thermal capacity of Perspex
d = dimple depth
D_d = dimple diameter
D_j = jet hole diameter
h = heat transfer coefficient
H = distance measured from nozzle plate to target plate
k = thermal conductivity of Perspex
$\dot{m}$ = mass flow rate
$\mathrm{Nu_d}$ or Nu−d = Nusselt number of dimpled surface
$\mathrm{Nu_o}$ or Nu−o = Nusselt number of flat surface
Re = Reynolds number based on a single jet, $\frac{VD_j}{\nu}$ where $V=\frac{\dot{m}}{\rho_j A_j}$
t = elapsed time
T_i = initial temperature of target plate before impingement began
T_m = bulk fluid temperature
V = jet velocity
$-X$ = streamwise distance of target plate
Y = spanwise distance of target plate
z = heat penetration depth in substrate
α = thermal diffusivity of Perspex
ν = dynamic viscosity of air
ρ = density of Perspex
ρ_j = density of air

References

[1] Chyu, M. K., Yu, Y., Ding, H., and Down, J. P., and Soechting, F. O., 1997, "Concavity Enhanced Heat Transfer in an Internal Cooling Passage," ASME Paper No. 97-GT-437.

[2] Kesarev, V. S., and Kozlov, A. P., 1993, "Convection Heat Transfer in Turbulized Flow Past a Hemispherical Cavity," Heat Transfer Res., **25**(2) pp. 156–160.

[3] Moon, H. K., O'Connell, T., and Glezer, B., 1999, "Channel Height Effect on Heat Transfer and Friction in a Dimpled Passage," ASME Paper No. 99-GT-163.

[4] Kanokjaruvijit, K., and Martinez-Botas, R. F., 2004, "Jet Impingement onto a Dimpled Surface with Different Crossflow Schemes," Paper IGTC2003 Tokyo TS-074, 8th International Gas Turbine Congress Tokyo, November 2–7, 2003.

[5] Kanokjaruvijit, K., and Martinez-Botas, R. F., 2004, "Parametric Effects on Heat Transfer of Impingement on Dimpled Surface," ASME J. Turbomach., **126**, pp. 287–296.

[6] Schultz, D. L., and Jones, T. V., 1973, "Heat-Transfer Measurements in Short-Duration Hypersonic Facilities," AGARD-AG-165.

[7] Camci, C., Kim, K., and Hippensteele, S. A., 1992, "A New Hue Capturing

Downloaded 30 May 2010 to 128.113.26.88. Redistribution subject to ASME license or copyright; see http://www.asme.org/terms/Terms_Use.cfm

Technique for the Quantitative Interpretation of Liquid Crystal Images Used in Convective Heat Transfer Studies," ASME J. Turbomach., **114**, pp. 765–775.
[8] Moffat, R., 1990, "Experimental Heat Transfer," 9th International Heat Transfer Conference, Jerusalem, Israel, August 20–24.
[9] Martinez-Botas, R. F., 1993, "Annular Cascade Aerodynamics and Heat Transfer," D.Phil. Thesis, St. John's College, Oxford University.
[10] Andrews, G. E., and Hussain, C. I., 1983, "Impingement Cooling of Gas Turbine Component," *Proceeding of Tokyo International Gas Turbine Congress and Exhibition*, October 23–29.
[11] Obot, N. T., and Trabold, T. A., 1987, "Impingement Heat Transfer Within Arrays of Circular Jets: Part I- Effects of Minimum, Intermediate and Complete Crossflow for Small and Large Spacings," ASME J. Heat Transfer, **109**, pp. 872–879.
[12] Huber, A. M., and Viskata, R., 1994, "Convective Heat Transfer to a Confined Impinging Array of Air Jets with Spent Air Exits," ASME J. Heat Transfer, **116**, pp. 570–576.
[13] Cornaro, C., Fleischer, A. S., and Goldstein, R. J., 1999, "Flow Visualization of a Round Jet Impinging on Cylindrical Surfaces," Exp. Therm. Fluid Sci., **20**, pp. 66–78.
[14] Kanokjaruvijit, K., and Martinez-Botas, R. F., 2004, "An Experimental Investigation of the Heat Transfer Due to Multiple Jets Impinging Normally on a Dimpled Surface," J. Mech. Eng. Sci., **218**, pp. 1337–1347.
[15] Ekkad, S., and Kontrovitz, D., 2002, "Jet Impingement Heat Transfer on Dimpled Target Surfaces," Int. J. Heat Fluid Flow, 23(1), pp. 22–28.

Downloaded 30 May 2010 to 128.113.26.88. Redistribution subject to ASME license or copyright; see http://www.asme.org/terms/Terms_Use.cfm

Control of Three-Dimensional Separations in Axial Compressors by Tailored Boundary Layer Suction

Semiu A. Gbadebo
Siemens Industrial Turbomachinery Ltd.,
Lincoln LN5 7FD, United Kingdom

Nicholas A. Cumpsty
Imperial College,
London SW7 2AZ, United Kingdom

Tom P. Hynes
University of Cambridge,
Whittle Laboratory,
Cambridge CB3 0DY, United Kingdom

One of the important ways of improving turbomachinery compressor performance is to control three-dimensional (3D) separations, which form over the suction surface and end wall corner of the blade passage. Based on the insights gained into the formation of these separations, this paper illustrates how an appropriately applied boundary layer suction of up to 0.7% of inlet mass flow can control and eliminate typical compressor stator hub corner 3D separation over a range of operating incidence. The paper describes, using computational fluid dynamics, the application of suction on the blade suction surface and end wall boundary layers and exemplifies the influence of end wall dividing streamline in initiating 3D separation in the blade passage. The removal of the separated region from the blade suction surface is confirmed by an experimental investigation in a compressor cascade involving surface flow visualization, surface static pressure, and exit loss measurements. The ensuing passage flow field is characterized by increased blade loading (static pressure difference between pressure and suction surface), enhanced average static pressure rise, significant loss removal, and a uniform exit flow. This result also enables the contribution of the 3D separation to the overall loss and passage blockage to be assessed. [DOI: 10.1115/1.2749294]

Introduction

Boundary layer suction has long been used both in external and internal aerodynamics to control flow separations, particularly two-dimensional (2D) boundary layer separation. In turbomachinery, the use of suction or aspiration has been focused mainly on enhancing the loading capacity of the compressor. Typical examples are the works of Kerrebrock et al. [1,2], who employed suction on the blade suction surface to control shock-boundary layer interactions. Merchant [3] and Dang et al. [4] also studied the impact of suction on the aerodynamic design and performance of compressor airfoils, again with emphasis on improving the blade loading. Suction has also been used to manage compressor stability, as carried out by Greitzer et al. [5]. However, little attention has been drawn to the use of suction in controlling three-dimensional (3D) separations in axial compressors, which occur in the corner formed by the blade suction surface and the end wall. This is perhaps due to the complex nature of the separated flow regions as well as limited understanding of their formation. In this paper, the emphasis leading to the use of suction is different; it is not explicitly aimed at enhancing blade loading but in eliminating the 3D separated region, which will in turn remove its deleterious consequences such as reduced blade loading itself, blockage, (which leads to limited static pressure rise) and rise in total pressure loss caused by entropy increase due to mixing of nonuniform separated flow with the main flow downstream.

One of the earliest studies on the use of suction to control 3D corner separation in compressor cascades was carried out by Peacock [6]. A slot equal in length to blade chord and about 2.1% chord wide was created on the end wall and bounded by the blade suction surface. With a bleed flow of 0.6% of inlet mass flow, the 3D separation was removed. Attempts were also made to optimize the slot length and width to obtain the minimum bleed mass flow. However, the mechanism involved in the formation of the corner separation itself was not addressed. Also, the effect of bleed flow on bleed pressure (hence efficiency of bleed) and the effect on the blade loading were not investigated.

A description of how a 3D separation forms on the suction surface/end wall corner of compressors is given in Ref. [7], and with greater detail in Ref. [8]. The 3D separation is characterized by the appearance of separation lines along which limiting streamlines or skin-friction lines converge on the suction surface and the end wall. The separated region is bounded by these separation lines, both of which are found to originate from a common singular point on the end wall corner. This description is illustrated in Fig. 1, which shows the computed suction surface and end wall streamlines in the separated region of a linear cascade of modern prescribed velocity distribution (PVD) stators, operated at 0.0 deg incidence. At this incidence, this common origin of the suction surface and end wall separation lines is located at a distance of about 37% axial chord from the leading edge. The behavior of the limiting streamlines that surround the point shows it to be a multiple node-saddle singular point (N and S) wherein it appears as a node on the end wall and a saddle point on the suction surface. A brief description of nodes, saddle point, and other singularities that occur in general can be found in Ref. [7]. The cascade was also operated at −7.0 deg incidence when the separated region was reduced in size, causing the origin of the separation lines to be moved downstream to a distance of about 46% axial chord from the leading edge.

As can be seen from Fig. 1, the suction-side leg of the leading edge horseshoe vortex system, which originates from the leading edge stagnation (saddle) point, terminates on the nodal point N from which the end wall separation line originates. The same point takes the form of a saddle S on whose arm forms the separation line on the suction surface. Hence, the dividing streamline plays a significant role in the formation of 3D separation in the blade passage. This streamline, like other limiting streamlines in the end wall boundary layer, turns more sharply toward the suction surface due to the imposition on the boundary layer of the

Contributed by the Turbomachinery Division of ASME for publication in the JOURNAL OF TURBOMACHINERY. Manuscript received November 18, 2005; final manuscript received January 25, 2007; published online December 19, 2007. Review conducted by Greg Walker.

 Copyright © 2008 by ASME

Downloaded 30 May 2010 to 128.113.26.88. Redistribution subject to ASME license or copyright; see http://www.asme.org/terms/Terms_Use.cfm

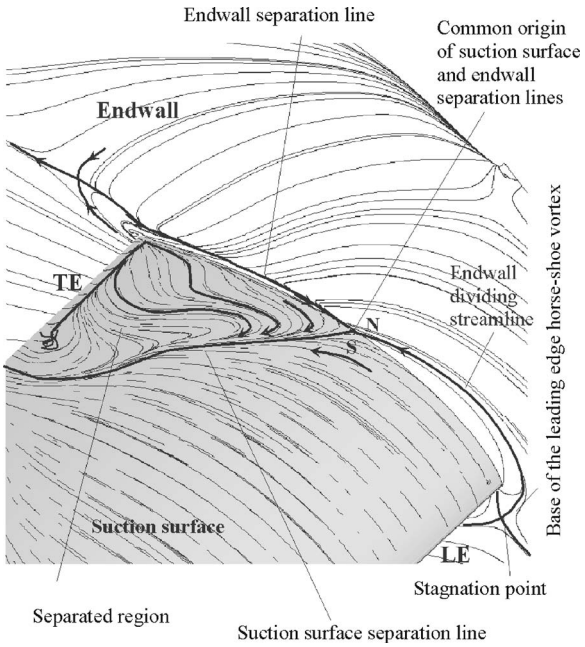

Fig. 1 Computed suction surface and end wall limiting streamlines showing 3D separated surface flow pattern on the compressor cascade of PVD stators, *i*=0.0 deg (S=saddle; N =nodes)

bulk circumferential pressure gradient needed to turn the main flow. As explained in Ref. [7], the dividing streamline, which presumably is characterized by relatively low shear stress (since it originates from a zero shear stress point), experiences the greatest influence of the adverse streamwise pressure gradient building up along the corner. This causes its shear stress to drop back to zero on the nodal point (N) as it interacts with the suction surface. A close inspection of Fig. 1 shows that the overturned limiting streamlines reverse direction as they converge on the end wall separation line near the suction surface. This is due to the strong adverse pressure gradient imposed on the low momentum fluid particles in the boundary layer. With increased incidence or flow turning, the adverse pressure gradient along the corner can also be steep enough to cause the dividing streamline itself to reverse direction before interacting with the suction surface, as observed in Ref. [7].

Since 3D separation is observed to be initiated from the end wall, it is believed that any control method should be applied there to be most effective. The use of suction in the present analysis is therefore intended to target the suction-side leg of the dividing streamline by sucking it off before it reaches the suction surface, in order to prevent bifurcation from taking place on the end wall corner (i.e., splitting to form into the separation lines on the suction surface and end wall). A second and related function is to bleed the overturned and reversed end wall boundary layer from the suction surface so that the suction surface boundary layer near the end wall can develop unhindered, just like the flow near the midspan. A computational fluid dynamics (CFD) investigation was carried out to assess the influence of suction by modeling the flow in the passage of the linear cascade of blades, shown in Fig. 1, to represent the predicted limiting streamlines for the datum case without bleed. This was then followed by an experimental study involving flow visualization, surface static pressure, and exit total pressure loss and flow angle measurements.

Cascade Description

A low-speed compressor cascade used in this study consists of five modern PVD blades. Details of the cascade are given in Ref. [7] in which it is referred to as cascade 2. The cascade geometry, measured flow, and inlet boundary layer parameters are shown in Table 1. Surface mounted tufts were used for the experimental flow visualization on the cascade, area traverses were performed with a three-hole probe located at about 50% axial chord downstream of the trailing edge (where the radial velocities are negligible), and the measurement procedure is the same as that given in Ref. [7].

Table 1 Compressor cascade geometry and inlet boundary layer parameters

Cascade geometry	
Profile	PVD
Chord (m)	0.1515
s/c	0.926
h/c	1.32
t/c	0.1
α_1	34° and 41.0°
Blade inlet angle	41.0°
Blade exit angle	−1°
Aerodynamic parameters	
Incidence	−7.0° and 0.0°
Re (inlet)	2.3×10^5
2D diffusion factor	0.49
de Haller No.	0.8
Inlet boundary layer parameters	
δ (mm)	5.23
δ^* (mm)	0.507
θ (mm)	0.29
H	1.75

Computational Procedure

The code employed is MULTALL, a fully 3D multistage Reynolds averaged Navier–Stokes (RANS) solver of Denton [9], which, in simple terms, is capable of modeling shroud, bleed, and cooling flows in turbomachinery. It is a more robust version of MULTIP also by Denton [10]. The code uses a scheme that is second order accurate in space and solutions can be obtained for flows from very low Mach number of about 0.1 to supersonic flows. The calculations are carried out using a control volume formulation on an "H-type" mesh. The wall shear stress is modeled using wall functions that assume the first grid point from the surface to lie at the start of the logarithmic region of a turbulent boundary layer. Away from the surfaces, shear stresses are obtained by a simple eddy-viscosity mixing-length turbulence model. The suction or bleed is modeled in this code as a "boundary condition." Hence, details of the flow field within the bleed slot or plenum need not be considered. As a normal physical boundary condition, the mass flux normal to the wall is set to zero. With suction applied, the boundary condition of zero mass flux is replaced by the mass flux being bled off from the surface, which, in this case, could be either the end walls or the blade surfaces. The overall mass bleed-off is specified, but the local velocity normal to the wall is fixed by the local static pressure in the flow above the wall

About 11 grid points were used to resolve the boundary layer on the blade surfaces, while 17 grid points were used for the boundary layer on the end wall; together these were found adequate to resolve the 3D boundary layer along the corner. The grid points in the pitchwise, streamwise, and spanwise directions were $49\times159\times99$. The experimentally measured inlet profiles of stagnation pressure and absolute flow angles were used to define the inlet conditions, while the measured inlet and exit static pressures were used as a guide for fixing the pressure ratio. The solutions converged smoothly to an average residual error in the midspan meridional velocity of between 0.02% and 0.08%, depending on

Downloaded 30 May 2010 to 128.113.26.88. Redistribution subject to ASME license or copyright; see http://www.asme.org/terms/Terms_Use.cfm

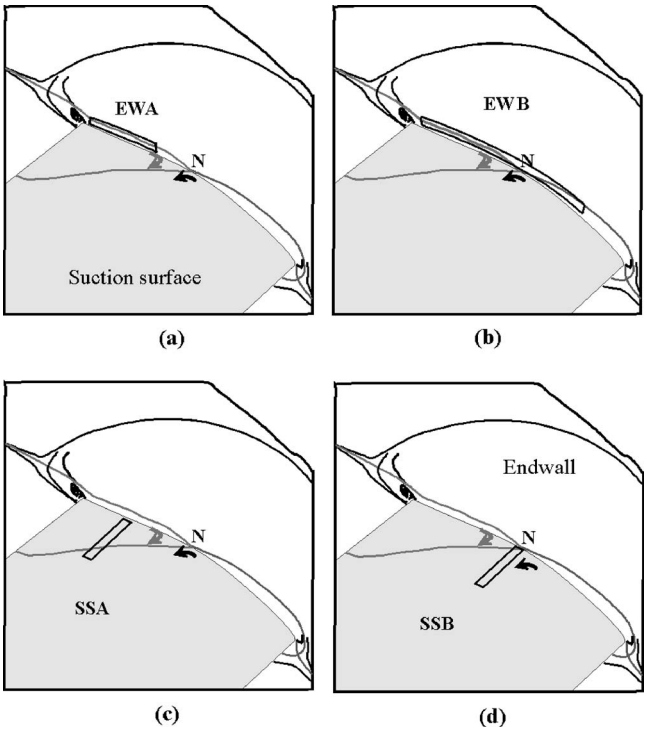

Fig. 2 Illustration of the suction slot configurations (not to scale) on the end wall and the blade suction surface: (*a*) EWA, (*b*) EWB, (*c*) SSA, and (*d*) SSB.

the magnitude of separations, at an average of about 14,000 time steps. Calculations with suction, however, converged faster as the 3D separation was being controlled.

Five separate "numerical" slot arrangements were considered using CFD: three on the end wall and two on the suction surface. Four are illustrated schematically in Fig. 2, and the fifth EWC is similar to EWA but further upstream to run from 15% chord. For comparison, where the blade joins the other end wall, there are no slots.

The slot arrangements can be described as follows.

End Wall Slots, EWA and EWB. Each of the two end wall slots is located at about 2% chord from the suction surface and is also about 2% chord wide. They both run parallel to the suction surface. The first one, referred to as EWA, as shown in Fig. 2, runs from 55% to 90% axial chord. This is purposely located beyond the point of bifurcation such that the dividing streamline would be allowed to interact with the suction surface. In the other configuration (referred to as EWB), the slot extends from about 16% to 90% axial chord. In this case, the dividing streamline together with other neighboring weak limiting streamlines would be sucked off, preventing their interaction with the suction surface.

Suction Surface Slots, SSA and SSB. Slots were also positioned on the blade suction surface used for CFD in order to investigate the role of suction surface boundary layer. In the first case, a rectangular slot of width of about 3% chord and a length of a quarter of blade span was positioned at about 2% chord from the end wall and centered at about 70% axial chord. In this position, the slot lies fairly within the original separated region such that after sucking off the low-energy fluid, new boundary layer can grow just downstream of it. This configuration is referred to as SSA. In order to specifically target the singular point from which the original suction surface separation line develops, the slot was moved upstream and centered at about 37% and 41% axial chords at 0.0 deg and −7.0 deg incidence, respectively. This is designated as SSB.

Suction Rates. A number of calculations were performed at −7.0 deg and 0.0 deg incidence with suction rate gradually increased at each incidence until the minimum suction mass flow just enough to remove 3D separations (but only for EWB was it fully removed) from the suction surface was achieved. This was carried out for each slot configuration. At 0.0 deg incidence, a minimum suction mass flow of about 0.7% of the bulk inlet mass flow was found to be significant in controlling the size of 3D separation. This suction mass flow was then fixed for all the slot configurations. At −7.0 deg incidence, about 0.4% of inlet mass flow was found to be effective because of reduced size of the separated region. Rather than expressing the suction mass flow as a percentage of the bulk inlet mass flow, a more appropriate way is to make the suction mass flow dimensionless using the end wall inlet boundary layer mass flow over a pitch, which is given as

$$\dot{m}_{\mathrm{bl}} = \rho s V(\delta - \delta^*) \tag{1}$$

This is because it is the boundary layer that is being removed and also, the mass flow into the boundary layer at the inlet does not change when the bulk inlet mass flow changes, for example, due to alterations in the blade span or hub-to-tip ratio. Computational analysis carried out in Ref. [8] suggests that the spatial extent of the 3D separated region on the suction surface remains almost constant when the aspect ratio is varied due to the changes in blade span, while other blade geometric parameters such as pitch-chord ratio, stagger angle, blade inlet, and exit angles are held fixed. Hence, while the suction mass flow needed to control the size of the separated region in this case will be fixed for different blade spans, the bulk inlet mass flow will vary. In the present analysis, the suction mass flows of 0.4% and 0.7% of the inlet mass flows at −7.0 deg and 0.0 deg incidence are equivalent to about 14% and 25.6% of the end wall inlet boundary layer mass flows, respectively.

Thickness of 3D Separated Layer. The concept of relative displacement thickness was presented in Ref. [7] for estimating the thickness of the 3D separated layer perpendicular to the suction surface at the trailing edge. It is the displacement thickness at other radial locations minus that at the midspan. It can be normalized as a fraction of blade chord as

$$\{\delta^*(r) - \delta^*_{\mathrm{mid}}\}/c \tag{2}$$

where displacement thickness is given as

$$\delta^*(r) = \int_0^{\delta} \left[1 - \frac{\rho\nu(r,s)}{\rho_{\mathrm{fs}} V_{\mathrm{fs}}}\right] ds \tag{3}$$

This is used here to further judge the extent of removal of 3D separation by suction. As mentioned in Ref. [8], the close coupling between the suction surface and the end wall boundary layer at the trailing edge corner does not allow a clear edge of the blade surface boundary layer until some distance from the end wall, say, about 5% span. The local midpitch velocity is therefore used to approximate the freestream velocity V_{fs}, where the latter is not properly defined close to the end wall.

Calculation of Exit Blockage. The overall exit blockage is determined using a method somewhat similar to the approach of Khalid et al. [11], where blockage is related to one-dimensional static pressure rise. In this particular case, the entire flow field is treated as one-dimensional using pitchwise and spanwise averaged quantities.

From Bernoulli's equation, an ideal static pressure coefficient can be written as

$$C_{P2} = \frac{P_2 - P_1}{(1/2)\rho V_1^2} = 1 - \left(\frac{V_2}{V_1}\right)^2 \tag{4}$$

If the overall (pitchwise and spanwise) averaged exit velocity is denoted by $\bar{V}_2$, then the overall velocity ratio can be expressed in terms of the actual pressure rise coefficient and the flow areas as

Downloaded 30 May 2010 to 128.113.26.88. Redistribution subject to ASME license or copyright; see http://www.asme.org/terms/Terms_Use.cfm

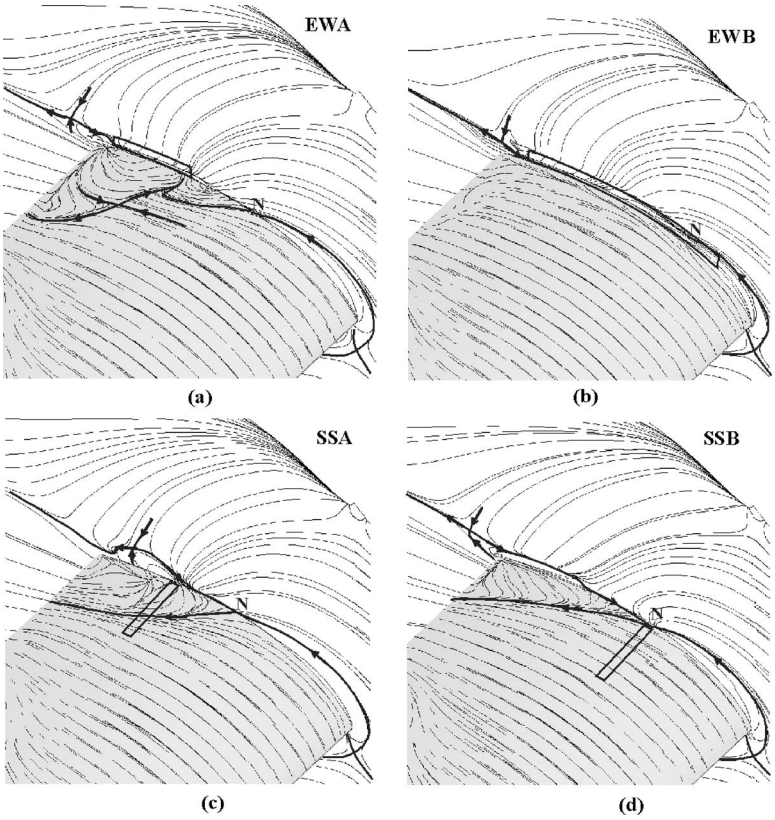

Fig. 3 Predicted limiting streamlines on the end wall and the blade suction surface of the cascade for the four suction slot configurations, *i*=0.0 deg: (*a*) EWA, (*b*) EWB, (*c*) SSA, and (*d*) SSB

$$\frac{\bar{V}_2}{V_1} = (1 - C_{P2})^{1/2} = \frac{A_1}{A_{2e}} \tag{5}$$

where A_1 and A_{2e} are the inlet and the effective exit flow areas, respectively. With A_2 denoting the geometric exit area, blockage as defined in Ref. [12] can be written as

$$B = 1 - \frac{A_{2e}}{A_2} \tag{6}$$

which can now be related to the average exit static pressure rise coefficient as

$$B = 1 - \frac{A_1}{A_2}(1 - C_{P2})^{-1/2} = 1 - \frac{\cos \alpha_1}{\cos \alpha_2}(1 - C_{P2})^{-1/2} \tag{7}$$

where α_1 and α_2 are the nominal inlet and exit flow angles at the midspan.

It will be realized that a reduction in blockage, such as suction produces, leads to an increase in the static pressure rise in the blade row.

Numerical Results

Figure 3 shows the suction surface and end wall limiting streamlines for the four slot configurations at zero incidence. For EWA, Fig. 3(*a*), a region of 3D separation is still clearly visible on the suction surface. This is because the slot is placed downstream of the point of origin (N) of the separation lines. The extent of the separated region is, however, reduced when compared to the datum in Fig. 1. The original end wall separation line has largely been sucked into the suction slot with only the part downstream of the slot near the trailing edge remaining. For the EWB configuration, shown in Fig. 3(*b*), it can be seen that the entire separated region has been practically eliminated; since the slot EWB has been extended upstream in order to capture the dividing streamline, the removal of separation confirms the argument that under the inherent adverse streamwise pressure gradient, the formation of 3D separation is associated with the interaction of the dividing streamline with the suction surface. A closer look at the end wall for both EWA and EWB configurations shows a strong curvature of the limiting streamlines as they are being drawn into the slot.

The limiting streamlines for the suction surface slot (SSA and SSB) clearly show that for both configurations, the extent of the 3D separated region is reduced but, as can be seen, neither of the two is able to remove it fully. For SSA and SSB, the suction surface and end wall separation lines appear in a similar way to the datum and originate where the dividing streamline interacts with the suction surface, as in the datum case in Fig. 1. From here, it can be concluded that 3D separation is not initiated from the suction surface but from the end wall.

Figure 4 compares the spanwise variation of relative displacement thickness (i.e., the extra thickness of the separated layer over the midspan value) at the trailing edge for the datum and the four suction configurations at incidence of 0.0 deg. Apparently, all the slot arrangements are able to reduce the thickness of the 3D separation when compared to the datum case. However, it can be seen that the entire thickness of the 3D separated layer is virtually removed with EWB configuration in which the suction slot is able to capture the dividing streamline and also suck off bulk of the drifted end wall boundary layer from the suction surface in the end wall region.

Experimental Investigation

The numerical results prompted an experimental investigation to be carried out and, following the conclusion drawn above, only the experiment on end wall slot configurations was considered. The end wall suction slot was approximated by a series of holes

Downloaded 30 May 2010 to 128.113.26.88. Redistribution subject to ASME license or copyright; see http://www.asme.org/terms/Terms_Use.cfm

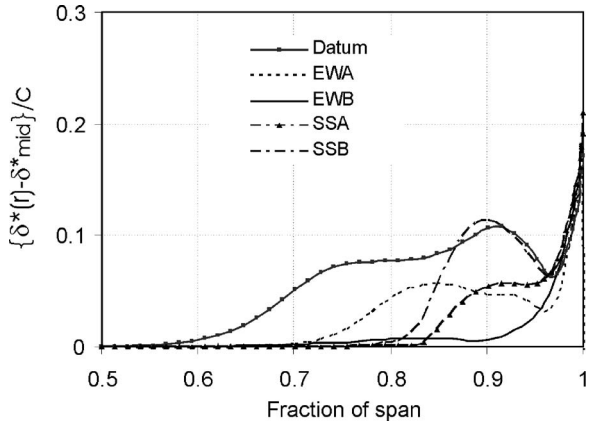

Fig. 4 Computed spanwise variation of the thickness of the separated layer at the trailing edge of the cascade for the four suction slot configurations, *i*=0.0 deg

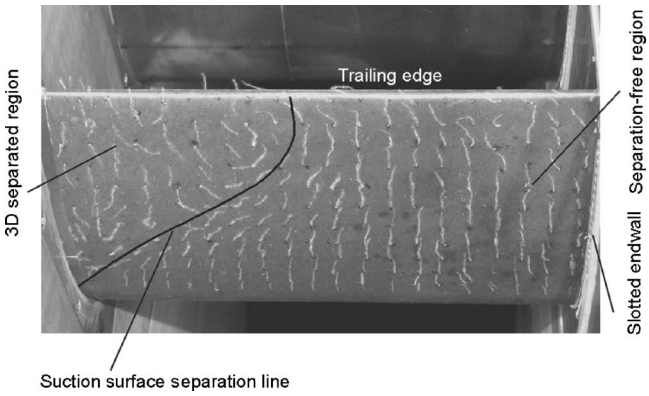

Fig. 6 Suction surface tuft flow visualization with end wall suction EWB configuration, *i*=0.0 deg

that covers the entire length of slot configuration EWB and has constant diameter equivalent to the width of the slot. The holes were drilled on a "perspex" plate, replacing the original end wall, and were repeated in all passages of the cascade. The slotted perspex then formed part of the wall of the plenum within which an equilibrium average bleed pressure can be measured. Calibration of the plenum was carried out in terms of the bleed characteristic. This relates the average bleed pressure to the bleed mass flow and was measured for the equivalents of the EWA and EWB configurations.

Results and Discussion

Figure 5 shows the measured variation of the average bleed pressure coefficient with bleed mass flow for the end wall slots. It can be seen that for the same operating incidence, the extended slot EWB displays a relatively gently sloped bleed characteristics, with less pressure loss for the same bleed mass flow when compared with EWA. Also shown is the bleed characteristic for a short slot similar to EWA but located upstream to run from 15% axial chord, EWC, for which its steep characteristic indicates an increased bleed pressure loss, relative to EWB, for bleed mass flow at the level needed to have any effect. This is to be expected since the bleed pressure is anticipated to reflect the average of the local

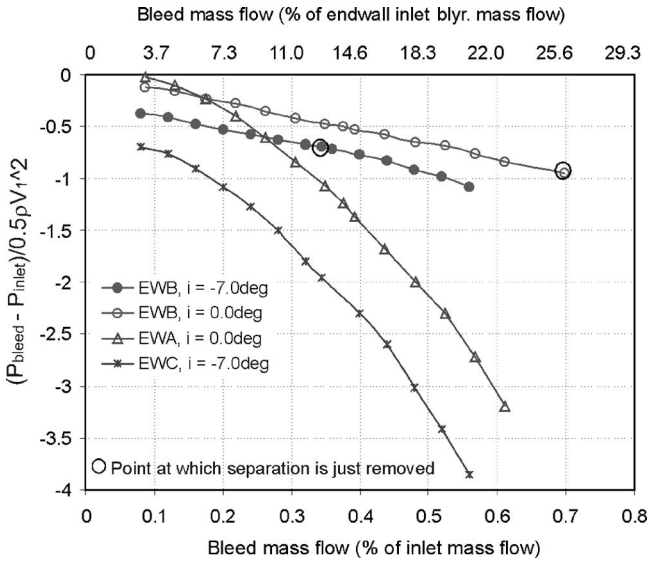

Fig. 5 Bleed characteristics for end wall slot configurations

static pressures on the wall/suction surface corner where the slot is located and EWC is nearer to the blade suction peak. It can, therefore, reasonably be concluded that bleeding with the longer slot EWB will require less suction power than the shorter slots. Furthermore, as the magnitude of 3D separation varies with incidence, as illustrated in Ref. [7], so does the position of the nodal point N depicted in Fig. 2. Thus, a long slot such as EWB will be able to intercept the dividing streamline at different operating points of the compressor with a high probability of being able to prevent the interaction with the suction surface.

As can be seen from Fig. 5, for the same slot geometry, the variation of average bleed pressure with bleed mass flow is a function of incidence. The bleed mass flow, at which 3D separation was just removed for EWB slot configurations at the two levels of incidence tested, is also indicated on the symbols by the circles. At $i=-7.0$ deg, the figure shows that separation was removed at a bleed static pressure in the plenum of about 70% of inlet dynamic head below cascade inlet static and at a bleed mass flow of 0.35% of inlet mass flow. At 0.0 deg incidence, the corresponding bleed plenum static pressure when separation was removed increased to about 95% of inlet dynamic head with 0.7% flow removed. In agreement with the numerical prediction, separation was only partly reduced with both the EWA and EWC configurations.

It should be pointed out that for the same bleed mass flow into slots of the same width but different lengths, mass flow per unit slot length will be different, which would imply different velocities into the slots and hence different bleed pressure coefficients. However, because the flow into the slot itself depends on the blade suction surface pressure distribution along the corner, which is not uniform, the bleed pressure coefficient for slots of the same size but placed at different locations along the corner will also be different. It is, therefore, not physically possible in the experiment or numerically (if the bleed slot geometry is modeled with pressure-driven flow) to achieve the same mass flow per unit slot length for similar slot size, but located differently along the end wall corner.

Cascade Performance With End Wall Suction (EWB). The suction surface tuft flow visualization at zero incidence with the EWB slot is depicted in Fig. 6. This matches well the computed limiting streamlines and thus confirms the predicted removal of 3D separation. The contours of total pressure loss measured at 50% axial chord downstream of the trailing edge at 0.0 deg incidence are presented in Fig. 7 for the datum and end wall suction. As a consequence of the removal of 3D separation, it is clear from the figure that the loss core caused by the interaction of the separated flow with the mainstream has been eliminated: what is left now is the loss due to the wakes and the end wall boundary layer. Consequently, when suction was applied, the overall mass-

Downloaded 30 May 2010 to 128.113.26.88. Redistribution subject to ASME license or copyright; see http://www.asme.org/terms/Terms_Use.cfm

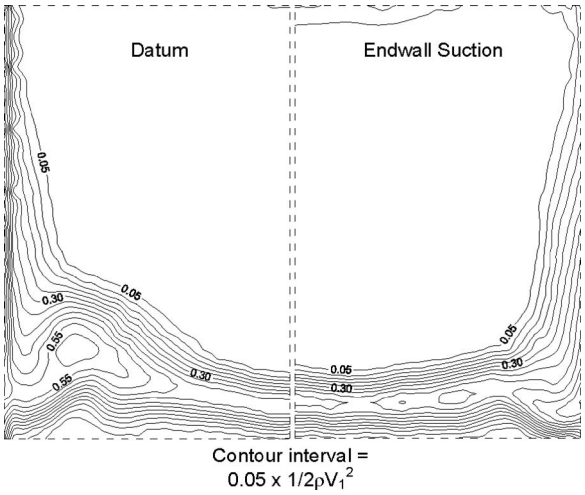

Fig. 7 Comparison of contours of measured exit total pressure loss for the compressor cascade with and without end wall dividing streamline suction, *i*=0.0 deg

averaged total pressure loss was found to reduce by about 22% relative to the datum without slots. This reduction is equivalent to about 2% of the inlet dynamic head. The measured and computed reduction in exit blockage and total pressure loss with suction is illustrated in Table 2, which shows a fair agreement between measurement and computation. It can be seen that 3D separation contributes up to about 35% of the overall blockage at −7.0 deg incidence and to over 40% of the total blockage at 0.0 deg incidence.

The blade used here is characteristic of a compressor stator. In the Appendix, an approximate calculation is carried out to compare the gains to the mainstream flow with the inevitable lost work associated with compressing air, which is then bled off to a lower pressure. Suppose this blade row forms part of a repeating stage with mean flow coefficient (V_x/U) of 0.5. Further suppose that the bled air is allowed to reenter the stream ahead of the upstream rotor (forming the stage), as illustrated in the Appendix, and that it does so with no effect on the primary flow. An estimate for the lost work to the bled air (i.e., the cost of bleeding air) can be compared with the reduction in total pressure loss to the main flow in the stator (i.e., the benefit to the primary flow). The gain in mainstream primary stagnation pressure is found to be worth 1.5 times the work lost in the bled air for the zero incidence case.

If the blade row with end wall suction were the exit guide vanes upstream of the combustor, then it would be static pressure rather than stagnation pressure which would matter. (There might be a downstream diffuser, and the reduction in blockage would then further increase the static pressure rise.) In this particular case, the increase in exit static pressure rise is estimated to be worth about four times the loss associated with the bled air for the zero incidence case.

Figures 8(*a*) and 8(*b*) shows the measured and computed surface static pressure distributions for the cascade near the end wall

Table 2 Total pressure loss and blockage reduction due to end wall suction (EWB) configuration

	Blockage reduction (%)		Loss reduction (%)	
i (deg)	Expt.	CFD	Expt.	CFD
−7.0	35.8	35.3	18.3	19.9
0.0	41.9	49.3	21.9	24.6

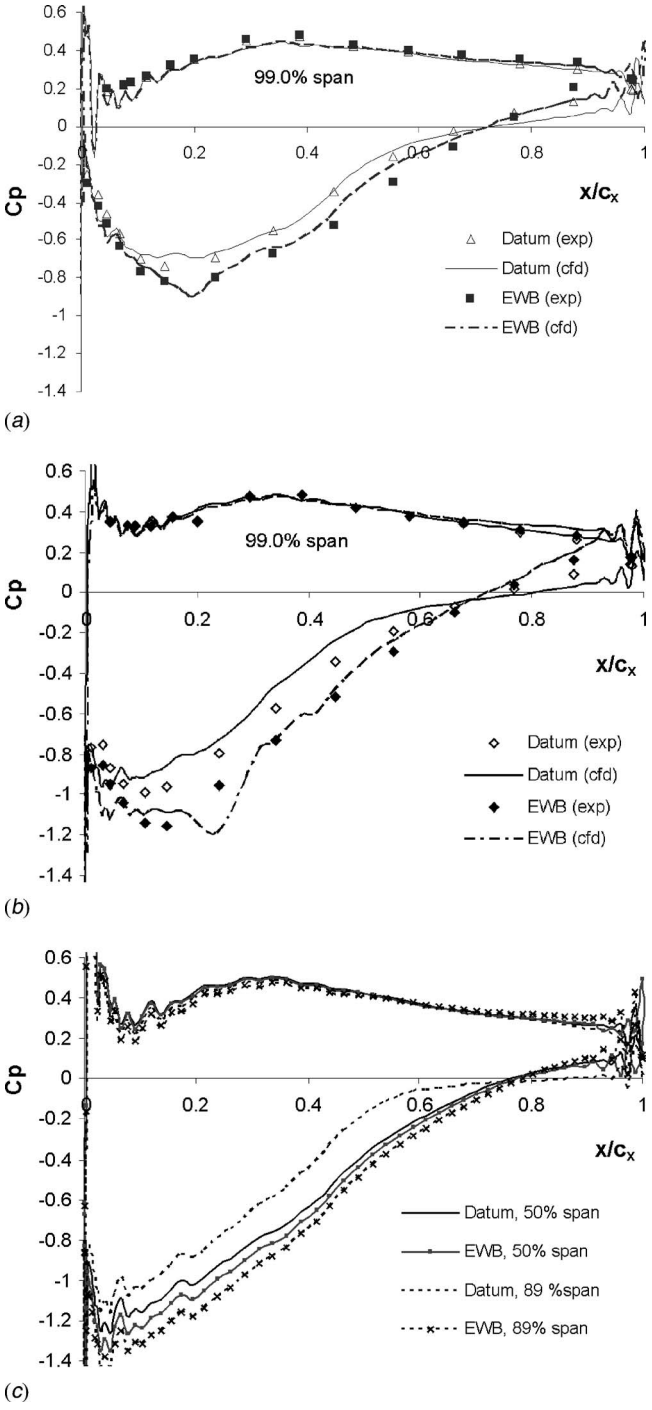

Fig. 8 (*a*) Measured and computed surface static pressure distribution near the end wall of the compressor cascade; datum and end wall suction EWB configuration (a) *i*=−7.0 deg, (*b*) *i* =0.0 deg, and (*c*) comparison of computed surface static pressure distribution at midspan and 89% span of the compressor cascade; datum and end wall suction EWB configuration, *i* =0.0 deg

at 99% span for −7.0 deg and 0.0 deg incidence cases, respectively, for the datum and with EWB slots. Figure 8(*c*) also compares the computed surface static pressure distribution at midspan and 89% span for datum and the EWB configuration at 0.0 deg incidence. Agreement between measurement and CFD is generally good, giving confidence in the use of CFD to draw conclusions about details of the flow. The removal of 3D separation and block-

Downloaded 30 May 2010 to 128.113.26.88. Redistribution subject to ASME license or copyright; see http://www.asme.org/terms/Terms_Use.cfm

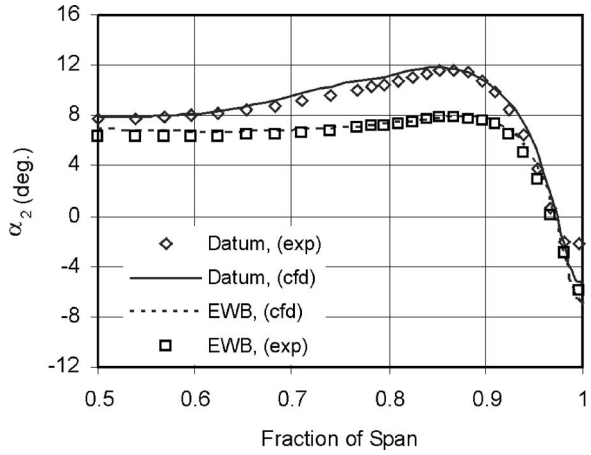

Fig. 9 Comparison of measured and computed exit flow angles of the compressor cascade for datum and end wall suction EWB configuration, *i*=0.0 deg

age associated with it can be seen to lead to increased blade loading (pressure difference between suction and pressure surfaces) and increased average static pressure rise. The increase in blade loading can also be seen to extend up to midspan, as shown in Fig. 8(*c*).

It can be noted in Fig. 8 that the datum case still supports some diffusion (static pressure rise) in the separated region. In a 2D description of the flow, where only the streamwise pressure gradient matters, the surface static pressure is not expected to increase in the streamwise direction once separation has occurred at the point at which the shear stress vanishes, and beyond which the flow reverses. In 3D, however, separation can occur with nonzero friction [13]. Thus there can be a pressure rise in a region of 3D separated flow because separation in this case does not necessarily imply zero velocity at the wall.

The measured and computed exit flow angles at zero incidence for the datum and end wall suction are compared in Fig. 9. This clearly shows a reduced deviation when suction is applied to remove the separated region. It is interesting to note that the reduction in deviation extends to the midspan, as indicated by both the experiment and CFD. The gain in pressure rise suggested from the blockage reduction might be thought to lead to a thickening of the suction surface boundary layer in the midspan region, which in a 2D sense would lead to an increase in deviation. However, as can be seen from the suction surface limiting streamlines in Fig. 1, the strong convergence of the limiting streamlines toward the separation line is an indication of the drifting of the unseparated suction surface boundary layer toward midspan near the trailing edge due to the separated flow in the end wall region. If continuity is applied to a stream tube bounded by the surface and adjacent limiting streamlines of distance n apart and of height h above the surface, then, as first pointed out by Lighthill [14] and further elaborated by Tobak and Peake [15], h can be expressed as

$$h = C\left(\frac{\nu}{n\tau_w}\right)^{1/2} \tag{8}$$

where C is a constant, ν is the kinematic viscosity, and τ_w is the wall shear stress.

Equation (8) indicates that the height h increases rapidly when the limiting streamlines converge, i.e., when n decreases or when the resultant skin friction τ_w drops to a minimum as the separation line is approached. Because of this, streamlines around the midspan are displaced away from the suction surface, near the trailing edge, producing deviation. This is in addition to the displacement already caused by the thickening of the suction surface boundary layer itself (as happens in 2D flow) as a result of the adverse streamwise pressure gradient and in addition to any "potential flow" deviation. This displacement of the streamlines from the suction surface implied by Eq. (8) leads to a higher exit flow angle (α_2) (higher deviation) in the midspan region in the 3D case for a given inlet flow angle (α_1). The removal of the separated flow by suction, as shown in Figs. 3(*b*) and Fig. 6, has enabled the flow to be nearly two-dimensional within the half-passage where it is applied.

Conclusions

The underlying premise of this work is that the corner separations of a 3D nature dominate blockage, loss, and the tendency to stall at higher loading. To improve compressor performance, therefore requires controlling and, if possible, removing the effect of these 3D separations. Some of the important conclusions that can be drawn from this study are as follows.

(1) Calculations and experiments have confirmed that the 3D separation in the suction/end wall corner arises at the place where the limiting streamline springing from the saddle point near the leading edge meets the suction surface. Removing this limiting streamline with suction effectively removes the 3D separation in the corner.
(2) Suction, which does not remove the limiting streamline before it intersects the suction surface, reduces but does not remove the 3D separation, at least for levels of suction corresponding to less than the total flow in the end wall boundary layer.
(3) Removing the 3D separation with suction reduces the stagnation pressure loss downstream of the blade row with suction as well as decreasing deviation and blockage and increasing static pressure rise. The reduction in deviation will tend to increase stagnation pressure and enthalpy rise in later stages; the increase in static pressure would be extremely valuable in outlet guide vanes just ahead of the combustion chamber. For this configuration, the increases in stagnation pressure and static pressure rise are, respectively, worth about 1.5 and 4 times the loss in work for the bled air.
(4) The optimum slot should be long enough to be sure to remove the limiting streamline and is recommended to run close to the suction surface from a position just downstream of the peak suction on the blade to near the trailing edge.

Acknowledgment

This work was supported by Rolls-Royce Plc, the Applied Research Programme of the Ministry of Defence, and the Department of Trade and Industry Aeronautic Research Programme. The authors are very grateful for this and for their permission to publish. The authors would also like to thank Professor J. D. Denton for the use of his CFD code.

Nomenclature

A = area
B = blockage
c = chord
C_p = static pressure coefficient $(P-p_1)/(0.5\rho V_1^2)$
h = blade height (span), height from surface
H = enthalpy, shape factor $=\delta^*/\theta$
i = incidence
$\dot{m}$ = mass flow rate
P = pressure
r = radius, radial distance
Re = Reynolds number
s = blade pitch, pitchwise distance
U = mean blade speed
V = velocity, free stream velocity

Downloaded 30 May 2010 to 128.113.26.88. Redistribution subject to ASME license or copyright; see http://www.asme.org/terms/Terms_Use.cfm

Greek Symbols

α = absolute flow angle
β = blade (metal) angle
δ = boundary layer thickness
δ^* = displacement thickness
θ = momentum thickness
ρ = density
ν = kinematic viscosity
ω = loss coefficient $(P_{01}-P_{02})/(0.5\rho V_1^2)$

Subscripts

b = bleed
bl = boundary layer
mid = midspan
fs = free stream
s = static
x = axial
0 = stagnation
1 = inlet
2 = exit
θ = tangential

Descriptors

F = focus
LE = leading edge
N = node
PS = pressure surface/side
S = saddle point
SS = suction surface/side
TE = trailing edge
Δ = change

Appendix

Illustration of Potential Performance Benefits From Suction

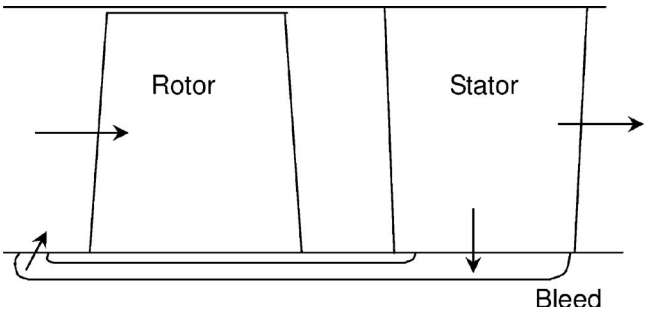

At zero incidence, inlet flow angle to the stator $\alpha_1=41.0$ deg and, using Fig. 9, the average exit flow angle $\alpha_2 \approx 7.0$ deg. Assuming a repeating stage with constant mean flow coefficient, $\phi = v_x/U = 0.5$, with absolute flow angles into and out of the rotor of 7 deg and 41 deg, then

$$\Delta H_0/U^2 = \Delta V_\theta/U = v_x(\tan 41 \text{ deg} - \tan 7 \text{ deg})/U = 0.373 \tag{A1}$$

With bleed flow of 0.7% of inlet mass flow (the value required to remove the separation at zero incidence), the lost work in dumping the bleed air back ahead of the rotor can be given as

$$(\dot{m}_b/\dot{m}_1)\Delta H_0/U^2 = 0.007 \times 0.373 = 0.0026 \tag{A2}$$

For these estimates, it suffices to take $\Delta P_0/\rho = \Delta H_0$.

The loss coefficient and the cascade static pressure rise are specified in terms of inlet dynamic pressure, based on the inlet velocity V_1. The inlet velocity

$$V_1/U = v_x/(U\cos\alpha_1) = 0.5/\cos 41 \text{ deg} = 0.6625$$

and the inlet dynamic head is given by

$$1/2 \times \rho V_1^2 = 0.219\rho U^2 \tag{A3}$$

The measured datum loss coefficient ω at zero incidence is about 9% of inlet dynamic pressure, so datum loss in stagnation pressure

$$\Delta P_0 = \omega \times 0.219 \times \rho U^2 = 0.01975\rho U^2 \tag{A4}$$

The measured exit static pressure rise coefficient for datum $C_{P2} = 0.284$, so rise in static pressure

$$\Delta P = C_{P2} \times 0.219 \times \rho U^2 = 0.0624\rho U^2 \tag{A5}$$

The 21% drop in loss coefficient by suction slot EWB, Table 2, therefore represents a reduction in ΔP_0 equal to $0.21 \times 0.0195 \times \rho U^2 = 0.0041 \times \rho U^2$, which is about 1.5 times the lost work (Eq. (A2)). Also, the 17% rise in exit static pressure coefficient corresponds to an increase in static pressure ΔP equal to $0.17 \times 0.219 \times \rho U^2 = 0.0106 \times \rho U^2$, which is about four times the lost work (Eq. (A2)).

In summary, the gain in stagnation pressure and increase in static pressure rise for the mainstream are worth about 1.5 and 4 times, respectively, the extra work in dumping the bled air back ahead of the rotor.

References

[1] Kerrebrock, J. L., Reinjen, D. P., Ziminsky, W. S., Smilg, L. M., 1997, "Aspirated Compressors," ASME Paper No. 97-GT-525.
[2] Kerrebrock, J. L., Drela, M., Merchant, A. A., and Schuler, B. J., 1998, "Family of Designs for Aspirated Compressors," ASME Paper No. 98-GT-196.
[3] Merchant, A., 2002, "Aerodynamic Design and Performance of Aspirated Airfoils," ASME J. Turbomach., **25**, pp. 141–148.
[4] Dang, T. Q., Van Rooij, M. P. C., and Larosiliere, L. M., 2003, "Design of Aspirated Compressor Blades Using Three-Dimensional Inverse Method," ASME Paper No. GT-2003-30369.
[5] Lee, N. K. W., and Greitzer, E. M., 1990, "Effects of Endwall Suction and Blowing on Compressor Stability Enhancement," ASME J. Turbomach., **112**, pp. 133–144.
[6] Peacock, R. E., 1965, "Flow Control in the Corners of Cascades," Aeronautical Research Council, ARC Paper No. 27291.
[7] Gbadebo, S. A., Cumpsty, N. A., and Hynes, T. P., 2005, "Three-Dimensional Separations in Axial Compressors," ASME J. Turbomach. **127**, pp. 331–339.
[8] Gbadebo, S. A., 2003, "Three-Dimensional Separations in Compressors," Ph.D thesis, University of Cambridge, Cambridge, UK.
[9] Denton, J. D., 2000, MULTALL, *Multistage Turbomachinery Flow Calculation Program*, Whittle Laboratory, University of Cambridge, Cambridge, UK.
[10] Denton, J. D., 1999, MULTIP, *Multistage Turbomachinery Flow Calculation Program*, Whittle Laboratory, University of Cambridge, Cambridge, UK.
[11] Khalid, S. A., Khalsa, A. S., Waitz, I. A., Tan, C. S., Greitzer, E. M., Cumpsty, N. A., Adamczyk, J. J., and Marble, F. E., 1999, "Endwall Blockage in Axial Compressors," ASME J. Turbomach., **121**, pp. 499–509.
[12] Cumpsty, N. A., 1989, *Compressor Aerodynamics*, Longman Scientific and Technical, Reprinted, 2004, Krieger, FL, ISBN 1-57524-247–8.
[13] Chang, P. K., 1970, *Separation of Flow*, Interdisciplinary and Advanced Topics in Science and Engineering, Pergamon, New York, Vol. 3.
[14] Lighthill, M. J., 1963, "Attachment and Separation in Three-Dimensional Flows," *Laminar Boundary Layers*, L. Rosenhead, ed., Oxford University Press, New York, pp. 72–82.
[15] Tobak, M., and Peake, D. J., 1982, *Topology of Three-Dimensional Separated Flows*, Annual Review of Fluid Mechanics, Vol. 14, pp. 61–85.

Downloaded 30 May 2010 to 128.113.26.88. Redistribution subject to ASME license or copyright; see http://www.asme.org/terms/Terms_Use.cfm

Large Eddy Simulation of Flow and Heat Transfer in the Developing Flow Region of a Rotating Gas Turbine Blade Internal Cooling Duct With Coriolis and Buoyancy Forces

Evan A. Sewall

Danesh K. Tafti

Mechanical Engineering Department,
Virginia Tech,
Blacksburg, VA 24061

The problem of accurately predicting the flow and heat transfer in the ribbed internal cooling duct of a rotating gas turbine blade is addressed with the use of large eddy simulations (LES). Four calculations of the developing flow region of a rotating duct with ribs on opposite walls are used to study changes in the buoyancy parameter at a constant rotation rate. The Reynolds number is 20,000, the rotation number is 0.3, and the buoyancy parameter is varied between 0.00, 0.25, 0.45, and 0.65. Previous experimental studies have noted that leading wall heat transfer augmentation decreases as the buoyancy parameter increases with low buoyancy, but heat transfer then increases with high buoyancy. However, no consistent physical explanation has been given in the literature. The LES results from this study show that the initial decrease in augmentation with buoyancy is a result of larger separated regions at the leading wall. However, as the separated region spans the full pitch between ribs with an increase in buoyancy parameter, it leads to increased turbulence and increased entrainment of mainstream fluid, which is redirected toward the leading wall by the presence of a rib. The impinging mainstream fluid results in heat transfer augmentation in the region immediately upstream of a rib. The results obtained from this study are in very good agreement with previous experimental results. [DOI: 10.1115/1.2437779]

Introduction

In an effort to increase the power output and efficiency of gas turbine engines, it is desirable to increase the temperature of the fluid exiting the combustor. To prevent the hot gases from melting the blades of the high-pressure turbine, they are cooled by compressor air that has bypassed the combustor. Two of the most common methods of cooling the turbine blades are internal cooling through ducts running throughout the blades and film cooling through holes leading from the internal ducts to the blade surfaces. In internal cooling, turbulators are often included on the channel walls to increase turbulent mixing and, as a result, heat transfer to the fluid. Accurate prediction of the flow and heat transfer characteristics of this highly turbulent flow is an important step in achieving a balance between bleeding as little compressor air as possible to prevent the engine's efficiency from being decreased and obtaining enough cooling flow to effectively cool the blades. This project is part of an effort to improve and demonstrate the prediction capability of large eddy simulations (LES) as an accurate prediction tool for turbulent flow in ribbed internal cooling ducts.

Previous Works. Of the many experiments conducted to measure the flow and heat transfer of rotating ducts with 45 deg and 90 deg ribs, a few of these studies varied the buoyancy parameter (a measure of density variation, rotation speed, and rotation radius) and found that the heat transfer augmentation on the trailing wall increases steadily with an increase in buoyancy. However, the heat transfer on the leading wall decreases initially until the buoyancy parameter reaches a value near 0.3, at which point the heat transfer begins to increase again with an increasing buoyancy parameter [1–3]. This effect has also been observed in smooth wall studies, such as those by Wagner et al. [4,5]. Though the study mentioned in [2] above was for large ribs angled at 60 deg, no cases with 45 deg ribs were found that demonstrated this effect. As these three studies were all strictly based on heat transfer measurements (many rotating flow measurement studies are not done in heated ducts), no concrete explanations of this effect were provided other than conjectures about the interaction of Coriolis and buoyancy effects.

Of the many computational studies on smooth wall heat transfer in rotating ducts, only a few address the effects of variations of buoyancy. One of them showed some differences in heat transfer between different buoyancy parameters at a high rotation number, but the results were inconsistent with the trend mentioned above [6]. A number of computational studies of rotating ducts with 90 deg ribs [7,8] and with 45 deg or V-shaped ribs [9–12] varied the buoyancy parameter, but none of them could reproduce the experimental observations of decreasing heat transfer augmentation followed by increasing heat transfer at higher buoyancy parameters.

One LES study by Murata and Mochizuki [13] of a periodic duct with 60 deg ribs did correctly show the trend of decreasing heat transfer on the leading wall when buoyancy parameter was increased from zero to a small number and increasing heat transfer as the buoyancy parameter was increased further to a large number. No explicit explanation was given as to why the heat transfer

Contributed by the International Gas Turbine Institute of ASME for publication in the JOURNAL OF TURBOMACHINERY. Manuscript received March 17, 2006; final manuscript received June 8, 2006; published online December 19, 2007. Review conducted by David Wisler. Paper presented at the ASME Turbo Expo 2005: Land, Sea and Air (GT2005), June 6–9, 2005, Reno, NV.

 Copyright © 2008 by ASME

Downloaded 30 May 2010 to 128.113.26.88. Redistribution subject to ASME license or copyright; see http://www.asme.org/terms/Terms_Use.cfm

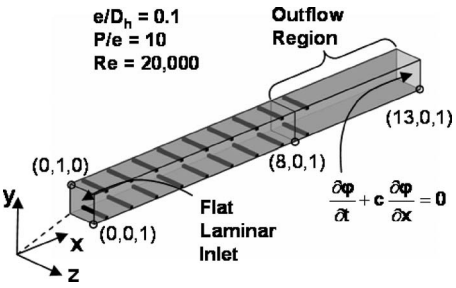

Fig. 1 Developing flow domain consisting of nine ribs followed by a downstream extension region

trend shifted and began to increase again as buoyancy was increased. Two other LES studies, one by Abdel-Wahab and Tafti [14] of a periodic channel and the other by Murata and Mochizuki [15] of an entire ribbed channel both studied the effects of buoyancy, but the buoyancy parameter only reached a maximum value of 0.35, so the high buoyancy effect could not be studied.

Objective. The goal of this study is to understand the interaction between the Coriolis and buoyancy forces and their combined effect on friction factor, mean flow, turbulence, and heat transfer in the developing region of a square duct with 90 deg ribs attached to opposite walls. Of particular interest is the anomalous behavior of heat transfer on the leading edge which decreases initially and then increases with an increase in buoyancy parameter. This has been observed in previous experiments, but no physical explanation is available. To resolve this subtle effect, high-resolution LES calculations are performed in the developing flow region of the duct.

Computational Model and Governing Equations

The computational domain used for studying the developing flow region, shown in Fig. 1, consists of an inlet with a flat velocity profile and zero turbulence, eight ribs in succession, and a final rib followed by an extended smooth region used to allow the turbulence to dissipate before the flow reaches the outlet boundary conditions. The duct surfaces, as well as the ribs, are heated with a uniform heat flux boundary condition. The governing flow and energy equations are nondimensionalized by a characteristic length scale, given by the channel hydraulic diameter (D_h), a characteristic velocity scale, given by the channel bulk velocity ($\overline{u_{\text{in}}}$), and a characteristic temperature scale, given by the nondimensional heat flux ($q''D_h/k$).

The equations governing the flow are the time-dependent Navier-Stokes and energy equations in transformed coordinates, $\vec{\xi}=\vec{\xi}(\vec{x})$. The equations, as well as all results presented in this paper, are given in terms of nondimensional variables

Continuity:

$$\frac{\partial}{\partial \xi_j}(\sqrt{g}\bar{U}^j)=0 \tag{1}$$

Momentum:

$$\frac{\partial}{\partial t}(\sqrt{g}\bar{u}_i)+\frac{\partial}{\partial \xi_j}(\sqrt{g}\bar{U}^j\bar{u}_i) = -\frac{\partial}{\partial \xi_j}(\sqrt{g}(\vec{a}^j)_i\bar{p})+\frac{\partial}{\partial \xi_j}\left[\left(\frac{1}{\text{Re}}+\frac{1}{\text{Re}_t}\right)\sqrt{g}g^{jk}\frac{\partial \bar{u}_i}{\partial \xi_k}\right] - 2\sqrt{g}\text{Ro}\bar{u}_m\in_{i3m}-\sqrt{g}\text{Ri}(\bar{\theta}-\bar{\theta}_{\text{ref}})\delta_{i1} \tag{2}$$

Energy:

$$\frac{\partial}{\partial t}(\sqrt{g}\bar{\theta})+\frac{\partial}{\partial \xi_j}(\sqrt{g}\bar{U}^j\bar{\theta})=\frac{\partial}{\partial \xi_j}\left[\left(\frac{1}{\text{Pr Re}}+\frac{1}{\text{Pr}_t\,\text{Re}_t}\right)\sqrt{g}g^{jk}\frac{\partial \bar{\theta}}{\partial \xi_k}\right] \tag{3}$$

where $\vec{a}^i$ are the contravariant basis vectors (the notation $(\vec{a}^j)_k$ is used to denote the kth component of vector $\vec{a}^j$, $(\vec{a}^j)_k=\partial\xi_j/\partial x_k$), $\sqrt{g}$ is the Jacobian of the transformation, g^{ij} are the elements of the contravariant metric tensor, $\sqrt{g}U^j=\sqrt{g}(\vec{a}^j)_k u_k$ is the contravariant flux vector, u_i is the Cartesian velocity vector, and θ is the nondimensional temperature. The overbar denotes grid filtered quantities with an implicit top-hat filter, $\bar{G}$.

In Eq. (2), both the rotational Coriolis forces and the centrifugal buoyancy forces are included in the formulation. In formulating Eq. (2), the following assumptions are made: the mean centrifugal force is combined with the mean pressure gradient term; the effect of variable density due to temperature differences only manifests itself through the centrifugal force term; and centrifugal buoyancy is only consequential in the balance of x momentum, as its contribution to the balance of y momentum is deemed to be negligible (the radial vector has a small component in the y direction).

The effects of centrifugal buoyancy are defined by the Richardson number in Eq. (2). The inlet rotation radius and rotation number do not change throughout the study, while the value of β is varied to model different magnitudes of centrifugal buoyancy. The buoyancy parameter is defined as $\overline{\text{Ri}(\theta_s-\theta_{\text{ref}})}$ where θ_s is the local surface temperature and θ_{ref} is the reference temperature at a given x location. The overbar denotes a spatial average. Since in the developing flow region the quantity under the overbar varies with x, the buoyancy parameter is defined as an average over the first eight ribs.

The inverse of the nondimensional eddy-viscosity, Re_t, is modeled by the Smagorinsky model as

$$\frac{1}{\text{Re}_t}=C_s^2(\sqrt{g})^{2/3}|\bar{S}| \tag{4}$$

where $|\bar{S}|$ is the magnitude of the strain rate tensor and the Smagorinsky constant C_s^2 is obtained via the dynamic subgrid stress model [16]. The model is described in more detail in [17].

A uniform laminar plug flow velocity profile is applied as the inlet boundary condition. This is the same inlet flow condition applied in the previous LES studies of developing flow in stationary and rotating ribbed ducts [18,19]. The inlet test conditions in the experimental rigs used by Liou and Hwang [20] and Han and [21], as well as many others in the open literature, are simulated by flow exiting a plenum through a sharp contraction into the test section. This produces separated flow with a low level of turbulence at the inlet. The only difference between these two studies and the LES studies is the absence of separated flow. This difference, however, is inconsequential by the time the flow reaches the second rib. Another set of calculations with fully developed turbulent flow profiles were also performed in a stationary duct, and it was found that the calculated heat transfer coefficients were nearly identical after the second rib. The nondimensional inlet temperature field is zero by definition.

The governing equations for momentum and energy are discretized with a conservative finite-volume formulation using a second-order central difference scheme on a nonstaggered grid topology. The Cartesian velocities, pressure, and temperature are calculated and stored at the cell center, whereas contravariant fluxes are stored and calculated at the cell faces. For the time integration of the discretized continuity and momentum equations, a projection method is used. The temporal advancement is performed in two steps, a predictor step, which calculates an intermediate velocity field, and a corrector step, which calculates the updated velocity field at the new time step by satisfying discrete

Downloaded 30 May 2010 to 128.113.26.88. Redistribution subject to ASME license or copyright; see http://www.asme.org/terms/Terms_Use.cfm

continuity. The energy equation is advanced in time by the predictor step. Details about the algorithm, functionality, and capabilities can be found in Tafti [22].

The computer program GenIDLEST (Generalized Incompressible Direct and Large-Eddy Simulations of Turbulence) used for these simulations has been applied to fully developed flow and heat transfer in a ribbed duct geometry similar to the one used in this study [17], with rotation and buoyancy effects [14,23], and in a channel with 45 deg ribs [24]. It has also been applied to both stationary and rotating developing flow domains (but with no buoyancy effects) [18,19]. In all of these cases, it has been consistently established through comparison to experiments that predictions of mean flow, turbulent quantities, and heat transfer, are accurate to within ±10% of experiments and in some cases within experimental uncertainty.

Computational Details

The calculation domain presented in this paper is a straight duct representing the developing flow region of a cooling duct. A grid independence study between a periodic channel with 96^3 and 128^3 grid points in Tafti [17] showed no significant differences between the low- and high-resolution cases when the dynamic Smagorinsky subgrid scale model was used. Both meshes predicted the local and mean heat transfer augmentations within experimental uncertainty on the ribbed wall and smooth walls. A study by Abdel-Wahab and Tafti [23] in a rotating duct showed less than a 9% difference between the 128^3 and 96^3 meshes in the predictions of heat transfer augmentation, with the majority of the comparisons being within 5%. In this study, we use a mesh of 96^3 for each rib pitch. The total mesh size for this calculation is 8.9×10^6 computational cells.

The channel aspect ratio is 1:1, and the geometric ratios governing the rib placement are $e/D_h = 0.1$ and $P/e = 10$, which is typical in many computational and experimental studies. The ribs are square in cross section, placed in an in-line (i.e., not staggered) configuration, and are angled at 90 deg to the flow direction. A uniform heat flux boundary condition is imposed on both the walls and the ribs (Pr=0.7), and the Reynolds number based on the inlet velocity, which is also the bulk fluid velocity, is 20,000. The duct is rotating at a constant rate with a rotation number of 0.3.

The nondimensional time step in the calculations is set to 5×10^{-5}. The diffusion terms are treated implicitly, and the average L_1 residual norm of global mass balance is converged to 1×10^{-8}, while the momentum and energy equations are converged to 1×10^{-7}. The calculations utilized 160 processors of an IA-64 Itanium Linux cluster. Each time step took ~ 0.12 μs/grid node of wall clock time.

Each calculation was initiated by assuming initial conditions similar to a fully developed channel and integrating in time until the flow reached a statistically stationary state. The time evolution of bulk quantities, such as Nusselt number, friction drag losses, and form drag losses, were observed until all values reached a uniform state. Once stationary conditions were established, sampling to obtain mean and turbulent quantities was carried out for approximately 10 time units. Initial mean quantities were obtained by sampling over one time unit before obtaining turbulent statistical quantities. The sampling time was doubled by using the z symmetry of the duct and presenting the averaged and turbulent quantities for 1/2 of the duct cross section. The coordinate system used for reporting results is shown in Fig. 1.

The local Nusselt number as related to the nondimensional temperature is calculated as

$$\mathrm{Nu} = \frac{1}{\theta_s - \theta_{\mathrm{ref}}} \tag{5}$$

where θ_s is the calculated surface temperature and θ_{ref} is the reference temperature defined as

$$\theta_{\mathrm{ref}} = \frac{\int\int |u_1| \theta dA_x}{\int\int |u_1| dA_x} \tag{6}$$

where θ is the non dimensional temperature defined as

$$\theta = \frac{T - T_{\mathrm{in}}}{\frac{q'' D_h}{k}} \tag{7}$$

The surface-averaged Nusselt number is area weighted as

$$\bar{\mathrm{Nu}} = \frac{\int\int_{\Omega} \mathrm{Nu} dS}{\int\int_{\Omega} dS} \tag{8}$$

where S denotes the surface under consideration.

The Fanning friction factor is calculated in terms of the nondimensional pressure gradient as

$$f = -\frac{1}{2}\frac{\Delta p}{\Delta L} \tag{9}$$

The reference value for the Nusselt number is obtained from the Dittus-Boelter correlation,

$$\mathrm{Nu}_0 = 0.023 \mathrm{Re}^{0.8} \mathrm{Pr}^{0.4} \tag{10}$$

and the friction factor is normalized by the following equation [25]:

$$f_0 = 0.046 \mathrm{Re}^{-0.2} \tag{11}$$

Results

In general, as the buoyancy parameter is increased from Bo=0.00 through Bo=0.65, overall friction factor increases by a factor of two; leading wall heat transfer augmentation decreases when the buoyancy parameter is increased from Bo=0.00 to Bo=0.25 but increases after that; and trailing wall heat transfer increases monotonically with the increase in buoyancy parameter. A significant change takes place in the size of the recirculation regions behind leading wall ribs and the reattachment length while little to no change occurs at the trailing wall.

Rotation induced Coriolis forces have two significant effects on the flow and heat transfer. The first effect is the destabilization and augmentation of turbulence at the trailing side of the duct together with stabilization and attenuation on the leading side. Another effect of Coriolis forces is the generation of secondary flow cells in the cross section of the duct, which develop strong upwash and/or downwash regions. Centrifugal buoyancy can either complement or oppose the effect of Coriolis forces. Through the action of Coriolis forces, fluid in the vicinity of the trailing duct wall is cooler than at the leading wall for radially outward flow. To first order, the higher density exposes the fluid at the trailing wall to a larger centrifugal force than at the leading side of the duct and complements the effect of Coriolis forces. If the flow is radially inward, then the leading wall of the duct will have cooler fluid temperatures in its vicinity than the trailing wall by the action of Coriolis forces. In this case, the centrifugal buoyancy body force is larger at the leading wall but opposes the action of Coriolis forces because of its outward direction.

A comparison of the mean velocity profiles across a vertical line between the eighth and ninth ribs in the symmetry plane of the duct is shown in Fig. 2. In the rotating case with no buoyancy effects (Bo=0.00), the peak velocity is skewed toward the leading wall, but as Bo increases and the reverse flow region at the lead-

Downloaded 30 May 2010 to 128.113.26.88. Redistribution subject to ASME license or copyright; see http://www.asme.org/terms/Terms_Use.cfm

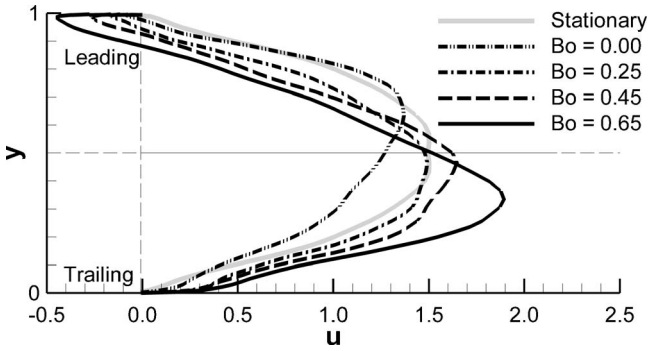

Fig. 2 Mean velocity profiles along a vertical line between ribs 8 and 9 in the symmetry plane (Ro=0.30 in the rotating cases)

ing wall gains strength, the maximum velocity is pushed towards the trailing wall to compensate for the reversed flow.

The change in the recirculation zones downstream of the ribs is another important characteristic of changes in buoyancy. The effect of rotation has a stabilizing and destabilizing effect on the leading and trailing walls, respectively. As fluid is forced away from the leading wall, the turbulence along that wall is decreased while the turbulence along the trailing wall is increased. As the buoyancy parameter increases, the trailing wall reattachment lengths approach a constant value of ~3.5 rib heights. On the leading side, the only case in which flow reattaches to the wall downstream of every rib is at Bo=0.00. At Bo=0.25, the recirculation regions, which form behind and in front of each rib, start merging together as shown in Fig. 3. At the two highest buoyancy parameters, a near-continuous recirculating zone extends throughout the cooling duct at the leading wall, which gathers strength as the flow moves into the duct. On the other hand, at the trailing wall, the recirculation zones do not experience large changes with increase in buoyancy. These observations agree with the fully developed calculations of Abdel-Wahab and Tafti [23]; at low buoyancy parameters (Bo<0.3), they reported an increase in the recirculation regions at the leading wall with no or little change at the trailing wall.

A close-up of the streamlines on the leading wall between the seventh and eight ribs is shown in Fig. 4. In the case with no buoyancy, flow reattaches to the leading wall between the two ribs, but with Bo=0.25, the recirculation zone behind Rib 7 and the recirculation zone upstream of Rib 8 bridge together, not allowing any flow to attach to the leading wall. In the two higher buoyancy cases, the two zones merge into a single large recirculating zone. The vertical size of the recirculation zones is also important to note. With Bo=0.00 (Ro=0.30), the recirculation

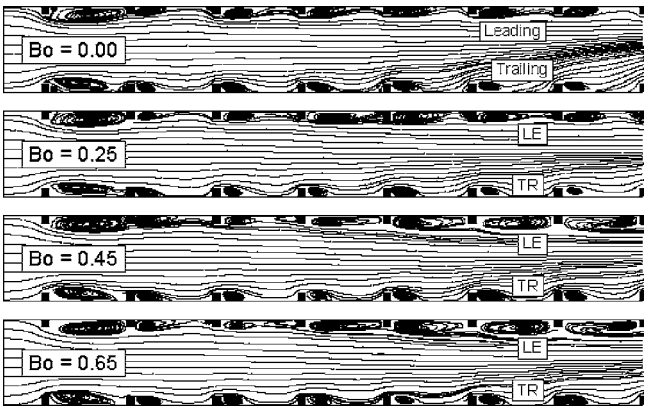

Fig. 3 Streamlines in the symmetry plane of the ducts for buoyancy parameters of 0.00, 0.25, 0.45, and 0.65

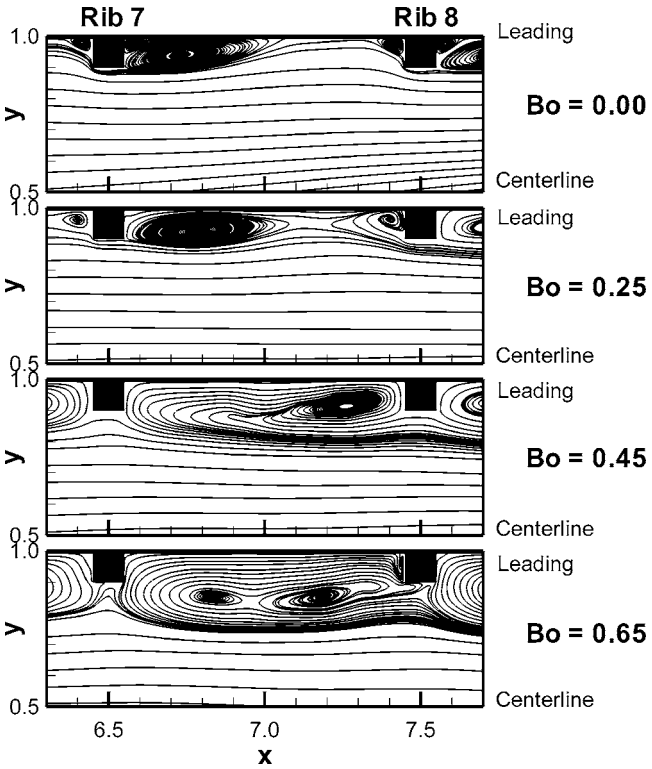

Fig. 4 Close-up views of the leading wall recirculating zones

zones are entirely below the shear layers formed above the ribs. When Bo=0.25, the recirculation zone begins to enlarge, stretching towards the mainstream. Once the two recirculation zones merge, the size becomes much larger. When Bo=0.45, the height of the recirculation zone is more than twice the height of the ribs, affecting channel flow at $y=0.8$ that was not directly affected by recirculation zones at lower buoyancy parameters. At the highest buoyancy parameter, Bo=0.65, the recirculation zone is ~2.5 times larger than the rib height.

More critical to the heat transfer is a close examination of the streamlines. At Bo=0.00, fluid from the center of the duct (freestream) is directed toward the leading wall in the reattachment region. This is usually the region where heat transfer augmentation is higher than the rest of the leading wall surface. At Bo=0.25, the merging of the two recirculation regions blocks freestream fluid from coming in the vicinity of the wall. However, an important change takes place in the structure of the recirculating zone as the buoyancy parameter increases further. At high buoyancy, as the recirculating zones get bigger, they draw in fluid from the center of the duct to the wall just upstream of the rib. This can be clearly observed in the streamline pattern upstream of the rib. As will be shown later this has consequences on heat transfer augmentation.

In addition to drawing in fluid from the duct center, the recirculating regions at the leading wall at the higher buoyancy parameters are highly energetic and unsteady compared to their low-buoyancy counterparts. A vertical profile of the turbulent kinetic energy between ribs 7 and 8 in Fig. 5 shows the increased turbulence near the trailing wall. The turbulence level of the fluid near the wall reaches magnitudes of 11%, 17%, 22%, and 26% for buoyancy parameters of 0.00, 0.25, 0.45, and 0.65, respectively. The turbulent kinetic energy of the fluid near the leading wall does not increase significantly, remaining at values <4%, indicating that turbulence near the wall is not a major contributor to the heat transfer. In the separated shear layer at the trailing wall, the turbulence reaches as high as 30%. The unexpected trend is in the increase in turbulent kinetic energy at $y=0.7$, near the leading side

Downloaded 30 May 2010 to 128.113.26.88. Redistribution subject to ASME license or copyright; see http://www.asme.org/terms/Terms_Use.cfm

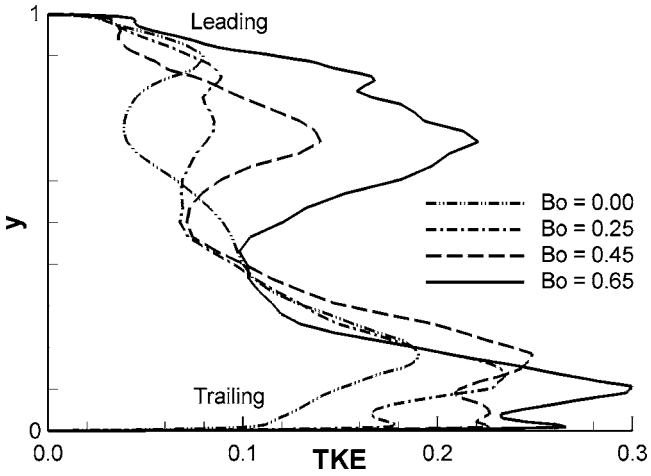

Fig. 5 Vertical profile of turbulent kinetic energy in the symmetry plane (z=0.5) directly between ribs 7 and 8

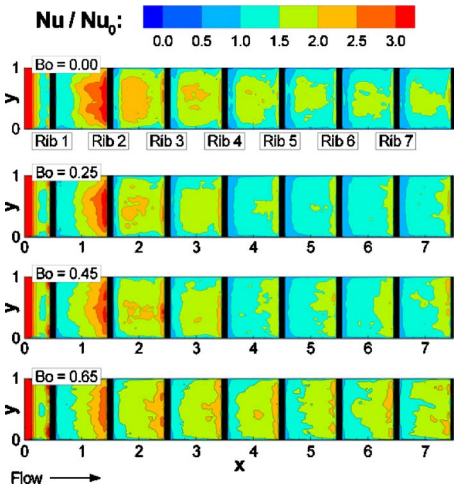

Fig. 7 Heat transfer augmentation contours on the leading wall

of the duct. This is a result of an energetic shear layer forming between the growing recirculation zones and the mainstream flow. In the two cases with low buoyancy (Bo=0.00 and 0.25), the peak is at rib height and has a magnitude of ~8%, but in the high buoyancy cases (Bo=0.45 and 0.65), TKE increases to a value of 22% at Bo=0.65.

Figure 6 shows heat transfer augmentation contours on the leading wall for the four buoyancy parameters. The recirculation zones between the ribs have a significant effect on the mainstream flow. In the first two cases (Bo=0.00 and 0.25), streamlines injected at rib height simply pass over the ribs, while in the higher buoyancy cases (Bo=0.45 and 0.65), much of the flow is entrained into the recirculation zone, which increases the heat transfer augmentation immediately upstream of the ribs because of impingement from the cooler mainstream fluid.

In Fig. 7, the heat transfer augmentation contours on the leading wall are shown for the four different buoyancy parameters. In all cases, the heat transfer is highest near the duct inlet and decreases downstream. In the case with no buoyancy, the peak heat transfer augmentation is observed directly between two ribs and is the result of reattachment of the separated flow from the ribs. As the buoyancy parameter is increased and the flow fails to reattach, the heat transfer augmentation decreases in this area. Conversely, as the recirculation zones upstream and downstream of the ribs begin to merge, a region of high heat transfer augmentation immediately upstream of the ribs begins to grow as mainstream flow is entrained into the recirculation zones. At Bo=0.00 and 0.25, there is a steady decrease in augmentation as the flow moves into the duct. As the buoyancy parameter increases further and the recirculation zones become large and extend all the way through the duct, the separated shear layer now impinges on the downstream rib and is redirected toward the wall. The combined effect of impingement, high turbulent fluctuations, and cold fluid from the center of the duct steadily increases the augmentation ratio in this region.

The rib-averaged values of heat transfer are shown for both the leading and trailing walls in Fig. 8 close-up of the values on the leading wall is plotted on the top of the figure. On the trailing side, the heat transfer shows a consistent increase as flow moves through the duct and as the buoyancy parameter is increased. The leading wall heat transfer shows a decrease in heat transfer between the case with no buoyancy and the lowest buoyancy (Bo =0.25). At the higher buoyancy parameters, however, the heat transfer augmentation on the leading wall increases. The increase in heat transfer augmentation is largest between the two highest buoyancy parameters (Bo=0.45 and 0.65).

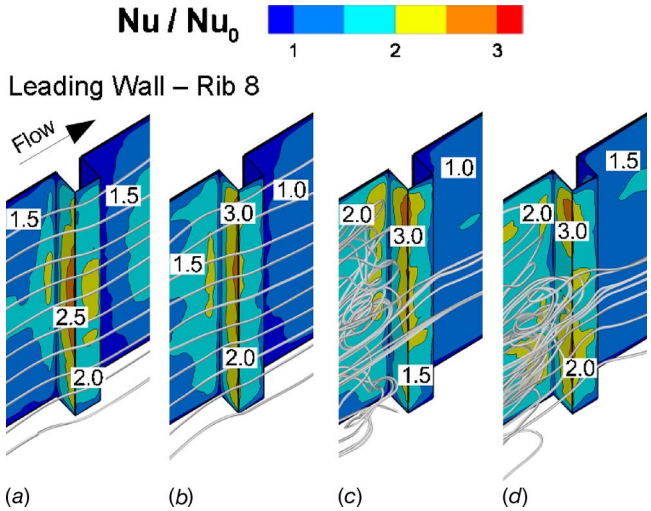

Fig. 6 Streamlines injected upstream of rib 8 in the four buoyancy cases of (*a*) Bo=0.00, (*b*) Bo=0.25, (*c*) Bo=0.45, and (*d*) Bo=0.65 (Ro=0.30 in all cases)

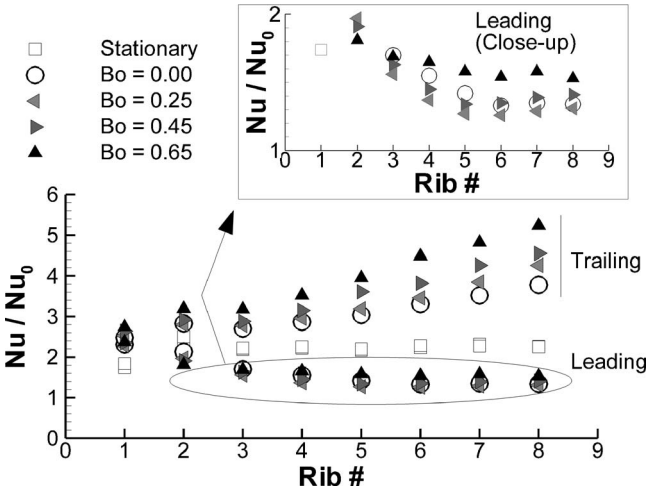

Fig. 8 Rib-averaged heat transfer augmentation on the leading and trailing walls and a close-up of the leading wall

Downloaded 30 May 2010 to 128.113.26.88. Redistribution subject to ASME license or copyright; see http://www.asme.org/terms/Terms_Use.cfm

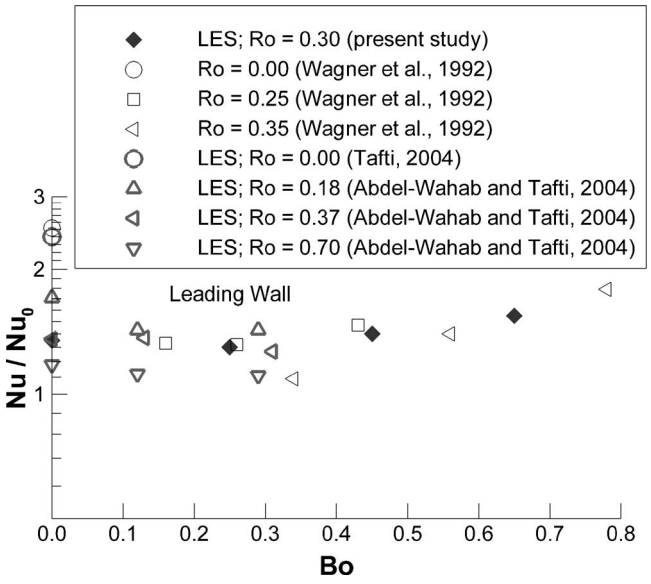

Fig. 9 Fully developed heat transfer augmentation as compared to previous LES calculations [17,14] and the experiments of Wagner et al. [1]

To compare to Wagner et al.'s [1] fully developed results, the average heat transfer augmentation over ribs 7 and 8 was used. This comparison is shown in Fig. 9. The test section in Wagner's experiments was similar to those of the present study, and a number of previous experiments in stationary [26–28] and rotating [29] ducts have shown a weak dependence on Reynolds number (Re=25,000 in the experiments) when the normalized heat transfer is considered. In addition to the experiments, previous LES computations are included from a fully developed stationary calculation [17] and a fully developed rotating calculation with varying buoyancy effects [14]. The other experimental studies showing a shift in heat transfer trends due to changes in buoyancy are not shown because [2] has angled ribs and therefore very different flow properties, and [3] only has five ribs and would not compare well to data from the ribs 7 and 8 (current study) or ribs 8–11 [1]. In the fully developed rotating calculations [14], the highest buoyancy parameter used was near Bo=0.3, which was not high enough to capture the heat transfer increase between two calculations at higher buoyancy parameters.

At buoyancy parameters smaller than 0.3, the average heat transfer augmentation changed very little, decreasing slightly, with increases in buoyancy. At Bo$>$0.3, however, the heat transfer augmentation increased steadily. This increase is larger than the initial decrease observed at the low-buoyancy parameters, quickly surpassing the initial heat transfer at Bo=0.00, resulting only from Coriolis forces.

Friction factors are calculated for each individual rib by calculating the area averaged pressure drop across a pitch surrounding the rib. The results are plotted in Fig. 10. The calculation of the friction factor does not include the effects of centrifugal pumping, which would depend on the radius from the rotation axis. When this effect is not included the friction factor increases with the buoyancy parameter. The large positive and negative values at ribs 1 and 2 are due to entrance effects and the large recirculation regions which form behind rib 1 and the subsequent pressure recovery at rib 2. Abdel-Wahab and Tafti noted in [23] that the form drag on the trailing wall accounted for about two-thirds of the overall pressure losses in the duct. Since the flow structures remain fairly constant on this side of the duct, most of the increase in the friction factor is expected to come from the increase in form and friction drag at the leading wall as the recirculating regions become larger and stronger with increase in buoyancy.

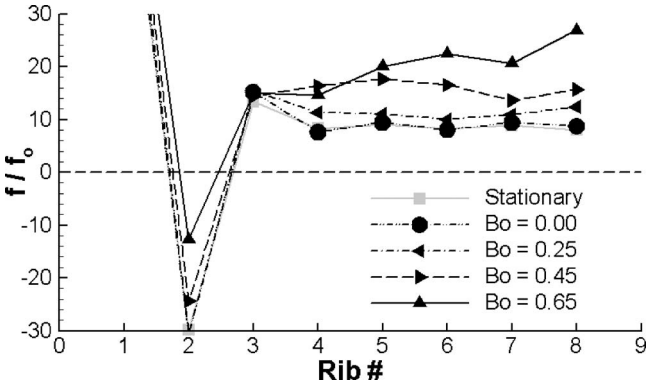

Fig. 10 The friction factor augmentation for the stationary ribbed case and the four buoyancy cases

The results are consistent with an LES study by Abdel-Wahab and Tafti [14], which showed an increase in friction factor with an increase in buoyancy at three different rotation numbers (Ro =0.18, 0.35, and 0.70) and three different buoyancy parameters for each rotation number (Bo=0.00, 0.12, and 0.30). They are also consistent with what has been reported in [15], in which an increase in the buoyancy parameter brought about an increase in friction factor in the first pass of a straight ribbed duct at Re =5000 and low buoyancy parameters (Bo=0.00, 0.15, 0.23, and 0.34).

Conclusion

Variations in buoyancy parameter in a ribbed rotating duct have a significant effect on the flow, pressure drop, and heat transfer augmentation on the channel walls. To study this effect, the rotation number was kept constant at Ro=0.30 and the buoyancy parameter was varied between values of Bo=0.00, 0.25, 0.45, and 0.65. In this study, it was found that the trailing wall heat transfer increased with a corresponding increase in buoyancy. On the leading wall, the heat transfer augmentation decreased when the buoyancy parameter was varied from zero to Bo=0.25 but increased when the buoyancy parameter was increased beyond Bo=0.25. This has been observed in previous experiments [1–3]. However, no definitive explanation about the underlying physics has been given.

By using LES it was found that at low buoyancy parameters, the growth of the separated region behind each rib was responsible for the decrease in heat transfer augmentation. However, as the separated region spanned the full pitch between ribs with an increase in buoyancy parameter, it led to entrainment of fluid from the mainstream of the duct into the separated shear layer, which was redirected by the rib downstream into the vicinity of the leading wall. The combined effect of an increase in turbulent fluctuations in the shear layer separating the recirculating region from the mainstream flow, increased entrainment of mainstream fluid, and subsequent redirection and impingement leads to an overall increase in heat transfer augmentation at the leading wall as the buoyancy parameter increases above 0.3.

It is noted that in spite of the Boussinesq approximation, the high-resolution LES calculations are capable of accurately predicting the subtle changes in heat transfer resulting from changes in buoyancy. Friction factors were found to increase monotonically with buoyancy, and the increase is attributed mostly to the increased form drag losses at the leading wall.

Acknowledgment

This research was supported by the US DOE, Office of Fossil Energy, National Energy Technology Laboratory. Any opinions, findings, conclusions, or recommendations expressed herein are

Downloaded 30 May 2010 to 128.113.26.88. Redistribution subject to ASME license or copyright; see http://www.asme.org/terms/Terms_Use.cfm

those of the author and do not necessarily reflect the views of the DOE. This work was also supported by National Computational Science Alliance under Grant No. MCA98N042N and utilized the Teragrid Linux cluster at the National Center for Supercomputing Applications.

Nomenclature

a^i = contravariant basis vector
Bo = buoyancy parameter $[=(\Delta\rho/\rho)(r/D_h)R^2]$
C_s = square root of the Smagorinsky constant
D_h = hydraulic diameter, characteristic length
e = rib height
f = fanning friction factor
g = square of the jacobian of the coordinate transformation
$\bar{G}$ = implicit top-hat filter
k = thermal conductivity
ΔL = change in streamwise position between two pressure measurements
Nu = local Nusselt number
$\overline{\text{Nu}}$ = spatially averaged Nusselt number
P = rib pitch
p = nondimensional pressure
Pr = Prandtl number $(=\mu C_p/k)$
q'' = nondimensional heat flux on duct walls and ribs, the characteristic temperature is $q''D_{hi}/k$
r = nondimensional rotation radius
r_0 = nondimensional rotation radius at duct entrance
Re = Reynolds number $(=\bar{u}_{\text{in}}D_h/\nu)$
Ri = Richardson number $(=\beta(r_0+x)R^2)$
Ro = rotation number $(=\Omega D_h/\bar{u}_{\text{in}})$
S = strain rate tensor
t = nondimensional time
T = temperature
TKE = turbulent kinetic energy described by TKE $=(\overline{u'^2}+\overline{v'^2}+\overline{w'^2})/2\bar{u}_{\text{in}}^2$
$\vec{u}$ = Cartesian velocity vector (u,v,w) or (u_1,u_2,u_3)
$\bar{u}_{\text{in}}$ = inlet flow velocity/mean bulk flow velocity, characteristic velocity
$\vec{x}$ = physical coordinates (x,y,z) or (x_1,x_2,x_3)
β = thermal expansion coefficient
Ω = heat transfer surface area
ρ = density
θ = nondimensional temperature, $(T-T_{\text{in}}/q''D_h/k)$
$\vec{\xi}$ = computational coordinates (ξ,η,ζ)

Subscripts

in = inlet to calculation domain; average bulk velocity
ref = reference
rms = root mean square
s = surface; Smagorinsky constant
t = turbulent
0 = normalizing parameter
1 = streamwise component of velocity vector

References

[1] Wagner, J. H., Johnson, B. V., Graziani, R. A., and Yeh, F. C., 1992, "Heat Transfer in Rotating Serpentine Passages With Trips Normal to the Flow," ASME J. Turbomach., **114**, pp. 847–857.
[2] El-Husayni, H. A., Taslim, M. E., and Kercher, D. M., 1994, "Experimental Heat Transfer Investigation of Stationary and Orthogonally Rotating Asymmetric and Symmetric Heated Smooth and Turbulated Channels," ASME J. Turbomach., **116**, pp. 124–132.
[3] Chang, S. W., and Morris, W. D., 2003, "Heat Transfer in a Radially Rotating Square Duct Fitted With In-Line Transverse Ribs," Int. J. Therm. Sci., **42**, pp. 267–282.
[4] Wagner, J. H., Johnson, B. V., and Hajek, T. J., 1991, "Heat Transfer in Rotating Passages With Smooth Walls and Radial Outward Flow," ASME J. Turbomach., **113**, pp. 42–51.
[5] Wagner, J. H., Johnson, B. V., Kopper, F. C., 1991, "Heat Transfer in Rotating Serpentine Passages With Smooth Walls," ASME J. Turbomach., **113**, pp. 321–330.
[6] Prakash, C., and Zerkle, R., 1992, "Prediction of Turbulent Flow and Heat Transfer in a Radially Rotating Square Duct," ASME J. Turbomach., **114**, pp. 835–846.
[7] Sleiti, A. K., and Kapat, J. S., 2004, "Comparison Between EVM and RSM Turbulence Models in Predicting Flow and Heat Transfer in Rib-Roughened Channels," *Proc. of ASME Heat Transfer/Fluids Engineering Summer Conference*, Charlotte NC, ASME, New York, ASME Paper No. HT-FED04-56250.
[8] Saha, A. K., and Acharya, S., 2003, "Flow and Heat Transfer in an Internally Ribbed Duct With Rotation: An Assessment of LES and URANS," ASME Paper No. GT2003-38619.
[9] Stephens, M. A., and Shih, T. I.-P., 1997, "Computation of Compressible Flow and Heat Transfer in a Rotating Duct With Inclined Ribs and a 180-Degree Bend," ASME Paper No. 97-GT-192.
[10] Jang, Y.-J., Chen, H.-C., and Han, J.-C., 2001, "Flow and Heat Transfer in a Rotating Square Channel With 45 Deg Angled Ribs by Reynolds Stress Turbulence Model," ASME J. Turbomach., **123**, pp. 124–132.
[11] Al-Qahtani, M., Chen, H.-C., and Han, J.-C., 2002, "A Numerical Study of Flow and Heat Transfer in Rotating Rectangular Channels (AR=4) With 45° Rib Turbulators by Reynolds Stress Turbulence Model," ASME Paper No. GT-2002–30216.
[12] Su, G., Teng, S., Chen, H.-C., and Han, J.-C., 2003, "Computation of Flow and Heat Transfer in Rotating Rectangular Channels (AR=4) With V-Shaped Ribs by a Reynolds Stress Turbulence Model," ASME Paper No. GT2003-38348.
[13] Murata, A., and Mochizuki, S., 2001, "Effect of Centrifugal Buoyancy on Turbulent Heat Transfer in an Orthogonally Rotating Square Duct With Transverse or Angled Rib Turbulators," Int. J. Heat Mass Transfer, **44**, pp. 2739–2750.
[14] Abdel-Wahab, S., and Tafti, D. K., 2004, "Large Eddy Simulation of Flow and Heat Transfer in a 90° Ribbed Duct With Rotation—Effect of Coriolis and Centrifugal Buoyancy Forces," ASME Paper No. GT2004-53799.
[15] Murata, A., and Mochizuki, S., 2004, "Aiding and Opposing Contributions of Centrifugal Buoyancy on Turbulent Heat Transfer in a Two-Pass Transverse- or Angled-Rib-Roughened Channel With Sharp 180° Turns," Int. J. Heat Mass Transfer, **47**, pp. 3721–3743.
[16] Germano, M., Piomelli, U., Moin, P., and Cabot, W. H., 1991, "A Dynamic Subgrid-Scale Eddy Vscosity Model," Phys. Fluids A **3**(7), pp. 1760–1765.
[17] Tafti, D. K., 2005, "Evaluating the Role of Subgrid Stress Modeling in a Ribbed Duct for the Internal Cooling of Turbine Blades," Int. J. Heat Fluid Flow **26**(1), pp. 92–104.
[18] Sewall, E. A., and Tafti, D. K., 2004, "Large Eddy Simulation of the Developing Region of a Stationary Ribbed Internal Turbine Blade Cooling Channel," ASME Paper No. GT2004-53832.
[19] Sewall, E. A., and Tafti, D. K., 2004, "Large Eddy Simulation of the Developing Region of a Rotating Ribbed Internal Turbine Blade Cooling Channel," ASME Paper No. GT2004-53833.
[20] Liou, T.-M., and Hwang, J.-J., 1992, "Developing Heat Transfer and Friction in a Ribbed Rectangular Duct With Flow Separation at Inlet," ASME J. Heat Transfer, **114**, pp. 565–573.
[21] Han, J. C., and Park, J. S., 1988, "Developing Heat Transfer in Rectangular Channels With Rib Turbulators," Int. J. Heat Mass Transfer, **31**, pp. 183–195.
[22] Tafti, D. K., 2001, "GenIDLEST—A Scalable Parallel Computational Tool for Simulating Complex Turbulent Flows," *Proc. of ASME Fluids Engineering Division*, ASME New York, Vol. FED 256, pp. 347–356.
[23] Abdel-Wahab, S., and Tafti, D. K., 2004, "Large Eddy Simulation of Flow and Heat Transfer in a 90° Ribbed Duct with Rotation—Effect of Coriolis Forces," ASME Paper No. GT2004-53796.
[24] Abdel-Wahab, S., and Tafti, D. K., 2004, "Large Eddy Simulation of Flow and Heat Transfer in a Staggered 45° Ribbed Duct," ASME Paper No. GT2004-53800.
[25] Incropera, F. P., and DeWitt, D. P., 2002, *Fundamentals of Heat and Mass Transfer*, 5th ed., Wiley, New York.
[26] Sewall, E. A., Tafti, D. K., Graham, A., and Thole, K. A., 2006, "Experimental Validation of Large Eddy Simulations of Flow and Heat Transfer in a Stationary Ribbed Duct," Int. J. Heat Fluid Flow **27**(2), pp. 243–258.
[27] Han, J. C., 1988, "Heat Transfer and Friction Characteristics in Rectangular Channels With Rib Turbulators," ASME J. Heat Transfer, **110**, pp. 321–328.
[28] Fann, S., Yang, W.-J., and Zhang, N., 1994, "Local Heat Transfer in a Rotating Serpentine Passage With Rib-Roughened Surfaces," Int. J. Heat Mass Transfer, **37**, pp. 217–228.
[29] Taslim, M. E., Rahman, A., Spring, S. D., 1991, "An Experimental Investigation of Heat Transfer Coefficients in a Spanwise Roating Channel With Two Opposite Rib-Roughened Walls," ASME J. Turbomach., **113**, pp. 75–82.

Downloaded 30 May 2010 to 128.113.26.88. Redistribution subject to ASME license or copyright; see http://www.asme.org/terms/Terms_Use.cfm

Carlos Martel
E.T.S.I. Aeronáuticos,
Universidad Politécnica de Madrid,
28040 Madrid, Spain
e-mail: martel@fmetsia.upm.es

Roque Corral[1]
Associate Professor
Industria de Turbopropulsores S.A.,
28830 Madrid, Spain
e-mail: roque.corral@itp.es

José Miguel Llorens
E.T.S.I. Aeronáuticos,
Universidad Politécnica de Madrid,
28040 Madrid, Spain
e-mail: jmillor@fmetsia.upm.es

Stability Increase of Aerodynamically Unstable Rotors Using Intentional Mistuning

A new simple asymptotic mistuning model, which constitutes an extension of the well known fundamental mistuning model for groups of modes belonging to a modal family exhibiting a large variation of the tuned vibration characteristics, is used to analyze the effect of mistuning on the stability properties of aerodynamically unstable rotors. The model assumes that both the aerodynamics and the structural dynamics of the assembly are linear, and retains the first-order terms of a fully consistent asymptotic expansion of the tuned system where the small parameter is the blade mistuning. The simplicity of the model allows the optimization of the blade mistuning pattern to achieve maximum rotor stability. The results of the application of this technique to realistic welded-in-pair and interlock low-pressure-turbine rotors are also presented. [DOI: 10.1115/1.2720503]

Introduction

Bladed disks used in turbine engines are nominally designed to be cyclically symmetric. However, in practice, small variations that result from the manufacturing process and wear break the symmetry, split the eigenvalue pairs, and prevent the existence of traveling-wave modes. Numerous studies have been conducted to understand mistuning effects on the dynamics of bladed disk assemblies (see the survey paper of Srinivasan [1]). The main conclusions are that while mistuning has an undesirable effect on forced response, increasing the maximum amplitude of some blades, it has often a beneficial (stabilizing) effect on flutter (see Ref. [2])

There is numerical ([3,4,2], among others) and experimental [5] evidence that mistuning has a strong beneficial effect on self-excited vibrations. However recent attempts to analyze [6] or devise design methods [7] retaining the effect of flutter on mistuning are scarce and concentrated on fans.

Flutter has been a common problem for fans and compressors. Recently, due to the increasing relevance in terms of cost and weight of low-pressure turbines (LPTs) in the architecture of modern large civil aero-engines, and the continuous trend to reduce them while keeping the same efficiency, the stiffness of LPT rotor blades has been gradually reduced, making them more flutter prone. It has been reported [8] that some LPTs may operate safely even if the rotor is aerodynamically unstable. However, it is evident that the design of LPT rotors may be constrained by flutter criteria and thus the search for mechanisms to alleviate this problem is desirable.

Several authors have suggested to increase the design space of aerodynamically unstable rotors by using intentional mistuning [3,4,9,2]. Although both intentional and random mistuning increases the stability of the assembly the difference between the statistically minimum and maximum values of damping is large enough to favor the implementation of mechanisms that ensure values close to the statistically maximum damping.

The analysis of mistuned rotors usually leads to the use of either statistical or optimization methods [9] to obtain the best mistuning pattern. In any case the need of reduced order models (ROMs) to reduce the computational time is required. The simplest form of ROMs are lumped models where the structure is modeled by mass-spring systems [10]. Lumped models, however, provide a qualitative description of the dynamics of the assembly. To obtain a more accurate description finite-element-based reduced order methods are required. During the past few years two approaches based on a component mode synthesis and the use of a subset of nominal modes (SNMs) have been developed. Methods based on component mode synthesis consider the blades and disk as separate substructures [11,12], while the ones using SNM consider the bladed disk as a single structure [13].

Recently an extension of the SNM, known as the fundamental mistuning model (FMM), that takes advantage of reducing the set of nominal modes to a single family has been developed [14]. The method only requires the natural frequencies and aerodynamic damping of the tuned system and has been used to predict the stability increase due to mistuning of LPT bladed disks [15].

This paper presents a further reduction of the FMM for cases in which all the modes of the family do not share the same frequency and mode shape (apart from differences in the interblade phase angle). This is important for LPT bladed disks that feature either very flexible disks or interlocked shrouds. The method is derived by means of a fully consistent asymptotic analysis of the mistuned rotor where the small parameter is the mistuning amplitude. The resulting model, referred to hereafter as asymptotic mistuning model (AMM), is not significantly faster than the FMM but helps to uncover the basic physical mechanisms of mistuning since it accounts for only the minimum subset of degrees of freedom that play a relevant role in the mistuning process.

In this paper we will first review the methodology currently applied to compute the aerodynamic effects on the stability of tuned bladed disks, with special emphasis in its asymptotic character. Then we will describe the AMM and its application to mistuned rotors. And finally, the application of the AMM to increase the stability of two realistic bladed disks (representative of an interlocked and a welded-in-pair LPT rotor, (see Fig. 1) using intentional mistuning will be presented.

Tuned System

The equations of motion for the small amplitude vibration of a perfectly tuned bladed disk with N identical sectors, in the absence of any external forcing except for the linear aerodynamic effects, take the form

[1]Also Associate Professor at E.T.S.I. Aeronáuticos, Universidad Politécnica de Madrid, 28040 Madrid, Spain.

Contributed by the International Gas Turbine Institute of ASME for publication in the JOURNAL OF TURBOMACHINERY. Manuscript received July 18, 2006; final manuscript received August 8, 2006; published online December 19, 2007. Review conducted by David Wisler. Paper presented at the ASME Turbo Expo 2006: Land, Sea and Air (GT2006), Barcelona, Spain, May 8–11, 2006. Paper No. GT2006-90407.

 Copyright © 2008 by ASME

Downloaded 30 May 2010 to 128.113.26.88. Redistribution subject to ASME license or copyright; see http://www.asme.org/terms/Terms_Use.cfm

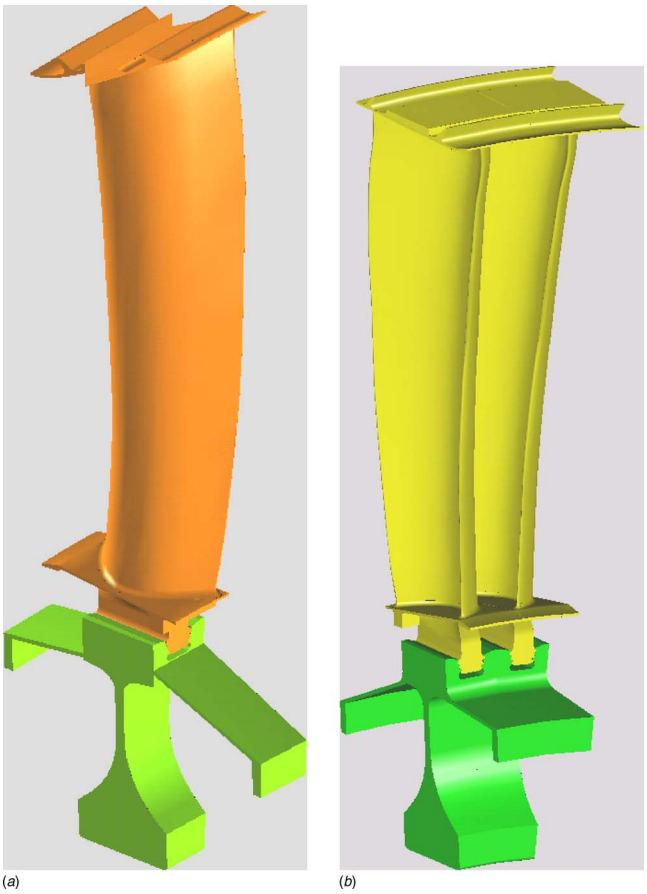

Fig. 1 Geometry of an interlock (left) and welded-in-pair (right) LPT bladed disks

$$\mathbf{M}\ddot{\mathbf{x}} + \mathbf{K}\mathbf{x} = \mathbf{L}(\mathbf{x})_{\text{aero}} \tag{1}$$

where the bladed disk degrees of freedom (after an appropriate FEM discretization) are stored in $\mathbf{x}(t)$, $\mathbf{M}$ and $\mathbf{K}$ are the mass and stiffness matrices, both symmetric and positive definite, and $\mathbf{L}_{\text{aero}}$ accounts for the aerodynamic forces. Structural damping has been neglected; the only source of damping considered in the formulation above is that coming from the aerodynamic terms, which is typically the dominating one (see e.g., Ref. [16]). Friction damping effects can be very important in tip shrouded LPTs with interlocked shrouds like the one depicted in Fig. 1, but this nonlinear effect will not be considered here because it is far away from the scope of the linear analysis presented in this paper.

The vibration modes of the system can be written using complex notation as

$$\mathbf{x} = \mathbf{X}e^{i\omega t} + \text{c.c.} \tag{2}$$

where the vibration mode shape $\mathbf{X}$ and the mode oscillation frequency and damping ω (c.c. stands for the complex conjugate) are given by the following eigenvalue problem

$$(\mathbf{K} - \omega^2\mathbf{M})\mathbf{X} = \mathbf{M}_{\text{aero}}(\omega)\mathbf{X} \tag{3}$$

which requires the knowledge of the matrix of aerodynamic forces $\mathbf{M}_{\text{aero}}$ as a function of ω. The calculation of $\mathbf{M}_{\text{aero}}$ for a given ω value involves the solution of the linearized Navier–Stokes equations that prescribe the airflow around the blades for all linearly independent blade displacements. Therefore, the computation of the bladed disk vibration characteristics using the fully coupled structural-aerodynamic formulation given by Eq. (3) is extremely costly and simply not realizable for any realistic configuration of practical interest.

The computational cost of this problem is drastically reduced if one takes into account the fact that the aerodynamic effects produce only small variations of the purely structural vibration frequencies. With this idea in mind, we will first rewrite Eq. (3) using the structural mode basis and then apply an asymptotic perturbation method to obtain the first-order aerodynamic correction of the purely structural vibration characteristics. This is a well known procedure to compute the aerodynamic stability properties of tuned bladed disks (see Refs. [15] for a recent application of this approach in two- and three-dimensional configurations), but we will briefly outline it below because it constitutes a necessary previous step before the analysis of the mistuned case.

Structural Vibration Modes. If the response vector Eq. (2) is partitioned as

$$\mathbf{X} = \begin{bmatrix} X_1 \\ X_2 \\ \vdots \\ X_N \end{bmatrix} \tag{4}$$

with the vector X_j containing the displacements of the m degrees of freedom associated with sector j, then the problem that gives the natural oscillations of the tuned bladed disk without aerodynamic effects (Eq. (3) with $\mathbf{M}_{\text{aero}}=0$) takes the form

$$\left(\begin{bmatrix} K & K_c & 0 & \cdots & K_c^{\mathrm{T}} \\ K_c^{\mathrm{T}} & K & K_c & \cdots & 0 \\ & \ddots & \ddots & & \\ K_c & 0 & \cdots & K_c^{\mathrm{T}} & K \end{bmatrix} - \omega^2 \begin{bmatrix} M & M_c & 0 & \cdots & M_c^{\mathrm{T}} \\ M_c^{\mathrm{T}} & M & M_c & \cdots & 0 \\ & & \ddots & \ddots & \\ M_c & 0 & \cdots & M_c^{\mathrm{T}} & M \end{bmatrix} \right) \times \begin{bmatrix} X_1 \\ X_2 \\ \vdots \\ X_N \end{bmatrix} = \begin{bmatrix} 0 \\ 0 \\ \vdots \\ 0 \end{bmatrix} \tag{5}$$

where the $m \times m$ sector stiffness and mass matrices K and M are symmetric and the coupling between adjacent sectors is represented by the coupling stiffness and mass matrices K_c and M_c.

The cyclic symmetry of the bladed disk (that is composed of a sector repeated N times and arranged periodically) is now evident in the matrices in Eq. (5) that exhibit a block circulant structure, i.e., each row can be obtained from the previous one after a wrap-around forward block shift. The associated complex eigenvectors

$$\begin{bmatrix} X_1 \\ \vdots \\ X_j \\ \vdots \\ X_N \end{bmatrix} = \begin{bmatrix} Z_k e^{i(2\pi k/N)1} \\ \vdots \\ Z_k e^{i(2\pi k/N)j} \\ \vdots \\ Z_k e^{i(2\pi k/N)N} \end{bmatrix}, \quad \text{for } k = 1 \ldots N \tag{6}$$

correspond to traveling waves with k nodal diameters that, taking into account Eq. (2), rotate around the annulus with constant angular velocity ω/k. The complex vector Z_k of size m contains the mode shape details and the only eigenvector variation from sector to sector is just a phase increment of amount $2\pi k/N$ (the so-called "interblade phase angle"). The vector Z_k can be regarded as the kth mode of the discrete Fourier transform of the N periodic sequence of the sector degrees of freedom along the complete structure, $X_1, \ldots X_N$; recall that the relation between Fourier modes $F_1, \ldots F_N$ and sector degrees of freedom $S_1, \ldots S_N$ is given by

$$S_j = \sum_{k=1}^{N} F_k e^{i(2\pi k/N)j}, \quad \text{for } j = 1 \ldots N \tag{7}$$

and

Downloaded 30 May 2010 to 128.113.26.88. Redistribution subject to ASME license or copyright; see http://www.asme.org/terms/Terms_Use.cfm

$$F_k = \frac{1}{N}\sum_{j=1}^{N} S_j e^{-i(2\pi j/N)k}, \quad \text{for } k = 1 \ldots N \tag{8}$$

Note also that it is enough to consider the value of k modulo N; the change $k \to k+N$, that corresponds to the addition of a complete turn around the rotor, leaves all the above expressions unchanged.

If we now insert expression (6) into Eq. (5), N decoupled eigenvalue problems of size m are obtained

$$((K_c - \omega^2 M_c)e^{i(2\pi k/N)} + (K_c - \omega^2 M_c)^T e^{-i(2\pi k/N)} + K - \omega^2 M)Z_k = 0 \quad \text{for } k = 1 \ldots N \tag{9}$$

which, for each k, have m real eigenvalues, $\omega_{k1}^2, \ldots, \omega_{km}^2 \geqslant 0$, that give the oscillation frequencies of the structure. The associated eigenvectors, $Z_{k1}, \ldots, Z_{km}$, are, in general, complex and can be taken to be such that the square matrix

$$P_k = [Z_{k1}|Z_{k2}| \ldots |Z_{km}] \tag{10}$$

verifies

$$P_k^H (M_c e^{i(2\pi k/N)} + M_c^T e^{-i(2\pi k/N)} + M) P_k = I \tag{11}$$

and

$$P_k^H (K_c e^{i(2\pi k/N)} + K_c^T e^{-i(2\pi k/N)} + K) P_k = \Omega_k^2 = \begin{bmatrix} \omega_{k1}^2 & & 0 \\ & \ddots & \\ 0 & & \omega_{km}^2 \end{bmatrix} \quad \text{for } k = 1 \ldots N \tag{12}$$

that is, the eigenvectors are orthonormal with respect to the mass matrix and turn into diagonal form the sector stiffness matrix (the superindex ^{H} stands for the conjugate transpose matrix), see e.g., Ref. [17]. Notice that the cyclic symmetry allows us to drastically reduce the computational effort required to obtain the vibration modes of the tuned bladed disk: from $O(\mathrm{N}^3\,\mathrm{m}^3)$ for solving Eq. (5) to only $O(\mathrm{N}\,\mathrm{m}^3)$ for the N eigenvalue problems in Eq. (6).

The eigenvalue equation Eq. (9) remains invariant under the changes

$$k \to N - k, \quad \omega_k^2 \to \omega_{N-k}^2, \quad \text{and} \quad Z_k \to \bar{Z}_{N-k} \tag{13}$$

and thus, for every traveling wave rotating in one direction, there is also another identical one that rotates in the opposite direction with the same velocity. This symmetry comes from the fact that the original system Eq. (1) remains unchanged after time is reversed, $t \to -t$, because it does not exhibit any dissipation at all. Traveling wave modes come thus in counterpropagating pairs, except for those associated with $k=0$ and $k=N/2$ (present only for $N=2$), which have real Z_k and can be seen as nonpropagative standing waves. Property (13) implies that the plot of the natural frequencies versus the number of nodal diameters, k, is symmetric, and only its first half (interblade phase angle from 0 to π) is normally plotted.

Figure 2 represents the natural frequencies of the purely structural problem, corresponding to a LPT rotor blade with an interlocked shroud (left plot in Fig. 1) whose characteristics have been previously reported [15]. The main effect of interlocking the rotor is twofold: first, it significantly raises the frequencies of the high nodal diameter modes, which in first approximation are torsion modes, and, second, it creates a region with a steep change in frequency that corresponds to shroud-dominated complex bending–torsion modes.

Figure 3 is the equivalent counterpart for a welded-in-pair LPT rotor blade (right plot in Fig. 1). The geometry of both configurations is strictly the same and the differences between the modal characteristics are solely associated with the shroud boundary conditions. The frequency characteristics of this type of bladed disks do not differ significantly from the ones with single cantilever rotor blades. Two regions may be clearly distinguished. First,

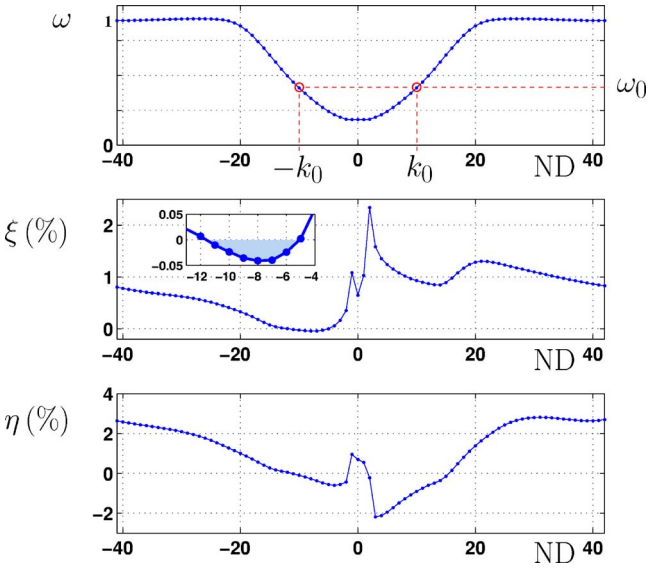

Fig. 2 Tuned vibration characteristics versus number of nodal diameters for the first family of modes of an interlocked rotor [15] (*N*=84): (top) normalized vibration frequency (active modes encircled); (middle) aerodynamic damping relative to the critical damping; (inset) zoom of the unstable modes (shading indicates instability); and (bottom); aerodynamic frequency correction (see Eq. (23))

a small region of disk dominated modes at low nodal diameters, which is an indication that the disk is very stiff compared to the blades. And second, a large high nodal diameter region corresponding to flap modes with almost no disk coupling effect.

It is important to highlight that the steep variation of the natural frequencies seen in the shroud-dominated or disk-dominated nodal diameter region is characteristic of LPT bladed disks. Modern unshrouded fans or blisks exhibit frequency variations much smaller than the ones presented in this work, at least for the first families of modes.

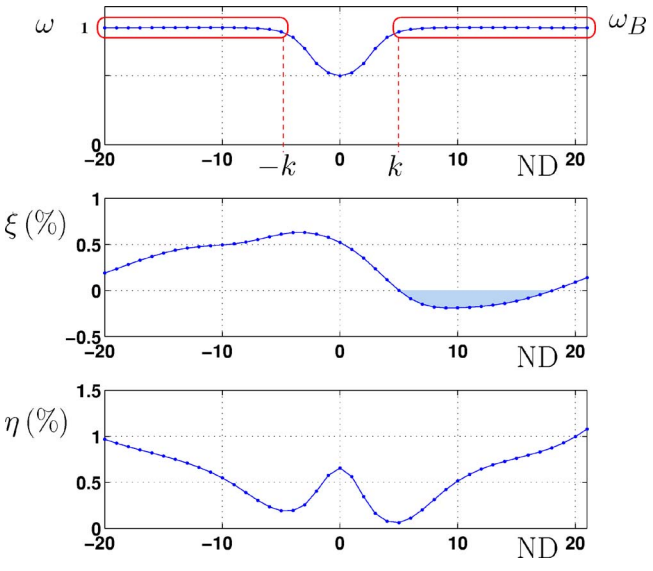

Fig. 3 Tuned vibration characteristics versus number of nodal diameters for the first family of modes of a welded-in-pair rotor [15] (*N*=42): (top) normalized vibration frequency (active modes encircled); (middle) aerodynamic damping relative to the critical damping (shading indicates instability); and (bottom) aerodynamic frequency correction (see Eq. (23))

Downloaded 30 May 2010 to 128.113.26.88. Redistribution subject to ASME license or copyright; see http://www.asme.org/terms/Terms_Use.cfm

Aerodynamic Correction. In order to evaluate the aerodynamic correction of the vibration characteristics of the bladed disk it is convenient to first perform in Eq. (3) the following change of variables to a purely structural traveling wave basis

$$\mathbf{X} = \mathbf{P}\mathbf{A} \tag{14}$$

with

$$\mathbf{P} = \frac{1}{\sqrt{N}} \begin{bmatrix} P_1 e^{i(2\pi 1/N)1} & \cdots & P_N e^{i(2\pi N/N)1} \\ \vdots & & \vdots \\ P_1 e^{i(2\pi 1/N)j} & \cdots & P_N e^{i(2\pi N/N)j} \\ \vdots & & \vdots \\ P_1 e^{i(2\pi 1/N)N} & \cdots & P_N e^{i(2\pi N/N)N} \end{bmatrix} \quad \text{and} \quad \mathbf{A} = \begin{bmatrix} A_1 \\ \vdots \\ A_j \\ \vdots \\ A_N \end{bmatrix} \tag{15}$$

and where the vectors $A_j = [A_{j1}, \ldots, A_{jm}]^T$ contain the amplitudes of the different traveling wave modes. The eigenvalue problem in Eq. (3) now takes the form

$$\begin{bmatrix} \Omega_1^2 - \omega^2 I & \cdots & 0 \\ \vdots & \ddots & \vdots \\ 0 & \cdots & \Omega_N^2 - \omega^2 I \end{bmatrix} \begin{bmatrix} A_1 \\ \vdots \\ A_N \end{bmatrix} = \mathbf{P}^H \mathbf{M}_{\text{aero}}(\omega) \mathbf{P} \begin{bmatrix} A_1 \\ \vdots \\ A_N \end{bmatrix} \tag{16}$$

with diagonal mass and stiffness matrices, see Eqs. (11) and (12), and block diagonal aerodynamic matrix

$$\mathbf{P}^H \mathbf{M}_{\text{aero}}(\omega) \mathbf{P} = \begin{bmatrix} M_1(\omega) & \cdots & 0 \\ \vdots & \ddots & \vdots \\ 0 & \cdots & M_N(\omega) \end{bmatrix} \tag{17}$$

as a result of the fact that the linearized aerodynamic flow problem has also cyclic symmetry and, therefore, the modes with different nodal diameters are completely independent.

The aerodynamic terms are small and give rise to a small correction of the purely structural vibration frequencies. For a given structural tuned frequency $\omega_{\tilde{k}\tilde{j}}$ (corresponding to the $\tilde{j}$th traveling wave mode with $\tilde{k}$ nodal diameters), its aerodynamically corrected counterpart ω is given by Eq. (16), and it can be approximately estimated if one takes into account the following:

1. The modes with a different number of nodal diameters are decoupled and do not play any role in the correction of $\omega_{\tilde{k}\tilde{j}}$, that is

$$A_k = 0, \quad \text{for all } k \neq \tilde{k} \tag{18}$$

2. The $\tilde{k}j$th equation in Eq. (16) reads

$$(\omega_{\tilde{k}j}^2 - \omega^2) A_{\tilde{k}j} = \sum_{h=1}^{m} [M_{\tilde{k}}(\omega)]_{jh} A_{\tilde{k}h} \tag{19}$$

The corrected frequency ω is close to $\omega_{\tilde{k}\tilde{j}}$, but not to the other frequencies $\omega_{\tilde{k}j}$ (we are implicitly assuming here that $\omega_{\tilde{k}\tilde{j}}$ is well apart from the rest of the frequencies corresponding to the same number of nodal diameters $\tilde{k}$). Therefore, if $j \neq \tilde{j}$ the term $(\omega_{\tilde{k}j}^2 - \omega^2)$ in the equation above is not small, but the aerodynamic terms, $[M_{\tilde{k}}(\omega)]_{jh}$, are small and we can neglect them to obtain

$$A_{\tilde{k}j} = 0, \quad \text{for all } j \neq \tilde{j} \tag{20}$$

In other words, the rest of the traveling wave modes with $\tilde{k}$ nodal diameters and different frequencies do not contribute either to the correction of the $\omega_{\tilde{k}\tilde{j}}$ in first approximation.

3. And finally, taking into account Eqs. (18) and (20), the $\tilde{k}\tilde{j}$th equation in Eq. (16) simplifies to

$$(\omega_{\tilde{k}\tilde{j}}^2 - \omega^2) A_{\tilde{k}\tilde{j}} = [M_{\tilde{k}}(\omega_{\tilde{k}\tilde{j}})]_{\tilde{j}\tilde{j}} A_{\tilde{k}\tilde{j}} \tag{21}$$

where the coefficients $(\omega_{\tilde{k}\tilde{j}}^2 - \omega^2)$ and $[M_{\tilde{k}}(\omega_{\tilde{k}\tilde{j}})]_{\tilde{j}\tilde{j}}$ are now both small, and we have also made use of the fact that ω is close to $\omega_{\tilde{k}\tilde{j}}$ to approximate

$$[M_{\tilde{k}}(\omega)]_{\tilde{j}\tilde{j}} = [M_{\tilde{k}}(\omega_{\tilde{k}\tilde{j}})]_{\tilde{j}\tilde{j}} + \cdots$$

In summary, the shape of the purely structural vibration modes remains, in first approximation, unchanged by the aerodynamic effects, while the mode frequencies $\omega_{\tilde{k}\tilde{j}}$ experience a small correction that, according to Eq. (21), can be expressed as

$$\omega = \omega_{\tilde{k}\tilde{j}} \left(1 - \frac{[M_{\tilde{k}}(\omega_{\tilde{k}\tilde{j}})]_{\tilde{j}\tilde{j}}}{2\omega_{\tilde{k}\tilde{j}}^2} + \cdots \right) \tag{22}$$

where the term $[M_{\tilde{k}}(\omega_{\tilde{k}\tilde{j}})]_{\tilde{j}\tilde{j}}$ represents the work of the aerodynamic forces over the blades, for a prescribed blade displacement that corresponds to the $\tilde{k}\tilde{j}$ vibration mode.

The computation of the work of the aerodynamic forces can be reduced to solving a set of linearized Navier–Stokes equations in a single sector with phase-shifted boundary conditions (see, e.g., Refs. [15]). The resulting aerodynamic correction in Eq. (22) is, in general, a complex number that can be written as

$$[M_{\tilde{k}}(\omega_{\tilde{k}\tilde{j}})]_{\tilde{j}\tilde{j}} = -2\omega_{\tilde{k}\tilde{j}}^2 (\eta + i2\xi) \tag{23}$$

where the real part η represents a small relative correction of the oscillatory frequency and the (positive/negative) imaginary part ξ is the small (stable/unstable) aerodynamic damping relative to the critical damping. The aerodynamic damping has to be evaluated for all system modes in order to know whether the bladed disk is stable or, on the contrary, some modes are unstable and flutter sets in. Moreover, the aerodynamic terms are not invariant under the changes in Eq. (13) and, therefore, the aerodynamic correction for a pair of identical traveling waves that rotate in opposite directions is, in general, different and has to be separately computed.

Figures 2 and 3 (middle) represent the aerodynamic damping relative to the critical damping of the interlock and welded-in-pair configurations, respectively. Both configurations are aerodynamically unstable, however there are three very noticeable differences, namely,

1. The instability level of the interlock is much more moderated than the one of the welded-in-pair (for the same steady aerodynamics);
2. The unstable modes of the interlock are complex, shroud dominated, bending–torsion modes, while those in the welded-in-pair correspond to an in-phase bending of the two in-sector blades with almost no disk coupling effect; and
3. The unstable modes of the interlock rotor are located in a region of steep variation of the natural frequency, while the ones of the welded-in-pair rotor are located in a flat region in terms of frequency.

The one that is relevant from the point of view of the resulting AMM description is in the third point. We will call the modes isolated or clustered depending on their relative difference in terms of frequency with the rest of the modes.

Figures 2 and 3 (bottom) show the frequency correction of the purely structural modes due to the aerodynamics. This correction is seldom taken into account in the standard design practice of LPT rotors. The average frequency correction for the interlock rotor due to the aerodynamics is about 2%, while for the welded-in-pair it is 1%, and the largest correction occurs for the highest nodal diameters.

Downloaded 30 May 2010 to 128.113.26.88. Redistribution subject to ASME license or copyright; see http://www.asme.org/terms/Terms_Use.cfm

Asymptotic Mistuning Model

The equations of motion for the vibration modes of a mistuned bladed disk with linear aerodynamic effects can be written as

$$((\mathbf{K}+\Delta\mathbf{K})-\omega^2(\mathbf{M}+\Delta\mathbf{M}))\mathbf{X}=\mathbf{M}_{\text{aero}}(\omega)\mathbf{X} \tag{24}$$

which are simply the tuned Eqs. (3) with the mistuning stiffness, $\Delta\mathbf{K}$, and mass, $\Delta\mathbf{M}$, matrices added. $\Delta\mathbf{K}$ and $\Delta\mathbf{M}$ are block diagonal matrices that contain the deviations from the mean stiffness K and mass M sector matrices (see Eq. (5)), that is

$$\Delta\mathbf{K}=\begin{bmatrix}\Delta K_1 & 0 & \cdots & 0\\ 0 & \Delta K_2 & \cdots & 0\\ & & \ddots & \\ 0 & 0 & 0 & \Delta K_N\end{bmatrix}$$
$$\Delta\mathbf{M}=\begin{bmatrix}\Delta M_1 & 0 & \cdots & 0\\ 0 & \Delta M_2 & \cdots & 0\\ & & \ddots & \\ 0 & 0 & 0 & \Delta M_N\end{bmatrix} \tag{25}$$

with

$$\sum_{j=1}^{N}\Delta K_j=0,\quad \sum_{j=1}^{N}\Delta M_j=0 \tag{26}$$

and

$$\Delta K_j=\Delta K_j^T,\quad \Delta M_j=\Delta M_j^T\quad \text{for } j=1\ldots N \tag{27}$$

The mistuning of the sector coupling block matrices has not been included in the model above; the coupling matrices involve only a very small subset of the degree of freedom (DOF) of the sector and, thus, its mistuning is negligible as compared with that of the main sector.

As we did in the previous section, we first rewrite Eq. (24) using the tuned traveling wave mode basis, Eqs. (14) and (15), to obtain

$$\begin{bmatrix}\Omega_1^2-\omega^2 I & \cdots & 0\\ \vdots & \ddots & \vdots\\ 0 & \cdots & \Omega_N^2-\omega^2 I\end{bmatrix}\begin{bmatrix}A_1\\ \vdots\\ A_N\end{bmatrix}=\mathbf{P}^H\mathbf{M}_{\text{aero}}(\omega)\mathbf{P}\begin{bmatrix}A_1\\ \vdots\\ A_N\end{bmatrix}$$
$$-\mathbf{P}^H(\Delta\mathbf{K}-\omega^2\Delta\mathbf{M})\mathbf{P}\begin{bmatrix}A_1\\ \vdots\\ A_N\end{bmatrix} \tag{28}$$

where the aerodynamic matrix is block diagonal, see Eq. (17). The structure of the mistuning correction matrix can be more easily analyzed if we make use of the Fourier modes of the sector distribution of the mistuning mass and stiffness, ΔK_k^{F} and ΔM_k^{F} which, according to Eq. (7), are given by

$$\Delta K_j=\sum_{k=1}^{N}\Delta K_k^F e^{i(2\pi k/N)j}$$

and

$$\Delta M_j=\sum_{k=1}^{N}\Delta M_k^F e^{i(2\pi k/N)j}\quad \text{for } j=1\ldots N$$

and verify (see Eqs. (26) and (27))

$$\Delta K_N^F=0,\quad \Delta M_N^F=0 \text{ and } \Delta K_k^F=\overline{\Delta K_{-k}^F},\quad \Delta M_k^F=\overline{\Delta M_{-k}^F}$$
$$\Delta K_k^F=(\Delta K_k^F)^T,\quad \Delta M_k^F=(\Delta M_k^F)^T,\quad \text{for } k=1\ldots N \tag{29}$$

After inserting the above expressions into Eq. (28), the mistuning matrix takes the form

$$\mathbf{P}^H(\Delta\mathbf{K}-\omega^2\Delta\mathbf{M})\mathbf{P}=\begin{bmatrix}0 & \Delta_{12} & \cdots & \Delta_{1N}\\ \Delta_{21} & 0 & \cdots & \Delta_{2N}\\ \vdots & \vdots & \ddots & \vdots\\ \Delta_{N1} & \Delta_{N2} & \cdots & 0\end{bmatrix} \tag{30}$$

where each block is related to the Fourier components of the mistuning by

$$\Delta_{kj}=P_k^H(\Delta K_{k-j}^F-\omega^2\Delta M_{k-j}^F)P_j \tag{31}$$

Note that the mistuning matrix in Eq. (30) exhibits off diagonal blocks and, thus, mistuning couples traveling waves with different number of nodal diameters. Moreover, according to Eq. (31), the coupling between the traveling waves with k and j nodal diameters takes place precisely through the (k-j) Fourier mode of the mistuning.

The mistuning and aerodynamic effects are small and give rise to small corrections of the purely structural natural oscillation frequencies. We will now use exactly the same arguments as in the previous section in order to derive a set of simplified equations that allow us to obtain an estimate of the mistuning and aerodynamic correction ω of a given purely structural tuned frequency $\tilde{\omega}$.

The solution ω of Eq. (28) that we are looking for is close to $\tilde{\omega}$ and this allow us to distinguish between two different kinds of traveling wave modes as follows:

1. Modes with frequencies that are not close to $\tilde{\omega}$, that is, modes whose frequency ω_{kj} is such that $|\tilde{\omega}-\omega_{kj}|$ is large as compared with the typical aerodynamic and mistuning frequency corrections. The corresponding equation for this kind of modes in Eq. (28) is of the form

$$(\omega_{kj}^2-\omega^2)A_{kj}=\sum_{i,h=1}^{m}(\text{small terms})A_{ih}$$

where the coefficient on the left hand side is large as compared with the small aerodynamic and mistuning terms on the right-hand side because ω is close to $\tilde{\omega}$ but not to ω_{kj}. After neglecting the small terms, the equation above yields

$$A_{kj}=0 \tag{32}$$

and, as it was already obtained in Item 2 of the previous section, all traveling wave modes with frequencies well apart from $\tilde{\omega}$ do not contribute in first approximation to its correction.

2. Modes with frequencies close to $\tilde{\omega}$, i.e., with frequencies that are at a distance from $\tilde{\omega}$ of the same order of the small aerodynamic and mistuning frequency corrections. We will hereafter refer to these modes as "active" modes because they are, in first approximation, the only ones that take part in the correction of $\tilde{\omega}$. After removing the unactive modes of the previous item from Eq. (28), the resulting equation for an active mode with amplitude A_a and tuned structural frequency ω_a reads

$$(\omega_a^2-\omega^2)A_a=-2\omega_a^2(\eta_a+i2\xi_a)A_a-\sum_{a'\neq a}\delta_{aa'}A_{a'} \tag{33}$$

where all coefficients are now small. The aerodynamic term was obtained in the previous section, the sum goes over all active modes except A_a, and according to Eq. (31), the mistuning coupling coefficients can be written as

$$\delta_{aa'}=Z_a^H(\Delta K_{k-k'}^F-\tilde{\omega}^2\Delta M_{k-k'}^F)Z_{a'} \tag{34}$$

where Z_a, $Z_{a'}$, k, and k' are, respectively, the mode shapes and the number of nodal diameters of the active modes A_a and $A_{a'}$, and the frequency ω has been approximated by $\tilde{\omega}$ (note also that the mistuning coupling terms verify $\delta_{aa'}=\overline{\delta_{a'a}}$ because mistuning constitutes a purely structural, con-

Downloaded 30 May 2010 to 128.113.26.88. Redistribution subject to ASME license or copyright; see http://www.asme.org/terms/Terms_Use.cfm

servative perturbation). Finally, we introduce the frequency correction $\omega=\tilde{\omega}(1+\Delta\omega)$ (with $|\Delta\omega|\ll 1$), in order to write Eq. (33) in the more convenient form

$$((\omega_a^2-\tilde{\omega}^2)-2\tilde{\omega}^2\Delta\omega)A_a=-2\omega_a^2(\eta_a+i2\xi_a)A_a-\sum_{a'\neq a}\delta_{aa'}A_{a'} \tag{35}$$

In a general situation, we have as many equations like Eq. (35) as active modes, which form a reduced eigenvalue problem that allow us to estimate correction of the frequencies close to $\tilde{\omega}$. We call this reduced problem the asymptotic mistuning model (AMM) because the above described procedure can be seen as an asymptotic perturbation expansion in which we have computed only the first correction term. The small parameters in this expansion are the size of the aerodynamic correction ($\sim$1–2% in the examples shown in Figs. 2 and 3) and the mistuning amplitude, which is considered of the same order: the smaller the aerodynamic and mistuning effects, the better the approximation given by the AMM.

The AMM description retains only the minimal set of traveling wave modes that are relevant for the estimation of the correction of a given purely structural, tuned frequency (and the nearby ones) due to aerodynamic and mistuning effects. It also reveals the coupling mechanism of mistuning: the only mistuning modes that are relevant are those that couple active modes, i.e., those modes with wave number equal to the difference of the number of nodal diameters of two active modes (see Eq. (34)).

In the next section we focus on two frequent bladed disk modal configurations in order to illustrate the use of the AMM formulation and its capability to provide a simplified description of the combined effect of aerodynamics and mistuning on the linear stability characteristics.

Applications

The AMM has been used to determine the optimal mistuning pattern required for the stabilization of two bladed disks. Their frequency characteristics have been obtained using a finite-element model. The unsteady aerodynamics has been computed assuming that its influence is negligible in the structural modes. The purely structural mode shapes and natural frequencies have been injected in a linearized Navier–Stokes solver and the unsteady aerodynamics associated to each mode shape computed [15].

It has already been mentioned that the two cases have been carefully chosen to represent two different problems: the aerodynamic instability of an interlock and a welded-in-pair LPT bladed disks. Both cases are substantially different because since in the former the unstable modes are separated in terms of frequency from the rest of the modes, in the latter there is a cluster of modes that share nearly the same frequency.

Isolated Modes. For the family of modes represented in Fig. 2, the marked vibration frequency ω_0 is well apart from the rest, i.e., its distance to the rest of the frequencies is large as compared with the corresponding aerodynamic corrections (represented in the lower plots of Fig. 2). In this case, in order to take into account the effect of the mistuning it is enough to consider the two counter rotating wavetrains with frequency ω_0 and nodal diameters $\pm k_0$. In other words, these two modes are the only active modes in the AMM description, which now takes its simplest form

$$\begin{aligned}-2\omega_0^2\Delta\omega A_+&=-2\omega_0^2(\eta_+ + i2\xi_+)A_+-\delta A_-\\ -2\omega_0^2\Delta\omega A_-&=-2\omega_0^2(\eta_- + i2\xi_-)A_--\bar{\delta}A_+\end{aligned} \tag{36}$$

where $A_\pm$, $\eta_\pm$, and $\xi_\pm$ are, respectively, the amplitude, the relative aerodynamic correction frequency, and damping of the $\pm k_0$ modes. The mistuning correction of the stability characteristics takes place only through its $2k_0$ Fourier mode

$$\delta=Z_{k_0}^H(\Delta K_{2k_0}^F-\omega_0^2\Delta M_{2k_0}^F)\overline{Z_{k_0}} \tag{37}$$

The eigenvalue problem Eq. (36) can be explicitly solved to give

$$\Delta\omega=\frac{(\eta_+ + \eta_-)+2i(\xi_+ + \xi_-)}{2}\pm\sqrt{\left(\frac{(\eta_+ - \eta_-)+2i(\xi_+ - \xi_-)}{2}\right)^2+\frac{|\delta|^2}{4\omega_0^4}}$$

and, if we now decompose the frequency correction as $\Delta\omega=\eta+2i\xi$, the resulting mistuned relative critical dampings can be expressed as

$$\xi=\frac{(\xi_+ + \xi_-)}{2}\pm\frac{1}{2}\sqrt{\frac{\sqrt{a^2+b^2}-a}{2}}$$

with

$$a=\frac{(\eta_+ - \eta_-)^2}{4}-(\xi^+ - \xi^-)^2+\frac{|\delta|^2}{4\omega_0^4}$$

and

$$b=(\eta^+ - \eta^-)(\xi^+ - \xi^-)$$

which are plotted in Fig. 4 as functions of the mistuning amplitude $|\delta|$.

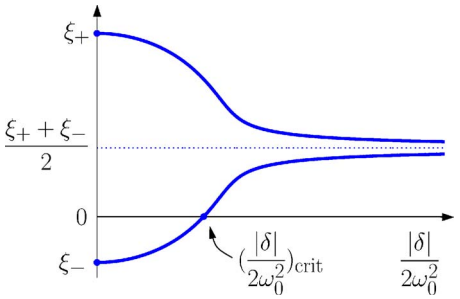

Fig. 4 Damping variation for a pair of isolated modes as the mistuning amplitude $|\delta|$ is increased

As it can appreciated from Fig. 4, in the absence of mistuning the tuned aerodynamic stability characteristics are recovered (one of the modes is stable $\xi_+>0$ and the other unstable and $\xi_-<0$, see Fig. 2). When the mistuning size is increased both dampings approach the tuned average damping $(\xi_+ + \xi_-)/2$ (in fact, the average of the mistuned dampings remains constant and equal to its tuned value). The shape of the curve in Fig. 4 is completely similar to that obtained via numerical optimization in Ref. [9]. There is an initial region for small mistuning with very little change in the stability margin, then comes a region of stability variation due to mistuning, and finally, the sensitivity to mistuning decays again as mistuning is increased and the asymptotic limit of stability is approached.

The mistuning is always stabilizing, but the stability increase of the unstable mode reduces the stability of the stable one. For positive averaged damping, i.e., for $(\xi_+ + \xi_-)/2>0$, both modes can be stabilized just by increasing the mistuning above the critical value

$$\left(\frac{|\delta|}{2\omega_0^2}\right)_{\text{crit}}=\sqrt{-\xi_+\xi_-\left(4+\frac{(\eta_+ - \eta_-)^2}{(\xi_+ + \xi_-)^2}\right)} \tag{38}$$

On the other hand, if the averaged damping is negative, then the stabilization through a small intentional mistuning is not possible.

The expression for the mistuning coefficient given in Eq. (37)

Downloaded 30 May 2010 to 128.113.26.88. Redistribution subject to ASME license or copyright; see http://www.asme.org/terms/Terms_Use.cfm

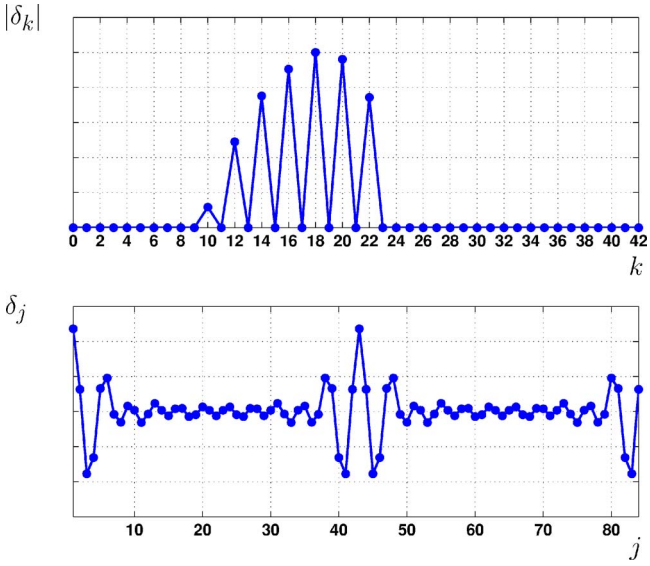

Fig. 5 (Top) Fourier coefficient distribution of the mistuning pattern required to stabilize the mode family in Fig. 2 according to Eq. (38); (bottom) corresponding physical mistuning pattern

can be easily interpreted in terms of the vibration frequency splitting produced by the mistuning when no aerodynamics effects are present. In this purely structural vibration case, the corrections of the frequency are given by Eq. (36) with $\xi_{\pm}=0$ and $\eta_{\pm}=0$ that yields

$$\Delta\omega = \pm \frac{|\delta|}{2\omega_0^2}$$

and thus the size of the relative frequency splitting due to mistuning is precisely $|\delta|/\omega_0^2$. Now, going back to the critical mistuning in Eq. (38), we can conclude that the mistuning required to achieve stabilization is the one that, in the absence of any aerodynamic effect, gives rise to a frequency splitting equal to twice the value in Eq. (38).

Note also that the only relevant mistuning component is its $2k_0$ Fourier mode, and that Eq. (37) indicates that, in order to be effective, the inclusion of intentional mistuning (via e.g., the addition of small masses) should take place in the sector regions with large local alternate stresses.

Finally, concerning the mode family depicted in Fig. 2, the unstable modes, which correspond to $k=-11,-10,-9,-8,-7,-6,-5$ (see the inset in the middle plot of Fig. 2), belong to isolated mode pairs and, according to the above results, can be stabilized just by the addition of a small mistuning pattern with the following six Fourier modes: 10, 12, 14, 16, 18, 20, and 22 (the resulting normalized profile of the Fourier coefficient distribution of the mistuning pattern required to achieve stabilization according to Eq. (38) is represented in Fig. 5). The remaining modes simply do not play any role, in first approximation, in the mistuning process.

Another interesting conclusion is that alternate mistuning, which has been argued to be suboptimal [9], has no effect on this type of configuration. This is somehow more surprising if we consider that one of the few experimental attempts to assess the effect of mistuning on the aerodynamic damping of LPT airfoils (Ref. [5]) was performed using alternate mistuning.

Clustered Modes. A frequency distribution like the one plotted in Fig. 3, in which the natural frequencies of a family of modes fast approach a constant value, ω_B, as the number of nodal diameters is increased, is frequently obtained in the vibration analysis of realistic tuned bladed disks. In this case, no interaction between the shrouds has been implemented in the finite-element method (FEM) used to compute the vibration characteristics in Fig. 3, and the frequency ω_B corresponds to an in-phase cantilever bending mode of the two blades with their shrouded tips contained in the basic sector of this welded-in-pair bladed disk (see Fig. 1), with almost no disk coupling effect. The AMM description again permits us to easily compute the mistuning-induced corrections of the frequency and damping.

In this case, the group of active modes are those with k or more nodal diameters (see Fig. 3), and we thus have $N_a=N-2k+1$ active modes, where N is the number of sectors of the bladed disk. The AMM formulation simplifies this problem to the computation of the eigenvalues $\Delta\omega$ of a matrix of size N_a that, according to Eq. (35), can be written in the form

$$\begin{bmatrix} d_k & & & & \\ & d_{k+1} & & \Delta & \\ & & \ddots & & \\ & \Delta^H & & d_{-(k+1)} & \\ & & & & d_{-k} \end{bmatrix} \begin{bmatrix} A_k \\ A_{k+1} \\ \vdots \\ A_{-(k+1)} \\ A_{-k} \end{bmatrix} = 0 \tag{39}$$

where the active modes have been ordered consecutively in k (recall that the number of nodal diameters has to be considered only modulo N) and the diagonal elements are given by

$$d_j = (\omega_j^2 - \omega_B^2) + 2\omega_j^2(\eta_j + i2\xi_j) - 2\omega_B^2\Delta\omega \tag{40}$$

The sub- and superdiagonal mistuning terms (Δ in the matrix above) can be further simplified if one takes into account that, in the almost constant frequency region that we are describing, the different mode shapes are approximately equal to the in-phase cantilever bending of the two in-sector blades, but with a different sector to sector phase change (i.e., a different interblade phase angle). That is, after arranging the blade and disk sector DOFs in the form

$$X_j = \begin{bmatrix} X_j^{\text{blade}} \\ X_j^{\text{disk}} \end{bmatrix}$$

the j sector displacement associated with the k mode can be approximately written as

$$X_j = \begin{bmatrix} Z_B \\ 0 \end{bmatrix} e^{i(2\pi k/N)j}$$

where the real vector Z_B contains the in-phase displacements of the two in-sector blades and their shrouded tips with frequency ω_B. This implies that the Fourier components of the modes in this near constant frequency region are equal and real

$$Z = \begin{bmatrix} Z_B \\ 0 \end{bmatrix} \tag{41}$$

and that the mistuning terms (see Eq. (34)) can be reduced to

$$\delta_{kk'} = Z^T(\Delta K_{k-k'}^F - \omega_B^2 \Delta M_{k-k'}^F)Z \tag{42}$$

The above expression for the mistuning terms depends only on $(k-k')$ and allows us to write the eigenvalue problem Eq. (39) as

$$\begin{bmatrix} d_k & \delta_1 & \delta_2 & \dots & \delta_{N_a-1} \\ \overline{\delta_1} & d_{k+1} & \delta_1 & \dots & \delta_{N_a-2} \\ & & \ddots & & \\ \overline{\delta_{N_a-2}} & \dots & & d_{-(k+1)} & \delta_1 \\ \overline{\delta_{N_a-1}} & \dots & & \overline{\delta_1} & d_{-k} \end{bmatrix} \begin{bmatrix} A_k \\ A_{k+1} \\ \vdots \\ A_{-(k+1)} \\ A_{-k} \end{bmatrix} = 0 \tag{43}$$

where the mistuning appears only through the complex numbers $\delta_1, \delta_2, \dots, \delta_{N_a-1}$.

Proceeding as in Ref. [14], it is possible to relate the mistuning coefficients δ_k to the mistuned frequencies ω_{Bj} of in-phase bending oscillation of each blade pair of the bladed disk. To this end we assume that the mode shapes of the mistuned blade pair

Downloaded 30 May 2010 to 128.113.26.88. Redistribution subject to ASME license or copyright; see http://www.asme.org/terms/Terms_Use.cfm

$$Z_j = \begin{bmatrix} Z_{Bj} \\ 0 \end{bmatrix}$$

are very close to that of the tuned blade pair in Eq. (41) and then, in first approximation, we have

$$\begin{aligned} Z^T(\Delta K_j - \omega_B^2 \Delta M_j)Z &= Z^T((K+\Delta K_j) - \omega_B^2(M+\Delta M_j))Z \\ &\simeq Z_j^T((K+\Delta K_j) - \omega_B^2(M+\Delta M_j))Z_j \\ &= \omega_{Bj}^2 - \omega_B^2 \end{aligned} \tag{44}$$

where we have made use of the fact that ω_B and Z_B in Eq. (41) are the tuned in-phase blade pair bending frequency and mode shape and thus verify

$$Z^T(K - \omega_B^2 M)Z = (\omega_B^2 - \omega_B^2)I = 0$$

If we now introduce the blade pair in-phase bending mistuned frequency relative variation, $\Delta\omega_{Bj}$, given by

$$\omega_{Bj} = \omega_B(1 + \Delta\omega_{Bj}) \quad \text{with } |\Delta\omega_{Bj}| \ll 1$$

Eq. (44) can be further simplified to

$$Z^T(\Delta K_j - \omega_B^2 \Delta M_j)Z \simeq 2\omega_B^2 \Delta\omega_{Bj}$$

and then, the δ_k coefficients in Eq. (43) can be written as

$$\delta_k = 2\omega_B^2 \Delta\omega_{Bk}^F$$

where $\Delta\omega_{Bk}^F$ is the kth Fourier mode of the mistuned blade pair in-phase bending relative frequency variation pattern.

After collecting all the above results, the eigenvalue problem produced by the AMM formulation takes the final form

$$\begin{bmatrix} \tilde{d}_k & \Delta\omega_{B1}^F & \Delta\omega_{B2}^F & \dots & \Delta\omega_{BN_a-1}^F \\ \overline{\Delta\omega_{B1}^F} & \tilde{d}_{k+1} & \Delta\omega_{B1}^F & \dots & \Delta\omega_{BN_a-2}^F \\ & & \ddots & & \\ \overline{\Delta\omega_{BN_a-2}^F} & \dots & \overline{\Delta\omega_{B1}^F} & \tilde{d}_{-(k+1)} & \Delta\omega_{B1}^F \\ \overline{\Delta\omega_{BN_a-1}^F} & \dots & & \overline{\Delta\omega_{B1}^F} & \tilde{d}_{-k} \end{bmatrix} \begin{bmatrix} A_k \\ A_{k+1} \\ \vdots \\ A_{-(k+1)} \\ A_{-k} \end{bmatrix} = 0 \tag{45}$$

where the diagonal elements can be written, in first approximation, as

$$\tilde{d}_j = \frac{(\omega_j^2 - \omega_B^2)}{2\omega_B^2} + (\eta_j + i2\xi_j) - \Delta\omega \tag{46}$$

and the mistuning terms verify $\Delta\omega_{BN}^F = \overline{\Delta\omega_{BN-k}^F}$, because they come from the Fourier transform of a real sequence (see Eq. (29)). Note that in this case the AMM can be seen as a simplification of the FMM [14], which takes into account a complete family of modes. The AMM includes only the active modes of the family and the final problem is smaller in size, with an associated matrix (see Eq. (45)) that is a submatrix of the one that is obtained from the FMM [15].

It is also interesting to mention that, as it happened in the isolated modes case, the resulting averaged damping remains constant and equal to its tuned value

$$\frac{1}{N_a}\sum_j \frac{\mathrm{Im}(\Delta\omega_j)}{2} = \frac{1}{N_a}\sum_j \xi_j \tag{47}$$

where the sums go over all active modes in Eq. (45), $\Delta\omega_j$ are the eigenvalues from Eq. (45), and the mistuned dampings are given by $\mathrm{Im}(\Delta\omega_j)/2$. This invariance follows from the basic linear algebra property that states that the sum of the eigenvalues of a matrix is equal to its trace, and indicates that the increase of stability of a mode inevitably reduces the stability of other modes. Moreover, this property allows us to conclude that if the average of the tuned dampings is negative, then it is not possible to achieve complete stabilization through the inclusion of small mistuning.

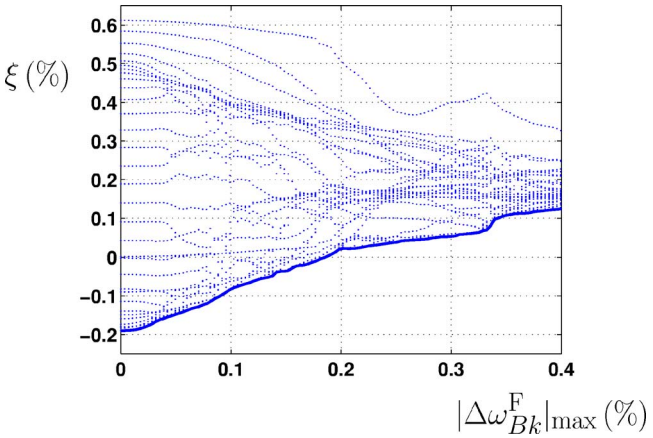

Fig. 6 Critical damping of the optimum mistuned configuration for the active modes indicated in Fig. 3 as a function of the maximum frequency deviation $|\Delta\omega_{Bk}^F|_{\max}$: (thick line) minimum damping envelope; (dotted lines) damping of all active modes

Another interesting property can be derived by premultiplying Eq. (45) by the row vector $[\overline{A_k}, \overline{A_{k+1}}, \dots, \overline{A_{-(k+1)}}, \overline{A_{-k}}]$ with the complex conjugates of the active mode amplitudes, and taking the imaginary part to obtain

$$\sum_j (2\xi_j - \mathrm{Im}(\Delta\omega))|A_j|^2 = 0$$

which implies that

$$\min_j \xi_j \leqslant \frac{\mathrm{Im}(\Delta\omega)}{2} \leqslant \max_j \xi_j \tag{48}$$

that is, the resulting mistuned dampings are always inbetween the maximum and the minimum tuned dampings of the active modes. This allows us to ensure that the effect of the mistuning on a stable family of modes with nearly equal frequencies can never be destabilizing.

The AMM formulation above is now used to look for the optimal mistuning patterns that stabilize the rotor in Fig. 3. The total number of sectors is $N=42$ and we now have $N_a=33$ active modes (all those with $|k|>5$ encircled in red in the top plot of Fig. 3).

For every value of $|\Delta\omega_{Bk}^F|_{\max}$, we use a a numerical optimization method to locate the mistuning pattern with Fourier coefficients below $|\Delta\omega_{Bk}^F|_{\max}$ that maximizes the minimum damping (i.e., the mistuning pattern that gives maximum stabilization). The results are presented in Fig. 6, where it can be appreciated that complete stabilization can be achieved from $|\Delta\omega_{Bk}^F|_{\max} \sim 0.2\%$ on. The Fourier modes of the resulting optimal mistuning patterns at several different stages of the optimization process are plotted in Fig. 7. The optimal mistuning pattern grows with $|\Delta\omega_{Bk}^F|_{\max}$ but its

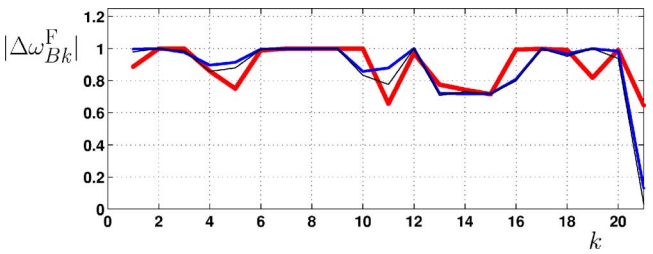

Fig. 7 Normalized Fourier coefficients of the optimal blade frequency deviation patterns for several different maximum frequency deviations in Fig. 6, $|\Delta\omega_{Bk}^F|_{\max}=0.2$, 0.3, and 0.4 (thick, medium, and thin line, respectively)

Downloaded 30 May 2010 to 128.113.26.88. Redistribution subject to ASME license or copyright; see http://www.asme.org/terms/Terms_Use.cfm

mode distribution appears to relax to a profile where the most important contributions are approximately located: (i) around $k=18$ that, as it can be seen from Fig. 6, corresponds to couplings between the most unstable and the most stable modes; and (ii) from $k=1$ to $k=9$, which can be related to the coupling only among the unstable modes and only among the stable modes.

Concluding Remarks

The derivation of a new reduced order model (AMM) based on the use of a subset of nominal modes has been presented. The AMM is, from a practical point of view, a further extension of the FMM [14,18], from which it differs on three crucial points

1. The AMM is derived recurring solely to the use of consistent asymptotic perturbation techniques;
2. The AMM uses only the active modes of a given family of modes, i.e., those who are relevant from the point of view of mistuning, and in this sense is more reduced than the FMM. Its simplicity unveils the physical mechanism of the mistuning induced coupling between different traveling-wave modes and provides valuable information on how to use intentional mistuning in order to increase the stability of aerodynamically unstable rotors.
3. The FMM can only describe the effect of mistuning on a complete modal family with almost equal frequencies and mode shapes with nearly identical sector displacements and different interblade phase angles. Even in the derivation of the improved FMM presented in Ref. [18], the above assumption on the mode shapes is made (precisely at p. 157, right below Eq. (31)) and the FMM is applied only to a mode family with a frequency variation smaller than 3% (see Fig. 8 of this paper). For these modal families with almost constant frequency, the FMM and the AMM are identical. But the AMM can go further and allows us to also describe the effect of small mistuning on modes belonging to families exhibiting a non-small variation of the frequency and the mode shapes, like the ones considered in this paper and encircled in red in Figs. 2 and 3, which are found, respectively, on interlocked and welded-in-pair LPT bladed disks.

The method has been used to increase the stability of two aerodynamically unstable LPT rotors. The first case corresponds to a rotor with an interlocked shroud. The unstable modes correspond to separated modes and the AMM provides an analytical description of the optimum mistuning pattern. The second case is representative of a welded-in-pair rotor. The unstable modes are clustered about a single frequency and an optimization process is conducted in order to find the optimum mistuning pattern. The FMM has also been previously used to describe the mistuning effect on flutter analysis (see Ref. [19]) but again, as mentioned in Item 3 above, the analysis is applied to a complete family of modes sharing similar mode shapes, while in this paper the AMM is used to analyze the effect of mistuning on groups of modes with similar tuned frequencies and belonging to modal families displaying large variations of the vibration characteristics.

As a final remark, it is interesting to comment on the work in Ref. [15] on the effect of random mistuning on the aerodynamic stability of the interlocked and welded-in-pair bladed disks in Figs. 2 and 3. Their results indicate that the minimum damping remains unaffected (and equal to its tuned value) for the interlock case while, for the welded-in-pair rotor, there is a clear increase of the minimum damping (i.e., a clear stabilization). This can be appreciated from Fig. 8 where the minimum damping, ξ, is plotted for a population of random mistuning patterns (σ is the standard deviation of the frequencies of the mistuning patterns). These two different responses to random mistuning can be explained using the AMM results from the previous section: The increase on the stability of one of the isolated unstable, e.g., $k=-8$, modes in the interlock mode family in Fig. 2 takes place precisely only through the $k=16$ mode of the mistuning, which induces a coupling with the $k=8$ stable mode. On the other hand, the stability of one of the unstable modes, $k=10$, for instance, of the welded-pair family in Fig. 3 is increased by the effect of many mistuning modes (approximately all modes from $k=9$ to 36 modulo 42) that provide coupling with the rest of the stable active modes. Therefore, an increase of stability as a result of a random mistuning pattern is much more probable for the welded-pair family, and this is what is reflected in the plots in Fig. 8.

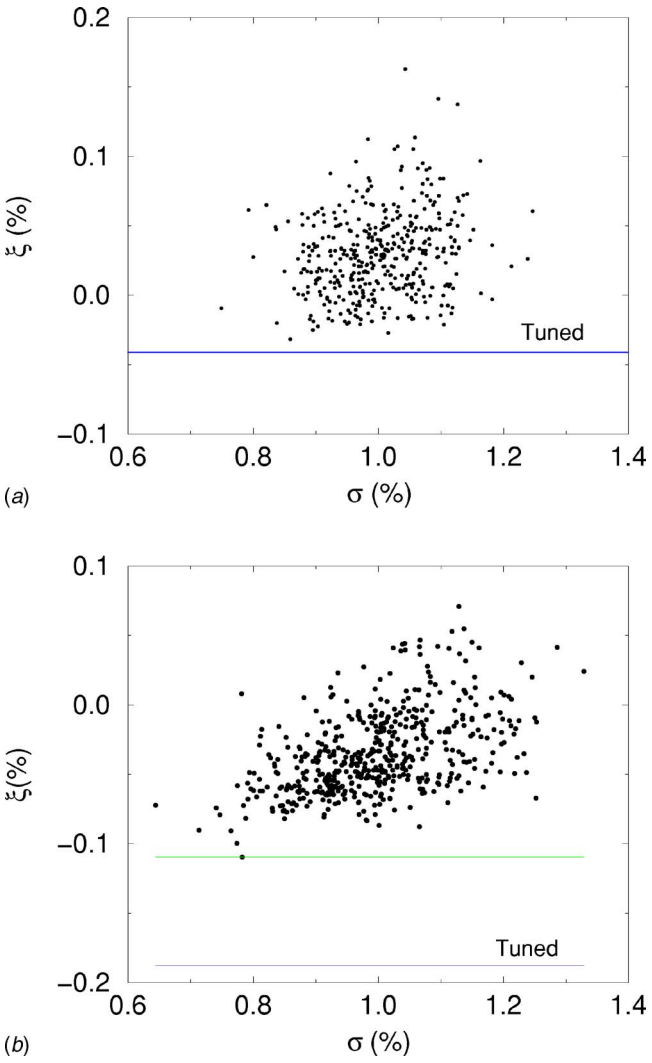

Fig. 8 Minimum damping as a function of the standard deviation, σ, of the natural frequencies of an interlock (top) and a welded pair (bottom) bladed disk (taken from Ref. [15])

Acknowledgment

The authors wish to thank ITP for the permission to publish this paper and for its support during the project. This work has been partially supported under Grant No. TRA2005-09331-C03-01 of the Spanish Ministry of Science and Technology. The work of J.M.L. was funded through a collaboration fellowship of Spanish Ministry of Science and Technology. The work of C.M. has also been supported by the Universidad Politécnica de Madrid under Grant No. CCG06-UPM/IME-328.

Nomenclature

$\mathbf{M}$ = mass matrix

Downloaded 30 May 2010 to 128.113.26.88. Redistribution subject to ASME license or copyright; see http://www.asme.org/terms/Terms_Use.cfm

$\mathbf{K}$ = stiffness matrix
$\mathbf{M}_{\text{aero}}$ = matrix of aerodynamic forces
$\mathbf{X}$ = DOF displacements vector
$\mathbf{A}$ = traveling wave mode amplitude vector
$\Delta\mathbf{M}$ = mass mistuning matrix
$\Delta\mathbf{K}$ = stiffness mistuning matrix
$\tilde{\omega}, \omega_{kj}, \omega_{\widetilde{kj}}$ = purely structural tuned vibration frequencies
ω = aerodynamically and mistuning corrected frequency $\omega = \tilde{\omega}(\eta + 2i\xi)$
η = relative frequency correction
ξ = damping relative to the critical damping

References

[1] Srinivasan, A. V., 1984, "Vibrations of Bladed-Disc Assemblies: A Selected Survey," ASME J. Vib., Acoust., Stress, Reliab. Des., **106**(2), pp. 165–168.
[2] Kaza, K. R. V., and Kielb, R. E., 1982, "Flutter and Response of a Mistuned Cascade in Incompressible Flow," AIAA J., **20**(8), pp. 1120–1127.
[3] Srinivasan, A. V., 1980, "Influence of Mistuning on Blade Torsional Flutter," Paper No. NASA CR-165137, (1).
[4] Bendiksen, O. O., 1984, "Flutter of Mistuned Turbomachinery Rotors," J. Eng. Gas Turbines Power, **106**, pp. 25–33.
[5] Nowinsky, M., and Panovsky, J., 2000, "Flutter Mechanisms in Low Pressure Turbine Blades," J. Eng. Gas Turbines Power, **122**, pp. 82–88.
[6] Sadeghi, M., and Liu, F., 2001, "Computation of Mistuning Effects on Cascade Flutter," AIAA J., **39**(1), pp. 22–28.
[7] Seinturier, E., Dupont, C., Berthillier, M., and Dumas, M., 2002, "A New Method to Predict Flutter in Presence of Structural Mistuning With Application to a Wide Chord Fan Stage," *Proceedings 9th International Symposium on Unstaedy Aerodynamics, Aeroacoustics and Aeroelasticity of Turbomachines*, Lyon, France, September 4–8, 2000, pp. 739–749.
[8] Corral, R., and Gallardo, J. M., 2005, "Strain-Gauge Prediction of Self-Excited Vibrations on Low Pressure Turbine Blades," *Proceedings AVT-121 RTO Symposium on Evaluation, Control and Prevention of High Cycle Fatigue in Gas Turbine Engines for Land, Sea and Air*, Granada, Spain, October 3–7.
[9] Crawley, E. F., and Hall, K. C., 1985, "Optimization and Mechanisms of Mistuning in Cascades," J. Eng. Gas Turbines Power, **107**, pp. 418–426.
[10] Ewins, D. J., 1969, "The Effects of Detuning Upon the Forced Vibrations of Bladed-Disks," J. Sound Vib., **9**(1), pp. 65–79.
[11] Yang, M.-T., and Griffin, J. H., 1997, "A Reduced Order Approach for the Vibration of Mistuned Nalded Disk Assemblies," J. Eng. Gas Turbines Power, **119**, pp. 161–167.
[12] Castanier, M. P., Ottarson, G., and Pierre, C., 1997, "A Reduced Order Modeling Technique for Mistuned Bladed-Disks," J. Vibr. Acoust., **119**(3), pp. 439–447.
[13] Yang, M. T., and Griffin, J. H., 1999, "A Reduced Order Model of Mistuning Using a Subset of Nominal Modes," ASME Paper No. 99-GT-288.
[14] Feiner, D. M., and Griffin, J. H., 2002, "A Fundamental Model of Mistuning for a Single Family of Modes," J. Turbomach., **124**, pp. 597–605.
[15] Corral, R., Gallardo, J. M., and Vasco, C., 2004, "Aeroelastic Stability of Welded-in-Pair Low Pressure Turbine Rotor Blades: A Comparative Study Using Linear Methods," ASME J. Turbomach., **129**, pp. 72–83.
[16] Kielb, J. J., and Abhari, R. S., 2003, "Experimental Study of Aerodynamic and Structural Damping in a Full-Scale Rotating Turbine," J. Eng. Gas Turbines Power, **125**, pp. 102–112.
[17] Wilkinson, J. H., 1988, *The Algebraic Eigenvalue Problem*, Oxford University Press, New York.
[18] Feiner, D. M., and Griffin, J. H., 2004, "Misuning Identification of Bladed Disks Using Fundamental Mistuning Model—Part I: Theory," J. Turbomach., **126**, pp. 150–158.
[19] Kielb, R. E., Feiner, D. M., Griffin, J. H., and Miyakozawa, T., 2004, "Flutter of Mistuned Bladed Disks With Aerodynamic and FMM Structural Damping," ASME Paper No. 2004-GT-54315.

Downloaded 30 May 2010 to 128.113.26.88. Redistribution subject to ASME license or copyright; see http://www.asme.org/terms/Terms_Use.cfm

Fully Automated Model-Based Performance Analysis Procedure for On-Line and Off-Line Applications

Michael Bauer
MTU Aero Engines GmbH,
Dachauer Str. 665,
Munich 80995, Germany

Stephan Staudacher
University of Stuttgart,
Institute for Aircraft Propulsion Systems (ILA),
Stuttgart 70569, Germany

The development of modern gas turbines is accompanied by an extensive prototype testing. To evaluate performance, the engines are fitted with a substantial number of sensors measuring pressures, temperatures, shaft speeds, etc. The test data are analyzed by procedures calculating data that are not directly measured, e.g., component efficiencies and turbine temperatures. Engine manufacturers usually apply such procedures for a detailed analysis after the test (off-line) as well as to ensure a safe and efficient engine operation during the test (on-line). Especially for the latter application, a fast and reliable assessment of the performance of the engine and its components as well as a fast and reliable detection of measurement faults are required. The paper describes a fully automated performance analysis procedure for off-line as well as on-line applications. The basis of the procedure is a full thermodynamic model representing the expected behavior of the engine to be tested. By such a model-based analysis procedure, a comparison between test data and the expected engine behavior is performed. The way the comparison is done allows detecting and isolating measurement faults and component malfunctions. In case of a detected measurement fault, the measurement will be excluded automatically from the analysis. At MTU Aero Engines GmbH the procedure is regularly applied for on-line and off-line test data analysis of different engine types. Compared to the procedures used thus far, many measurement faults can be detected quickly and reliably.
[DOI: 10.1115/1.2720875]

1 Introduction

Gas turbine engine manufacturers usually apply full thermodynamic models for the prediction of engine performance. The performance calculation tools are thereby modularly structured and synthesize the performance of the engine, based on the characteristics of its individual components. Using these tools, a full thermodynamic model of any engine configuration can be set up, which allows the calculation of the engine performance with high accuracy. These models represent thereby existing knowledge and interpretation of the component characteristics of the engine being developed.

Alongside performance calculations, the development of gas turbine engines is accompanied by an extensive prototype testing. This is necessary to validate the results of the development work and to demonstrate fulfillment of customer and airworthiness authority requirements. Besides tests with individual engine parts and modules, tests with the whole engine are performed. These tests are thereby conducted in different installations, such as the sea-level test cell and the altitude test facility.

To evaluate the performance characteristics of the engine and its components, analysis procedures are applied. In general, such procedures calculate data, which are not directly measured (e.g., turbine temperatures, efficiencies, and specific fuel consumption). The procedures are applied during the test (on-line) to ensure safe and efficient tests as well as after the test (off-line) for detailed analysis; see Fig. 1.

For on-line analysis, simply structured procedures are in use for a long time. On the one hand, such so-called quick analysis programs (QAP) calculate mean values, where there are a number of sensors measuring the same quantity. On the other hand, they calculate engine performance parameters, which are not directly measured. Because of the simple structure, only a few parameters, e.g., bypass ratio, have to be evaluated by a numerical iteration procedure. Consequently, a reliable and numerically robust calculation is ensured. To detect measurement faults due to deficiencies of the measuring device, QAPs can include automated measurement checking-algorithms, as, for example, range checks and filter algorithms. Nevertheless, the abilities of QAPs to translate the measured data into engine performance parameters, e.g., at standard conditions, are limited. A reliable comparison between test data and expectation, and thus a reliable assessment of the test data, cannot be performed. Furthermore, not every measurement fault can be detected by applying the measurement-checking algorithms. Hence, a detailed off-line analysis is absolutely required.

For detailed off-line analysis, engine manufacturers usually apply procedures based on the corresponding performance prediction model. Such model-based analysis procedures allow calculations with high accuracy and flexibility. Contrary to QAPs, a comparison between the real data and the expected component characteristics is done and the performance of the components can be assessed. Furthermore, engine performance parameters, e.g., at standard conditions, can be calculated and compared to requirements. However, the amount of parameters, which have to be evaluated by a numerical iteration procedure, is higher, and thus a numerically robust calculation is not always ensured. Model-based analysis procedures can also include measurement-checking algorithms, which are similar to those used for on-line analysis. But again, not every measurement fault can be detected by applying these algorithms. Thus, for an accurate performance analysis, the performance engineer has to check the quality of the measure-

Contributed by the International Gas Turbine Institute of ASME for publication in the JOURNAL OF TURBOMACHINERY. Manuscript received August 18, 2006; final manuscript received September 7, 2006; published online December 19, 2007. Review conducted by David Wisler. Paper presented at the ASME Turbo Expo 2006: Land, Sea and Air (GT2006), May 8–11, 2006, Barcelona, Spain. Paper No. GT2006–91050.

 Copyright © 2008 by ASME

Downloaded 30 May 2010 to 128.113.26.88. Redistribution subject to ASME license or copyright; see http://www.asme.org/terms/Terms_Use.cfm

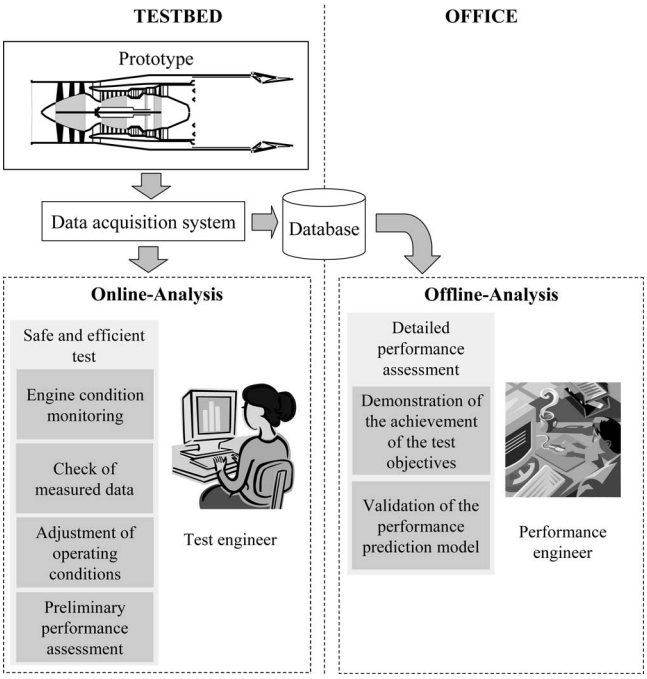

Fig. 1 Application of performance analysis procedures

ments manually and to exclude them from the analysis. The accuracy of the analysis is thereby strongly dependent on the engineer's experience.

Because of the increasing competitive environment of gas turbine manufacturers and the resulting demand for continuously decreasing development cost and time, the importance of safe and efficient development tests, a fast and reliable performance analysis, and the elimination of the maintenance effort of two different analysis programs increases. Moreover, automated procedures are already required during the test to ensure timely detection of problems that might otherwise remain undetected. Possibly, undetected problems could cause a costly repetition of the whole test. Consequently, the following requirements for a modern performance analysis procedure can be deduced:

- high degree of automation
- high accuracy
- high flexibility
- on-line and off-line capability
- fast and reliable assessment of the performance of the engine and its components
- fast and reliable detection and isolation of component malfunctions and measurement faults

In this paper, a model-based performance analysis procedure is presented that fulfills these increasing demands.

2 Engine Performance Simulation

Performance calculation programs are used for engine-development purposes to perform design, off-design, and test data analysis for a wide range of engine types and application cases. The performance calculation program described in this paper is modularly structured and synthesizes the performance of the engine based on the characteristics of its individual components (see [1,2]). Each component is thereby represented by a specific source code module. As shown in Fig. 2, the module arrangement reflects the layout of the engine. Using such modularly structured tools, a full thermodynamic model of any engine configuration can be set up that allows the calculation of the engine performance with high

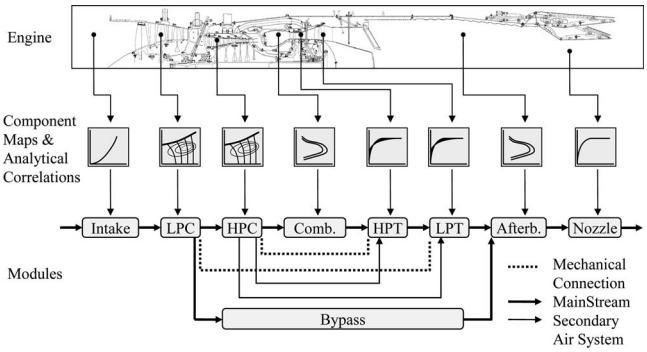

Fig. 2 Module arrangement for a given engine configuration

accuracy. Furthermore, the modular approach allows a clear understanding of engine operation as a component contribution to overall performance is visualized.

The component characteristics are described by maps or analytical equations, which represent the correlations between the main parameters of the components. The characteristics are based on calculation procedures or are derived from component rig tests and engine tests. The degree of component detailing depends on the purpose of the calculation and the availability of component data.

Considering the boundary conditions u defining flight condition and power level, the calculation starts with the front components and proceeds to the rear components following the gas path. Thereby, at every station between the components mean values of the mass flow and the thermodynamic variables of state, e.g., pressure and temperature, are determined. At certain points of the calculation process, it is necessary to estimate some parameters X, as for example the bypass ratio, compressor working points, and combustion fuel-to-air ratio. These parameters are balanced by an equal number of matching conditions H, such as flow continuity and power balance. This results in solving a system of nonlinear equations

$$H(u,X) = 0 \tag{1}$$

This equation system is solved by using an iterative technique, e.g., the Newton-Raphson algorithm (see [3]).

3 Model-Based Performance Analysis

Prior to any development test, a so-called pretest model is prepared that represents the predicted characteristics of the engine and its components. On the one hand, the pretest model is used to support the test planning activities; on the other hand, it is applied to assess the test data after the test.

3.1 Typical Prototype Performance Instrumentation. To evaluate the real performance of the engine and its components, the engine is fitted with sensors measuring pressures and temperatures at virtually every station, as well as thrust, spool speeds, fuel flow, air flow, etc. To measure the nonuniform flow, the various engine stations are equipped with several pressure and temperature rakes measuring data at different radial and circumferential positions. In Fig. 3, the general arrangement of a two-spool mixed flow afterburner turbofan engine with a convergent-divergent nozzle is shown. The general arrangement includes typical development engine performance instrumentation. With such instrumentation it is possible to accurately evaluate the real in-engine characteristics of all major components, particularly of the turbo components.

3.2 Analysis by Synthesis (ANSYN). Test data requires considerable processing before conclusions can be drawn. First, suitable representative mean values have to be calculated for stations

Downloaded 30 May 2010 to 128.113.26.88. Redistribution subject to ASME license or copyright; see http://www.asme.org/terms/Terms_Use.cfm

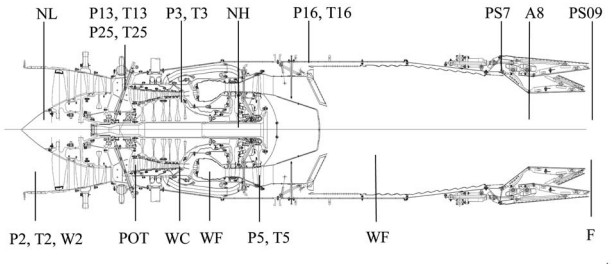

Fig. 3 General arrangement of a two-spool mixed-flow afterburner turbofan engine including typical instrumentation

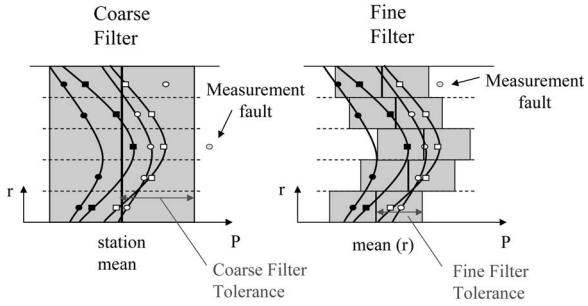

Fig. 4 Coarse filter and fine filter

with a number of sensors measuring the same quantity (see [4,5]). For off-line analysis purposes, engine manufacturers usually apply a model-based performance analysis procedure called analysis by synthesis (ANSYN) (see [1,6,7]). The basic idea of the procedure is to match the model to real engine test data on a component level by using so-called modifiers. On the one hand, this allows calculating all data, which are not directly measured (e.g., thermodynamic variables of state in engine stations, such as turbine inlet temperature; component performance parameters, such as efficiencies; and overall engine parameters, such as specific fuel consumption or net thrust). On the other hand, the procedure includes assumptions of the component characteristics derived from the pretest model. Thus, in addition to a pure test data analysis, a comparison between real data and expected component characteristics is performed by a model-based analysis. The deviations between real and expected component data are represented by modifiers, which are related to parameters describing the predicted behavior of the components. The modifiers can be adders or scalers. For turbocomponents modifiers for

$$\text{flow } M_{W\sqrt{T}/P} = \frac{\left(\frac{W\sqrt{T}}{P}\right)_{\text{analyzed}}}{\left(\frac{W\sqrt{T}}{P}\right)_{\text{model}}}$$

$$\text{pressure ratio } M_{\Pi} = \frac{\Pi_{\text{analyzed}} - 1}{\Pi_{\text{model}} - 1}$$

$$\text{and efficiency } M_{\eta} = \frac{\eta_{\text{analyzed}}}{\eta_{\text{model}}}$$

are usually used. The way the comparison is done allows considering the components almost separately from each other. Thus, matching effects are nearly eliminated.

To perform a model-based analysis, the nonlinear equation system (1) is extended by introducing modifiers M together with extra matching quantities considering the measurements y

$$H(M,X,u,y) = 0 \tag{2}$$

With a detailed test data analysis, one can end up with 20–30 variables within the equation system to be solved.

When using numerical iteration procedures, the convergence is always a challenging task. In the case of a model-based analysis, the convergence is strongly dependent on the quality of the estimation values and of the measured data. If a measurement is not reasonable and the value is out of the analysis model's range, then the iteration will not converge.

3.3 On-line Capability. To apply the procedure described in Sec. 3.2 for on-line analysis, an automated and numerically robust calculation is mandatory. Any problems with the convergence are not acceptable for monitoring the test and might have fatal consequences for the engine's and test bed's health.

A numerically robust calculation is achieved by a reliable detection and isolation of measurement faults and a reasonable estimation of the iteration variables.

3.3.1 Check of Single Measurements. Where there are a number of sensors at a station, each single measurement can be checked by applying filter algorithms. The use of so-called coarse filters and fine filters has been state of the art for some time.

Figure 4 shows the principle of the applied filter algorithms. One can see typical total pressure measurements dependent on radial position plotted for different circumferential positions. By the coarse filter algorithm, each single measurement is checked with the station mean value. Thereby, the specified tolerance has to consider the real radial and circumferential variation of the parameter as well as the measurement accuracy [8]. By the fine filter algorithm, each single measurement is checked with the mean value of the measurements installed at the same radial position. The specified tolerance has to consider only the circumferential variation of the parameter as well as the measurement accuracy. Appropriate values of the tolerances can be evaluated by investigating test data from previous engine tests or by using data calculated by aerodynamic calculation procedures.

Every incorrect measurement, which is detected by the filter algorithms, is then automatically substituted by a more realistic value calculated by an interpolation algorithm.

However, with the described filter algorithms, not all measurement faults can be detected. For example, if all measurements of a parameter are processed by an incorrect calibration curve, all measurements, and consequently the mean values, include the same fault. Furthermore, parameters measured only by one sensor, e.g., thrust, cannot be checked by a filter algorithm.

3.3.2 Check of Mean Values. To manage the described deficiencies of the filter algorithms, the analysis procedure is extended by calculating expected values y_{exp} derived by the pretest model before the analysis. To identify flight condition and power level, appropriate measurements are chosen. Thereby, measurements should be applied, which can be well monitored by the test engineer, e.g., P0, T0, PS09, and NL.

The approach implies that a numerically robust calculation of the expected values is guaranteed. This can be reached, for example, by reading suitable estimation functions for X, dependent on flight condition and power level, before the calculation is performed. Usually, it is sufficient to establish such estimation functions only once for an "average" engine of any given engine type.

The expected values y_{exp} are then used to check the measurements y with the help of specified tolerances δ defining the maximal allowed deviations between the measured and the expected values (see Fig. 5). Thereby, the tolerances δ have to consider the measurement accuracy as well as the model accuracy. Of course, this has to be done carefully. The higher the values of δ are, the fewer measurement faults can be detected and the risk increases that the model-based analysis procedure will not converge. In contrast, the lower the values of δ are, the risk increases that correct measurements will be flagged as incorrect.

Preliminary values of δ can be evaluated by investigating test

Downloaded 30 May 2010 to 128.113.26.88. Redistribution subject to ASME license or copyright; see http://www.asme.org/terms/Terms_Use.cfm

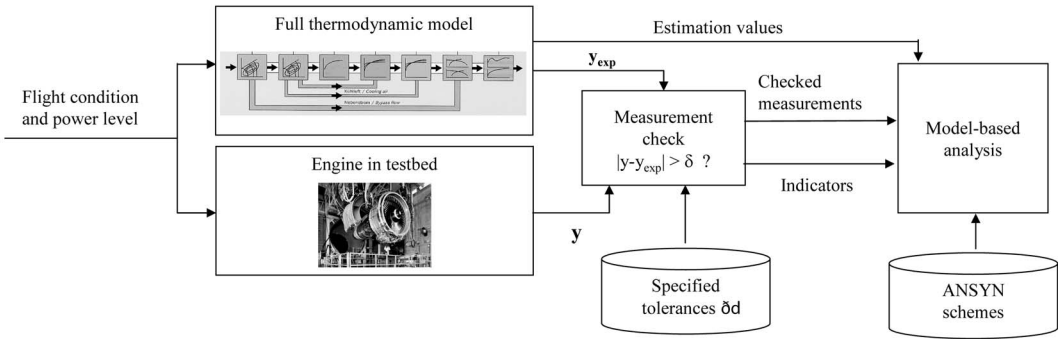

Fig. 5 Measurement check and determination of estimation values

data from previous engine tests. In Fig. 6, typical deviations between correct measurements of P25 and the expected values calculated by a pretest model can be seen for three different engines of the same type. The scatter is within ±3%.

3.3.3 Determination of Suitable Estimation Values. Applying the pretest model, expected values of every performance parameter are calculated, e.g., bypass ratio. The derived values are used as estimation values of X to be solved by equation system (2); see Fig. 5. Because the real performance of an engine usually does not vary much from the pretest model, it is sufficient to estimate the scalers and adders to 1 and 0, respectively.

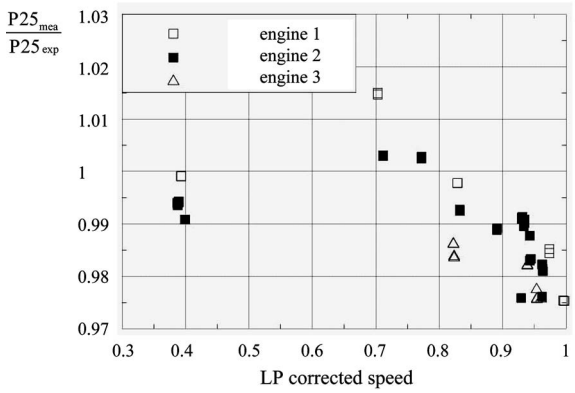

Fig. 6 Typical deviations between measurement and expectation

3.3.4 Automatic Use of a Valid Analysis Scheme. In the case of a detected measurement fault, the measurement has to be excluded from the analysis. Consequently, the original ANSYN scheme is no longer valid and an alternative ANSYN scheme has to be chosen. An on-line application of the procedure implies that this has to be done fully automated.

To reach the on-line capability of the procedure, a variety of different ANSYN schemes are provided before the test. There are always different possibilities to establish an alternative ANSYN scheme,

- consideration of measurements not used thus far by the original ANSYN scheme
- consideration of measurements of the in-service instrumentation, e.g., PS3, EGT, etc.
- reduction of the equation scheme (2) by eliminating modifiers and matching conditions, which correspond to the incorrect measurement faults,
- consideration of expected values derived by the pretest model.

Especially, expected values derived by the pretest model are always available.

If the measurement check algorithm described in Sec. 3.3.2 detects a measurement fault, then a corresponding indicator is set. Dependent on these indicators, the analysis procedure defines automatically an appropriate ANSYN scheme. Figure 7 shows an example of the principle for the measurement $P3$. When the measurement $P3$ is flagged as incorrect, then an alternative ANSYN scheme is used, which considers P_S3 instead of $P3$. If both mea-

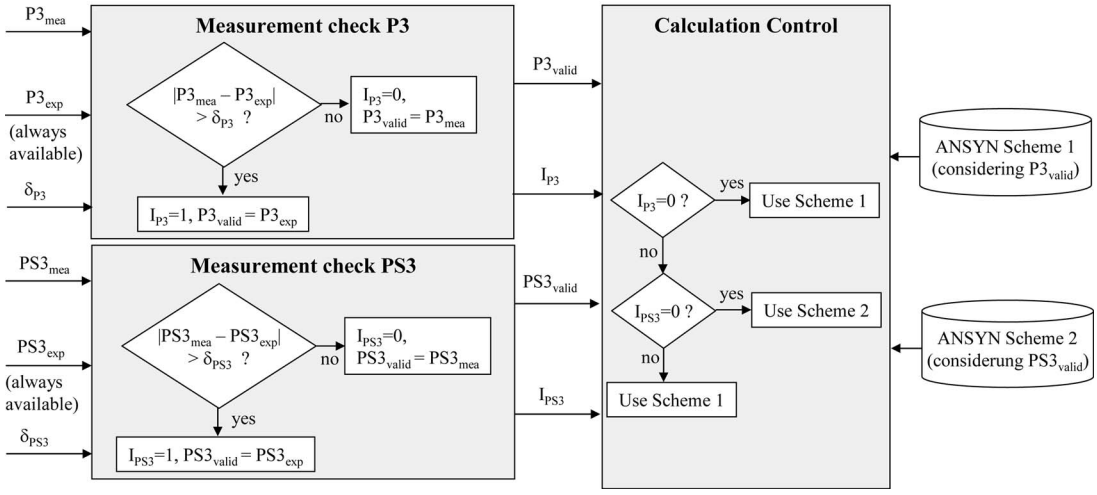

Fig. 7 Automatic use of a valid ANSYN scheme

Downloaded 30 May 2010 to 128.113.26.88. Redistribution subject to ASME license or copyright; see http://www.asme.org/terms/Terms_Use.cfm

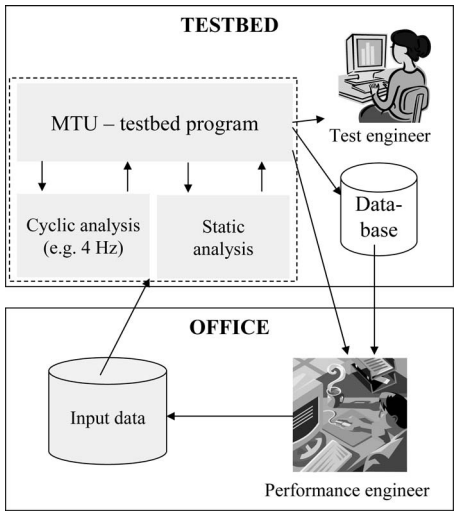

Fig. 8 Test-bed integration

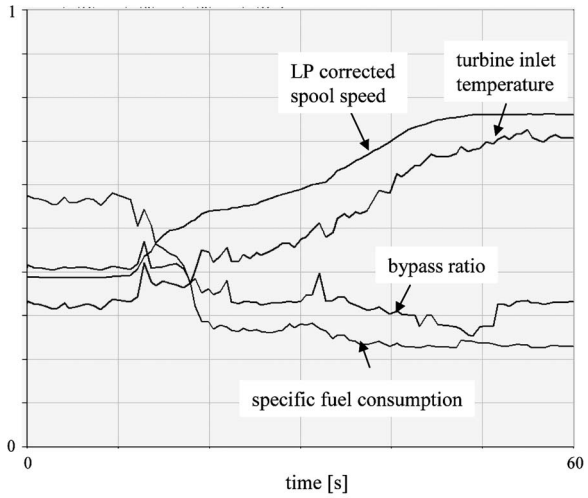

Fig. 9 On-line visualization of calculated data

surements $P3$ and P_S3 are flagged as incorrect, then the analysis is performed by the original ANSYN scheme considering the expected value for $P3$, which is always available.

4 Application

4.1 Test-Bed Integration. The performance calculation program described in this paper has been implemented in a modern data acquisition system of MTU Aero Engines GmbH (MTU). Both, the test-bed program and the performance-calculation program are running on the same PC (Pentium 2 GHz) with the WINDOWS® XP Operating System (see Fig. 8). An interface between the test-bed program and the performance-calculation program transfers the measured data to the analysis program and the calculated data back to the test-bed program.

The analysis is performed in two different modes. The so-called cyclic mode calls the procedure continuously, e.g., with a 4 Hz rate. When a snapshot is taken manually by the test engineer, e.g., a snapshot at stabilized conditions, this snapshot is then analyzed by the so-called static mode.

Besides the application of the analysis procedure, the test-bed program of MTU incorporates the following capabilities (see also [9]):

- storage of all measured and calculated data on a database
- on-line visualization of measured and calculated data
- monitoring of measured and calculated data applying range checks and raising corresponding alarms

With the on-line application of the analysis procedure used thus far off-line, the work of a performance engineer changes significantly. Already before the test, the engineer has to carefully prepare the input data of the analysis procedure, including the corresponding pretest model. Thereby, the engineer has to carefully review which instrumentation will be available during the test.

4.2 Test Support. The fully automated model-based analysis procedure described in this paper is regularly applied during development tests of different engine types at MTU. It is used during tests of modern military engines, conventional civil aircraft engines, and turboshaft engines. The tests are carried out in sea-level tests beds as well as in altitude test facilities. Furthermore, the analysis procedure has been used during a test campaign with a technology demonstrator called CLEAN [10]. A numerically robust calculation has been always observed.

With the capabilities of the model-based analysis procedure and the test-bed program, all requirements for a safe and efficient development test can be fulfilled.

4.2.1 Visualization of Calculated Data. As an example, Fig. 9 shows an on-line visualization of calculated parameters plotted over time during engine acceleration. Thus, the test engineer can adjust specified parameters, e.g., specified turbine temperatures, which are not directly measured. Furthermore, the test engineer has an accurate view of critical parameters.

4.2.2 Check of Measured Data. To check the measured data, the indicators of the measurement check algorithm described in Sec. 3.3.2 are monitored by the test-bed program. In the case of a detected measurement fault, a corresponding alarm is raised to the test engineer. Thus, the test crew can solve measurement problems immediately.

Figure 10 shows an on-line visualization of ratios and differences between the measurements and expectations for different pressures and temperatures of an engine. Besides the measurement of $T3$, all measurements are in the specified tolerances. However, the measurement $T3$ deviates too much from the expected value due to wrongly applied calibration curves.

As an example, the following are typical measurement faults that have been detected by the analysis procedure:

- pressure lines not installed (measurements show ambient pressure)
- pressure lines installed wrongly (e.g., total pressure measurements show static pressure values)
- leakages of pressure lines (measured values are lower than the expected values)
- calibration curves defined incorrectly
- fuel flow measurement not installed

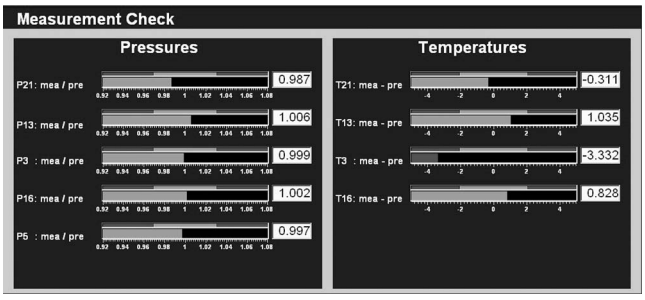

Fig. 10 Detection of a measurement fault

Downloaded 30 May 2010 to 128.113.26.88. Redistribution subject to ASME license or copyright; see http://www.asme.org/terms/Terms_Use.cfm

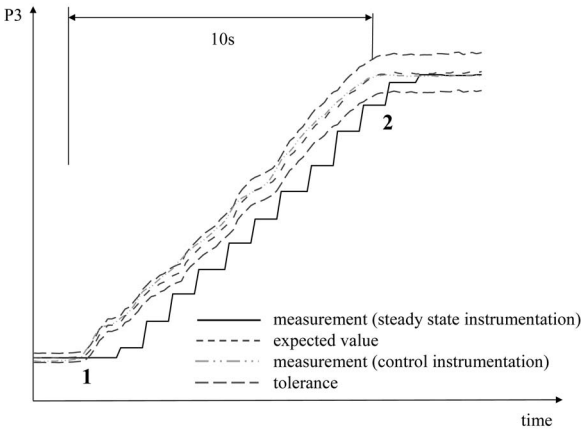

Fig. 11 Measurement check during an engine acceleration

- defect thrust measurement

Compared to the on-line analysis procedure used thus far at MTU, many measurement faults can be detected. Especially, during the first run of a development engine with the aim to check the whole instrumentation work, the advantages of the analysis procedure are evident. It is important to mention that no false alarm has appeared thus far.

The functionality of the analysis procedure can be demonstrated when checking instrumentation optimized to measure stabilized conditions. To prevent disturbances from the engine, pressure transducers are installed outside the test bed. Thus, the pressure lines have several meters of length, and the measurements response is slow. Figure 11 shows the measurement of a typical steady-state instrumentation of $P3$ during an acceleration of an engine. Furthermore, the expected values calculated by the pretest model, the specified tolerances, and the measurement of the control system are plotted. One can see that the measurement of the steady-state instrumentation responds delayed compared to the expectation and to the measurement of the control system. Thus, the measurement of the steady-state instrumentation is not adequate to analyze the acceleration. At time 1, the measurement exceeds the tolerance range and a measurement fault is detected. Subsequently, the analysis is performed with the measurement of the control system. Alternatively, the analysis can also be carried out with the expected value. At time 2, the measurement reenters the tolerance range and the analysis is performed again with this measurement. The steps in the diagram are caused by a lower test data acquisition frequency than the frequency of the analysis.

4.2.3 Engine Condition Monitoring. For engine condition monitoring purposes, the derived modifiers are used as "health indices". The modifiers are monitored by the test-bed program. In the case of a deviation too far from a nominal value, a corresponding alarm is raised. As an example, Fig. 12 shows an on-line visualization of the derived modifiers.

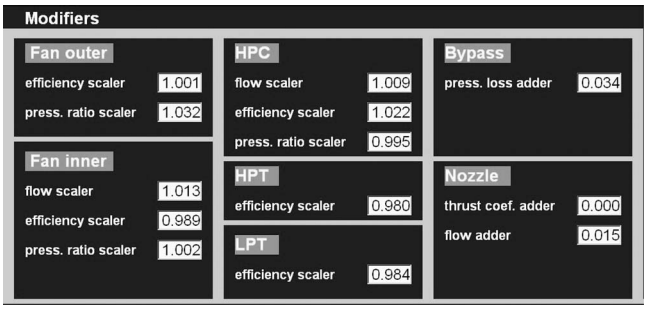

Fig. 12 On-line visualization of derived modifiers

4.2.4 Preliminary Performance Assessment. The results of cyclic and static analysis are available to the performance engineer already during the test. The results have the same accuracy as the results of the analysis procedure used thus far off-line. Consequently, the engineer has a good overview of the quality of the measurements and the behavior of the individual components of the engine already during the test. The engineer also has a high confidence in these data because the results are produced by the input data established by himself.

4.2.5 Model Calibration. When all problems raised during the first run of a development test have been solved, then the pretest model is calibrated with the test data gained thus far, and the specified tolerances δ are reduced. This procedure guarantees a reliable monitoring of the development engine. The calibration is especially valuable for endurance tests run over several months.

5 Conclusion

In this paper, a fully automated model-based analysis procedure is presented that can be used for on-line as well as for off-line applications. The on-line capability of the procedure has been obtained by calculating expected values by a pretest model. These values are used to check the measurements and to derive suitable estimation values to resolve the nonlinear equation system. If measurements faults are detected, these measurements are excluded from the analysis and an alternative analysis scheme is used.

At MTU Aero Engines GmbH this model-based analysis procedure is regularly applied during development tests of different engine types in sea-level test beds as well as in altitude test facilities. Thereby, the performance calculation program has successfully been linked to a modern data acquisition system.

The described analysis procedure gives the following advantages:

- Critical parameters can be monitored on-line more accurately.
- Parameters that are not directly measured can be adjusted more accurately during the test.
- Measurement faults and component malfunctions can be quickly and reliably detected on-line. Many measurement faults have not been detected by the on-line analysis procedure used in the past. No false alarm has occurred thus far.
- The performance engineer obtains a fast and reliable assessment of the performance of the engine and its components already during the test.
- Only one single analysis program has to be maintained.
- A high degree of automation, accuracy, and flexibility has been obtained.

Acknowledgment

The authors wish to thank their colleagues for inspiring discussions and MTU Aero Engines GmbH for the permission to publish this paper.

Nomenclature

A = area
EGT = exhaust gas temperature
F = thrust
H = matching constraint
I = indicator
M = modifier
NH = HP spool speed
NL = LP spool speed
P = total pressure
P_S = static pressure
r = radius

Downloaded 30 May 2010 to 128.113.26.88. Redistribution subject to ASME license or copyright; see http://www.asme.org/terms/Terms_Use.cfm

T = total temperature
u = boundary condition
W = mass flow
W_C = customer bleed flow
W_F = fuel flow
X = model parameter
y = measurement
δ = tolerance
η = efficiency
Π = pressure ratio

Acronyms

exp = expected
HP = high pressure
HPC = high-pressure compressor
HPT = high-pressure turbine
LP = low pressure
LPC = low-pressure compressor
LPT = low-pressure turbine
mea = measured
POT = power offtake

References

[1] RTO, 2002, "Performance Prediction and Simulation of Gas Turbine Engine Operation," AVT Working Group 018, RTO Technical Report No. TR-044, April.
[2] Kurzke, J., 1992, "Calculation of Installation Effects Within Performance Computer Programs," AGARD-LS-183, pp. 7.1–7.19.
[3] Selder, H., 1973, *Einführung in die Numerische Mathematik für Ingenieure*, Carl Hanser Verlag, München.
[4] AGARD, 1983, "Suitable Averaging Techniques in Non-Uniform Internal Flows," AGARD Working Group 14, AGARD-AR-182.
[5] Walsh, P. P., and Fletcher, P., 1998, *Gas Turbine Performance*, Blackwell, London.
[6] Habrard, A. G., 1976, "Characterization of Components Performance and Optimization of Matching in Jet-Engine Development," AGARD-LS-83, pp. 7.1–7.19.
[7] Riegler, C., Bauer, M., and Schulte, H., 2003, "Validation of a Mixed Flow Turbofan Performance Model in the Sub-Idle Operating Range," ASME Paper No. GT 2003-38223.
[8] 1998, "Test Uncertainty," ASME PTC 19.1-1998.
[9] Preinesberger, E., and Mitterhuber, J., 2001, "Anforderungen an die Systeme der neuen Generation zur Datenerfassung und Überwachung an Triebwerksprüfstände," DGLR-JT-2001-041.
[10] Gerlach, C., Staudacher, S., Filipovic, D., and Lippl, F., 2005, "CLEAN—Bench Adaptation and Test for a Complex Demo Engine Concept at ILA Stuttgart," ISABE-2005-1134, Sept.

Downloaded 30 May 2010 to 128.113.26.88. Redistribution subject to ASME license or copyright; see http://www.asme.org/terms/Terms_Use.cfm

Three-Component LDV Measurements in the Wake of a Compressor Cascade With Flow Separation

G. V. Hobson

T. M. Caruso

J. R. Carlson

Department of Aeronautics and Astronautics,
Turbopropulsion Laboratory,
Naval Postgraduate School,
Monterey, CA 93943

Measurements were taken of the vortex system and turbulent flow that resulted from the interaction between a stator blade and the approaching endwall boundary layer in a linear cascade of compressor blades. Data were taken at a Reynolds number based on blade chord of 640,000. Five-hole pressure measurements were conducted upstream and downstream of the blade row. The approaching boundary layer was also characterized with the laser-Doppler velocimeter. Downstream three-component laser-Doppler velocimetry surveys were conducted at three streamwise stations to map the location and velocity characteristics of the wake and vortex system. Results clearly showed the extent of the vortex emanating from the separation of the boundary layer on the suction side of the blade. Finally, all components of mean flow velocity and turbulence are documented for the last survey station. These data will form a challenging test case for numerical code validation. [DOI: 10.1115/1.2364883]

Introduction

The trend of axial turbomachine design is toward higher blade loading and lower aspect ratios, which places more emphasis on endwall effects and tip clearance losses [1]. Endwall effects and tip clearance losses are results of secondary flows around blade tips and within blade passages. Secondary flows are highly complex in nature and require full three-dimensional analysis to be fully understood, which in turn require detailed three-dimensional measurements of the flow field [2]. Data on these flow fields can be measured either intrusively or nonintrusively. The two major methods for measuring flow fields intrusively are hot wires and pneumatic probes. Both measuring instruments are able to acquire extremely accurate data but require extensive calibration. Furthermore, both instruments will display some sort of flow field interference that will become more significant as the distance from the instrument to a solid surface decreases. Gregory-Smith and Graves [3], Moore and Adhye [4], and Moore et al. [5] performed probe and hot wire measurements in turbine cascades.

The laser-Doppler-velocimetry (LDV) technique, which is nonintrusive, has been used for a number of years. Two decades ago the first results of using LDV for three-dimensional flow field measurements were published. One of the first attempts [6] used a one-component LDV system that rotated through three different positions to map the three-dimensional flow field downstream of a set of airfoils in a non-rectilinear cascade. Only within the last few years has three-dimensional LDV been used specifically for turbomachinery applications. A two-component LDV system that was orientated in different directions was used to measure the three-dimensional flow field in the inlet scroll of a radial-inflow turbine [7]. A three-component LDV system has been used to measure the three-dimensional flow field in the rotor blade passage of an axial-flow compressor [8]. A three-component LDV system was used to measure the unsteady flow field in the rotor of a radial-inflow turbine [9]. Many studies have considered tip clearance flows, primarily on axial compressors [10,11] and centrifugal compressors [12]. Most recently a study has been initiated to perform detail flow field surveys of a highly loaded compressor cascade for code validation [13].

The intent of the present study is that it will be a challenging computational fluid dynamics (CFD) test case, particularly for the validation of codes capable of either large eddy simulation (LES) or direct numerical simulation (DNS). The present work was focused on the secondary flow that existed downstream of a set of stator blades in a linear cascade. A three-component fiber-optic LDV system was used to map the flow field in the endwall region of the cascade. The corner vortex on the suction side of the blade was convected along the blade surface due to the secondary flow within the passage. This vortex gave rise to three-dimensional separation close to the trailing edge of the blade at mid span. Measurements were made at the design Reynolds numbers of 640,000 based on blade chord.

Experimental Setup

The cascade wind tunnel test facility is shown in Fig. 1. The facility, test section, and blade profiles, which had a chord length of 127.25 mm, were fully described by Hobson et al. [14]. The inlet guide vanes on the cascade tunnel were set for an inlet flow angle, β_1, of 38 deg, which was measured from the vertical. Pneumatic five-hole probe surveys were conducted at a traverse slot located two chords upstream of the leading edge of the blades. Five-hole pressure measurements were also taken downstream of the blades in a traverse slot located 2.78 axial chords from the leading edges of the blades. The figure also shows the position where seed particles were introduced in the tunnel for LDV measurements. Glycerin oil was used as the seeding material and the particle generator was a TSI six-jet atomizer. The average particle size produced by the oil-mist generator was 0.9 μm with a standard deviation of 0.45 μm. Seeding material was injected into the flow upstream of the inlet guide vanes, which were situated at the end of the inlet bellmouth. Blade profile information can also be found in [14]

The LDV system utilized for this work was a TSI three-component fiber-optic system. Figure 2 depicts the connections between system components.

Contributed by the International Gas Turbine Institute (IGTI) of ASME for publication in the JOURNAL OF TURBOMACHINERY. Manuscript received October 1, 2001; final manuscript received March 1, 2002; published online January 14, 2008. Review conducted by E. Benvenuiti. Paper presented at the International Gas Turbine and Aeroengine Congress and Exhibition, Atlanta, GA, June 16–19, 2003, Paper No. GT2003-38980.

 Copyright © 2008 by ASME

Downloaded 30 May 2010 to 128.113.26.88. Redistribution subject to ASME license or copyright; see http://www.asme.org/terms/Terms_Use.cfm

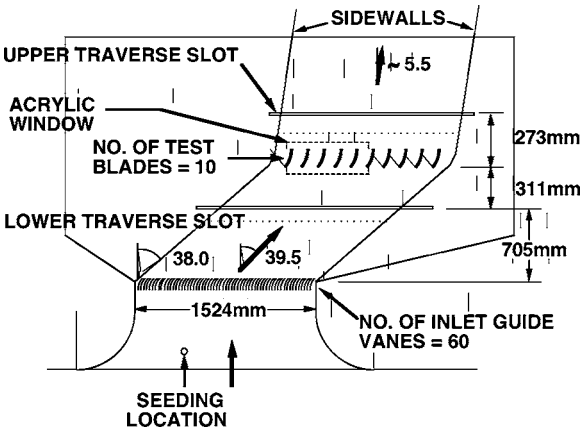

Fig. 1 Schematic of the low-speed cascade tunnel

Upstream pitchwise LDV surveys were conducted at a station 30% of an axial chord (121.9 mm) ahead of the leading edge at nine different spanwise locations close to the endwall. Downstream pitchwise surveys were taken at 5%, 10%, and 20% of an axial chord downstream of the trailing edge also at nine different spanwise locations. Measurements closest to the endwall resulted in saturation of the receiving optics, which rendered the data inaccurate and these locations are noted on the figure below, which depicts the LDV measurement grid. Figure 3 also shows the three-axis traverse mechanism coordinate system (primed). The cascade coordinate systems was x—axial, y—blade-to-blade, and z—spanwise.

Error Analysis. The estimated measurement uncertainties are given in Table 1. The uncertainties in parameters κ, L, and λ were given by the manufacturer. The fringe spacing was calculated as $d_f=\lambda/\sin\kappa$. Since particles do not follow the flow exactly, the uncertainty in the velocity can be larger than the uncertainty in the particle velocity.

Laser-Doppler-velocimetry measurements are also subject to additional errors. The nonorthogonal measurement of velocity components leads to the coupling of measurement errors. The spanwise velocity, W, was determined by taking the difference of two relatively large quantities (the velocity components measured by the blue and violet beam pairs), and then dividing by the sine of the angle between the probes. Thus to reduce this error required that the angle be made as large as possible. The magnitude of the angle between the two probes was 30 deg, which was dictated by the required immersion distance of the probe volume to the mid-span of the cascade.

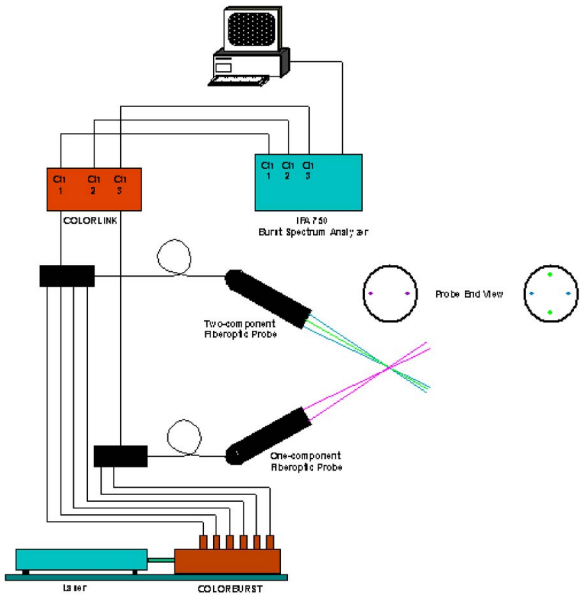

Fig. 2 Three-component LDV setup and plan view of the optical arrangement

Another source of error, which was difficult to quantify, was that the laser beam from one probe reflected off the acrylic window back into the receiving optics of the opposing probe. This only occurred at particular immersion depths of the LDV system, however when this occurred it did result in saturation of the photomultipliers as the wavelength of the blue (488 nm) and violet (476 nm) was relatively close.

All LDV data were acquired in the coincidence mode and averaging was performed over 1024 data points at each measurement location. Data were edited, i.e., they were processed using refinement bounds set at plus or minus two standard deviations. These refinement bounds gave a 95% confidence level associated with the uncertainty levels quoted in Table 1.

Results and Discussion

Flow Visualization. Surface flow visualization was performed on blades 3 and 4 in the cascade at the design Reynolds number. The flow pattern is shown in Fig. 4, which revealed that the suction surface of the blade was separated due to the roll up of the corner vortex on either side of the blade. This pattern was similar to that proposed by Delery and Meauze [13], who described the "tornado like vortices" on the suction side of the blade. The recirculation in the center of the blade in the present study was closer to the trailing edge than that shown in Fig. 5.

Blade Surface Pressure Distribution. Mid-span pressure distribution (here defined as the difference between local and upstream static pressures divided by the inlet dynamic pressure) on the fully instrumented blade (blade no. 6) is shown in Fig. 6. The pressure was a minimum at 0.4 of a chord, on the suction surface, and then rose continuously to the trailing edge even though three-dimensional flow separation was evident from about 70% chord as shown in Fig. 4.

Five-Hole Probe Data. The wakes of the inlet guide vanes were evident in the nondimensional total pressure (here defined as the ratio of the local total pressure to the upstream plenum pressure) and nondimensional velocity (X) distribution at the upstream slot. The inlet guide vanes were spaced 25.4 mm (1 in.) apart, however they were cantilevered alternately from either side of the cascade. Thus the tip vortices off the blades were spaced 50.8 mm (2 in.) apart. The effect of three of the inlet-guide-vane, tip-leakage vortices was evident for one blade passage, as can be seen in Figs. 7 and 8.

Both surface plots, Figs. 9 and 10, clearly show the total pressure and velocity deficit in the wakes, which become more complex as the endwall region was approached, i.e., double peaks appeared at approximately 20% span ($z/h=-0.3$).

Loss coefficients (ω_i) were calculated for each spanwise survey, such that;

$$\varpi_i = \frac{\bar{C}p_{t1} - \bar{C}p_{t2}}{\bar{C}p_{t1} - \bar{C}p_{s1}}$$

$$\bar{C}p_{tj} = \frac{\Delta z_i \int_0^S (P_{tj}/P_p) U_j \, dy}{\Delta z_i \int_0^S U_j \, dy} \tag{1}$$

and a similar expression for $\bar{C}p_{s1}$ where P_{tj} is the local total pressure and P_p is the upstream plenum pressure. Stations 1 and 2

Downloaded 30 May 2010 to 128.113.26.88. Redistribution subject to ASME license or copyright; see http://www.asme.org/terms/Terms_Use.cfm

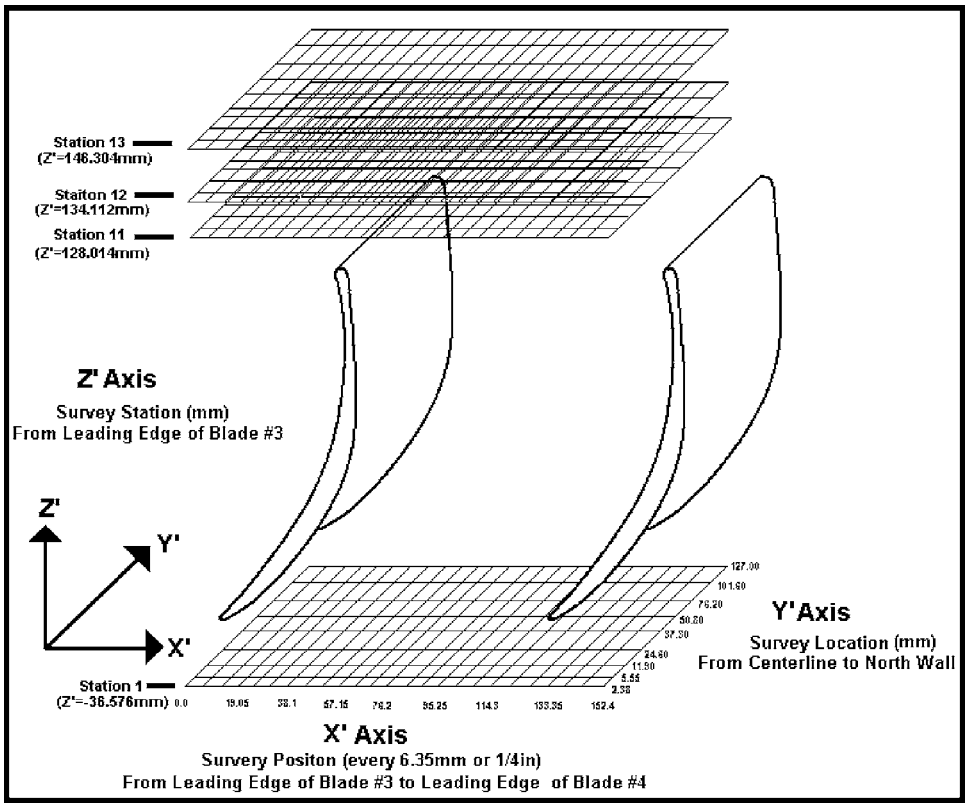

Fig. 3 LDV measurement grid and traverse mechanism coordinate system

denote the inlet and exit five-hole probe survey locations. Figure 11 shows the spanwise mass-averaged loss coefficient from centerline to the endwall. The loss coefficient showed a minimum between 20% and 30% span, which was associated with the double peaks in the total pressure distribution, or narrowing of the wake width in that region.

Three-Component LDV Data. A surface plot of the nondimensionalized velocity ($U_{\text{tot}}/V_{\text{ref}}$) from the centerline ($z/h=0$) to the end-wall region is shown in Fig. 12 as a summary of all station 1 surveys. The surface shows little or no effect of the inlet guide vanes on the total velocity at this station. However, a single-perturbation one-blade pitch in extent was evident, which was due to the upstream influence of the test blades on the approaching flow field.

The effect of the inlet guidevanes was, however, still evident in the approaching turbulence field, as can be seen in Fig. 13, which is a surface plot of the turbulent kinetic energy nondimensionalized by the upstream reference velocity. Close to the endwall three regions of high turbulence ($\sim$30%) are seen, which are spaced two inlet guidevanes apart. The mid-span turbulence was at a reduced level of approximately 7.7%, which corresponded to an inlet freestream turbulence intensity of approximately 2.2%. Figure 14 is a mass average of Figs. 12 and 13 or the spanwise mean velocity and turbulent kinetic energy distributions, obtained in a similar manner to mass averaged spanwise loss distribution in Fig. 11. Both distrubutions are essential inlet boundary conditions for any CFD simulation. Previous hot wire measurements [15] showed that the length scale of the approaching turbulence was of the order of the spacing of the inlet guide vanes, which was on a

Table 1 Estimated measurement uncertainty

Item	Description	Uncertainty
x, y, z	Traverse coordinates	0.025 mm
P_t	Plenum pressure	25 Pa
P	Pressure (Scanivalve)	12 Pa
P_{atm}	Atmospheric pressure	35 Pa
T_t	Plenum temperature	0.2°C
X	Five-hole velocity	4% @ 10 m/s 2% @ 100 m/s
κ	Beam half angle	0.3 deg
L	Focal length	8.0 mm
λ	Wavelength	0.1%
d_f	Fringe spacing	0.3%
U, V	Particle velocity	0.5% @ 10 m/s 1.0% @ 100 m/s
W	Particle velocity	2.0% @ 10 m/s 4.0% @ 100 m/s

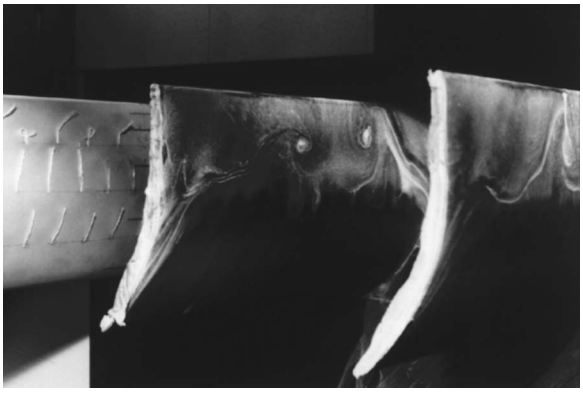

Fig. 4 Suction side surface flow visualization

Downloaded 30 May 2010 to 128.113.26.88. Redistribution subject to ASME license or copyright; see http://www.asme.org/terms/Terms_Use.cfm

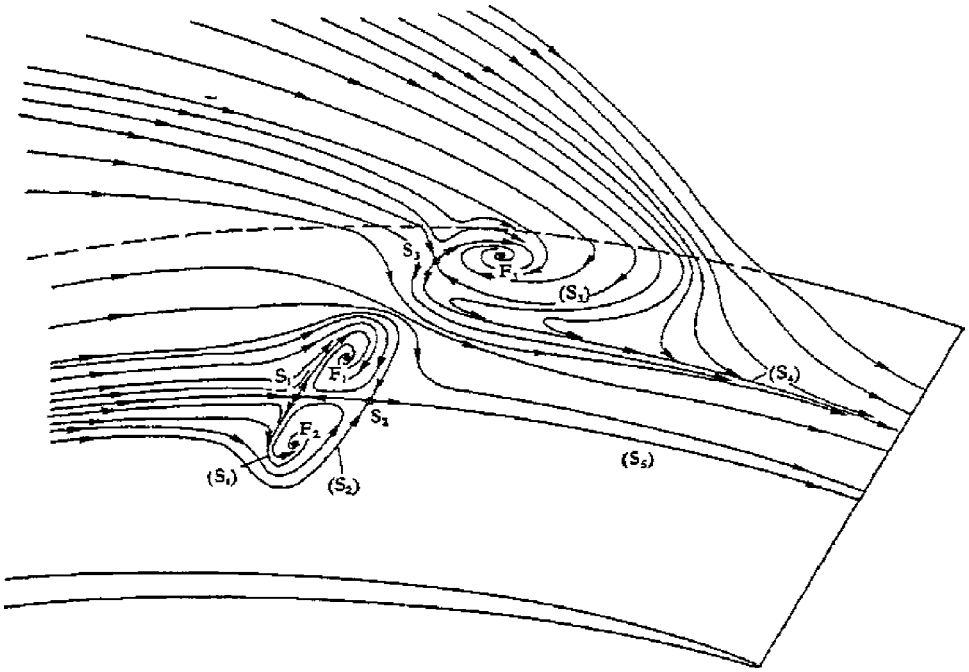

Fig. 5 Schematic flow topology proposed by Delery and Meauze [13]

sixth of a blade pitch.

Figures 15 and 16 show the mean flow axial velocity profile measured at stations 11 and 12, respectively. These surveys were incomplete as stated earlier due to saturation of the optics as the endwall was approached. However, they do show the depth of the velocity deficit in the wake and its development ahead of station 13 (Fig. 17), which was the most complete survey grid measured.

At station 13 the endwall boundary layer was most evident, as was the narrowing of the wake at the spanwise location (z/h) of 0.3–0.4. The narrowing of the wake was due to the secondary flow resulting from the three-dimensional separation on the blade surface. The secondary flow vectors are superimposed on the axial velocity contours for stations 11, 12, and 13 in Fig. 18, which shows the development of the endwall vortex in the wake.

Counter-rotating vortices emanated from the suction surface of the blade, which caused the mid-span flow to separate close to the trailing edge. The pressure-side corner vortex hugged the endwall and was convected across the passage to the suction side of the adjacent blade. This vortex then continued to be convected in the same direction such that it was located on the pressure side of the wake at the downstream survey location. The suction side vortex was convected spanwise along the blade surface away from the endwall. In doing so it became significantly distorted, to the point where it was not readily distinguished at the downstream measurement location.

The turbulent kinetic energy distribution associated with the mean flow profile (Figs. 17 and 18) at station 13 is presented in Fig. 19.

This distribution showed three distinct features. Two peaks in intensity were measured along the pitchwise direction at mid span, which coincided with the maximum velocity gradients on either side of the wake. Second the localized peak at $z/h=-0.3$ on the suction side of the blade, which corresponded to the minimum thickness of the wake and highest mean flow gradient. Third, there was an increase of turbulence in between the blades close to the endwall. The modest (when compared to the high turbulence in the wake) levels of k/V_{ref}^2 close to the endwall were approximately 40%, compared to the 30% level from the inlet turbulence profile as shown in fig. 14. Figure 20 shows the development of

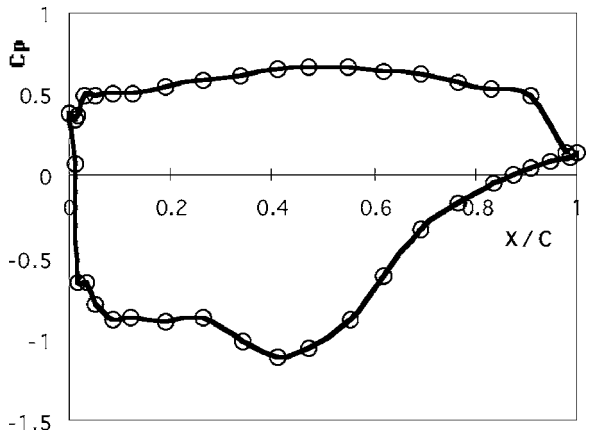

Fig. 6 Mid-span blade surface pressure distribution

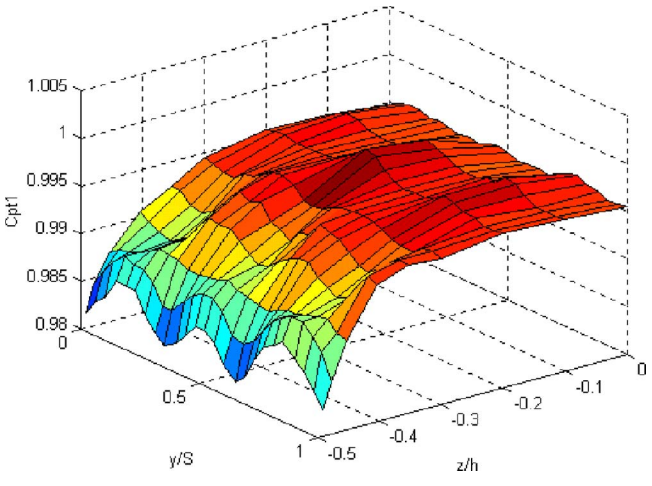

Fig. 7 Inlet total pressure distribution (two axial chords upstream)

Downloaded 30 May 2010 to 128.113.26.88. Redistribution subject to ASME license or copyright; see http://www.asme.org/terms/Terms_Use.cfm

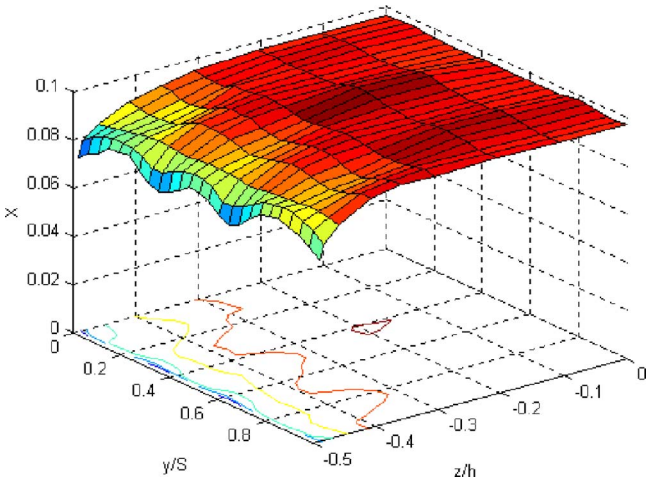

Fig. 8 Inlet nondimensional velocity distribution (two axial chords upstream)

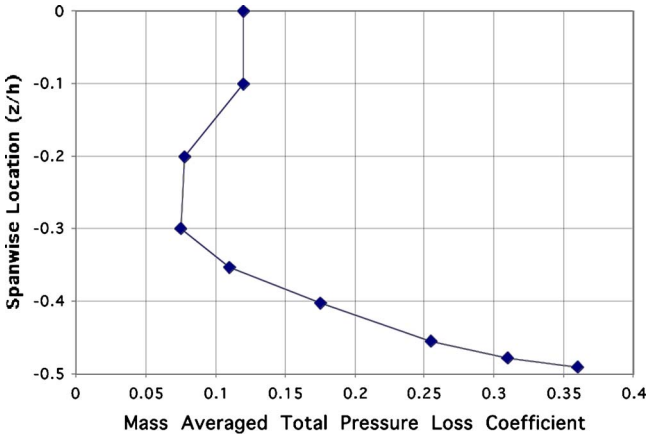

Fig. 11 Spanwise total pressure loss distribution

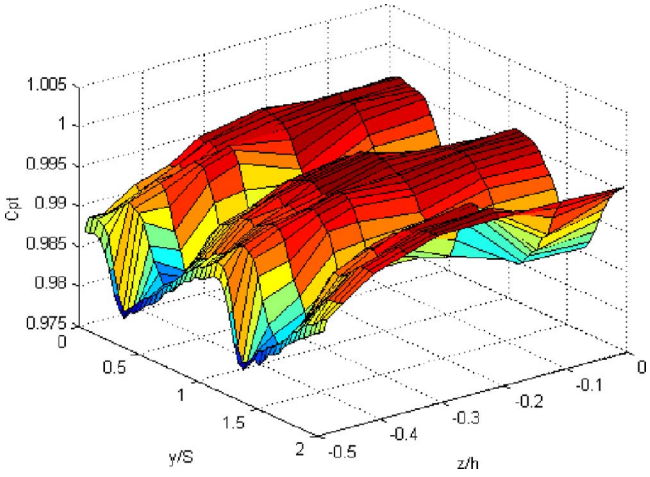

Fig. 9 Exit total pressure distribution over blade passages (2.78 axial chords downstream from leading edge)

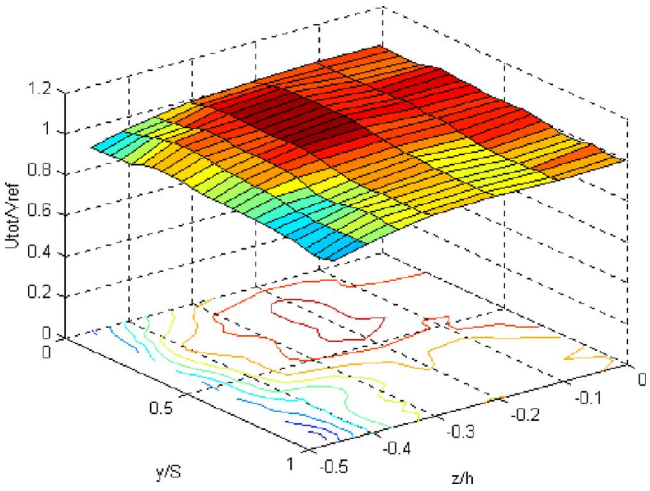

Fig. 12 Inlet nondimensional velocity distribution (30% of an axial chord upstream of the leading edge)

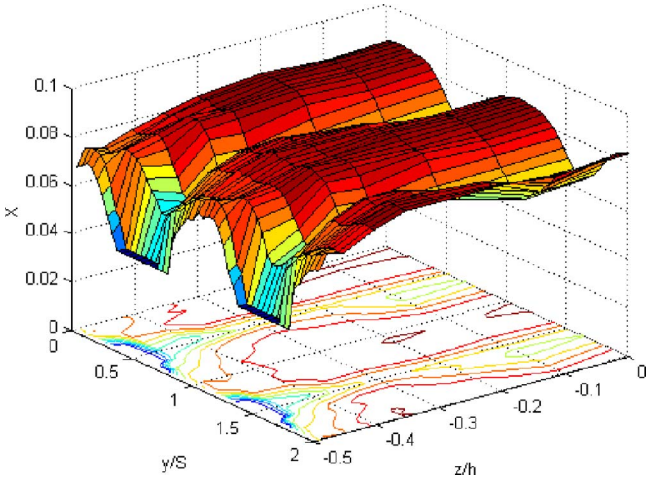

Fig. 10 Exit nondimensional velocity distribution (2.78 axial chords downstream of the leading edge)

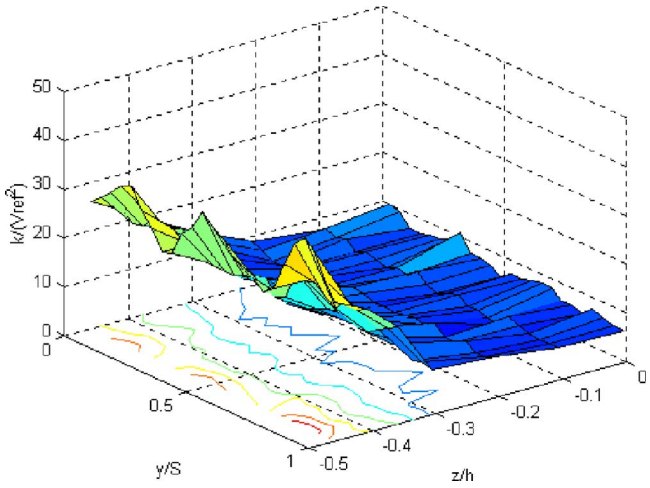

Fig. 13 Inlet nondimensional turbulent kinetic energy distribution at station 1 (30% of an axial chord upstream of the leading edges)

Downloaded 30 May 2010 to 128.113.26.88. Redistribution subject to ASME license or copyright; see http://www.asme.org/terms/Terms_Use.cfm

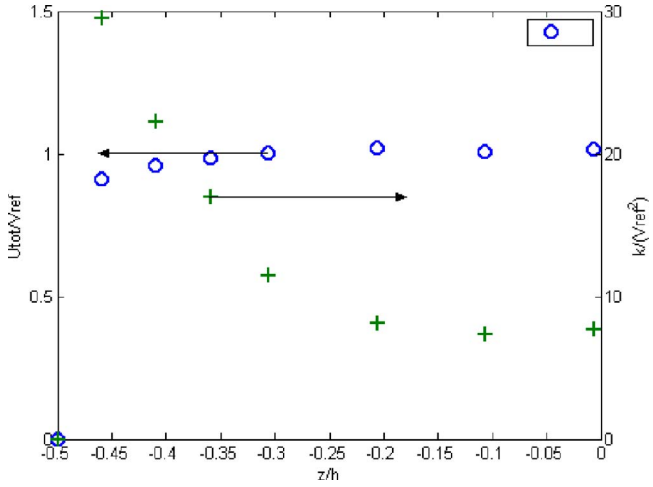

Fig. 14 Mass average spanwise inlet velocity and turbulent kinetic energy profiles 30% ahead of the leading edges

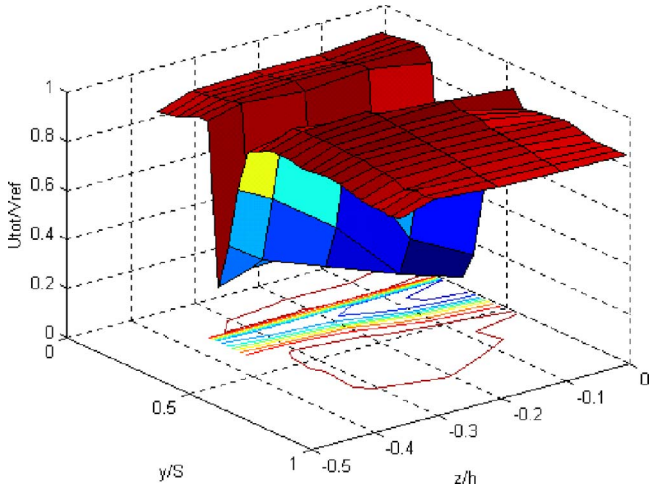

Fig. 15 Wake nondimensional velocity distribution at station 11

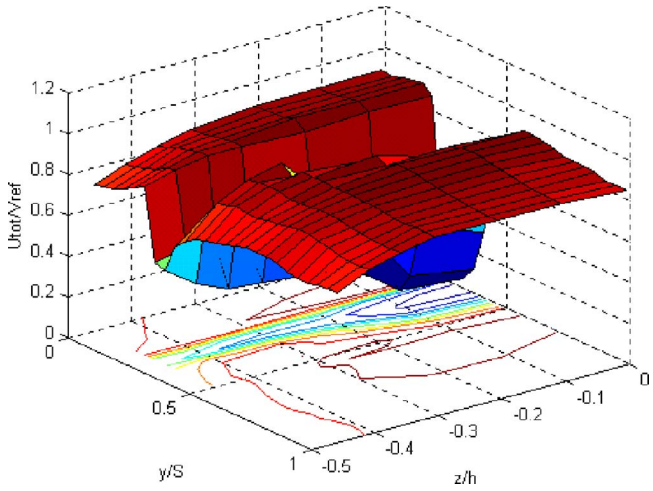

Fig. 16 Wake nondimensional velocity distribution at station 12

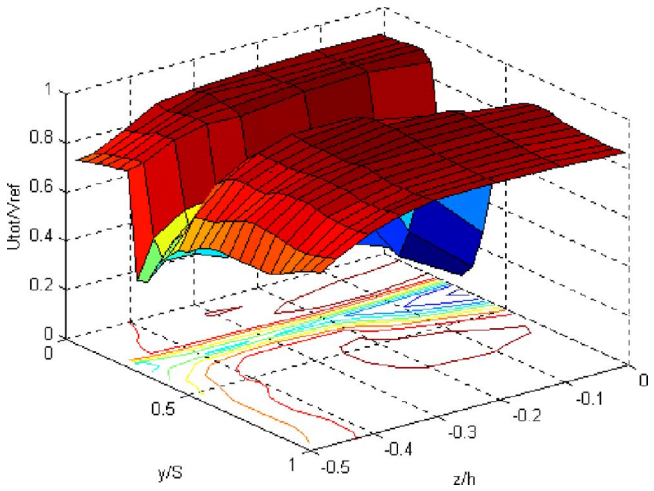

Fig. 17 Wake nondimensional velocity distribution at station 13

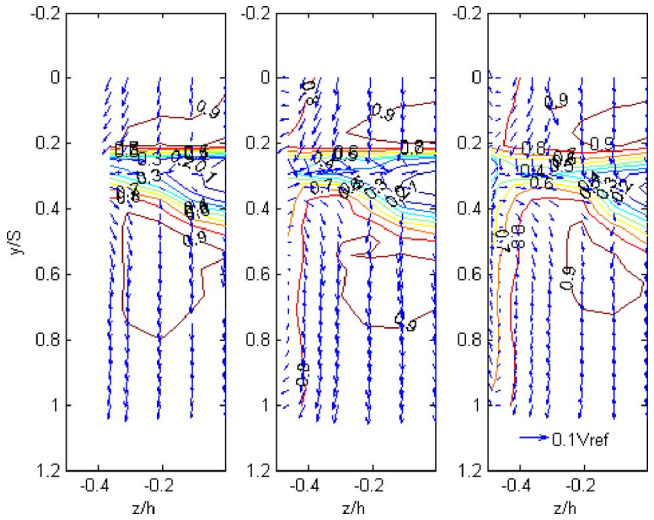

Fig. 18 Secondary flow development downstream of the trailing edges at 5%, 10%, and 20% axial chord

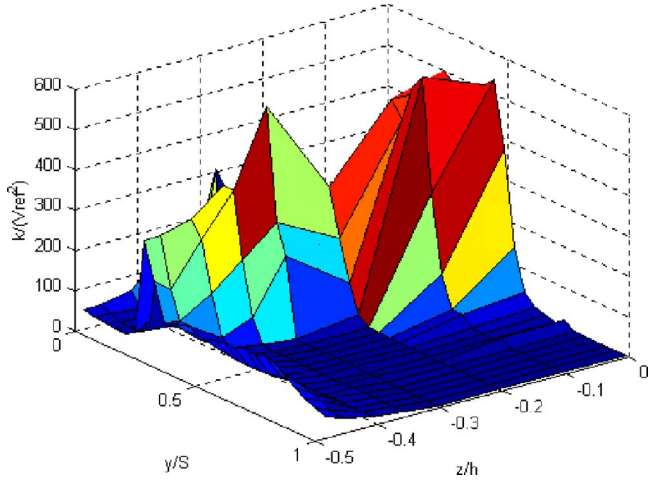

Fig. 19 Wake nondimensional turbulent kinetic energy distribution at station 13

Downloaded 30 May 2010 to 128.113.26.88. Redistribution subject to ASME license or copyright; see http://www.asme.org/terms/Terms_Use.cfm

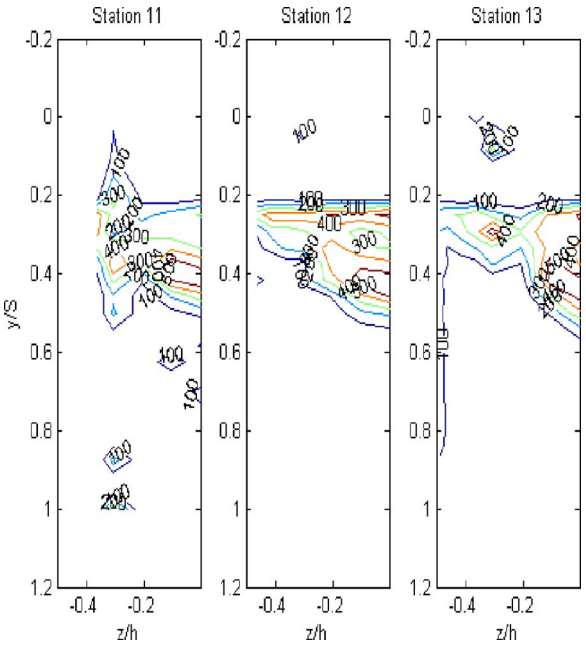

Fig. 20 Turbulent kinetic energy distribution at stations 11, 12, and 13

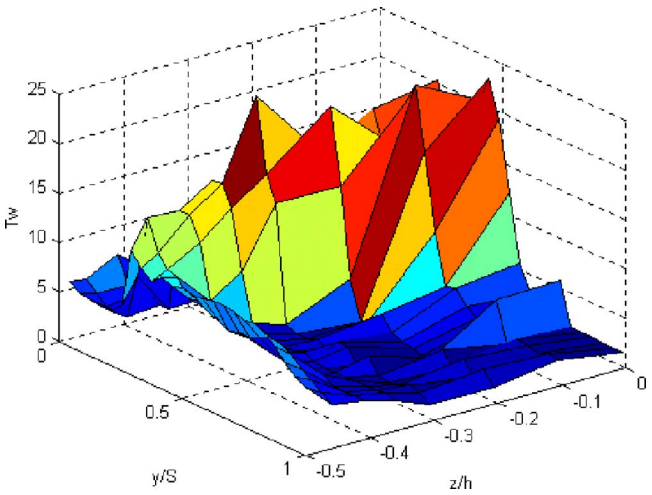

Fig. 23 Spanwise turbulence intensity distribution at station 13

the turbulent kinetic energy field in the wake for stations 11–13.

The individual components of the turbulent kinetic energy profile are presented as streamwise (axial), pitchwise (blade-to-blade), and spanwise turbulence intensity profiles in Figs. 21–23.

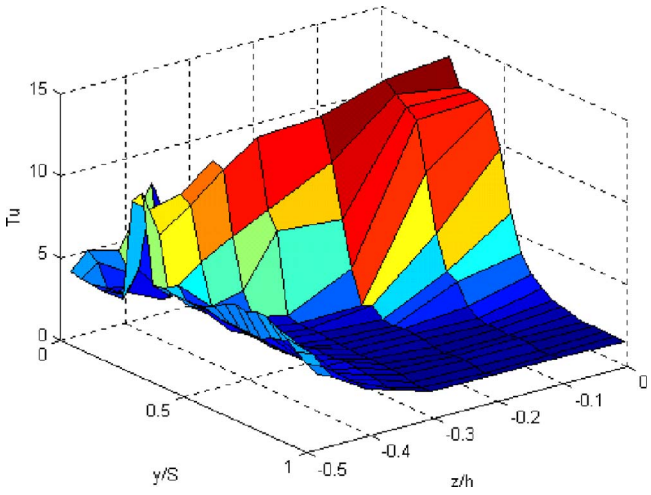

Fig. 21 Streamwise turbulence intensity distribution (30% of an axial chord downstream of the trailing edge (station 13))

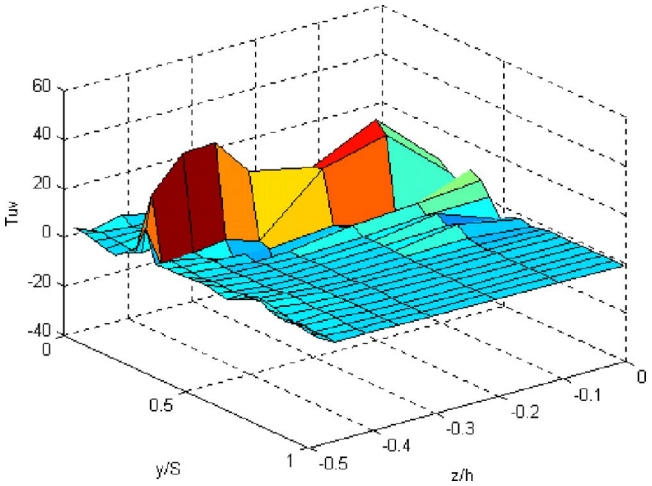

Fig. 24 Reynolds stress ($\overline{u'v'}$) distribution

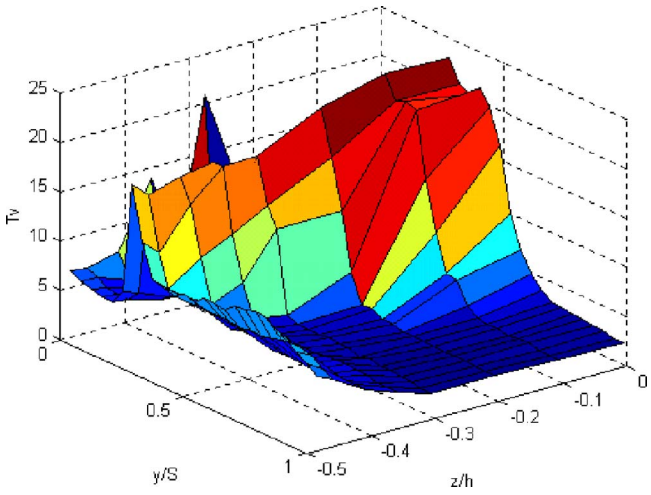

Fig. 22 Station 13 pitchwise turbulence intensity distribution

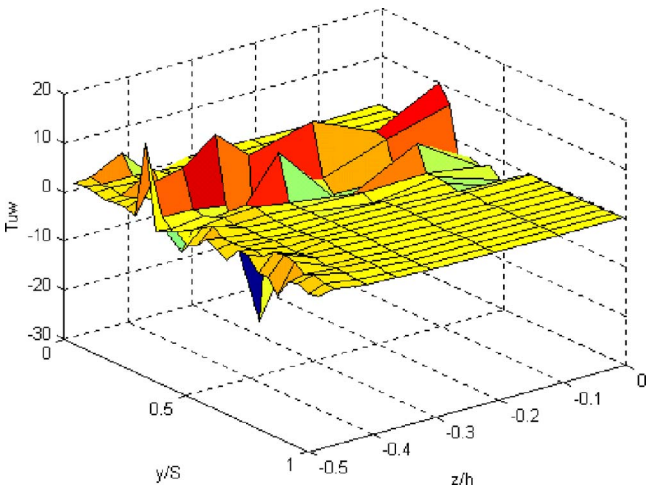

Fig. 25 Reynolds stress ($\overline{u'w'}$) distribution

Downloaded 30 May 2010 to 128.113.26.88. Redistribution subject to ASME license or copyright; see http://www.asme.org/terms/Terms_Use.cfm

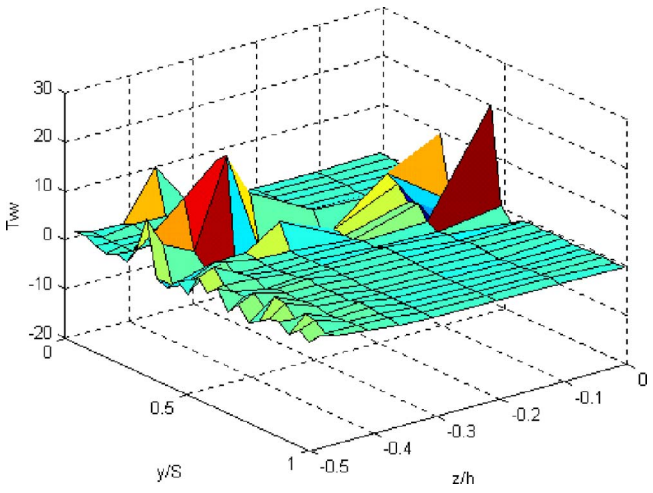

Fig. 26 Reynolds stress ($\overline{v'w'}$) distribution

Finally, for completeness the, remainder of the components of the Reynolds stress tensor are presented as dimensional cross correlations in Figs. 24–26.

Conclusions

The setup and utilization of a three-component LDV system with traverse were successfully demonstrated. The introduction of full three-dimensional analysis to cascade flows should eventually lead to refined modeling and improved data for turbomachinery design.

The upstream LDV surveys showed the inlet flow to be nearly two-dimensional, and the results of the downstream LDV surveys documented the complex three-dimensional wake flow. Counter-rotating vortices, which emanated from the suction surface of the blade, were measured at their downstream location in the wake of the cascade. The effect of the overall secondary flow within the blade passage was more than expected at the moderately high inlet-flow angle. The maximum secondary-flow values were as high as 10% of inlet freestream velocity. Turbulence intensity distributions showed maximum levels, which corresponded to regions of high mean-flow shear. Maximum turbulence-intensity levels in the wake were 25%, up from the inlet freestream values of 2.2%.

Nomenclature

Cp = coefficient of pressure
C = blade chord (127 mm)
h = blade span (254 mm)
k = turbulent kinetic energy, $1/2(u'^2+v'^2+w'^2)$
Re_c = Reynolds number based on chord length
S = blade pitch (152 mm)
Tu = axial turbulence intensity, $\sqrt{u'^2}/v_{\mathrm{ref}}$
Tuv = cross-correlation, $\overline{u'v'}$ ($\mathrm{m}^2/\mathrm{s}^2$)
Tuw = cross-correlation, $\overline{u'w'}$ ($\mathrm{m}^2/\mathrm{s}^2$)
Tv = pitchwise turbulence intensity, $\sqrt{v'^2}/v_{\mathrm{ref}}$
Tvw = cross-correlation, $\overline{v'w'}$ ($\mathrm{m}^2/\mathrm{s}^2$)
Tw = spanwise turbulence intensity, $\sqrt{w'^2}/v_{\mathrm{ref}}$
U = axial mean velocity component
U_{tot} = $\sqrt{\mathrm{U}^2+\mathrm{V}^2+\mathrm{W}^2}$
u' = axial fluctuating velocity component
V = pitchwise mean velocity component
$\mathrm{V}_{\mathrm{ref}}$ = upstream reference total velocity
v' = pitchwise fluctuating velocity component
W = spanwise mean velocity component
w' = spanwise fluctuating velocity component
X = nondimensional velocity, $U_{\mathrm{tot}}/\sqrt{2C_pT_t}$
x = axial direction
y = pitchwise, or tangential, direction
z = spanwise direction
β = inlet flow angle from the axial direction, in the x-y plane

References

[1] Dong, Y., Gallimore, S. J., and Hodson, H. P., 1987, "Three-Dimensional Flows and Loss Reduction in Axial Compressors," ASME J. Turbomach., **109**, pp. 354–361.
[2] Enomoto, S., Hah, C., and Hobson, G. V., 2000, "Numerical and Experimental Investigation of Low Reynolds Number Effects on Laminar Flow Separation and Transition in a Cascade of Compressor Blades," ASME Paper No. 2000-GT-0276.
[3] Gregory-Smith, D. G., and Graves, C. P., 1983, "Secondary Flow and Losses in a Turbine Cascade," *AGARD Conference Proceedings No. 351 on Viscous Effects in Turbomachines*, Copenhagen, Denmark.
[4] Moore, J., and Adhye, R. Y., 1985, "Secondary Flows and Losses Downstream of a Turbine Cascade," ASME J. Eng. Gas Turbines Power, **107**(4), pp. 961–968.
[5] Moore, J., Schaffer, D. M., and Moore, J. G., 1987, "Reynolds Stresses and Dissipation Mechanisms Downstream of a Turbine Cascade," ASME J. Turbomach., **109**, pp. 258–267.
[6] Lasser, R., and Rouleau, W. T., 1983, "Measurements of Secondary Flow Within a Cascade of Curved Blades and in the Wake of the Cascade," ASME Paper No. 83-GT-24.
[7] Malak, M. F., Hamed, A., and Tabakoff, W., 1987, "Three-Dimensional Flow Field Measurements in a Radial Inflow Turbine Scroll Using LDV," ASME J. Turbomach., **109**, pp. 163–169.
[8] Chesnakas, C. J., and Dancey, C. L., 1990, "Three-Component LDA Measurements in an Axial-Flow Compressor," J. Propul. Power, **6**, pp. 474–481.
[9] Pasin, M., and Tabakoff, W., 1993, "Laser Measurements of the Flow Field in a Radial Turbine Rotor," AIAA Paper No. 93-0156.
[10] Stauter, R. C., 1992, "Measurement of the Three-Dimensional Tip Region Flow Field in an Axial Compressor," ASME Paper No. 92-GT-211.
[11] Doukelis, A., Mathioudakis, K., Founti, M., and Papailiou, K., 1997, "3-D LDA Measurements in an Annular Cascade for Studying Tip Clearance Effects," AGARD CP-598, Advanced Non-Intrusive Instrumentation for Propulsion Engines, Brussels.
[12] Skoch, G. J., Prahst, P. S., Wernet, M. P., Wood, J. R., and Strazisar, A. J., 1997, "Laser Anemometer measurements of the Flow Field in a 4:1 Pressure Ration Centrifugal Impeller," ASME Paper No. 97-GT-342.
[13] Delery, J., and Meauze, G., 2003, "A Detailed Experimental Analysis of the Flow in a Highly Loaded Fixed Compressor Cascade: The ISO-Cascade Co-Operative Programme on Code Validation," Aerosp. Sci. Technol., **7**(1), pp. 1–9.
[14] Hobson, G. V., Hansen, D. J., Schnorenberg, D. G., and Grove, D. V., 2001, "Effect of Reynolds Number on Separation Bubbles on Controlled-Diffusion Compressor Blades in Cascade," J. Propul. Power, **17**(1), pp. 154–162.
[15] Hobson, G. V., and Shreeve, R. P., 1993, "Inlet Turbulence Distortion and Viscous Flow Development in a Controlled-Diffusion Compressor Cascade at Very High Incidence," J. Propul. Power, **9**(3), pp. 397–407.

Downloaded 30 May 2010 to 128.113.26.88. Redistribution subject to ASME license or copyright; see http://www.asme.org/terms/Terms_Use.cfm

The Influence of Compressor Blade Row Interaction Modeling on Performance Estimates From Time-Accurate, Multistage, Navier–Stokes Simulations

Dale Van Zante
NASA Glenn Research Center,
Cleveland, OH 44135

Jenping Chen
Ohio State University,
Columbus, OH 43210

Michael Hathaway
ARL Vehicle Technology Directorate,
Cleveland, OH 44135

Randall Chriss
NASA Glenn Research Center,
Cleveland, OH 44135

The time-accurate, multistage, Navier–Stokes, turbomachinery solver TURBO *was used to calculate the aeroperformance of a 2* 1/2 *stage, highly loaded, high-speed, axial compressor. The goals of the research project were to demonstrate completion times for multistage, time-accurate simulations that are consistent with inclusion in the design process and to assess the influence of differing approaches to modeling the effects of blade row interactions on aeroperformance estimates. Three different simulation setups were used to model blade row interactions: (1) single-passage per blade row with phase lag boundaries, (2) multiple passages per blade row with phase lag boundaries, and (3) a periodic sector (*1/2 *annulus sector). The simulations used identical inlet and exit boundary conditions and identical meshes. To add more blade passages to the domain, the single-passage meshes were copied and rotated. This removed any issues of differing mesh topology or mesh density from the following results. The* 1/2 *annulus simulation utilizing periodic boundary conditions required an order of magnitude fewer iterations to converge when all three simulations were converged to the same level as assessed by monitoring changes in overall adiabatic efficiency. When using phase lag boundary conditions, the necessity to converge the time history information requires more iterations to obtain the same convergence level. In addition to convergence differences, the three simulations gave different overall performance estimates where the* 1/2 *annulus case was 1.0 point lower in adiabatic efficiency than the single-passage phase lag case. The interaction between blade rows in the same frame of reference sets up spatial variations of properties in the circumferential direction, which are stationary in that reference frame. The phase lag boundary condition formulation will not capture this effect because the blade rows are not moving relative to each other. Thus, for simulations of more than two blade rows and strong interactions, a periodic simulation is necessary to estimate the correct aeroperformance.* [DOI: 10.1115/1.2775486]

Keywords: blade row interaction, numerical modeling, multi-stage compressor

Introduction

The NASA ultraefficient engine technology (UEET) Program is developing and transferring turbine engine propulsion technologies to improve the performance of future aerospace systems. The MSU-TURBO suite of time-accurate, multistage, analysis software is a technology being matured and demonstrated by the program. The two stage axial compressor which was designed for the highly loaded light weight compressor and turbine subproject is used as a test case to demonstrate the computational capability of TURBO. This compressor is referred to as the proof of concept compressor (POCC).

Unsteady Reynolds-averaged Navier–Stokes (RANS) flow solvers for turbomachinery rotor-stator flows have been under development since the 1980s, see, for example, Rai [1], Janus and Whitfield [2], Giles [3], Lewis et al. [4], Chen and Whitfield [5], among others. An impediment to the common use of these techniques is the large computational cost of direct computation of multiple blade row simulations and rapid turnaround time required, usually within 24 h, if simulations are to have timely impact on new designs. This requirement limits the routine use of unsteady RANS codes in the industrial environment. Fortunately, contemporary computer capability has advanced significantly both in processor speed and memory size concurrently with falling cost since the adoption of high performance parallel computing. TURBO has already proven excellent scalability on parallel systems. One focus of this work is to demonstrate the feasibility of unsteady multi-blade-row turbomachinery simulations with substantial reduction of turnaround time by using the parallel computing power that is now more readily available.

The TURBO code incorporates multiple boundary condition treatments from which the user can choose: phase lag boundary conditions, periodic boundary conditions, and a combination of periodic and phase lag boundaries. All three of the above boundary condition treatments were evaluated with the POCC test case for numerical efficiency and to ascertain any differences in aeroperformance estimates. The three modeling approaches are as follows.

Phase lag boundary conditions are a commonly used practice to reduce computing resources for unsteady simulations without changing the blade count (Erdos et al. [6]). This allows modeling

Contributed by the International Gas Turbine Institute of ASME for publication in the JOURNAL OF TURBOMACHINERY. Manuscript received July 14, 2006; final manuscript received August 21, 2006; published online January 14, 2008. Review conducted by David Wisler. Paper presented at the ASME Turbo Expo 2005: Land, Sea and Air (GT2005), Reno, NV, June 6–9, 2005, Paper No. GT2005-68463.

 Copyright © 2008 by ASME

Downloaded 30 May 2010 to 128.113.26.88. Redistribution subject to ASME license or copyright; see http://www.asme.org/terms/Terms_Use.cfm

of rotor-stator interaction using only a single blade passage in each blade row. This technique can greatly reduce the computing resources needed for simulations of stages with irreducible blade counts and is useful for time-accurate analyses dominated by unsteadiness at the adjacent blade passing frequency (see Chen and Barter [7] for a detailed description of this modeling technique). The single-stage phase lag capability was implemented in TURBO using a more general approach suitable for simulating multiple stage interaction (Wang and Chen [8]). Although it generally reduces computing resources in terms of CPUs and memory, direct-storage phase lag simulation typically requires longer computing time to converge the stored history data for the phase lag boundary. In an effort to speed up the convergence performance, a partial frequency mode acceleration technique was implemented to increase the convergence of the phase lag simulations. This method will be discussed in more detail later.

While temporal periodicity due to adjacent blade passing can be modeled with the single-passage phase lag modeling, there were concerns over its inability to fully capture the spatial periodicity resulting from interactions of blade rows in the same reference frame, stator-stator or rotor-rotor interactions. These interactions can produce significant circumferential nonuniformities in multistage machines (He et al. [9]). This concern is addressed in this study by modifying the single-passage model to use multiple passages in each blade row so that the total circumferential extent of a blade row is always greater than the pitch of the next upstream blade row which is in the same frame of reference. This is an attempt to achieve adequate spatial coverage to capture the incoming wakes while keeping the number of passages computed at a minimum. However, it is recognized that this approach enforces a spatial periodicity that is not necessarily consistent with the spatial periodicity associated with the relative blade counts.

Finally, a half-annulus simulation of the entire 2.5 stage machine which captures the inherent periodicity associated with integer multiples of blade counts is also presented in this study. Application of circumferential periodicity models the blade row interactions directly, thereby eliminating concerns over the modeling assumptions in the phase lag simulations and also enforces the correct spatial periodicity. Note, however, that harmonics that are not associated with integer multiples of shaft frequency, for example, stall cells, are improperly constrained to grow at integer multiples of shaft frequency unless a full annulus simulation is done. Since this work is done at the design point for the machine, all temporal harmonics are dominated by shaft speed and a half-annulus simulation is sufficient. Although substantially more computing resources are needed, it will be demonstrated that a half-annulus simulation of the 2.5 stage compressor converges much faster than the phase lag simulations. The half-annulus simulation also provides the base-line solution for evaluating the respective merits of the three different approaches, i.e., direct periodicity associated with relative blade counts, single-passage phase lag, and multipassage phase lag.

What follows is a brief discussion of the TURBO code numerics and recent changes to the code which improved convergence time. Next, the setup of the three simulations is discussed followed by the timing and aeroperformance results. The paper concludes with an analysis of the interactions that lead to the observed differences in aeroperformance.

TURBO Numerical Technique. The TURBO code is a three-dimesional (3D), viscous, time-accurate code which solves the RANS equations in a rotating cartesian coordinate system. The equations are spatially discretized using a modified upwind scheme (Whitfield et al. [10]) based on Roe [11] and Osher and Chakravarthy [12]. Temporal discretization is second-order accurate backward differencing. The governing equations are time marched with an implicit scheme based on the iterative Newton algorithm with flux Jacobians computed using the flux-vector splitting technique of Steger and Warming [13] and analytical viscous Jacobians. Matrix inversion is accomplished using a symmetric Gauss–Siedel technique and multiple Newton subiterations are performed at each time step to minimize linearization error. The effects of turbulence are incorporated using a NASA/CMOTT κ-ε turbulence model (Zhu and Shi [14]) with wall functions. TURBO computes the flow fields of single or multiple blade passages within either a complete blade row or a periodic circumferential sector of a blade row, and it is capable of simulating unsteady interaction between multiple blade rows using a dynamic sliding interface. Further information on the numerical aspects of TURBO can be found in Chen and Briley [15].

One goal of the present research is to demonstrate large-scale simulations using parallel computing. It is important that the code is portable across different parallel computing platforms and this was accomplished through use of the message passing interface (MPI) for interprocessor communications. Distributed memory computation is the architectural paradigm of the code, so that each processor (CPU) has exclusive access to its own partition of memory, which typically resides in the processor. The parallel code is implemented by a single-program multiple-data (SPMD) parallelization strategy. In this strategy, a single program is replicated for each processor and run with the data associated with a subdomain of the original computational domain.

The parallel communication framework has been coded to support solution of problems using multiblock structured grids in which the block connectivity of the grid blocks is arbitrary (Chen and Briley [15]). The grids, one per blade passage, need to be partitioned before the execution of the flow solver. The grid partitioning is done with the preprocessor GUMBO (Remotigue [16]), which features a graphical user interface. To reduce the initial transient, an APNASA (Adamczyk [17]) solution (or any 3D RANS solution) can be used to provide initial flow fields. This approach has been shown to greatly speed up the convergence of the unsteady simulations (Chen et al. [18]). In addition to existing capabilities, two new features have been developed to help improve the turnaround time and are described next.

Analytical Flux Jacobians. For implicit schemes, flux Jacobians are needed to linearize the physical flux vectors, which contain both inviscid and viscous components. The viscous Jacobians are computed with a numerical formulation in the older versions of the code. Redundant computation of viscous fluxes had consumed almost one-third of the entire computing time. To improve numerical efficiency, an analytical formulation was implemented which resulted in a 30% reduction in CPU time and enhanced code robustness.

Partial Frequency Mode. A direct-storage method is used in the phase lag simulations (Chen and Barter [7]), which is based on the assumption that passage flow is periodic in time at a prescribed frequency. For embedded blades, the unsteady frequency is a combination of the adjacent blade passing frequencies, which in turn depends on the smallest common divisor of their blade counts. With the typical blade counts found in contemporary compressor designs, it is common to store a full revolution of phase lag boundary history data. Previous experience indicates that the convergence rate of the phase lag simulations is strongly related to the storage, size; i.e., the smaller the storage the faster the convergence. To reduce the storage size, a modification to the unsteady frequency of each passage is done so that it only accounts for the dominating disturbance from one of the two neighboring blades. For example, in blades where incoming wakes are the dominating disturbances, the phase lag frequency can be temporarily changed to that of the upstream blade passing frequency. The size of the phase lag boundary history data then reduces to only account for the upstream blade count which requires less storage than to account for both upstream and downstream blade counts. This procedure has been shown to be an effective way to move quickly through the initial transient phase when starting from a condition

Downloaded 30 May 2010 to 128.113.26.88. Redistribution subject to ASME license or copyright; see http://www.asme.org/terms/Terms_Use.cfm

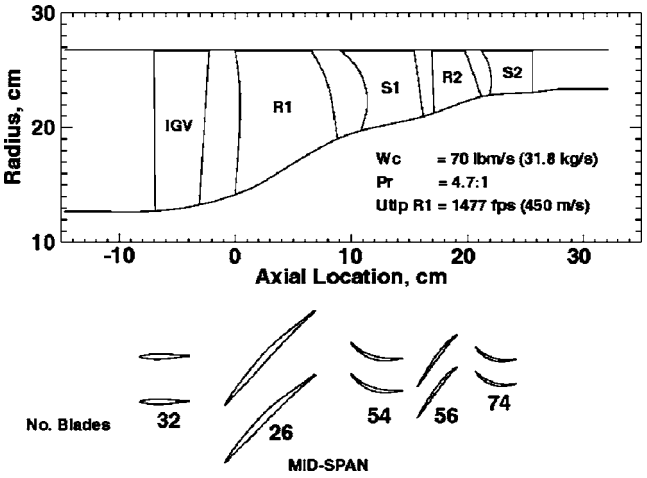

Fig. 1 The UEET 2.5 stage compressor (from Larosiliere et al. [19])

that is far from being converged. As the primary periodicity due to the upstream disturbance is established, the downstream disturbance can then be included.

Simulation Setup

Proof of Concept Processor Test Case. The test case used in this study is the NASA UEET POCC. The goal of this design is to demonstrate a highly loaded axial compressor technology capable of delivering 12:1 pressure ratio (PR) in four stages with a high level of polytropic efficiency. The POCC compressor, which is the first 2.5 stages of a four stage design, is shown in Fig. 1.

Grid Topology and Inlet/Exit Conditions. The APG code of Beach and Hoffman [20] was used to produce one-block-per-blade-passage, elliptically smoothed, H meshes with 80 nodes along the blade chord, 71 points spanwise with eight cells in the tip/hub clearances packed at the wall, and (except for the IGV) 71 points pitchwise. Mesh size was chosen so that convected features and clearance flows would be adequately modeled based on experience from Refs. [21,22]. The spacing of the first node off of solid surfaces was consistent with using wall functions (y^+ of 15–100 with most nodes at 50). GUMBO was used to partition the meshes and to duplicate the meshes for multiple passages per blade row. All three simulations used the identical base meshes. Meshes were simply copied and rotated to create additional passages. The single-passage solution contains 3.1×10^6 nodes, the multipassage 6.9×10^6 nodes, and the half-annulus solution 76.4×10^6 nodes.

The only change to blade counts was done early in this research project because the computational resources available were not adequate to simulate a periodic sector. Thus, a modification to S2 blade count from 74 to 75 was made to the single-passage and multiple passage simulations to keep the computational resources for the multiple passage simulation manageable. The blade count change was only done to allow the comparison of the single-passage and multiple passage simulations. The single-passage phase lag simulation has no inherent restriction on blade count. The addition of a single S2 blade was done without rescaling the blade chord or changing the axial spacing. An APNASA simulation of the POCC showed less than 0.1 point change in adiabatic efficiency due to the S2 blade count change. This was considered acceptable. When additional computer resources became available, a periodic sector simulation with exact blade counts was added to the suite of cases.

One-dimensional (1D) nonreflecting inlet and exit conditions were used with the base flow derived from an APNASA solution. These 1D boundary conditions were derived from small perturbation theory to allow the base flow to adjust as the flow inside the computational domain evolves (Chen et al. [18]). The same inlet and exit conditions were used for all three simulations. The history data time extent for each blade row is set by the user within the constraints that it must be consistent with the temporal periodicity as determined by the relative blade counts. Because of blade counts, the longest time history record of the five blade rows is for R2, 1/3 revolution for the single-passage case and 1 revolution for the multipassage case. The influence of this time history record length is discussed further in the simulation convergence section. Detailed setup for the three simulation cases is as follows.

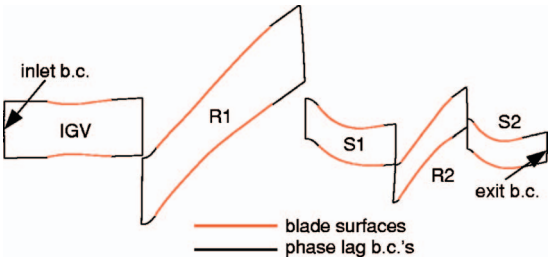

Fig. 2 Case 1: Single-passage phase lag

Case 1: Single-Passage Phase Lag. The standard phase lag modeling is used for this case in which only one blade passage is computed for each blade row. This technique uses the least amount of computer resources and therefore allows smaller grid size per processor to reduce computing time. The phase lag boundary conditions were applied at the circumferential interface between blade passages, as indicated in Fig. 2, and the sliding interface between blade rows.

With approximately 50,000 grid nodes per processor, the simulation used 60 processors. The unsteady frequency for each blade row is a combination of the blade passing frequencies of the two adjacent blade rows.

Case 2: Multiple-Passage Phase Lag. While temporal periodicity arising from adjacent blade rows can be modeled with the single-passage phase lag simulations, the spatial periodicity from upstream blade rows in the same reference frame cannot. A different simulation methodology is proposed here to examine the importance of this effect. Multiple passages are used in each blade row so the circumferential coverage of a particular blade row is always greater than the pitch of the next upstream blade row in the same frame of reference, see Fig. 3. For example, the circumferential extent of the S1 domain is greater than the IGV domain. It was hoped that the increased circumferential extent of the domain would better capture the rotor-rotor and stator-stator interactions while keeping the number of passages computed at a minimum. The additional meshes were created by copying and rotating the original mesh without changing mesh topology or node count. The modified geometry resulted in the computation of 11 passages

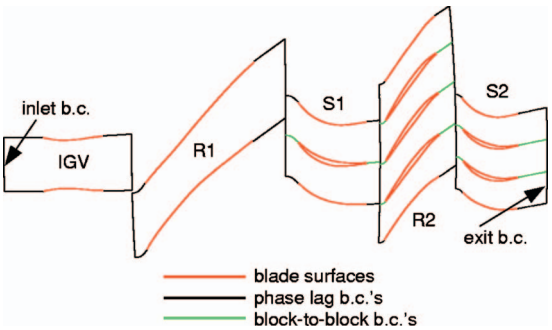

Fig. 3 Case 2: Multipassage phase lag

Downloaded 30 May 2010 to 128.113.26.88. Redistribution subject to ASME license or copyright; see http://www.asme.org/terms/Terms_Use.cfm

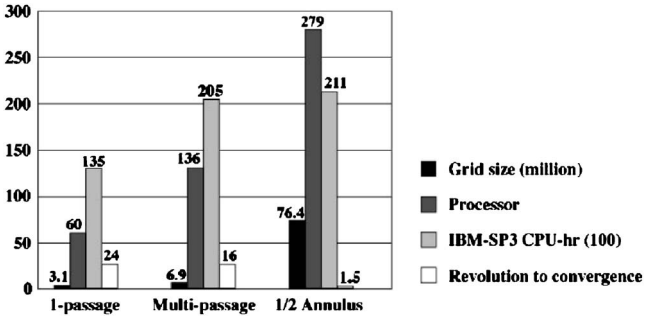

Fig. 4 Computer resources used

with 1-1-2-4-3 blade count.

The multiple passages within each blade row form a group where phase lag boundary conditions can be applied at the outer boundaries. Note that this enforces a spatial periodicity that is inconsistent with the actual spatial periodicity (i.e., two S1 passages are not equal to an IGV passage). Block-to-block interface communication was applied to passage interfaces within the group. For interfaces between blade rows, the sliding interface was used. 136 processors were used with approximately 50,000 grid nodes per processor.

Case 3: Periodic Sector Simulation (Half-Annulus). The blade count (32-26-54-56-74) of this geometry allows for the periodic simulation to compute 1/2 annulus (16-13-27-28-37) of the entire five-blade-row compressor with circumferential periodicity. Dynamic sliding interface is applied between blade rows for time-accurate blade interactions. This simulation used 279 processors with approximately 270,000 nodes per processor. The periodic simulation uses the least modeling assumptions and therefore will be used as the base-line result for comparison in this study.

Results

Computing Resources Required. An IBM SP3 system was used for the POCC simulations. Computer resources for each case are shown in Fig. 4 in terms of CPUs and time. The overall resource requirements can be expressed in total CPU hours used for the simulation (number of processors multiplied by time used). The half-annulus simulation seemed to provide the best return on investment as it produces the highest fidelity (least assumptions) result with only a small increase in total CPU hours. If the number of CPUs is a constraint, the single-passage phase lag simulation provides the most viable means to conduct the unsteady simulation.

Simulation Convergence. Simulation convergence was determined by monitoring adiabatic efficiency from the TURBO performance history file. Adiabatic efficiency is computed at each iteration from mass average properties at the exit of the computational domain. The convergence of adiabatic efficiency is slower than mass flow or PR and thus represents a stringent test of convergence. All three simulations were started from equivalent 3D base flows. Figure 5 shows the convergence history for the three simulations. Convergence of the 1/2 annulus simulation is considered first.

The 1/2 annulus case was considered converged when the instantaneous value of efficiency was ±0.1 point from the mean computed over 1/2 revolution (1300 iterations),

$$\max|\eta(t) - \bar{\eta}| \leq 0.1 \text{ point}$$

where

$$\bar{\eta} = \frac{1}{T}\int_{t}^{t+T} \eta dt \quad \text{T} = 1300 \text{ iterations}$$

(see the callout of Fig. 5 for a graphical illustration of this). The simulation was considered converged at 1.5 rotor revolutions but was run for a total of 2.5 revolutions to be certain. The convection time from inlet to exit of the computational domain is 0.5 revolutions. Pressure wave propagation time is 0.2 revolution downstream and 0.5 revolution upstream going. Therefore, it is reasonable to assume that adequate convection/propagation transit times have occurred for simulation convergence especially since the initial base flow state is close to the converged time-accurate flow state.

The efficiency history of the phase lag simulations must be analyzed differently than that of a periodic simulation because the phase lag computational domain does not encompass a spatially periodic sector. This leads to a "fuzz" in the convergence history (shown in orange line in Fig. 5) that is a result of the limited circumferential domain over which the average properties are determined. Additionally, the phase lag time history has a record length which is set by the user, for example, one revolution or 2600 iterations is the maximum record length needed for the multipassage case. TURBO uses a direct-storage method where the time history is updated by averaging the instantaneous values at the boundary with previously stored values. Once the entire record length is updated, the process starts again at the beginning of the record. This reset to the beginning leads to a step change in efficiency and thus convergence is quantized by time history record length in that the user must wait for the next pass through the time history to ascertain if the efficiency value remains within the tol-

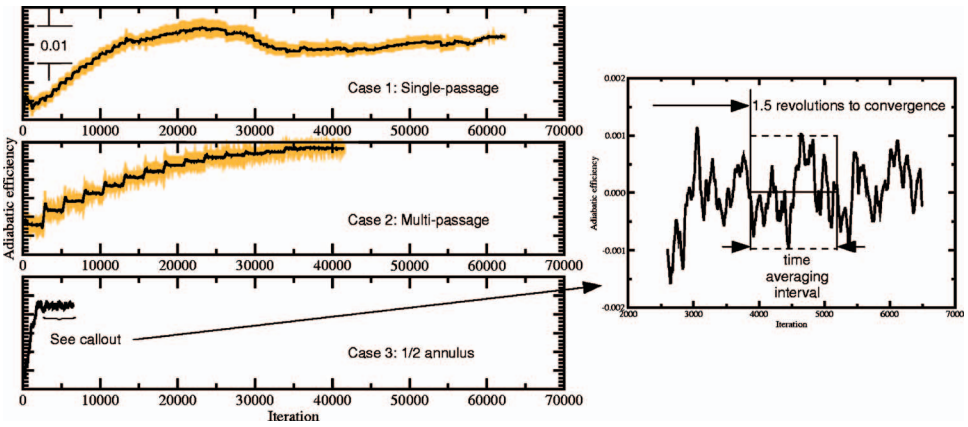

Fig. 5 Adiabatic efficiency convergence history (0.01=1 point)

Downloaded 30 May 2010 to 128.113.26.88. Redistribution subject to ASME license or copyright; see http://www.asme.org/terms/Terms_Use.cfm

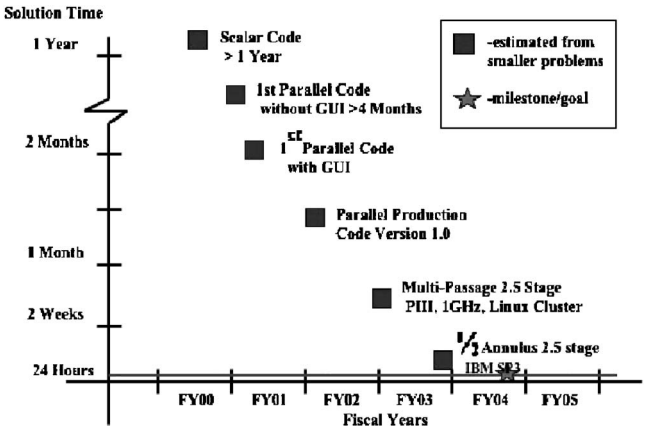

Fig. 6 Time to complete solution for 2.5 stage compressor

erance band and if the trend is stable.

This process is best illustrated by the multipassage case shown in Fig. 5. The orange line is the performance history directly from TURBO. The black line is a running average mean and shows the step changes in efficiency due to the time history record length. The changes in running average efficiency become smaller from revolution to revolution until the change is smaller than 0.1 point for two consecutive revolutions.

The assumption of phase lag periodicity is valid only when the unsteady flow frequencies are multiples of neighboring blade passing frequency. Although it generally reduces computing resources in terms of CPUs and memory, phase lag simulation typically requires longer computing time because of the need to converge the history data in addition to the questions raised above as to the resolution of the spatial periodicity being adequately accounted for in multistage environments.

The single-passage case required 24 revolutions, the multiple-passage case required 16 revolutions, and the periodic case required 1.5 revolutions to converge. Even though more computing resources are needed for the half-annulus periodic simulation, the convergence speed is at least one order of magnitude faster than the phase lag simulations, as shown by Fig. 5.

Simulation Turnaround Time. Hardware improvement is a major factor in realizing the 24 h turnaround. TURBO has been used on computers based on 800 MHz Pentium II processors for Linux clusters to 1.3 GHz Power 4 processors for the IBM P4 supercomputer. The scalable parallel architecture of TURBO is able to utilize these improved hardware capabilities as they become available. In view of the hardware advances, as shown in Fig. 6, the combination of hardware and software improvements has resulted in at least two orders of magnitude reduction in turnaround time over the past five years in addressing problems as large as the POCC case. The computation time is decreasing even as the size of the simulation increases during the evolution of the TURBO code. The move from scalar to parallel code architecture resulted in both reduced solution times and also the ability to compute larger problems. The addition of a GUI greatly simplified the solution setup. Unsteady simulations of the entire compression system using RANS techniques are now within reach of current computing capacity. The demonstration of 24 h turnaround time was a UEET program milestone. The 24 h turnaround is based on timing studies done with the IBM P4.

Aero Performance Estimates. To determine overall performance, the simulations must be appropriately time and spatially averaged. The performance calculation method used for results presented here is explained in detail in the Appendix. The aerodynamic performance estimates from the three simulations are summarized in Table 1.

Table 1 Overall performance results

	Mass flow, (kg/s)	Total Pressure ratio, Pt/Pref	Adiabatic efficiency, 0.01=1 point
Single-passage phase lag	32.24	−0.03	+0.010
Multipassage phase lag	32.23	−0.03	+0.006
1/2 annulus	32.24	Base line	Base line

The simulations converged to identical mass flow but showed a small difference in PR and a 1.0 point maximum difference in adiabatic efficiency. This compressor has a nearly vertical design speed characteristic so mass flow is not a good indicator of operating point. Instead, the APNASA code has been used to generate the design speed line and the efficiency versus PR relationship obtained, Fig. 7. With the 1/2 annulus simulation as a base line, the single- and multipassage simulation efficiencies can be adjusted based on their difference in PR from base line. The adjustment is negligible being only 0.025 point in efficiency for both simulations. This indicates that the differences in efficiency are a result of differences in modeling and not due to a change in operating point.

Discussion

A more detailed analysis of the three simulations is undertaken to establish a possible cause of the differing overall adiabatic efficiencies. Figure 8 shows the axisymmetric average static pressure on the casing for the three TURBO cases to compare pressure rise and mean rotor shock locations. The differences in static pressure rise between the simulations are very small and the rotor shock structure is the same in all. The pressure rise differences between simulations occur gradually with axial distance through the machine and no large change in matching/performance for an individual blade row is noticeable. The effects of the different simulation methodologies appear to be subtle and cumulative through the machine.

The work of He et al. [9] notes that phase lag boundary conditions will not capture the effects of rotor-rotor and stator-stator interactions because these interactions are stationary in the reference frame of a blade row. These interactions lead to circumferential flow field variations and differing passage to passage time average flow fields. He illustrates what he calls "aperiodic efficiency" variations of 0.65 point in polytropic efficiency at the exit

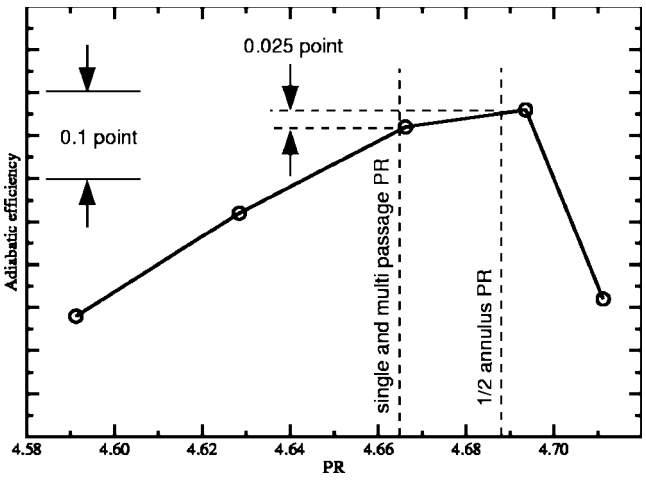

Fig. 7 Sensitivity of efficiency to operating point (PR characteristic from APNASA).

Downloaded 30 May 2010 to 128.113.26.88. Redistribution subject to ASME license or copyright; see http://www.asme.org/terms/Terms_Use.cfm

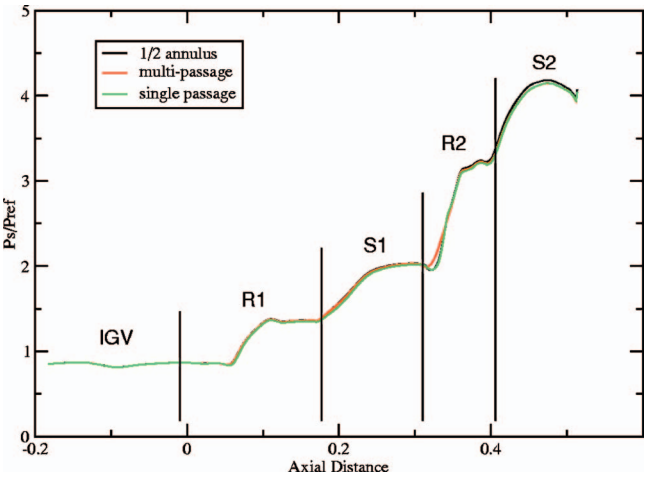

Fig. 8 Axisymmetric static pressure on the POCC casing

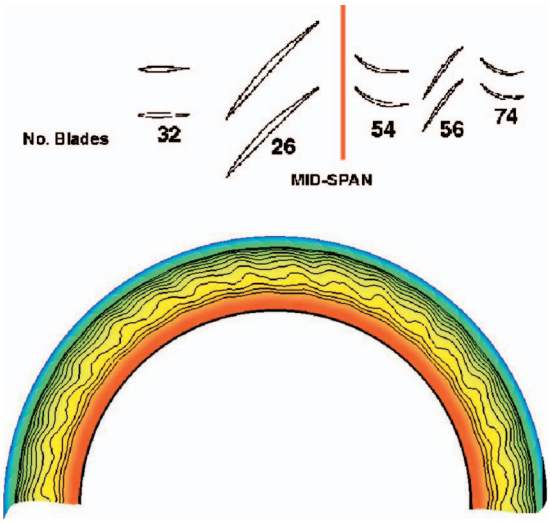

Fig. 9 Adiabatic efficiency at the inlet plane of the stator 1 mesh, 1/2 annulus solution. Contour increments are 1 point in efficiency.

of a rotor row. Similar passage to passage variations in time average flow were observed when studying the POCC flows in detail. For example, Fig. 14 in the Appendix illustrates the passage to passage differences in the R2 shock structure due to the circumferentially nonuniform inlet conditions to the rotor.

It should be noted that the mechanism that creates the circumferential variations described in this work differs from that described by Shang et al. [23]. Their work involved a single-stage machine where the local back pressure effect of the stator caused a change in rotor loss production. Thus, flow into the stator had nonuniform circumferential properties due to the change in rotor loss. This is an "unsteady" effect and differs from rotor-rotor or stator-stator interactions. The degree of blade row coupling will determine the amplitude of the passage to passage variation and thus the impact of the modeling methodology on the overall performance results.

Circumferential Variations of Time Average Properties. The three simulations were completed using different modeling methods but with careful attention to maintain identical grid topology and identical inlet and exit boundary conditions. Time unsteady features are modeled by direct periodicity or phase lag boundary conditions with the more general formulation of phase lag boundary capable of simulating the multiple frequencies present for an embedded blade row. Thus, assuming that the time unsteady character of all simulations is essentially equivalent, the feature that differentiates the simulations from each other is the ability of the modeling assumptions to capture the spatial nonuniformities due to rotor-rotor and stator-stator interactions.

As shown by He et al.[9] and reconfirmed for the results shown here, efficiency and entropy show equivalent trends for circumferential nonuniformities. Because it is more intuitive, efficiency will be used in the following analysis.

Using the time average state variables, the adiabatic efficiency was calculated near the R1/S1 mesh interface in the S1 flow field (absolute frame) for the half-annulus solution (Case 1), see Fig. 9. The figure shows significant variation of adiabatic efficiency with circumferential position. For a more quantitative view, the adiabatic efficiency with the mean value removed is plotted along the 50% span line, Fig. 10(*a*).

In Fig. 10(*a*), the peak to peak amplitude of the efficiency variation is nearly 1.0 point. The primary spatial period seen corresponds to the IGV spacing which would be expected due to the IGV wakes. However, several other longer and shorter spatial periods are also present. Following the ideas of Williams [24], a spatial fast Fourier transform (FFT) is done to better understand circumferential wave number content and contribution, see Fig. 10(*b*).

Fig. 10(*b*), shows the IGV (circumferential wave number 32) to be the primary contributor to the circumferential variation. However, modes corresponding to the S1 first (circumferential wave number 54), second (circumferential wave number 108), and third (circumferential wave number 162) harmonics have peaks within an order of magnitude of the IGV mode. Beat modes of sums and differences (circumferential wave numbers 76 and 86) are also readily apparent which indicates an interaction between the IGV and S1.

The 1/2 annulus simulation encompasses the correct periodic spatial extent and thus results from the simulation will contain all the correct coupling for rotor-rotor and stator-stator interactions. As seen in Figs. 10(*a*) and 10(*b*), the inflow to S1 has a circumferential structure that is relatively complex in terms of the circumferential wave number content due to IGV-S1 interaction. This will also be true of the inflow to R2 (R1/R2 interaction) and S2 (S1/S2 interaction). The spatial nonuniformities will drive subtle but cumulative changes in aeroperformance through the machine.

Cases 1 and 2 using phase lag boundaries will not completely capture the stator/stator or rotor/rotor interactions due to the limited circumferential extent of the computation domain. A representation of 1/2 the compressor annulus, as is shown in Fig. 9, can be recreated from phase lag simulation results by a postprocessing procedure which is based on the phase lag methodology. This was done for the single- and multipassage cases. The adiabatic efficiency profiles from 50% span S1 inlet were extracted and are shown in Figs. 11(*a*) and 12(*a*). It is evident that the circumferential wave number content is substantially different from the 1/2 annulus case.

Spatial FFTs of the single- and multipassage efficiency profiles are shown in Figs. 11(*b*) and 12(*b*). The circumferential wave number content of the single-passage case, Fig. 12(*b*), is almost entirely composed of S1 content and harmonics. The IGV wave number content is more than an order of magnitude lower than the S1 peaks. The circumferential extent of the S1 domain is small (1/54th of the annulus) and is not able to capture the IGV-S1 interaction. This results in a "spatial filtering" of the information that is passed between blade rows. Similarly, information will be filtered from R1 to R2 and from S1 to S2 as well.

A simplified but illustrative way of understanding the spatial filtering is shown schematically in Fig. 13. Blade passages shown in black are the only passages included in the computational domain. The influence of the neighboring passages (shown in red) is

Downloaded 30 May 2010 to 128.113.26.88. Redistribution subject to ASME license or copyright; see http://www.asme.org/terms/Terms_Use.cfm

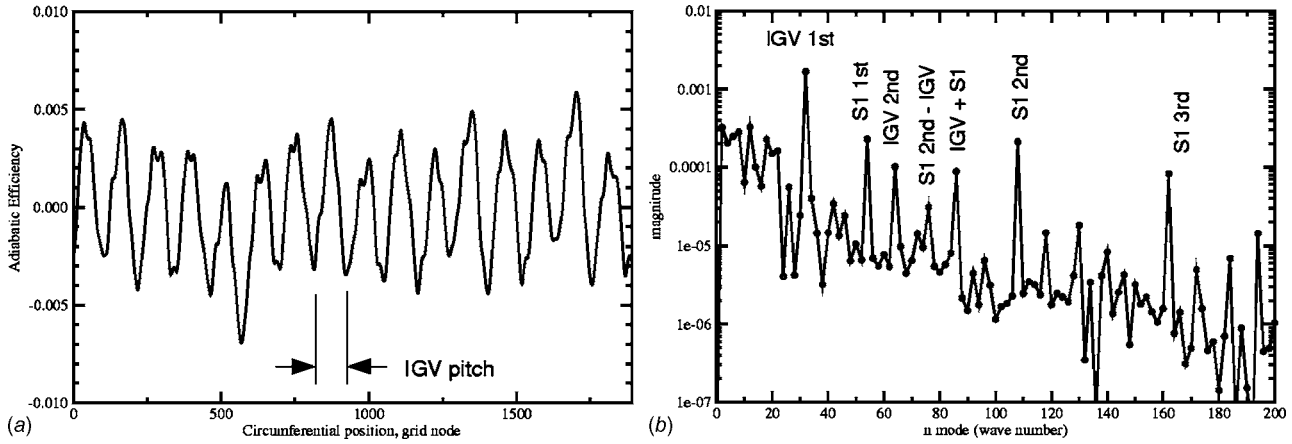

Fig. 10 (*a*) **Circumferential variation of adiabatic efficiency at 50% span, stator 1 inlet plane for the 1/2 annulus solution (average value has been removed).** (*b*) **Modes present in the 1/2 annulus solution.**

modeled with the phase lag boundary condition. For example, the phase lag boundary condition will take the time history at point "A" and apply it at "B" with a phase shift. This is shown by the black curves in the time history plot of Fig. 13. For a two blade row simulation, this is all that is needed to represent both the mean and time varying flow. With the addition of a third (or more) blade row, the flow field at B is phase shifted in time from A but also would require a shift in mean value due to the influence of the IGV or IGV/S1 coupling, as is illustrated by the red curve in the time history of Fig. 13. The shift in mean is due to the "footprint" of the IGV flow field as it was processed by R1 resulting in a time average flow at the R1 exit that has variations in the circumferential direction. The phase lag boundary condition has no mechanism to account for these spatial variations due to the IGV

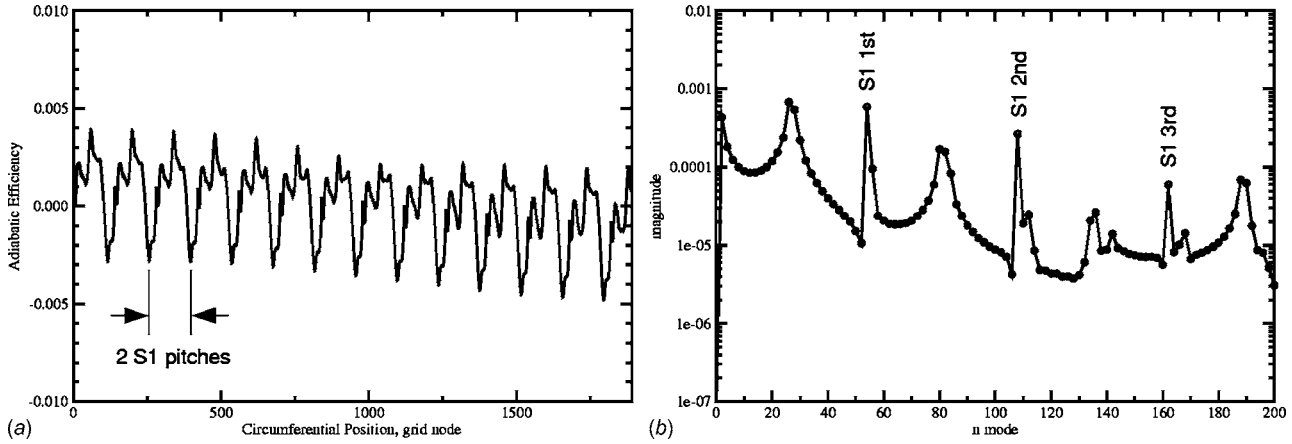

Fig. 11 (*a*) **Adiabatic efficiency at 50% span, stator 1 inlet for the multipassage case.** (*b*) **Modes present in the multipassage case.**

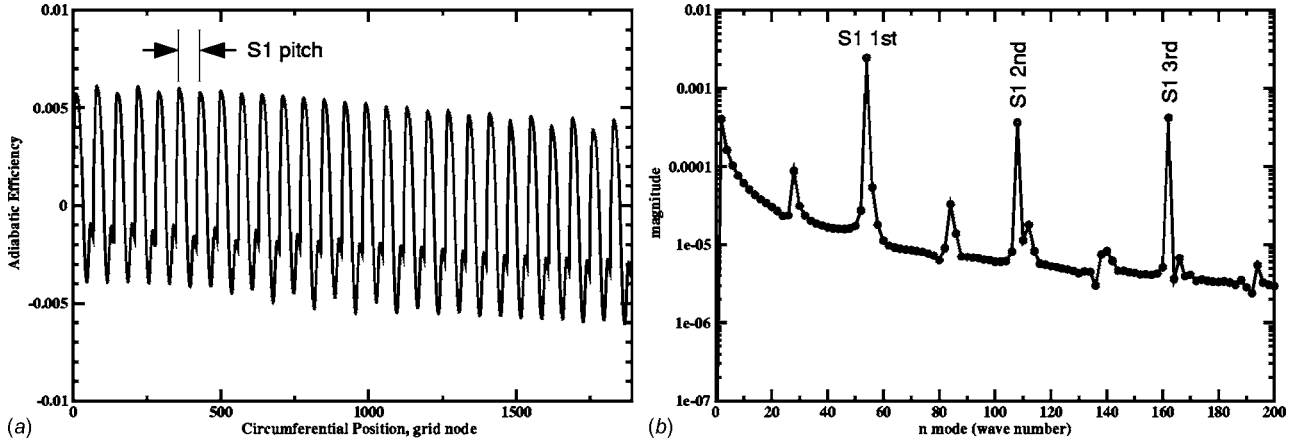

Fig. 12 (*a*) **Adiabatic efficiency at 50% span, stator 1 inlet for the single-passage case.** (*b*) **Modes present in the single passage case.**

Downloaded 30 May 2010 to 128.113.26.88. Redistribution subject to ASME license or copyright; see http://www.asme.org/terms/Terms_Use.cfm

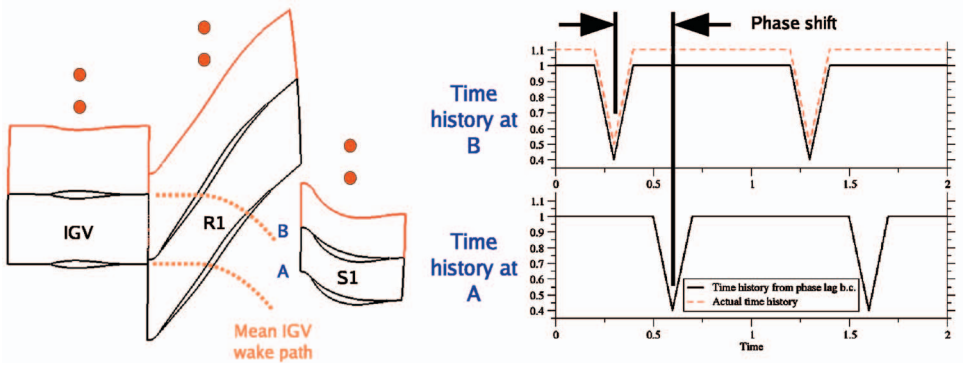

Fig. 13 The phase lag boundary condition behavior for more than two blade rows. To create the time history at "B," the boundary condition will apply a phase shift but not the necessary change in the mean.

since they are steady in time. Also, due to the limited computational domain, there is no mechanism for true IGV/S1 coupling to occur. Therefore, there is an inherent inconsistency between what the flow field "wants" to do and what the boundary condition is imposing on it. A further example of this inconsistency is that the running average mean changes with circumferential position in Figs. 11(*a*) and 12(*a*). Note that the scale is highly magnified so that the total "drift" in the mean is only about 0.002 (0.2 point in efficiency). This drift is not due to solution convergence issues but rather is a consequence of applying phase lag boundary conditions in a flow field that has circumferential nonuniformities.

The intent of the multipassage case (Case 2) was to include a greater circumferential domain to better capture the blade row interactions. As shown by the circumferential wave number content in Fig. 11(*b*), the results are somewhat improved over the single-passage case for the IGV/S1 interaction. There is now some IGV content as indicated by the larger amplitude at circumferential wave number 32, although the peak is smeared over several wave numbers. Note the two S1 pitch periods present in Fig. 11(*a*), indicating that results are strongly influenced by the spatial extent of the domain used for the calculation. The multipassage case has captured some of the IGV-S1 interaction as evidenced by increased IGV wave number content but does not contain the beat wave numbers which would indicate a true coupling of the IGV and S1.

The 1/2 annulus simulation (Case 3) results include the blade row coupling present in the POCC. The single- and multipassage cases are not able to capture the coupling. The greatest difference in circumferential wave number content and thus largest filtering of information occurs between the single passage (Case 1) and 1/2 annulus (Case 3) which is consistent with the largest difference in overall performance. Adding additional circumferential extent to the computational domain, the multipassage case (Case 2) improved the circumferential wave number content somewhat and brought the overall performance estimates into better agreement with the 1/2 annulus case. However, to achieve full coupling, a circumferential domain corresponding to the periodic sector is needed.

Conclusions

A 2.5 stage compressor has been simulated with the time-accurate, multistage, turbomachinery solver TURBO using three different modeling strategies: single passage per blade row with phase lag boundary conditions, multiple passages per blade row with phase lag boundary conditions, and a 1/2 annulus sector. The simulations all used identical meshes and inlet/exit boundary conditions. Major findings are as follows:

1. The 1/2 annulus simulation converged an order of magnitude faster than the simulations which incorporated phase lag boundary conditions. Even though the computer resource requirements are large in terms of the number of processors for the 1/2 annulus simulation, the actual computing time for which the resources are required is small. The 1/2 annulus simulation is then competitive with the phase lag simulations when consideredon a combined resource-time basis.
2. Different modeling strategies employed in the simulations resulted in different overall adiabatic efficiency predicted with the greatest difference of 1.0 point between the single-passage case and the 1/2 annulus simulation.
3. The 1/2 annulus simulation shows substantial circumferential variation of thermodynamic properties at the S1 inlet plane due to interactions of blade rows in the same frame of reference. This will be true of R2 and S2 as well. Simulations using the phase lag boundary conditions were not able to completely capture this effect even with multiple passages per blade row. The consequence of this information filtering is a subtle and cumulative change in performance through the machine as shown by the differences in overall performance.

Acknowledgment

The authors would like to thank Tony Strazisar and John Adamczyk for many useful comments and discussions, Chuck Niggley of NAS for computing resources, and the Naval Oceanographic Major Shared Resource Center for computing resources. Thanks to Mark Turner for assistance with axisymmetric averaging tools for general meshes with acknowledgement to Lyle Dailey as the primary tool developer. Support for one of the authors J. C. is from NASA Contract No. NAS3-00181, Eric McFarland, Contract Monitor. His support is gratefully acknowledged. This work was supported by the NASA UEET Program.

Nomenclature

GUI = graphical user interface
IGV = inlet guide vane
POCC = proof-of-concept compressor
PR = pressure ratio (Fig. 1)
R1, R2 = rotor 1, rotor 2
S1, S2 = stator 1, stator 2
UEET = ultraefficient engine technology
Utip = tangential tip speed (Fig. 1)
Wc = corrected weight flow (Fig. 1)
η = adiabatic efficiency

Appendix: Computation of Losses in Unsteady Flows

The only accurate measure of loss in an unsteady flow is entropy (Denton and Cumpsty [25]). However, entropy cannot be measured directly in an experiment but is instead inferred by mea-

Downloaded 30 May 2010 to 128.113.26.88. Redistribution subject to ASME license or copyright; see http://www.asme.org/terms/Terms_Use.cfm

surements of total pressure and total temperature. In multistage compressors, these interstage measurements of total pressure and total temperature are typically done using stator leading edge instrumentation. Overall performance might be determined by rake measurements downstream of the last blade row. The stator leading edge instrumentation is in an especially unsteady flow field and is thought to, at best, measure an approximation of the time average total pressure and total temperature (Kronauer and Grant [26]).

From a numerical simulation, there are several possible methods of computing loss or efficiency, although not all methods are consistent with what the experimental instrumentation is believed to be measuring. TURBO has a time averaging routine, which runs concurrently with the flow solver and averages the code's state variables, $(\rho, \rho u, \rho v, \rho w, \rho e)$. This is convenient for the user since time averaging is no longer a postprocessing step and file storage requirements are minimized. However, total pressure and total temperature (and thus adiabatic efficiency) are nonlinear functions of the state variables and thus

$$\eta(\bar{P}_T, \bar{T}_T) \neq \eta(\bar{\rho}, \overline{\rho u}, \overline{\rho v}, \overline{\rho w}, \overline{\rho e})$$

for an unsteady flow. However, estimating the efficiency based on time average state variables may be satisfactory if the efficiency calculation locations are chosen judiciously in areas of relatively low unsteadiness.

The time averaging routine of TURBO was modified to output both time averages of the state variables but also time averages of pressure, total pressure, total temperature, mass-weighted total temperature, and mass-weighted entropy. The multipassage simulation (Case 2) was time averaged with the modified routine.

Using the modified time average results, adiabatic efficiency was calculated by three different methods: (1) using total temperature and total pressure calculated from the time average state variables, (2) using time average total pressure and total temperature directly, and (3) using the time average mass-weighted total temperature and entropy to calculate total pressure and then adiabatic efficiency. Time average total pressure and total temperature are used so that the analysis is consistent with what is measured experimentally. Method 3 represents a thermodynamically rigorous but experimentally unrealizable method to determine efficiency. It is included for completeness.

The difference in the efficiency values is shown on a 50% span surface for S1, R2, and S2 in Fig. 14 for method 2 versus 1 and Fig. 15 for method 3 versus 1. The base line is the efficiency calculated using time average state variables (method 1). For example, a contour value of 0.005 in Fig. 13 would indicate that calculating efficiency with time average Pt and Tt results in a value 0.5 point higher than using state variables.

The rating plane for the compressor is the S2 exit plane. The maximum error at that axial location is less than 0.1 point. Therefore, any of the calculation methods would give an estimate of overall performance to within engineering accuracy.

Additionally, the largest errors occur for all blade rows in their central spans where narrow wakes and shocks are present. In the endwalls, the relative unsteadiness is much lower because, for instance, the rotor tip clearance flow and the rotor wake fill nearly the entire blade pitch and are seen as a quasisteady flow by the following blade row.

For the inlet region of embedded S1, the error associated with calculating efficiency based on time average state variables is 0.2–0.4 point depending on circumferential location. Errors downstream of S1 exceed 1 point in efficiency due to the presence of the bow shock from the transonic R2. Note that the S1 exit performance could be determined with less error by using the inlet plane of the R2 solution where the bow shock is essentially steady in the rotor frame of reference.

In summary, relative comparisons of efficiency at the same spatial location between the three simulations are valid. Comparison of absolute values is only valid if the errors at that spatial location are low. The entrance to S1 and the rating plane downstream of S2 are examples of locations where the time average state variables can be used to calculated performance to within engineering accuracy. With the above limitations noted, the analysis contained in this paper is based on the time average state variables.

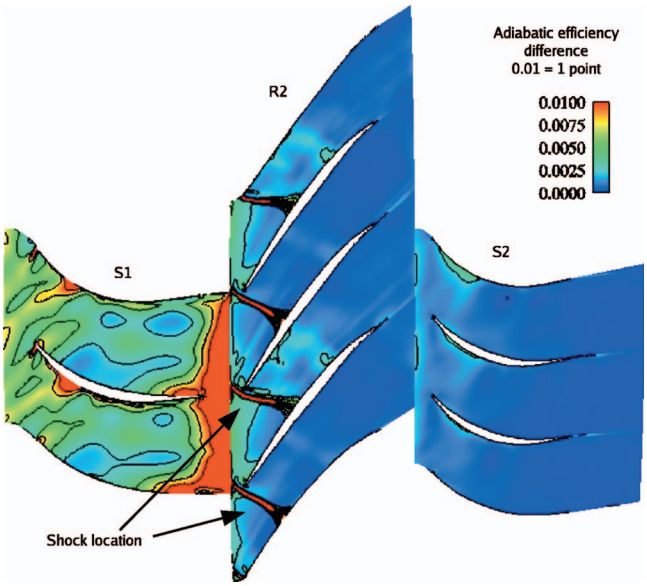

Fig. 14 Difference in adiabatic efficiency from a calculation using time average total temperature and total pressure and a calculation using time average state variables

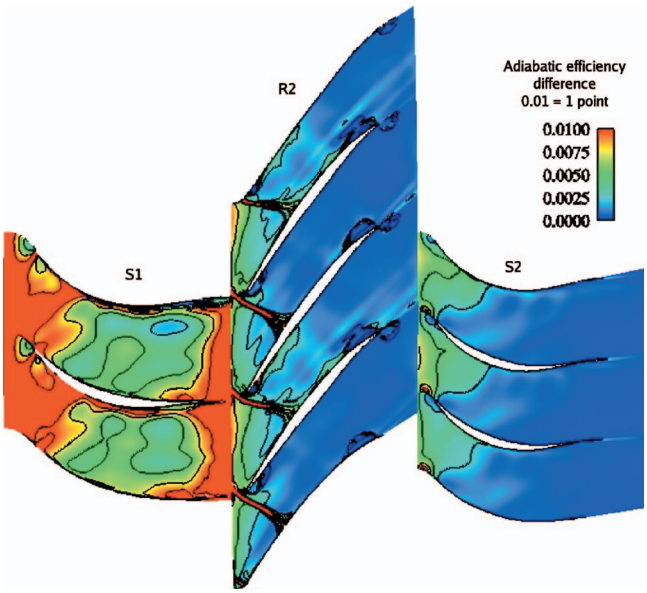

Fig. 15 Difference in adiabatic efficiency from a calculation using mass weighted, time average total temperature, and total pressure from mass-weighted entropy and a calculation using time average state variables

References

[1] Rai, M. M., 1986, "Navier–Stokes Simulations of Rotor/Stator Interactions Using Patched and Overset Grids," J. Propul. Power, **3**(5), pp. 387–396.

[2] Janus, J. M., and Whitfield, D. L., 1989, "A Simple Time-Accurate Turbomachinery Algorithm With Numerical Solutions of an Uneven Blade Count Configuration," Report No. AIAA-89-0206.

[3] Giles, M. B., 1988, "Stator/Rotor Interaction in a Transonic Turbine," Report No. AIAA-88-3093.

Downloaded 30 May 2010 to 128.113.26.88. Redistribution subject to ASME license or copyright; see http://www.asme.org/terms/Terms_Use.cfm

[4] Lewis, J. P., Delaney, R. A., and Hall, E. J., 1989, "Numerical Prediction of Turbine Vane-Blade Aerodynamic Interaction," ASME J. Turbomach., **111**, pp. 387–396.
[5] Chen, J. P., and Whitfield, D. L., 1993, "Navier–Stokes Calculations for the Unsteady Flowfield of Turbomachinery," Report No. AIAA-93-0676.
[6] Erdos, J. I., Alzner, E., and McNally, W., 1997, "Numerical Solution of Periodic Transonic Flow Through a Fan Stage," AIAA J., **15**(11), pp. 1559–1568.
[7] Chen, J. P., and Barter, J. W., 1998, "Comparison of Time-Accurate Calculations for the Unsteady Interaction in Turbomachinery Stage," Report No. AIAA-98-3292.
[8] Wang, X., and Chen, J. P., 2004, "A Post-Processor to Render Turbomachinery Simulations," Report No. AIAA-2004-615.
[9] He, L., Chen, T., Wells, R. G., Li, Y. S., and Ning, W., 2002, "Analysis of Rotor-Rotor and Stator-Stator Interferences in Multi-Stage Turbomachines," ASME J. Turbomach., **124**, pp. 564–571.
[10] Whitfield, D. L., Janus, J. M., and Simpson, L. B., 1988, "Implicit Finite Volume High Resolution Wave-Split Scheme for Solving the Unsteady Three-Dimensional Euler and Navier-Stokes Equations on Stationary or Dynamic Grids," Report No. MSSU-EIRS-ASE-88-2.
[11] Roe, P. L., 1981, "Approximate Riemann Solvers, Parameter Vectors, and Difference Schemes," J. Comput. Phys., **43**, pp. 357–372.
[12] Osher, S., and Chakravarthy, S. R., 1984, "Very High Order Accurate TVD Schemes," ICASE Report No. 84-44.
[13] Steger, J. L., and Warming, R. F., 1981, "Flux Vector Splitting of the Inviscid Gasdynamic Equations With Application to Finite-Difference Methods," J. Comput. Phys., **40**, pp. 263–293.
[14] Zhu, J., and Shih, T.-H., 1997, "CMOTT Turbulence Module for NPARC," NASA Report No. CR 204143.
[15] Chen, J. P., and Briley, W. R., 2001, "A Parallel Flow Solver for Unsteady Multiple Bladerow Turbomachinery Simulations," Report No. ASME-2001-GT-0348.
[16] Remotigue, M. G., 1999, "Structured Grid Technology to Enable Flow Simulation in an Integrated System Environment," Ph.D. Mississippi State University.
[17] Adamczyk, J. J., 1984, "Model Equation for Simulating Flow in Multistage Turbomachinery," Report No. ASME 85-GT-226.
[18] Chen, J. P., Celestina, M., and Adamczyk, J. J., 1994, "A New Procedure for Simulating Unsteady Flows Through Turbomachinery Blade Passages," Report No. ASME-94-GT-151.
[19] Larosiliere, L., Wood, J. R., Hathaway, M. D., Medd, A. J., and Dang, T. Q., 2002, "Aerodynamic Design Study of Advanced Multistage Axial Compressor," NASA Report No. TP-2002-211568.
[20] Beach, T. A., and Hoffman, G., 1992, "IGB Grid: User's Manual (A Turbomachinery Grid Generation Code)," NASA Contractor Report No. 189104.
[21] Van Zante, D. E., Strazisar, A. J., Wood, J. R., Hathaway, M. D., and Okiishi, T. H., 2000, "Recommendations for Achieving Accurate Numerical Simulation of Tip Clearance Flows in Transonic Compressor Rotors," J. Turbomach., **122**, pp. 733–742.
[22] Van Zante, D. E., To, W.-M., and Chen, J.-P., 2002, "Blade Row Interaction Effects on the Performance of a Moderately Loaded NASA Transonic Compressor Stage," Report No. ASME-GT2002-30575.
[23] Shang, T., Epstein, A. H., Giles, M. B., and Sehra, A. K., 1993, "Blade Row Interaction Effects on Compressor Measurements," J. Propul. Power, **9**(4), pp. 569–578.
[24] Williams, M. C., 1998, "Inter and Intrablade Row Laser Velocimetry Studies of Gas Turbine Compressor Flows," ASME J. Turbomach., **110**, pp. 369–376.
[25] Denton, J. D., and Cumpsty, N. A., 1987, "Loss Mechanisms in Turbomachines," IMechE Paper No. C260/87.
[26] Kronauer, R., and Grant, H., 1954, "Pressure Probe Response in Fluctuating Flow," *Proceedings of the Second US National Congress of Applied Mechanics*, Ann Arbor, MI, Jun.

Downloaded 30 May 2010 to 128.113.26.88. Redistribution subject to ASME license or copyright; see http://www.asme.org/terms/Terms_Use.cfm

Michele Marconcini
e-mail: michele.marconcini@arnone.de.unifi.it

Filippo Rubechini

Andrea Arnone

"Sergio Stecco" Department of Energy Engineering,
University of Florence,
via di Santa Marta 3,
50139 Firenze, Italy

Seiichi Ibaraki
Nagasaki R&D Center,
Mitsubishi Heavy Industries, Ltd.,
Nagasaki 851-0392, Japan

Numerical Investigation of a Transonic Centrifugal Compressor

A three-dimensional Navier-Stokes solver is used to investigate the flow field of a high-pressure ratio centrifugal compressor for turbocharger applications. Such a compressor consists of a double-splitter impeller followed by a vaned diffuser. The inlet flow to the open shrouded impeller is transonic, thus giving rise to interactions between shock waves and boundary layers and between shock waves and tip leakage vortices. These interactions generate complex flow structures which are convected and distorted through the impeller blades. Detailed laser Doppler velocimetry flow measurements are available at various cross sections inside the impeller blades highlighting the presence of low-velocity flow regions near the shroud. Particular attention is focused on understanding the physical mechanisms which govern the flow phenomena in the near shroud region. To this end numerical investigations are performed using different tip clearance modelizations and various turbulence models, and their impact on the computed flow field is discussed.
[DOI: 10.1115/1.2752186]

Introduction

In recent years the growing necessity of increasing specific output power of turbochargers and turboshaft engines has encouraged the design of high-pressure ratio, large capacity centrifugal compressors. Two-stage compressors, which can achieve the high-pressure ratio required, are not suitable for these applications due to volume and weight increases. In order to accommodate a large mass flow, increased inlet diameters are required and it is probable that supersonic velocity could be obtained near the shroud. The common design trend is thus to use single-stage highly loaded compressors with a supersonic region at the impeller inlet.

Hah and Krain [1] performed experimental and numerical analyses of a 4.7:1 pressure ratio backswept unshrouded impeller in order to study the development of secondary flows, vortex motion, and tip clearance flow effects on these flow structures. They found that the relative motion between the rotating impeller and the stationary shroud as well as the resulting tip leakage flow greatly influenced the swirling flow and the vortex motion inside the impeller. As a consequence they emphasized that tip clearance effects should be properly modeled when seeking a realistic flow prediction.

More recently, Higashimori et al. [2] investigated the high transonic flow of a centrifugal compressor double-splitter impeller with pressure ratio 11:1 and relative Mach number of about 1.6 at inlet, for aeronautical application. They conducted laser doppler velocimetry (LDV) measurements as well as computational fluid dynamics (CFD) calculation with the Dawes's BTOB3D code [3], finding that CFD was capable of estimating flow distribution with good accuracy in most of the flow range. Discrepancies were found in detecting a reverse flow region near the shroud due to the interaction of the leakage flow and the shock wave. Moreover their numerical results tended to overestimate the extension of a low-energy region near the shroud located in the suction side passage after the first splitter leading edge.

Ibaraki et al. [4,5] conducted flow measurements using LDV in a high-load and large capacity double-splitter transonic impeller followed by a vaned diffuser for turbocharger applications. They used Dawes's code with the Baldwin-Lomax [6] turbulence model for CFD computations and presented the complex three-dimensional flow field using vortex structures visualizations. From the comparison of measured and computed relative velocity distributions at various stations inside the impeller vanes, they showed how CFD results were in qualitative and quantitative agreement with experiment, except for location near the shroud where a low-energy region was overestimated.

The current study is aimed at analyzing the three-dimensional flow field of the transonic unshrouded impeller previously investigated by Ibaraki et al. [4,5]. The numerical analysis was carried out including both the impeller and the diffuser, because of its influence on the impeller operating condition. The goal was to closely match the operating point near the design flow rate, where detailed measurements are available for the impeller. Following the hints given in Ref. [5], attention was focused on the flow field structure in the near shroud region, which resulted in lesser agreement with experimental findings. Here an attempt is made to understand the physical mechanisms which govern the flow phenomena in this region, and clearance treatment and turbulence modeling are the issues considered.

Compressor Stage Description

The compressor stage is composed of a centrifugal impeller with seven blades and double splitters with seven and 14 blades, respectively (Fig. 1), and a vaned diffuser with 19 blades. The impeller is unshrouded with a tip clearance varying from 0.65 mm at the blade inlet to 1 mm at the exit. The diffuser vanes are of double-circular-arc type and constant height equal to the impeller exit width. A sketch of the compressor test rig with the transonic impeller, the vaned diffuser followed by a volute is shown in Fig. 2, while the main geometrical parameters are listed in Table 1.

Detailed LDV measurements for the transonic impeller are available, and the experimental procedure is described by Ibaraki et al.[4,5]. Figure 3 shows the meridional view of the impeller and the LDV measurement positions. The design rotational speed is 24,700 rpm, and pressure ratio is 3.9:1 with a volume flow, referred to the inlet conditions, of 6.8 m^3/s, leading to an inlet Mach number of about 1.3.

Computational Procedure

The multirow, multiblock release of the TRAF code [7] was used in the present work. The unsteady, three-dimensional, Reynolds averaged Navier-Stokes equations are written in conservative form in a curvilinear, body-fitted coordinate system and solved for density, absolute momentum components, and total energy.

Contributed by the International Gas Turbine Institute of ASME for publication in the JOURNAL OF TURBOMACHINERY. Manuscript received November 2, 2006; final manuscript received November 6, 2006; published online January 14, 2008. Review conducted by David Wisler. Paper presented at the ASME Turbo Expo 2006: Land, Sea and Air (GT2006), Barcelona, Spain, May 8–11, 2006, Paper No. GT2006-90098.

 Copyright © 2008 by ASME

Downloaded 30 May 2010 to 128.113.26.88. Redistribution subject to ASME license or copyright; see http://www.asme.org/terms/Terms_Use.cfm

Fig. 1 The transonic impeller

The code has recently been used for the design and optimization of transonic centrifugal compressor impellers [8,9] and for the analysis of components interaction in centrifugal compressor stages [10,11].

Numerical Scheme. The space discretization is based on a cell-centered finite volume scheme. Both scalar and matrix artificial dissipation models introduced by Jameson et al. [12] and Swanson and Turkel [13] are available in the code. In order to minimize the amount of artificial diffusion inside the shear layers an eigenvalue scaling was implemented to weigh these terms. The system of governing equations is advanced in time using an explicit four-stage Runge-Kutta scheme.

Residual smoothing, local time stepping, and multigridding are employed to speed up convergence to the steady-state solution. The time step is locally computed on the basis of the maximum allowable Courant number, typically 5.0, and accounts for both convective and diffusive limitations [14].

Inflow and outflow boundaries are treated according to the theory of characteristics: the flow angles, total pressure, and temperature are imposed at the subsonic first row inlet, while the outgoing Riemann invariant is taken from the interior. At the subsonic last row outlet, static pressure is prescribed, and the density and the momentum components are extrapolated. The link between rows is handled by means of mixing planes. Consecutive rows have a common interface plane and the match is provided through appropriate calculation of phantom cell values, keeping the spanwise distribution while averaging in the blade-to-blade direction.

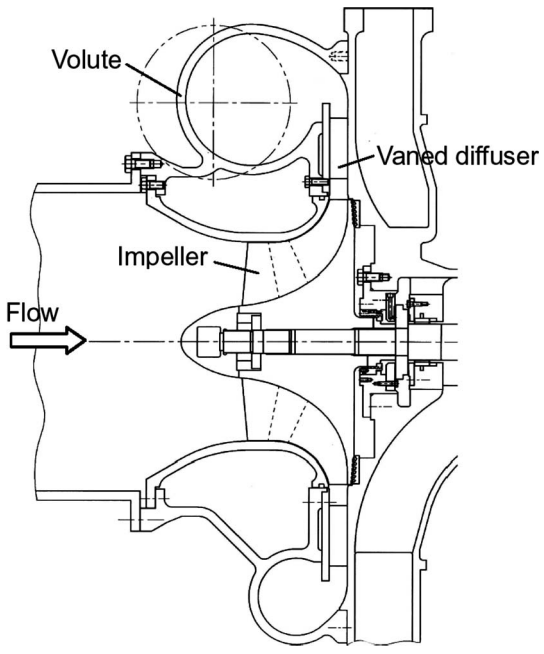

Fig. 2 Cross section of compressor stage

Table 1 Compressor stage geometrical data

Impeller	
Blade number	7+7+14 (double splitter)
Inlet hub diameter	94.6 mm
Inlet tip diameter	261.3 mm
Inlet tip angle	29.8 deg (from tangential)
Exit diameter	373 mm
Exit backsweep angle	25 deg
Diffuser	
Blade number	19
Inlet diameter	429 mm
Inlet angle	21 deg (from tangential)
Exit diameter	590.1 mm

Computational Grids. The impeller computational domain was divided into four mesh blocks, one for each of the four semivanes included between two main blades. Each of them was discretized using an H-type elliptic grid with $149 \times 41 \times 57$ points in the streamwise, pitchwise, and spanwise directions, respectively. In this way, the total number of mesh cells between two main blades in the pitchwise direction is 160, and the total number of grid points for the impeller is 1,392,852. The value of y^+ for the first grid point above the wall, was between 1.0 and 4.0 for all the blades. For the diffuser vane, a $105 \times 49 \times 57$ single-block H-type grid was adopted.

A three-dimensional view of the impeller grid is shown in Fig. 4(*a*). The impeller tip clearance was discretized with 16 cells and the clearance region was handled with two different models. The baseline tip gridding model is that proposed by [15]. It uses a periodic boundary across a nongridded region over the top of the blade tip to treat the clearance flow as an orifice flow with no

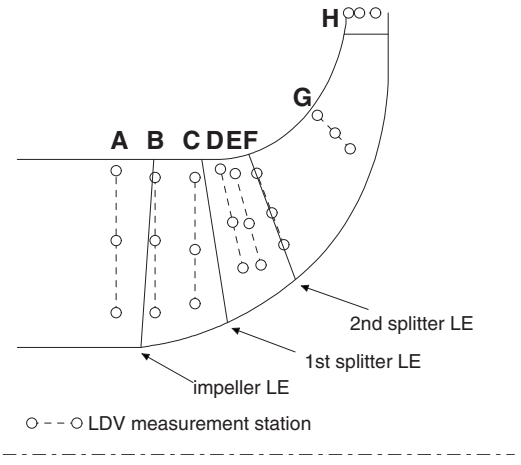

Fig. 3 Meridional section of the impeller with measurement sections

Downloaded 30 May 2010 to 128.113.26.88. Redistribution subject to ASME license or copyright; see http://www.asme.org/terms/Terms_Use.cfm

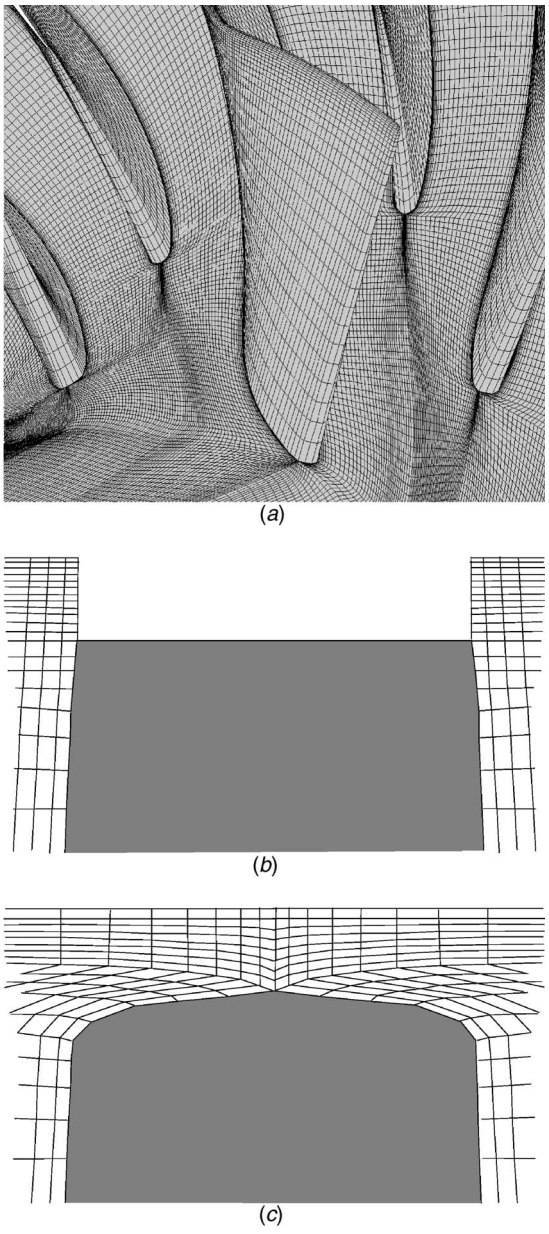

Fig. 4 Three-dimensional view of the impeller computational mesh and schematics of mesh in the tip region: (*a*) impeller grid (blade-to-blade at mid-span); (*b*) modeled tip gap; and (*c*) gridded tip gap

change in mass, momentum, and energy across the blade tip. The clearance region is obtained by extending the grid from the blade tip to the shroud while maintaining the tangential thickness of the blade (referred as "modeled tip gap" in Fig. 4(*b*)). In the second tip gridding model, the blade is pinched (e.g., Refs. [16,17]), and the tip gap is fully gridded (referred as "gridded tip gap" in Fig. 4(*c*)). Following the suggestions of Van Zante et al. [18], the two models employ the same spanwise spacing in the clearance gap, and pitchwise and chordwise grid spacings are unchanged.

Turbulence Modeling. Three turbulence models are used in the present work, namely the algebraic Baldwin-Lomax (BL) model [6], the one-equation Spalart-Allmaras (SA) model [19], and the two-equation Wilcox's k-ω model [20].

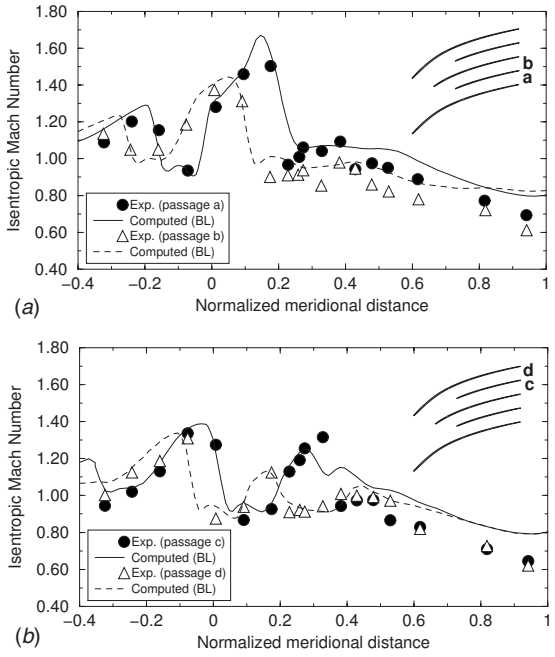

Fig. 5 Streamwise distributions of isentropic Mach number at the shroud: (*a*); and (*b*)

The rotation/streamline curvature correction for the SA model developed by Spalart and Shur [21] and Shur et al. [22] was used (SARC). The SARC model introduces a heuristic function f_{r1} that multiplies the model's production term $c_{b1}\tilde{S}\tilde{\nu}$. This function includes three constants whose default values are $c_{r1}=1$, $c_{r2}=12$, and $c_{r3}=1$. In the current study, we use the value of 0.6 for the model constant c_{r3} (cf. Refs. [21,23]).

For the two-equation model, the Durbin [24] realizability correction is used to compute the eddy viscosity value. The freestream value of the specific dissipation rate ω is determined by using the following estimate proposed by Menter [25]: $\omega_\infty = 10 \cdot V_\infty / L$. The freestream eddy viscosity is set to $\mu_{t\infty}=10^{-2} \cdot \mu_l$, and the turbulent kinetic energy is calculated from the definition of the eddy viscosity $k_\infty = \mu_{t\infty}\omega_\infty$. At the solid walls, the value of k is set to zero and the value of ω is computed using Wilcox's roughness model for smooth surfaces.

Flow Analysis and Discussion

Measured pitchwise relative velocity distributions are available near the shroud (85–90% blade span), near midspan, and near the hub (20–30% blade span) between blade pitches in the respective cross sections A–H (see Fig. 3).

Following the approach suggested by [26], the comparison between calculations and experiments was carried out using the mass flow rate nondimensionalized with the choke mass flow rate as equivalence criterion. In a transonic compressor rotor this criterion is applied to ensure that the same operating condition is matched by both the experiments and the computations.

Figure 5 shows the streamwise distribution of isentropic Mach number (M_{is}) at the shroud along the midpitch of the four flow passages. The meridional distance has its zero on the full blade leading edge and it is normalized with the full blade length. The static temperature in the definition of M_{is} is computed using the static pressure and the isentropic relation with the inlet total quantities as reference status. The comparison with experimental data shows that the shock wave locations as well as the shape of the distributions are nearly matched.

Downloaded 30 May 2010 to 128.113.26.88. Redistribution subject to ASME license or copyright; see http://www.asme.org/terms/Terms_Use.cfm

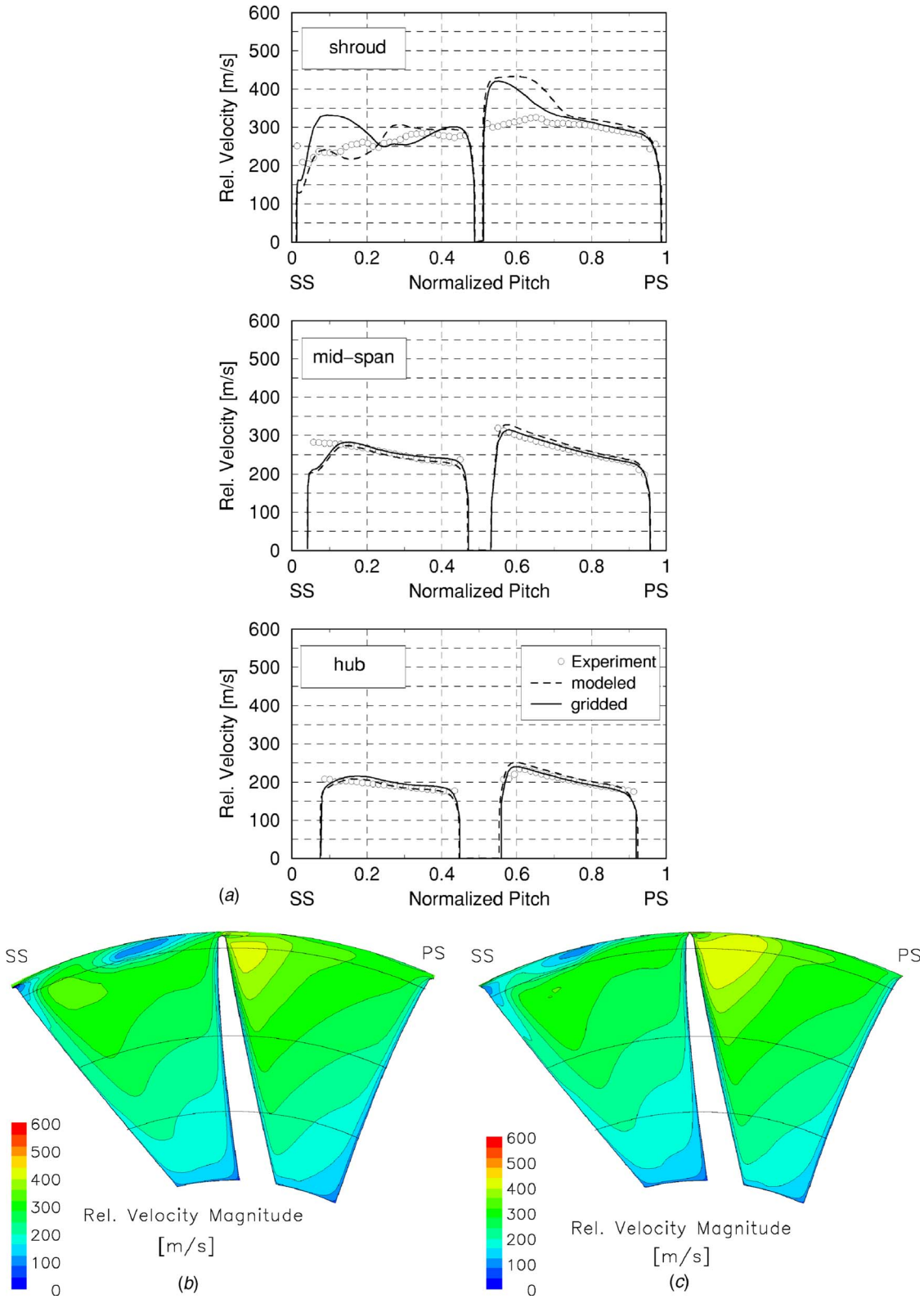

Fig. 6 Pitchwise relative velocity distribution and contours in section D (BL model): (*a*) section D; (*b*) gridded tip gap; and (*c*) modeled tip gap

Clearance Model Influence. A first set of computations was performed using the BL turbulence model in order to determine the clearance model to adopt. Two cross sections representative of the clearance model impact on the computed flow field were selected, namely sections D and G in Fig. 3. Pitchwise relative velocity distributions at section D are reported in Fig. 6(*a*) and relative velocity contours obtained with the two clearance models in Figs. 6(*b*) and 6(*c*). As expected the clearance model mostly influences the near shroud distributions: the low-velocity region generated by the interaction between the full blade tip leakage

Downloaded 30 May 2010 to 128.113.26.88. Redistribution subject to ASME license or copyright; see http://www.asme.org/terms/Terms_Use.cfm

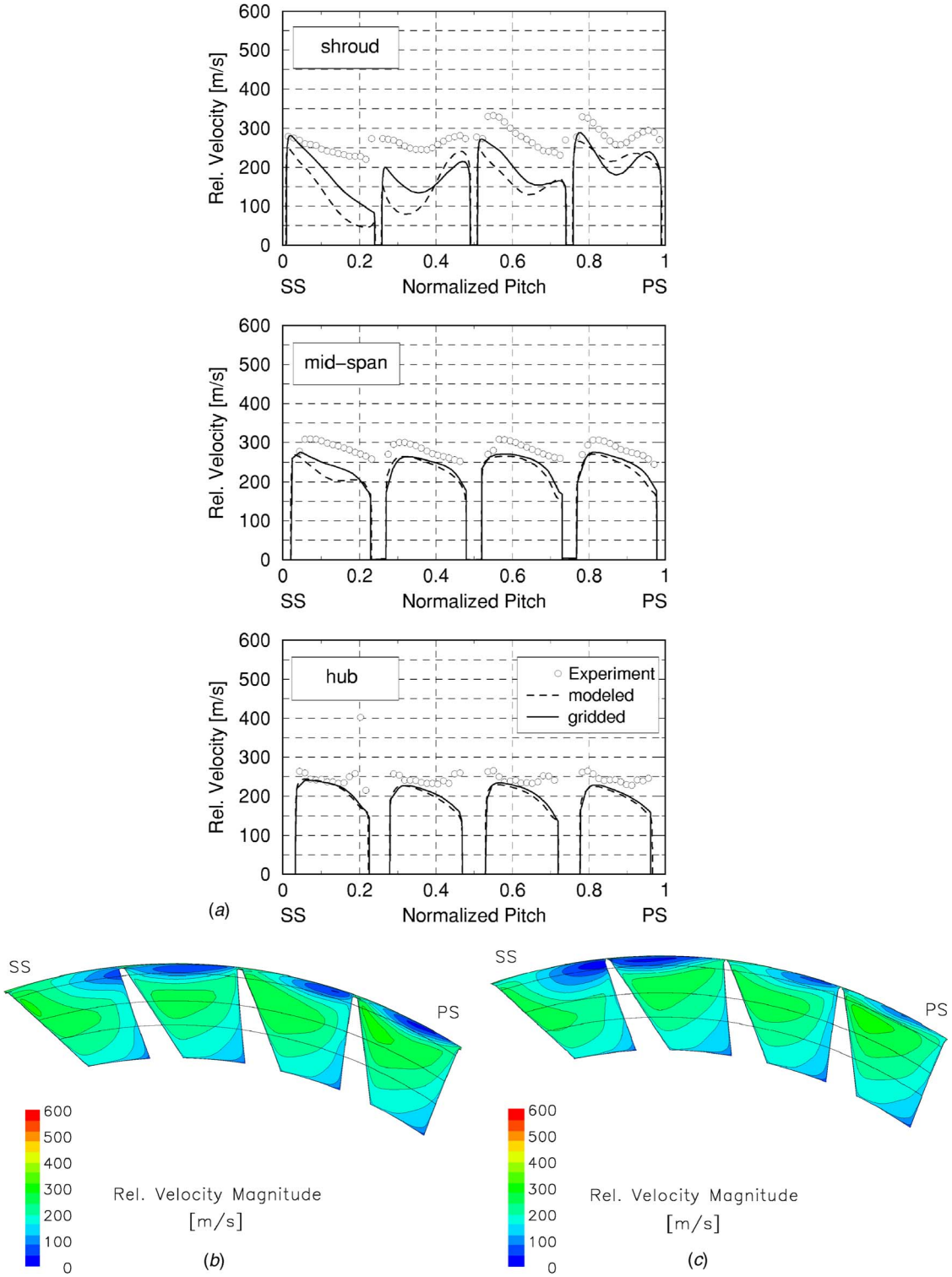

Fig. 7 Pitchwise relative velocity distribution and contours in section G (BL model): (*a*) section G; (*b*) gridded tip gap; and (*c*) modeled tip gap

vortex and the shock wave is more extended in the pitchwise direction and positioned closer to the splitter (PS) for the gridded tip gap. The high-velocity region near the shroud of the splitter (SS), due to the root of the shock wave, is more extended for the modeled than for the gridded tip gap.

In cross section G (Figs. 7(*a*)–7(*c*)) low-velocity regions are present near the shroud in all the four passages formed by the first and the second splitter blades. Velocity defects detected with the modeled gap seem to be more pronounced in the first three passages starting from the full blade SS, whereas the shape is less influenced by the clearance model. The same behavior is observable in the first passage at midspan where the low-velocity region extends over a larger portion of the span (see Fig. 7(*c*)).

In light of the observed differences, and since in other cross sections these differences are also smaller, it may be concluded that no major arguments arise in favor of one of the two clearance

Downloaded 30 May 2010 to 128.113.26.88. Redistribution subject to ASME license or copyright; see http://www.asme.org/terms/Terms_Use.cfm

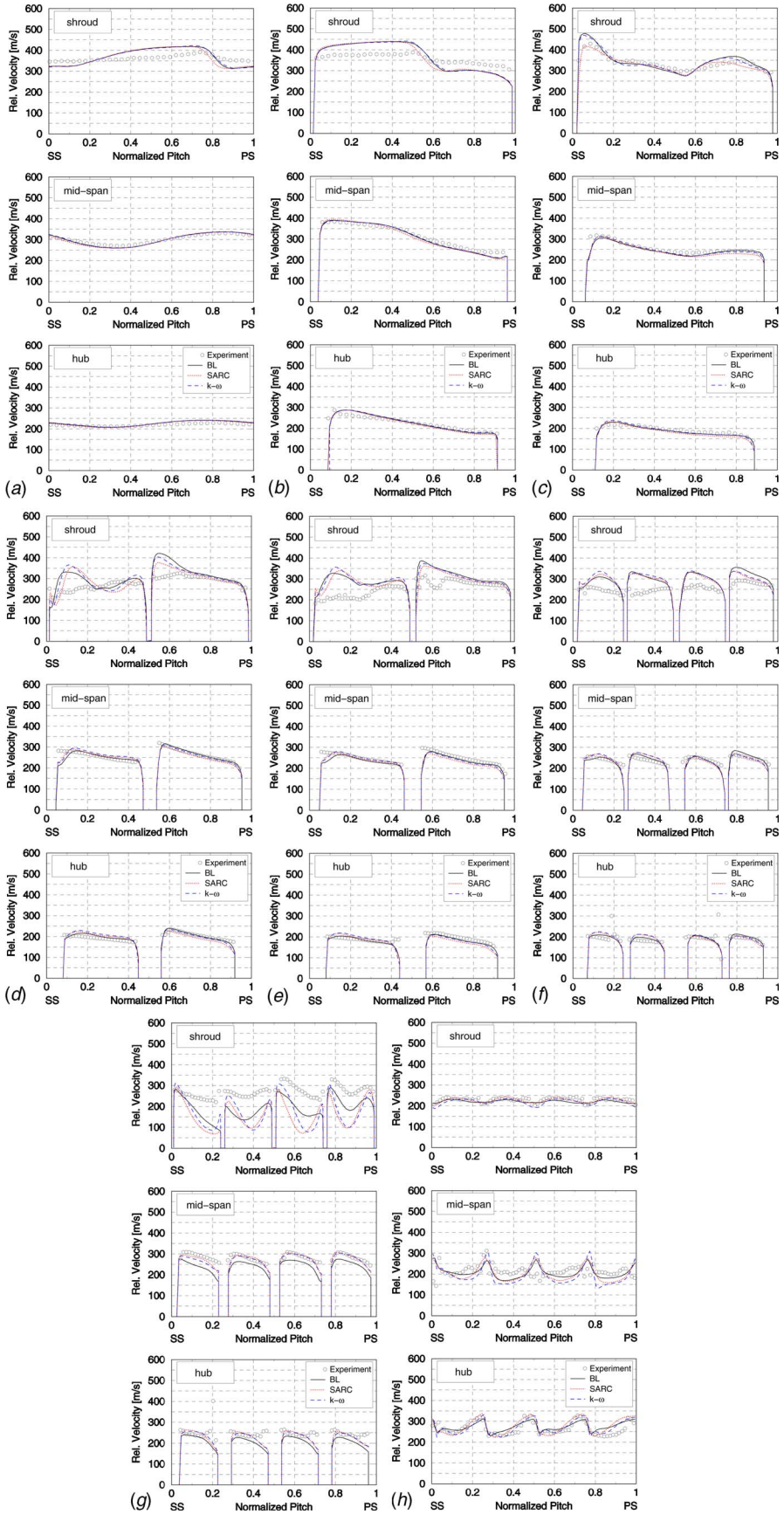

Fig. 8 Comparison of pitchwise relative velocity distribution: (*a*) section A; (*b*) section B; (*c*) section C; (*d*) section D; (*e*) section E; (*f*) section F; (*g*) section G; and (*h*) section H

Downloaded 30 May 2010 to 128.113.26.88. Redistribution subject to ASME license or copyright; see http://www.asme.org/terms/Terms_Use.cfm

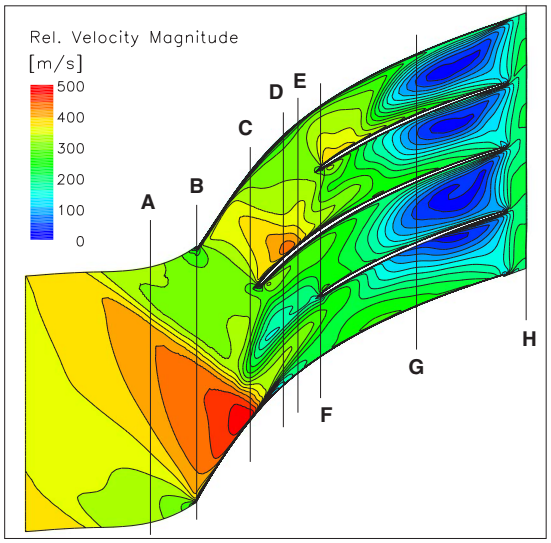

Fig. 9 Computed relative velocity contours near shroud at about 90% span (BL model)

models with respect to the experiments. Nevertheless, since the gridded tip gap model globally predicts higher velocity levels in section G, better resembling the experimental patterns, this model was chosen for the successive analyses.

Flow Field Analysis. It can be expected that the physical mechanisms governing the flow field in the near shroud region would be influenced by turbulence modelization and transport through the computational domain. In light of this, the algebraic BL model was compared with two widely used turbulence closures, such as the Spalart-Allmaras model with rotation/curvature correction (SARC) and the Wilcox's k-ω model.

In Fig. 8 the pitchwise relative velocity distributions are shown in cross sections A–H. Figure 9 shows a blade-to-blade view of the computed relative velocity contours near the impeller shroud at about 90% span height, while Fig. 10 depicts an overview of tip leakage vortices, leakage, and secondary flows evolution in the impeller passages. Figures 9 and 10 will be referred to in the flow

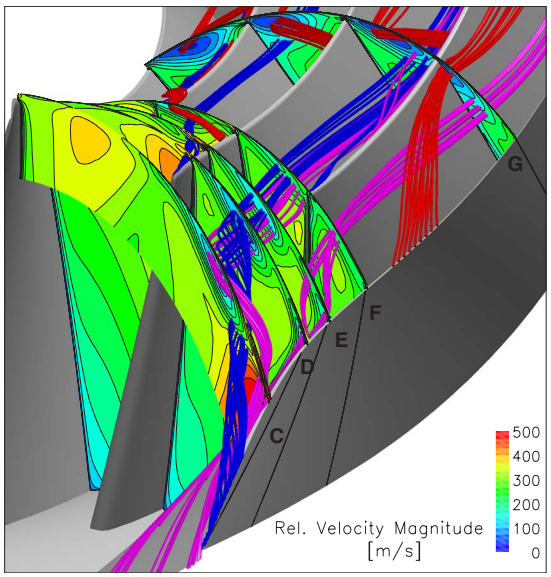

Fig. 10 Tip leakage vortices, leakage, and secondary flows evolution in the impeller passages (BL model)

field analysis to support the discussion of the velocity distributions of Fig. 8. In the midspan and near hub locations CFD distributions exhibit the same shape as well as the same global magnitude as the measured ones. Therefore attention will be focused on the discussion of the near shroud distributions.

Referring to Fig. 9, section A (Fig. 8(a)) crosses the shock wave located in front of the full blade leading edge at about 0.1 of the normalized pitch, and the expansion region starting near the midpitch. It can be seen that the velocity drop across the shock is larger in the computed distributions. Similarly, in section B (Fig. 8(b)), the position of the shock wave is correctly predicted to be between 0.5 and 0.6 of the normalized pitch but the computed shock intensity is about three times the measured one. In both sections A and B the SARC model tends slightly to anticipate the shock position with respect to BL and k-ω models.

In cross section C (Fig. 8(c)), the predicted velocity distributions agree quite well with the experimental one. Starting from the full blade SS the section crosses the maximum velocity region before the shock root, the shock wave, and then a low-velocity region due to a secondary flow coming from the SS of the full blade. Finally, it encounters the expansion region originated from the first splitter SS (see Fig. 9). Referring to Fig. 10, the aforementioned low-velocity region seems to be originated by both the tip leakage vortex of the full blade and, mostly, by the boundary layer flow which undergoes a momentum loss through the shock, migrates toward the shroud, and is captured by the leakage flow and drawn in the midpassage. The SARC model better predicts the velocity near the full blade SS, whereas it slightly underestimates the expansion region extension.

In cross section D (Fig. 8(d)), a low momentum region formed by the flow which has run up towards the shroud, due to the shock-boundary layer interaction, is observed close to the full blade SS. This low momentum region visible in Fig. 10 is also present in the experimental distribution, and is better captured by the SARC and the k-ω models than the BL model. The tip leakage vortex of the full blade, which moves toward the passage center when interacting with the shock wave, is clearly visible as a hollow in the relative velocity magnitude near 0.3 of the normalized pitch. Although this behavior is not confirmed by the experiments, the consequent blockage induces an acceleration effect on the adjacent flow: the leakage vortex is acting as a flow obstruction, which causes the flow entering the blade passage to pass around it rather than through it. On the SS of the first splitter, all the turbulence models predict an accelerating flow (see Fig. 9) that is not present in the experimental distribution. Similar considerations as for section D hold for section E (Fig. 8(e)), located slightly downstream. In the experimental distribution a velocity drop is visible around 0.6 of the normalized pitch. This seems not to be related to the first splitter tip leakage vortex which is located closer to the shroud (see Fig. 10), but may be due to a shock-induced separation.

Cross section F in Fig. 8(f) corresponds to the portion immediately after the leading edge of the second splitter blade. The predicted velocity magnitude on the four passages is generally overestimated with respect to experiments. In the last passage, adjacent to the full blade PS, the distributions predicted by the SARC and the k-ω models are in better agreement, with the exception of a region near the splitter SS where a stronger expansion is visible (see Fig. 9).

In cross section G (Fig. 8(g)), the SARC and the k-ω models are in good agreement with the experimental distributions both near hub and midspan, whereas the BL model tends to predict lower velocity levels. In the near shroud section there is an evident discrepancy between the measured and the computed magnitudes, the latter being much smaller. The BL model exhibits a better agreement in terms of shape of the velocity distribution on all the four passages. A similar behavior was found in the near shroud section by [5]. They supposed the different velocity levels were influenced by the centrifugal forces acting on the seeding

Downloaded 30 May 2010 to 128.113.26.88. Redistribution subject to ASME license or copyright; see http://www.asme.org/terms/Terms_Use.cfm

particles used for the experiment. As shown in Fig. 10 the low momentum regions seem to be formed mainly by tip leakage flows coming from the adjacent passages and, concurrently, by tip leakage vortices and secondary flows migrated from hub to shroud.

Cross section H (Fig. 8(*h*)) is located downstream of the impeller at a radius of about 1.05 times the exit radius. In the midspan section the velocity pattern is influenced by the wakes and by the low momentum regions coming from the upstream passages and observed in section G. In spite of discrepancies found in section G it can be noticed that at the impeller exit the flow is almost mixed and a good agreement is observed between computations and measurements in both the level and the shape of the velocity distributions.

Conclusions

A three-dimensional Navier-Stokes solver was used to investigate the high-pressure ratio transonic centrifugal compressor for turbocharger applications. Attention was focused on the flow field structure in the near shroud region which, based on previous analyses [4,5], resulted in lesser agreement with experimental findings. At this end an attempt was made to investigate the impact of some specific features of CFD modeling, such as tip clearance discretization and turbulence models, on the numerical solution. Based on the computed results and comparison with experimental data, the following conclusions are made.

As expected, the tip gap modelization has an impact on the predicted flow structures. The two models used to handle the tip leakage gap, a simple modeled or nongridded tip gap and a pinched blade or gridded tip gap, yielded some differences both in terms of relative velocity distribution shape and magnitude in the near shroud region. The gridded tip gap model showed a better agreement with the experiments in terms of overall velocity levels.

The flow field analysis in the impeller passages was conducted by comparing the computed and measured relative velocity distributions at several stations. The physical mechanisms associated with the observed flow structures were identified through particle path visualization. The influence of turbulence modeling was assessed by comparing the algebraic model of Baldwin-Lomax, the Spalart-Allmaras one-equation model with rotation/streamline curvature correction and the Wilcox's k-ω model. The overall results yielded by the one and two equation turbulence models are similar to the algebraic eddy viscosity model. Although some variations in the predicted velocity distributions are evident, these are restricted to some flow field details. The major impact is observed in the measurement station located in the region of maximum curvature of the meridional channel, where turbulence transport models are in closer agreement with experiments near hub and midspan while present larger velocity defects are near the shroud. At the impeller exit all the turbulence models predict similar mixing levels in good agreement with the experimental findings.

Acknowledgment

The authors gratefully acknowledge Dr. Roberto Pacciani of the University of Florence for helpful discussions on turbulence models.

Nomenclature

$\tilde{S}$ = deformation rate in the Spalart-Allmaras (SA) model
c_{b1} = 0.1355 empirical constant of the SA model
c_p = specific heat at constant pressure
c_{r1}, c_{r2}, c_{r3} = constants of the SA rotation/curvature model (SARC)
f_{r1} = rotation/curvature function of the SARC model
I = rothalpy
k = turbulent kinetic energy
L = computational domain length
M_{is} = isentropic Mach number ($M_{is} = \sqrt{2[I - c_p T_{is} + (\Omega r)^2/2]/(\gamma R T_{is})}$)
R = gas constant
r = radius
T = temperature
V = absolute velocity magnitude
PS = pressure surface
SS = suction surface

Greek

γ = specific heats ratio
μ = eddy viscosity
Ω = angular velocity
ω = specific turbulent dissipation rate
$\tilde{\nu}$ = modified eddy viscosity of the SA model

Subscripts

l = laminar
∞ = freestream value
t = turbulent

References

[1] Hah, C., and Krain, H., 1990, "Secondary Flow and Vortex Motion in a High-Efficiency Backswept Impeller at Design and Off-Design Conditions," ASME J. Turbomach., **112**(1), pp. 7–13.
[2] Higashimori, H., Hasagawa, K., Sumida, K., and Suita, T., 2004, "Detailed Flow Study of Mach Number 1.6 High Transonic Flow With a Shock Wave Pressure Ratio 11 Centrifugal Compressor Impeller," ASME J. Turbomach., **126**(4), pp. 473–481.
[3] Dawes, N. W., 1987, "Application of a Three-Dimensional Viscous Compressible Flow Solver to a High-Speed Centrifugal Compressor Rotor—Secondary Flow and Loss Generation," *Proceedings IMechE Conference on Turbomachinery*, Robinson College, Cambridge, UK, Paper No. C261/87.
[4] Ibaraki, S., Higashimori, H., and Matsuo, T., 2001, "Flow Investigation of a Transonic Centrifugal Compressor for Turbocharger," *Proceedings 23rd CIMAC Congress Proceedings*, Hamburg, Germany, May 7–10, pp. 339–346.
[5] Ibaraki, S., Matsuo, T., Kuma, H., Sumida, K., and Suita, T., 2003, "Aerodynamics of a Transonic Centrifugal Compressor Impeller," ASME J. Turbomach., **125**(2), pp. 346–351.
[6] Baldwin, B. S., and Lomax, H., 1978, "Thin Layer Approximation and Algebraic Model for Separated Turbulent Flows," *Proceedings 16th Aerospace Sciences Meeting*, Huntsville, AL, January 16–18, AIAA Paper No. 78-257.
[7] Arnone, A., 1994, "Viscous Analysis of Three-Dimensional Rotor Flow Using a Multigrid Method," ASME J. Turbomach., **116**(3), pp. 435–445.
[8] Bonaiuti, D., Arnone, A., Ermini, M., and Baldassarre, L., 2006, "Analysis and Optimization of Transonic Centrifugal Compressor Impellers Using the Design of Experiments Technique," ASME J. Turbomach., **128**(4), pp. 786–797.
[9] Arnone, A., Bonaiuti, D., Ermini, M., Milani, A., and Baldassarre, L., 2003, "Development of a Procedure for the Aerodynamic Design of Transonic Centrifugal Compressor Impellers," *Proceedings of the 5th European Turbomachinery Conference*, Prague, Czech Republic, March 17–21.
[10] Bonaiuti, D., Arnone, A., Hah, C., and Hayami, H., 2002, "Development of Secondary Flow Field in a Low Solidity Diffuser in a Transonic Centrifugal Compressor Stage," *Proceedings ASME Turbo Expo*, Amsterdam, The Netherlands, June 3–6, ASME Paper No. 2002-GT-30371.
[11] Bonaiuti, D., Arnone, A., Milani, A., and Baldassarre, L., 2003, "Aerodynamic Analysis of a Multistage Centrifugal Compressor," *Proceedings ASME Turbo Expo*, Atlanta, GA, June 16–19, ASME Paper No. 2003-GT-38495.
[12] Jameson, A., Schmidt, W., and Turkel, E., 1981, "Numerical Solutions of the Euler Equations by Finite Volume Methods Using Runge-Kutta Time-Stepping Schemes," *Proceedings 14th Fluid and Plasma Dynamics Conference*, Palo Alto, CA, June 23–25, AIAA Paper No. 81-1259.
[13] Swanson, R. C., and Turkel, E., 1992, "On Central-Difference and Upwind Schemes," J. Comput. Phys., **101**, pp. 292–306.
[14] Arnone, A., and Swanson, R. C., 1993, "A Navier-Stokes Solver for Turbomachinery Applications," ASME J. Turbomach., **115**(2), pp. 305–313.
[15] Kirtley, K. R., Beach, T. A., and Adamczyk, J. J., 1990, "Numerical Analysis of Secondary Flow in a Two-Stage Turbine," *Proceedings 26th SAE, ASME, and ASEE, Joint Propulsion Conference*, Orlando, FL, July 16–18, AIAA Paper No. 90-2356.
[16] Storer, J. A., and Cumpsty, N. A., 1991, "Tip Leakage Flow in Axial Compressors," ASME J. Turbomach., **113**(2), pp. 252–259.
[17] Crook, A. J., Greitzer, E. M., Tan, C. S., and Adamczyk, J. J., 1993, "Numerical Simulation of Compressor Endwall and Casing Treatment Flow Phenomena," ASME J. Turbomach., **115**(3), pp. 501–512.
[18] Van Zante, D. E., Strazisar, A. J., Wood, J. R., Hathaway, T. H., and Okiishi, T. H., 2000, "Recommendations for Achieving Numerical Simulation of Tip Clearance Flows in Transonic Compressor Rotor," ASME J. Turbomach.,

Downloaded 30 May 2010 to 128.113.26.88. Redistribution subject to ASME license or copyright; see http://www.asme.org/terms/Terms_Use.cfm

122(4), pp. 733–742.
[19] Spalart, P. R., and Allmaras, S. R., 1994, "A One-Equation Turbulence Model for Aerodynamic Flows," La Rech. Aerosp., **1**, pp. 5–21.
[20] Wilcox, D. C., 1998, *Turbulence Modeling for CFD*, 2nd ed., DCW Industries Inc., La Cañada, CA, ISBN 1-928729-10-X.
[21] Spalart, P. R., and Shur, M., 1997, "On the Sensitization of Turbulence Models to Rotation and Curvature," Aerosp. Sci. Technol., **1**(5), pp. 297–302.
[22] Shur, M. L., Strelets, M. K., Travin, A. K., and Spalart, P. R., 2000, "Turbulence Modeling in Rotating and Curved Channels: Assessing the Spalart-Shur Correction," AIAA J., **38**(5), pp. 784–792.
[23] Rumsey, C. L., and Gatski, T. B., 2001, "Isolating Curvature Effects in Computing Wall-Bounded Turbulent Flows," *Proceedings 39th AIAA Aerospace Sciences Meeting & Exhibit*, Reno, NV, January 8–11, AIAA Paper No. 2001-0725.
[24] Durbin, P. A., 1996, "On the k-ε Stagnation Point Anomaly," Int. J. Heat Fluid Flow, **17**, pp. 89–90.
[25] Menter, F. R., 1992, "Influence of Freestream Values on k-ω Turbulence Models Predictions," AIAA J., **30**(6), pp. 1657–1659.
[26] Pierzga, M. J., and Wood, J. R., 1985, "Investigation of the Three-Dimensional Flow Field Within a Transonic Fan Rotor: Experiment and Analysis," ASME J. Turbomach., **107**(2), pp. 436–449.

Downloaded 30 May 2010 to 128.113.26.88. Redistribution subject to ASME license or copyright; see http://www.asme.org/terms/Terms_Use.cfm

Minimizing Maximum Modal Force in Mistuned Bladed Disk Forced Response

Keith W. Jones
Propulsion Directorate,
Air Force Research Laboratory,
Wright-Patterson Air Force Base, OH 45433

Amplitude magnification is defined as the maximum forced response amplitude of any blade on a mistuned bladed disk divided by the maximum response amplitude of any blade on a tuned bladed disk over a range of engine order excitation frequencies. This paper shows that amplitude magnification can be approximated as the maximum ratio of modal force divided by modal vector magnitude in an isolated family of turbine engine bladed disk modes. An infinite linear mistuning pattern, defined by a constant interblade stiffness increment between an infinite number of blades, is found to minimize the maximum modal force when subjected to engine order N/4 excitation. Linear mistuning, an approximation of the infinite linear mistuning pattern, approximately minimizes the maximum modal force for bladed disks with a finite number of blades when subjected to engine order N/4 excitation. From this theory, $\sqrt{2/N}$ is proposed to be a lower boundary for amplitude magnification. The linear mistuning method is demonstrated to produce very low amplitude magnifications numerically and experimentally. The numerical examples suggest that linear mistuning may produce amplitude magnifications near the absolute minimum possible. [DOI: 10.1115/1.2749291]

1 Introduction

Bladed disks, such as those in fans, compressors, and turbines, rotate through circumferential pressure disturbances caused by struts, vanes, stators, or other obstructions in the gas path of turbine engines. These disturbances cause engine order excitation, where the engine order refers to the number of equally spaced disturbances either upstream or downstream of the bladed disk. The resulting blade vibration can lead to high cycle fatigue (HCF) failures as cycles quickly accumulate at the high rotational rates of turbine engines. HCF has historically led to the premature failure of major aircraft engine components and, in some instances, has resulted in the loss of the total engine and aircraft. Estimates put the cost of HCF at over $400 million per year [1].

HCF is exacerbated by mistuning, a breakdown in the cyclic symmetry of bladed disks. A tuned bladed disk is defined as one in which all sectors have identical properties. Manufacturing tolerances and asymmetric wear inevitably introduce differences in the geometries, material properties, or interface boundary conditions of blades, resulting in a mistuned bladed disk. The maximum blade response to engine order excitation, or maximum response for short, is usually greater for a mistuned bladed disk than for a tuned bladed disk. Therefore, mistuning tends to shorten component life and negatively impacts the durability and reliability of engines. Because of the importance of mistuning to turbine engine durability, a large amount of research has been published on the subject. Srinivasan [2] has surveyed much of the literature.

The effect of mistuning on turbine bladed disk forced vibration is often described using the term *amplitude magnification*, which is the maximum mistuned blade response across a range of excitation frequencies divided by the maximum tuned blade response. Whitehead [3–5] and Kenyon et al. [6] showed that the maximum amplitude magnification possible due to mistuning is $g_{\max}=(1+\sqrt{N})/2$, where N is the number of blades on the disk. Kenyon et al. [6] also presented a method for finding the mistuning required to achieve a maximum amplitude magnification. Both Whitehead [3–5] and Kenyon et al. [6] maximized amplitude magnification by creating a mode that produces an extremely high response on one blade. In these papers, the other mode shapes in the family are unimportant since the maximum blade response is known to occur at resonance in the optimized mode.

Since Whitehead [3] published his first result for maximum amplitude magnification mistuning nearly 40 years ago, no analogous solution for the mistuning that minimizes amplitude magnification has been published despite the fact that such a solution would be of great practical interest for designing bladed disks with maximum HCF lives. This paper attempts to find the mistuning that minimizes amplitude magnification. The problem definition and assumptions will parallel those of Kenyon et al. [6] by formulating the problem in terms of the distortion of individual modes. However, one major difference is that instead of maximizing the response in one distorted mode, the maximum response must be minimized for a family of N distorted modes simultaneously.

The remainder of the paper demonstrates the linear mistuning theory both numerically and experimentally, showing the lowest numerical and experimental amplitude magnifications published to date. A spring mass model is used to investigate how close linear mistuning comes to minimizing amplitude magnification and to investigate the effectiveness of linear mistuning for bladed disks with various coupling, damping, and numbers of blades. The linear mistuning method is then numerically demonstrated on a finite element model (FEM) of a realistic geometry bladed disk. Lastly, linear mistuning is experimentally demonstrated on a bladed disk of simple geometry.

2 Theory

The goal of this section is to find the mistuning that minimizes the maximum resonant forced response amplitude of any blade in any mode for an isolated family of bladed disk modes excited by an engine order excitation.

2.1 Derivation of Amplitude Magnification. The undamped equations of motion for a FEM of a bladed disk assembly can be written as

Submitted to ASME for publication in the JOURNAL OF TURBOMACHINERY. Manuscript received September 16, 2003; final manuscript received January 11, 2007; published online January 25, 2008. Review conducted by Marc P. Mignolet.

 Copyright © 2008 by ASME

Downloaded 30 May 2010 to 128.113.26.88. Redistribution subject to ASME license or copyright; see http://www.asme.org/terms/Terms_Use.cfm

$$\tilde{\mathbf{M}}\ddot{\tilde{\mathbf{x}}} + \tilde{\mathbf{K}}\tilde{\mathbf{x}} = \tilde{\mathbf{f}} \tag{1}$$

where $\tilde{\mathbf{M}}$ and $\tilde{\mathbf{K}}$ are the full mass and stiffness matrices, respectively, $\tilde{\mathbf{x}}$ is a vector containing the displacements of each degree of freedom, and $\tilde{\mathbf{f}}$ is a vector of forces on each degree of freedom. Tildes indicate that the variables correspond to the full FEM.

If the mode shapes are normalized with respect to the mass matrix, then they can be diagonalized via the following transformations involving the modal matrix, where $\mathbf{I}$ is the identity matrix and $\mathbf{\Lambda}$ is the diagonal matrix of the system's natural frequencies squared:

$$\mathbf{I} = \tilde{\boldsymbol{\phi}}^T\tilde{\mathbf{M}}\tilde{\boldsymbol{\phi}} \tag{2}$$

$$\mathbf{\Lambda} = \tilde{\boldsymbol{\phi}}^T\tilde{\mathbf{K}}\tilde{\boldsymbol{\phi}} \tag{3}$$

Therefore, the physical mass and stiffness matrices can be recovered using the following inverse transformations:

$$\tilde{\mathbf{M}} = (\tilde{\boldsymbol{\phi}}^T)^{-1}\mathbf{I}\tilde{\boldsymbol{\phi}}^{-1} \tag{4}$$

$$\tilde{\mathbf{K}} = (\tilde{\boldsymbol{\phi}}^T)^{-1}\mathbf{\Lambda}\tilde{\boldsymbol{\phi}}^{-1} \tag{5}$$

If all columns of the modal matrix are eliminated, except those corresponding to the N mode shapes in a single family of modes in the frequency range of interest, and all rows of the modal matrix are eliminated, except those corresponding to a single retained degree of freedom at an identical location of interest (not on any nodal point of any mode shape) on each sector of the bladed disk, then Eqs. (4) and (5) produce N by N reduced order model mass and stiffness matrices. If the forces in $\tilde{\mathbf{f}}$ are only applied at the retained degrees of freedom, then the same rows deleted in the modal matrix may be deleted in $\tilde{\mathbf{x}}$ and $\tilde{\mathbf{f}}$, resulting in the equations of motion of the reduced order model,

$$\mathbf{M}^0\ddot{\mathbf{x}} + (\mathbf{K}^0 + \mathbf{\Delta K})\mathbf{x} = \mathbf{f} \tag{6}$$

where $\mathbf{M}^0$ and $\mathbf{K}^0$ are the circulant matrices of the tuned bladed disk and $\mathbf{\Delta K}$ represents the mistuning in the reduced order model. The reduced order model, having the same eigenstructure as that of the full model in the frequency range of interest, will produce the exact same frequency response functions as that of the full size model as long as all forces and measurements are taken at the retained degrees of freedom.

The vector of engine order excitation forces ($\mathbf{f}$) is assumed to be a harmonic excitation that differs from blade to blade by a constant interblade phase angle (θ),

$$\mathbf{f} = \mathbf{M}^0\hat{\mathbf{b}}u \tag{7}$$

where

$$u = e^{i\omega t} \tag{8}$$

$$b_j = \sqrt{1/N}e^{ij\theta} \quad j = 0, 1, \ldots, N-1 \tag{9}$$

$$\theta = 2\pi E/N \tag{10}$$

In Eq. (7), $\hat{\mathbf{b}}$ is a unit magnitude force shape vector, u is a scalar that characterizes the temporal properties of the forces, j is the index for the blade number, i is $\sqrt{-1}$, E is the engine order of the excitation, N is the number of blades, ω is the excitation frequency, and t is time. Because the mass matrix is a circulant matrix, its premultiplication in Eq. (7) scales the forces on the blades by a complex constant but does not alter their interblade phase angle relationships.

It is convenient to have a diagonal mass matrix in the following derivation. Therefore, Eq. (6) is premultiplied by the inverse of the mass matrix,

$$\mathbf{I}\ddot{\mathbf{x}} + \mathbf{M}^{0^{-1}}(\mathbf{K}^0 + \mathbf{\Delta K})\mathbf{x} = \hat{\mathbf{b}}u \tag{11}$$

The steady-state solution to Eq. (11) for the forced response in the frequency domain may be written as a summation of modal responses,

$$x_j(\omega) = \sum_{n=0}^{N-1} \frac{\phi_{jn}\boldsymbol{\phi}_n^H\hat{\mathbf{b}}}{\boldsymbol{\phi}_n^H\mathbf{I}\boldsymbol{\phi}_n(\omega_n^2 - \omega^2 + 2\zeta\omega_n\omega i)} \tag{12}$$

where ω_n and $\boldsymbol{\phi}_n$ are the nth natural frequency and the nth mode shape, ϕ_{jn} is the jth element or blade of the nth mode, and H denotes the Hermitian transpose. Damping is incorporated into the model through a modal damping ratio ζ, which is assumed to be the same value for all modes, tuned or mistuned.

The resonant response of any blade in any mode is now considered. It is assumed that the resonant responses are dominated by a single mode at resonance where $\omega \approx \omega_n$ for a lightly damped system. As in Ref. [7], the frequency dependence of the damping term $2\zeta\omega_n\omega$ is neglected by assuming that the natural frequencies are approximately the arithmetic mean of the tuned natural frequencies, i.e., $\omega_n \approx \omega_{\text{avg}}^0$. This assumption is valid in a system where the natural frequencies are closely spaced. Inserting these simplifying assumptions into Eq. (12) results in an expression for the magnitude of the resonant response for each blade in each mode,

$$x_{jn} \approx \left| \frac{\phi_{jn}\boldsymbol{\phi}_n^H\hat{\mathbf{b}}}{\boldsymbol{\phi}_n^H\boldsymbol{\phi}_n 2\zeta(\omega_{\text{avg}}^0)^2} \right| \tag{13}$$

The same development applies to a tuned bladed disk with modes given by [7]

$$\phi_{jn}^0 = \sqrt{1/N}e^{ij2\pi(n/N)} \tag{14}$$

resulting in

$$x_{jn}^0 \approx \left| \frac{\phi_{jn}^0\hat{\boldsymbol{\phi}}_n^{0H}\hat{b}}{\hat{\boldsymbol{\phi}}_n^{0H}\hat{\boldsymbol{\phi}}_n^0 2\zeta(\omega_{\text{avg}}^0)^2} \right| \tag{15}$$

The tuned modes are normalized to have a unit vector magnitude in Eq. (14) and therefore written as $\hat{\boldsymbol{\phi}}_n^0$ in Eq. (15). Note from Eqs. (9) and (14) that $\hat{\mathbf{b}} = \hat{\boldsymbol{\phi}}_E^0$. Since $\hat{\boldsymbol{\phi}}_E^0$ is orthogonal to all of the other tuned modes, x_{jn}^0 in Eq. (15) is only nonzero when $n = E$ [8]. Using this fact and the fact that the magnitudes of all ϕ_{jn}^0 are $1/\sqrt{N}$ gives the maximum resonant tuned response amplitude

$$x_{\max}^0 \approx [2\zeta(\omega_{\text{avg}}^0)^2\sqrt{N}]^{-1} \tag{16}$$

Dividing Eq. (13) by Eq. (16) gives g_{jn}^*, an approximation of the true amplitude magnification g,

$$g_{jn}^* = \left| \sqrt{N}\frac{\phi_{jn}\boldsymbol{\phi}_n^H\hat{\mathbf{b}}}{\boldsymbol{\phi}_n^H\boldsymbol{\phi}_n} \right| \tag{17}$$

Note that there are N^2 g^*'s defined, one for the resonant response of each blade in each mode. It can be shown from Eq. (17) (see Appendix A) that the amplitude magnifications must satisfy

$$\sum_{n=0}^{N-1}\sum_{j=0}^{N-1} g_{jn}^{*2} = N \tag{18}$$

Equation (18) shows the difficulty in minimizing the maximum resonant blade response; any reduction in one blade's resonant response amplitude in a particular mode must be accompanied by increases in other blade resonant response amplitudes.

The overall amplitude magnification is defined by the maximum mistuned response divided by the maximum tuned response, where the maximum response indicates that $\phi_{jn} = \phi_{(\max)n}$, where $\phi_{(\max)n}$ is the maximum of the elements in the nth mode. Normalizing the modes in Eq. (17) so that $\phi_{(\max)n} = 1$ gives

Downloaded 30 May 2010 to 128.113.26.88. Redistribution subject to ASME license or copyright; see http://www.asme.org/terms/Terms_Use.cfm

$$g^* = \sqrt{N}\max\left(\left|\frac{\boldsymbol{\phi}_n^H\hat{\mathbf{b}}}{\boldsymbol{\phi}_n^H\boldsymbol{\phi}_n}\right|\right) \tag{19}$$

Equation (19) can be written in terms of a normalized modal force defined as

$$Q_n^{\text{norm}} = \frac{\boldsymbol{\phi}_n^H\hat{\mathbf{b}}}{\|\boldsymbol{\phi}_n\|} = \hat{\boldsymbol{\phi}}_n^H\hat{\mathbf{b}} \tag{20}$$

Then, Eq. (19) becomes

$$g^* = \sqrt{N}\max\left(\frac{|Q_n^{\text{norm}}|}{\|\boldsymbol{\phi}_n\|}\right) \tag{21}$$

Equations (20) and (21) give a great deal of insight into minimizing amplitude magnification. The normalized modal force is simply the component of the mode shape vector in the direction of the force vector. The denominator is simply the vector magnitude of the mode shape. Recall that the modes are normalized so that their maximum value is unity. Therefore, the denominator will be largest for a mode with all elements equal to ± 1 and smallest for a mode with one element equal to one and all others zero. In other words, the denominator is largest for *extended modes*, those having participation in many blades, and smallest for *localized modes*, those having participation in few blades. Thus, Eq. (21) indicates that to minimize amplitude magnification, a family of modes where every mode shape is extended and produces a small normalized modal force is desired. Due to the difficulty in minimizing Eq. (21) directly, the following sections of the paper investigate the normalized modal force and the modal magnitude separately.

2.2 Minimizing Maximum Normalized Modal Force. The mode shape vectors $\hat{\boldsymbol{\phi}}_n$ form an orthonormal set of basis vectors that span the space of all possible displacements, $\mathbf{x}$, in Eq. (11). Therefore, the force vector $\hat{\mathbf{b}}$ can be written in terms of these basis vectors as

$$\hat{\mathbf{b}} = \sum_{n=0}^{N-1} Q_n^{\text{norm}}\hat{\boldsymbol{\phi}}_n \tag{22}$$

Since $\hat{\mathbf{b}}$ is a unit vector, the sum of the squares of all its components must equal 1,

$$\sum_{n=0}^{N-1} |Q_n^{\text{norm}}|^2 = 1 \tag{23}$$

Using Eq. (23), it can be shown (see Appendix B) that the maximum normalized modal force will be a minimum when all the normalized modal forces are equal to $\sqrt{1/N}$,

$$|Q_n^{\text{norm}}| = \sqrt{1/N} \quad \text{for all } n \tag{24}$$

One example of a family of mistuned modes that satisfies Eq. (24) is the uncoupled bladed disk modes,

$$\phi_{jn} = \delta_{jn} \tag{25}$$

where δ_{jn} is the Kronecker delta. These modes exist in coupled bladed disks where the mistuning is large compared to the coupling [8]. Although the uncoupled modes minimize the maximum Q_n^{norm} by satisfying Eq. (24), they also minimize $\|\boldsymbol{\phi}\|$ in the denominator of Eq. (21), resulting in an amplitude magnification of 1. Therefore, the uncoupled modes are too localized to minimize amplitude magnification. Fortunately, there may be other more extended modes that also satisfy Eq. (24).

It can be shown, as in the case of the uncoupled modes, that families of mode shapes where the modes differ only by a cyclic shift of an integer number of blade positions satisfy Eq. (24). This property can be described mathematically by

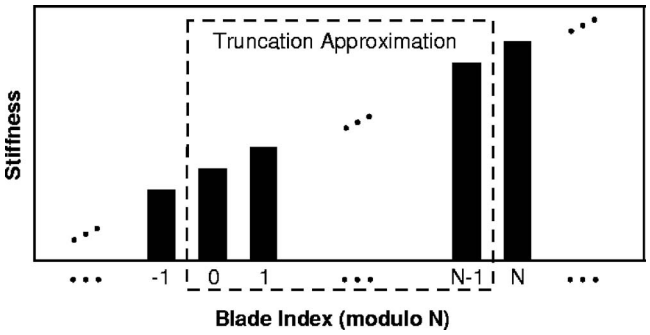

Fig. 1 Infinite linear mistuning and its truncated approximation

$$\phi_{jp} = \phi_{(j+s)q} \tag{26}$$

where ϕ_{jp} is the jth element of the pth mode shape, s is the integer shift in the blade position, and the blade number $(j+s)$ is taken mod N. Modes that have the property described by Eq. (26) are referred to as *shifted* in this paper. Due to the definition of $\hat{\mathbf{b}}$ in Eq. (9), Q_n^{norm} in Eq. (20) is a form of the Eth discrete Fourier transform (DFT) of $\hat{\boldsymbol{\phi}}$. Therefore, the DFT sample shift theorem [9] applies to shifted modes,

$$\text{DFT}[\boldsymbol{\phi}_q]_E = e^{isE(2\pi/N)}\text{DFT}[\boldsymbol{\phi}_p]_E \tag{27}$$

where $\text{DFT}[\boldsymbol{\phi}_p]_E$ is the Eth DFT of $\boldsymbol{\phi}_p$, and $\boldsymbol{\phi}_p$ and $\boldsymbol{\phi}_q$ are defined by Eq. (26). Since the magnitude of the exponential term is 1, the magnitudes of both sides of Eq. (27) are the same. Therefore, the DFT sample shift theorem says that any two shifted modes satisfy Eq. (24). Therefore, any family of shifted modes will minimize the maximum normalized modal force.

2.3 Mistuning to Obtain Shifted Modes. For a complete family of N shifted modes, every mode must be related to $\boldsymbol{\phi}_q$ by a unique integer shift index s,

$$\phi_{js} = \phi_{(j+s)q} \quad s = 1,2,\ldots,N-1 \tag{28}$$

and $(j+s)$ is taken mod N. The structural eigenvalue problem can be used to solve for the mistuning required to produce the shifted modes in Eq. (28),

$$[(\mathbf{K}^0 + \boldsymbol{\Delta}\mathbf{K}) - \omega_s^2\mathbf{M}^0]\boldsymbol{\phi}_s = 0 \tag{29}$$

For distinct natural frequencies, the nontrivial solution to the homogeneous linear system of algebraic equations in Eq. (29) for $\boldsymbol{\phi}_s$ is unique to within a scalar constant multiplier. Therefore, for two mode shapes to be identical, differing only by a shift in the blade position, the following condition is sufficient:

$$[(\mathbf{K}^0 + \boldsymbol{\Delta}\mathbf{K}) - \omega_s^2\mathbf{M}^0]_{(r+s)(c+s)} = [(\mathbf{K}^0 + \boldsymbol{\Delta}\mathbf{K}) - \omega_0^2\mathbf{M}^0]_{rc} \tag{30}$$

where $[\ ]_{rc}$ indicates an element in the rth row and cth column of the matrix, and $(r+s)$ and $(c+s)$ are taken modulo N. Expanding Eq. (30) using the fact that $\mathbf{K}^0$ and $\mathbf{M}^0$ are circulant matrices results in the following:

$$[\boldsymbol{\Delta}\mathbf{K}]_{(r+s)(c+s)} = [\boldsymbol{\Delta}\mathbf{K}]_{rc} + [\mathbf{M}^0]_{rc}(\omega_s^2 - \omega_q^2) \tag{31}$$

Letting $s=1$ shows that Eq. (31) describes an infinite linear mistuning pattern, where each blade's stiffness is increased (assuming $\omega_s > \omega_q$) by a constant amount relative to its lower numbered neighbor, as shown in Fig. 1. Therefore, the infinite linear mistuning pattern produces a family of shifted modes and, thus, minimizes the maximum normalized modal force.

An obvious contradiction exists in Eq. (31) because an infinite linear mistuning pattern cannot be applied to a cyclic structure where the mistuning pattern must eventually repeat. In fact, Eq. (31) requires $[\boldsymbol{\Delta}\mathbf{K}]_{(r+N)(c+N)} > [\boldsymbol{\Delta}\mathbf{K}]_{rc} \pmod N$, which is a contra-

Downloaded 30 May 2010 to 128.113.26.88. Redistribution subject to ASME license or copyright; see http://www.asme.org/terms/Terms_Use.cfm

diction because the same element of the matrix cannot have two different values. Therefore, a complete family of perfectly shifted modes is not possible for a bladed disk. However, infinite linear mistuning may be approximated by truncating the infinite pattern, as shown in Fig. 1. In this physically applicable linear mistuning pattern, every blade has an identical stiffness relationship with its neighboring blades, except where the highest frequency blade neighbors the lowest. It will be shown in a numerical example that modes where the lowest or the highest frequency blades participate substantially are not shifted versions of the other modes and, therefore, do not minimize the maximum modal force. However, it will also be shown that excitation of these modes can be avoided for engine orders near $N/4$. It is also expected that as N approaches infinity, linear mistuning will better approximate infinite linear mistuning and produce more perfectly shifted modes (at least for those excited by engine order $N/4$), and the maximum normalized modal force will approach $\sqrt{1/N}$, as predicted by Eq. (24).

2.4 Robustness. The recursive relationship in Eq. (31) also means that linear mistuning causes the difference between the squares of neighboring natural frequencies to be equal. For closely spaced bladed disk modes, an even spread of the squares of the natural frequencies implies an even spread of the natural frequencies themselves. Furthermore, from Eq. (31), the greater the linear mistuning ($[\mathbf{\Delta K}]_{(r+s)(c+s)}-[\mathbf{\Delta K}]_{rc}$), the more the natural frequencies will spread. Yang and Griffin [10] showed that the difference between two natural frequencies is inversely related to the sensitivity of the corresponding two mode shapes to mistuning. Therefore, in addition to reducing the maximum response, linear mistuning should also reduce the sensitivity of the mode shapes to mistuning by spreading the natural frequencies evenly, so that no two natural frequencies are left significantly closer than another two. Since amplitude magnification is solely a function of the modes in Eq. (19), the sensitivity of amplitude magnification to mistuning should also be reduced. Therefore, linear mistuning is expected to provide low amplitude magnification with a degree of robustness to additional random mistuning. This may make linear mistuning an attractive intentional mistuning pattern to implement in the design of some bladed disks [11,12].

2.5 Modal Magnitude. Recall that minimizing amplitude magnification in Eq. (21) involved finding families of modes with small normalized modal forces and large modal magnitudes. Sections 2.2 and 2.3 showed that linear mistuning approximately minimizes the maximum normalized modal force. However, the effect of linear mistuning on modal magnitude has not yet been addressed. It is known that any mistuning pattern can produce very extended modes (if the magnitude of the mistuning is small compared to the coupling between blades) or very localized modes (if the magnitude of the mistuning is large compared to the coupling) [13]. Therefore, the optimum amount of linear mistuning can be found by numerically solving for amplitude magnification across a range of linear mistuning amplitudes. The lowest amplitude magnification found by this procedure will likely be lower than 1, but may or may not be the absolute minimum amplitude magnification.

One conclusion can be made concerning the behavior of amplitude magnification for a linearly mistuned bladed disk as N approaches infinity. As N approaches infinity, it is expected that more blades will participate in each mode shape since there will be more blades of similar frequency to the natural frequency of any mode. (Note that mistuning stiffness perturbations are limited to a finite value by the nominal stiffness of the blade, whereas the number of blades is allowed to grow to infinity.) Since the modal magnitude in Eq. (21) is defined as the square root of the sum of the squares of the elements of the mode shape, modal magnitude will increase with increasing N due to more participating blades in the mode shape (i.e., more positive terms in the summation).

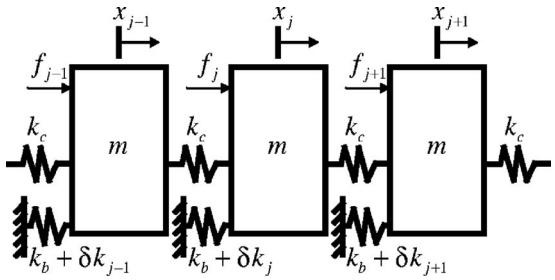

Fig. 2 Spring mass model

Therefore, with the numerator of Eq. (21) approaching $\sqrt{1/N}$—as predicted in Eq. (24)—and the denominator increasing with N, it is expected that amplitude magnification will approach zero as N approaches infinity for a linearly mistuned bladed disk.

2.6 Lower Boundary for Amplitude Magnification. Finally, a lower boundary for amplitude magnification can be proposed based on the previous development. First, assume that the mistuned bladed disk does not have any repeated natural frequencies, so that its mode shapes are real. Second, assume that no mistuned mode can be more extended than the tuned mode shapes written in their real form. For example, the tuned sine mode shape excited by engine order $E=N/4$ is

$$^{S}\phi_{jE}^{0}=\sin\left(\frac{\pi j}{2}\right) \tag{32}$$

The vector magnitude of this sine mode shape is $\sqrt{N/2}$. Substituting $\sqrt{N/2}$ for $\|\boldsymbol{\phi}_n\|$ in Eq. (21) and $\sqrt{1/N}$ for Q_n^{norm} in Eq. (24) gives

$$g_{\min}^{*}=\sqrt{2/N}\approx 1.414N^{-0.5} \tag{33}$$

This lower boundary is proposed in the sense that no mistuning can produce an amplitude magnification lower than $\sqrt{2/N}$. Since inconsistent mode shapes were substituted into Eq. (21), this lower limit may not be physically achievable. However, even if the boundary is unrealistically low, it serves as a reference for comparing how close linear mistuning comes to minimizing amplitude magnification in the numerical examples below.

3 Numerical Validation

Linear mistuning will be demonstrated numerically using a simple spring mass model of a bladed disk and a FEM of a complex geometry bladed disk. The spring mass model will be used to demonstrate the performance of linear mistuning for different engine orders, to investigate whether or not linear mistuning produces the absolute minimum maximum blade response, and to investigate the effectiveness of linear mistuning for bladed disks with different coupling, damping, and numbers of blades. The FEM will be used to demonstrate linear mistuning on a realistic bladed disk.

3.1 Spring Mass Model Example. An example of the linear mistuning method is presented using the spring mass model given in Fig. 2. The equations of motion for this system can be found in Refs. [8,13]. The properties of the bladed disk used in this example can be found in Table 1. Any system of units can be used for the mass and stiffness values in Table 1 because all results will be given in terms of dimensionless quantities.

The procedure for finding the minimum amplitude magnification possible with linear mistuning is illustrated in Fig. 3 by plotting amplitude magnification versus normalized linear mistuning amplitude A (defined as $\max(|\delta k_j|)/k_b$) for the spring mass model with an $E=3$ excitation. The minimum amplitude magnification ($g=0.6961$) occurs for a normalized linear mistuning amplitude of 0.0736. The forced response and mode shapes at this design point

Downloaded 30 May 2010 to 128.113.26.88. Redistribution subject to ASME license or copyright; see http://www.asme.org/terms/Terms_Use.cfm

Table 1 Properties of the spring mass model example

Parameter	Value
N	12
m	1
k_b	1
k_c	0.02
ζ	0.001

are shown in Figs. 4 and 5. Note in Fig. 5 that most modes are shifted versions of each other and that the resonant response amplitudes in Fig. 4 are nearly equal, as predicted by the theory.

3.2 Engine Order Limitation. As shown in Fig. 5, the lowest and highest frequency modes are not shifted versions of the other modes in the family. Therefore, they will not minimize modal force according to Sec. 2.2. These modes tend to be excited by engine orders N and $N/2$, just as the lowest and highest frequency modes in a tuned bladed disk tend to be excited by these engine orders. The effect of exciting these modes with engine orders N and $N/2$ is shown in Fig. 6. Large responses are present in the lowest frequency mode for $E=N$ and in the highest frequency mode for $E=N/2$. In general, linear mistuning does not produce amplitude magnifications less than 1 for engine orders near N and $N/2$, but does for engine orders near $N/4$. Therefore, the examples given in the rest of the paper will be for $E=N/4$.

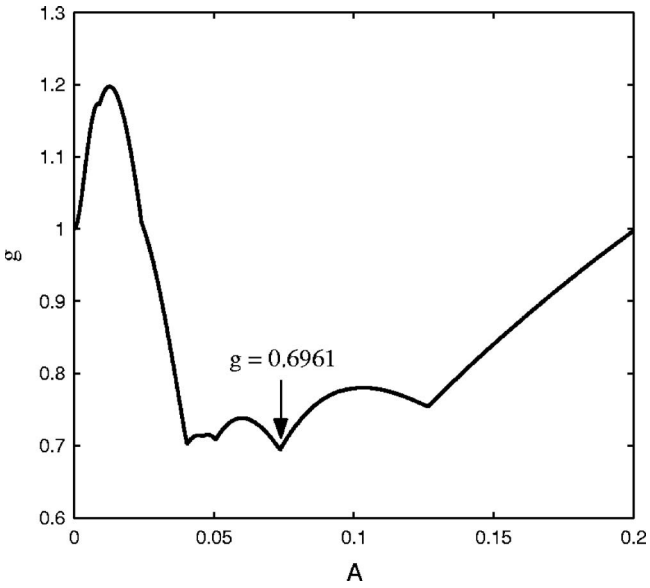

Fig. 3 Amplitude magnification versus normalized linear mistuning amplitude for the spring mass model ($E=N/4$)

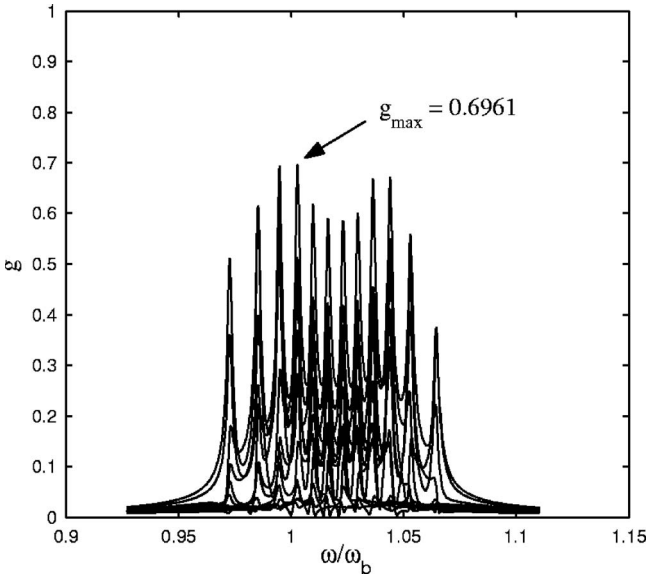

Fig. 4 Forced response of the spring mass model ($E=N/4$, $A=0.0736$)

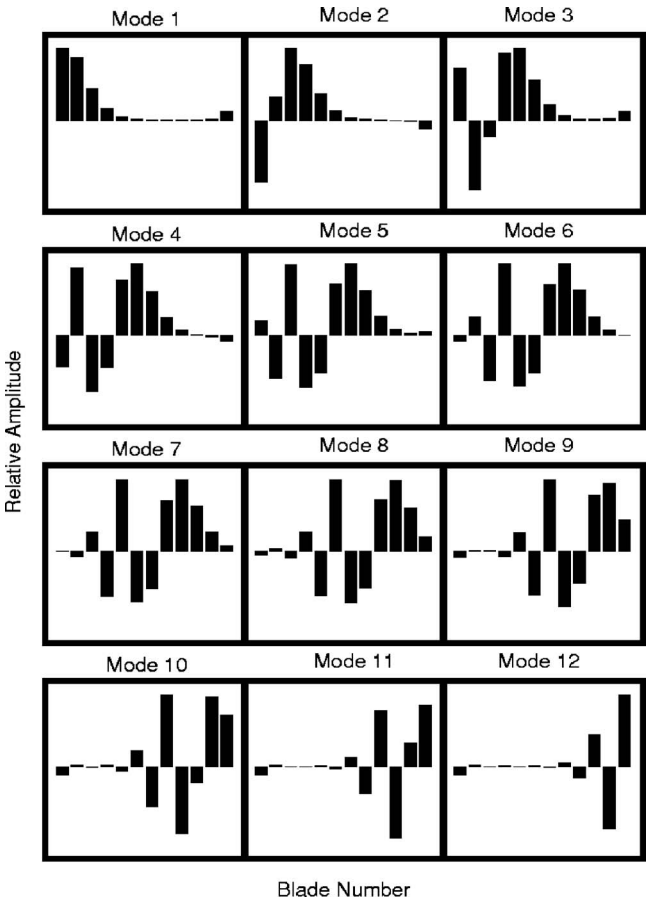

Fig. 5 Linearly mistuned spring mass model modes ($A=0.0736$)

3.3 Absolute Minimum Forced Response. As discussed in Sec. 2.5, linear mistuning may or may not produce the absolute minimum amplitude magnification. This section investigates how close the linear mistuning method comes to producing the absolute minimum amplitude magnification by comparing linear mistuning to randomly generated mistuning patterns and to numerically optimized mistuning patterns.

A Monte Carlo analysis was conducted by solving for the amplitude magnifications resulting from randomly generated mistuning patterns of the same standard deviation of mistuning as a linear mistuning pattern with an amplitude of 0.0742. Not one of 100,000 randomly generated mistuning patterns produced a lower amplitude magnification compared to the linear mistuning pattern. Figure 7 shows the probability density function for these 100,000 amplitude magnifications. Clearly, linear mistuning produces an amplitude magnification that is very low compared to the population of possible amplitude magnifications.

Next, an optimization study was conducted using the MATLAB™ optimization function *fminsearch*. The optimizations attempted to minimize amplitude magnification by varying the mistuning on

Downloaded 30 May 2010 to 128.113.26.88. Redistribution subject to ASME license or copyright; see http://www.asme.org/terms/Terms_Use.cfm

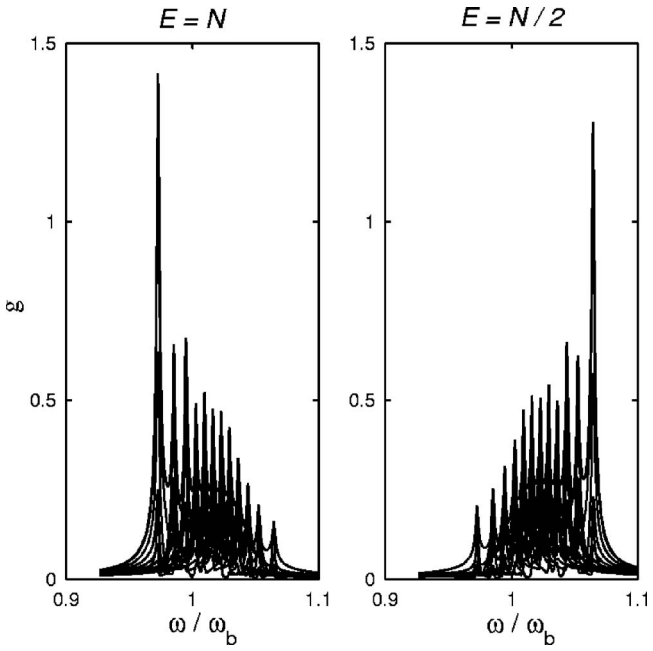

Fig. 6 Effect of the engine order on the forced response of the linearly mistuned spring mass model (*A*=0.0736)

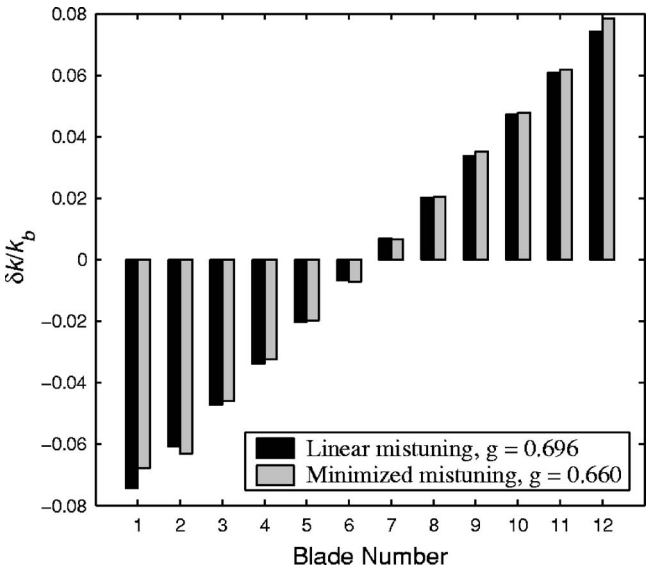

Fig. 8 Comparison of linear and numerically optimized mistuning from the spring mass model (*E*=*N*/4)

each blade. The optimizations were started from 1000 randomly selected mistuning patterns from the previous Monte Carlo analysis. All 1000 optimizations converged to a local minimum amplitude magnification. Of the 1000 optimizations, the lowest amplitude magnification was achieved when the optimization was started from the linear mistuning pattern. The resulting optimized mistuning pattern, shown in Fig. 8, still resembles a linear pattern. Overall, the optimization made a modest improvement to the linear mistuning pattern, reducing the amplitude magnification from 0.696 to 0.660. Although linear mistuning did not produce the global minimum for amplitude magnification, its shape was very similar to the optimized mistuning pattern that produced the lowest amplitude magnification found, indicating that it may be a reasonable approximate solution for the minimum amplitude magnification.

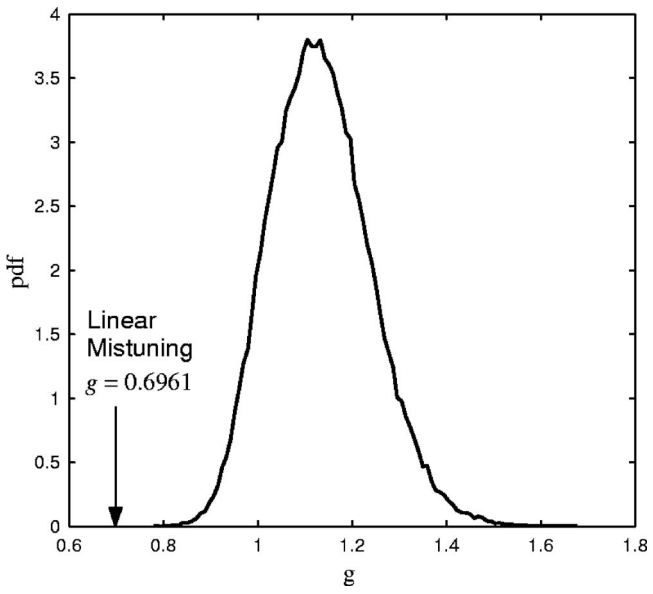

Fig. 7 Probability density function of spring mass model amplitude magnifications (*E*=*N*/4)

3.4 Parametric Spring Mass Model Study. The numerical examples presented so far were for a spring mass model with the properties given in Table 1. However, since the development of linear mistuning in Sec. 2 did not rely on any particular model of a bladed disk, linear mistuning should apply to a wide variety of bladed disks, including many realizations of the spring mass model. This section demonstrates the effectiveness of linear mistuning for spring mass models with different coupling ratios (k_c/k_b), damping ratios (ζ), and numbers of blades (N).

First, the effect of different coupling ratios is evaluated for a 12 bladed disk with $E=3$ excitation. The fundamental assumption inherent to Eq. (13) is that the maximum response is dominated by a single mode at resonance. If damping is allowed to go to zero, this assumption is satisfied. Therefore, the amplitude magnification for $\zeta \rightarrow 0$, as defined in Eq. (21), is plotted for different combinations of coupling and normalized linear mistuning amplitude in Fig. 9. Note that the coupling ratio simply determines the linear mistuning amplitude required to get low amplitude magnification. Linear mistuning is effective in producing amplitude magnifications less than 1 for all values of the coupling ratio.

Figure 9 also shows the effect of increasing the modal damping ratio to 0.001. In Fig. 9, the amplitude magnification is calculated using Eq. (12) since the maximum response can now be a combination of multiple modes. The area corresponding to low coupling and low mistuning now produces amplitude magnifications greater than 1. This is caused by closely spaced modal peaks with finite bandwidth (due to nonzero damping) overlapping in the forced response. In these regions, the assumption of response in a single mode is violated and the effectiveness of linear mistuning is reduced. Amplitude magnifications below 1 appear at higher levels of coupling and linear mistuning, where the natural frequencies are spread enough to create individual modal resonant peaks. Overall, linear mistuning is effective over a wide range of coupling ratios.

Since Fig. 9 shows that linear mistuning reduces amplitude magnification for almost all coupling ratios, the coupling ratio can be fixed at 0.02 and the effect of the number of blades can be evaluated. As stated in Sec. 2.4, it is expected that amplitude magnification for the linearly mistuned bladed disk will approach zero as N approaches infinity. Figure 10 shows the effect of the number of blades on amplitude magnification for $\zeta \rightarrow 0$ and for

Downloaded 30 May 2010 to 128.113.26.88. Redistribution subject to ASME license or copyright; see http://www.asme.org/terms/Terms_Use.cfm

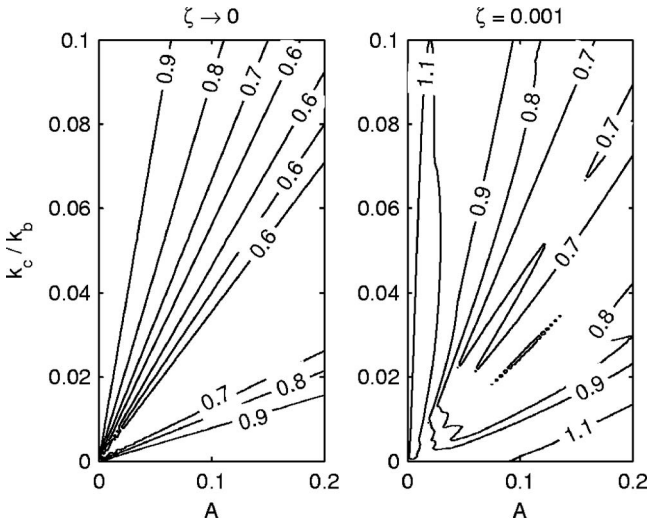

Fig. 9 Amplitude magnification contours for various combinations of coupling and linear mistuning (g^* plotted for $\zeta \to 0$, $E=N/4$)

$\zeta=0.0001$. Note that amplitude magnifications are higher when damping is added to the system. Again, this is explained by closely spaced modal peaks of finite bandwidth overlapping in the forced response. This problem increases with the number of blades as more modes are packed into the same frequency range. However, even in these cases, linear mistuning produces amplitude magnifications below or near 1, which are still favorable compared to large amplitude magnifications normally associated with mistuning.

3.5 Minimum Amplitude Magnification for Linear Mistuned Spring Mass Model. The path through the deepest valley of Fig. 10 is plotted in Fig. 11 to estimate the minimum amplitude magnification achievable by linearly mistuning a spring mass model. Figure 11 shows that extremely low amplitude magnifications are possible with large numbers of blades and very small damping. To the author's knowledge, these are, by far, the lowest amplitude magnifications ever published [11,12,14–16]. Figure 11 also shows the following curve fit equation of the $\zeta \to 0$ data for large N:

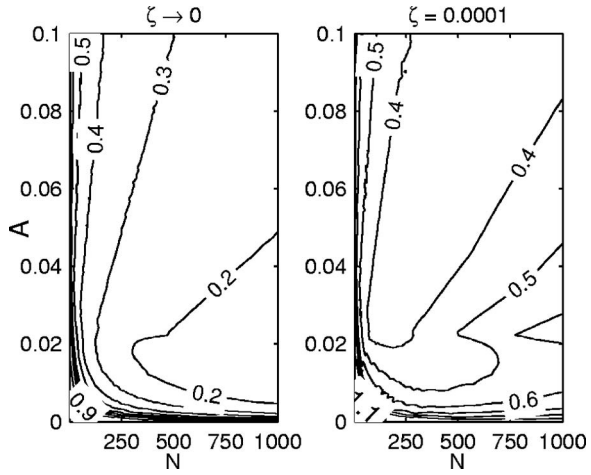

Fig. 10 Amplitude magnification contours for various combinations of numbers of blades and linear mistuning (g^* plotted for $\zeta \to 0$, $E=N/4$)

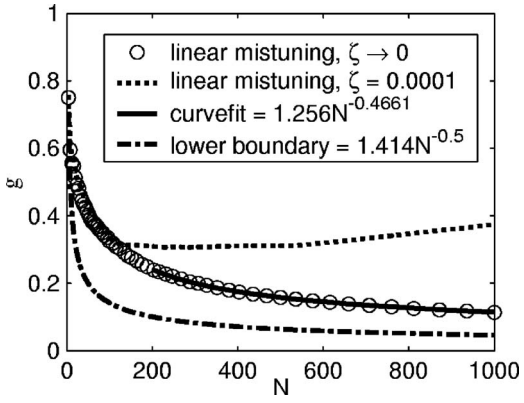

Fig. 11 Estimates of the minimum amplitude magnification for the spring mass model (g^* plotted for $\zeta \to 0$, $E=N/4$)

$$g^*_{\min} = 1.256N^{-0.4661} \quad 200 \geqslant N \geqslant 1000 \tag{34}$$

The amplitude magnification of the linearly mistuned bladed disk appears to approach zero as N approaches infinity, as predicted. Also, Eq. (34) shows a similar behavior to the $\sqrt{2/N}$ proposed lower boundary for amplitude magnification.

3.6 Realistic Bladed Disk Finite Element Model. Finally, linear mistuning is applied to the 16 bladed low aspect ratio fan in Fig. 12 to show its effectiveness on a realistic, complex geometry bladed disk. Although the full bladed disk is shown in Fig. 12, only a single sector was modeled, and the first family of tuned natural frequencies and mode shapes was found using the ANSYS™ cyclic symmetry modal analysis. The first mode family was characterized by a flapping or bending blade motion and was well separated from the next family of modes higher in frequency. Using the fundamental mistuning model (FMM) reduced order modeling method [7], amplitude magnification was found as a function of linear mistuning amplitude for an $E=4$ excitation and $\zeta=0.001$. The minimum amplitude magnification was found to occur for a linear mistuning amplitude of 0.0289 ($\max(\omega_j)/\omega^0_{\text{avg}}$). Figure 13 shows that this amount of linear mistuning resulted in an amplitude magnification of 0.753. Clearly, linear mistuning is effective in reducing the maximum response for both simple and realistic bladed disk models.

4 Experimental Validation

4.1 Experimental Setup. Linear mistuning was experimentally demonstrated on the 18 bladed steel disk shown in Fig. 14.

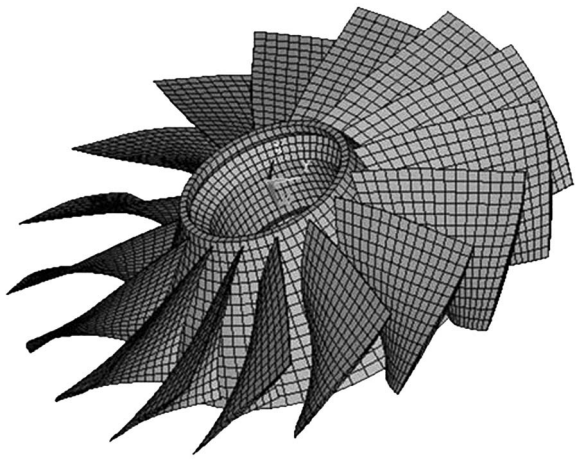

Fig. 12 FEM of a realistic bladed disk

Downloaded 30 May 2010 to 128.113.26.88. Redistribution subject to ASME license or copyright; see http://www.asme.org/terms/Terms_Use.cfm

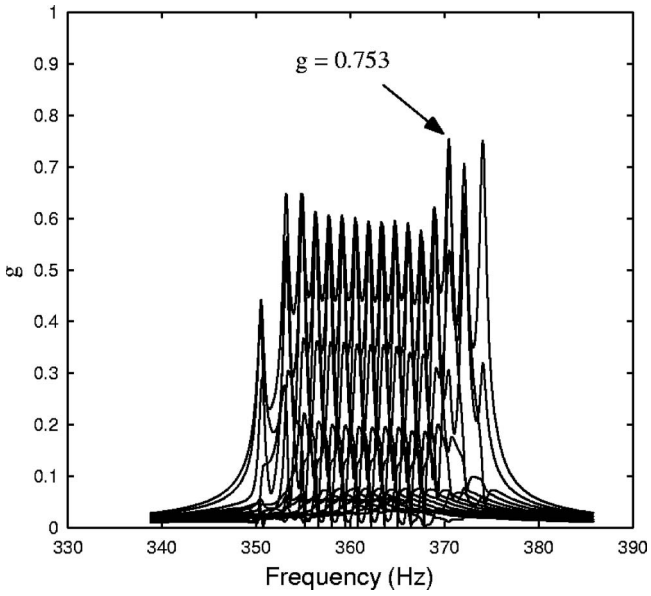

Fig. 13 Forced response of the linearly mistuned bladed disk FEM ($E=N/4$, $\zeta=0.001$, $A=0.0289$)

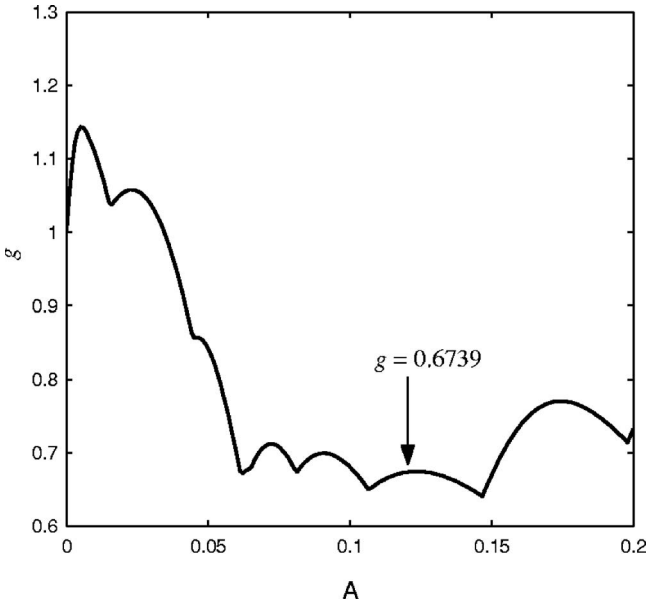

Fig. 15 Predicted amplitude magnification versus normalized linear mistuning amplitude ($E=4$)

Feiner and Griffin showed that the modes and forced response of a mistuned system are determined by the frequency variations of the sectors of a bladed disk [7]. Whether or not those frequency variations are created by perturbing the mass or stiffness properties is unimportant. Therefore, due to the difficulty of experimentally changing stiffnesses, mistuning was added to the bladed disk by attaching masses, made from aluminum bar stock, to the blades with accelerometer wax. A traveling wave excitation system generated an $E=4$ excitation by exerting the forces in Eq. (7) to the blade tips with noncontacting electromagnets [17]. Measurements of blade frequency responses were taken at the same point on each blade using a scanning laser vibrometer.

4.2 Predicted Result. First, the expected amplitude magnification reduction from linear mistuning needed to be predicted. This required a tuned forced response prediction and a mistuned forced response prediction, both of which were found via modal summation using Eq. (12). For the tuned forced response prediction, Eq. (12) requires the tuned natural frequencies, tuned modes, and tuned modal damping ratios. The tuned modes were theoretically known from Ref. [8]. The tuned modal damping ratios were assumed to be equal to the modal damping ratios from the nominal (no masses attached) bladed disk because the nominal modes were very similar to tuned modes. A standard experimental modal analysis was performed on the nominal bladed disk using the STAR™ modal software to get the nominal modal damping ratios as well as the nominal modes and nominal natural frequencies. From the experimentally measured nominal modes and natural frequencies, the tuned natural frequencies were found using Feiner and Griffin's FMM based mistuning identification (FMMID) method [18]. A predicted tuned forced response was then generated using Eq. (12).

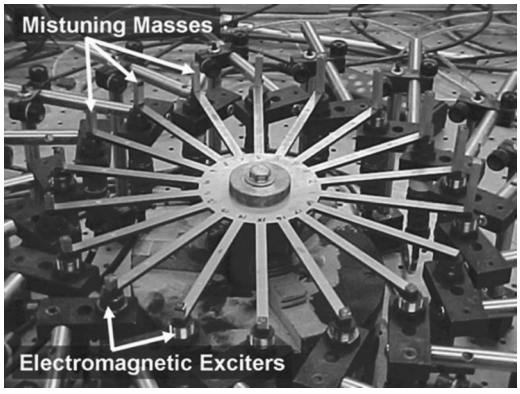

Fig. 14 Linear mistuning experimental setup

For the mistuned forced response prediction, the mistuned natural frequencies, modes, and modal damping ratios were required in Eq. (12). The mistuned natural frequencies and mode shapes were predicted by FMM, using the tuned natural frequencies and the assumed linear mistuning blade frequency deviations. The mistuned modal damping ratios were found from the tuned modal damping ratios and mistuned modes using the following equation, which is developed in Appendix C:

$$\mathbf{z} = \mathrm{diag}((\boldsymbol{\varphi}^{0^{-1}}\boldsymbol{\varphi})^T\mathbf{Z}^0\boldsymbol{\varphi}^{0^{-1}}\boldsymbol{\varphi}) \tag{35}$$

where $\mathbf{z}$ is the vector of mistuned modal damping ratios, $\mathbf{Z}^0$ is the diagonal matrix of the tuned modal damping ratios, $\boldsymbol{\varphi}^0$ is the tuned modal matrix, and $\boldsymbol{\varphi}$ is the mistuned modal matrix. Finally, the mistuned forced response was predicted from Eq. (12) and divided by the maximum tuned forced response prediction to find the predicted amplitude magnification. Figure 15 shows the predicted amplitude magnification versus normalized linear mistuning amplitude plot. From Fig. 15, a decision was made to demonstrate linear mistuning with a normalized amplitude of 0.12, which was predicted to result in an amplitude magnification of 0.6739.

4.3 Designing the Experiment. Feiner and Griffin's FMMID method [18] was used to create an experimental correlation between added blade mass and sector frequency. The process consisted of adding several different masses to a blade and identifying the resulting mistuning on that blade. This correlation provided the blade masses that were required to achieve a linear mistuning pattern with a normalized amplitude of 0.12. Since sector frequencies can only be reduced by adding mass, the linear mistuning pattern was implemented with sector frequency perturbations that ranged from 0% to −24% of the nominal sector frequency. Also, a tuned bladed disk experiment was required to provide the tuned

Downloaded 30 May 2010 to 128.113.26.88. Redistribution subject to ASME license or copyright; see http://www.asme.org/terms/Terms_Use.cfm

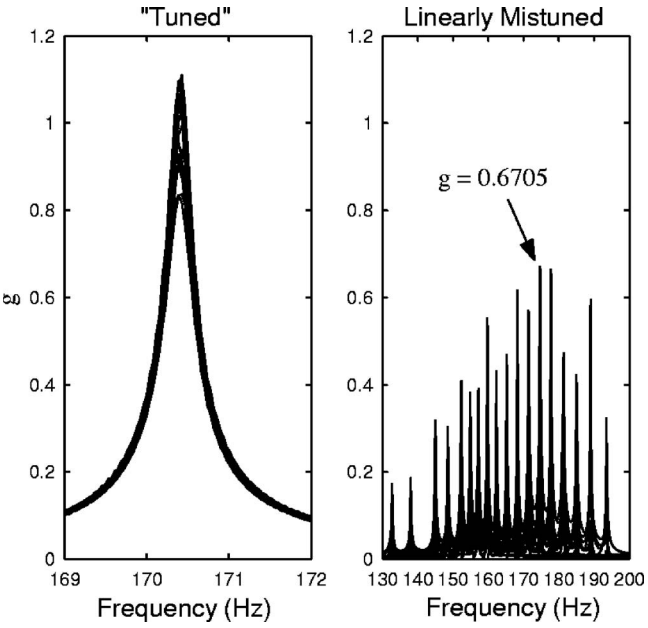

Fig. 16 Linear mistuning experimental results (*E*=4)

maximum response reference needed to calculate amplitude magnification. Therefore, a tuned bladed disk forced response experiment was also conducted on the bladed disk with masses added such that all sector frequencies were approximately 12% below nominal. The mistuning was iteratively identified using FMMID and corrected to produce as close to a perfectly tuned bladed disk as possible.

The tuned and mistuned experiments were designed to produce maximum responses at approximately the same frequency, so that any effect of frequency dependent damping on the maximum response could be ignored. Similarly, the blade excitation force amplitudes were adjusted, so that the tuned and mistuned maximum forced response amplitudes were approximately the same. Therefore, the damping could be assumed to be the same in the two experiments even if damping was amplitude dependent. The amplitude magnification was then computed from the ratio of the maximum mistuned response over the maximum tuned response, where the responses were actually the frequency response functions between the measured response and the excitation amplitude.

4.4 Experimental Results. The results of the two experiments are shown in Fig. 16. Because the tuned responses in Fig. 16 show some peak splitting and variation in blade response amplitudes due to small amounts of mistuning, the true tuned maximum response had to be estimated from the experimental tuned responses. Kenyon [19] used MacBain and Whaley's theory on peak splitting [20] to extract the true tuned maximum forced response amplitude from similar experimental data. Using this method and normalizing the tuned and mistuned responses by the true maximum tuned response, linear mistuning was found to produce an amplitude magnification of 0.6705, which is within 0.5% of the FMM predicted amplitude magnification of 0.6739.

5 Conclusions

This paper solved for the mistuning the required to minimize the maximum modal force, which is closely related to producing a low amplitude magnification in a bladed disk forced response. The problem was simplified by assuming that damping was small enough such that the maximum response was dominated by a single mode. It was found that to minimize amplitude magnification, every mode in the family needed to produce low modal force and to have an extended mode shape. An infinite linear mistuning pattern with engine order $N/4$ was shown to minimize the maximum modal force by making the mode shapes shifted versions of each other, resulting in all normalized modal forces equaling $\sqrt{1/N}$. The infinite linear mistuning pattern was truncated to produce a linear mistuning pattern that approximately minimizes the maximum modal force for bladed disks with finite N. The effectiveness of linear mistuning is limited to engine orders near $N/4$ because engine orders near N and $N/2$ tend to excite nonshifted modes with large participation in blades near the truncation, resulting in larger modal forces. Finally, a lower boundary for amplitude magnification was proposed to be $\sqrt{2/N}$.

The effectiveness of linear mistuning in minimizing maximum response was investigated numerically using a spring mass model. It was found that linear mistuning compared very favorably to the population of similarly sized mistuning patterns, producing the lowest amplitude magnification of 100,000 randomly generated others. In addition, numerical optimizations were unable to produce a lower maximum response compared to the linear mistuning pattern, except when the optimization used the linear mistuning pattern as its starting point. Even in this case, the numerical optimization made a modest further reduction in amplitude magnification, from 0.696 to 0.660, and the optimized mistuning pattern still closely resembled the linear mistuning pattern. Therefore, it was concluded that linear mistuning may be a reasonable approximate solution for the minimum amplitude magnification.

Linear mistuning was then shown to be effective for nearly all realizations of the spring mass model, regardless of the coupling, damping, or number of blades. Linear mistuning was shown to be most effective when the damping approached zero and the assumption of maximum response, being dominated by a single mode, was fully satisfied. As N approached infinity, the amplitude magnification of a linearly mistuned bladed disk approached zero, as predicted. Also, linear mistuning amplitude magnifications showed a similar behavior to the proposed $\sqrt{2/N}$ lower boundary for amplitude magnification.

Since the development of linear mistuning did not rely on any particular bladed disk model, linear mistuning should apply to many different bladed disks with isolated families of modes. In addition to the spring mass model simulations, this was confirmed by a numerical demonstration of linear mistuning on a FEM of a realistic bladed disk, resulting in an amplitude magnification of 0.753. An amplitude magnification of 0.671 was also experimentally demonstrated on a simple geometry bladed disk.

Acknowledgment

This work was supported by a grant from the Air Force Office of Scientific Research. The author would like to give special thanks to Dr. James Kenyon of the Air Force Research Laboratory for many fruitful discussions on the topics of mistuning and reducing amplitude magnification. Specifically, the author is indebted to Dr. Kenyon for his recognition that the success of linear mistuning in reducing amplitude magnification was related to the fact that it distorted the modes such that they had equal nodal diameter
content.

Appendix A

If the modal vectors are normalized such that they have a unit magnitude, then Eq. (17) becomes

$$g_{jn}^{*} = \sqrt{N}|\phi_{jn}\hat{\boldsymbol{\phi}}_n^H\hat{\mathbf{b}}| \tag{A1}$$

or using the definition of normalized modal force in Eq. (20),

Downloaded 30 May 2010 to 128.113.26.88. Redistribution subject to ASME license or copyright; see http://www.asme.org/terms/Terms_Use.cfm

$$g_{jn}^{*} = \sqrt{N}|\phi_{jn} Q_n^{\text{norm}}| \tag{A2}$$

Now, consider the sum of the squares of all g^{*}'s,

$$\sum_{n=0}^{N-1}\sum_{j=0}^{N-1} g_{jn}^{*2} = \sum_{n=0}^{N-1}\sum_{j=0}^{N-1} N|\phi_{jn}|^2 |Q_n^{\text{norm}}|^2 \tag{A3}$$

Removing Q^{norm} from the summation on j gives

$$\sum_{n=0}^{N-1}\sum_{j=0}^{N-1} g_{jn}^{*2} = N\sum_{n=0}^{N-1} |Q_n^{\text{norm}}|^2 \sum_{j=0}^{N-1} |\phi_{jn}|^2 \tag{A4}$$

On the right hand side of Eq. (A4), the summation on j equals 1 by definition of a unit vector, and therefore the summation on n equals 1 by Eq. (23). Therefore,

$$\sum_{n=0}^{N-1}\sum_{j=0}^{N-1} g_{jn}^{*2} = N \tag{A5}$$

Appendix B

This appendix shows that the maximum normalized modal force is a minimum when all modal forces are equal to $\sqrt{1/N}$. First, assume that all normalized modal forces have equal magnitudes,

$$|Q_0^{\text{norm}}|^2 = |Q_1^{\text{norm}}|^2 = \cdots = |Q_{N-1}^{\text{norm}}|^2 \tag{B1}$$

Then, Eq. (23) and (B1) give

$$|Q_0^{\text{norm}}| = |Q_1^{\text{norm}}| = \cdots = |Q_{N-1}^{\text{norm}}| = \sqrt{1/N} \tag{B2}$$

Now, assume that one normalized modal force has a greater magnitude than all the others,

$$|Q_0^{\text{norm}}|^2 > |Q_n^{\text{norm}}|^2 \quad n = 1,2,\ldots,N-1 \tag{B3}$$

The inequalities in Eq. (B3) can be rewritten as equalities using scalar slack variables s_n,

$$|Q_n^{\text{norm}}|^2 = |Q_0^{\text{norm}}|^2 - s_n^2 \quad n = 1,2,\ldots,N-1 \tag{B4}$$

Then, Eq. (23) becomes

$$|Q_0^{\text{norm}}|^2 + \sum_{n=1}^{N-1} (|Q_0^{\text{norm}}|^2 - s_n^2) = 1 \tag{B5}$$

Solving for $|Q_0^{\text{norm}}|$ gives

$$|Q_0^{\text{norm}}| = \sqrt{\frac{1}{N}\left(1 + \sum_{n=1}^{N-1} s_n^2\right)} \tag{B6}$$

Since the sum of the squares of the slack variables is greater than zero, $|Q_0^{\text{norm}}| > \sqrt{1/N}$. Comparing this result to the maximum normalized modal force of $\sqrt{1/N}$, found when all normalized modal force magnitudes are equal, leads to the following conclusion. Maximum normalized modal force magnitudes are at a minimum when all normalized modal force magnitudes are equal. All other cases, where one normalized modal force magnitude is larger than all the others, produce a larger maximum normalized modal force magnitude.

Appendix C

This appendix shows how the mistuned modal damping ratios $\mathbf{z}$ can be found from the tuned modal damping ratios $\mathbf{z}^0$ and the tuned and mistuned modal matrices $\boldsymbol{\varphi}^0$ and $\boldsymbol{\varphi}$.

First, the bladed disk is assumed to be proportionally damped,

$$\mathbf{C}^0 = a\mathbf{M}^0 + b\mathbf{K}^0 \tag{C1}$$

It is also assumed that mistuning does not affect the damping matrix

$$\mathbf{C} = \mathbf{C}^0 \tag{C2}$$

The mistuned modes are assumed to be a linear combination of the tuned modes [21],

$$\boldsymbol{\varphi} = \boldsymbol{\varphi}^0 \boldsymbol{\beta} \tag{C3}$$

The tuned modal damping ratio matrix $\mathbf{Z}^0$ is defined as

$$\mathbf{Z}^0 = \boldsymbol{\varphi}^{0T} \mathbf{C}^0 \boldsymbol{\varphi}^0 \tag{C4}$$

The mistuned modal damping ratio matrix $\mathbf{Z}$ is defined as

$$\mathbf{Z} = \boldsymbol{\varphi}^T \mathbf{C} \boldsymbol{\varphi} \tag{C5}$$

Substituting Eq. (C3) into Eq. (C5), rearranging the terms, and using the definition in Eq. (C4) gives

$$\mathbf{Z} = \boldsymbol{\beta}^T \mathbf{Z}^0 \boldsymbol{\beta} \tag{C6}$$

Since $\boldsymbol{\varphi}^0$ is an invertible matrix, $\boldsymbol{\beta}$ can be written as

$$\boldsymbol{\beta} = \boldsymbol{\varphi}^{0^{-1}} \boldsymbol{\varphi} \tag{C7}$$

Substituting Eq. (C7) into Eq. (C6) gives

$$\mathbf{Z} = (\boldsymbol{\varphi}^{0^{-1}} \boldsymbol{\varphi})^T \mathbf{Z}^0 \boldsymbol{\varphi}^{0^{-1}} \boldsymbol{\varphi} \tag{C8}$$

In practice, $\mathbf{Z}$ will not be a diagonal matrix even though $\mathbf{Z}^0$ was. However, the diagonal elements are usually larger than the off-diagonal elements, so that the mistuned modal damping ratios may be taken as the diagonal elements of $\mathbf{Z}$,

$$\mathbf{z} = \text{diag}[(\boldsymbol{\phi}^{0^{-1}} \boldsymbol{\phi})^T \mathbf{Z}^0 \boldsymbol{\phi}^{0^{-1}} \boldsymbol{\phi}] \tag{C9}$$

References

[1] Garrison, B., "High Cycle Fatigue (HCF) Science and Technology Program 2000 Annual Report," Propulsion Directorate, Air Force Research Laboratory, Air Force Material Command, Wright-Patterson AFB, Report No. AFRL-PR-WP-TR-2001-2010.

[2] Srinivasan, A. V., 1997, "Flutter and Resonant Vibration Characteristics of Engine Blades," ASME J. Eng. Gas Turbines Power, **119**(4), pp. 742–775.

[3] Whitehead, D. S., 1966, "Effect of Mistuning on the Vibration of Turbomachine Blades Induced by Wakes," J. Mech. Eng. Sci., **8**(1), pp. 15–21.

[4] Whitehead, D. S., 1976, "Research Note: Effect of Mistuning on Forced Vibration of Blades With Mechanical Coupling," J. Mech. Eng. Sci., **18**(6), pp. 306–307.

[5] Whitehead, D. S., 1998, "The Maximum Factor by Which Forced Vibration of Blades Can Increase Due to Mistuning," ASME J. Eng. Gas Turbines Power, **120**(1), pp. 115–119.

[6] Kenyon, J. A., Griffin, J. H., and Feiner, D. M., 2003, "Maximum Bladed Disk Forced Response From Distortion of a Structural Mode," ASME J. Turbomach., **125**(2), pp. 352–363.

[7] Feiner, D. M., and Griffin, J. H., 2002, "A Fundamental Model of Mistuning for a Single Family of Modes," ASME J. Turbomach., **124**(4), pp. 597–605.

[8] Wei, S.-T., and Pierre, C., 1988, "Localization Phenomena in Mistuned Assemblies With Cyclic Symmetry—Part II: Forced Vibrations," ASME J. Vib., Acoust., Stress, Reliab. Des., **110**(4), pp. 439–449.

[9] Elliott, D. F., 1987, *Handbook of Digital Signal Processing Engineering Applications*, Academic, San Diego, CA, p. 34.

[10] Yang, M.-T., and Griffin, J. H., 1997, "A Normalized Modal Eigenvalue Approach for Resolving Modal Interaction," ASME J. Eng. Gas Turbines Power, **119**(3), pp. 647–650.

[11] Castanier, M. P., and Pierre, C., 1997, "Consideration on the Benefits of Intentional Blade Mistuning for the Forced Response of Turbomachinery Rotors," *Analysis and Design Issues for Modern Aerospace Vehicles*, ASME, New York, **AD-55**, pp. 419–425.

[12] Castanier, M. P., and Pierre, C., 1998, "Investigation of the Combined Effects of Intentional and Random Mistuning on the Forced Response of Bladed Disks," Paper No. AIAA-98-3720.

[13] Wei, S.-T., and Pierre, C., 1988, "Localization Phenomena in Mistuned Assemblies With Cyclic Symmetry—Part I: Free Vibrations," ASME J. Vib., Acoust., Stress, Reliab. Des., **110**(4), pp. 429–438.

[14] Judge, J., Pierre, C., and Mehmed, O., 2001, "Experimental Investigation of Mode Localization and Forced Response Amplitude Magnification for a Mistuned Bladed Disk," ASME J. Eng. Gas Turbines Power, **123**(4), pp. 940–950.

[15] Choi, B., Lentz, J., Rivas-Guerra, A., and Mignolet, M., 2003, "Optimization of Intentional Mistuning Patterns for the Reduction of the Forced Response Effects of Unintentional Mistuning: Formulation and Assessment," ASME J. Eng. Gas Turbines Power, **125**(1), pp. 131–140.

[16] Jones, K., and Cross, C., 2003, "On Antiresonance in the Forced Response of

Downloaded 30 May 2010 to 128.113.26.88. Redistribution subject to ASME license or copyright; see http://www.asme.org/terms/Terms_Use.cfm

Mistuned Bladed Disks," Shock Vib., **10**(2), pp. 135–146.
[17] Jones, K., and Cross, C., 2003, "Traveling Wave Excitation System for Bladed Disks," J. Propul. Power, **19**(1), pp. 135–141.
[18] Feiner, D. M., and Griffin, J. H., 2004, "Mistuning Identification of Bladed Disks Using a Fundamental Mistuning Model—Part I: Theory," ASME J. Turbomach., **126**(1), pp. 150–158.
[19] Kenyon, J. A., 2002, "Robust Maximum Forced Response in Mistuned Turbine Engine Bladed Disks," Ph.D. thesis, Carnegie Mellon University.
[20] MacBain, J. C., and Whaley, P. W., 1984, "Maximum Resonant Response of Mistuned Bladed Disks," ASME J. Vib., Acoust., Stress, Reliab. Des., **106**, pp. 218–223.
[21] Yang, M.-T., and Griffin, J. H., 2001, "A Reduced-Order Model of Mistuning Using a Subset of Nominal System Modes," ASME J. Eng. Gas Turbines Power, **123**(4), pp. 893–900.

Downloaded 30 May 2010 to 128.113.26.88. Redistribution subject to ASME license or copyright; see http://www.asme.org/terms/Terms_Use.cfm

Combustion Instability and Emission Control by Pulsating Fuel Injection

Christian Oliver Paschereit
Chair of Fluid Dynamics
Hermann-Föttinger-Institute,
Technical University Berlin,
10623 Berlin, Germany
e-mail: oliver.paschereit@tu-berlin.de

Ephraim Gutmark
Aerospace Engineering and Engineering
Mechanics Department,
University of Cincinnati,
Cincinnati, OH 45221-0070
e-mail: ephraim.gutmark@uc.edu

Open-loop control methodologies were used to suppress symmetric and helical thermoacoustic instabilities in an experimental low-emission swirl-stabilized gas-turbine combustor. The controllers were based on fuel (or equivalence ratio) modulations in the main premixed combustion (premixed fuel injection (PMI)) or, alternatively, in the secondary pilot fuel. PMI included symmetric and asymmetric fuel injection. The symmetric instability mode responded to symmetric excitation only when the two frequencies matched. The helical fuel injection affected the symmetric mode only at frequencies that were much higher than that of the instability mode. The asymmetric excitation required more power to obtain the same amount of reduction as that required by symmetric excitation. Unlike the symmetric excitation, which destabilized the combustion when the modulation amplitude was excessive, the asymmetric excitation yielded additional suppression as the modulation level increased. The NO_x *emissions were reduced to a greater extent by the asymmetric modulation. The second part of the investigation dealt with the control of low frequency symmetric instability and high frequency helical instability by the secondary fuel injection in a pilot flame. Adding a continuous flow of fuel into the pilot flame controlled both instabilities. However, modulating the fuel injection significantly decreased the amount of necessary fuel. The reduced secondary fuel resulted in a reduced heat generation by the pilot diffusion flame and therefore yielded lower* NO_x *emissions. The secondary fuel pulsation frequency was chosen to match the time scales typical to the central flow recirculation zone, which stabilizes the flame in the burner. Suppression of the symmetric mode pressure oscillations by up to* 20 dB *was recorded. High frequency instabilities were suppressed by* 38 dB*, and CO emissions reduced by using low frequency modulations with 10% duty cycle.* [DOI: 10.1115/1.2749292]

Introduction

Thermoacoustic instabilities and emission of pollutants, such as NO_x, CO, and soot, are two major problems in the design of power plants and propulsion systems. The large mechanical vibrations and enhanced heat transfer induced by the instabilities can damage the system and lead to total failure. The high-pressure oscillations may cause flame blowout. At the same time, designers of combustion systems have to comply with increasingly strict regulations and maintain low-emission levels. Combustion processes are quite complex and may involve spray dynamics, mixing of fuel and oxidizer, chemical reactions, heat transfer, and acoustic interaction in confined systems. The interaction between these diverse processes may lead to combustion instabilities (see reviews by Candel [1] and Kailasanath and Gutmark [2]).

The suppression of thermoacoustic instabilities while maintaining low emissions became a major challenge and a subject of extensive research in the last two decades. Passive techniques were developed to control the combustion characteristics by modifications of the fuel distribution pattern and changes in the combustor geometry (Schadow and Gutmark [3]). Active control systems, which have the potential to be more adaptable to variable operational conditions, decouple physical processes that excite combustion instabilities, such as mixing, acoustics, and heat release. They require sensors, actuators, and feedback control algorithm that are used to drive the actuators and process output from the sensors. The actuators are used to modulate the air or fuel supply to the combustor. An extensive review of active control work was published by McManus et al. [4] and, more recently, by Docquier and Candel [5].

Unsteady fuel injection was investigated as an actuation method for control systems that can potentially be adopted in full-scale power generation or propulsion applications. Langhorne et al. [6] demonstrated an active control of a 250 kW ducted flame. They obtained 12 dB reduction in peak pressure oscillations by injecting 3% additional unsteady fuel upstream of the flame holder. An active control system with spatially distributed actuators was proposed by Fung et al. [7]. They developed a model that included modulated secondary fuel injection into the combustion chamber controlled by a PI system. An adaptive active control algorithm was developed by Billoud et al. [8], who used a microphone and a photomultiplier as sensors and a driver unit coupled to the fuel supply line to modulate the fuel injection. An active control of instabilities in rocket combustors by modulating the heat release in conjunction with a unique real time identification controller was proposed by Neumeier and Zinn [9]. Menon [10] used large eddy simulation (LES) to obtain a reduction of 10 dB in the rms fluctuation level in a dump combustor with a secondary fuel injection. A pulsed secondary injection of liquid fuel was used to control oscillations in ducted premixed flames (Sivasegaram et al. [11]). They obtained 12–16 dB reduction in pressure oscillations and showed that control by oscillating liquid fuel is sensitive to atomization and the location of injection. A closed-loop active control of instabilities in a 500 kW dump combustor using a modulated liquid fuel injection was reported by Yu et al. [12]. They emphasized the importance of the injection timing of the modulated fuel relative to the formation of air vortices during instability on the droplet dispersion. McManus et al. [13] modulated the main fuel flow using a high speed solenoid valve in open-loop and closed-loop control systems aimed to study com-

Submitted to ASME for publication in the JOURNAL OF TURBOMACHINERY. Manuscript received July 21, 2005; final manuscript received January 28, 2007; published online January 25, 2008. Review conducted by Je-Chin Han.

 Copyright © 2008 by ASME

Downloaded 30 May 2010 to 128.113.26.88. Redistribution subject to ASME license or copyright; see http://www.asme.org/terms/Terms_Use.cfm

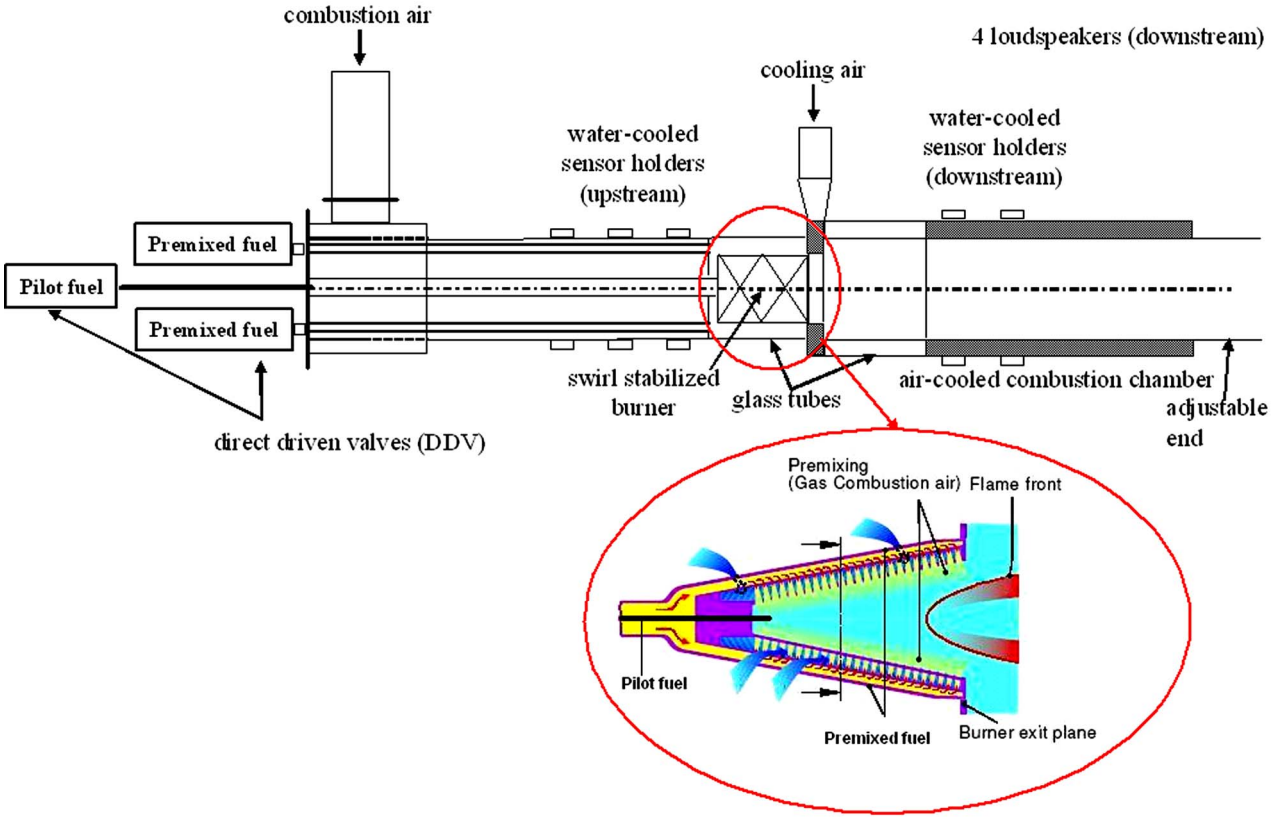

Fig. 1 Experimental facility. The figure in the inset is taken from Zajadatz et al. [27].

bustion instabilities in a simulated afterburner. Their experiments showed a strong response of the combustion process to the fuel modulations. Secondary fuel modulations were also shown to be effective in reducing combustion instabilities in gas-turbine combustors (Cohen et al. [14]).

Lubarski et al. [15] used pulsed secondary fuel injection in an open-loop control system at a nonresonant frequency to suppress thermoacoustic instabilities. Park et al. [16] developed a closed-loop control system that was based on sensing the distributed heat release by a linear array of photodetectors and pulsing the fuel using a solenoid valve. Sato et al. [17] used piezoelectric fast valves to modulate secondary fuel injection in a dump combustor configuration. The fuel was injected into the recirculation zone behind the sudden expansion. Using secondary flow of 3–5% of the main fuel, they obtained 10–20 dB reduction in flame oscillations. Yi and Gutmark [18] introduced a secondary heat release rate perturbation using a high frequency fuel valve. They developed an observer-based adaptive controller and demonstrated it in an unstable combustor that had a large system delay and two unstable modes with comparable amplitudes.

In earlier investigations, Paschereit et al. ([19–23]) studied instability modes in an experimental low-emission swirl-stabilized combustor and used acoustical control methods. They studied partially premixed-diffusion flame and premixed combustion. The diffusion flame was tuned to an unstable operation with axisymmetric and helical modes. The premixed instability mode, which was obtained by adjusting the acoustic boundary conditions, was predominantly axisymmetric. Pressure fluctuations were detected only for the axisymmetric modes, but heat release fluctuations, which were measured by OH chemiluminescence, indicated a dual mode behavior.

The present work extends the previous thermoacoustic instability control work to include a more practical (compared to acoustic excitation) fuel modulation strategy (Paschereit et al. [24]). The specific design of the experimental burner enables the testing of the effects of symmetric and antisymmetric fuel pulsations on the combustion instability modes. The tests were conducted with symmetric and helical instability modes. Open-loop control systems that modulated either the premixed fuel injection (PMI) or the secondary pilot fuel injection (SPI) were investigated, including their effect on pressure and heat release oscillations and emissions.

Experimental Setup

Combustion Facility. The combustion facility is shown in Fig. 1. The atmospheric test rig consists of a plenum chamber upstream of the swirl-inducing burner and a combustion chamber downstream of the burner. The plenum chamber contains perforated plates to reduce the turbulence level of the flow. The circular combustion chamber consists of an air-cooled double wall quartz glass to provide full visual access to the flame. The exhaust system is an air-cooled tube with the same cross section as the combustion chamber to avoid acoustic reflections at area discontinuities. The acoustic boundary conditions of the exhaust system could be adjusted from an almost anechoic (reflection coefficient $|r| < 0.15$) to an open end reflection. An experimental swirl-stabilized premixed burner was used. A detailed cross section of the burner is shown in the inset in Fig. 1. The burner's body comprises two displaced half cones with air entering the inner volume through two longitudinal slots (Doebbeling et al. [25]). The premixed operation is accomplished by injecting the fuel through multiple holes in the two premixed fuel channels that are placed along the slots. The pilot fuel can be injected at the vertex of the cone. The flame was stabilized in a recirculation region near the burner outlet. The burner was operated at atmospheric conditions. A controlled excitation of the burner was achieved by modulating the PMI or the SPI using direct driven valves which have high frequency response ($f > 200$ Hz). Two different instability modes were excited and tested in this paper: a low symmet-

Downloaded 30 May 2010 to 128.113.26.88. Redistribution subject to ASME license or copyright; see http://www.asme.org/terms/Terms_Use.cfm

ric instability at a normalized frequency of St=0.58, and helical low frequency instability at St=1.16 and a high frequency instability at St=7.77 (Paschereit et al. [19]). The specific design of the experimental burner allowed for symmetric and antisymmetric fuel injection schemes. For premixing fuel excitation, two direct driven valves were mounted and were driven at 0 deg phase difference (symmetric excitation) or 180 deg phase difference. Pressure fluctuations were measured using Brüel & Kjær water-cooled microphones, which were mounted on the sidewall of the combustor. Time varying heat release was recorded using a pair of filtered fiber optic probes, which detected the OH radiation. Since the OH data were acquired at two fixed locations (centerline and shear layer), they intend to show qualitative local trends of heat release pattern rather than overall changes in the combustor heat release. All the data presented in this paper were normalized by the base line values (steady fuel flow without control by fuel modulations) obtained at the same test conditions.

Control System. Two open-loop active control systems were utilized: one controlled the PMI and another controlled the SPI. The total fuel input was kept constant during the secondary fuel injection. In the premixed open-loop operation, the amplified output of a signal generator was used to drive the valves in a range of forcing frequencies. The driving signal consisted of dc and ac components that could be independently set. The dc voltage determined the amount of continuous fuel injection, while the ac amplitude determined the amount of fuel modulations and the rms level of the forcing amplitude F. In the SPI experiments, modulated fuel was injected into the pilot flame in addition to continuous fuel supply to the premixed combustion. The duty cycle of the secondary fuel injection was varied by changing the length of time that the valve was open during each modulation period.

Phase locked images of the flame were obtained using an amplified (microchannel plate) charge coupled device (CCD) camera with an exposure time of 20 μs. The camera was triggered by using either the pressure or OH signals which were bandpass filtered at the instability frequency and phase shifted. The images were filtered using a bandpass filter with low and high cutoff wavelengths of 290 nm and 390 nm, respectively. The phase locked exposures were then averaged over 64 events. The operating conditions of the burner have been maintained by analyzing the exhaust gas composition using a physical gas analysis system. The nitric oxides NO and NO_2, combined in NO_x, have been detected with a chemiluminescence analyzer. The detection of the remaining O_2 in the exhaust gas was made, utilizing the paramagnetic properties of oxygen in the analyzing device. Unburned hydrocarbons (UHCs) have been analyzed by a flame ionization detector. All emissions were measured in ppm units.

Structure of the Instability

Three different thermoacoustic instability modes were forced to occur by adjusting the acoustic boundary conditions for different combustor operating conditions. All the instability modes were related to combustion within large-scale structures, which were excited in the combustion chamber due to interaction between various flow instabilities and the acoustic resonant modes of the combustor, as determined by the combustion chamber acoustic boundary conditions. The instabilities associated with the premixed mode of operation were at a normalized frequency St $=fD/\bar{U}=0.58$, which was the predominant mode, where f is the instability frequency, D the burner diameter, and $\bar{U}$ the burner exit velocity. Another instability mode at St=1.16 was observed for nonreflecting boundary conditions at the combustor exit ($|r|<0.15$). The St=0.58 instability was forced to occur by increasing the reflection coefficient at the combustor exit ($|r|>0.5$) and was related to the interaction between flow instabilities and a longitudinal plane wave acoustic resonant mode. A typical level of the St=0.58 was 29 dB above the background noise level. High frequency instabilities at St=7.77 could be forced to occur with amplitudes of up to 40 dB above the background noise. This instability was excited for nonreflecting boundary conditions and with a 20% increase in operating power. It was linked to the first azimuthal acoustic mode in the combustion chamber.

The mode structure of the different instabilities was visualized using an amplified and filtered CCD camera, which was triggered at different phase angles relative to the zero crossing of the instability pressure signal to obtain a sequence of phase locked images over one cycle of instability. Phase-averaged OH images were obtained for different modes of the thermoacoustic instabilities. The St=0.58 instability is shown in Figs. 2(*a*) and 2(*b*) at two phase angles of 0 deg and 180 deg during a premixed operation. The visualization indicated that this instability was axisymmetric and demonstrated the variable heat release during the cycle. The highest heat release as indicated by the large OH intensity was measured at a phase angle of 0 deg, while the lowest level was measured at 180 deg. A helical unstable mode was measured during a premixed operation at a normalized frequency St=1.16 (Figs. 2(*c*) and 2(*d*)). The high OH intensity shifted from the top shear layer for a phase angle of 0 deg to the bottom shear layer at 180 deg. A similar helical mode behavior was observed for the high frequency instability at St=7.77 (Figs. 2(*e*) and 2(*f*)). The three modes were associated with different flow instabilities. When the frequency of the flow instabilities matched one of the resonant acoustic modes in the combustion chamber, they were strengthened and caused periodic changes in the heat release, which further enhanced the flow instabilities. This feedback loop was the underlying mechanism for the excitation of the thermoacoustic instabilities.

Results and Discussion

Open-loop active control tests were performed in a premixed combustion mode by modulating the fuel injection through the PMI ports and by modulating SPI. Tests were performed at lean equivalence ratio conditions. The fuel to air mixture ratio was varied by 20%, relative to the nominal operating conditions. Most of the tests were performed when the combustor was destabilized in the axisymmetric mode at a normalized frequency of St=0.58. Some tests were repeated with excited high frequency helical mode of St=7.77. In all tests, the pressure fluctuations were monitored using a microphone which was placed near the dump plane. OH chemiluminescence was measured at a distance of $x/D=0.046$ from the burner exit, on the combustor centerline, and in the shear layer. Emissions of NO_x, CO, and UHCs were measured at the combustor exhaust.

Premixed Combustion Open-Loop Control

Symmetric Fuel Pulsations. Tests were performed during the onset of symmetric mode combustion instability at St=0.58. The response of the combustion oscillations to fuel modulation was determined by pulsating the fuel at normalized frequencies between $0<\mathrm{St}<2.15$. The rms of the forcing amplitude was fixed at $F/F_{\max}=15\%$ for all forcing frequencies, where $F_{\max}$ corresponds to a forcing level that induced 100% fuel modulations (Fig. 3).

The pressure fluctuations remained essentially unchanged in the entire range of frequencies except near the instability frequency in the range of $0.54<\mathrm{St}<0.70$. Fuel pulsations at this frequency reduced the oscillations by more than 10 dB. A similar behavior was observed for the OH fluctuations in the shear layer and the centerline. However, the shear layer OH detector measured an initial reduction of heat release oscillations at a normalized frequency of St=0.27. A small reduction of the OH fluctuation levels was measured at Strouhal numbers above 0.8, particularly along the combustor's centerline. Once the most effective symmetric fuel injection frequency was determined in the open-loop system, the pulsation amplitude was varied at that frequency, i.e., St =0.61 (Fig. 4). The most effective suppression of both the pres-

Downloaded 30 May 2010 to 128.113.26.88. Redistribution subject to ASME license or copyright; see http://www.asme.org/terms/Terms_Use.cfm

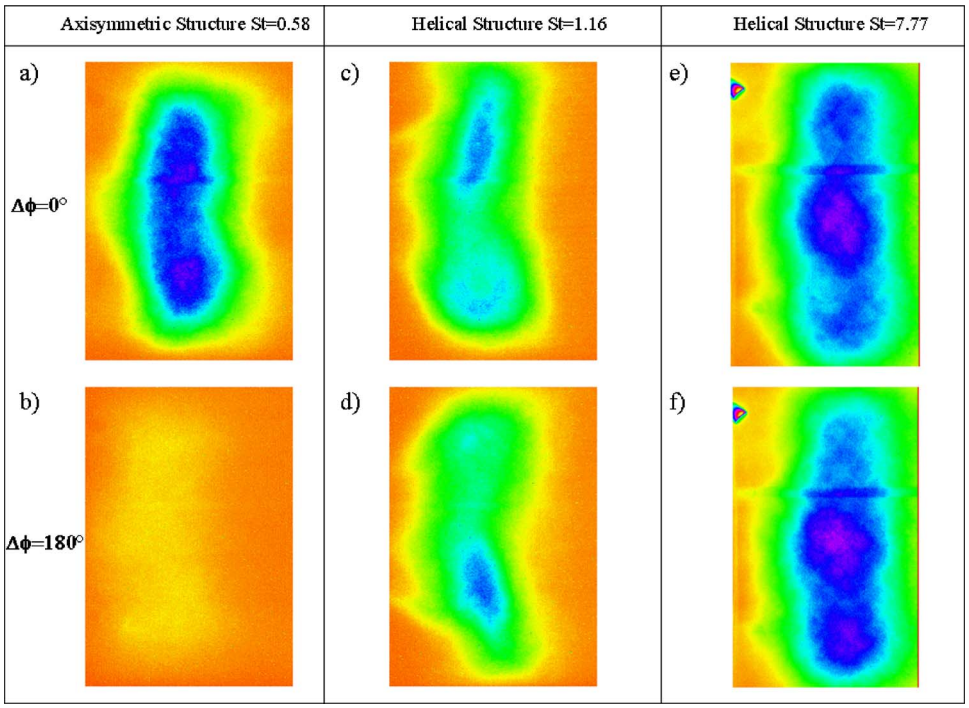

Fig. 2 Visualization of phase averaged OH images at two phase angles of 0 deg and 180 deg. (*a*), (*b*) Axisymmetric structure (premixed, St=0.58). (*c*), (*d*) Helical structure (premixed, St =1.16). (*e*), (*f*) Helical structure (premixed flame, St=7.77).

sure and heat release fluctuations was obtained at a forcing amplitude of $F/F_{max}=15\%$. The reduction in oscillation amplitude was initially proportional to the increase in pulsation amplitude. However, a further increase of the amplitude resulted in a corresponding increase in the amplitude of the pressure and OH fluctuations. The recovery of the oscillation's intensity was particularly noticeable in the OH measurements. The initial suppression was likely caused by a mismatch of the fuel injection phase to that of the instability in the swirling flow environment. However, a further increase in the forcing amplitude caused locking of the unstable mode, since the forcing frequency matched that of the instability frequency.

A small decrease in NO_x production was measured at the Strouhal number that yielded the highest reduction in pressure oscillations ($St>0.61$) and a progressively large decrease was obtained at Strouhal numbers above $St>1.7$ (Fig. 5). Since the combustor pressure remained essentially atmospheric during the tests, the changes in NO_x production were mainly due to modified temperature distribution as a result of changes in fuel distribution, mixing patterns, and heat release locations. The amount of CO in the exhaust gases increased slightly at low level forcing. At higher forcing amplitudes ($F/F_{max}=25\%$), for which the pressure fluctuations increased, the CO emission was reduced by up to 13%, indicative of more complete combustion at that forcing level.

Antisymmetric Fuel Pulsations. Open-loop control tests were repeated with an antisymmetric pulsed fuel injection. The response to different forcing frequencies is depicted in Fig. 6. The measurements were performed for the symmetric instability mode, and the forcing amplitude was $F/F_{max}=50\%$. Since antisymmetric

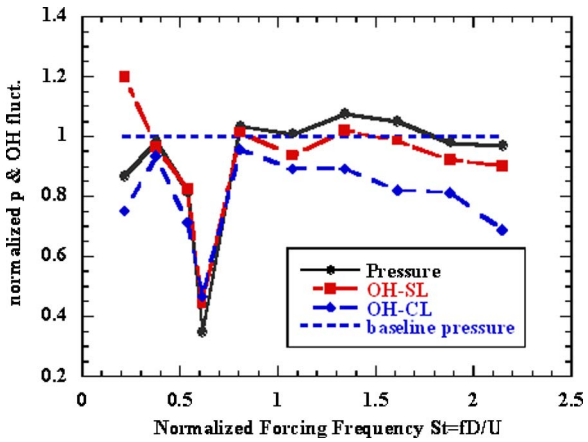

Fig. 3 Frequency response of pressure and OH fluctuations to an open-loop controller with a symmetric pulsed fuel injection ($F/F_{max}=15\%$)

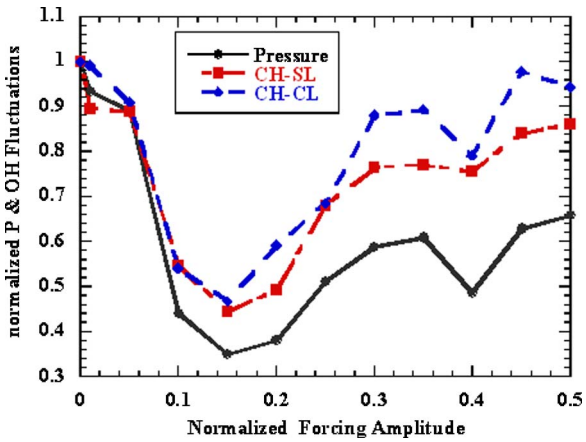

Fig. 4 Amplitude response of pressure and OH fluctuations to an open loop-controller with a symmetric pulsed fuel injection (St=0.61)

Downloaded 30 May 2010 to 128.113.26.88. Redistribution subject to ASME license or copyright; see http://www.asme.org/terms/Terms_Use.cfm

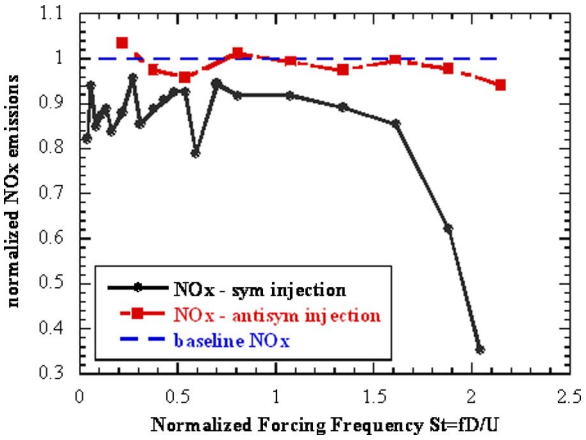

Fig. 5 NO_x emissions as a function of frequency using an open-loop controller with a symmetric pulsed fuel injection (F/F_{max}=15%) and with an antisymmetric pulsed fuel injection (F/F_{max}=50%)

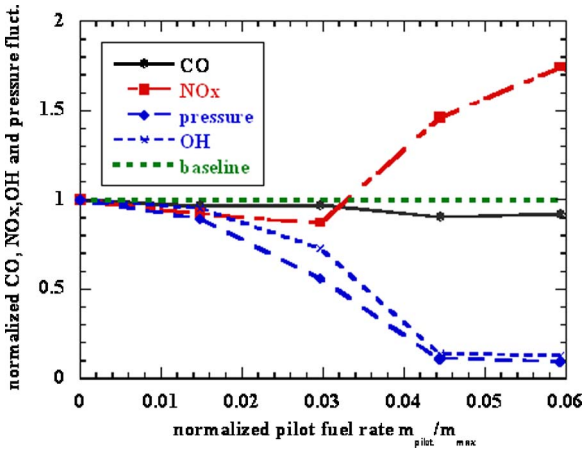

Fig. 7 Suppression of pressure and OH fluctuations by SPI and its effect on NO_x and CO emissions

forcing was applied here to suppress symmetric instability, the forcing level was significantly higher than that of the symmetric excitation (50% compared to 15%), indicative of a less effective method. The pressure and OH fluctuations remained close to the uncontrolled level up to a forcing frequency of St=1.88. At an injection frequency of St=2.05, the pressure oscillations were reduced by nearly 24 dB. A small decrease of 6 dB was also documented at a frequency of St=0.59, corresponding to the unstable frequency. It is conjectured that the high frequency suppression is related to the interference with the formation of coherent vortices in the shear layer, as proposed by Huang and Ho (1990)[26]. The suppression at the instability frequency could be attributed to antisymmetric fuel injection which interferes with the periodic heat release of the symmetric mode. The necessary pulsation amplitude was determined to be at least F/F_{max}=45% for a forcing frequency of St>2.

NO_x was slightly reduced for all forcing frequencies, with the largest reduction measured at the frequency which was also most efficient in the suppression of pressure oscillations (Fig. 5). The present results show a simultaneous reduction of pressure oscillations and of NO_x emissions. The NO_x emission level depend exponentially on temperature. Due to this exponential dependency, the average emissions are higher than their level at the operating point for steady state conditions. Therefore, in an unstable lean premixed combustion, fluctuations in heat release and, consequently, in temperature may lead to increase in NO_x emissions. By stabilizing the combustion process, it was possible to decrease NO_x emission levels.

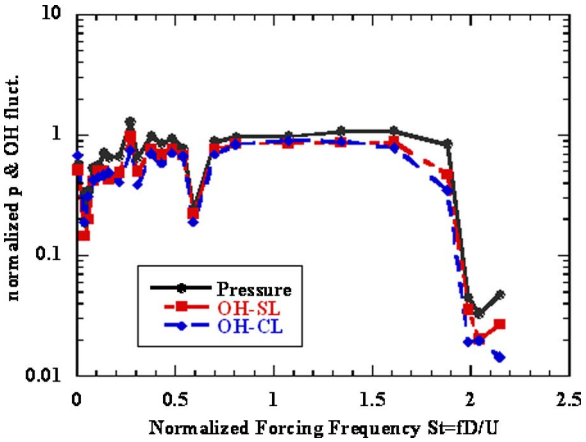

Fig. 6 Frequency response of pressure and OH fluctuations to an open-loop controller with an antisymmetric pulsed fuel injection (F/F_{max}=50%)

Control of Symmetric Instability by Pilot Flame Modulations. The axisymmetric instability mode (St=0.58) was stabilized by injecting secondary fuel into a pilot diffusion flame. The level of the pressure and OH fluctuations decreased with increased secondary fuel mass flow rate, until a low plateau was reached for 4.4% pilot fuel addition (Fig. 7). At this point, the axisymmetric instability was reduced by 20 dB. It is usually undesirable to add a diffusion flame to a premixed combustion due to a potential increase in emissions. In the present case, NO_x emissions decreased while the secondary fuel addition was less than 3% and rapidly increased as the amount of secondary fuel exceeded this level (Fig. 7). Concurrently, the amount of CO decreased slightly with an increase in secondary fuel, indicating improved combustion efficiency (Fig. 7).

To minimize the amount of fuel injected into the pilot flame, pulsed injection at very low frequencies relative to the instability frequency was utilized. The low frequency pulsations were adjusted to be in a range commensurate with the time scales associated with the growth rate of the instability, i.e., corresponding to number of instability cycles during the transition from linear growth to limit cycle. The pulsed injection also enabled modification of the duty cycle to minimize the total amount of secondary fuel injected while maintaining sufficient heat release at each injection cycle. An illustration of the mode of operation of this controller is depicted in Fig. 8, where the time traces of the pressure signal (solid line) are shown with the control signal (dashed square wave) that opens and closes the pilot fuel injector. The pilot fuel injector is shown to be open 20% of the cycle when the voltage is positive. The interval between pulses allows an occasional onset of combustion instability, as manifested by the exponential increase of the pressure oscillation amplitude. The pilot fuel injection suppresses the instability within a few instability cycles. The forcing frequency is thus determined from the rise time of the combustion instability and has to be large enough to prevent the instability from reaching a saturation level or any other predetermined unacceptable amplitude.

The fuel flow rate was set at an intermediate level of 4.4% such that the increase in NO_x will not be excessive, and the duty cycle was fixed at 20%. The pressure and OH fluctuation levels decreased monotonically with increasing normalized frequency (Strouhal number), until they reached a flat minimum level at St =0.065, yielding a suppression level of over 20 dB (Fig. 9). The base line level in this figure is the fluctuations level with the

Downloaded 30 May 2010 to 128.113.26.88. Redistribution subject to ASME license or copyright; see http://www.asme.org/terms/Terms_Use.cfm

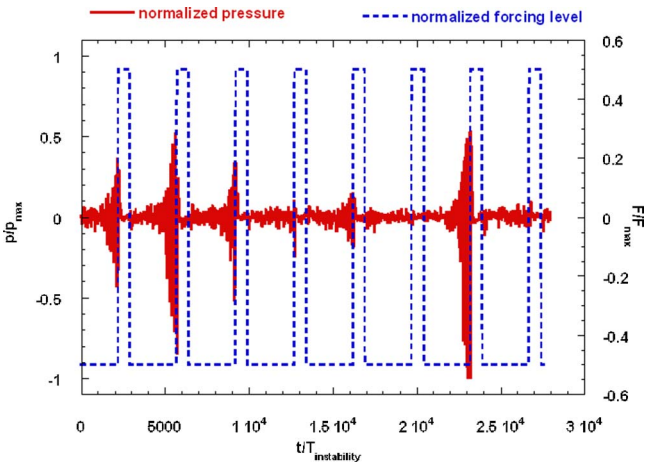

Fig. 8 Temporal combustion-pressure variation during the control of the periodical onset of high frequency instability by pulsed secondary fuel injection. 20% duty cycle.

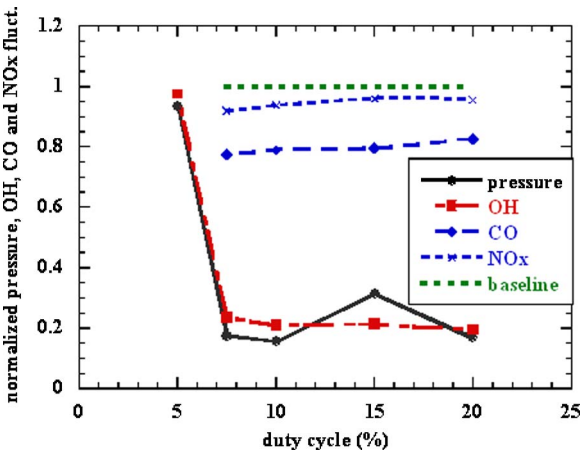

Fig. 10 Variation of pressure and OH fluctuations, and NO_x and CO emissions as a function of the duty cycle. Secondary fuel at 4.4% and forcing frequency: St=0.066.

continuous secondary fuel injection at the same flow rate. Emissions of NO_x increased at the lowest pulsation frequency, followed by a continuous decrease with increasing frequency until reaching a lower level than the reference conditions for St >0.055 (Fig. 9). CO emissions exhibited a similar behavior, except that the CO level decreased below the base line for St >0.01.

Changes in duty cycle were tested at two forcing frequencies: a low normalized frequency of St=0.022, which reduced the pressure fluctuations by 4.5 dB at a duty cycle of 20%, and a higher frequency of 0.066 Hz, which yielded nearly 14 dB reduction at the same conditions. The low frequency was tested, varying the duty cycles from 20% to 80%. There was no effect of the lengthened duty cycle on the amplitude of the pressure and OH fluctuations up to a duty cycle of 40%. At a higher duty cycle, the oscillations decreased continually, reaching a level of 1/3 of the initial value at 80% duty cycle. NO_x emissions increased for low duty cycles and decreased to a level below the base line at 80%, and CO emissions decreased for all duty cycles.

A forcing frequency frequency of St=0.066 was tested at duty cycles between 5% and 20% (Fig. 10). This forcing frequency was effective in reducing the pressure fluctuations by 14 dB even at a short duty cycle of 7.5%. The same suppression level was maintained at longer duty cycles. Both NO_x and CO emissions were reduced for all duty cycles tested by an average of 5% and 20%, respectively (Fig. 10).

The effect of changing the equivalence ratio and combustion power on the suppression level was tested at optimal pulsation conditions of a normalized frequency of St=0.066, 10% duty cycle, and 4.4% secondary fuel injection. The results were also compared to the effect of continuous secondary fuel injection. The normalized equivalence ratio (normalized by the nominal equivalence ratio of the combustor) was varied from $0.83<\Phi/\Phi_n<1.18$ (Fig. 11). The controlled pressure oscillations were nearly independent of the equivalence ratio, unlike the base line case for which the pressure oscillations peaked at $\Phi/\Phi_n=0.95$. The difference between continuous and pulsating injection was minimal. For $0.85<\Phi/\Phi_n<1.05$, continuous injection was slightly more effective, but required ten times more fuel to obtain the same results. No significant difference was detected in the UHC between the continuous and pulsed injection. For lean mixtures ($\Phi/\Phi_n<1.1$), the heat release intensity and, therefore, OH chemiluminescence fluctuations were low, and they increased with increased normalized equivalence ratio in the uncontrolled combustion (Fig. 12). The secondary fuel injection reduced their normalized level by 60–80%. There was no notable difference between the results of the continuous secondary fuel injection and the pulsating injection. The proportional increase in temperature

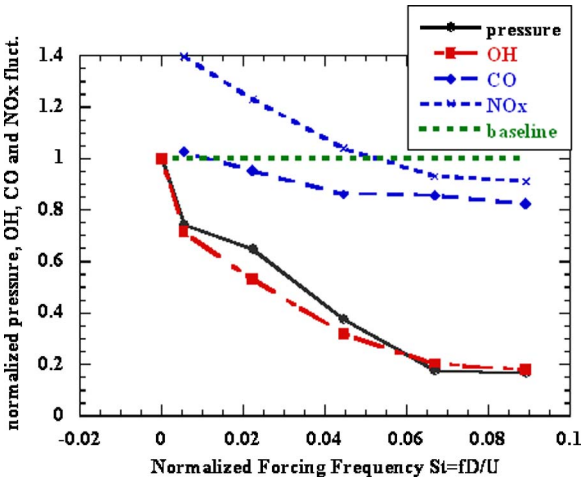

Fig. 9 Response of pressure and OH fluctuations to modulations of pilot flame, and the effect on NO_x and CO emissions. Pilot fuel at 20% duty cycle.

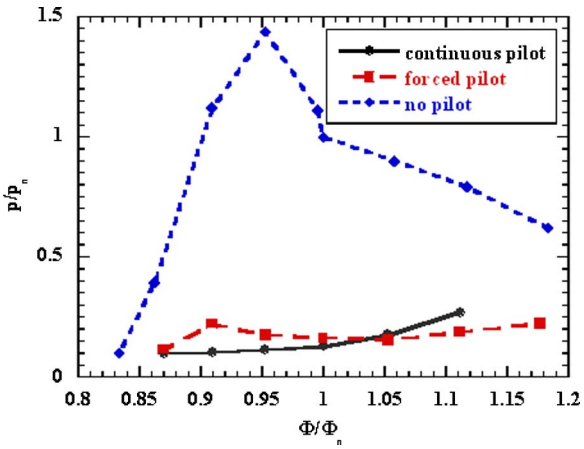

Fig. 11 Variation of pressure fluctuations with an equivalence ratio for continuous and pulsed secondary fuel injection. Secondary fuel flow rate of 4.4%, 10% duty cycle, and St=0.066.

Downloaded 30 May 2010 to 128.113.26.88. Redistribution subject to ASME license or copyright; see http://www.asme.org/terms/Terms_Use.cfm

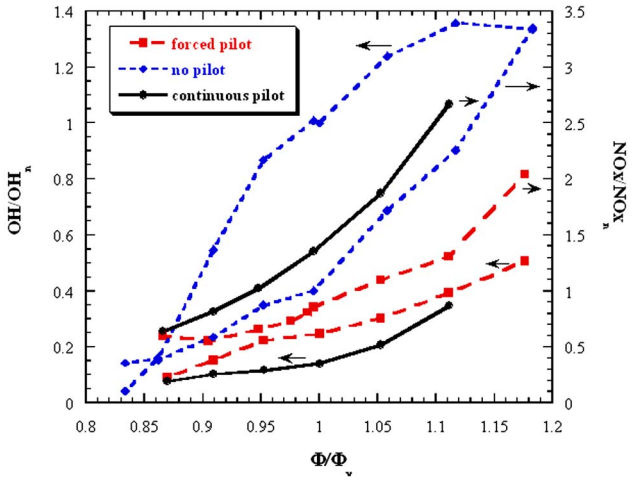

Fig. 12 Variation of NO_x and OH fluctuations with an equivalence ratio for continuous and pulsed secondary fuel injection. Secondary fuel flow rate of 4.4%, 10% duty cycle, and St =0.066.

with the heat release for a higher equivalence ratio resulted in a commensurate increase in NO_x (Fig. 12). At the small amount of 4.4% secondary fuel injection, the NO_x emissions were only marginally increased with continuous fuel injection. With pulsating injection, NO_x emissions were reduced for all $\Phi/\Phi_n > 0.91$.

CO emission was not affected by the pulsating secondary fuel injection. For continuous injection, it was significantly reduced by the pilot fuel at the low normalized equivalence ratio range ($\Phi/\Phi_n < 0.95$) (Fig. 13). The sudden increase of CO at low equivalence ratios is indicative of the loss of flame anchoring, resulting in a subsequent liftoff of the flame. The small amount of secondary continuous fuel enhanced the flame stabilization at the burner exit and thus led to a decrease in CO.

The pilot fuel pulsations were effective for an increase of 20% in the nominal combustion power. The suppression level was higher at the nominal power compared to higher power levels at which the base line instability was reduced (Fig. 14).

Control of Helical High Frequency Instability by Pilot Flame Modulations. High frequency helical instability at St =7.77 was excited at a normalized power of $P/P_n = 1.14$ and nominal equivalence ratio. Continuous fuel injection into the pilot diffusion flame was used to stabilize this mode. The pressure and

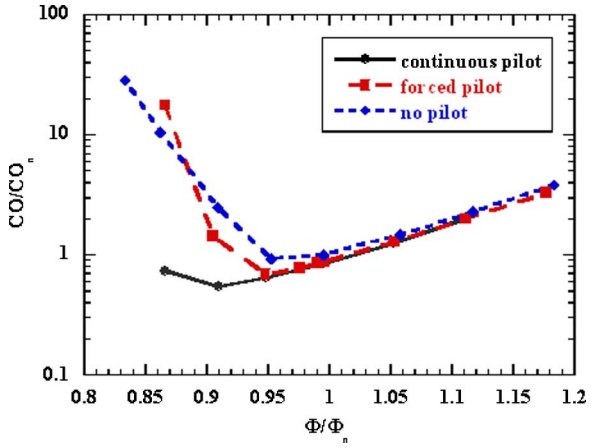

Fig. 13 Variation of CO with an equivalence ratio for continuous and pulsed secondary fuel injection. Secondary fuel flow rate of 4.4%, 10% duty cycle, and St=0.066.

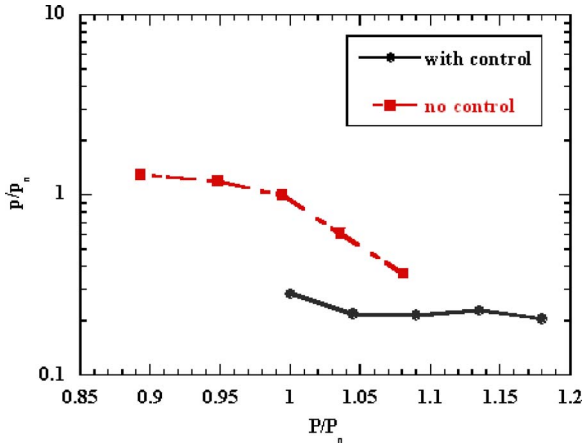

Fig. 14 Variation of pressure oscillations with a combustion power at a nominal equivalence ratio. Secondary fuel flow rate of 4.4%, 10% duty cycle, and St=0.066.

OH fluctuations remained unchanged up to a threshold of 2.8% secondary fuel injection. At that point, an abrupt reduction of 22.5 dB was measured. Above this level of fuel injection, the amplitude of the pressure and OH oscillations was reduced proportionally to the fuel flow rate until 38 dB was achieved at 5.6% (Fig. 15). Pilot fuel addition resulted in the reduction of CO emissions by up to 11%.

To minimize the amount of fuel utilized in the pilot diffusion flame, the secondary fuel was injected periodically at varying frequencies with a duty cycle of 20% (Fig. 16). A continuous reduction in pressure fluctuations was obtained with increasing pulsation frequency. A maximum suppression of 32 dB was measured at a normalized frequency of St=0.0056.

Duty-cycle variation at a forcing frequency of St=0.0022 showed that at least 10% duration of pilot fuel injection was needed to effectively control this instability.

Summary and Conclusions

Premixed fuel modulations, which cause equivalence ratio modulations, and secondary pilot fuel pulsations were used to control thermoacoustic instabilities in an experimental swirl-stabilized gas-turbine combustor. The instabilities included symmetric and helical modes.

The first series of tests included an open-loop control by modulating part of the premixed fuel. Two methods of fuel injection modulations were tested: symmetric and asymmetric injection.

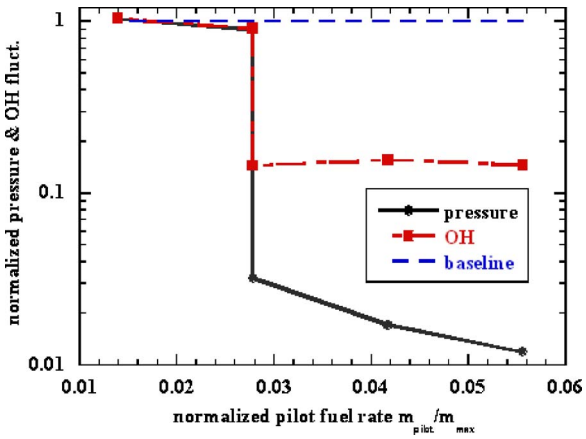

Fig. 15 Suppression of high frequency pressure and OH fluctuations by continuous pilot fuel injection

Downloaded 30 May 2010 to 128.113.26.88. Redistribution subject to ASME license or copyright; see http://www.asme.org/terms/Terms_Use.cfm

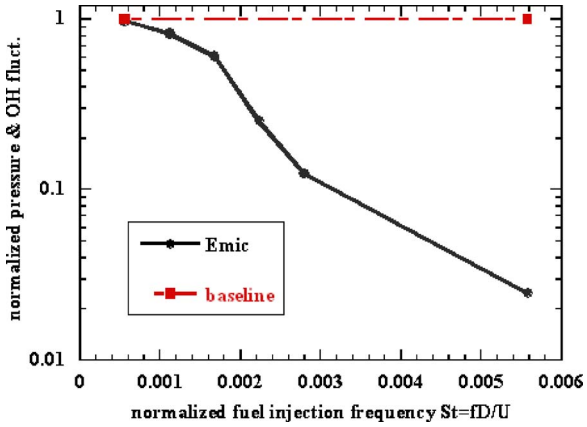

Fig. 16 Response of high frequency pressure and OH fluctuations to modulations of pilot flame. Pilot fuel at 20% duty cycle.

This control method is not only more practical than the previously tested acoustic control but was also shown here to be more effective. The fuel was modulated at a wide range of frequencies, and the response of the combustion process was determined from the resulting amplitude of the pressure and OH oscillations. It was found that the symmetric mode responded to symmetric excitation only when the two were at the nearly same frequency range. Thus, this method could be applied only at a very narrow range of frequencies. The asymmetric fuel injection affected the symmetric mode only at frequencies that were at least four times higher than the instability mode. Due to the limitation in the frequency response of the fuel modulation system, it was not possible to modulate the fuel effectively at higher frequencies. Therefore, the full range of frequencies at which this method can be applied could not be determined. The response of combustion when the modulating frequency matched the instability was minimal. The asymmetric excitation required more power to obtain the same amount of reduction than that which was required by symmetric excitation. But unlike the symmetric excitation, which destabilized the combustion when the modulation amplitude was excessive, the asymmetric excitation yielded additional suppression at higher modulation levels. The NO_x emissions were reduced to a greater extent by the asymmetric modulation.

The second open-loop control system utilized modulations of a secondary pilot flame. Control of low frequency symmetric instability and high frequency helical instability was investigated. Adding a continuous flow of fuel into the pilot flame controlled both instabilities. However, modulating the fuel injection significantly decreased the amount of needed fuel. The reduced secondary fuel resulted in a reduced heat release by the pilot flame and therefore yielded lower NO_x emissions. The pulsation frequency was chosen to match the time scales typical to the central flow recirculation zone that is used to stabilize the flame in the burner. Low frequency required a longer duty cycle, while at high frequency modulations a duty cycle of less than 10% was necessary. Suppression of pressure oscillations by up to 20 dB was recorded.

High frequency instabilities were suppressed by 38 dB and CO emissions reduced by using low frequency modulations with 10% duty cycle. The forcing frequency was determined by the typical rise time of the high frequency instabilities. A brief injection of secondary fuel was sufficient to suppress the instability before it reached a predetermined threshold.

Acknowledgment

We gratefully acknowledge the support of Dr. J. Hellat and Dr. K. Doebbeling, ALSTOM (Switzerland) Ltd. in carrying out this research.

References

[1] Candel, S. M., 1992, "Combustion Instabilities Coupled by Pressure Waves and Their Active Control," *Proceedings of the Combustion Institute*, The Combustion Institute, Vol. 24.
[2] Kailasanath, K., and Gutmark, E. J., 1998, "Combustion Instability," *Propulsion Combustion: Fuels to Emissions*, G. Roy, ed., Taylor and Francis, London.
[3] Schadow, K., and Gutmark, E. J., 1992, "Combustion Instability Related to Vortex Shedding in Dump Combustors and Their Passive Control," Prog. Energy Combust. Sci., **18**, pp. 117–132.
[4] McManus, K. R., Poinsot, T., and Candel, S. M., 1993, "A Review of Active Control of Combustion Instabilities," Prog. Energy Combust. Sci., **19**, pp. 1–29.
[5] Docquier, N., and Candel, S., 2002, "Combustion Control and Sensors: A Review," Prog. Energy Combust. Sci., **28**, pp. 107–150.
[6] Langhorne, P. J., Dowling, A. P., and Hooper, N., 1990, "Practical Active Control System for Combustion Oscillations," J. Propul. Power, **6**, pp. 324–333.
[7] Fung, Y. T., Yang, V., and Sinha, A., 1991, "Active Control of Combustion Instabilities With Distributed Actuators," Combust. Sci. Technol., **78**, pp. 217–245.
[8] Billoud, G., Galland, M. A., Huy, C. H., and Candel, S., 1991, "Adaptive Active Control of Instabilities," J. Intell. Mater. Syst. Struct., **2**, pp. 457–471.
[9] Neumeier, Y., and Zinn, B. T., 1994, "Active Control of Combustion Instabilities Using Real Time Identification of Unstable Combustor Modes," *Proceedings of the Combustion Institute*, The Combustion Institute, Vol. 25.
[10] Menon, S., 1991, "Active Control of Combustion Instability in a Ramjet Using Large-Eddy Simulations," Paper No. AIAA-91-0411.
[11] Sivasegaram, S., Tsai, R. F., and Whitelaw, J. H., 1995, "Control of Combustion Oscillations by Forced Oscillation of Part of the Fuel Supply," Combust. Sci. Technol., **105**, pp. 67–83.
[12] Yu, K., Wilson, K. J., Parr, T. P., Schadow, K. C., and Gutmark, E. J., 1996, "Active Control of Liquid Fueled Combustion Using Periodic Vortex-Droplet Interaction," *Proceedings of the Combustion Institute*, The Combustion Institute, Vol. 26.
[13] McManus, K. R., Magill, J. C., and Miller, M. F., 1998, "Combustion Instability Suppression in Liquid Fueled Combustors," Paper No. AIAA-98-0642.
[14] Cohen, M. F., Rey, N. M., Jacobsen, C. A., and Anderson, T. J., 1998, "Active Control of Combustion Instability in a Liquid-Fueled Low-NO_x Combustor," ASME Paper No. 98-GT-267.
[15] Lubarski, E., Shcherbik, A., Bibik, A., and Zinn, B., 2004, "Open Loop Control of Severe Combustion Instability by Fuel Flow Modulation at Nonresonant Frequencies," Paper No. AIAA-2004-0634.
[16] Park, S., Wachsman, A., Annaswamy, A., and Ghoniem, A., 2004, "Experimental Study of POD Based Control for Combustion Instability Using a Linear Photodiode Array," Paper No. AIAA-2004-0639.
[17] Sato, H., Yasunami, Y., Hayashi, A.-K., and Ogawa, S., 2004, "Optimization of Oscillatory Flame in a Swirler Combustor Using an Active Control Method," Paper No. AIAA-2004-640.
[18] Yi, T., and Gutmark, E., 2004, "Adaptive Control of Combustion Instability Based on Dominant Acoustic Modes Reconstruction," Paper No. AIAA-2004-751.
[19] Paschereit, C. O., Gutmark, E., and Weisenstein, W., 1998, "Structure and Control of Thermoacoustic Instabilities in a Gas-Turbine Combustor," Combust. Sci. Technol., **138**, pp. 213–232.
[20] Paschereit, C. O., Gutmark, E., and Weisenstein, W., 1998, "Control of Thermoacoustic Instabilities and Emissions in an Industrial Type Gas-Turbine Combustor," *Proceedings of the Combustion Institute*, 27, pp. 1817–1824.
[21] Paschereit, C. O., Gutmark, E., and Weisenstein, W., 1998, "Suppression of Combustion Instabilities by Acoustic Control of Shear Layer Properties," *Advances in Turbulence*, U. Frisch, ed., Kluwer Academic, Dordrecht, pp. 293–296.
[22] Paschereit, C. O., Gutmark, E., and Weisenstein, W., 1999, "Coherent Structures in Swirling Flows and Their Role in Acoustic Combustion Control," Phys. Fluids, **11**, pp. 2667–2678.
[23] Paschereit, C. O., Gutmark, E., and Weisenstein, W., 2000, "Excitation of Thermoacoustic Instabilities by the Interaction of Acoustics and Unstable Swirling Flow," AIAA J., **38**, pp. 1025–1034.
[24] Paschereit, C. O., Gutmark, E., and Weisenstein, W., 1999, "Control of Combustion Driven Oscillations by Equivalence Ratio Modulations," ASME Turbo Expo 99, Indianapolis, IN, June 7–10.
[25] Doebbeling, K., Eroglu, A., Joos, F., and Hellat, J., 1999, "Novel Technologies for Natural Gas Combustion in Turbine Systems," Eurogas 99, Ruhr University Bochum, Germany, May 25–27.
[26] Huang, L. S., and Ho, C. H., 1990, "Small Scale Transition in a Plane Mixing Layer," J. Fluid Mech., **210**, pp. 475–500.
[27] Zajadatz, M., Lachner, R., Bernero, S., Duckers, J., and Flohr, P., 2006, "Development and Design of ALSTOM's Staged Fuel Gas Injection EV Burner for NO_x Reduction," Power-Gen Europe, Kölnmesse, Cologne, Germany, May 30–June 1.

Downloaded 30 May 2010 to 128.113.26.88. Redistribution subject to ASME license or copyright; see http://www.asme.org/terms/Terms_Use.cfm

Alok Sinha
Professor
Department of Mechanical Engineering,
The Pennsylvania State University,
University Park, PA 16802

Benjamin Hall
Pratt & Whitney,
E. Hartford, CT 06108

Brice Cassenti
Associate Fellow
Pratt & Whitney,
E. Hartford, CT 06108

Gary Hilbert
Fellow
Aeromechanics and Structures,
Pratt & Whitney,
E. Hartford, CT 06108

Vibratory Parameters of Blades From Coordinate Measurement Machine Data

This paper deals with the development of a procedure to model geometric variations of blades. Specifically, vibratory parameters of blades are extracted from coordinate measurement machine (CMM) data on an integrally bladed rotor (IBR). The method is based on a proper orthogonal decomposition of CMM data, solid modeling, and finite element techniques. In addition to obtaining natural frequencies and mode shapes of each blade on an IBR, statistics of these modal parameters are also computed and characterized. Numerical results are validated by comparison with experimental results.
[DOI: 10.1115/1.2749293]

Introduction

Blades on integrally bladed rotors (IBRs) are manufactured by milling machines [1]. During this milling process, the geometry of blades deviates from the nominal geometry. This variation in the geometry of blades due to the manufacturing process is known as geometric mistuning. It is well known that the forced response of a blade can be very sensitive to geometric mistuning. Therefore, it is important to accurately model variations in vibratory parameters of blades due to geometric mistuning. Geometries of blades are measured by a coordinate measurement machine (CMM). The objective of this paper is to present a procedure for extracting vibratory parameters of blades from CMM data.

In the absence of CMM data, system identification techniques [2,3] have been developed in the literature to determine natural frequencies of mistuned blades. Blair and Annis [4] have used the sensitivity of a frequency to the variation in the nodal thickness, which is directly available in commercial finite element packages, to predict the changes in the frequency. To account for correlations among various nodal thicknesses, they have constructed variograms. Garzon and Darmofal [5], Ghiocel [6], and Brown et al. [7] have used the Karhunen–Loeve (KL) expansion method [8] to model geometric variations of blades. Garzon and Darmofal [5] have examined the sensitivities of aerodynamic performance parameters to geometric mistuning. Ghiocel [6] has characterized the statistical variations of airfoil thicknesses. In addition, he has also found that leading-edge dynamic stresses in blades can change drastically because of variations in airfoil thicknesses.

Coordinates of a blade surface are measured at many points on a selected grid. Compiling these data for all blades, statistics of coordinates can be characterized for each point. It is clear that there will be correlations among the statistics of coordinates of different points. Therefore, the KL expansion method, which involves a singular value decomposition of the covariance matrix is used to identify independent random variables. It is also of interest to determine the nature of distributions of these random variables, particularly if they are Gaussian or non-Gaussian. Deviations of blades' geometries from their mean values are quite small. Therefore, it is reasonable to expect that the relationship between a modal parameter and independent random variables can be linearized without any significant loss of accuracy. If the linearization is valid, then sensitivities or partial derivatives of modal parameters to independent random variables will be sufficient to describe the variations in modal parameters of blades due to geometric mistuning.

The relationship between CMM data and modal parameters of blades is modeled by solid modeling (UNIGRAPHICS) and finite element (ANSYS) techniques. First, a solid model of a blade is constructed from CMM data in UNIGRAPHICS. Next, this solid model is provided as an input to ANSYS for meshing, creation of mass and stiffness matrices, and computation of natural frequencies (eigenvalues) and mode shapes (eigenvectors). Thus, there are a number of numerical steps that define the mapping between CMM data and modal parameters of blades. There are some approximations involved at many of these steps; for example, the solid model is based on an interpolation technique, the computation of eigenvalues and eigenvectors would involve convergence criteria, etc. Since the variations in geometries of blades or in CMM data are small, it is important to know whether the number of samples obtained by CMM, solid modeling, and finite element techniques provide results with sufficient fidelity so as to accurately compute the variations in modal parameters of blades due to geometric mistuning.

Karhunen–Loeve/Proper Orthogonal Decomposition Expansion of Coordinate Measurement Machine Data on Integrally Bladed Rotors

Data obtained from the CMM are available in computer files. These data are measurements of blade surface coordinates at many sections of a blade, where measurements are made at many points of each section. Therefore, the number of measured coordinates of blades equals the number of sections multiplied by the number of points on each section. We define the following variables:

(1) $\boldsymbol{p}_i$: locations of points in space where blade surface coordinates are measured ($i=1,2,\ldots,nm$)
(2) nm: number of measured coordinates on a blade
(3) $\boldsymbol{v}_{sj}(\boldsymbol{p}_i)$: measured blade surface coordinates of the jth blade in the sth IBR group at $\boldsymbol{p}_i(j=1,2,\ldots,nb(s))$

Contributed by the International Gas Turbine Institute of ASME for publication in the JOURNAL OF TURBOMACHINERY. Manuscript received October 13, 2005; final manuscript received June 27, 2006; published online January 25, 2008. Review conducted by David Wisler. Paper presented at the ASME Turbo Expo 2005: Land, Sea and Air (GT2005), Reno, NV, June 6–9, 2005, Paper No. GT2005-69004.

Downloaded 30 May 2010 to 128.113.26.88. Redistribution subject to ASME license or copyright; see http://www.asme.org/terms/Terms_Use.cfm

(4) $nb(s)$: number of blades which have been measured in the sth IBR group

It should be noted that vectors $\boldsymbol{p}_i$ and $\boldsymbol{v}_j(\boldsymbol{p}_i)$ are three dimensional with x, y, and z components, i.e.,

$$\boldsymbol{p}_i = \begin{bmatrix} x_i \\ y_i \\ z_i \end{bmatrix} \tag{1a}$$

and

$$\boldsymbol{v}_{sj}(\boldsymbol{p}_i) = \begin{bmatrix} v_{si}^x \\ v_{si}^y \\ v_{si}^z \end{bmatrix} \tag{1b}$$

We define the CMM data vector for the jth blade in the sth group of IBR as

$$\boldsymbol{w}_{sj} = [\boldsymbol{v}_{sj}^T(\boldsymbol{p}_1) \ \cdots \ \boldsymbol{v}_{sj}^T(\boldsymbol{p}_{nm})]^T \quad j = 1,2, \ldots, nb(s) \tag{2}$$

The dimension of this vector is

$$nd = 3 * nm \tag{3}$$

The mean of $\boldsymbol{w}_{sj}$ is computed as

$$E(\boldsymbol{w}_s) = \frac{1}{nb(s)} \sum_{j=1}^{nb(s)} \boldsymbol{w}_{sj} \tag{4}$$

and the covariance matrix $\boldsymbol{C}_s$ is computed as follows:

$$\boldsymbol{C}_s = \frac{1}{nb(s)} \sum_{j=1}^{nb(s)} \delta\boldsymbol{w}_{sj} \delta\boldsymbol{w}_{sj}^T \tag{5}$$

where

$$\delta\boldsymbol{w}_{sj} = \boldsymbol{w}_{sj} - E(\boldsymbol{w}_s) \tag{6}$$

The order of the covariance matrix $\boldsymbol{C}_s$ is nd. Eigenvalues λ_{sj} and eigenvectors $\boldsymbol{u}_{sj}$ of the covariance matrix are related by

$$\boldsymbol{C}_s \boldsymbol{u}_{s\ell} = \lambda_{s\ell} \boldsymbol{u}_{s\ell} \quad \ell = 1,2, \ldots, nd \tag{7}$$

Then, the KL expansion (Appendix) of the CMM data is

$$\delta\boldsymbol{w}_{sj} = \sum_{\ell=0}^{nd} \xi_{s_\ell} \sqrt{\lambda_{s\ell}} \boldsymbol{u}_{s\ell} \tag{8}$$

where $\xi_{s\ell}$ are uncorrelated random variables with zero mean and unity standard deviation.

In other words,

$$E(\xi_{s\ell}) = 0 \quad E(\xi_{s\ell}^2) = 1 \tag{9}$$

and

$$E(\xi_{s\ell}\xi_{sp}) = 0 \quad \text{when} \ \ \ell \neq p \tag{10}$$

For the aforementioned example, nd=9408. Hence, the order of the matrix $\boldsymbol{C}_s$ is large and the MATLAB routine *eig* requires a large amount of computation time to determine eigenvalues and eigenvectors. For an efficient computation of these eigenvalues and eigenvectors, Eq. (5) is rewritten as

$$\boldsymbol{C}_s = \frac{1}{nb(s)} \delta W_s \delta W_s^T \tag{11}$$

where

$$\delta W_s = [\delta\boldsymbol{w}_{s1} \ \cdots \ \delta\boldsymbol{w}_{snb(s)}] \tag{12}$$

Since the dimension of δW_s is $ndxnb(s)$, and $nb(s) < nd$, the rank of the matrix $\boldsymbol{C}_s$ cannot exceed $nb(s)$. An efficient computational algorithm is developed by realizing the connection between eigenvalues of $\boldsymbol{C}_s$ and singular values of δW_s. The well-known singular value decomposition is

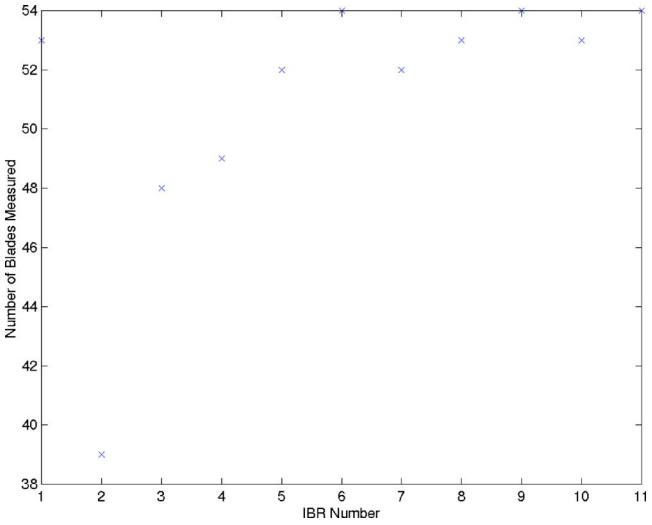

Fig. 1 Number of blades measured on an IBR

$$\delta W_s = U_s \Sigma_s V_s^T \tag{13}$$

where

$$U_s = [\boldsymbol{u}_{s1}, \ \boldsymbol{u}_{s2}, \ \cdots, \ \boldsymbol{u}_{snb(s)}] \tag{14}$$

$$V_s = [\boldsymbol{v}_{s1}, \ \boldsymbol{v}_{s2}, \ \cdots, \ \boldsymbol{v}_{snb(s)}] \tag{15}$$

$$\Sigma_s = \text{diag}[\sigma_{s1}, \ \sigma_{s2}, \ \cdots, \ \sigma_{snb(s)}] \tag{16}$$

σ_{si} is the ith singular value of δW_s. Singular values, vectors $\boldsymbol{u}_{si}$ and $\boldsymbol{v}_{si}$, are related to eigenvalues and eigenvectors of the covariance matrix as follows:

$$\delta W_s^T \delta W_s \boldsymbol{v}_{si} = \sigma_{si}^2 \boldsymbol{v}_{si} \tag{17}$$

$$\delta W_s \delta W_s^T \boldsymbol{u}_{si} = \sigma_{si}^2 \boldsymbol{u}_{si} \tag{18}$$

Therefore, from Eqs. (5), (7), (11), and (18),

$$\lambda_{si} = \frac{\sigma_{si}^2}{nb(s)} \tag{19}$$

Numerical Results

Consider the CMM data that are available for 11 IBRs for a rotor stage in an engine:

$$s = i\text{: IBR No. } i \quad i = 1,2, \ldots, 11 \tag{20}$$

The number of blades on an IBR equals 54. However, CMM data are not available for each blade on an IBR (Fig. 1).

Convergence of Mean. An important issue is to determine the sample size to capture the statistics of the manufacturing process. Therefore, the following data are computed:

$$\Delta E(i) = EW(i+1) - EW(i) \tag{21}$$

where

$$EW(i) = \frac{1}{nbb(i)} \sum_{\ell=1}^{i} \sum_{j=1}^{nb(\ell)} \boldsymbol{w}_{\ell j} \tag{22}$$

$$nbb(i) = \sum_{\ell=1}^{i} nb(\ell) \tag{23}$$

Here, $EW(i)$ and $nbb(i)$ are the mean of the CMM data and the total number of measured blades, respectively, when the number of measured IBR is i. Therefore, $\Delta E(i)$ is the change in the mean

Downloaded 30 May 2010 to 128.113.26.88. Redistribution subject to ASME license or copyright; see http://www.asme.org/terms/Terms_Use.cfm

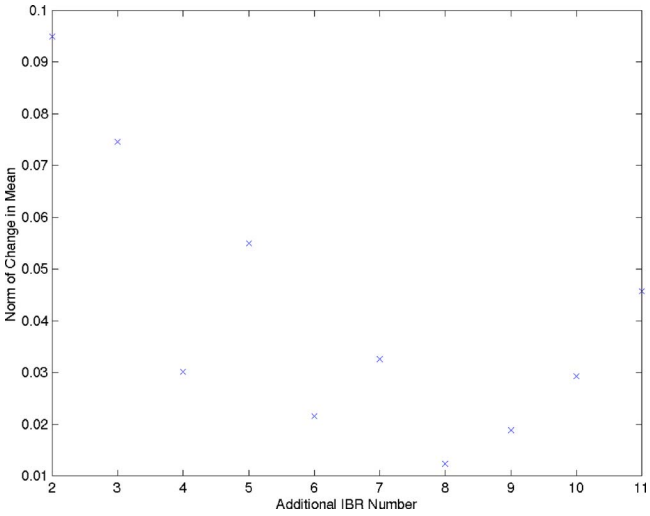

Fig. 2 Change in mean as a function of additional IBR

of the CMM data when the data for the $i+1$ IBR is added.

Figure 2 indicates that the norm of $\Delta E(i)$ oscillates around 0.025 after the sixth IBR is added. It almost seems that the mean does not change significantly after the sixth IBR has been added to the database. Hence, the CMM data are divided into two sets of the first six IBRs and the last five IBRs

$$s = 12\text{: first six IBRs } (s = 1 - 6) \tag{24a}$$

$$s = 13\text{: last five IBRs } (s = 7 - 11) \tag{24b}$$

The objective is to determine if the proper orthogonal decomposition (POD) modes obtained from the first six IBRs are related to those obtained from the last five IBRs. Many POD modes for these two sets of IBRs are found to be similar (see, for example, Figs. 3 and 4). Color scales on these plots indicate norms of deviations in x, y, and z coordinates from their mean values. Results shown in Figs. 3 and 4 indicate that the POD features present in the measured CMM data can represent those to be found for IBRs that will be manufactured in the future.

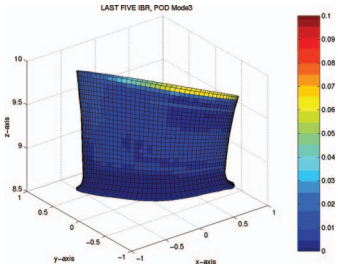

Fig. 4 POD mode 3 of CMM data for the last five IBRs

Distributions of Proper Orthogonal Decomposition Random Variables ξ_i. Premultiplying Eq. (8) by $\boldsymbol{u}_{sp}^T$,

$$\boldsymbol{u}_{sp}^T \delta \boldsymbol{w}_{sj} = \sum_{\ell=0}^{nd} \xi_{s\ell} \sqrt{\lambda_{s\ell}} \boldsymbol{u}_{sp}^T \boldsymbol{u}_{s\ell} \tag{25}$$

Because of the orthonormality of vectors $\boldsymbol{u}_{s\ell}$,

$$\boldsymbol{u}_{sp}^T \delta \boldsymbol{w}_{sj} = \xi_{sp} \sqrt{\lambda_{sp}} \Rightarrow \xi_{sp} = \frac{\boldsymbol{u}_{sp}^T \delta \boldsymbol{w}_{sj}}{\sqrt{\lambda_{sp}}} \tag{26}$$

Distributions of random variables are generated (Figs. 5–13) by considering all the CMM data:

$$s = 14\text{: all 11 IBRs } (s = 1 - 11) \tag{27}$$

For this case, the total number of measured blades is 561. For this set of data, relations (9) and (10) have been verified to be true. Many of the plots in Figs. 5–13 resemble a Gaussian distribution. Deviations from the Gaussian distribution can also result from a limited (561) number of samples.

Natural Frequencies and Mode Shapes of Blades. Using linearization,

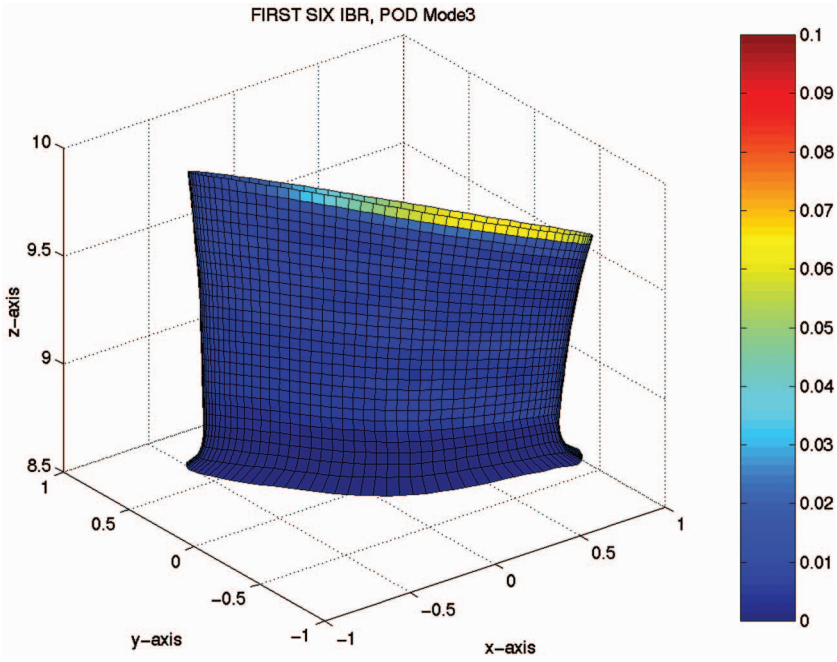

Fig. 3 POD mode 3 of CMM data for the first six IBRs

Downloaded 30 May 2010 to 128.113.26.88. Redistribution subject to ASME license or copyright; see http://www.asme.org/terms/Terms_Use.cfm

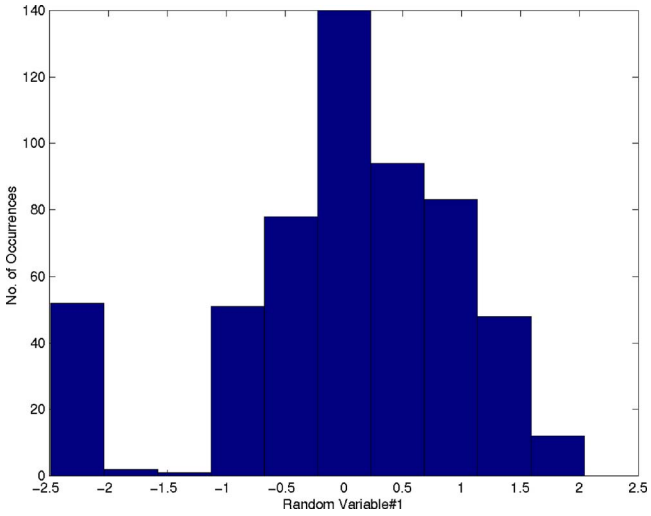

Fig. 5 Probability distribution of ξ_{s1} (s=14)

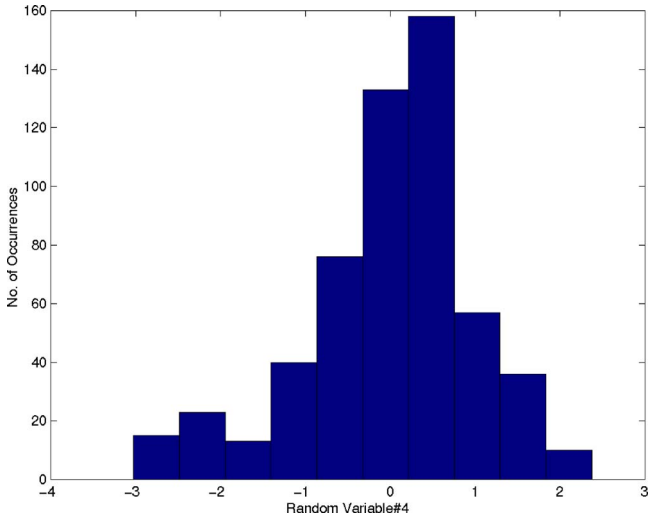

Fig. 8 Probability distribution of ξ_{s4} (s=14)

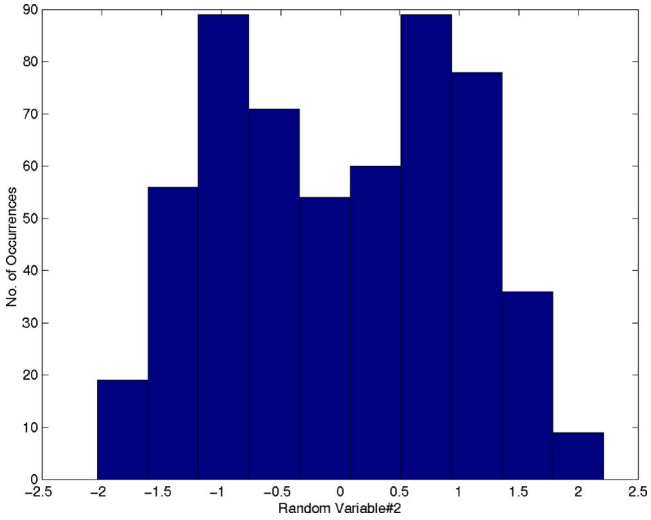

Fig. 6 Probability distribution of ξ_{s2} (s=14)

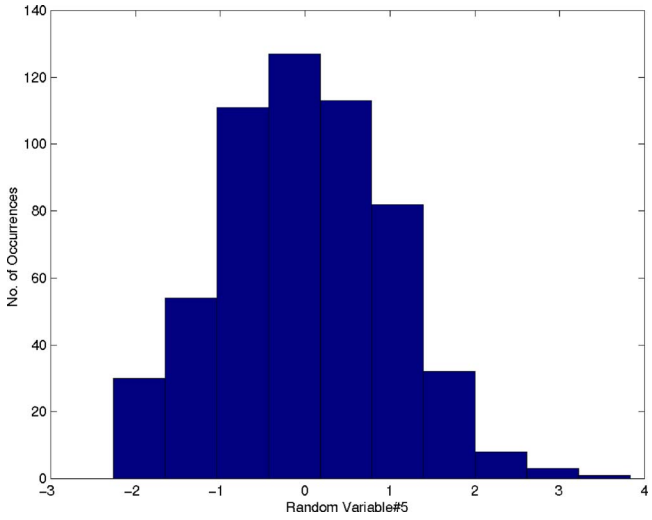

Fig. 9 Probability distribution of ξ_{s5} (s=14)

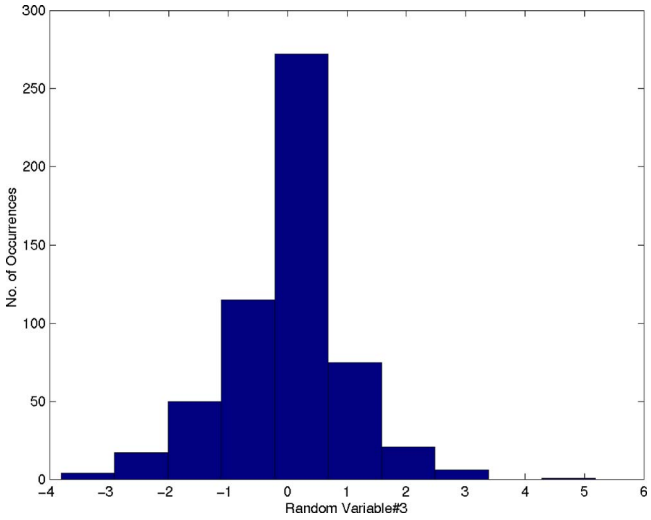

Fig. 7 Probability distribution of ξ_{s3} (s=14)

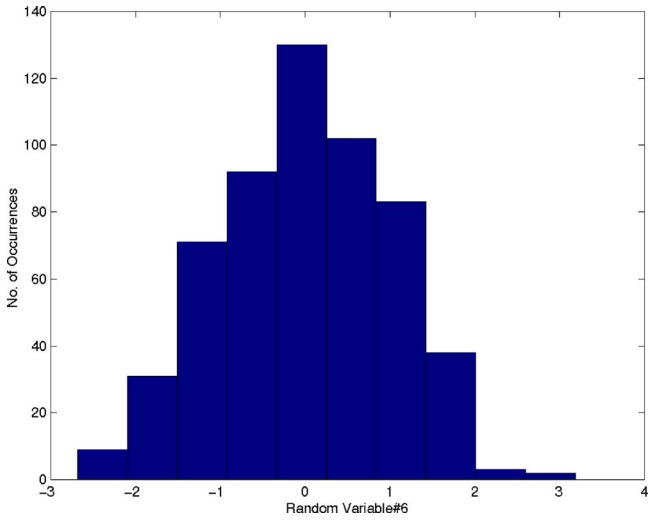

Fig. 10 Probability distribution of ξ_{s6} (s=14)

Downloaded 30 May 2010 to 128.113.26.88. Redistribution subject to ASME license or copyright; see http://www.asme.org/terms/Terms_Use.cfm

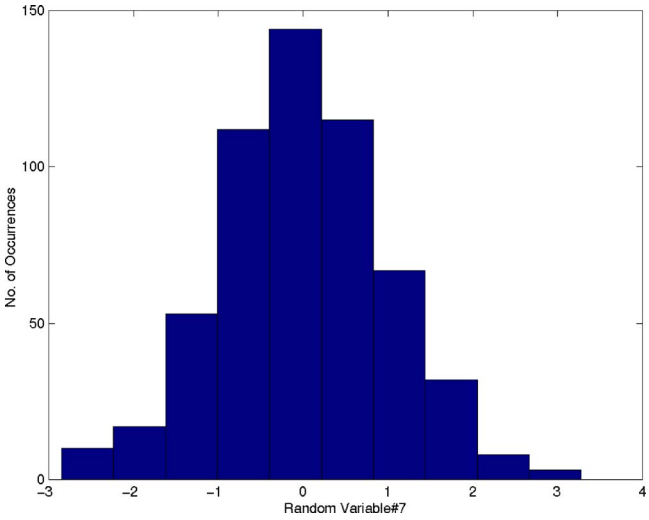

Fig. 11 Probability distribution of ξ_{s7} (s=14)

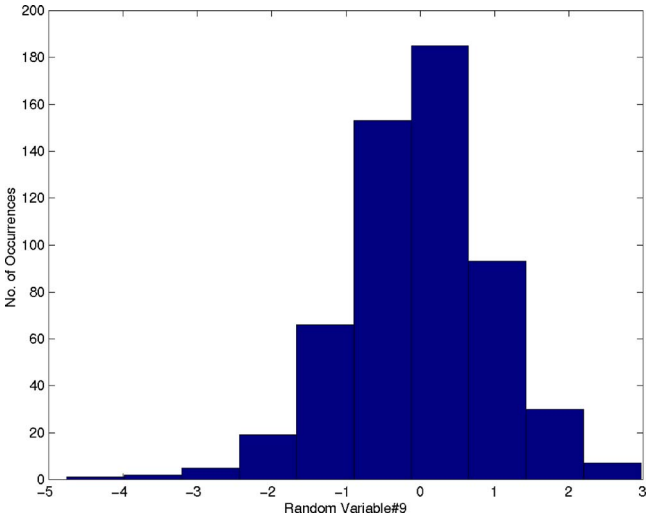

Fig. 13 Probability distribution of ξ_{s9} (s=14)

$$\omega_j = \bar{\omega}_j + \sum_{i=1}^{np} \left(\frac{\partial \omega_j}{\partial \xi_i} \right) \xi_i \tag{28}$$

$$\boldsymbol{\phi}_j = \bar{\boldsymbol{\phi}}_j + \sum_{i=1}^{np} \left(\frac{\partial \boldsymbol{\phi}_j}{\partial \xi_i} \right) \xi_i \tag{29}$$

where ω_j and $\boldsymbol{\phi}_j$ are the jth natural frequency and modal vector of a blade, respectively, and $\bar{\omega}_j$ and $\boldsymbol{\phi}_j$ are, respectively, the jth natural frequency and modal vector of the blade with a mean geometry, i.e., ξ_i=0.

From Eqs. (28), (9), and (10), the mean and variance of a blade's natural frequency are given by

$$E(\omega_j) = \bar{\omega}_j \tag{30}$$

and

$$E[(\omega_j - \bar{\omega}_j)^2] = \sum_{i=1}^{np} \left(\frac{\partial \omega_j}{\partial \xi_i} \right)^2 \tag{31}$$

Partial derivatives of natural frequencies with respect to POD random variables are computed via finite-difference approximations,

$$\left(\frac{\partial \omega_j}{\partial \xi_{si}} \right) = \frac{\omega_j(\xi_{si} = 0.5) - \bar{\omega}_j}{0.5} \tag{32}$$

or

$$\left(\frac{\partial \omega_j}{\partial \xi_{si}} \right) = \frac{\omega_j(\xi_{si} = 0.5) - \omega_j(\xi_{si} = -0.5)}{1} \tag{33}$$

Similarly, partial derivatives of modal vectors with respect to POD random variables are computed as

$$\left(\frac{\partial \boldsymbol{\phi}_j}{\partial \xi_{si}} \right) = \frac{\boldsymbol{\phi}_j(\xi_{si} = 0.5) - \boldsymbol{\phi}_j}{0.5} \tag{34}$$

or

$$\left(\frac{\partial \boldsymbol{\phi}_j}{\partial \xi_{si}} \right) = \frac{\boldsymbol{\phi}_j(\xi_{si} = 0.5) - \boldsymbol{\phi}_j(\xi_{si} = -0.5)}{1} \tag{35}$$

Frequencies and modal vectors $\bar{\omega}_j$, $\boldsymbol{\phi}_j$, $\omega_j(\xi_{si}=0.5)$, $\boldsymbol{\phi}_j(\xi_{si}=0.5)$, $\omega_j(\xi_i=-0.5)$, and $\boldsymbol{\phi}_j(\xi_i=-0.5)$ are computed via solid modeling with UNIGRAPHICS and via finite element analysis with ANSYS. First, the blade geometry is created for the perturbation along the ith POD mode,

$$\boldsymbol{w}_{si} = E(\boldsymbol{w}_s) + \xi_{si} \sqrt{\lambda_i} \boldsymbol{u}_i \tag{36}$$

Then, the data file is created for this blade geometry. To this data file, data files for geometries of end walls are attached, and the solid model of the blade is created in UNIGRAPHICS. After this, portions beyond end walls in the solid model are trimmed. This solid model is imported into the ANSYS program. Boundary conditions for the modal analysis are taken to be zero nodal displacements at the root of the blade. In Figs. 14 and 15, frequencies $\omega_j/\bar{\omega}_j$ of a blade in a commercial rotor are plotted as a function of the random variable ξ_1. The objective is to examine the nature of the relationship between the natural frequencies and the random variable ξ_1. For the first frequency, the relationship is quadratic because the changes are small, and, as a result, the first derivative is almost zero. This result also indicates that the precision level of the ANSYS/UNIGRAPHICS process is sufficient to detect small changes in frequencies due to changes in the random variable ξ_1.

In Fig. 16, predictions of natural frequencies from Eq. (28) are presented for a blade where partial derivatives are computed by Eq. (33) and the number of POD features is taken to be 10. In this figure, natural frequencies are divided by the first natural frequency predicted by the POD method. It is seen that POD results compare very well with ANSYS and experimental results as well. In Fig. 17, statistics of natural frequencies are presented. Standard

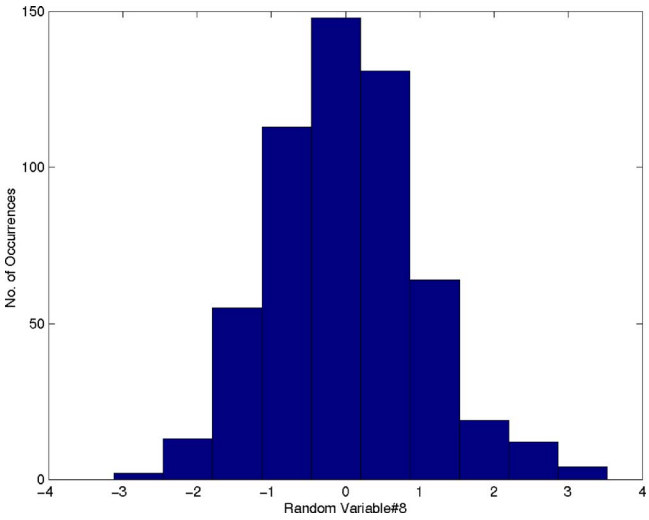

Fig. 12 Probability distribution of ξ_{s8} (s=14)

Downloaded 30 May 2010 to 128.113.26.88. Redistribution subject to ASME license or copyright; see http://www.asme.org/terms/Terms_Use.cfm

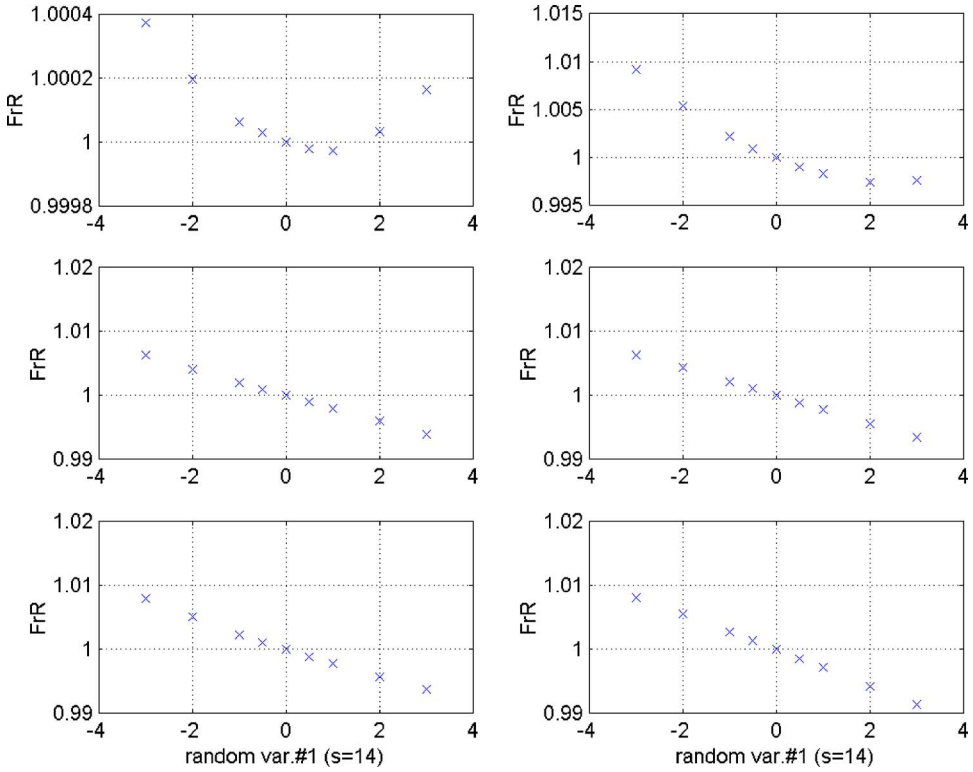

Fig. 14 Frequencies $\omega_j/\bar{\omega}_j$, $j=1,2,\ldots,6$, of a blade on an IBR

deviations predicted by the POD method compare very well with experimental results for few modes of vibration. For many modes of vibration, standard deviations of natural frequencies are not close. A major source of experimental error is due to the fact that the predictions are for an isolated blade while the measurements are for a full IBR. In the experimental procedure, natural frequen-

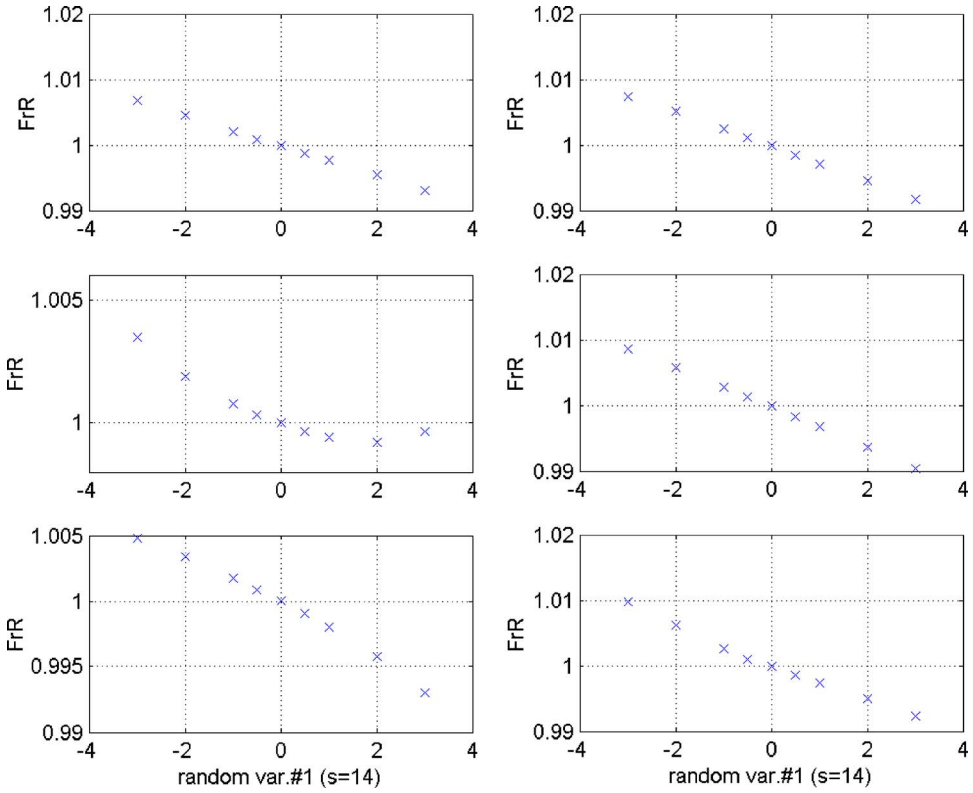

Fig. 15 Frequencies $\omega_j/\bar{\omega}_j$, $j=7,8,\ldots,12$, of a blade on an IBR

Downloaded 30 May 2010 to 128.113.26.88. Redistribution subject to ASME license or copyright; see http://www.asme.org/terms/Terms_Use.cfm

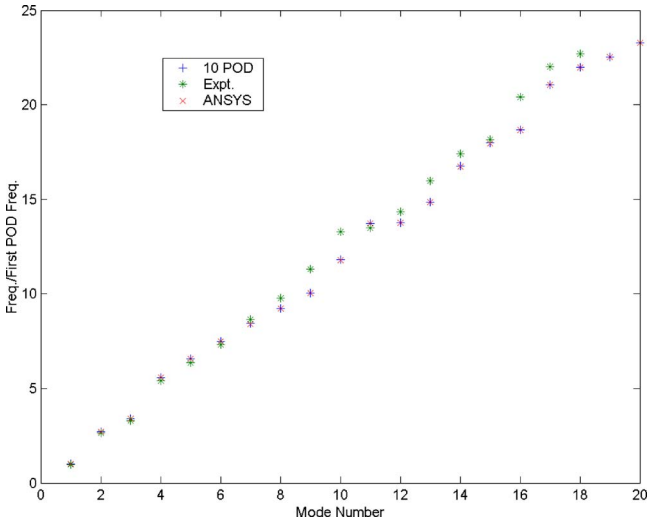

Fig. 16 Prediction of natural frequencies of a blade on an IBR

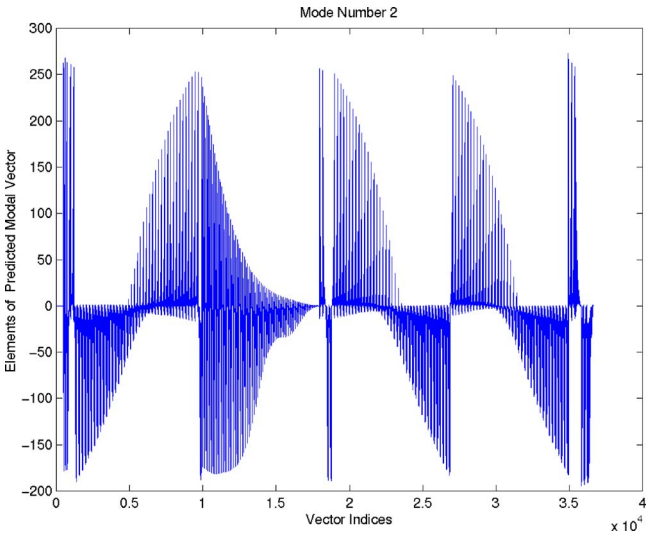

Fig. 19 Modal vector predicted by the POD method

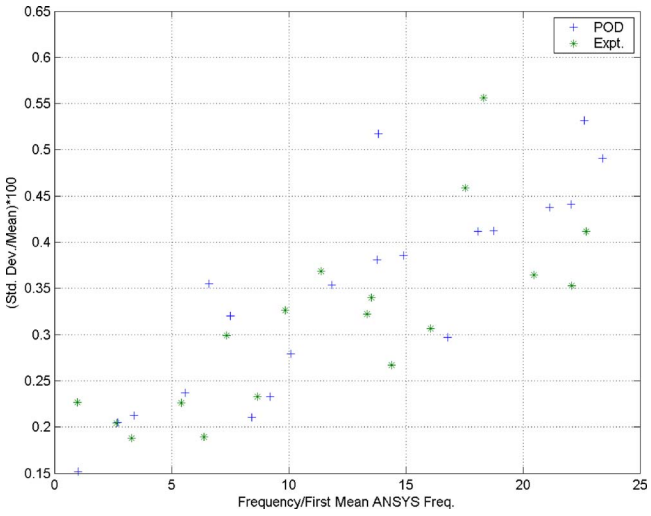

Fig. 17 Statistics of natural frequencies

cies are obtained by examining peaks in the frequency response when only one blade is excited on an IBR. Because of this, some of these peaks are related to system (bladed disk) frequencies rather than to frequencies of the blade alone.

In Figs. 18–20, results for mode shapes are plotted. In Fig. 18, one of the mode shapes obtained from the direct use of the blade's CMM data along with ANSYS and UNIGRAPHICS is presented. For this blade, POD random variables (ξ_i) are also computed. Then, the first ten POD modes are selected, and mode shapes are computed by Eq. (29), where partial derivatives are computed by Eq. (35). In Fig. 19, the mode shape corresponding to Fig. 18 is presented. The error in the mode shape predicted by Eq. (29) is small (Fig. 20).

Conclusions

When variations in geometries of blades are measured by a CMM, the POD analysis (or KL expansion), along with the solid modeling and the finite element method, can accurately yield natural frequencies and mode shapes of a blade on the IBR, along with their means and standard deviations. This technique is based on the linearization process. Therefore, a careful study has been conducted to establish the validity of the linearization approach. It

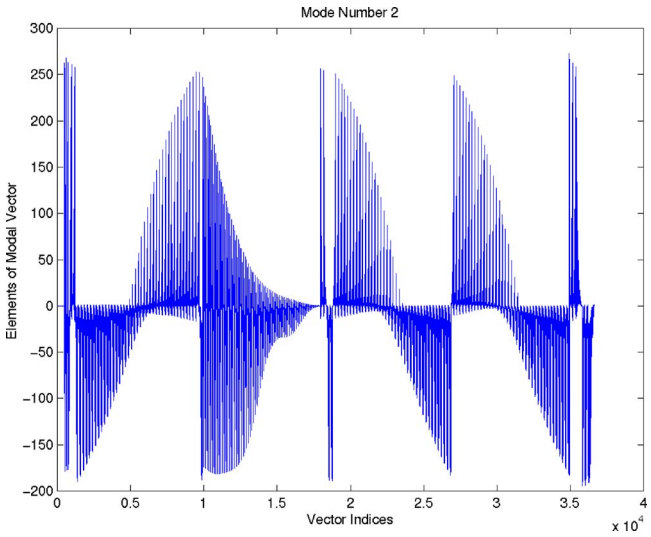

Fig. 18 A modal vector of a blade

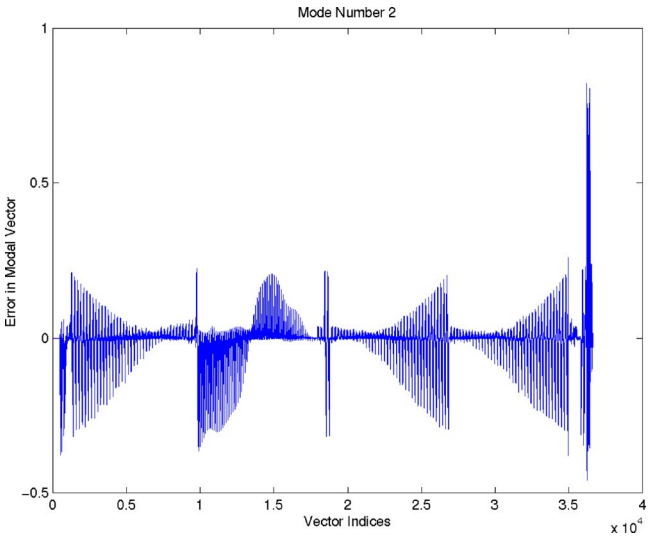

Fig. 20 Error in the predicted modal vector

Downloaded 30 May 2010 to 128.113.26.88. Redistribution subject to ASME license or copyright; see http://www.asme.org/terms/Terms_Use.cfm

is also shown that the ANSYS/UNIGRAPHICS approach has sufficient numerical precision to capture the effects of a very small change in the geometry on the modal parameters of blades.

A comparison with experimental results clearly corroborates the validity of the POD method. It is also seen that POD features present in the measured CMM data can represent IBRs that will be manufactured in the future. Therefore, predicted statistics of modal parameters of blades will also apply to IBRs that will be manufactured in the future.

Acknowledgment

Most of this work has been performed during the first author's sabbatical at Pratt & Whitney, E. Hartford, CT. The first author gratefully acknowledges the financial support from Pratt & Whitney.

Appendix

Karhunen–Loeve Expansion [8]

Consider a random process $w(x,\theta)$ which is a function of the position vector x defined over the domain D, with θ belonging to the space of random events Ω. Let $\bar{w}(x)$ and $\boldsymbol{C}(x_1,x_2)$ be the expected value and the covariance function of $w(x,\theta)$, respectively. Then,

$$w(x,\theta) = \bar{w}(x) + \alpha(x,\theta) \tag{A1}$$

where

$$\alpha(x,\theta) = \sum_{n=0}^{\infty} \xi_n(\theta)\sqrt{\lambda_n} f_n(x) \tag{A2}$$

Here, $\xi_n(\theta)$ are random variables satisfying $E[\xi_n(\theta)]=0$ and $E[\xi_n(\theta)\xi_m(\theta)]=\delta_{nm}$, where δ_{nm} are the dirac-delta function. Furthermore, λ_n and $f_n(x)$ are eigenvalues and eigenvectors of the covariance function $C(x_1,x_2)$ satisfying the following properties:

$$\int_D C(x_1,x_2) f_n(x_1) dx_1 = \lambda_n f_n(x_2) \tag{A3}$$

$$\int_D f_n(x) f_m(x) dx = \delta_{nm} \tag{A4}$$

References

[1] Wu, C. Y., 1995, "Arbitrary Surface Flank Milling of Fan, Compressor, and Impeller Blades," ASME J. Turbomach., **117**, pp. 534–539.

[2] Judge, J., Pierre, C., and Ceccio, S. L., 2001, "Identification of Mistuning in Blisks," *Proceedings of the Sixth National High Cycle Fatigue (HCF) Conference*, Jacksonville, FL.

[3] Feiner, D., and Griffin, J. H., 2003, "Mistuning Identification of Bladed Disks Using a Fundamental Mistuning Model. Part I. Theory,"ASME Paper No. GT2003-38952; 2003, "Mistuning Identification of Bladed Disks Using a Fundamental Mistuning Model. Part II. Application," ASME Paper No. GT2003-38953.

[4] Blair, A., and Annis, C., 2002, "Development of Probabilistic Methods for Campbell Diagram Frequency Placement," *Proceedings of the Seventh National Turbine Engine High Cycle Fatigue Conference*, Palm Beach, FL.

[5] Garzon, V. E., and Darmofal, D. L., 2003, "Impact of Geometric Variability on Axial Compressor Performance," ASME Paper No. GT2003–38130.

[6] Ghiocel, D. M., 2001, "Stochastic Field Models for Aircraft Jet Engine Applications," J. Aerosp. Eng., **14**(4), pp. 127–139.

[7] Brown, J. M., Slater, J., and Grandhi, R. V., 2003, "Probabilistic Analysis of Geometric Uncertainty Effects on Blade Modal Response," ASME Paper No. GT2003–38557.

[8] Ghanem, R. G., and Spanos, P. D., 1991, *Stochastic Finite Elements: A Spectral Approach*, Springer, New York.

Downloaded 30 May 2010 to 128.113.26.88. Redistribution subject to ASME license or copyright; see http://www.asme.org/terms/Terms_Use.cfm

Improved Diffuser/Volute Combinations for Centrifugal Compressors

T. Steglich

J. Kitzinger

J. R. Seume

Institute for Turbomachinery and Fluid Dynamics,
Leibniz University Hannover,
30167 Hannover, Germany

R. A. Van den Braembussche

J. Prinsier

von Karman Institute for Fluid Dynamics,
Sint-Genesius-Rode, Belgium

Internal volutes have a constant outer radius, slightly larger than the diffuser exit radius, and the circumferential increase of the cross section is accommodated by a decrease of the inner radius. They allow the design of compact radial compressors and hence are very attractive for turbochargers and high-pressure pipeline compressors, where small housing diameters have a favorable impact on weight and cost. Internal volutes, however, have higher losses and lower pressure rise than external ones, in which the center of the cross sections is located at a larger radius than the diffuser exit. This paper focuses on the improvement of the internal volute performance by taking into account the interaction between the diffuser and the volute. Two alternative configurations with enhanced aerodynamic performance are presented. The first one features a novel, nonaxisymmetric diffuser/internal volute combination. It demonstrates an increased pressure ratio and lower loss over most of the operating range at all rotational speeds compared with a symmetric diffuser/internal volute combination. The circumferential pressure distortion at off design operation is slightly larger than in the original configuration with a concentric vaneless diffuser. Alternatively, a parallel-walled diffuser with low-solidity vanes and an internal volute allows a reduction of the unsteady load on the impeller and an improved performance, approaching that of a vaneless concentric diffuser with a large external volute. [DOI: 10.1115/1.2749296]

Introduction

The maximum volume of centrifugal/radial compressors is often limited by the available space and by the material—the manufacturing costs being proportional to size. This favors the use of internal volutes, i.e., volutes with a constant outer radius and the center of the cross sections at a smaller radius than the diffuser outlet. The main disadvantages of internal volutes are a lower static pressure rise and larger total pressure losses. The pressure recovery through the deceleration of the flow in the diffuser with increasing radius is annihilated by the subsequent reacceleration in the volute due to the decreasing volute centerline radius.

External volutes have the inner wall at constant (diffuser exit) radius. They show a higher pressure ratio and efficiency because of the extra diffusion that takes place in the volute. However, they are much larger because the outer radius increases circumferentially with the increasing volute cross section.

Detailed measurements and numerical studies of the flow in internal and external volutes with different cross-section shapes, realized by Ayder et al. [1–3], have provided a better understanding of the flow structure and confirmed the importance of the two main loss mechanisms used in the 1D models of Japikse [4] and Weber et al. [5]. The first one is the friction and diffusion of the volute throughflow velocity. The losses depend on the diffuser exit tangential velocity and the circumferential variation of the volute cross-sectional area. The second one is the dissipation of the secondary vortex in the volute cross sections. The corresponding losses are proportional to the square of the radial velocity at the diffuser outlet. Both indicate a strong interaction between the diffuser and the volute flow and suggest a simultaneous optimization of both components.

The circumferential variation and radial location of the volute cross section critically influence the pressure conversion and define the circumferential pressure distortion at design and off-design operation (Hagelstein et al. [6]). The latter one causes unsteady impeller flow, periodic variation of the impeller blade forces, and an additional loading of the bearings (Binder and Knapp [7], Knapp [8], and Brown and Bradshaw [9]). The impact of the volute geometry on the circumferential pressure distortion at the impeller outlet confirms the strong interaction between impeller, diffuser, and volute.

Lee et al. [10] presented performance improvements by an optimization of a radial vaneless diffuser. Many attempts have been made to improve the volute performance by studying the optimum cross-sectional shape and area variation (Mishina and Gyobu [11] and Reunanen et al. [12]). However, the strong interaction between the diffuser and the volute suggests that further improvements require a simultaneous optimization of both.

The present paper is the continuation of the theoretical and experimental studies by Hagelstein et al. [6,13] on a centrifugal compressor with a vaneless diffuser and an external, central, and internal volute. It aims at an improvement of performance of the compressor with a compact internal volute, without compromising on the operating range. Reunanen et al. [12] claim that the shape of the volute cross section is not so important because the tangential velocity at the volute inlet is much larger than the radial one. Hence, the present results, obtained for a volute of rectangular cross section, can be extrapolated to other geometries.

Two modifications are proposed in this paper. The first one aims at a reduction of the diffuser and volute friction losses by cutting out the wall between them. This relates the diffuser outlet radius to the volute inner wall radius and results in a nonaxisymmetric diffuser. The second modification aims at a weaker secondary vortex in the volute by reducing the diffuser exit radial velocity.

Test Facility and Instrumentation

The performance of the original and the redesigned geometries has been experimentally verified on the radial compressor test facility of the Institute for Turbomachinery and Fluid Dynamics at

Contributed by the International Gas Turbine Institute of ASME for publication in the JOURNAL OF TURBOMACHINERY. Manuscript received January 11, 2006; final manuscript received January 23, 2007; published online January 25, 2008. Review conducted by Michael Casey. Paper presented at the ASME Turbo Expo 2005: Land, Sea and Air (GTO2005), Reno, NV, June 6–9, 2005, Paper No. GT2005-68894.

 Copyright © 2008 by ASME

Downloaded 30 May 2010 to 128.113.26.88. Redistribution subject to ASME license or copyright; see http://www.asme.org/terms/Terms_Use.cfm

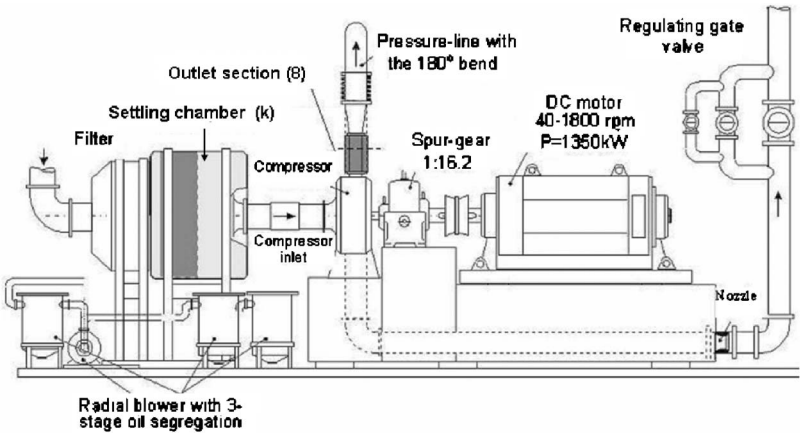

Fig. 1 Schematic of the test facility

the Leibniz University Hannover. It is schematically shown in Fig. 1. Air is supplied to the compressor at atmospheric conditions through a settling chamber and an axial inlet pipe.

The compressor geometry is the same as that used by Hagelstein [6]. The impeller has 20 blades with 30° backward lean at the trailing edge. Ten of them are cut back at the inlet (splitter blades). The impeller has an outer diameter of 400 mm. It is fitted with a convergent diffuser of radius ratio $r_3/r_2=1.5$ resulting in a 13% area increase. An internal volute connects the diffuser exit to the discharge pressure line where three valves allow an accurate setting of the mass flow.

The test compressor is driven by a dc motor through a gear box. The compressor rotational speed can be varied continuously between 650 and 29,000 rpm. It is measured with an inductive eddy-current sensor and monitored online. The reproducibility of the speed is 0.1%, the uncertainty is 0.02%, and the standard deviation is 0.1%. The mass flow is measured according to DIN 1952 with an orifice in the discharge pipe. The reproducibility of mass flow is 0.6%, the uncertainty is 0.07%, and the standard deviation is 0.7%. The performance map data and the diffuser static pressure distributions are acquired using an automatic data acquisition device with 80 pressure and 20 temperature channels.

Design of an Asymmetric Diffuser

The new geometries have been optimized by means of the 3D commercial Navier–Stokes solver CFX-TASC flow on a grid with 650,000 cells covering the diffuser and volute volume. The diffuser inlet conditions are defined based upon the measured impeller exit conditions at three operating points, corresponding to near surge (low), optimum efficiency (nominal), and near choking (maximum) mass flows. They are indicated by black dots on the experimental performance map shown in Fig. 2.

All performance maps in this paper show the total to total pressure ratio Π_{tot} (experimental reproducibility of 0.2%, uncertainty of 0.7%, and standard deviation of 0.01%) and total to total efficiency (experimental reproducibility of 0.3%, uncertainty of 0.7%, and standard deviation of 0.01%). They are based on pressure and temperature measurements in the upstream settling chamber of the compressor (denoted k) and at the discharge flange (denoted 8).

The many computational fluid dynamics (CFD) studies, which have been made on diffuser/volute combinations with time-averaged flow conditions imposed at the diffuser inlet (Miner et al. [14], Chen et al. [15], Flathers et al. [16], and Ayder et al. [3]), confirm the importance and validity of those simulations for the optimization of these components.

A major source of losses in a vaneless diffuser/internal volute combination is the reacceleration of the tangential velocity in the volute after it has been decelerated in the vaneless diffuser according to the conservation of angular momentum ($c_u \cdot r=$const). The result is friction losses in both the diffuser and the volute without a net increase in pressure. The reacceleration could be counteracted by an increase of the internal volute cross-sectional area, but this would result in a circumferential pressure distortion or flow separation from the inner wall of the volute.

Friction on the wall between the diffuser and the volute can be decreased by removing part of it (Fig. 3). The result is an asymmetric vaneless diffuser, as shown in Fig. 4(b). In addition to a reduction of the friction losses, this also results in a small increase of the volute cross-section area without a change in the overall dimensions.

The flow between the impeller exit and stage outlet is calculated at 14,000 rpm with the common diffuser/volute wall reduced to 50%, 25% (shown in Fig. 3(b)), and 0% of its original height and with two different height changes in the vicinity of the tongue (shown in Fig. 5). One has a step increase of the diffuser radial extent at the tongue (Fig. 5(a)) and the other has a gradual in-

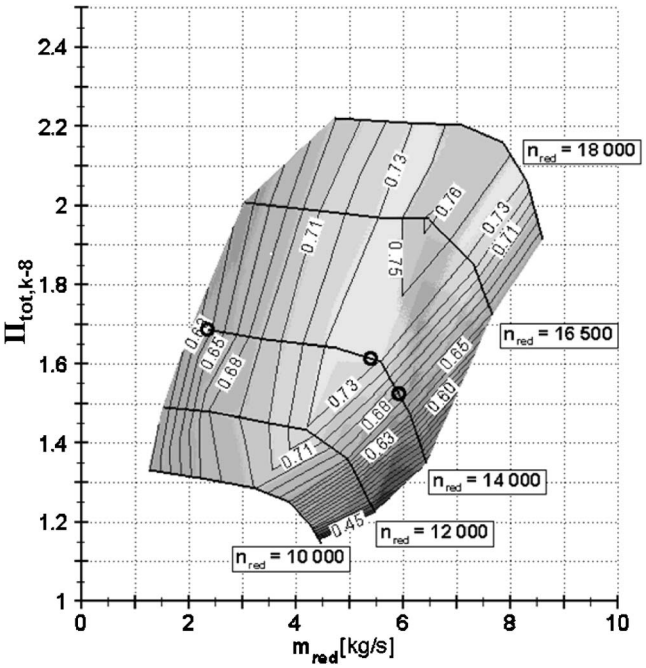

Fig. 2 Experimental performance map of the original compressor with concentric diffuser and an internal volute indicating the points of low, nominal, and maximum mass flows

Downloaded 30 May 2010 to 128.113.26.88. Redistribution subject to ASME license or copyright; see http://www.asme.org/terms/Terms_Use.cfm

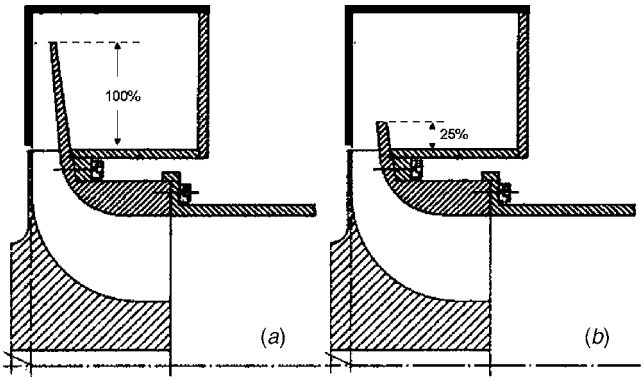

Fig. 3 Meridional cross sections at θ=300 deg of an internal volute with a conventional concentric diffuser (*a*) and an asymmetric one with the diffuser wall reduced to 25% (*b*)

crease between point B and the tongue (Fig. 5(*b*)). The vaneless diffuser radius ratio decreases from 1.5 in section (A) to 1.07 in section (B) (θ=300°).

The loss and pressure rise coefficients at the exit of the axisymmetric vaneless diffuser (100%) and the asymmetric one, in which the wall between the diffuser and the volute is cut back to 25% of its initial value, are listed in Table 1. The latter ones are given for the case of a gradual variation of the diffuser in the vicinity of the tongue. C_p and ω are nondimensionalized with the diffuser inlet kinetic energy. Average values are based on the conservation of mass, momentum, and energy. The variation of the diffuser and

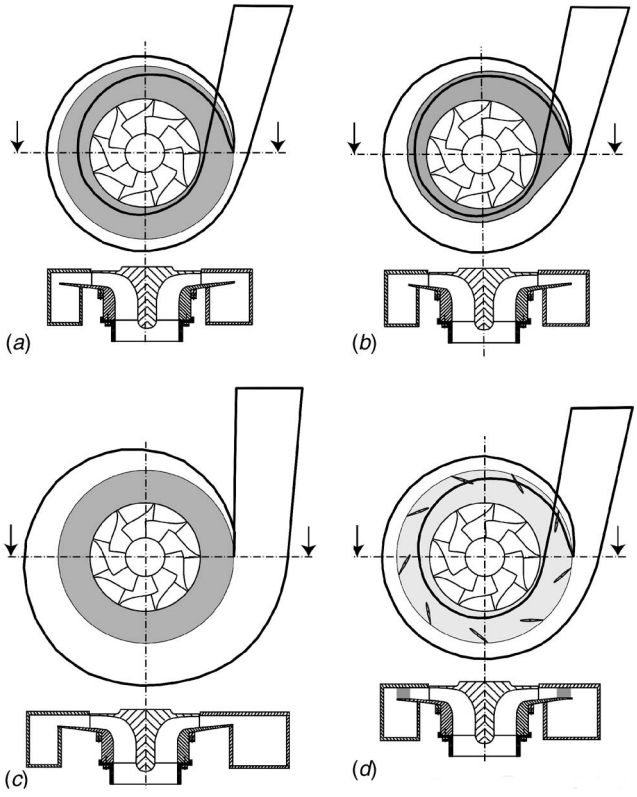

Fig. 4 Schematic of the four compressor configurations (the dark gray area defines the convergent vaneless diffuser wall, and the light gray area defines the parallel LSD wall): (*a*) internal volute+concentric diffuser (IN), (*b*) internal volute +asymmetric diffuser (AD), (*c*) external volute+concentric diffuser (EX), and (*d*) internal enlarged volute+LS diffuser (LSD)

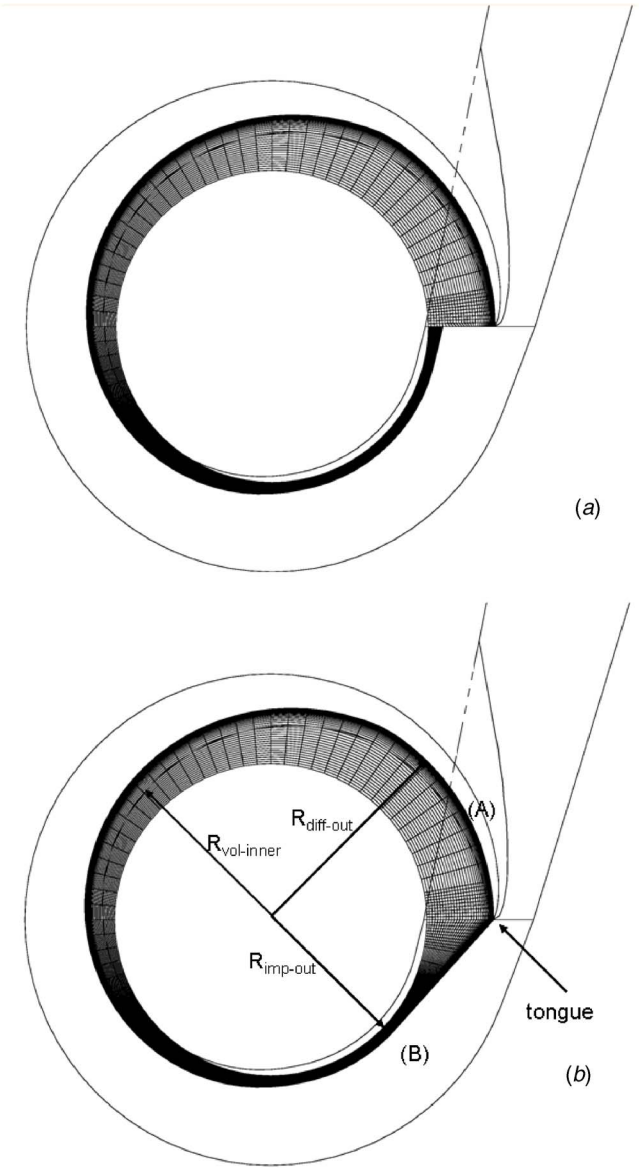

Fig. 5 Axial view of the asymmetric diffuser with a 25% wall and a stepwise (*a*) or gradual (*b*) variation of the diffuser wall in the tongue region

volute pressure rise coefficient and loss coefficient is plotted in Fig. 6 as a function of the remaining fraction of diffuser wall. The calculations of the diffuser with an abrupt (step) increase (Fig. 5(*a*)) resulted in a similar performance as the diffuser with a gradual increase, but this option was not evaluated further because CFD predictions indicate a local flow separation at the tongue.

The significant decrease of the pressure recovery in the vaneless diffuser, after cutting back the diffuser wall, is due to the decreased radius ratio. However, shortening the vaneless diffuser transforms the internal volute into a partially external one (Fig. 4(*b*)) and the corresponding volute pressure rise compensates for the lower pressure rise in the diffuser. A combination of both effects results in better performance at high and medium mass flow than with the axisymmetric diffuser, shown in Figs. 3(*a*) (100%) and 4(*a*). The higher volute inlet tangential velocity and increase of the volute cross-sectional area lead to a flow separation at minimum mass flow. This results in an increase of losses and a limitation of the volute pressure rise. Hence, the lower pres-

Downloaded 30 May 2010 to 128.113.26.88. Redistribution subject to ASME license or copyright; see http://www.asme.org/terms/Terms_Use.cfm

Table 1 Summary of the calculated loss and pressure rise coefficients at the vaneless diffuser outlet and stage outlet for a concentric diffuser (100%) and an asymmetric diffuser with a wall cut back to 25% (14,000 rpm)

		Nom. mass flow rate		Min. mass flow rate		Max. mass flow rate	
Diff. inlets	α (deg)	75.0		64.8		54.0	
	$\dot{m}$ kg/s	2.026		5.573		5.871	
	%	100	25	100	25	100	25
Up to diff. outlets	ω	0.106	0.112	0.083	0.061	0.056	0.053
	C_p	0.438	0.289	0.413	0.264	0.396	0.229
Up to stage outlet	ω	0.372	0.413	0.500	0.408	0.817	0.638
	C_p	0.579	0.534	0.364	0.461	−0.070	0.115

sure recovery in the diffuser cannot be fully recuperated in the volute, which results in a small decrease of the overall pressure rise.

A theoretical approach shows that $C_p+\omega=C_{p\ \text{isentropic}}$, in which $C_{p\ \text{isentropic}}$ depends only on the diffuser inlet flow and discharge flange cross-section area. The sum of $C_p+\omega$ is, therefore independent of the diffuser and volute geometry between these sections. This is confirmed by the data in Table 1 showing that any change in static pressure coefficient is the consequence of an equal and opposite change in total pressure losses.

The pressure recovery between the diffuser exit and the volute outer wall (Fig. 7) results from the centrifugal force generated by the tangential velocity in the volute. The radial velocity diffuses quickly at the diffuser exit and results in a weaker secondary vortex inside the volute than with a longer axisymmetric diffuser.

The volute with a 25% diffuser wall and a gradual (tangential) transition in the vicinity of the tongue was verified experimentally. The corresponding performance map is shown in Fig. 8. Efficiency and pressure ratio are considerably higher than those measured for the same volute and a concentric diffuser. However, the useful operating range being limited to the mass flows between maximum pressure rise and choking, it turns out that the price for a higher efficiency and pressure ratio is a reduction of the operating range. One also observes a more pronounced circumferential static pressure variation at the impeller outlet when operating the asymmetric diffuser outside the nominal point (Fig. 9 versus Fig. 10). This causes higher dynamic loads on rotor and bearings. The low-solidity diffuser, presented in the next chapter, is an attempt to remedy this disadvantage.

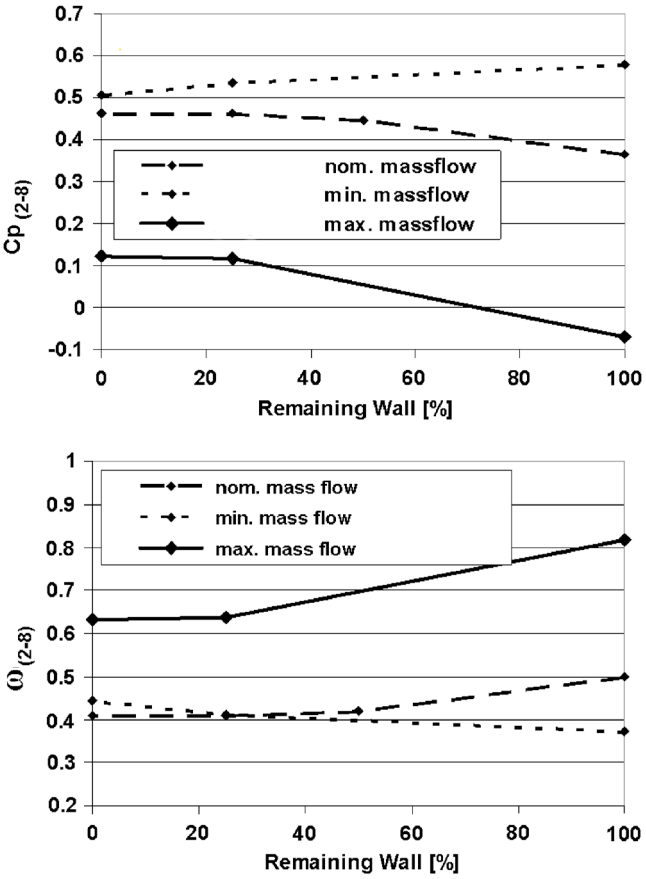

Fig. 6 Calculated static pressure rise and loss coefficients of the internal volute as a function of the remaining fraction of diffuser wall (14,000 rpm)

Design of a Low-Solidity Diffuser With a Larger Internal Volute

A volute cannot convert the kinetic energy in the secondary vortex into a pressure rise and the dissipation of this kinetic energy is a first and major contribution to the volute losses. The increased total pressure losses and lower static pressure in the vortex center cause a blockage of the effective volute cross section. This leads to an increase of the circumferential velocity component and an additional increase of the volute friction losses. The latter contribution is particularly important at high mass flow because of the stronger vortex blockage in a volute that is already too small. Hence, any reduction of the secondary flow vortex contributes in two ways to a decrease of the losses. Volute optimization, in terms of efficiency, therefore requires a maximum reduction of the radial velocity at the diffuser outlet.

Continuity imposes that the product of radial velocity, diffuser cross-sectional area, and fluid density is constant. Minimizing the radial velocity can be achieved by maximizing the diffuser outlet area and/or increase of the fluid density by an increase of the diffuser static pressure rise. This requires parallel-walled or even divergent diffusers in which, in the vaneless version, the flow is likely to become unstable, i.e., separate. CFD calculations confirm a performance increase with a parallel wall vaneless diffuser at medium and high mass flow, but at the cost of a considerable reduction of the operating range due to exceeded limits of diffuser flow stability at low mass flow.

Low solidity diffusers (LSDs), first mentioned by Senoo [17], are well suited to increase the diffuser static pressure rise without limiting the operating range (Engeda [18]). Combined with parallel wall diffusers, they allow a considerable reduction of the diffuser exit velocity without reducing the flow stability. The very low solidity (0.9 or less) does not lead to a geometrical throat section and minimizes the impact of the vanes on diffuser choking mass flow.

Downloaded 30 May 2010 to 128.113.26.88. Redistribution subject to ASME license or copyright; see http://www.asme.org/terms/Terms_Use.cfm

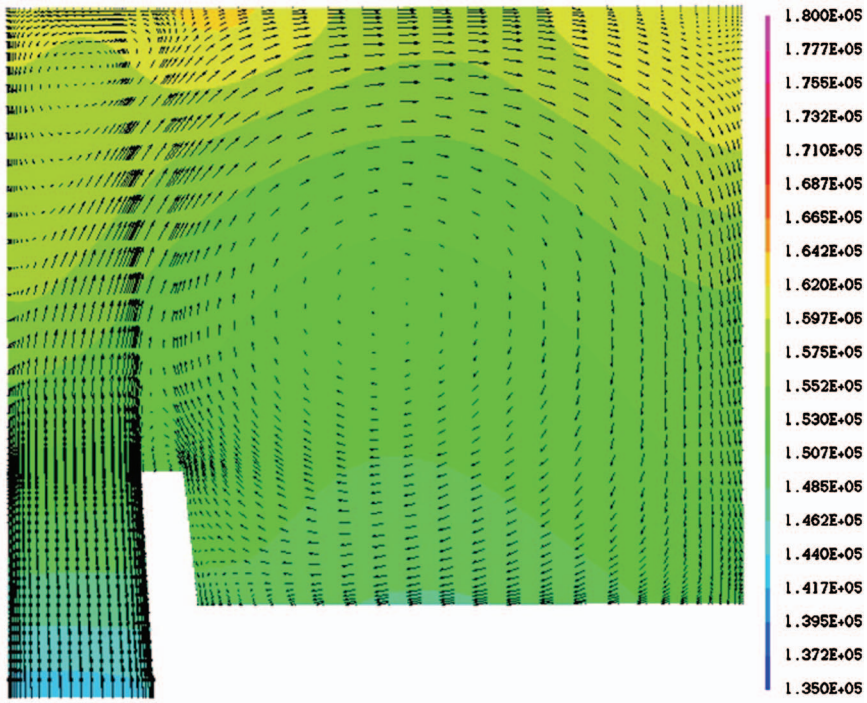

Fig. 7 Static pressure distribution (predicted by CFD, in Pa) at θ=180° in the internal volute with the diffuser wall reduced to 25% (m_{red}=4.573 kg/s, n_{red}=14,000 rpm)

Designing a LSD requires a multipoint optimization to guarantee good performance from surge to choking mass flow. Two LSDs have been designed and analyzed at an impeller speed of 18,000 rpm. Both have nine vanes to avoid interference with the 20 impeller blades. The vanes have a constant height and a NACA65 thickness distribution with 10% maximum thickness. The "13° camber" design provides nominally 13° turning compared with the fluid path of a logarithmic spiral, and the "17° camber" provides nominally 17° turning. The original convergence of the diffuser walls is conserved up to the vane leading edge at a diameter ratio of 1.29. The results of the CFD analysis at the three operating points under consideration are listed in Table 2 and visualized in Fig. 11.

The upper part of Fig. 11 shows an increase of the static pressure rise between the rotor exit and the diffuser exit when replacing the convergent diffuser by the LSD. This increase in pressure is associated with an increase of the total pressure loss coefficient due to the increased incidence and friction losses on the blade. The increase of the static pressure rise is not contradicted by this larger total pressure loss because of the smaller exit kinetic energy resulting from a more radial exit flow in a wider diffuser.

The total pressure distributions at midsection of the 13° camber LSD, shown in Figs. 12(*a*)–12(*c*) for the three operating points, indicate a small separation on the vane suction side near the trailing edge at minimum mass flow. Increasing the vane camber to 17° resulted in a small improvement at maximum mass flow but

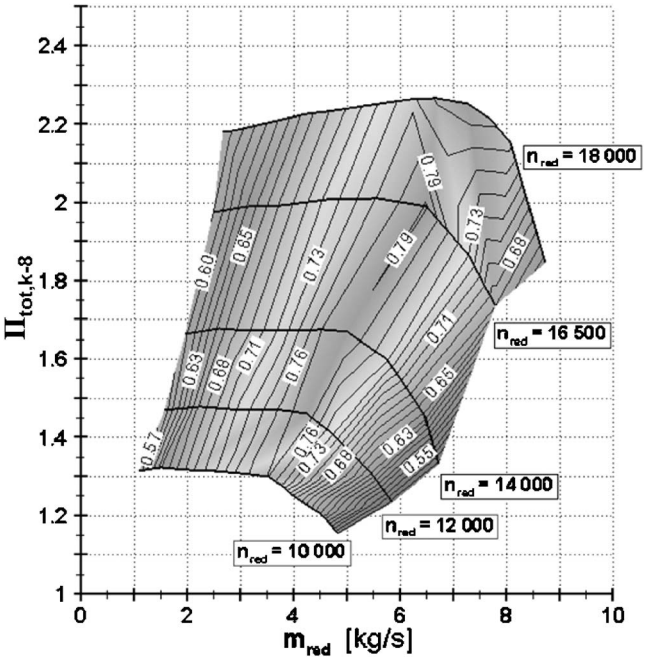

Fig. 8 Experimental performance map of the compressor with an asymmetric diffuser

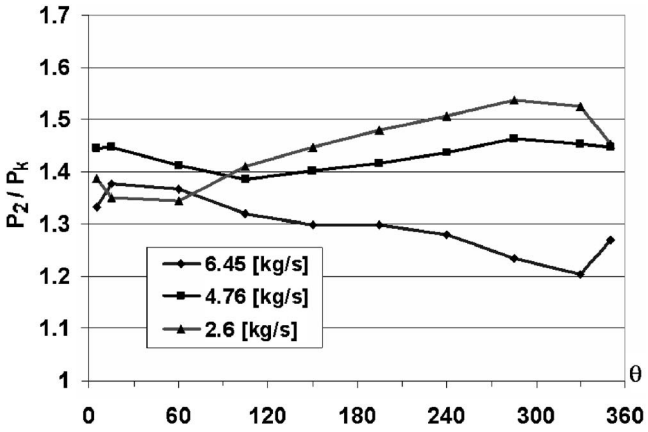

Fig. 9 Circumferential static pressure distribution at impeller outlet (asymmetric diffuser, 14,000 rpm)

Downloaded 30 May 2010 to 128.113.26.88. Redistribution subject to ASME license or copyright; see http://www.asme.org/terms/Terms_Use.cfm

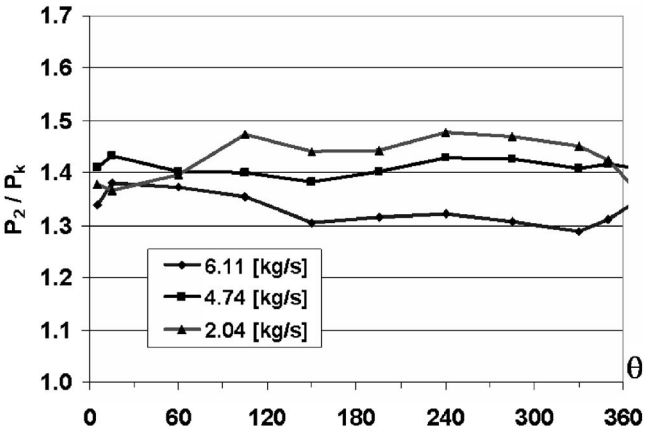

Fig. 10 Circumferential static pressure distribution at impeller outlet (concentric diffuser, 14,000 rpm)

lowered the diffuser pressure rise at minimum and medium mass flow because of an increased flow separation on the vanes.

The higher pressure rise in the LSD results in a smaller volume flow in the volute but with a considerably lower diffuser exit tangential velocity. Not adapting the volute means that the flow will reaccelerate, resulting in a decrease of the static pressure and an increase of the friction losses in the volute. The extra pressure rise in the LSD is then annihilated in the volute. This is shown in the lower half of Table 2 and in Fig. 11 where, in spite of the larger pressure rise in the diffuser, the static pressure at the volute exit is lower with both parallel-walled LSDs than with the convergent diffuser. This means that an optimum volute is larger for a LSD than for a vaneless diffuser.

Adapting the internal volute to the LSD exit flow conditions requires a 34% increase of its cross section. The corresponding results are listed in the last line of Table 2. One observes a considerable increase of the performance of the 13° cambered LSD when fitted with a larger volute. The test section exit flange, where the performance is measured, is unchanged so that the results are comparable to the ones of the original convergent vaneless diffuser and smaller volute. This also means that the sum of $C_p+\omega$ must remain unchanged for all geometries at each operating point and remain equal to $C_{p\ \text{isentropic}}$. This is again rather well confirmed by the data in Table 2.

A comparison of the experimental performance map in Fig. 13 with the one of the original concentric vaneless diffuser (Fig. 1) confirms the predicted increase of the pressure ratio and stage efficiency with the optimized LSD and larger volute combination. Pressure ratio and operating range approach the ones obtained for a concentric diffuser with an external volute (Fig. 14), of which the geometry is specified in Refs. [6,13] and Fig. 4(*c*).

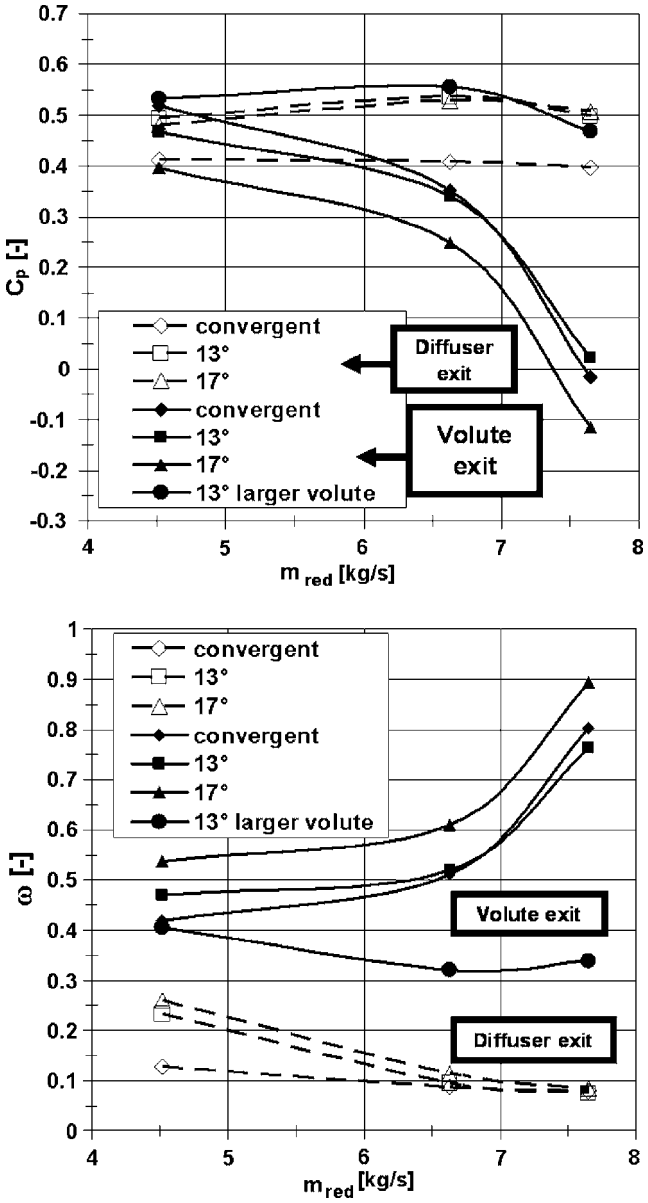

Fig. 11 Calculated static pressure rise and total pressure loss coefficients for different geometries and mass flows

Table 2 Predicted performance of LSDs at different inlet conditions

	4.52 kg/s		6.63 kg/s		7.65 kg/s	
At diff. exit	C_p	ω	C_p	ω	C_p	ω
Convergent	0.412	0.127	0.409	0.086	0.396	0.078
13° camber	0.494	0.232	0.536	0.094	0.497	0.074
17° camber	0.480	0.260	0.528	0.115	0.507	0.085
At volute exit						
Convergent	0.519	0.420	0.352	0.511	–0.015	0.803
13° camber	0.466	0.471	0.341	0.519	0.023	0.763
17° camber	0.397	0.538	0.249	0.610	–0.115	0.894
13° camber+ larger volute	0.533	0.405	0.557	0.321	0.469	0.338

Downloaded 30 May 2010 to 128.113.26.88. Redistribution subject to ASME license or copyright; see http://www.asme.org/terms/Terms_Use.cfm

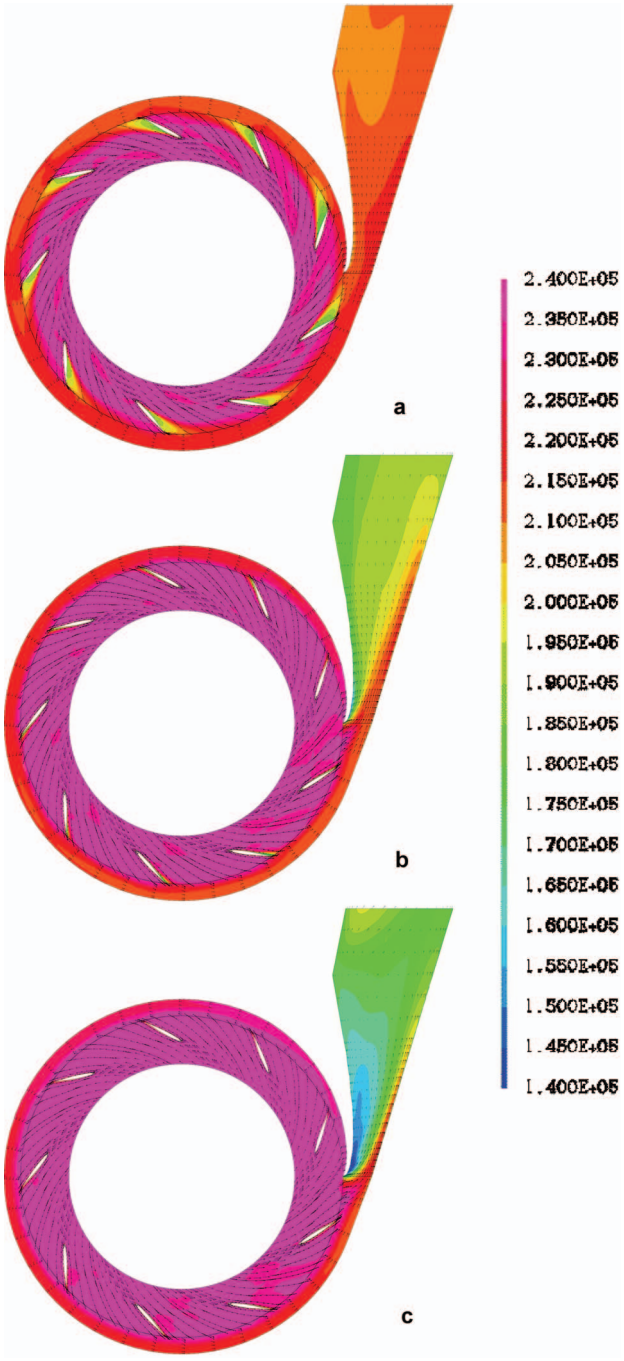

Fig. 12 Total pressure distribution (predicted by CFD in Pa) at midspan of the optimized LSD at 18,000 rpm for m_{red}=(*a*) 4.525, (*b*) 6.632, and (*c*) 7.655 kg/s

The circumferential static pressure distributions in the LSD near optimum mass flow are shown in Fig. 15. Measurements are taken on the diffuser hub wall near the impeller exit (r/r_2 =1.05), halfway along the vanes (r/r_2=1.395), and at the diffuser exit (r/r_2=1.50). The calculated static pressure distributions are at the same radial positions but at midspan. One observes a large pressure variation from the suction to the pressure side halfway along the diffuser vanes and its upstream influence on the circumferential pressure distribution at the impeller outlet. The measurements agree well with the calculations except at the diffuser exit where the pressure measured on the hub wall is higher than the one calculated at midspan. This is due to the large spanwise pressure variation at the diffuser outlet, resulting from the 90° turning of the flow (from radial at diffuser exit to axial at the internal volute inlet, Fig. 4(*d*)). Compared to the combination of the concentric diffuser with an external volute, the LSD has the advantage of reducing the upstream pressure distortion at the impeller exit.

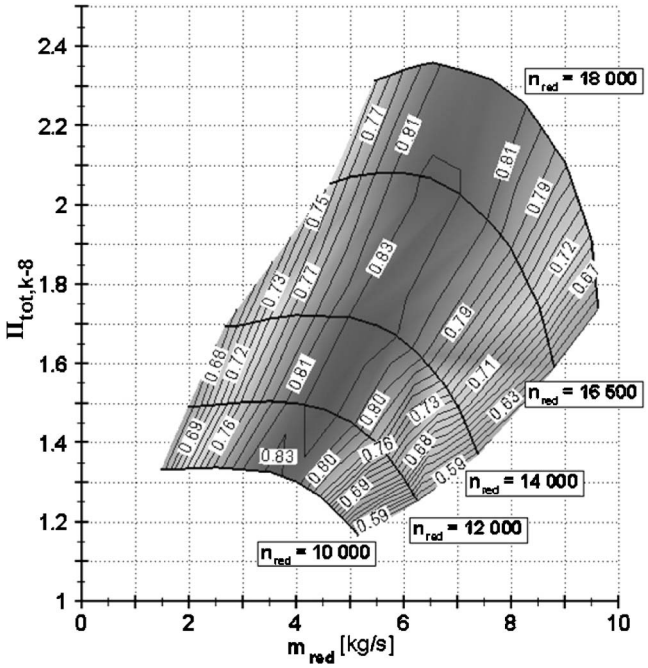

Fig. 13 Experimental performance map of the compressor with a LSD

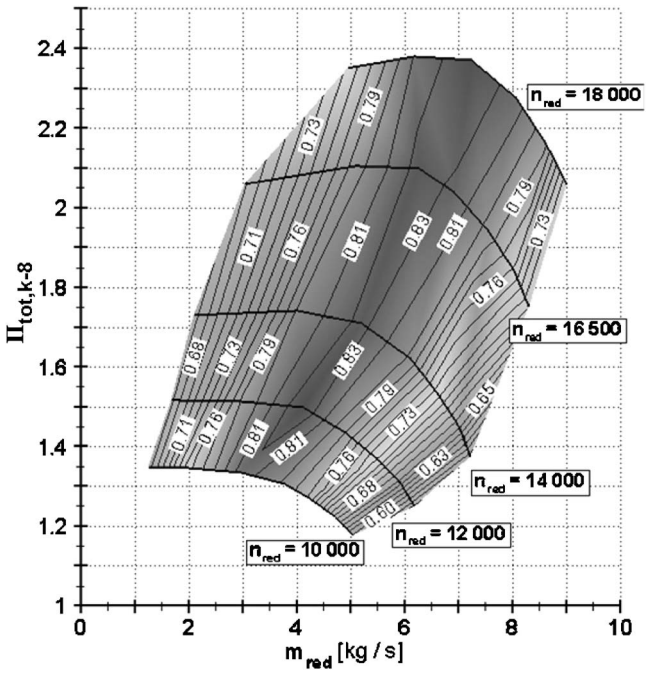

Fig. 14 Experimental performance map of the compressor with a concentric diffuser and an external volute

Downloaded 30 May 2010 to 128.113.26.88. Redistribution subject to ASME license or copyright; see http://www.asme.org/terms/Terms_Use.cfm

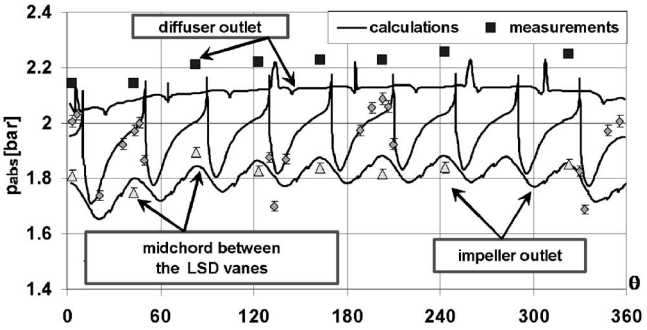

Fig. 15 Circumferential static pressure distributions on the hub wall at the diffuser inlet, midchord, and the trailing edge radius of the LSD (m_{red}=6.9 kg/s, n_{red}=18,000 rpm)

Comparison of Performance for the Different Diffuser Geometries

The pressure ratio $\Pi_{tot,k\text{-}8}$ and efficiency $\eta_{tot,k\text{-}8}$ of the different compressor geometries are compared in Figs. 16–18 for different speeds. The legend is shown in Fig. 16 only and refers to the different diffuser/volute combinations depicted schematically in Fig. 4. Although the asymmetric diffuser achieved a non-negligible increase of performance over the concentric diffuser, its performance falls short of that of the external volute with a concentric diffuser.

The higher performance of the external volute results from the extra deceleration, according to the conservation of angular momentum, between the diffuser exit and the center of the volute cross section. A similar deceleration has already taken place upstream of the volute when the flow is deflected by the LSD vanes. This increased diffusion results in a lower velocity at the volute inlet and, hence, in a decrease of friction and swirl losses in the volute. This explains how a pressure ratio, comparable to the one obtained with an external volute, could be obtained with a LSD/internal volute combination.

The weaker secondary vortex in the volute cross section also results in a lower blockage. Together with the larger cross section, this contributes to a higher choking mass flow for the LSD than for all other diffusers. The shift in surge limit to higher mass flows, when increasing n_{red} from 16,500 rpm to 18,000 rpm, is due to a reduction of the LSD incidence range with increasing inflow Mach number.

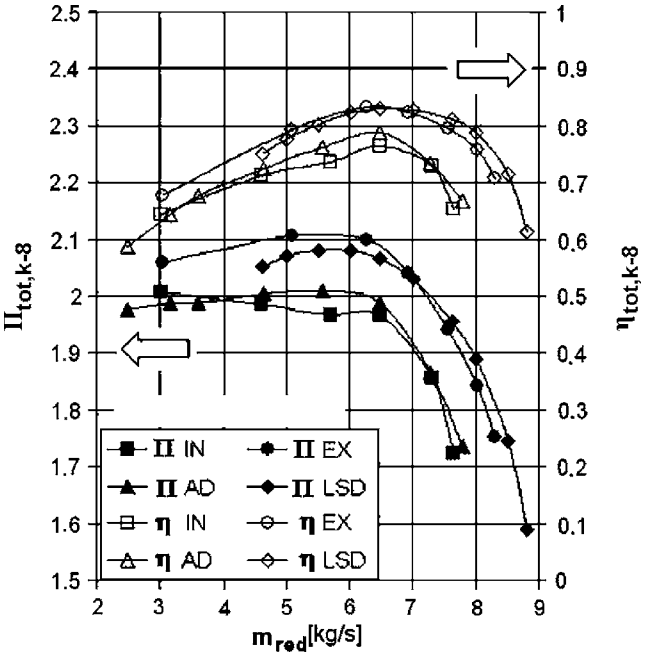

Fig. 17 Comparison of pressure ratio and isentropic efficiency for all four configurations at 16,500 rpm

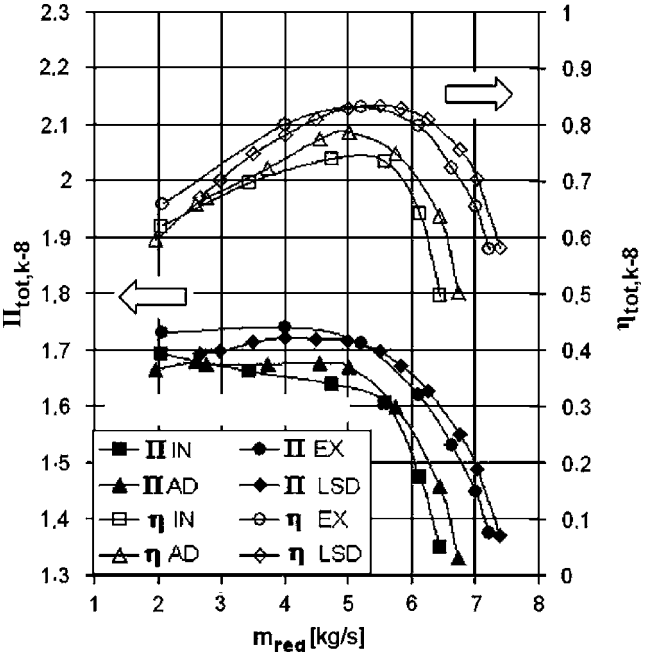

Fig. 16 Comparison of pressure ratio and isentropic efficiency for all four configurations at 14,000 rpm: (*a*) internal volute+concentric diffuser (IN), (*b*) internal volute+asymmetric diffuser (AD), (*c*) external volute+concentric diffuser (EX), and (*d*) internal enlarged volute+LS diffuser (LSD)

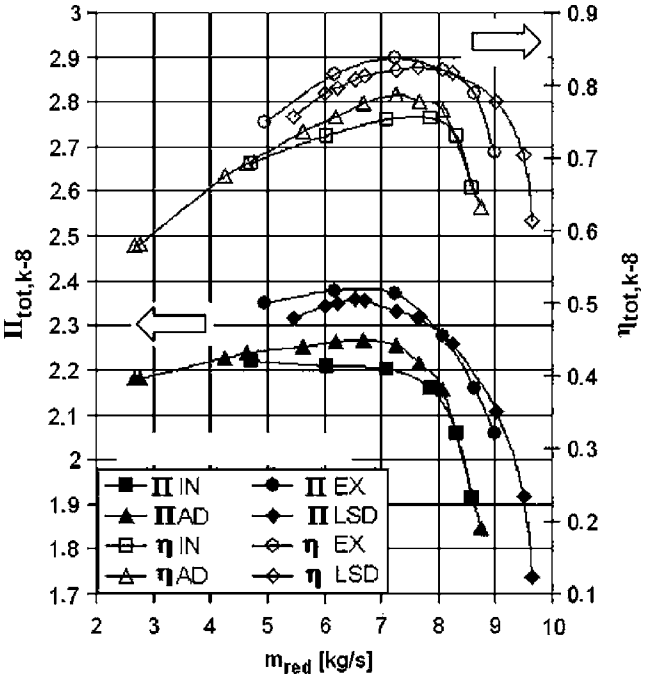

Fig. 18 Comparison of pressure ratio and isentropic efficiency for all four configurations at 18,000 rpm

Downloaded 30 May 2010 to 128.113.26.88. Redistribution subject to ASME license or copyright; see http://www.asme.org/terms/Terms_Use.cfm

The useful operating range of process compressors is limited to the zone of negative gradient of the pressure ratio versus mass flow. It is as large with the LSD as in the configuration with the external volute and a concentric vaneless diffuser.

Conclusions

Two geometry modifications of a diffuser with an internal volute have been described and their impact on performance has been analyzed. The internal volute with a nonaxisymmetric diffuser shows higher pressure ratio and efficiency than that with the axisymmetric diffuser over almost the complete operating range and all rotational speeds. The improvements are the consequence of lower friction losses by reducing the diffuser and volute surface and by avoiding a reacceleration of the flow in the volute.

The impeller outlet circumferential pressure variation at off design operation is slightly larger with the asymmetric diffuser than with the original concentric one. This may result in a small increase of dynamic loads on the impeller and the bearings.

The LSD and internal volute combination achieves pressure ratios and efficiencies that are close to the ones obtained with a concentric vaneless diffuser and a larger external volute, if the volute cross section is adapted to the new volute inlet conditions.

This paper illustrates the advantage of a simultaneous optimization of the diffuser and volute. The proposed modifications of the diffuser/internal volute system were both successful in terms of efficiency increase but resulted in a reduction of the operating range.

Design considerations, such as the higher dynamic load on the impeller or reduced operating range, will influence the decision on what option is the most appropriate to improve a specific internal volute design.

Acknowledgment

This paper is part of the scientific results of a research project, sponsored by the FVV ("Forschungsvereinigung Verbrennungskraftmaschinen e. V." = Combustion Machinery Research Association, Frankfurt, Germany) and was carried out at the Institute for Turbomachinery and Fluid Dynamics of Leibniz University Hannover and the von Karman Institute. This FVV project was partially (50%) financed by the German Ministry for Economics (BMWi) through the Society for Industry Research (AiF) (AiF-No. 12478 N) and partially through participating industry. The authors would like to thank FVV for funding the project. The guidance of Dr.-Ing. Rudof Keiper, Aktiengesellschaft Kühnle, Kopp & Kausch (KKK), and of the entire steering committee of the "FVV Spirale II" project was the key to success, to the innovative idea of an asymmetric diffuser, and is gratefully acknowledged.

Nomenclature

c_u = circumferential velocity (m/s)
C_p = pressure rise coefficient
m = mass flow rate (kg/s)
n_{red} = reduced rotor speed in rpm (min^{-1})
r = radius (mm)

Greek Letters

α = flow angle (measured from radial) (degree)
Π = pressure ratio
θ = circumferential angle (measured from tongue position) (degree)
ω = total pressure loss coefficient
ρ = density (kg/m^3)

Subscripts

isentropic = isentropic value
k = inlet settling chamber
red = quantity at standard inlet conditions
tot = total value
2 = impeller exit
3 = diffuser exit
8 = compressor exit flange

References

[1] Ayder, E., and Van den Braembussche, R. A., 1991, "Experimental Study of the Swirling Flow in the Internal Volute of a Centrifugal Compressor," ASME Paper No. 91-GT-7.
[2] Ayder, E., Van den Braembussche, R. A., and Brasz, J., 1993, "Experimental and Theoretical Analysis of the Flow in a Centrifugal Compressor Volute," ASME J. Turbomach., **115**(3), pp. 582–589.
[3] Ayder, E., and Van den Braembussche, R. A., 1994, "Numerical Analysis of the Three-Dimensional Swirling Flow in a Centrifugal Compressor Volute," ASME J. Turbomach., **116**(3), pp. 462–468.
[4] Japikse, D., 1982, "Advanced Diffusion Levels in Turbocharger Compressors and Component Matching," *Proceedings of the First International Conference on Turbocharging and Turbochargers*, IMECHE, London, pp. 143–155.
[5] Weber, C. R., and Koronowski, M. E., 1986, "Meanline Performance Prediciton of Volutes in Centrifugal Compressors," ASME Paper No. 86-GT-216.
[6] Hagelstein, D., Hillewaert, K., Van den Braembussche, R. A., Engeda, A., Keiper, R., and Rautenberg, M., 2000, "Experimental and Numerical Investigation of the Flow in a Centrifugal Compressor Volute," ASME J. Turbomach., **122**(1), pp. 22–31.
[7] Binder, R. C., and Knapp, R. T., 1936, "Experimental Determination of the Flow Characteristics in the Volutes of Centrifugal Pumps," Trans. ASME, **58**, pp. 649–663.
[8] Knapp, R. T., 1941, "Centrifugal Pump Performances Affected by Design Features," Trans. ASME, **63**(2), pp. 251–260.
[9] Brown, W. B., and Bradshaw, G. R., 1947, "Design and Performance of Family of Diffusing Scrolls With Mixed-Flow Impeller and Vaneless Diffuser," Flight Propulsion Research Laboratory, National Advisory Committee for Aeronautics, Cleveland, OH.
[10] Lee, Y., Luo, L., and Bein, T. W., 2000, "Direct Method for Optimization of a Centrifugal Compressor Vaneless Diffuser," ASME J. Turbomach., **123**(1), pp. 73–79.
[11] Mishina, H., and Gyobu, I., 1978, "Performance Investigations of Large Capacity Centrifugal Compressors," ASME Paper No. 78-GT-3.
[12] Reunanen, A., Pikänen, H., Siikonen, T., Heiska, H., Larjola, J., Esa, H., and Sallinen, P., 2000 "Computational and Experimental Comparison of Different Volute Geometries in a Radial Compressor," ASME Paper No. 2000-GT-469.
[13] Hagelstein, D., Van den Braembussche, R. A., Keiper, R., and Rautenberg, M., 1997, "Experimental Investigation of the Circumferential Static Pressure Distortion in Centrifugal Compressor Stages," ASME Paper No. 97-GT-50.
[14] Miner, S. M., Flack, R. D., Allaire, P. E., 1992, "Two Dimensional Flow Analysis of a Laboratory Flow Pump," J. Turbomach., **144**, pp. 333–339.
[15] Chen, S. H., and Liaw, L. F., 1997, "The Flowfield Calculations of a Centrifugal Pump With Volute," ASME Paper No. 97-GT-49.
[16] Flathers, B., and Bache, G. E., 1999, "Aerodynamically Induced Radial Forces in Centrifugal Compressor—Part 2: Computational Investigation," ASME J. Eng. Gas Turbines Power, **121**(4), pp. 725–734.
[17] Senoo, Y., Hayami, H., and Ueki, H., 1983, "Low Solidity Tandem-Cascade Diffusers for Wide-Flow-Range Centrifugal Blowers," ASME Paper No. 83-GT-3.
[18] Engeda, A., 2001, "The Design and Performance Results of Simple Flat Plate Low Solidity Diffusers," Proc. Inst. Mech. Eng., Part A, **215**, pp. 109–118.

Downloaded 30 May 2010 to 128.113.26.88. Redistribution subject to ASME license or copyright; see http://www.asme.org/terms/Terms_Use.cfm

Numerical Investigation of End Wall Boundary Layer Removal on Highly Loaded Axial Compressor Blade Rows

V. Gümmer
e-mail: volker.guemmer@rolls-royce.com

M. Goller

M. Swoboda

Compressor Engineering,
Rolls-Royce Deutschland Ltd. & Co. KG,
Eschenweg 11,
D-15827 Dahlewitz, Germany

This paper presents results of numerical investigations carried out to explore the benefit of end wall boundary layer removal from critical regions of highly loaded axial compressor blade rows. At the loading level of modern aero engine compressors, the performance is primarily determined by three-dimensional (3D) flow phenomena occurring in the end wall regions. Three-dimensional Navier–Stokes simulations were conducted on both a rotor and a stator test case in order to evaluate the basic effects and the practical value of bleeding air from specific locations at the casing end wall. The results of the numerical survey demonstrated substantial benefits of relatively small bleed rates to the local flow field and to the performance of the two blade rows. On the rotor, the boundary layer fluid was removed from the main flow path through an axisymmetric slot in the casing over the rotor tip. This proved to give some control over the tip leakage vortex flow and the associated loss generation. On the stator, the boundary layer fluid was taken from the flow path through a single bleed hole within the passage. Two alternative off-take configurations were evaluated, revealing a large impact of the bleed hole shape and the location on the cross-passage flow and the suction side corner separation. On both blade rows investigated, rotor and stator, the boundary layer removal resulted in a reduction of the local reverse flow, blockage, and losses in the respective near-casing region. This paper gives insight into changes occurring in the 3D passage flow field near the casing and summarizes the effects on the radial matching and pitchwise-averaged performance parameters, namely loss and deviation of the rotor and stator when suction is active. Primary focus is put on the aerodynamics in the blade rows in the main flow path; details of the internal flow structure within the bleed off-take cavities/ports are not discussed here. [DOI: 10.1115/1.2749297]

Introduction

The compression system of an aeroengine has a high potential to contribute to weight and cost reduction of the unit. In order to allow the desired reduction in stage and part count, the aerodynamic loading of the individual blade rows must rise, but highly loaded compressors can only be designed for high efficiency if the boundary layers on both aerofoil and end wall are well controlled.

In the 1980s, controlled-diffusion aerofoils were introduced to control the two-dimensional (2D) profile boundary layers [1,2]. In the 1990s the deliberate use of sweep and dihedral was widely explored and applied in numerous compressor designs [3–6]. further potential enhancement of the compressor aerodynamic design is the use of new features providing passive or even active flow control, such as casing treatment, flow removal, and flow injection. In order to allow a successful application of these features, the flow phenomena to be controlled need to be understood in detail. At the loading level of modern axial compressors, the performance is largely dependent on three-dimensional (3D) secondary flows occurring in the end wall regions.

A prime contributor to secondary flows in rotor blade passages is the tip leakage, which is generated in the radial tip clearance gap. The leakage flow interacts with the casing end wall boundary layer and forms an area of reverse flow occurring within the blade passage near the casing. In transonic rotors, as well as in highly loaded subsonic rotors, the reverse-flow region covers a major portion of the rotor passage and comes fairly close to the blade leading edge [7–10]. On these types of rotors, stall inception usually occurs in the tip region of the blade. In this case, the flow reversal instantaneously progresses into regions upstream of the rotor leading edge (spill forward mechanism), which triggers the development of a rotating stall in the time span of just a few rotor revolutions. A number of tip injection concepts have recently been investigated to suppress or delay tip stall inception [11–14]. Some of the work published on rotor tip flow control reports the use of bleed/suction [15], applied on a shrouded rotor of a fully aspirated fan stage. To the knowledge of the authors, no published work has dealt with the effects of tip suction on highly loaded unshrouded rotors. The rotor investigations reported in the present paper were carried out on a low-speed research compressor (LSRC) to gain an additional understanding of the rotor tip flow physics in the presence of bleed, taken to remove the end wall boundary layer fluid from the rotor tip clearance region.

A major driver of secondary flow in stator blade passages is the cross-passage flow, which occurs at fixed ends and usually leads to flow separation in the end wall suction side corner [16,17]. Depending on the turning and local loading of the blade row, the corner separation may cover a significant part of the span and may feature a complicated 3D topology [4,18]. Some publications [19,20] deal with air injection or recirculation aimed at controlling the 2D suction surface boundary layer on the aerofoil. Limited work has addressed the control of end wall separation. Early cascade experiments [21] have demonstrated the potential of local suction/bleeding to reduce the size of corner separation. In Ref. [15], suction was used to improve the outer end wall flow in a

Contributed by the International Gas Turbine Institute of ASME for publication in the JOURNAL OF TURBOMACHINERY. Manuscript received February 9, 2006; final manuscript received September 22, 2006; published online January 25, 2008. Review conducted by David Wisler. Paper presented at the ASME Turbo Expo 2005: Land, Sea and Air (GT2005), Reno, NV, June 6–9, 2005, Paper No. GT2005-68699.

 Copyright © 2008 by ASME

Downloaded 30 May 2010 to 128.113.26.88. Redistribution subject to ASME license or copyright; see http://www.asme.org/terms/Terms_Use.cfm

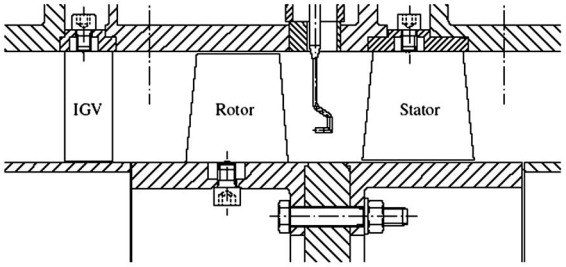

Corrected Inlet Flow	6.82 kg/s
Corrected Tip Speed	88 m/s
Work Coefficient	> 0.5
Reaction	0.64
Diffusion Factor (R, S)	0.50
Outer Diameter	0.6 m

Fig. 1 Low-speed research compressor

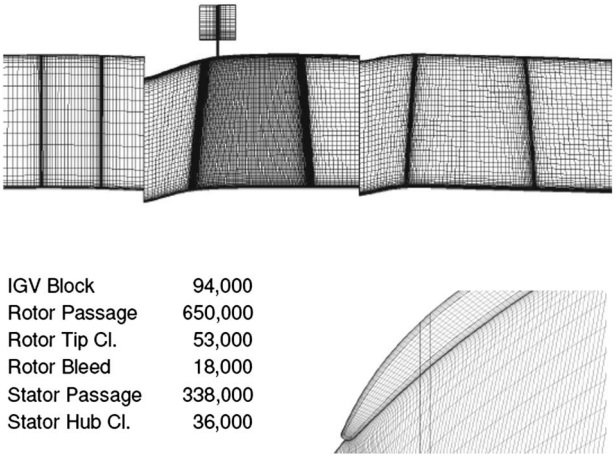

IGV Block	94,000
Rotor Passage	650,000
Rotor Tip Cl.	53,000
Rotor Bleed	18,000
Stator Passage	338,000
Stator Hub Cl.	36,000

Fig. 2 LSRC model grid topology

transonic stator. In general, taking bleed is a normal measure in multistage compressors to supply air for cooling of high-temperature components and pressurization of cavities. In Ref. [22], the predictive accuracy of different bleed models is investigated. The conclusion is drawn that the off-take (OT) geometry needs to be fully modeled to resolve the complex flow structure and that the OT is best located downstream of the aerofoil trailing edge plane to obtain maximum efficiency. The complexity and the problems present in the flow field in the vicinity of casing bleed holes and slots, which are located within the aerofoil passage, were investigated only recently in adequate detail [23,24]. These works focused on bleed OTs that were sized to allow bleed mass flows significantly higher than the nominal flow to allow for an off-design operation of the compressor. The stator investigations reported in the present paper are based on the approach of combining secondary air OT with end wall flow control. This novel concept was developed to fulfill the requirement of continually supplying a fixed amount of air at the outer wall of an embedded highly loaded stator of a multistage high-speed compressor.

In the present paper, highly loaded rotor and stator configurations are investigated numerically, each of the two featuring a local bleed OT at an aerodynamically critical location of the flow path.

Rotor Casing Flow Removal

As the effectiveness of the casing boundary layer removal increases with the aerodynamic loading of the rotor in the tip region, a relatively highly loaded machine was selected for the numerical study presented in the next paragraphs. The respective LSRC has been designed and built for investigations of the tip leakage flow and different 3D rotor designs in a past research program. The aerodynamic and mechanical designs of the single-stage machine are reported in Refs. [8,9]. For convenience, some details of the LSRC are given in Fig. 1.

The present study of the casing boundary layer removal was limited to the base line stage configuration using a 2D-style rotor, which features straight radial stacking of the blade sections. The LSRC is designed at a hub-to-tip ratio of 0.75 within parallel annulus lines at constant inner and outer radii. The stage is equipped with an inlet guide vane (IGV) to provide some preswirl to the rotor. The axial length of the annulus was fixed to give a low aspect ratio arrangement on both rotor and stator. The stator is cantilevered, and the design assumes a radial clearance gap of 1% annulus height at rotor tip and stator hub. The aerodynamic loadings and geometry of the LSRC are derived from the middle stages of a multistage HP compressor for application in modern two-shaft civil engines.

Numerical Model. Simulations of the steady, 3D viscous flow field were carried out on the full compressor stage, including the IGV, using the 3D CFD package Numeca FINE TURBO, (see Fig. 2). The whole stage was modeled in order to capture the impact on the stator flow field and to allow a comparison to existing designs of the stage which are not reported here. The code solves the Reynolds-averaged Navier–Stokes equations on structured multi block arbitrary grids using mixing planes between blade rows. An explicit time marching, implicit residual smoothing four-step Runge–Kutta procedure, and a cell-centered second-order finite-volume discretization are employed. Local time stepping and multigrid functionality improve convergence. The turbulence model of Spallart–Almaras was used for the present study.

A circumferential slot of a small axial width was implemented as a bleed device at the casing over the rotor tip. This bleed modeling approach allows standard grid topologies in both domains. Due to the axisymmetric geometry of the slot, 3D Navier–Stokes the (3DNS) simulations can be run in a steady-state mode. The bleed slot is 1 mm wide, equivalent to about 1.5% of the rotor chord length, and takes 1% of the inlet flow. Based on an existing mesh of the stage, the axial resolution of the mesh in the rotor was significantly refined to give a sufficient coverage with the bleed slot grid block at any axial location between the blade leading and trailing edge. The radial and circumferential grid resolutions were increased across the rotor and the stator. Comparisons of the existing original model and the refined model were carried out to ensure that the predicted results remained closely similar.

The passages of all blade rows were modeled using a standard elliptical *H*-grid. The number of cells in the radial direction on the IGV, rotor, and stator are 37, 81, 73, respectively. The true tip geometry of the rotor and the stator was modeled introducing separate tip clearance grid blocks (13 cells in the radial direction). On both rotor and stator, a butterfly grid topology was used, which consists of an inner *H*-type core portion encapsulated by an *O*-type grid domain.

The bleed device was modeled using a simple *H*-grid, covering at least two cells of the passage/tip clearance grid block. A nonmatching grid interface (interpolation) is used to connect the tip clearance blocks and the bleed slot block. Except in the region around the blade edges, grid cell aspect ratios were kept below 8, expansion ratios below 10, and $y+$ below 8.

Rotor Near-Casing Three-Dimensional Flow Field. As reported in Ref. [8], the growth of losses at the tip clearance end of

Downloaded 30 May 2010 to 128.113.26.88. Redistribution subject to ASME license or copyright; see http://www.asme.org/terms/Terms_Use.cfm

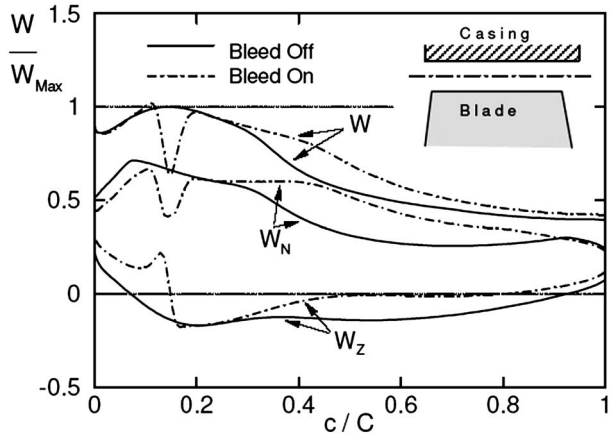

Fig. 3 Chordwise midgap velocity distributions, operation at DP with bleed off/on

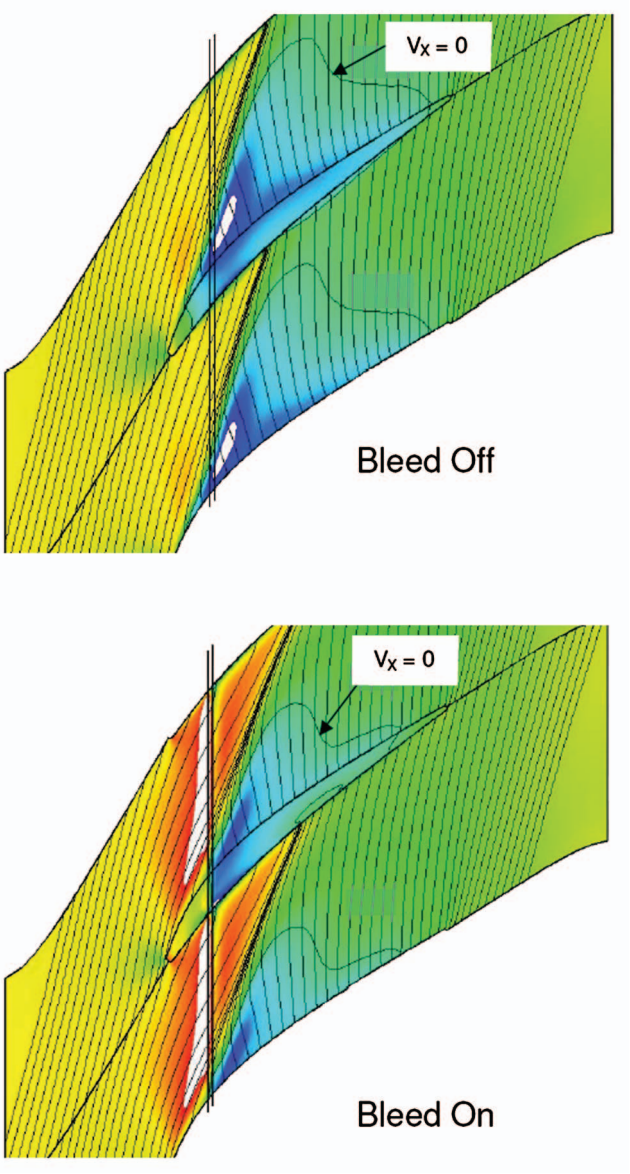

Fig. 4 Contours of axial velocity and relative velocity streamlines at midgap radial height

the rotor is primarily driven by the axial and radial extent of the reverse-flow patch occurring across part of the tip chord in the region of maximum pressure gradients across the gap. In this region, a strong tip leakage vortex is generated, which rapidly loses its vortical structure when interacting with the low-momentum end wall flow and being exposed to the high adverse axial pressure gradient through the blade passage. Additional low-momentum fluid passing the radial gap in the rear part of the blade also tends to stagnate due to the blocking effect and the flow direction imposed by the reverse-flow patch in the front part of the blade passage.

Figure 3 shows the distribution of the relative velocity, the relative velocity component normal to the tip chord line, and the axial velocity component, all determined in the center of the tip clearance gap (i.e., at half the radial gap height and along a projection of the profile camber line) at the design operating point. For the given profile loading distribution, the maximum relative velocity in the gap occurs at 15% chord and continuously reduces toward the trailing edge, similar to the normal velocity component, which has its peak somewhat further upstream at 10% chord. The axial velocity changes sign to negative at this position, reaches a minimum at 20% chord, and indicates a reverse flow down to 90% chord. When the bleed is taken, the relative and relative normal velocity distributions show a deep local reduction at the bleed position and an increase over the remaining downstream part of the chord. The axial velocity is positive up to the bleed position, rapidly reduces down to the original minimum at 20% chord, but returns to zero at 50% chord, and shows positive values from 80% chord on.

As a consequence of the bleed removing some of the low-momentum fluid a significantly larger portion of the end wall flow tends to travel downstream without stagnation. The area of reverse flow and the associated blockage are largely reduced. The near-end-wall flow field is depicted in Fig. 4, showing contours of axial velocity in an axisymmetric blade-to-blade plane located at a midgap height close to the casing at the design point condition. The flow field of the rotor configuration without the bleed slot is not shown here, as it was found to be virtually identical to that with the bleed slot attached but nonactive.

When no bleed is taken, the flow enters the passage at an almost uniform axial velocity and approaches a 3D separation line, which is originated at the suction side near the leading edge and ends at about 30% chord at the pressure surface of the adjacent blade. The separation line is closely linked to the development of the tip leakage vortex and is located immediately upstream the vortex casing trajectory. Downstream of the 3D separation line, there is a region of much lower axial velocity, showing a reverse-flow patch that originated along the suction surface. The axial forward (reverse) component of the flow direction is also apparent from the streamlines derived using rotor relative velocity and also shown in the figure.

When the bleed is active, axial velocity is increased in a region just upstream of the bleed slot, covering approximately 10% of the axial passage length. In this narrow region, the flow angle is visibly reduced, supporting the desired turning in the blade passage. This bleed effect occurs almost uniformly across the full blade pitch, indicating that the bleed OT flow is sufficiently high to avoid pitchwise recirculation along the slot, even when being exposed to the fairly high blade-to-blade pressure gradients given on this rotor. As a consequence of a more axially directed flow behind the bleed slot, the 3D separation line is more oblique. In this case, the triangular region of high-momentum flow between the slot and the separation line is larger. The tip leakage vortex is more aligned with the main flow and therefore represents less endwall blockage in the tip region of the rotor passage. Downstream of the 3D separation line a markably smaller region of reverse flow occurs. The reverse-flow patch is still located near

Downloaded 30 May 2010 to 128.113.26.88. Redistribution subject to ASME license or copyright; see http://www.asme.org/terms/Terms_Use.cfm

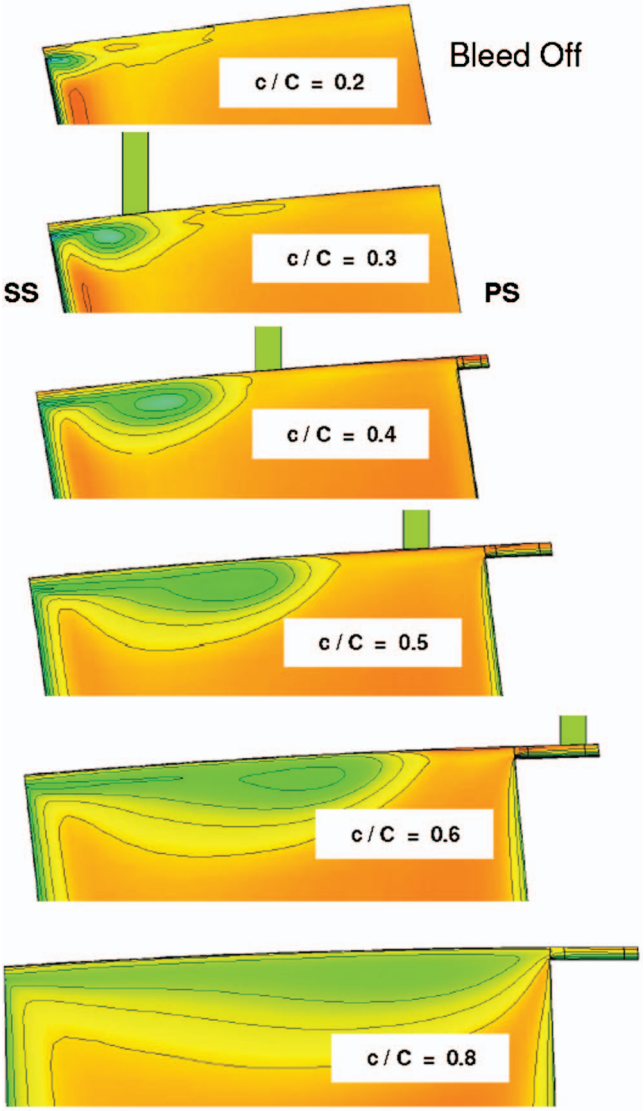

Fig. 5 Development of near-casing relative total pressure contours through the rotor passage, bleed off

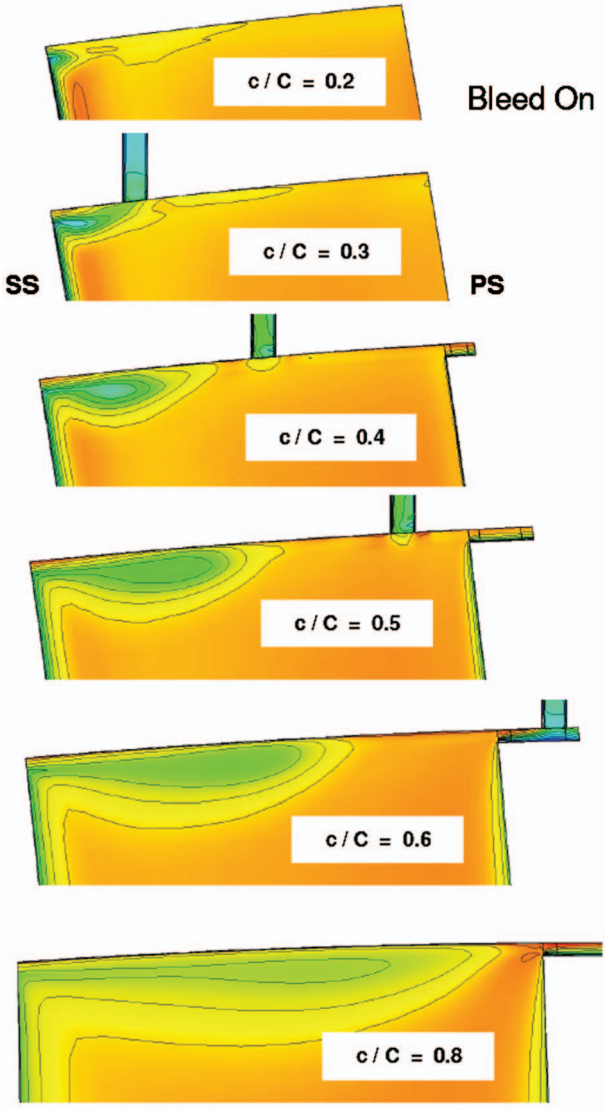

Fig. 6 Development of near-casing relative total pressure contours through the rotor passage, bleed on

the suction surface, but is limited by the bleed slot in upstream direction and shows a reduction of 30% extent in pitchwise and downstream direction.

Since a large portion of the low-momentum fluid either entering the passage or leaking over the blade tip is rolled up into the tip leakage vortex and transported downstream, there is a significant impact of the bleed on the development of losses across the rotor passage. Figures 5 and 6 show contours of relative total pressure in selected planes normal to the rotor tip chord direction. At 20% chord, which is just ahead of the bleed slot position, the vortex loss core shows up as a very local and concentrated feature of the flow field in both cases, bleed off and on. Downstream of this front location, the loss core rapidly grows and, in the case of no bleed taken, almost occupies the full blade pitch when approaching the exit of the passage. Since the radial growth of the vortex loss core is not as strong, the loss region changes its shape from "circular" to "oval" when passing through the passage. A significant radial immersion of the vortex loss region of about 10% blade height can be observed at the exit of the rotor. When bleed is taken, the growth and radial immersion of the vortex loss core is reduced. Already in front of the bleed slot at 20% chord, the loss core is sucked toward the casing wall, and at 30% chord, part of the loss core is removed through the bleed slot. Caused by this mechanism, the vortex loss core is deflected toward the suction surface and takes a more streamwise orientation, which is maintained all the way down the passage. This is consistent with the previous observation of the vortex separation at the casing getting more oblique. At the exit of the rotor, the loss region covers a smaller portion of the blade pitch and gives less blockage due to the reduced growth and interaction of the vortex with the main flow than in the case of no bleed being taken.

Pitchwise-Averaged Results. The reduction of blockage caused by the flow removal at the tip of the rotor has an effect not only on the flow field near the casing but, to some degree, also near the hub. Figure 7 shows the radial distribution of deviation and pressure loss coefficient at the design operating point. When taking bleed, deviation is reduced across the upper 50% of blade height although the bleed is acting very locally at the casing. In the area of 10% to 50%, blade height deviation is increased by almost the same amount due to the slightly higher loading generated by a reduced blockage at the tip. However, the differences in deviation are small and the total average remains virtually unchanged.

The radial distribution of the pitchwise-averaged loss coefficient shows the huge magnitude of loss generation in the tip leak-

Downloaded 30 May 2010 to 128.113.26.88. Redistribution subject to ASME license or copyright; see http://www.asme.org/terms/Terms_Use.cfm

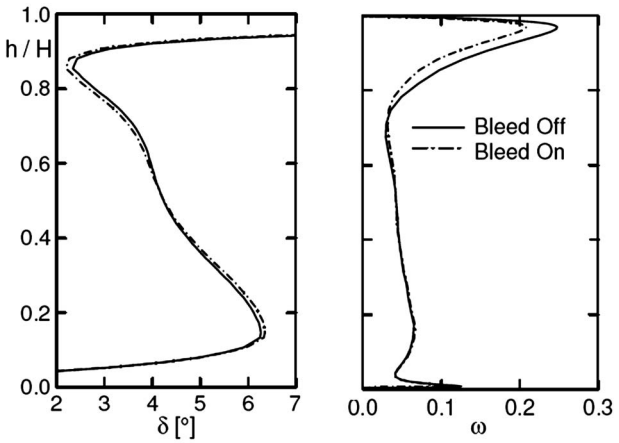

Fig. 7 Rotor pitchwise-averaged deviation and loss coefficient

age flow region of the present rotor. Local losses near the casing are five times as high as at midheight. The tip losses still dominate when bleed is taken. However, the bleed leads to a local 20% reduction of losses across the upper quarter of the blade span.

Although the bleed air taken has no specific destination and has to be accounted for as a loss for the compression system, the overall performance of the rotor benefits from the casing boundary layer removal, as the tip leakage flow reduction and the associated loss and blockage reduction—locally as well as averaged—is dominant.

Stator Casing Flow Removal

The numerical investigations carried out on a stator have been initiated with a slightly different scope. In this case, a certain amount of permanent bleed air was to be provided by the middle stages of a multistage axial compressor for secondary use in the engine. The stator considered here is a high-speed derivative of the LSRC stator used in the previously discussed rotor simulations. Figure 8 gives an arrangement of the embedded stator geometry. The aerofoils are aerodynamically highly loaded and of small physical size. The performance of the stator, which had to incorporate the OT hole due to mechanical design limitations, was found to be unexpectedly sensitive to taking bleed air, even at the design flow rate of about 3% of core flow. Therefore, a variety of different bleed OTs were investigated to improve the stator/OT configuration. The baseline design is a circular-hole OT located midway between two aerofoils in the rear half of the stator passage (see Fig. 9(*a*)). The study eventually led to a tailored bleed OT, which is relatively slim, located close to the suction side of the aerofoil, and which uses less cross-sectional area to remove the air more efficiently from the flow path (see Fig. 9(*b*)).

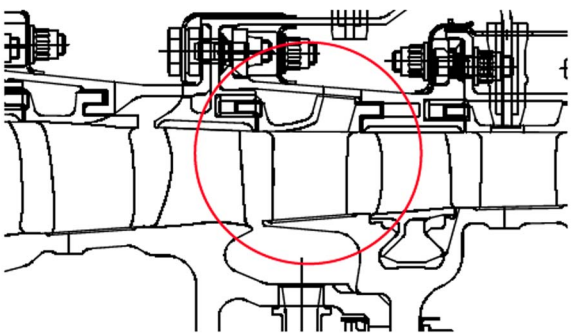

Fig. 8 Embedded stator arrangement

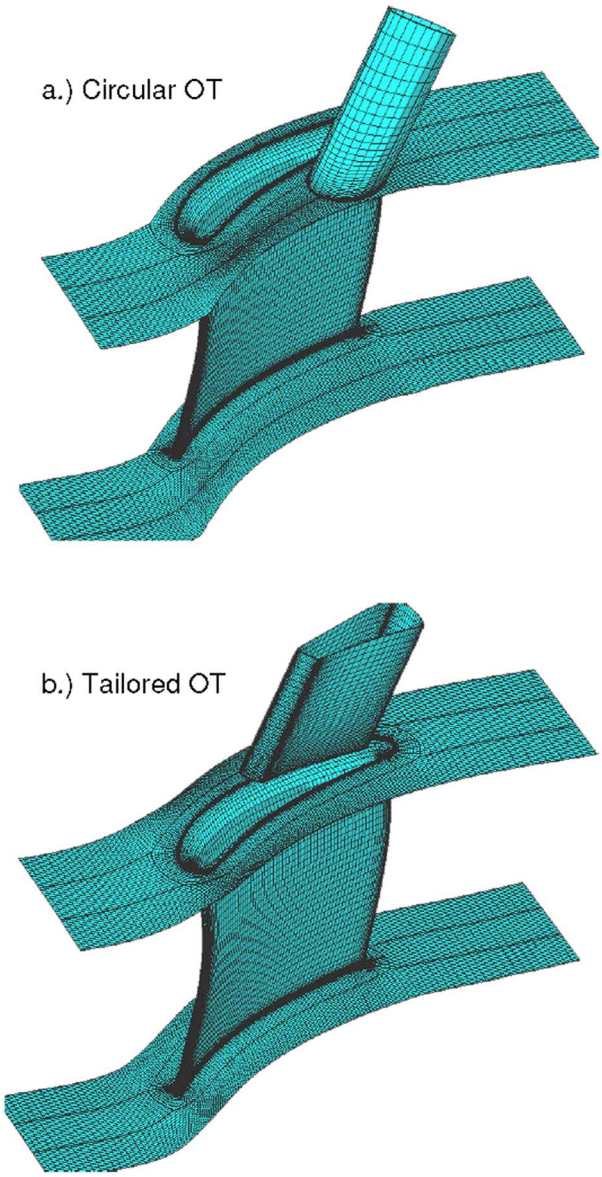

Fig. 9 Stator grid model featuring different bleed geometries: (*a*) circular OT; (*b*) tailored OT

Throughout the whole investigation, the stator aerofoil geometry was not changed. However, the downstream rotor was redesigned to match the improved stator exit conditions.

Numerical Model. The 3DNS simulations were carried out on a single blade row model featuring a fine mesh of approximately 500.000 grid points in the main flow passage. This grid is divided into a number of individual blocks, two adjacent *H*-grid blocks located in the center domain of the passage, an *O*-grid block in the vicinity around the aerofoil, and one *H*-grid block each to fill the remaining gap upstream and downstream of the *O* grid. The tip clearance at the hub is gridded using a so-called butterfly topology in which a central *H* grid is encased by an outer *O* grid. The hub clearance is resolved with 17 points in the radial direction. At the casing, a fillet radius has been implemented. The bleed OT geometry was fully modeled in order to resolve the interaction of the main and bleed flow domain correctly. The OT is represented by a separate block, which corresponds to the passage blocks across a fully nonmatching interface, which hugely reduces the meshing effort and ensures that the same blade passage grid can be used in

Downloaded 30 May 2010 to 128.113.26.88. Redistribution subject to ASME license or copyright; see http://www.asme.org/terms/Terms_Use.cfm

all computations. All investigated bleed blocks were resolved with approximately 50.000 grid points. An elliptical smoothing procedure was applied to the entire grid, improving to high quality in terms of aspect ratio and cell skewness angle. The stator has a cantilevered arrangement and, therefore, features a radial clearance at the hub. All simulations assumed a relative clearance gap size of 1.5% annulus height. The boundary conditions in terms of total pressure and temperature profile at the inlet and back static pressure at the outlet of this single-row calculation were provided by a multistage calculation previously performed for the entire compressor. The effect of the stagewise mixing and the effect of the vortex reducer OT upstream the stator have been taken into account. The simulations were done at the design point and for the nominal bleed off-take rate, equally for all computations. At the outlet of the bleed hole, a mass flow boundary condition was applied. This ensures identical bleed rates for all configurations investigated.

Passage Three-Dimensional Flow Field. The base line stator model features a circular bleed hole in the rear part of the passage, positioned slightly off mid-passage toward the pressure side of the aerofoil (region of maximum static pressure). The OT center line is inclined against the radial direction by about 30 deg to ease flow entry. This configuration was expected to give high bleed OT pressures. However, 3DNS simulations revealed large regions of separation giving poor stator performance. In order to quantify the impact of the bleed, additional simulations were carried out on a "clean" configuration without bleed OT, (see Fig. 10). The upper part of the figure shows the stator aerofoil and the casing end wall, viewed from the rear. Mach number contours and surface streak lines illustrate the intrapassage flow field. The blue color designates regions of low-momentum flow. Near the casing end wall, cross-passage flow develops due to the strong pitchwise pressure gradient present in the passage. A large portion of the end wall low-momentum fluid is driven toward and down the suction surface. The corner separation is of relatively simple topology. Reverse flow occurs only locally near the trailing edge at 80% span. A smaller portion of the end wall boundary layer reaches the stator exit with little distortion and, therefore, without reverse flow. The lower part of the figure shows total pressure contours in a plane at 10% of chord downstream of the stator. The region of low total pressure spreads across 35% of the span, but the pitchwise extent and, therefore, the amount of annulus blockage generated by the corner separation are still moderate. The boundary layers leaving the passage at the hub and casing have similar thicknesses and occupy approximately 15% of the annulus height.

The flow field within and downstream of the stator changes when the circular OT is attached to the model and bleed is taken (see Fig. 11). The corner stall in this configuration is considerably larger than observed in the stator flow field without bleed. The surface streak lines show a pattern of 3D separation lines and attachment lines in the corner stall region, which has primarily grown in the pitchwise direction. It is now dominated by flow stagnation and reverse flow. On both the hub and the suction surface, a focus is formed as additional elements of the complicated 3D flow structure. This type of corner stall topology is usually associated with high flow path blockage and high entropy rise. In the remaining fraction of the pitch, which is not blocked by the corner stall, very little end wall boundary layer leaves the passage. At midchord, some boundary layer moves down the suction surface to feed the corner stall, but at and beyond the bleed position, the cross-passage flow mechanism is almost eliminated as the responsible boundary layer is removed. Taking bleed within the passage generally increases the level of diffusion, but the aerofoil should cope with this without any significant deterioration of its performance. However, the way the circular bleed hole takes the air from the passage generates most of the diffusion locally in the vicinity of the end wall suction side corner, causing the sensitive corner stall region to grow. The total pressure contours at the stator exit show the huge corner stall blockage, which has

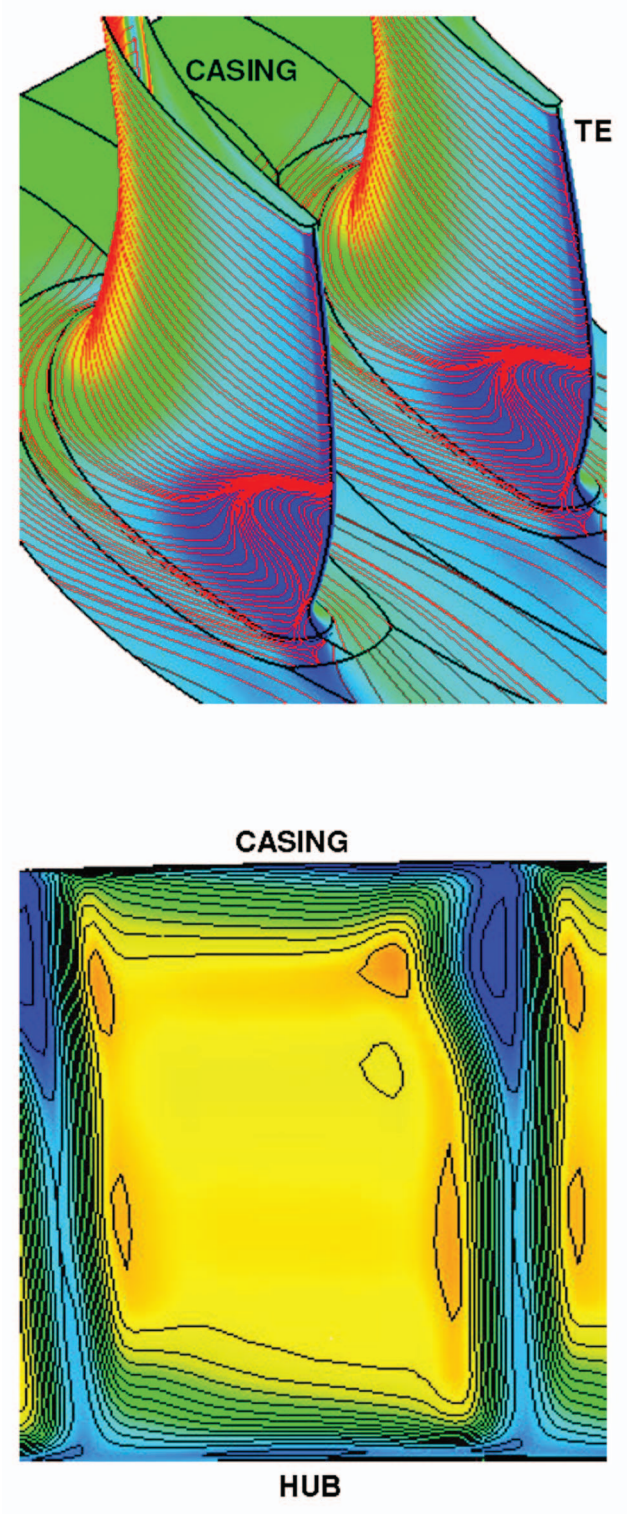

Fig. 10 Stator surface Mach number contours and streak lines, stator exit total pressure contours, no OT

doubled relative to the clean configuration, and confirm the removal of the casing boundary layer in the region left of it. The trailing edge wake across the inner 70% of span and the pressure deficit in the hub tip clearance region have slightly reduced.

In order to avoid the detrimental effects observed, the position and shape of the bleed OT were changed to fit the specific needs of the stator flow field. The tailored bleed OT is also located in the

Downloaded 30 May 2010 to 128.113.26.88. Redistribution subject to ASME license or copyright; see http://www.asme.org/terms/Terms_Use.cfm

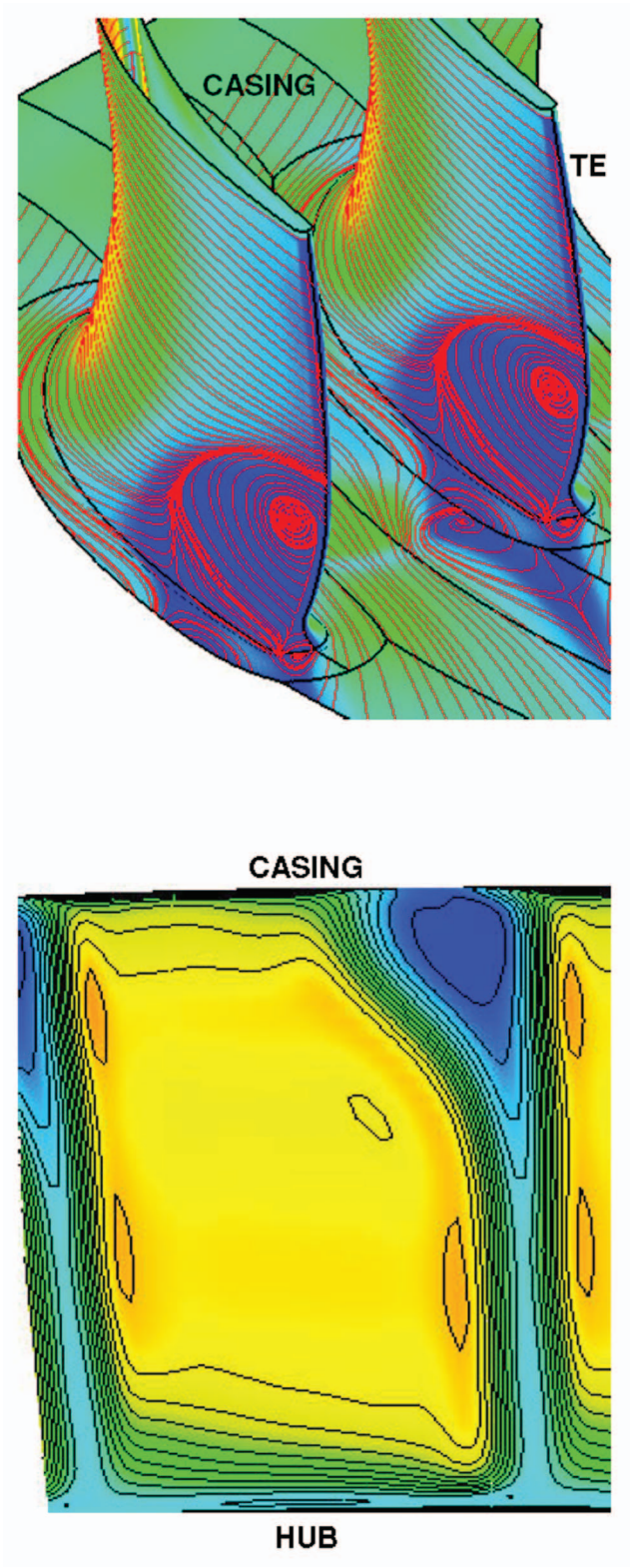

Fig. 11 Stator surface Mach number contours and streak lines, stator exit total pressure contours, circular OT

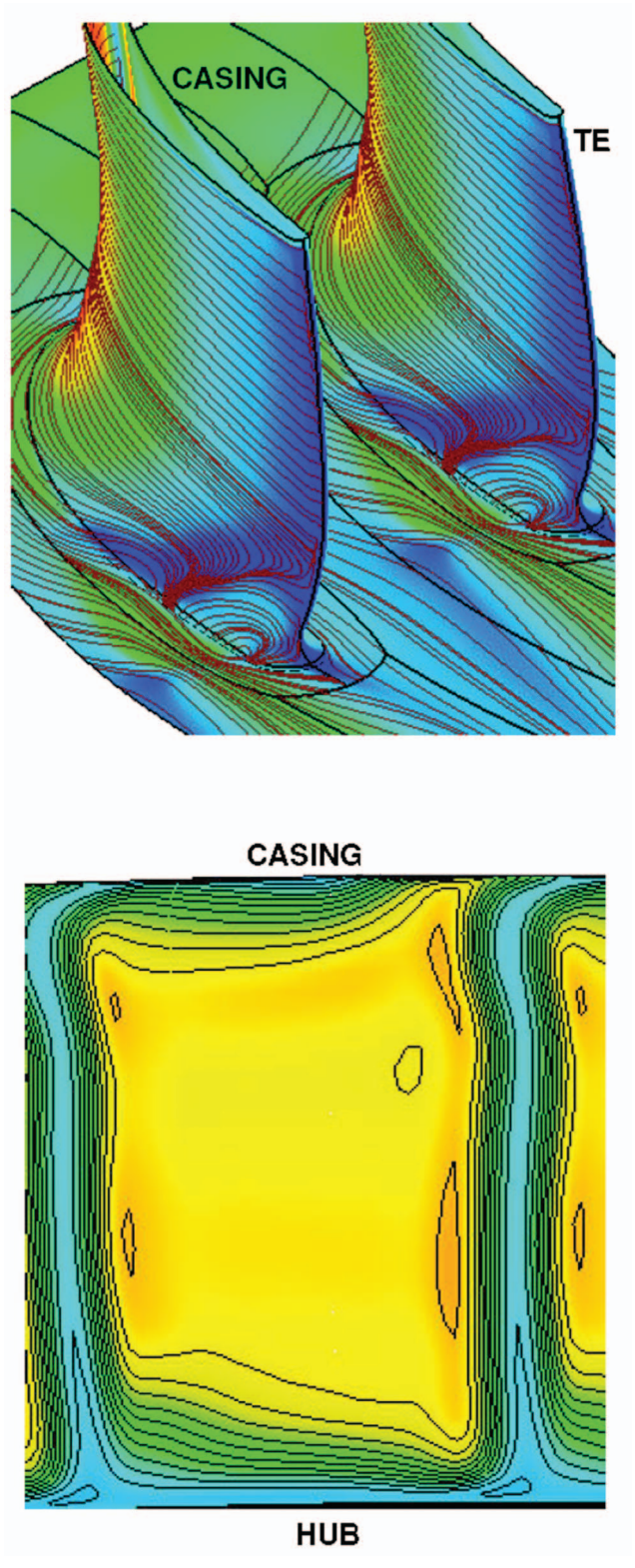

Fig. 12 Stator surface Mach number contours and streak lines, stator exit total pressure contours, tailored OT

casing end wall, but further downstream and closer to the aerofoil suction surface. This arrangement allows a close-link control of the corner stall region. The OT area is reduced by about 30%, and its shape is more lengthy in streamwise direction. Relative to the circular OT configuration, the flow field has drastically improved (see Fig. 12). The streak lines show a 3D surface flow pattern in the suction side corner, which still features a separation line on the aerofoil but—in contrast to normal corner stall topologies—shows associated secondary flows directed toward the casing end wall. The tailored OT removes less casing boundary layers at the stator exit than the circular OT, but is able to capture the bulk of the cross-passage flow approaching the suction surface. Only at 70%

Downloaded 30 May 2010 to 128.113.26.88. Redistribution subject to ASME license or copyright; see http://www.asme.org/terms/Terms_Use.cfm

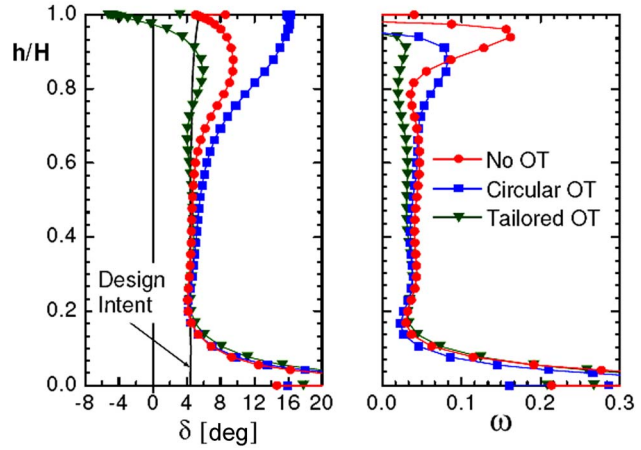

Fig. 13 Stator pitchwise-averaged deviation and loss coefficient

chord, a small fraction of the cross-passage flow travels some way onto the suction surface but is then drawn back toward the casing into the OT. At and beyond the bleed position, there are less boundary layers remaining near the end wall. The total pressure contours at the stator exit clearly show the benefit of the tailored OT geometry. At the casing, the corner separation wake is fully eliminated, but there is a compensatory effect occurring at the hub, where the trailing edge wake and the clearance leakage flow at the hub show an increased pressure deficit. This is due to the removal of the blockage at the casing and the resulting increase in diffusion at the hub. The thickness of the hub boundary layer and, therefore, the hub blockage are larger than in the configuration with a circular bleed OT. The trailing edge wake is uniform across the center region of the stator span. Tailoring the OT in terms of location and shape to suit to secondary flows actually given in regions of aerodynamic distress has resulted in an overall reduction and a balanced redistribution of blockage within the stator.

Pitchwise-Averaged Results. The 3D flow fields in the three OT configurations (no OT, circular OT, and tailored OT) were found to be considerably different in terms of local boundary layer growth and secondary flow topology. This is clearly reflected in the pitchwise-averaged performance parameters of the stator. Figure 13 shows the radial distribution of deviation and pressure loss coefficient at the stator design operating condition. In terms of deviation, the clean configuration (no OT) meets the design intended in the annulus height range between 20% and 60%. Toward the hub, underturning occurs, giving huge values directly near the end wall. Toward the casing, underturning is less strong but still gives a maximum of 3° at 85% annulus height. The overturning usually generated by the cross-passage flow at fixed stator ends is very weak due to the dominating effect of the corner separation. The losses predicted for the clean configuration show little variation between 25% and 75% spans, but high end wall losses on either side. Large tip leakage losses occur near the hub; near the casing, losses are as high as 18% in the region of 90% span, but—as typical for regions with a cross-passage flow—rapidly drop when further approaching the end wall.

On the circular bleed OT configuration, the casing corner separation leads to deviations of up to 16 deg in the outer half of the aerofoil. With respect to the losses, the detrimental effect of the huge corner stall is partly compensated by the benefit given by the removal of the boundary layer across a large portion of the stator pitch. Therefore, the casing end wall losses are reduced relative to the clean stator configuration. A positive side of the blockage caused by the corner stall is the resulting loading reduction and, hence, loss reduction in the lower 70% of the span. The present observations of how loss and deviation vary with bleed rate (0% for no OT and 3% for circular OT) are quite consistent with those made in Ref. [18].

Replacing the circular OT by the tailored off-take, a small increase in deviation occurs in the inner half of the span, including the hub tip clearance region, but a drastic improvement is achieved in the outer half of the span. In the tailored OT configuration, the actual deviations are close to the design intended across most of the annulus height. The outer 10% of annulus height shows a significant amount of overturning, which is in contrast to the huge underturning found on the circular OT configuration.

The stator loss distribution associated with the tailored OT is basically uniform all the way out to the casing, showing a profile loss level without indication of secondary losses in this end wall region. The reduced amount of blockage at the casing raised the loading at the hub, which gives rise to some higher leakage loss at the inner end of the stator.

Conclusions

Numerical simulations were carried out on highly loaded rotor and stator configurations to explore the benefit of the end wall boundary layer removal from aerodynamically critical locations of the casing end wall.

On the rotor, the use of 1% bleed rate taken at the radial tip clearance through an axisymmetric slot proved to give some control over the tip leakage vortex flow.

(i) The relative velocities within the tip clearance along the chord are redirected and show some reduction of the components pointing axially forward (reverse flow).
(ii) The tip leakage vortex and the associated 3D separation line upstream of the vortex trajectory are more aligned with the main flow.
(iii) The area covered by reverse-flow along the casing end wall is reduced, and there is less blockage generated in the rotor tip region.
(iv) Deviations are almost unaffected, but losses are well reduced.

On the stator, a bleed rate of 3% taken through casing holes within the stator passage proved to give control over the suction side corner separation.

(i) There is a risk of substantially increasing the corner separation when using bleed OTs unsuitably placed in the stator passage and causing additional diffusion in sensitive locations of the flow field.
(ii) Tailoring the bleed OT to the actual secondary flows within the passage allows a substantial reduction of the corner separation.
(iii) A rematch of aerodynamic loading across the stator span occurs, but a net performance benefit remains.
(iv) Deviations and losses are significantly improved.

Acknowledgment

The authors would like to thank Torsten Thiele for his contribution to conducting and evaluating the CFD simulations on the rotor configurations. The management of Rolls-Royce Deutschland Ltd. & Co. KG is gratefully acknowledged for supporting the work and permitting the presentation of results.

Nomenclature

Geometric and Flow Quantities

I, J, K = grid dimensions

$\omega = \frac{(P_1 - P_2)}{(P_1 - p_1)}$ = total pressure loss coefficient

X = axial coordinate (m)

C = chord length (m)

Downloaded 30 May 2010 to 128.113.26.88. Redistribution subject to ASME license or copyright; see http://www.asme.org/terms/Terms_Use.cfm

c = chordwise coordinate (m)
H = blade height (m)
h = radial coordinate (m)
W = relative velocity
W_N = normal relative velocity component
W_Z = axial velocity component
Ma = Mach number
P = total pressure (N m^{-2})
p = static pressure (N m^{-2})
δ = deviation angle (deg)

References

[1] Hobbs, D. E., and Weingold, H. D., 1983, "Development of Controlled Diffusion Airfoils for Multistage Compressor Application," ASME Paper No. 83-GT-211.

[2] Behlke, R. F., 1986, "The Development of a Second Generation of Controlled Diffusion Airfoils for Multistage Compressors," ASME J. Turbomach., **108**, pp. 32–41.

[3] Weingold, H. D., Neubert, R. J., Behlke, R. F., and Potter, G. E., 1995, "Reduction of Compressor Stator Endwall Losses Through the Use of Bowed Stators," ASME Paper No. 95-GT-380.

[4] Gümmer, V., Wenger, U., and Kau, H.-P., 2000, "Using Sweep and Dihedral to Control Three-Dimensional Flow in Transonic Stators of Axial Compressor," ASME-Paper No. 2000-GT-491.

[5] Gallimore, S. J., Bolger, J. J., Cumpsty, N. A., Taylor, M. J., Wright, P. I., and Place, J. M. M., 2002, "The Use of Sweep and Dihedral in Multistage Axial Flow Compressor Blading—Part I: University Research and Methods Development," ASME Paper No. GT-2002-30328.

[6] Gallimore, S. J., Bolger, J. J., Cumpsty, N. A., Taylor, M. J., Wright, P. I., and Place, J. M. M., 2002, "The Use of Sweep and Dihedral in Multistage Axial Flow Compressor Blading—Part II: Low and High Speed Designs and Test Verification," ASME Paper No. GT-2002-30329.

[7] Saathoff, H., and Stark, U., 2001, "Tip Clearance Flow in a Low-Speed Compressor and Cascade," Fourth European Conference on Turbomachinery, Firenze, Italy, March 20–23.

[8] Gümmer, V., Swoboda, M., Goller, M., and Dobat, A., 2003, "The Impact of Rotor Tip Sweep on the Three-Dimensional Flow in a Highly-Loaded Single-Stage Low-Speed Axial Compressor—Part 1: Design and Numerical Analysis," Fifth European Conference on Turbomachinery, Prague, Czech Republic, March 18–21.

[9] Rohkamm, H., Wulff, D., Kosyna, G., Saathoff, H., Stark, U., Gümmer, V., Swoboda, M., and Goller, M., 2003, "The Impact of Rotor Tip Sweep on the Three-Dimensional Flow in a Highly-Loaded Single-Stage Low-Speed Axial Compressor—Part II: Test Facility and Experimental Results," Fifth European Conference on Turbomachinery, Prague, Czech Republic, March 18–21.

[10] Hah, C., Rabe, D. C., and Wadia, A. R., 2004, "Role of Tip-Leakage Vortices and Passage Shock in Stall Inception in a Swept Transonic Compressor Rotor," ASME Paper No. GT2004-53867.

[11] Goto, A., 1998, "Stall Margin Improvement Using Circumferential High-Speed Fluid Injection (Experimental and Numerical Investigation on Flow Mechanism)," *Proceedings of 7th International Symposium on Transport Phenomena and Dynamics of Rotating Machinery*, Honolulu, HI, February 22–26.

[12] Suder, K. L., Hathaway, M. D., Thorp, S. A., Strazisar, A. J., and Bright, M. M., 2001, "Compressor Stability Enhancement Using Discrete Tip Injection," ASME J. Turbomach., **123**(1), pp. 14–23.

[13] Nie, C., Xu, G., Cheng, X., and Chen, J., 2002, "Micro Air Injection and Its Unsteady Response in a Low-Speed Axial Compressor," ASME Paper No. GT-2002-30361.

[14] Strazisar, A. J., Bright, M. M., Thorp, S., Culley, D. E., and Suder, K. L., 2004, "Compressor Stall Control Through Endwall Recirculation," ASME Paper No. GT2004-54295.

[15] Merchant, A., Kerrebrock, J. L., Adamczyk, J. J., and Braunscheidel, E., 2004, "Experimental Investigation of a High Pressure Ratio Aspirated Fan Stage," ASME Paper No. GT2004-53679.

[16] Joslyn, H. D., and Dring, R. P., 1985, "Axial Compressor Stator Aerodynamics," ASME J. Heat Transfer, **107**, pp. 485–493, ASME Paper No. 84-GT-90.

[17] Kang, S., and Hirsch, C., 1991, "Three Dimensional Flow in a Linear Compressor Cascade at Design Condition," ASME Paper No. 91-GT-114.

[18] Gbadebo, S. A., Cumpsty, N. A., and Hynes, T. P., 2004, "Three-Dimensional Separations in Axial Compressors," ASME Paper No. GT2004-53617.

[19] Kirtley, K. R., Graziosi, P., Wood, P., Beacher, B., and Shin, H.-W., 2004, "Design and Test of an Ultra-Low Solidity Flow-Controlled Compressor Stator," ASME Paper No. GT2004-53012.

[20] Car, D., Kuprowicz, N., Estevadeordal, J., Zha, G., and Copenhaver, W., 2004, "Stator Diffusion Enhancement Using a Recirculating Co-Flow Steady Jet," ASME Paper No. GT2004-53086.

[21] Stratford, B. S., 1973, "The Prevention of Separation and Flow Reversal in the Corner of Compressor Blade Cascades," Aeronaut. J., Technical Notes, pp. 249–256.

[22] Wellborn, S. R., and Koiro, M. L., 2002, "Bleed Flow Interactions With an Axial-Flow Compressor Powerstream," AIAA Paper No. 2002-4057.

[23] Leishman, B. A., Cumpsty, N. A., and Denton, J. D., 2004, "Effects of Bleed Rate and Endwall Location on the Aerodynamic Behaviour of a Circular Hole Bleed Off-Take," ASME Paper No. GT2004-54197.

[24] Leishman, B. A., Cumpsty, N. A., and Denton, J. D., 2004, "Effects of Inlet Ramp Surfaces on the Aerodynamic Behaviour of Bleed Hole and Bleed Slot Off-Take Configurations," ASME Paper No. GT2004-54331.

Downloaded 30 May 2010 to 128.113.26.88. Redistribution subject to ASME license or copyright; see http://www.asme.org/terms/Terms_Use.cfm

Correlative Analysis of Effusion Cooling Systems

Lorenzo Arcangeli

Bruno Facchini

Marco Surace
e-mail: marco.surace@htc.de.unifi.it

Lorenzo Tarchi

Department of Energy Engineering "Sergio Stecco,"
University of Florence,
Via Santa Marta 3,
50139 Firenze, Italy

Gas turbine cooling has steadily acquired major importance whenever engine performances have to be improved. Among various cooling techniques, film cooling is probably one of the most diffused systems for protecting metal surfaces against hot gases in turbine stages and combustor liners. Most recent developments in hole manufacturing allow us to perform a wide array of microholes, currently referred to as effusion cooling. Though some drawbacks of such a concept still need to be solved (manufacturing costs, holes blockage, and then system reliability), its potential is now worth investigating. This paper presents the validation of a simplified numerical two-dimensional conjugate approach through a comparison with the experimental results of effectiveness for an effusion plate. A preliminary test is performed with the steady-state technique, using thermochromic liquid crystal wide-band formulations. Results are obtained in terms of local distributions of adiabatic effectiveness. Average values are compared with calculations to validate the numerical code. Then, the design of experiment approach is used to perform several conjugate numerical tests (about 180), so as to derive the behavior of different effusion plates in terms of overall effectiveness and mass flow rate. Data are analyzed in detail, and a correlative approach for the overall effectiveness is proposed.
[DOI: 10.1115/1.2749298]

Introduction

In modern aircraft engines, the turbine hot section is always cooled by air coming from the compressor. Heat transfer engineers have to design the cooling system in order to obtain proper metal temperature distributions on vanes, blades, end walls, and shrouds. To increase engine performance, it is necessary to reduce cooling mass flow and to improve cooling effectiveness and efficiency. This implies a very accurate choice among different cooling techniques, suitable to the configuration selected for each location, depending on external constraints and the heat loads of each part to be cooled. This is one reason why there have been so many efforts to develop different cooling techniques and schemes. Among these, the injection of cooling air in the main flow through the walls is one of the most used techniques. The aim is to produce a thin film of cooling air that isolates the walls from the hot gases. Because of the complex mixing of air/hot gas and the structural and manufacturing requirements, many different injection hole shapes and arrays have been proposed and a great deal of research work is still ongoing.

The most diffused design criterion presents a limited number of injection rows, each one made by holes with a very complex geometry, at least at the exit. Examples are holes with a diverging exit section, such as fan shaped holes (Bell et al. [1]). The design of a properly diverging exit enables us to control the film spread and film coverage, i.e., the film adiabatic effectiveness, up to the next row or along the plate (Sechieder et al. [2]).

Only in recent years has the improvement of drilling capability allowed us to perform a large amount of extremely small cylindrical holes, whose application is commonly referred to as effusion cooling. Even if this solution does not guarantee the excellent wall protection achievable with film cooling, the most interesting aspect is the significant effect of wall cooling due to the heat removed by the passage of coolant inside the holes (Gustafsson [3]). In fact, a higher number of small holes, uniformly distributed over the whole surface, permits a significant improvement in lowering wall temperature. From this point of view, effusion can be seen as an approximation of transpiration cooling by porous wall means, with a slight decrease in performances but without the same structural disadvantages.

Studies on effusion cooling or on multirow hole injection have been performed for years. Sasaki et al. [4] presented film cooling adiabatic effectiveness results, using a scanning infrared camera, for a staggered array of discrete holes. Mayle and Camarata [5] proposed an adiabatic effectiveness correlation for multiholes with both streamwise and spanwise angles, i.e., compound angles. Due to the air injection and mixing with hot gases, the flow field near the wall is usually very complex, and the heat transfer coefficient changes compared to that of a flat plate. This means that not only the effectiveness has to be evaluated, but so does the heat transfer coefficient in order to correctly predict the heat flux. Crawford et al. [6] experimentally determined the Stanton number for an effusion cooling geometry.

As previously stated, when injection holes are distributed over the whole surface, the heat transfer between the wall and the air passing into the holes is not to be neglected. On the contrary, the wall temperature is quite affected by the heat transferred between air and wall before injection into the main stream, so the overall effectiveness must be evaluated and compared with adiabatic effectiveness. A detailed analysis was carried out by Andrews et al. [7,8], as a function of hole density and length to diameter ratio.

Many different experimental techniques have been used to measure wall temperature in such configurations, and high resolution temperature maps have been acquired. Martini et al. [9] used an infrared camera, but liquid crystal thermography has also been widely used, as in Mayhew et al. [10].

From the design point of view, it is important to develop a simulation tool in order to predict overall effectiveness whenever boundary conditions and geometry parameters change. This could permit us to properly design the hole array geometry depending on the location and the hot gas thermal loads. Moreover, such tools need to be fast and easy to manage because in the preliminary design stage, several different analyses need to be performed. It may also be used to perform design of experiment (DOE) calculations in order to indicate useful correlations or trends and the relative importance of the parameters involved.

The first aim of this paper is to verify and eventually tune a

Contributed by the International Gas Turbine Institute of ASME for publication in the JOURNAL OF TURBOMACHINERY. Manuscript received May 18, 2006; final manuscript received December 4, 2006; published online January 28, 2008. Review conducted by Je-Chin Han. Paper presented at the ASME Turbo Expo 2006: Land, Sea and Air (GT2006), Barcelona, Spain, May 8–11, 2006, Paper No. GT2006-90405.

Downloaded 30 May 2010 to 128.113.26.88. Redistribution subject to ASME license or copyright; see http://www.asme.org/terms/Terms_Use.cfm

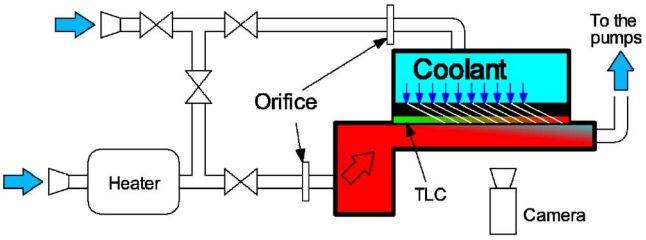

Fig. 1 Test rig

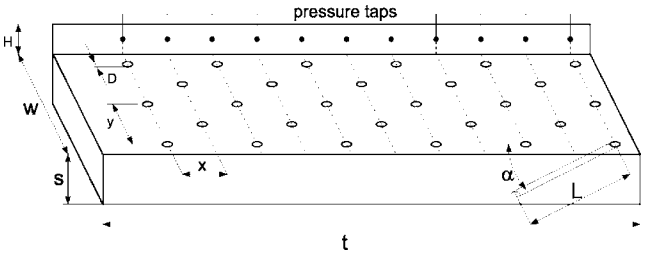

Fig. 2 Effusion plate

proper simulation tool using experimental data. Once verified, a DOE approach is used to deepen the understanding of the effusion cooling system behavior, investigating even very small holes. All results will then be exploited to select the most promising geometries to be experimentally studied in the following years. The foreseen application is on end wall cooling of highly thermally loaded vanes, as in high pressure turbine stages.

Tools Validation

Experiments. The experimental survey was performed at the Dipartimento di Energetica of the University of Florence. The final aim of this activity is the measurement of the adiabatic effectiveness over a flat plate of a specific cooling geometry. The test rig (Fig. 1) consists of a suction-type circuit that allows complete control of two separate flows, the mainstream and the coolant, in terms of both temperature and mass flow rate: a more detailed description can be found in Facchini et al. [11]. The mainstream air passes through a 9.0 kW electronically controlled electric heater; then, the flow rate is measured by an orifice. The coolant flow temperature is controlled by mixing heated air and cool air. Two rotary vane vacuum pumps, powered by two 7.5 kW electric motors, blow air outside and provide the suction for a maximum mass flow rate of 0.10 kg/s. The two flow rates are set up by guiding the motor speed between 300 rpm and 1300 rpm and by throttling the remote controlled motorized valves; the air temperature exiting the heater is controlled by means of a four wire Pt100 resistance temperature detector. Three pressure scanners Scanivalve® DSA 3217 with temperature compensated piezoresistive relative pressure sensors allow us to measure the total or static pressure in 48 different locations with an accuracy of 6.9 Pa. Several *T*-type thermocouples connected to a data acquisition/switch unit (HP/Agilent®34970A) measure the mainstream temperature, the coolant temperature and other temperatures inside the model. A digital three-charge-coupled-device (3CCD) camcorder (Canon®XM-1) records a sequence of color bitmap images (720×576 pixel, 25 frames/s) from the thermochromic liquid crystal (TLC) painted surface on a PC (IEEE-1394 standard). The illuminating system (Shott-Fostec®KL1500 LCD) uses an optical fiber ring light to ensure a uniform illumination on the test surface, and it allows us to keep both color temperature and light power constant. In order to reduce any undesired Plexiglas reflections, two polarized lens filters are fitted on both ring light and camcorder lenses.

TLCs are the devices used to evaluate surface temperature and, consequently, the adiabatic effectiveness. For our purpose, we used the 30'C20W formulation of Hallcrest active from 30°C to 50°C. Crystals are thinned with water and sprayed with an airbrush on the test surface after the application of a black background paint. TLCs have been calibrated, replicating the same optic conditions of the real test (more details in Facchini and Surace [12]).

The tested geometry consists of a flat plate with 11 rows of staggered holes, equally spaced in the spanwise and streamwise direction: Fig. 2 shows a schematic drawing of such a plate, and the geometric and flow parameter values are reported in Table 1. The plate is made by PVC and fitted inside a Plexiglas test article equipped with thermocouples and pressure probes and able to perform heat transfer measurements with two separated flows (see Facchini and Surace [12]). Three separate plenum chambers are present, one for the mainstream flow, one for the coolant, and the last at the exit. Between the first plenum chamber and the flat plate, there is a smooth converging duct and, afterward, a 250 mm long entrance region with a fixed cross section.

The measurement of the adiabatic effectiveness over the cooled plate consists of a steady-state test realized with assigned flow conditions (see Table 1). Starting from the definition,

$$\eta_{\text{ad}} = \frac{T_{\text{aw}} - T_g}{T_c - T_g} \tag{1}$$

where, according to the definition of Lakshminarayana [13], the adiabatic wall temperature T_{aw} represents the surface temperature of a perfectly insulated wall and the adiabatic effectiveness is evaluated measuring the mainstream temperature T_g and the coolant temperature T_c with several thermocouples, while T_{aw} is measured by means of a TLC sheet. Actually, this temperature is not exactly the adiabatic one since there is some heat transfer through the PVC plate; anyway, the maximum wall temperature difference between the adiabatic one and the measured one was verified with an isothermal test, as always below 1.0 K. Thus, this difference has not been taken into account for the calculation of the η_{ad}, but only in the uncertainty analysis.

The test was run after the steady condition was reached by all the measured quantities: mass flows, pressures, and temperatures. These measurements are performed all at once while recording with the camcorder for 10 s: afterward, an average value is used for the calculations.

In order to measure a row-by-row discharge coefficient and blowing ratio, 11 static pressure taps are present on the sidewall. These measurements are made taken from a cold test.

The uncertainty analysis was performed following the standard ANSI/ASME PTC 19.1 [14] based on the Kline and McClintock method [15]. The temperature accuracy is 0.5 K, the differential pressure is 6.9 Pa, the mass flow rate is 2%, and the maximum error in measuring the effectiveness is 0.05.

Code Features. In this section the numerical tool used to calculate the performances of effusion cooling geometries will be presented. The study aims at evaluating the external metal temperature of an effusion cooled flat plate, so as to determine the

Table 1 Experimental parameters

Geometric parameters		Flow parameters	
D (m)	4×10^{-3}	M_1-M_{11}	0.11–0.32
x (m)	30×10^{-3}	$\dot{m}_g$ (kg/s)	65×10^{-3}
y (m)	30×10^{-3}	$\dot{m}_c$ (kg/s)	3×10^{-3}
w (m)	108×10^{-3}	T_g (K)	50
H (m)	20×10^{-3}	T_c (K)	25
s (m)	40×10^{-3}	ρ_g (kg/m^3)	0.717
α	30°	ρ_c (kg/m^3)	0.791

Downloaded 30 May 2010 to 128.113.26.88. Redistribution subject to ASME license or copyright; see http://www.asme.org/terms/Terms_Use.cfm

overall effectiveness and influence on this parameter of design criteria (hole spacing, angle, and diameter) and external boundary conditions. Heat conduction inside the metal and then its temperature distribution are obtained by using a two-dimensional finite element method (2D FEM) model of the plate with a commercial code (ANSYS®9) and then by calculating metal conduction as far as hot and cold side boundary conditions are known. Hot side boundary conditions (heat transfer coefficient and adiabatic wall temperature) are evaluated using a typical fully turbulent flat plate correlation (specified in the next section); the analysis of the coolant fluid network is performed using a one-dimensional (1D) steady code, stator rotor blade cooling (SRBC), developed in-house during industrial research projects and successfully used in several works (Carcasci et al. [16], Carcasci and Facchini [17], Facchini et al. [11,18]). The cooling system consists of a fluid network connecting one basic component to another, each one representing a particular region of the cooling system. In this particular case, each simple model represents a single film cooling row. The specification of geometric characteristics of single components, such as hole diameter, pitch, length, roughness, inclination angle, and so on, can be custom selected. A coolant is considered a perfect gas subjected to wall friction and heat transfer, and a flow field is solved in subsonic regime using correlations to determine heat transfer coefficient (HTC) and friction factor. The user can specify boundary conditions for the fluid network in terms of inlet and outlet pressures or mass flow rate, depending on design specifications. Therefore, SRBC, solving the fluid network, provides coolant side thermal boundary conditions for thermal calculation, particularly heat sink effect of coolant holes and film cooling effectiveness. The heat sink effect is evaluated by applying to the FEM model, for each row, the heat removal given by the mean heat transfer coefficient and the adiabatic wall temperature inside the holes. Film cooling effectiveness is provided by SRBC using the correlation in L'Ecuyer and Soechting [19], which was derived in 1985 after an extensive search in the literature performed to assemble a comprehensive bibliography of film cooling (384 publications from 1964 to 1983) and to select the primary sources of data to be used in the development of a reliable flat plate adiabatic effectiveness correlation. It calculates the adiabatic film cooling effectiveness for each row (once the blowing ratio, velocity ratio, and row geometry are known), and then the principle proposed by Sellers [20] is used to superimpose the effects of each row. The achieved film cooling effectiveness is then used together with the gas temperature and outlet coolant temperature to evaluate the external adiabatic wall temperature. Since the actual component mass flow rate and pressure drop is wall temperature dependent, an iterative procedure is required. Convergence is achieved when differences in pressures and mass flow remain unchanged or below an error set by the user (0.01% in this case). The SRBC code can also be used without the thermal FEM model to perform fixed metal temperature or adiabatic calculations on fluid networks. In this paper, this feature has been used to validate adiabatic film cooling prediction and superposition criteria via experimental data.

Experimental Results and Comparison. First, a series of cold tests was performed in order to measure the C_D (i.e., the mass flow rate) of each effusion hole, varying the coolant mass flow rate (m_c=1–61 g/s) and keeping the mainstream flow at 65 g/s constant. Due to the relevant pressure losses in the mainstream channel, the expansion ratio of each single row grows significantly from the first (β=1.0027) to the last (β=1.0064). So, this variation results in an increasing coolant flow in the x direction.

Experimental data have been correlated in order to define a C_D typical of the tested geometry,

$$C_D = 0.75(1 - e^{-(\beta-1)/0.0072}) \tag{2}$$

which, in test conditions, was found to vary between 0.23 and 0.44 from the first to the last row. Using this correlation together with the measured expansion ratio of each row, it is possible to evaluate the mass flow rate of each hole. The validity of this correlation has also been tested, comparing the total coolant mass flow rate (measured with the orifice meter) with the sum of the flow of each hole,

$$\dot{m}_{\text{orifice}} = \sum_{i=1}^{11} C_D[f(\beta)]\dot{m}_{\text{is}}[f(\beta, p_{0c}, T_{0c}, i)] \tag{3}$$

This equation has been verified in various conditions, and the maximum error found is 2.4%.

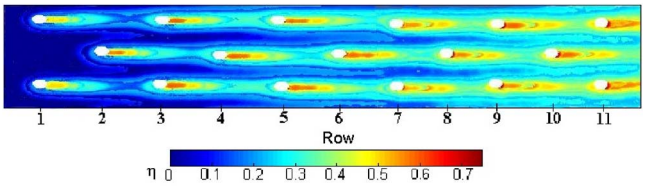

Fig. 3 Adiabatic effectiveness map over the effusion plate

As regards the heat transfer measurements, the adiabatic efficiency has been measured in the flow conditions reported in Table 1. Looking at Fig. 3, where a 2D map of the adiabatic efficiency is shown, the following comments can be made.

- The adiabatic effectiveness before the first row is equal to zero. Theoretically, this result is obvious and is a necessary validation of the measuring technique.
- Because of the low blowing ratio, film cooling is far from the penetration regime. Then, the effectiveness always decreases after each hole.
- The superposition of the coolant, together with an increasing blowing ratio from the first to the last row, results in a general increase of the streamwise effectiveness mean value.
- The presence of a small region before the first hole with adiabatic effectiveness slightly greater than zero shows the effect of nonperfect adiabaticity claimed in the previous section. This effect is taken into account in the experimental uncertainty evaluation.

In order to perform a validation of the SRBC prediction procedure, it is necessary to extract an adiabatic effectiveness profile from the experimental results. In particular, the target of this comparison is

- to verify L'Ecuyer Soechting correlation (single row adiabatic effectiveness prediction) for effusion cooling geometry
- to verify Sellers' superposition criterion for multirow geometries
- to verify the hypothesis of an undefined superposition length

In order to do that, experimental data have been used to properly set up the SRBC model (discharge coefficient and pressure ratio for each row), and a comparison has been made in terms of spanwise averaged adiabatic effectiveness. Results are shown in Fig. 4.

The agreement between experimental and numerical results seems to be quite good, especially for $x/D > 52$, where both peak values and decrease after each row are the same. For $x/D < 52$, the L'Ecuyer Soechting correlation slightly underpredicts the effectiveness between two adjacent rows but correctly predicts the peak value and the general trend.

Design of Experiment

General Assumptions. The comparison presented in the previous section was necessary to ensure the validity of the simplified 1D analysis for the adiabatic effectiveness evaluation by means of a correlative approach. As previously described, conjugate simulations take advantage of the solution of 2D conduction equations

Downloaded 30 May 2010 to 128.113.26.88. Redistribution subject to ASME license or copyright; see http://www.asme.org/terms/Terms_Use.cfm

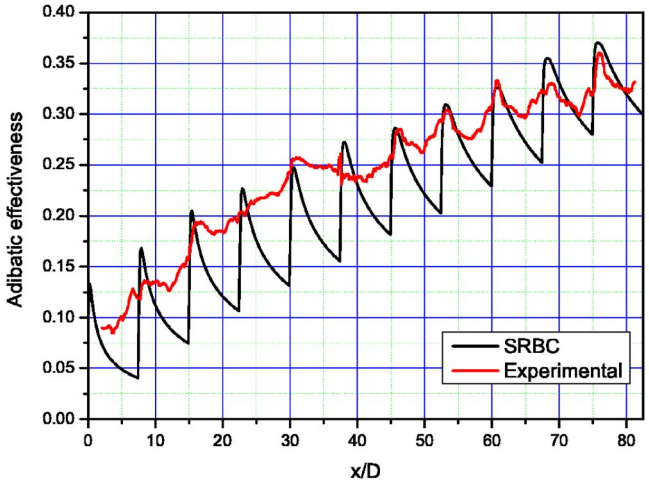

Fig. 4 Spanwise average adiabatic effectiveness comparison

through the metal. Validation was not retained worthwhile for the FEM tool, as it is well known that a 2D conduction in a thin metal plate can be easily solved with high accuracy.

Effusion cooling configurations were applied on a flat plate, representative of a HP stage platform, which conventionally presents few film cooling rows of bigger diameter holes, while the proposed solution features a large number of uniformly distributed microholes (Fig. 5). In fact, one of the aims of the broad investigation carried out is to show the possible increase in performance by adopting effusion instead of film cooling.

Table 2 shows the main input parameters fixed for all simulations. All other inputs were selected in a wide range, so as to allow the comprehension of general validity aspects. Starting with them, several significant design parameters can be derived, as reported in Table 3.

This passage requires a detailed explanation of the adopted assumptions and derived steps.

Referring to a subsonic HP stator vane, a hot gas Mach number usually varies from very low values at the beginning of the stage ($Ma_{is} \approx 0.2$), up to approaching sonic conditions ($Ma_{is} \approx 0.95$). Assuming an isentropic flow for the hot gas and fixing the total temperature and pressure for it and the coolant, the pressure in the main channel, coolant mass velocity (i.e., ρv_c, aside from heating

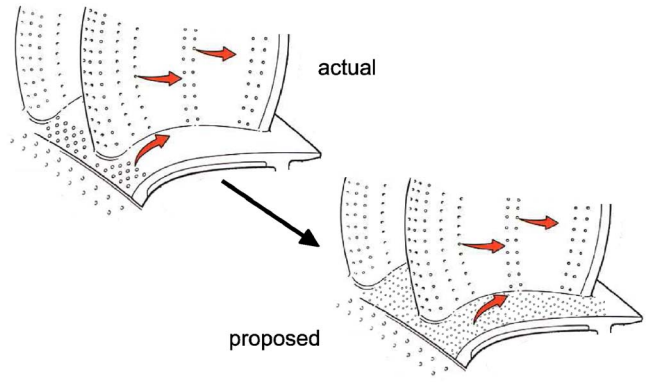

Fig. 5 Actual and proposed configurations

Table 2 Fixed flow and geometric conditions

T_{0g}/T_{0c}	p_{0g}/p_{0c}	t (mm)	s (mm)
2.24	1.02	0.05	1.5×10^{-3}

Table 3 Design parameters

Variable inputs	
Ma_{is}	0.2–0.95
D (m)	$(0.07–0.4) \times 10^{-3}$
α	30–90°
x/D	10–54
y/D	4–18
Derived parameters	
β	1.05–1.82
$Re_x = \left(\frac{\rho v}{\mu}\right)_g x$	$(1.0–6.0) \times 10^6$
$Re_c = \left(\frac{\rho v}{\mu}\right)_c D$	$(1.0–6.0) \times 10^4$
$G = \frac{\dot{m}}{tw}$ (kg/m^2 s)	1.0–26.0

effects along the hole), coolant pressure ratio, and blowing ratio are set once Ma_{is} is known. It implies that where the Mach number is high, the hot gas mass velocity is high, the static pressure is low, and the coolant pressure ratio and, with it, the coolant mass velocity are high. It derives that it is not possible to infer the blowing ratio trend by a qualitative approach, and the quantitative analysis will show that the blowing ratio variation range is limited.

Hole discharge coefficients C_D are inferred from data presented by Gritsch et al. [21,22], thus taking into account the dependence on the main flow Mach number, the coolant pressure ratio, and the injection angle. These data were not taken from the experimental results presented in the previous section as the main parameters range investigated afterward is much wider, requiring reference to more detailed cases.

Then, the geometric features have to be decided in terms of hole diameter and angle, streamwise and spanwise pitches, in order to achieve the desired result. The dimensionless pitches x/D and y/D assume particular importance: together with the C_D, they determine the coolant mass flow per unit platform area G (and then the overall coolant mass flow) independently of the diameter size. In detail, it can be easily demonstrated that

$$G = \frac{\dot{m}}{tw} = \frac{\pi}{4} \frac{(\rho v)_c C_D}{x/D y/D} \tag{4}$$

Each simulation was performed at a fixed Ma_{is}: On the one hand, such simplification causes some distance from the real flow conditions, as the actual gas accelerates across the stator. On the other hand, it allows us to investigate the performances of different effusion geometries independently of the vane profile and then the pressure distribution along the channel.

The hot side heat transfer coefficient was calculated as a function of position and gas Reynolds number Re_x, with the flat plate correlation from Lakshminarayana [13], and is reported below

$$Nu_x = 0.0288\, Re_x^{0.8}\, Pr_g^{1/3} \tag{5}$$

derived for an uncooled plate. It was found that h_g varied from 3000 W/m^2 K to 7000 W/m^2 K with Ma_{is} from 0.2 to 0.95, respectively. For each calculation (i.e., imposed Ma_{is}), the heat transfer coefficient decreased by about 10% along the plate.

The experimental comparison effected in the previous section was helpful in indicating that the complete effectiveness superposition guarantees a correct simulation of the 1D behavior. This assumption was maintained for all performed runs.

Numerical Procedure. To obtain the desired results, an iterative calculation procedure was followed for each geometry and

Downloaded 30 May 2010 to 128.113.26.88. Redistribution subject to ASME license or copyright; see http://www.asme.org/terms/Terms_Use.cfm

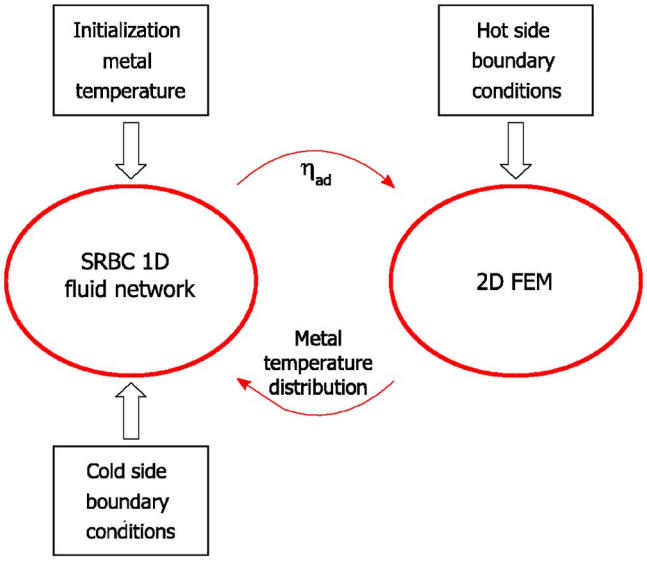

Fig. 6 Iterative procedure

flow condition. Once the 1D fluid network is generated with SRBC and the plate geometry is created and meshed in ANSYS®, the following calculation steps are followed, with reference to Fig. 6

- The fluid network is initialized with a first attempt metal temperature distribution (constant), and coolant boundary conditions are imposed in terms of pressure, temperature, and geometry.
- SRBC provides a distribution of adiabatic effectiveness (and then adiabatic wall temperature); it depends on the assumed metal temperature as the coolant exit conditions are affected by this value and consequently affect η_{ad}.
- The adiabatic effectiveness distribution is given as a boundary condition to the FEM calculation, together with hot side data; the solution, attained in terms of 2D wall temperature distribution, is used to reinitialize the SRBC run.
- The convergence is achieved when the maximum error on the hot surface metal temperature is below the desired value of 0.1 K.

Tests. To ensure a proper evaluation of the influence of the different input parameters on the overall effectiveness, reducing CPU time as much as possible, a DOE approach has been used to determine the test matrix for calculations. For each input variable reported in Table 3, three values have been chosen, particularly the lower, the average, and the higher value of the range. Since for each calculation the CPU time is about 25 min, a full factorial DOE sequence has not been considered suitable, and a reduced factorial approach has been adopted. The set of runs has been reduced from 243 for a three level full factorial DOE to 180 of the reduced factorial approach, reducing the calculation time by about 2/3, without affecting the reliability of results (Montgomery [23]). MODE-FRONTIER® code capabilities have been used to determine the DOE sequence to develop an automatic procedure able to prepare input files for each design and to post process the results. It was then possible to obtain, for each set of input variables, the coolant mass flow rate, the temperature distribution along the plate, and, thus, the overall effectiveness on the external surface.

Results and Discussion

Achieved results will now be presented in terms of adiabatic (Eq. (1)) and overall effectiveness, which is defined as follows:

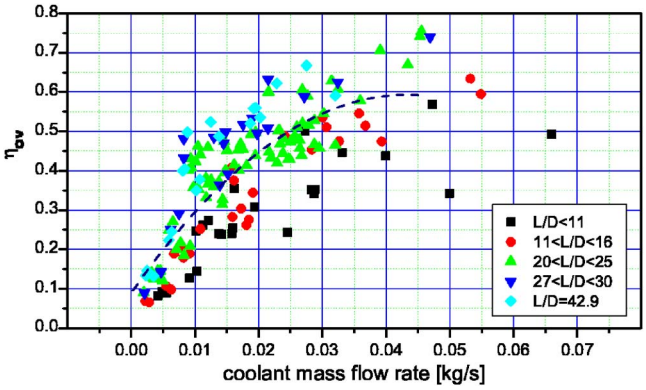

Fig. 7 Overall effectiveness of performed tests as a function of coolant mass flow rate, with reference to the length to diameter ratio

$$\eta_{ov} = \frac{T_w - T_g}{T_{cin} - T_g} \tag{6}$$

where T_w indicates the average wall temperature on the hot surface.

Figure 7 shows the overall effectiveness as a function of coolant mass flow rate for all the performed tests. Data are dispersed around the dotted line, which represents a parabolic fit. An increase of both effectiveness value and its dispersion as the mass flow rate increases is evident. Looking through the plotted data, the dispersion can be attributed to the length to diameter ratio, which acts as a fundamental parameter to distinguish among performances of different configurations. As a general trend, the highest effectiveness values are associated with the highest L/D ratios, which depend on both hole diameter D and angle α, as the plate thickness s is fixed.

The same considerations cannot be expressed, examining Fig. 8, which shows the adiabatic effectiveness as a function of coolant mass flow rate, with reference to the length to diameter ratio. The significant dispersion of data prevents us from deriving a direct relation between the plotted quantities or the influence of the hole length. Indeed, it underlines the importance of the heat transfer inside the hole and points out that a configuration showing a better adiabatic behavior can have a worse overall performance, thus indicating that η_{ad} cannot be used as an independent assessment parameter.

As previously stated, the blowing ratio M does not vary with an easily predictable trend; hence, it is not an input but rather an output of a complex combination of quantities. In particular, while

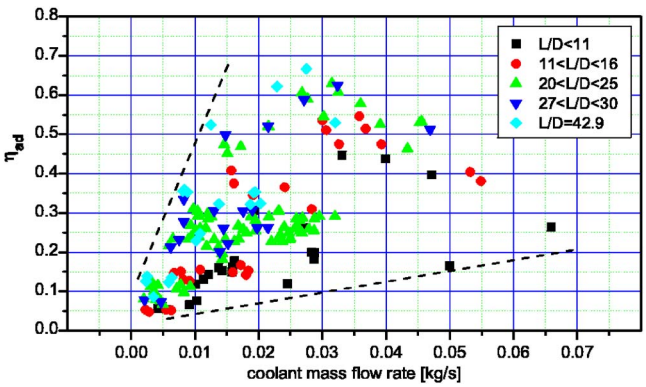

Fig. 8 Adiabatic effectiveness of performed tests as a function of coolant mass flow rate, with reference to the length to diameter ratio

Downloaded 30 May 2010 to 128.113.26.88. Redistribution subject to ASME license or copyright; see http://www.asme.org/terms/Terms_Use.cfm

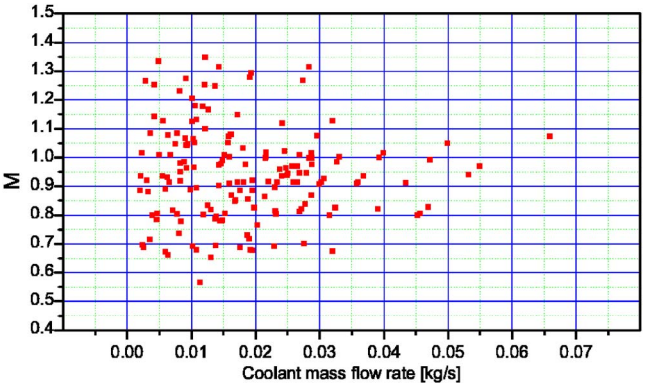

Fig. 9 Blowing ratio variation for all performed runs

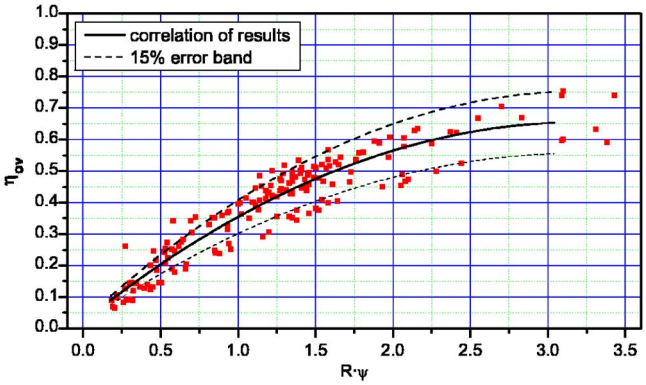

Fig. 11 Correlation of obtained results

the hot gas mass velocity ρv_g is uniquely identified by the selected Ma_{is} and static pressure, the coolant mass velocity ρv_c depends both on that pressure and on the heating effect across the plate. It is, in turn, affected by the wetted surface of the holes and by diameters, pitches, and angles. Looking at Fig. 9, we see how such geometric features influence the blowing ratio, which can change from 0.6 to 1.3 for the same coolant mass flow rate.

The best configurations, taken from the set previously shown, have been tested again, maintaining all dimensionless quantity and flow conditions and changing only the hole diameter. As to be expected from exposed comments, best configurations present the lowest hole size, i.e., $D=0.07$ mm. New simulations were performed at $D=0.4$ mm, thus adopting a value typical of conventional—though small—film cooling holes. The results of this comparison are shown in Fig. 10, which highlights the good potential of microhole solutions, which appear able to guarantee an improvement in cooling performances, other conditions being equal. A similar DOE approach including large holes was not carried out as was thought to be useless. As a consequence, obtained results probably do not represent the best configurations for $D=0.4$ mm, but previous considerations keep their validity.

Correlation. A statistical approach was followed to correlate all the results from performed tests. It was found that the main output, η_{ov}, was essentially dependent on the length to diameter ratio and the dimensionless quantity ψ, defined as

$$\psi = \frac{Gc_p}{\bar{h}_g} \tag{7}$$

where, in particular, $\bar{h}_g$ is calculated, averaging the local heat transfer coefficients on the hot side of the plate. This quantity deserves a detailed interpretation, as it takes into account several important effects: on the one hand, the pressure ratio, the coolant heating before injection, and the dimensionless streamwise and spanwise pitches, by means of G, as indicated by Eq. (4); on the other hand, the heat load on the hot side with $\bar{h}_g$. Thus, a lower ψ with the same η_{ov} (i.e., a lower metal temperature) implies a lower coolant mass flow rate or a higher thermal load, thus better performances.

Figure 11 shows the correlation of present data in terms of the overall effectiveness as a function of ψ and L/D,

$$\eta_{ov} = a_2(R\psi)^2 + a_1 R\psi + a_0 \tag{8}$$

with

$$R = b_2(L/D)^2 + b_1(L/D) + b_0 \tag{9}$$

Equation (8) fits all the test results with a correlation coefficient of 90%, determined through a regression analysis (Table 4). It was actually run with many cross products of terms, but only the subset reported here was found to be significant. This correlation format now identifies the important parameter relationships that affect effusion array performances. No extrapolation of the presented equation is feasible; rather, its use may be significant only within the selected range of input parameters (see Table 3). Summarizing, it should be $R\psi<3.0$, $30°<\alpha<90°$ and $10<L/D<43$.

It is interesting to show that the hole angle, despite being varied in a wide range, was not found to act directly on overall performances, but only to affect the hole length, which is in turn a correlation input.

Despite the unavoidable uncertainty of the expression, it is very interesting to underline the novelty of this correlation, which helps to increase the comprehension of effusion cooling related phenomena and whose alternative forms have not been published in the available literature to the best of the authors' knowledge. This tool can be extremely helpful in the first design stage of cooling systems for turbine blade and vane hottest regions.

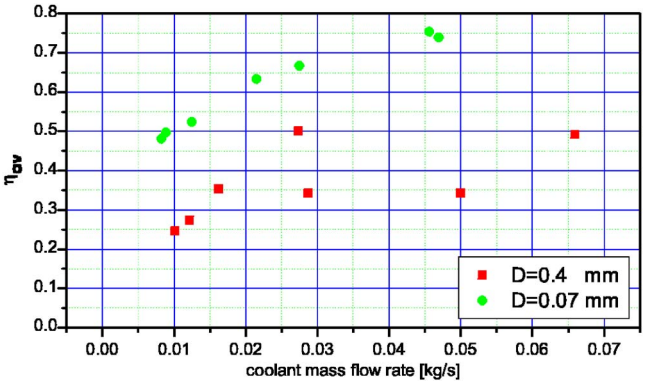

Fig. 10 Comparison between the best configurations of microholes and conventional holes

Conclusions

The present study has investigated the cooling performances for a series of effusion configurations of microholes applied to a flat

Table 4 Correlation coefficients

a_0	a_1	a_2
9.134×10^{-2}	4.060×10^{-1}	-6.381×10^{-2}
b_0	b_1	b_2
-9.0×10^{-2}	5.8×10^{-2}	-5.6×10^{-4}

Downloaded 30 May 2010 to 128.113.26.88. Redistribution subject to ASME license or copyright; see http://www.asme.org/terms/Terms_Use.cfm

plate. The analysis has initially focused on the validation of the available numerical tools, then a detailed DOE approach followed to investigate the effects of the main design parameters. A big influence on global performance has been shown by the hole length to diameter ratio, as it was found that the overall effectiveness always increases with L/D. Moreover, for a fixed geometry $(x/D, y/D, \alpha)$, a smaller diameter always implies better performance in terms of η_{ov}. Finally, all reported data have been analyzed, and the great number of performed tests has allowed the formulation of a simple correlation, covering the entire range of parameters tested.

Acknowledgment

The present work was supported by the European Commission as part of the FP6 STREP AITEB-2 research program, which is gratefully acknowledged together with consortium partners.

Nomenclature

c_p = specific heat ($J\,kg^{-1}\,K^{-1}$)
C_D = effusion hole discharge coefficient
D = effusion hole diameter (m)
G = coolant mass flow per unit platform area ($kg\,m^{-2}\,s^{-1}$)
$\bar{h}_g$ = average heat transfer coefficient ($W\,m^{-2}\,K^{-1}$)
L = hole length (m)
$\dot{m}$ = coolant mass flow rate (kg/s)
M = blowing ratio $(\rho v)_c/(\rho v)_g$
Ma = hot gas Mach number
Nu = Nusselt number
Pr = Prandtl number
R = correlation parameter
Re = Reynolds number
p = pressure (Pa)
s = plate thickness (m)
t = plate length (m)
T = temperature (°C)
v = velocity (m/s)
x = streamwise pitch (m)
y = spanwise pitch (m)
w = plate width (m)

Greek

α = effusion hole angle (°)
β = coolant pressure ratio $(p_0/p)_c$
η = effectiveness
μ = viscosity ($kg\,m^{-1}\,s^{-1}$)
ρ = density (kg/m^3)

Subscripts

0 = total quantity
1,…,11 = row number
ad = adiabatic
aw = adiabatic wall
c = coolant
g = hot gas
in = inlet
is = isentropic
ov = overall
x = abscissa along the plate
w = wall

References

[1] Bell, C. M., Hamakawa, H., and Ligrani, P. M., 2000, "Film Cooling From Shaped Holes," ASME J. Heat Transfer, **122**, pp. 224–232.
[2] Schnieder, M., Parneix, S., and von Wolfersdorf, J., 2003, "Effect of Showerhead Injection on Superposition of Multirow Pressure Side Film Cooling With Fan Shaped Holes," ASME Paper No. GT2003-38693.
[3] Gustafsson, K. M. B., 2001. "Experimental Studies of Effusion Cooling," Ph.D. thesis, Chalmers University of Technology; (www.tfd.chalmers.se/~lada/postscript_files/bernhard_phd.pdf).
[4] Sasaki, M., Takahara, K., Kumagai, T., and Hamano, M., 1979, "Film Cooling Effectiveness for Injection From Multirow Holes," ASME J. Eng. Power, **101**, pp. 101–108.
[5] Mayle, R. E., and Camarata, F. J., 1975, "Multihole Cooling Film Effectiveness and Heat Transfer," ASME J. Heat Transfer, **97**, pp. 534–538.
[6] Crawford, M. E., Kays, W. M., and Moffat, R. J., 1980, "Full-Coverage Film Cooling, Part 1," ASME J. Eng. Power, **102**, pp. 1006–1012.
[7] Andrews, G. E., Asere, A. A., Mkpadi, M. C., and Tirmahi, A., 1986, "Transpiration Cooling: Contribution of Film Cooling to the Overall Cooling Effectiveness," Int. J. Turbo Jet Engines, **3**, pp. 245–256.
[8] Andrews, G. E., Asere, A. A., Gupta, M. L., and Mkpadi, M. C., 1990, "Effusion Cooling: The Influence of Number of Hole," Power Eng. J., **204**, pp. 175–182.
[9] Martini, M., Schulz, A., and Witting, S., 1995, "Full Coverage Film Cooling Investigations: Adiabatic Wall Temperature and Flow Visualization," Paper No. 95-WA/HT-4.
[10] Mayhew, J. E., Baughn, J. W., and Byerley, A. R., 2002, "The Effect of Freestream Turbulence on Film Cooling Adiabatic Effectiveness," ASME Paper No. GT-2002-30172.
[11] Facchini, B., Surace, M., and Tarchi, L., 2005, "Impingement Cooling for Modern Combustors: Experimental Analysis and Preliminary Design," ASME Paper No. GT2005-68361.
[12] Facchini, B., and Surace, M., 2006, "Impingement Cooling for Modern Combustors: Experimental Analysis of Heat Transfer and Effectiveness," Exp. Fluids, **40**, pp. 601–611.
[13] Lakshminarayana, B., 1996, *Fluid Dynamics and Heat Transfer of Turbomachinery*, Wiley, New York.
[14] ASME, 1985, "Measurement Uncertainty," *Instrument and Apparatus*, Performance Test Code, Vol. ANSI/ASME PTC 19.1-1985, ASME, New York.
[15] Kline, S. J., and McClintock, F. A., 1953, "Describing Uncertainties in Single Sample Experiments," Mech. Eng. (Am. Soc. Mech. Eng.), **75**, pp. 3–8.
[16] Carcasci, C., Facchini, B., and Ferrara, G., 1995, "A Rotor Blade Cooling Design Method for Heavy Duty Gas Turbine Applications," Paper No. 95-CTP-90.
[17] Carcasci, C., and Facchini, B., 1996, "A Numerical Procedure to Design Internal Cooling of Gas Turbine Stator Blades," Rev. Gen. Therm., **35**, pp. 257–268.
[18] Facchini, B., Surace, M., and Zecchi, S., 2003, "A New Concept of Impingement Cooling for Gas Turbine Hot Parts and its Influence on Plant Performance," ASME Paper No. GT-2003-38166.
[19] L'Ecuyer, M. R., and Soechting, F. O., 1985, "A Model for Correlating Flat Plate Film Cooling Effectiveness for Rows of Round Holes," *AGARD Heat Transfer and Cooling in Gas Turbines*, Paper No. SEE N86-29823 21-07, provided by the Smithsonian/NASA Astrophysics Data System (http://adsabs.harvard.edu/cgi-bin/nph-bib_query?bibcode=1985htcg.agarQ....L&db_key=PHY).
[20] Sellers, J. P., 1963, "Gaseous Film Cooling With Multiple Injection Stations," AIAA J., **1**, pp. 2154–2156.
[21] Gritsch, M., Schulz, A., and Wittig, S., 1998, "Method for Correlating Discharge Coefficients of Film Cooling Holes," AIAA J., **36**, pp. 976–980.
[22] Gritsch, M., Schulz, A., and Wittig, S., 1998, "Discharge Coefficient Measurements of Film Cooling Holes With Expanded Exits," ASME J. Turbomach., **120**, pp. 557–563.
[23] Montgomery, D. C., 1991, *Design and Analysis of Experiments*, 4th ed., Wiley, New York.

Downloaded 30 May 2010 to 128.113.26.88. Redistribution subject to ASME license or copyright; see http://www.asme.org/terms/Terms_Use.cfm

Vasudevan Kanjirakkad
Richard Thomas
Howard Hodson

Whittle Laboratory,
University of Cambridge,
Cambridge CB3 0DY,
United Kingdom
e-mail: kpv20@cam.ac.uk

Erik Janke
Frank Haselbach

Turbine Aerodynamics & Cooling,
Rolls-Royce Deutschland,
D-15827 Dahlewitz,
Germany

Chris Whitney
ALSTOM Power Technology Centre,
Cambridge Road, Whetstone,
Leicester LE8 6LH,
United Kingdom

Passive Shroud Cooling Concepts for HP Turbines: Experimental Investigations

The cooling of rotor shrouds in the first stage of a high-pressure turbine requires special attention as flatter turbine inlet temperature profiles and more highly loaded blades result in increased thermal and mechanical stresses. The use of film cooling and/or internal convective cooling makes the rotor shroud heavier and oversized, restricting the maximum rotational speed. Alternative methods are, therefore, sought to achieve improved cooling of the shroud. This paper discusses the low-speed experimental investigation of two "passive" cooling concepts known as "rail cooling" and "platform cooling." It has been shown experimentally that the modified cooling method, namely, the platform cooling, substantially improves the rotor shroud coolant distribution in the critical areas while employing significantly lower amounts of coolant. [DOI: 10.1115/1.2749300]

Keywords: passive cooling, rotor shroud, adiabatic cooling effectiveness

Introduction

The rotor shrouds in high-pressure turbines are subjected to severe thermal and mechanical stresses. The conventional shroud cooling strategies, such as film cooling and internal convection cooling, result in heavier shrouds. This restricts the rotational speed and hence the stage work output. This is because higher rotational speeds can reduce the creep life of the blade due to increased centrifugal/hoop stresses. Furthermore, present day design trends toward employing larger pitch-chord ratios (highly loaded profiles) result in larger rotor shroud overhangs and, therefore, higher stresses.

The critical areas that need cooling on a first stage high-pressure (HP) turbine rotor shroud are the leading fin and the fillet area (joining the blade and the shroud) especially near the pressure side trailing edge. Maintaining an adequate life span for the rotor shroud therefore requires improved cooling methodologies, especially when one takes into account recent trends toward increases in turbine entry temperature and flatter combustor exit profiles. While there has been a renewed interest in the aerodynamics of turbine rotor shroud leakage (Wallis et al. [1] and Pfau et al. [2,3]), following earlier studies by Denton et al. [4,5], most of the tip cooling and heat transfer studies were confined to those on unshrouded/plain-tip blades (e.g., Epstein et al. [6] and Metzger et al. [7]). There is a notable paucity in the literature concerning the cooling and heat transfer of shrouded rotor blades. The present paper investigates the concept of *passive* shroud cooling where the rotor shroud is cooled by coolant air ejected from the stationary frame of reference. A base line concept called rail cooling is tested experimentally. The physical understanding gained from the measurements in conjunction with the numerical investigation, as explained in the companion paper of Janke et al. [8], is then used to arrive at an improved configuration. This improved configuration was labeled the platform-cooling configuration.

Aerodynamic measurements were carried out in a large-scale low-speed turbine facility at the University of Cambridge. Gas tracing and surface flow visualization measurements were carried out to track the evolution of coolant around the rotor shroud. A combination of the ammonia-diazo surface flow visualization, method and surface gas sampling technique is used to measure the adiabatic cooling effectiveness achieved on the shroud surfaces. It is shown experimentally that the improved platform-cooling configuration provides a much more uniform cooling effectiveness over the critical areas of the shroud, while requiring significantly less coolant flow and without added aerodynamic penalty.

Experimental Approach

Test Turbine and Stage Configuration. All the experiments described in this paper were carried out in the low-speed large-scale turbine rig at the Whittle Laboratory, University of Cambridge. The single stage model high-pressure turbine has been modified for testing the two shroud cooling geometries described in this paper. Figure 1 shows the arrangement of the low speed turbine and the measurement planes. More details of the test rig can be found in Ref. [9]. The test section has a parallel annulus with a hub to tip ratio of 0.8. The inlet boundary layers were tripped at a distance twice the stator midspan axial chord upstream of the stator leading edge. The shape factors were measured to be $H_{\text{hub}}=1.367$ and $H_{\text{casing}}=1.378$ (Kanjirakkad [9]). The stage geometry had a row of 26 stator blades (Fig. 2(*a*)) followed by a row of 45 shrouded rotor blades (Fig. 2(*b*)). The shrouds of the individual rotor blades are separated circumferentially by a 1.3 mm gap (Fig. 3(*a*)). The rotor shroud consisted of three forward leaning fins and the casing had backward facing steps (Fig. 1). The

Contributed by the International Gas Turbine Institute of ASME for publication in the JOURNAL OF TURBOMACHINERY. Manuscript received June 15, 2006; final manuscript received January 11, 2007; published online January 28, 2008. Review conducted by David Wisler. Paper presented at the ASME Turbo Expo 2006: Land, Sea and Air (GT2006), Barcelona, Spain, May 8–11, 2006, Paper No. GT2006-91250.

Downloaded 30 May 2010 to 128.113.26.88. Redistribution subject to ASME license or copyright; see http://www.asme.org/terms/Terms_Use.cfm

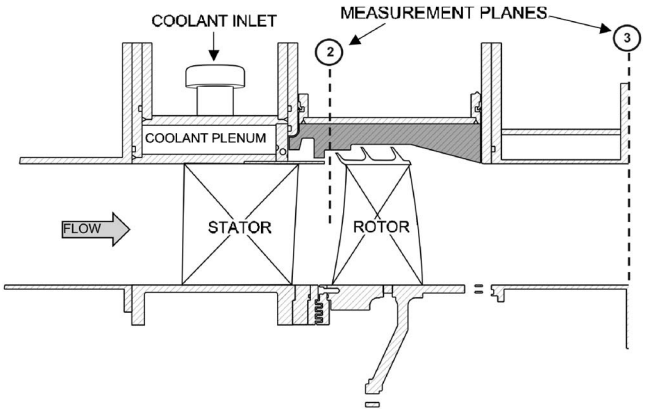

Fig. 1 Low-speed turbine rig (with rail-cooling geometry)

stage geometry and design test conditions are detailed in Table 1. The respective cooling/shroud geometries are presented in Figs. 5 and 13 later in the paper.

Results are presented from five-hole probe and gas sampling area traverses downstream of the stator (measurement plane 2). The measurement of adiabatic cooling effectiveness is described in detail in the next section. A rotor blade (Fig. 3(*b*)) instrumented with blade and shroud static pressure tappings was employed to collect surface gas samples for the cooling effectiveness measurements. The instrumented rotor blade, made of clear resin, was manufactured using stereo-lithography in order to include the pressure channels, of 1 mm diameter, that run through the blade and the shroud. A rotating scanivalve and slip-ring arrangement with a pneumatic coupling was employed for acquiring and transferring the gas samples from the rotating blade. The stage performance of both passive cooling configurations was measured by traversing a three-hole cobra style probe at a location of three rotor midspan axial chords downstream of the rotor trailing edge (measurement plane 3).

A 2.05 mm diameter five-hole cone probe (with 45° semicone angle) has been used for the stator exit area traverse. The probe was calibrated for yaw and pitch angles in the range ±30 deg. The calibration was carried out in a low-speed tunnel at the typical velocities encountered in the turbine and is found to be Reynolds number independent at those velocities.

Gas sampling is carried out using an infrared gas analyzer that collects air samples through an ordinary pitot-type probe that is traversed in an identical manner to the five-hole probe. The gas analyzer produces a voltage output proportional to the concentration of the foreign gas (ethylene) relative to a datum sample, usually the ambient air. The gas sampling technique is also employed in the adiabatic cooling effectiveness measurements for which air samples are collected through the blade and shroud surface tappings. In both cases, the sampling rates were low enough not to disturb the surface flow pattern.

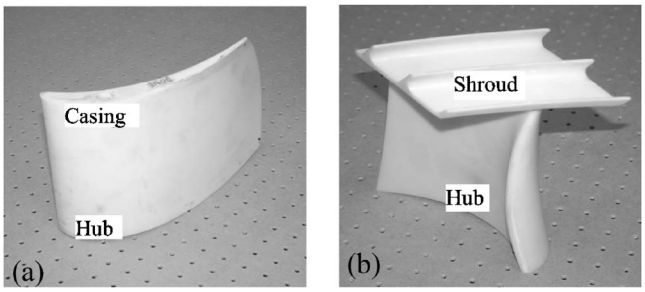

Fig. 2 Blades: (*a*) stator and (*b*) rotor

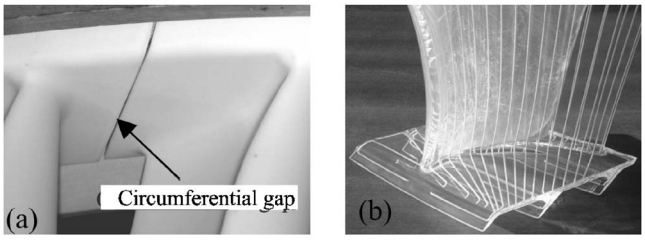

Fig. 3 (*a*) Intershroud gap and (*b*) rotor blade instrumentation

Table 1 Stage geometry and design conditions

Number of stator blades	26
Number of rotor blades	45
Mean radius (mm)	685.8
Hub-tip radius ratio	0.8
Stator axial chord (midspan) (mm)	137.7
Rotor axial chord (midspan) (mm)	93.9
Shroud tip clearance (% of blade span, nominal)	1.0
Stator chord based Reynolds number	1.2×10^6
Rotational speed in rpm	886
Inlet mass flow rate (kg/s)	20.0
Flow coefficient (V_x/U)	0.42
Stage pressure coefficient $[\Delta P_0/0.5\rho_1 V_{x1}/\cos 70)^2]$	1.69

Measurement of Adiabatic Cooling Effectiveness

The adiabatic cooling effectiveness is measured using a combination of methods based on the ammonia-diazo surface flow visualization technique and a conventional gas sampling technique. The ammonia-diazo method (Friedrichs et al. [10]) is used to form a trace of the coolant on the surfaces of interest, in this case the shroud surfaces. The shroud surfaces are coated with diazo paper and the experiment performed with the coolant air seeded with ~5000 ppm of ammonia, for about 2 h. The ammonia gas reacts with the diazo coated paper, resulting in a visible trace. Gas sampling is then used to sample the flow at selected locations on the shroud surface. The sampling is performed by drawing air samples through the surface static tappings on the instrumented blade and measuring the concentration of foreign gas. The foreign gas used in this study was ethylene. The coolant is seeded with controlled amounts of ethylene at the inlets to the plenum. Showerheads are used to spray the foreign gas into the inlet of the plenum in order to achieve uniform mixing with the coolant air. Typically, the air in the coolant plenum has an ethylene concentration of ~150 ppm (representing 100% coolant.) This, along with the ambient ethylene concentration (~0 ppm), forms the two reference concentrations from which the relative concentration (C_{rel}) in the test sample is calculated.

$$C_{\text{rel}} = \frac{C_{\text{sample}} - C_{\text{ambient}}}{C_{\text{plenum}} - C_{\text{ambient}}} \tag{1}$$

The ammonia trace obtained from the separate test was scanned (8 bits, gray scale, and 100 dpi resolution was found to be adequate) and processed to obtain the darkness index (1 −(pixel value/256)) corresponding to each pixel in the scanned image. A calibration curve was constructed by combining the darkness index at the locations where the gas sampling was carried out with the corresponding concentration data (Fig. 4). This calibration is then applied to the whole scanned image to obtain the relative concentration contours. Note that the calibration is accurate only within the range of concentration data available in the experiment.

The adiabatic cooling effectiveness is defined based on the adiabatic wall temperature (T_{aw}), i.e., the temperature assumed by an adiabatic wall in the presence of the coolant.

Downloaded 30 May 2010 to 128.113.26.88. Redistribution subject to ASME license or copyright; see http://www.asme.org/terms/Terms_Use.cfm

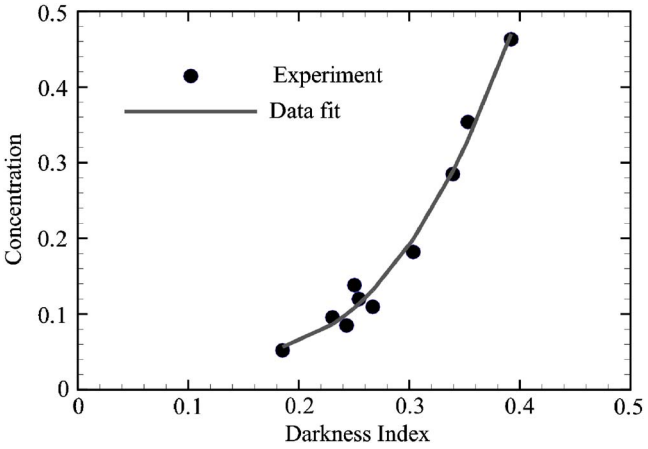

Fig. 4 Ammonia-diazo calibration plot

$$\eta_{\text{adiabatic}} = \frac{T_\infty - T_{\text{aw}}}{T_\infty - T_{\text{plenum}}} \tag{2}$$

However, in the present low-speed tests, with both the coolant air and the mainstream air having very similar thermodynamic properties, the adiabatic wall temperature is analogous to the impermeable wall concentration (C_{iw}) due to the coolant gas [10]. The adiabatic wall effectiveness thus becomes the impermeable wall effectiveness defined in the following way:

$$\eta_{\text{impermeable}} = \frac{C_{\text{iw}} - C_\infty}{C_{\text{plenum}} - C_\infty} \tag{3}$$

The adiabatic cooling effectiveness is, therefore, identical to the relative concentration defined previously and thus

$$\eta_{\text{adiabatic}} = \eta_{\text{impermeable}} = C_{\text{rel}} \tag{4}$$

Results and Discussion

The results from the rail-cooling and platform-cooling configurations are presented next. For each case, geometrical details of the cooling configurations are introduced first, followed by stator/coolant exit flow field results, foreign gas sampling, and the adiabatic cooling effectiveness data. A comparison of the stage performance of the two methods is presented at the end of the paper.

Rail Cooling. The first of the two passive cooling geometries presented is the rail-cooling configuration. The coolant air that is already employed for cooling the NGV rail/platform is subsequently guided toward the rotor shroud in an attempt to cool the latter. In the experimental rig, the coolant air is drawn into a plenum that is situated around the NGV casing into which atmospheric air is drawn through 26 (one per stator blade) equally spaced mouthpiece inlets arranged circumferentially (Fig. 1). The coolant contained in the plenum is ejected through a circumferential array (ten per stator pitch) of compound angled holes into the platform overhang area. The holes are 6 mm in diameter and have a circumferential and a radial inclination of 65° and 30°, respectively. Table 2 provides the geometry details of the rail-cooling holes. The radial inclination is such that the coolant impinges at about halfway along the platform overhang. The platform overhang forms a cavity (hereafter referred to as the coolant exit cavity) along with the outer casing into which the coolant is ejected before it joins the mainstream air in the shroud inlet cavity, where it mixes out with the latter. Figure 5 shows the rail-cooling concept and geometry in detail.

Table 2 Rail-cooling hole details

No. of coolant holes/stator pitch	10
Hole diameter (mm)	6
Circumferential inclination (deg)	65
Radial inclination (deg)	30
Length/diameter ratio	6.83
Coolant mass flow rate (%)	2.15

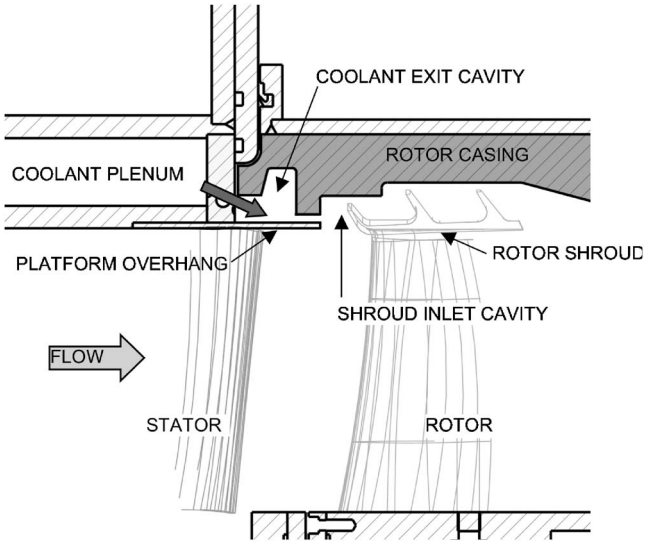

Fig. 5 Rail-cooling geometry/concept

Five-Hole Probe Area Traverse. As the coolant is ejected through the compound angled holes, it enters the coolant exit cavity before it passes into the shroud inlet cavity (see Fig. 5). A five-hole probe area traverse experiment has been conducted at 25% stator midspan axial chord downstream of the stator trailing edge (measurement plane 2). The traverse was carried out over one stator pitch circumferentially and from 50% span to 104% span in the radial direction (a full span traverse was not possible due to blade geometry restrictions). The traverse grid consisted of 29 equally spaced circumferential points and 33 spanwise points refined around the exit of the coolant exit cavity.

Figure 6 shows the contours of radial velocity as derived from the five-hole probe measurements, for the cases where (*a*) the coolant is turned off and (*b*) the coolant is turned on. The plots also show the secondary flow lines overlaid on top of the contours. The secondary flow velocity components are calculated by resolving the component velocities along the plane normal to the streamwise direction, using the equations

$$V_n = V_\theta \cos \alpha_{\text{mid}} - V_x \sin \alpha_{\text{mid}}, \quad V_s = V_r \tag{5}$$

where V_n and V_s are the streamwise-normal and spanwise components of velocity, respectively. Note that the regions in the plot that are above 100% span correspond to the exit region of the coolant exit cavity.

In the absence of coolant (Fig. 6(*a*)), it can be seen that the stator pressure field influences the flow near the exit of the coolant exit cavity. The cavity fluid, essentially mainstream fluid that has found its way into the cavity, is driven inside the cavity by the stator exit pressure field. The radial velocity is found to be negative in this region due to the existence of an inlet cavity vortex (Fig. 7(*a*)), as described by Wallis et al. [1] and Pfau et al. [2]. Figure 6(*a*) also shows the presence of the stator wake and the casing passage vortex (around 80% span). The wake fluid is identified with a negative velocity, indicating its inward motion as a result of the radial pressure gradient. However, the bulk of the flow outside the wake region, at this traverse plane, has a positive radial velocity. This is due to the radial migration of passage fluid into the leakage path, in the outer part of the span. Note that

Downloaded 30 May 2010 to 128.113.26.88. Redistribution subject to ASME license or copyright; see http://www.asme.org/terms/Terms_Use.cfm

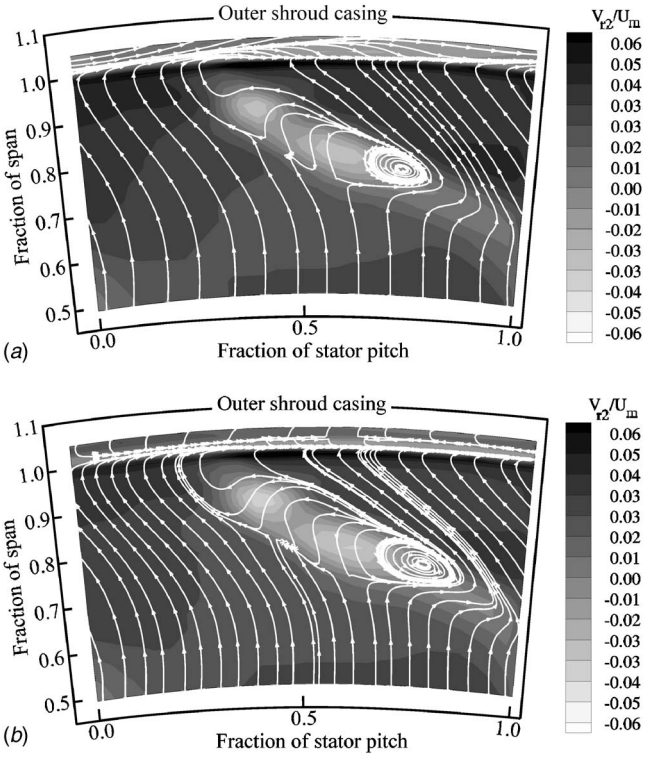

Fig. 6 Stator exit radial velocity contours: (*a*) without coolant and (*b*) with coolant

although the flow at this measurement location is greatly influenced by the rotor pressure field, the steady measurements as presented here average out the rotor related unsteady effects.

In the case with coolant (Fig. 6(*b*)), although most of the passage region looks identical to that in the "without coolant" case, the flow pattern in the exit region of the coolant exit cavity (fraction of span >1.0) is significantly different. The radial velocity in this region is no longer negative except in the lower regions of the cavity (fraction of span ~ 1.0). The in-and-out movement of the mainstream fluid within the cavity, induced previously by the stator exit pressure field, is no longer visible as the ejected coolant acts as a curtain restricting the mainstream fluid from entering the coolant exit cavity (Fig. 7(*b*)). There seems to be a clear region of positive radial velocity signifying the migration of cavity fluid (most of which is made up of the coolant) into the shroud leakage path. The coolant, therefore, or at least the majority of it, migrates into the overshroud leakage path and very little coolant manages to mix with the passage flow and find its way toward the shroud underside regions.

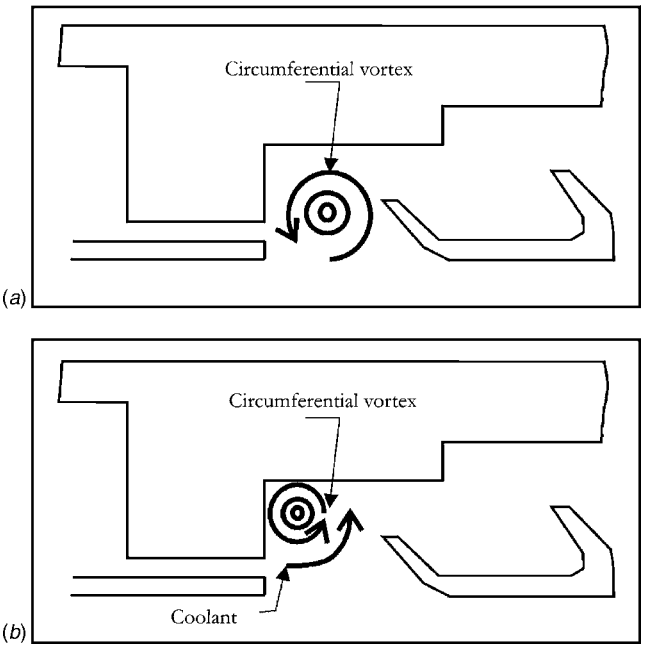

Fig. 7 Schematic of the shroud inlet cavity vortex: (*a*) without coolant and (*b*) with coolant

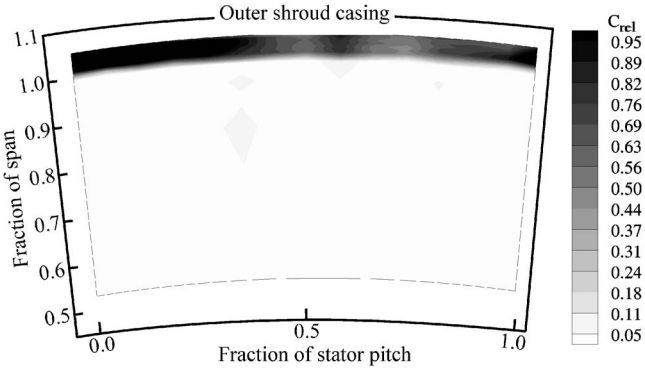

Fig. 8 Contours of relative coolant concentration at stator/coolant exit cavity (rail cooling)

All the configurations reported in this paper employ a 1% shroud tip clearance. This results in a leakage flow of approximately 1% of the inlet mass flow [5]. If this leakage consists of entirely coolant flow (at 2.15%), then only half of it would remain in the annulus for useful blade and undershroud cooling.

Ethylene Tracing. Gas tracing measurements were carried out in the form of an area traverse covering the same traverse window as in the case of the five-hole probe traverse above, but with fewer grid points (17 circumferential points and 16 spanwise points with a maximum spanwise resolution of 1 mm in the exit region of the coolant exit cavity). The air in the coolant plenum is seeded with controlled amounts of ethylene gas, such that the air sample within the plenum has an ethylene concentration of approximately 150 ppm. This, therefore, represents a 100% coolant sample when ejected into the cavity. A pitot-type probe is used to collect the gas samples at measurement plane 2. The air samples thus collected are analyzed in an infrared gas analyzer to assess the ethylene concentration (C_{sample}). Simultaneously, two reference concentration levels are measured, namely, the ambient (C_{ambient}) and that from the plenum (C_{plenum}). The relative concentration of the air sample collected by the probe is then calculated using Eq. (1).

The contours of ethylene concentration measured in the above manner are shown in Fig. 8. The white region in the contours, below a fraction of span of 1.0, shows that no coolant appears to be entering the main annulus area, whereas the exit region of the coolant exit cavity itself has a circumferentially varying concentration of coolant with regions of high concentration (dark area) repeated once per stator pitch. This implies that the coolant trajectory is clearly influenced by the stator field.

Upon comparing the coolant fraction contours with those of the radial velocity for the case with coolant, as presented in Fig. 6(*b*), it becomes apparent that the regions of high coolant concentration are also the regions of positive radial velocity. It can, therefore, be inferred that the coolant at the coolant cavity exit moves radially outward and joins the overshroud leakage path further downstream. However, the interaction of the coolant with main flow in the shroud inlet cavity could result in some of the coolant flow entering the rotor passage. Measurements in the inlet cavity carried out by Pfau et al. [11] revealed that only about 25% of the

Downloaded 30 May 2010 to 128.113.26.88. Redistribution subject to ASME license or copyright; see http://www.asme.org/terms/Terms_Use.cfm

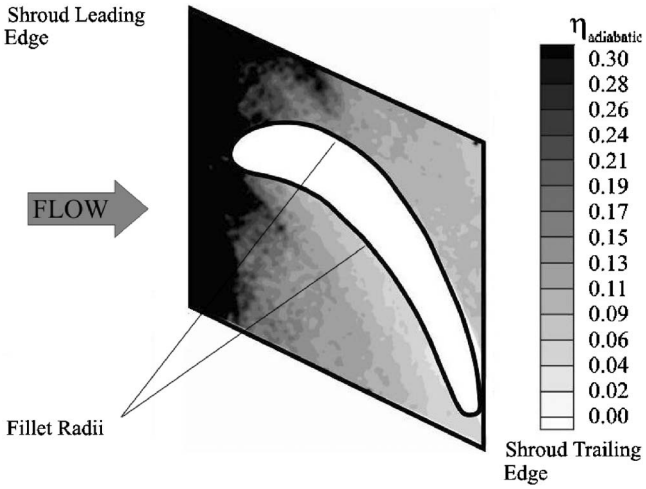

Fig. 9 Contours of adiabatic cooling effectiveness on the shroud underside surface (rail cooling)

total passage fluid that enters the inlet cavity finds its way into the leakage path and the rest is forced back into the rotor passage. This is an effect of the rotor pressure field that can only be seen in an unsteady measurement. Therefore, inevitably, some coolant is drawn into the rotor passage and the shroud bottom region. Since this is not visible in the coolant concentration plot, as shown in Fig. 8, the coolant must be entering the annulus in a downstream plane slightly upstream of the shroud leading edge. This is a significant observation because the shroud bottom needs to be cooled with particular attention given to the fillet radii and trailing edge regions.

Adiabatic Cooling Effectiveness Measurement. The gas tracing experiment along with the radial velocity contours, as described above, indicates that the majority of the rail-cooling air migrates radially outward and joins the shroud leakage flow, thus making less coolant available in the blade passage. The cooling effectiveness measurements described in this section provide quantitative information about the coolant distribution/availability on the shroud surfaces.

As described earlier, the adiabatic cooling effectiveness was measured over the various shroud surfaces using a combination of the ammonia-diazo method and the foreign gas sampling method. Figure 9 shows the cooling effectiveness distribution on the shroud underside surface measured in this manner. Note that the effectiveness data presented here are limited to the range of 0–0.3 for comparison with the platform-cooling test case, where the calibration data (not shown) are only accurate within this range. The dark contours correspond to a high cooling effectiveness and hence indicate the "cooled" regions, whereas the white contours reveal the "uncooled" regions. It is evident from this plot that the shroud leading edge region receives large amounts of coolant ($\eta_{adiabatic} \geq 0.3$), whereas the trailing edge regions remain uncooled ($\eta_{adiabatic} \leq 0.1$). Also noticeable from the coolant distribution pattern is the effect of the influence of the blade-to-blade pressure field. The effects of a classical endwall secondary flow pattern can be seen with the flow leaving the pressure side near the blade leading edge and overturning toward the blade suction surface. The fact that the ammonia gas contained in the coolant air is responsible for the formation of the contours, tells us that the ejected coolant that enters the blade passage is contained in the secondary flow, thus leaving little to no coolant available further downstream.

More evidence of the presence of coolant in the overturning endwall flow can be observed in the traces seen in the tip region of the blade suction side (Fig. 10). In Fig. 10, the blade surface looks longer than the shroud, as it is a developed view of the

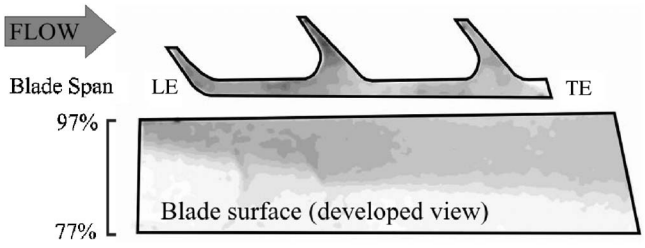

Fig. 10 Contours of adiabatic cooling effectiveness on the shroud/blade suction side surface (rail cooling)

otherwise curved suction surface. The blade-to-blade pressure field forces the endwall flow, containing the coolant air, away from the pressure side onto the suction side of the blade. This results in a larger coolant presence (and hence cooling effectiveness) on the blade suction side above 80% span. Seen also in the figure are the effectiveness contours on the side faces of the shroud. Note that as mentioned earlier, there exists a circumferential gap between the shroud platforms (Fig. 3(*b*)), allowing the rotor blade passage flow to interact with the leakage fluid. The dark contours over the fins are formed by the coolant that is present in the overshroud leakage as the circumferential gap allows this fluid to leak across the shroud chambers. However, the "hot" fluid that migrates from the rotor passage into the shroud leakage path is responsible for the lower cooling effectiveness that is seen away from the fins. The same features are seen on the pressure side of the shroud, (Fig. 11), with high coolant concentration on the fin sides and lower concentrations elsewhere. On the tip region of the pressure side of the blade, however, there is hardly any coolant visible as most of it is overturned, along with the endwall flow, toward the blade suction side.

Figure 12 shows the cooling effectiveness distribution on the top surfaces of the shroud that are in contact with the leakage flow. The high value of cooling effectiveness is clearly due to a greater presence of coolant in the leakage flow than that seen in the passage. This confirms the previous findings from the radial velocity contours and the ethylene gas concentration contours, indicating a strong migration of coolant flow into the leakage path. Note that the distribution is not circumferentially uniform. There is a lower concentration of the coolant near the midpitch compared to the suction and pressure side gap regions. This is thought to be the effect of the rotor pressure field forcing the coolant/leakage around the blade leading edge.

Note that in a real engine, the leakage mass flow is usually associated with a lower stagnation temperature than the mainstream. Therefore, a high coolant presence over the top surfaces of the shroud, except in the fin tip regions, is not particularly beneficial.

Rail Cooling Summary. Observations from the rail-cooling experimentation can be summarized in the following manner. The stator pressure field influences the coolant exit cavity in that the main passage fluid is driven in and out of this cavity in the ab-

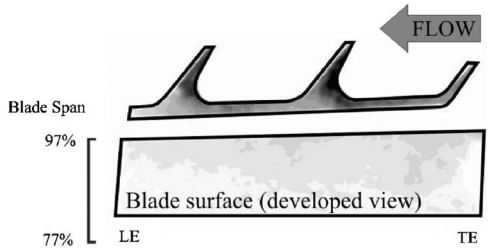

Fig. 11 Contours of adiabatic cooling effectiveness on the shroud/blade pressure side surface (rail cooling)

Downloaded 30 May 2010 to 128.113.26.88. Redistribution subject to ASME license or copyright; see http://www.asme.org/terms/Terms_Use.cfm

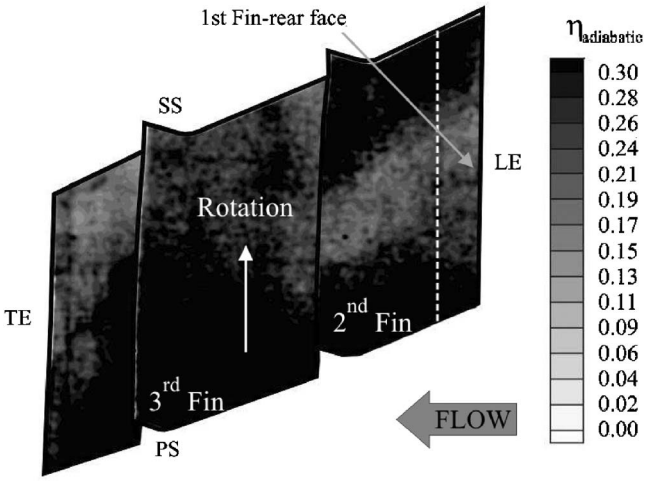

Fig. 12 Contours of adiabatic cooling effectiveness on the shroud top surfaces (rail cooling)

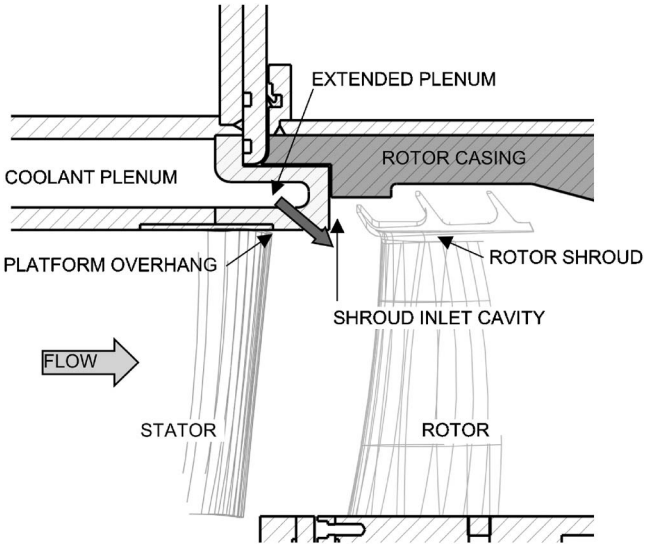

Fig. 13 Platform-cooling geometry/concept

sence of coolant ejection. The "loss" of the ejected coolant into the overshroud leakage path resulted in more coolant reaching the leading fin and the shroud top surfaces. The interaction of the passage fluid with the leakage flow through the circumferential intershroud gap resulted in "hotter" regions on the shroud side faces. The role of the secondary flow on the underside of the shroud in the redistribution of coolant in this region prevented the coolant from reaching the rear parts of the shroud. The average effectiveness on the shroud underside surface is found to be 0.19 and this includes the leading fin region where the coolant presence is the highest. On the top surfaces of the shroud, however, this value is 0.32, owing to the larger presence of coolant in the leakage flow. The average values on the pressure and suction side faces are 0.13 and 0.09, respectively.

These observations suggest that in order to achieve the objective of cooling the shroud under surface effectively, more coolant needs to be redirected from the overtip leakage path to the main passage region.

Platform Cooling. The inability of the rail-cooling method to effectively cool the shroud underside surface has been identified as being due to a lack of coolant in the blade passage. This is because most of the coolant ejected into the platform/coolant exit cavity region is drawn into the shroud leakage path. To overcome this difficulty, a modified passive cooling concept called platform cooling has been conceived, where the coolant from the coolant plenum is injected directly into the passage, downstream of the stator trailing edge. A near unity velocity ratio of the coolant jet ($V_{coolant}/V_2$) needs to be maintained, such that the jet penetrates the casing boundary layer locally and enters the freestream flow. This coolant, or most of it, is expected to remain in the mainstream flow as it approaches the rotor shroud so that the shroud underside surface receives a sufficient amount of coolant.

A feasibility study using the commercially available steady Navier–Stokes solver FLUENT and a 1D mixing loss calculation technique has been carried out. The details are presented in the companion paper of Janke et al. [8]. These studies suggested that the platform cooling could achieve an improved coolant distribution on the shroud surfaces employing a lower amount of coolant (1.5% of the stage inlet mass flow). The loss of efficiency due to the mixing of the coolant was predicted to be about 0.5% [8].

Figure 13 shows a schematic of the platform-cooling geometry in the test rig. The coolant plenum was extended axially to include the coolant exit cavity that was present in the rail-cooling geometry. In order to achieve a coolant jet velocity ratio of near unity, the coolant plenum was supplied with pressurized air from a centrifugal fan through the 26 circumferential mouthpieces. The exits of the coolant holes on the stator platform were located five hole diameters downstream of the stator trailing edge. A reduction in the coolant mass flow rate is achieved by reducing the coolant hole diameter from 6 mm as in the rail-cooling case to 4 mm. The coolant hole parameters are presented in Table 3. Note that the number of holes per stator pitch and the orientations of the holes were the same as those in the rail-cooling test case.

Five-Hole Probe Area Traverse. The five-hole probe area traverse was conducted in an identical fashion to the one carried out for the rail-cooling case. Since the traverse grid employed only 29 equally spaced circumferential grid points (i.e., three per cooling hole pitch), only the gross features of the individual jets are picked out. Figure 14 shows the radial velocity contours measured for the platform-cooling test case. Unlike in the case of the rail-cooling geometry, there is no coolant exit cavity present upstream of the shroud inlet cavity in this case. The distinctive coolant jets are visible below the stator platform (fraction of span=1)

Table 3 Platform-cooling hole details

No. of coolant holes/stator pitch	10
Hole diameter (mm)	4
Circumferential inclination (deg)	65
Radial inclination (deg)	30
Length/diameter ratio	6.0
Coolant mass flow rate (%)	1.5

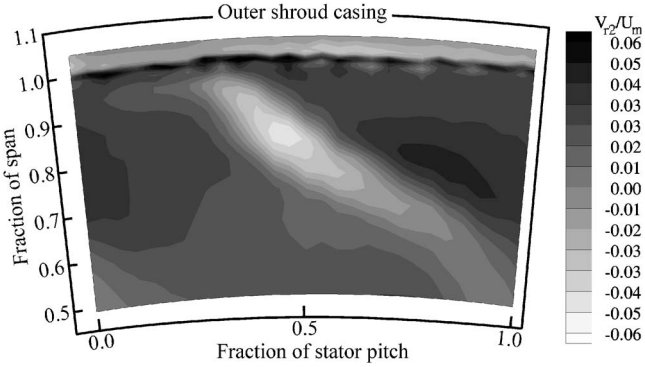

Fig. 14 Stator exit radial velocity contours with coolant ejected through the platform-cooling holes

Downloaded 30 May 2010 to 128.113.26.88. Redistribution subject to ASME license or copyright; see http://www.asme.org/terms/Terms_Use.cfm

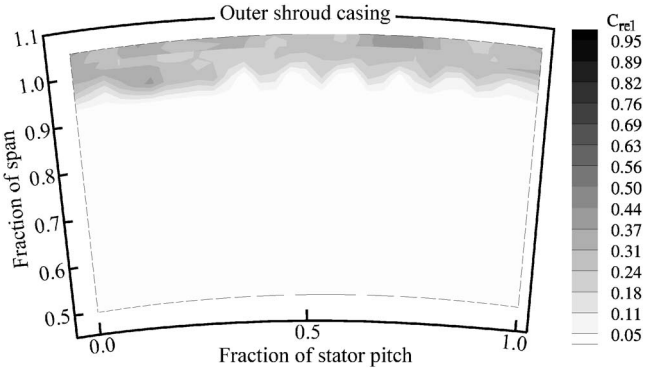

Fig. 15 Contours of relative coolant concentration at stator/coolant exit cavity (platform cooling)

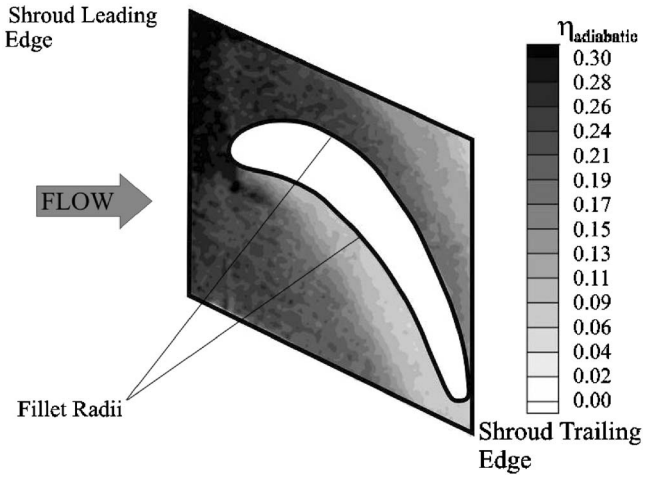

Fig. 16 Contours of adiabatic cooling effectiveness on the shroud underside surface (platform cooling)

as adjacent pairs of positive and negative radial velocities. It can be noted that these jets are not uniform across the pitch due to the stator pressure field. A stator platform flow visualization, (see Ref. [9]), also revealed a circumferential nonuniformity in the horseshoe vortex patterns around the individual jets. The flow features in the annulus are comparable to that in the rail-cooling case with an inward moving (negative V_r) wake surrounded by an outward moving (positive V_r) main flow. The coolant jets can be thought of as jets in a cross flow [12,13]. These jets, as they emerge from the hole, are known to contain streamwise components of vorticity that further help them to mix out laterally with one another as they move downstream. Such a mixing, if it exists, would assist in a better coolant distribution in the circumferential direction.

Ethylene Tracing. The coolant concentration was measured using the ethylene gas tracing experiment. The relative concentration contours are presented in Fig. 15. Compared to the rail-cooling case, the traverse grid near the casing has been refined circumferentially to contain three grid points per coolant hole. The distribution around the midspan is identical to that in the case of rail cooling (Fig. 8) in that there is no coolant present in this region. In the outer region of the annulus, however, there are noticeable differences from the rail-cooling configuration. First, the coolant jets penetrate into the annulus as far down as 95% of span. Note that the undulation in the contours due to the coolant jets, though captured, is not well defined due to the lack of grid resolution. Second, the distribution of coolant is much more uniform in the circumferential direction. This is possibly due to the lateral mixing of the individual coolant jets. Due to the mixing, the maximum coolant concentration in this plane is much lower ($\sim$40%) compared to that in the rail-cooling configuration ($>$95%). Unlike for the rail cooling, this result is encouraging in that there is evidence of coolant presence within the annulus, which can be made available for cooling the shroud underside surface. An ammonia-diazo experiment, as described below, was conducted to ascertain if the coolant was indeed available for cooling the shroud underside surface.

Adiabatic Cooling Effectiveness Measurement. The cooling effectiveness contours on the shroud underside surface are presented in Fig. 16. In comparison with the rail-cooling test case, the coolant distribution has improved substantially. The effectiveness values of the order of 0.2 are available even as far downstream as the trailing edge region of the suction side fillet. There is also more uniformity in the distribution on most of the surface, except close to the pressure side trailing edge where the secondary flow convects the coolant toward the blade suction side. On the leading fin, however, there is a reduction in the effectiveness compared to the rail-cooling case. This can be attributed to the fact that the total coolant ejected is only 1.5% of the stage inlet mass flow compared to the 2.15% coolant mass flow for the rail-cooling case. Despite the reduction in coolant mass flow in the platform-cooling case, the average effectiveness on the shroud underside face is found to be 0.19, which is identical to that in the rail-cooling case described previously. This is because a more uniform effectiveness has been achieved.

As in the rail-cooling case, evidence of the overturning of the endwall secondary flow and the presence of coolant within it can be established from the rotor suction side tip coolant distribution (Fig. 17). Also shown in the same plot is the suction side face of the rotor shroud. Note that here, again, the coolant distribution is much more uniform than in the rail-cooling case. All three fin sides and most of the shroud platform face have an effectiveness value of over 0.15. Note also that there is no trace of the hot passage fluid interacting with the leakage flow. It is not the absence of the passage-shroud gap interaction but the higher concentration of coolant air in the main passage fluid that is thought to be responsible for such an improvement in cooling effectiveness.

The pressure side face of the rotor shroud (Fig. 18) is also uniformly cooled compared to the rail-cooling test case. Here again the presence of coolant in the passage fluid interacting

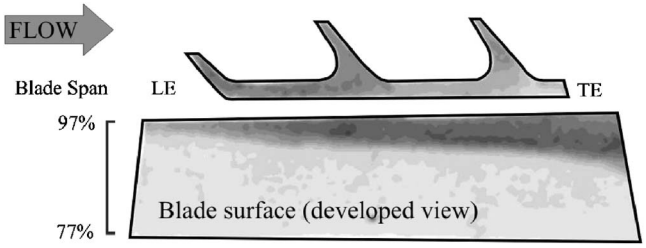

Fig. 17 Contours of adiabatic cooling effectiveness on the shroud/blade suction side surface (platform cooling)

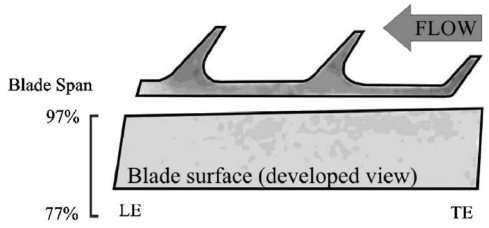

Fig. 18 Contours of adiabatic cooling effectiveness on the shroud/blade pressure side surface (platform cooling)

Downloaded 30 May 2010 to 128.113.26.88. Redistribution subject to ASME license or copyright; see http://www.asme.org/terms/Terms_Use.cfm

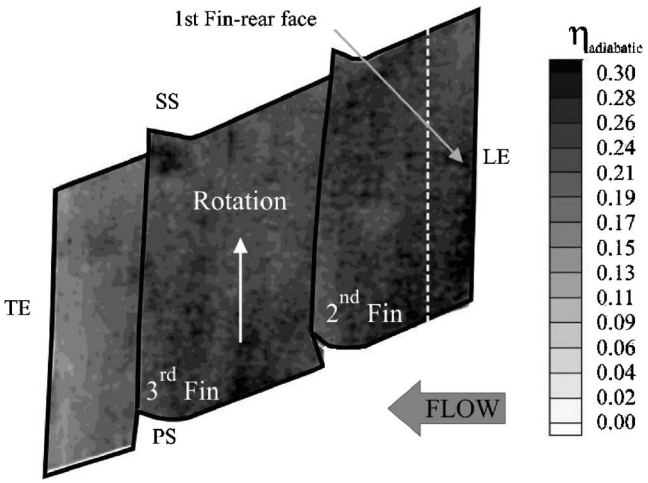

Fig. 19 Contours of adiabatic cooling effectiveness on the shroud top surfaces (platform cooling)

through the intershroud gap is the reason for the improved coolant distribution. Interestingly, the average effectiveness on both the suction side and pressure side faces of the fin was found to be 0.12 with a substantial improvement on the suction side in comparison with the rail-cooling test case. On the blade pressure surface, however, as in the rail-cooling case, there is hardly any coolant visible thus showing the effect of the cross passage pressure gradient in the coolant distribution.

Figure 19 shows the effectiveness contours on the top faces of the shroud. Although the distribution is more uniform with the influence of the rotor leading edge pressure field now less obvious, it can be noticed that in comparison with the rail-cooling case the effectiveness values are lower. The average effectiveness has dropped from 0.32 in the rail-cooling case to 0.22 in the present platform-cooling case. This reduction is proportional to the reduction in total coolant mass flow rate from 2.15% for the rail-cooling case to 1.5% in the present case. However, another reason for this reduction is that in the platform-cooling case, there is proportionately more coolant present in the passage and not all coolant is "lost" into the overshroud leakage path.

Platform-Cooling Summary. The platform cooling was designed in order to make more coolant available in the shroud region of the rotor passage, unlike the rail-cooling method where most of the cooling air managed to join the shroud leakage flow. The experiments showed that the process of injecting coolant into the annulus downstream of the stator trailing edge with a velocity ratio of 1.0 substantially improved the cooling of the shroud surfaces. Note that the coolant and the mainstream flow have the same density in the experiments. Although in the engine representative conditions the coolant to mainstream density ratio (and hence the blowing ratio, which is the product of the density ratio and the velocity ratio) is higher than in the experiments; a near unity velocity ratio is thought to be practically achievable. On the shroud underside surface the improvement is such that a near uniform effectiveness is achieved on most of the surface except the pressure side fillet region. Even with a 30% reduction in total coolant mass flow, the platform-cooling method could achieve the same average adiabatic cooling effectiveness on the shroud underside surface. Although, on the top faces, the effectiveness is reduced by a proportional amount, the shroud side faces saw a much higher and more uniform coolant distribution.

Overall Performance. Stage performance measurements were carried out by traversing a three-hole cobra probe at measurement plane 3 located three rotor midspan axial chords downstream of the rotor trailing edge. The calculation of stage efficiency accommodates the coolant ejection using the definition,

$$\eta = \frac{\rho_{01}\Omega\tau}{\dot{m}_{\text{inlet}}(P_{01} - \bar{P}_{03}) + \dot{m}_{\text{coolant}}(P_{0\text{coolant}} - \bar{P}_{03})} \tag{6}$$

The measurements were carried out for both the configurations and the stage efficiencies, calculated in the above manner, were respectively, 92.4% and 92.7% for the rail-cooling and platform-cooling configurations.

Estimation of measurement uncertainty based on the methods proposed by Kline and McClintock [14] showed that there is a $\pm 0.4\%$ uncertainty in the measured velocity, $\pm 2.4\%$ uncertainty in the adiabatic effectiveness, and $\pm 0.6\%$ uncertainty in the measured efficiency. Since the difference between the efficiencies of the two cooling configurations tested is within the range of uncertainty, the advantage of one over the other is not conclusive. Table 4 presents a comparison of the stage and the cooling performance of the two cooling configurations.

Table 4 Comparison of the overall performance of the cooling configurations

		Rail cooling	Platform cooling
Tip clearance (%)		1	1
Coolant flow (%)		2.15	1.50
Stage efficiency (%)		92.4	92.7
Average cooling effectiveness	Shroud top	0.32	0.22
	Shroud bottom	0.19	0.19
	Shroud pressure side	0.13	0.12
	Shroud suction side	0.09	0.12

Although no experimental data are available with the same coolant fractions for both rail-cooling and platform cooling, numerical studies were carried out by Janke et al., [8], with 1.5% coolant ejection on both the configurations. These studies showed that the platform-cooling configuration yields similar effectiveness values on the first fin and the shroud top as the rail-cooling configuration. However, the effectiveness values on all other shroud surfaces are significantly higher (90%) for the platform-cooling test case.

In a real engine scenario, one needs to take into account the local shroud surface heat transfer coefficients to fully appreciate the benefits of the cooling design. Estimation of shroud surface heat transfer coefficients is beyond the scope of the present work as here the attention is focused on achieving a more efficient coolant distribution as discussed above. However, since the flow patterns on the underside of the shroud, in particular, change little between the cases, the benefits indicated in this paper are believed to be valid as the heat transfer coefficient depends largely on the flow field.

Summary

This paper describes the concept of passive shroud cooling where attempts are made to cool the HP turbine rotor shroud using the spent cooling air from the NGV platform. Two different configurations, namely, "rail cooling" and "platform cooling," were experimentally tested. The inability of the rail-cooling strategy to cool the shroud underside surface due to the "loss" of coolant into the shroud leakage flow and the shroud/tip secondary flow has been identified.

The alternative concept of platform cooling has been shown to cool the shroud faces more effectively as it makes more coolant available in the tip region of the rotor blade passage. Furthermore, this is achieved with a 30% reduction in coolant mass flow rate and is, therefore, highly recommended as a future design methodology for rotor shroud cooling.

Downloaded 30 May 2010 to 128.113.26.88. Redistribution subject to ASME license or copyright; see http://www.asme.org/terms/Terms_Use.cfm

Stage performance measurements showed that the aerodynamic penalty associated with the through platform coolant injection is comparable to that of the rail cooling for the coolant flow rates tested.

Acknowledgment

The authors would like to thank the European Commission for funding the research programme through the project "Aerothermal Investigation on Turbine Endwalls and Blades" (AITEB, 5FP, G4RD-CT-1999-00055). Thanks are also due to Whittle Laboratory technical staff and especially Gavin Ross for his assistance with the experimental setup.

Nomenclature

C = concentration (coolant, ppm)
H = boundary layer shape factor (δ^*/θ)
P = pressure (Pa)
T = temperature (K)
U = blade speed (m/s)
V = fluid velocity (m/s)
V_{coolant}/V_2 = velocity ratio for the coolant jet
$\dot{m}$ = mass flow rate (kg/s)
α_{mid} = reference yaw angle at midspan (deg)
Ω = angular velocity (rad/s)
η = stage efficiency, cooling effectiveness
ρ = density of air (kg/m^3)
τ = torque (N m)

Subscripts

inlet = value at rig inlet
rel = value relative to a reference
adiabatic = adiabatic wall conditions
ambient = ambient room conditions
sample = pertaining to sampled gas
coolant = pertaining to coolant
impermeable = impermeable wall conditions
plenum = pertaining to the coolant plenum
aw = adiabatic wall
iw = impermeable wall
x = axial component
θ = circumferential component
r = radial component
n = streamwise-normal component
s = spanwise component
∞ = freestream value
1 = value at rig inlet (midspan, static)
2 = value at stator exit plane (static)
3 = value at rotor exit plane (static)
01 = value at rig inlet (midspan, stagnation)
02 = value at stator exit plane (stagnation)
03 = value at rotor exit plane (stagnation)

References

[1] Wallis, A. M., Denton, J. D., and Demargne, A. A. J., 2000, "The Control of Shroud Leakage Flows to Reduce Aerodynamic Losses in a Low Aspect Ratio Shrouded Axial Flow Turbine," ASME Paper No. 2000-GT-0475.
[2] Pfau, A., Trieber, M., Sell, M., and Gymrathy, G., 2000, "Flow Interaction From the Exit Cavity of an Axial Turbine Blade Row Labyrinth Seal," ASME Paper No. 2000-GT-0481.
[3] Pfau, A., Schlienger, J., Rusch, D., Kalfas, A. I., and Abhari, R. S., 2003, "Unsteady Flow Interactions within the Inlet Cavity of a Turbine Rotor Tip Labyrinth Seal," ASME Paper No. GT2003–38271.
[4] Denton, J. D., and Johnson, C. G., 1972, "The Tip Leakage Loss of Turbine Blades: A Review and a Theory for Shrouded Blades," CEGB Report No. R/M/N 627.
[5] Denton, J. D., and Johnson, C. G., 1976, "An Experimental Study of The Tip Leakage from Around Shrouded Turbine Blades," CEGB Report No. R/M/N 848.
[6] Epstein, A. H., Guenette, G. R., Norton, R. J. G., and Yuzhang, C., 1985, "Time Resolved Measurements of a Turbine Rotor Stationary Tip Casing Pressure and Heat Transfer Field," AIAA Paper No. 85-1220.
[7] Metzger, D. E., Dunn, M. G., and Hah, C., 1991, "Turbine Tip and Shroud Heat Transfer," J. Turbomach., **113**, pp. 502–507.
[8] Janke, E., Haselbach, F., Whitney, C., Kanjirakkad, V. P., Thomas, R. L., and Hodson, H. P., 2006, "Passive Shroud Cooling Concepts for HP Turbines: CFD Based Design Approach," ASME Paper No. GT2006-91194.
[9] Kanjirakkad, V. P., 2005, "Passive Shroud Cooling in High Pressure Turbines," Ph.D. thesis, University of Cambridge, Cambridge.
[10] Friedrichs, S., Hodson, H. P., and Dawes, W. N., 1996, "Distribution of Film-Cooling Effectiveness on a Turbine Endwall Measured Using the Ammonia and Diazo Technique," ASME J. Turbomach., **118**, pp. 613–621.
[11] Pfau, A., Kalfas, A. I., and Abhari, R. S., 2004, "Making Use of Labyrinth Interaction Flow," ASME Paper No. GT2004-53797.
[12] McGovern, K. T., and Leylek, J. H., 2000, "A Detailed Analysis of Film-Cooling Physics: Part I-Streamwise Injection With Cylindrical Holes," ASME J. Turbomach., **122**, pp. 102–112.
[13] McGovern, K. T., and Leylek, J. H., 2000, "A Detailed Analysis of Film Cooling Physics: Part 2-Compound-Angle Injection With Cylindrical Holes," ASME J. Turbomach., **122**, pp. 113–121.
[14] Kline, S. J., and McClintock, F. A., 1953, "Describing Uncertainties in Single-Sample Experiments," Mech. Eng. (Am. Soc. Mech. Eng.), **75**, pp. 3–8.

Downloaded 30 May 2010 to 128.113.26.88. Redistribution subject to ASME license or copyright; see http://www.asme.org/terms/Terms_Use.cfm

Tim Roediger[1]
e-mail: roediger@iag.uni-stuttgart.de

Helmut Knauss

Uwe Gaisbauer

Ewald Kraemer

Institute of Aerodynamics and Gas Dynamics (IAG),
University of Stuttgart,
Pfaffenwaldring 21,
Stuttgart, Germany 70569

Sean Jenkins

Jens von Wolfersdorf

Institute of Aerospace Thermodynamics (ITLR),
University of Stuttgart,
Pfaffenwaldring 31,
Stuttgart, Germany 70569

Time-Resolved Heat Transfer Measurements on the Tip Wall of a Ribbed Channel Using a Novel Heat Flux Sensor—Part I: Sensor and Benchmarks

A novel heat flux sensor was tested that allows for time-resolved heat flux measurements in internal ribbed channels related to the study of passages in gas turbine blades. The working principle of the atomic layer thermopile (ALTP) sensor is based on a thermoelectric field created by a temperature gradient over an yttrium-barium-copper-oxide (YBCO) crystal (the transverse Seebeck effect). The sensors very fast frequency response allows for highly time-resolved heat flux measurements up to the 1 MHz *range. This paper explains the design and working principle of the sensor, as well as the benchmarking of the sensor for several flow conditions. For internal cooling passages, this novel sensor allows for highly accurate, time-resolved measurements of heat transfer coefficients, leading to a greater understanding of the influence of fluctuations in temperature fields.* [DOI: 10.1115/1.2751141]

Introduction

Despite the progress in the field of optical measurement techniques for the determination of heat flux distributions at the surface by various methods, including infrared thermography, liquid crystal methods, and temperature sensitive paint, there is still a strong demand for highly time-resolved heat flux measurements at the surface. At the moment, optical methods do not reach sufficient levels of accuracy or spectral resolution for comparisons to numerical simulations, especially for complex geometries.

There are several methods for measuring the heat flux at the wall. However, for the determination of the time-resolved heat flux, two major principles are commonly used for single-point heat flux gauges. The use of thin-film resistance gauges for the measurement of required surface temperature histories in order to calculate the heat flux was described by Schultz and Jones [1]. However, the Cook and Felderman algorithm [2], which is used to reconstruct the heat flux, leads to a very noisy signal from the integration procedure and significantly reduces the theoretically possible frequency resolution of ~500 kHz.

Another method is to measure the temperature gradient in a material with known thermal resistance. This method, used by the so-called Gardon-gauges [3], was introduced in 1953. Differential thermopiles or thin-film gauges are used for the measurement of the temperature gradient. The use of microfabrication techniques has reduced the thickness of the gauges to ~1 μm and a frequency response of ~100 kHz has been achieved. The fabrication and properties of these gauges is extensively discussed in [4–9]. The disadvantages of this sensor are a significant reduction of sensitivity with decreasing sensor area and its limited spatial resolution.

The ALTP works on a different principle. The transverse Seebeck effect creates an output signal directly related to the temperature gradient over a thin-film crystal. Therefore, it has a large dynamic range because of a time constant smaller than 1 μs. The sensor responds to radiation over a very large wavelength range from infrared (IR) to ultraviolet (UV). Another advantage of the ALTP is that it does not require active heating of the film. The ALTP is a wall-isothermal sensor and does not produce thermal disturbances like hot wires or films. It is therefore very suitable for array measurements.

The application of the sensor is demonstrated in two benchmark experiments. Case 1 shows comparative stagnation point heat flux measurements of a blunt body configuration in the supersonic flow of a short duration facility. The second case exhibits its performance on the tip wall of a ribbed channel in subsonic flow conditions.

Atomic Layer Thermopile: Principle of Operation

The ALTP was developed as a detector for optical radiation. It has been used as a power meter for laser radiation and for laser beam diagnostics. The ALTP works on the thermopile effect created by a temperature gradient over an yttrium-barium-copper-oxide ($YBa_2Cu_3O_{3-d}$=YBCO) crystal. The thermoelectric effect for YBCO crystals was observed by Renk et al. [10] and Zeuner et al. [11] for the first time in 1993. Figure 1 shows a schematic cross section of a tilted YBCO film, consisting of CuO_2 layers and intermediate YBCO layers. The films are grown by laser ablation on $SrTiO_3$ substrates. The substrates can be cut at a certain angle to its crystallographic plane. Therefore, the YBCO film grows with a certain tilt angle α_c between the *c*-axis of the crystal and the surface normal *n* of the film.

The whole sensor can be regarded as an atomic layer thermopile because the copper oxide layers and its YBCO interlayers form atomic thermocouples connected in series. The thermopile works on the principle of the transverse Seebeck effect, caused by the anisotropy of the YBCO film in combination with the tilt angle of the crystal with respect to the film surface normal. Investigations of the dependency of the tilt angle and the thermoelectric

[1]Corresponding author.

Contributed by the International Gas Turbine Institute of ASME for publication in the JOURNAL OF TURBOMACHINERY. Manuscript received July 17, 2006; final manuscript received September 25, 2006; published online January 28, 2008. Review conducted by David Wisler. Paper presented at the ASME Turbo Expo 2006: Land, Sea and Air (GT2006). May 8–11, 2006, Barcelona, Spain.

Downloaded 30 May 2010 to 128.113.26.88. Redistribution subject to ASME license or copyright; see http://www.asme.org/terms/Terms_Use.cfm

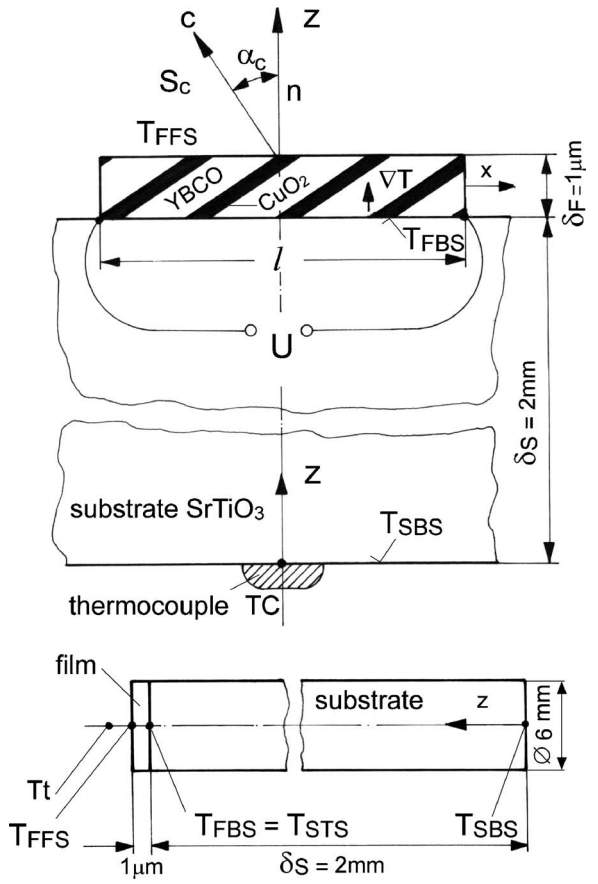

Fig. 1 Schematic cross section of a tilted YBCO film [12]

signal were carried out by Zeuner et al. [11], and it was shown that the signal of the ALTP is purely of thermoelectric origin. The created thermoelectric field $\vec{E}$ yields from

$$\vec{E} = \vec{S}\,\nabla\,\vec{T} \tag{1}$$

where $\vec{S}$ is the Seebeck tensor and $\nabla\vec{T}$ the temperature gradient. The elements of the Seebeck tensor defined with respect to the coordinate system in Fig. 1 can be written as

$$\vec{S} = \begin{bmatrix} S_{ab}\cos^2\alpha_c + S_c\sin^2\alpha_c & 0 & \left(\frac{\sin 2\alpha_c}{2}\right)(S_{ab}-S_c) \\ 0 & S_{ab} & 0 \\ \left(\frac{\sin 2\alpha_c}{2}\right)(S_{ab}-S_c) & 0 & S_{ab}\sin^2\alpha_c + S_c\cos^2\alpha_c \end{bmatrix} \tag{2}$$

where S_c and S_{ab} are the values for the thermopower of the anisotropic crystal with respect to the *c*-axis and the *ab*-axis (normal to c). The heating of an YBCO film by absorption of radiation or convective heat transfer leads to a temperature gradient over the film. The transversal component $\varepsilon_x = S_{xz}\nabla_z T = (\sin 2\alpha_c/2)(S_{ab} - S_c)\nabla_z T$ of the created thermoelectric field $\vec{E} = [\varepsilon_x, \varepsilon_y, \varepsilon_z]^T$, yields the thermoelectric voltage in the *x* direction

$$U = -\varepsilon_x l = -\left(S_{xz}\frac{l}{\delta_F}\right)\Delta T \tag{3}$$

where l is the length of the film (normal to the layer orientation), δ_F the film thickness, and $\Delta T = T_{\mathrm{FFS}} - T_{\mathrm{FBS}}$ is a temperature difference between the front (FFS) and back sides (FBS) of the film (see Fig. 1). The temperature gradient can be assumed to be essentially perpendicular to the film surface (i.e., $\nabla\vec{T} \approx \nabla_n\vec{T}$) due to the ratio of the film thickness to its length $(\delta_F/l) = 0.001$. Equations (2) and (3) can be simplified and yield the thermoelectric voltage U created by the film

$$U = \frac{l}{\delta_F}\Delta S\Delta T\frac{\sin 2\alpha_c}{2} \tag{4}$$

where $\Delta S = (S_c - S_{ab})$. The estimation of typical ALTP sensitivities yields $E = 3.5$ mV/K for $\alpha_c = 20$ deg, with dimensions of $\delta_F = 1$ μm and $l = 1$ mm and $\Delta S \approx S_c = 10$ μV/K. Laser calibration experiments carried out by Zeuner et al. [11] showed a linear characteristic of the sensor over more than 11 orders of magnitude. Heat flux rates of a few milliwatts per square centimeter up to 20 kW/cm^2 (damage threshold for a 1 ms pulse) were detectable with the ALTP.

Table 1 Thermal properties of ALTP components

Sensor component	Density ρ (g/cm^3)	Specific heat c (J/g K)	Thermal conductivity k (J/cm s K)	Thermal product $\sqrt{\rho c k}$ (J/cm^2 K$\sqrt{s}$)
YBCO/CuO_2-film	6.68	0.37	0.015	0.1925
$SrTiO_3$ substr.	5.116	0.538	0.10	0.5246

Thermal Properties of ALTP

For the application of the ALTP sensor to fluid and thermodynamics problems, the thermal properties and heat transfer through the sensor must be investigated and discussed. In Table 1 the thermal properties of the ALTP are listed.

For a stationary and uniform heat flux through the front surface of the film and substrate as well as through the substrate bottom side, the case of a stationary one-dimensional heat transfer problem can be applied

$$q = h(T_t - T_{\mathrm{FFS}}) = \left(\frac{k}{\delta}\right)_F (T_{\mathrm{FFS}} - T_{\mathrm{FBS}}) = \left(\frac{k}{\delta}\right)_S (T_{\mathrm{STS}} - T_{\mathrm{SBS}}) \tag{5}$$

where the nomenclature of the temperatures can be obtained from Fig. 1.

For the demonstration of the dominant driving temperature differences in the heat conduction process of the ALTP, the ratios of the temperature difference over the film, the substrate, and the convective temperature difference at the surface are compared as follows:

$$\frac{\Delta T_F}{\Delta T_S} = \frac{T_{\mathrm{FFS}} - T_{\mathrm{FBS}}}{T_{\mathrm{STS}} - T_{\mathrm{SBS}}} = \left(\frac{\delta}{k}\right)_F \left(\frac{k}{\delta}\right)_S = 3.3 \times 10^{-3} \tag{6}$$

$$\frac{\Delta T_S}{\Delta T_{\mathrm{conv}}} = \frac{T_{\mathrm{STS}} - T_{\mathrm{SBS}}}{T_t - T_{\mathrm{FFS}}} = h\left(\frac{\delta}{k}\right)_S = 6 \times 10^{-2} \tag{7}$$

The ratios have been evaluated for the thermal properties in Table 1 and $h \approx 300$ W/m^2 K, representing approximately the highest heat transfer coefficient in benchmark case 2. Equation (6) shows that the temperature difference over the film is much smaller than the one over the substrate ($\Delta T_F < \Delta T_S$). Therefore, it can be neglected and the wall temperature can be estimated by $T_w = T_{\mathrm{FBS}}$. Furthermore, Eq. (7) shows that the driving temperature difference is dominated by the convective heat transfer process at the wall. From these two ratios, the total temperature difference over the sensor can be formulated as

Downloaded 30 May 2010 to 128.113.26.88. Redistribution subject to ASME license or copyright; see http://www.asme.org/terms/Terms_Use.cfm

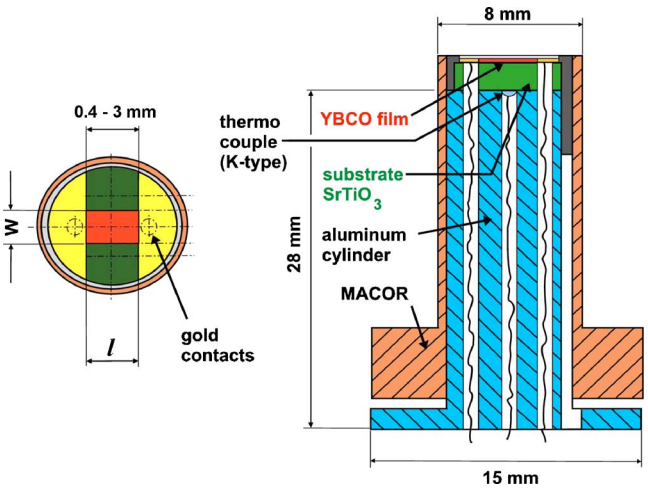

Fig. 2 Schematic cross section of the sensor module

$$\Delta T_{\mathrm{ALTP}} = T_{\mathrm{FFS}} - T_{\mathrm{SBS}} < \Delta T_{\mathrm{conv}} \tag{8}$$

From Eq. (8), it is clear that the temperature difference in the ALTP can be neglected in comparison to the convective one, which leads to the assumption

$$T_w \approx T_S \tag{9}$$

For higher heat transfer coefficients, as in benchmark case 1, the temperature difference in the substrate cannot be neglected and a transient heat transfer analysis has to be carried out. A transient analysis described in [12] resulted in a temperature change at the back side of the substrate of 1 K after ~350 ms.

The wall-mounted installation can lead to problems like casing effects and conduction errors as for nearly all wall-mounted surface measurement techniques and needs to be taken into account for large temperature differences.

Dynamic Properties and Protective Coating. In addition to the linear characteristic of the ALTP over 11 orders of magnitude [11], it also covers the wide spectral range from UV to the FIR range. In laboratory tests on very thin YBCO films ($\delta_F \approx$several nanometers), an electrical bandwidth up to ~1 GHz could be achieved [10]. The sensitivity of these sensors decreases with time due to the hygroscopic character of the YBCO film. A recalibration period of several months, depending on the test environment, is recommended for quantitative heat flux measurements without coating. Nevertheless, this sensor configuration can be used for heat flux fluctuation measurements with very good spatial and temporal resolution. Presently, sensors with a film thickness between 500 and 700 nm and an active area of 2×0.4 mm have been successfully used. The dynamic calibration shows a spectral resolution up to 1 MHz.

For quantitative intensity measurements, a protective coating was optimized for maximal absorption in the IR range. The coating stabilizes the sensitivity of the sensor significantly. Unfortunately, the spectral resolution is reduced to ~250 kHz at the same time. Nevertheless, this type of sensor achieved very good results in quantitative heat flux measurements, and for the investigation of gas turbine blade cooling, their spectral resolution is sufficient.

Sensor Module Design and Signal Amplification

A schematic cross section of the sensor module is displayed in Fig. 2. The YBCO film is connected by sputtered gold contacts to thin silver-coated copper wires. The substrate with the YBCO film is mounted on an aluminum cylinder. For the measurements of the substrate temperature, a thermocouple is installed on its back side. The housing of the whole module is made of a ceramic insulator (MACOR) to achieve a mainly one-dimensional heat flux through the substrate and the cylinder. At the back side of the aluminum cylinder, the contact wires are soldered to a shielded cable, which reduces the electric noise level of the ALTP sensor. The ALTP signal is amplified by special miniature low-noise amplifiers with adjustable gain from 100 to 10,000.

Static Calibration

The ALTP calibration is carried out with the intention to refer the absorbed part of a laser beam to a measured flow heat flux density. Figure 3 shows a scheme of the calibration setup. It consists of a CO_2-laser, a telescope ZnSe-lens configuration for beam broadening, and a attenuator for the variation of the laser power. The ALTP is placed behind a circular aperture (10 mm dia) in order to obtain a well-defined reference cross section (a_{ref}). The active area of the sensor (e.g., 3×3 mm) is considerably smaller than the reference area of the laser beam. Therefore, the sensor could be totally exposed to an incident radiation of known intensity i. The beam intensity $i = P_{\mathrm{laser}}/a_{\mathrm{ref}}$ can be determined with the power of the dissected laser beam P_{laser}, measured by a reference detector (COHERENT FIELDMASTER 10). Figure 4 shows a typical signal of the ALTP and the reference detector during exposure to the laser beam. From the measured step height of the two signals, a calibration curve may be produced for the variation of the laser power by the attenuator. In Fig. 5, a calibration curve (GAIN =1) with logarithmic scale on both axes of an ALTP after the exposure to a DC-excited CO_2 laser for low intensities and a pulsed one for higher intensities is presented. The slope of the curve shows a typical sensitivity of $s = 69\ \mu\mathrm{V}/(\mathrm{W}/\mathrm{cm}^2)$ for an ALTP. The total uncertainty of the calibration can be estimated

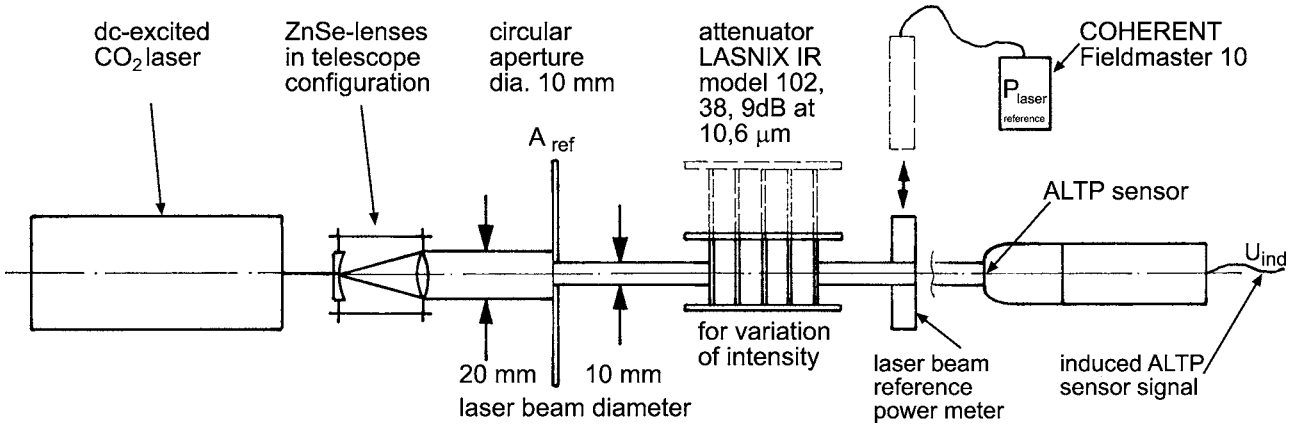

Fig. 3 Scheme of calibration setup

Downloaded 30 May 2010 to 128.113.26.88. Redistribution subject to ASME license or copyright; see http://www.asme.org/terms/Terms_Use.cfm

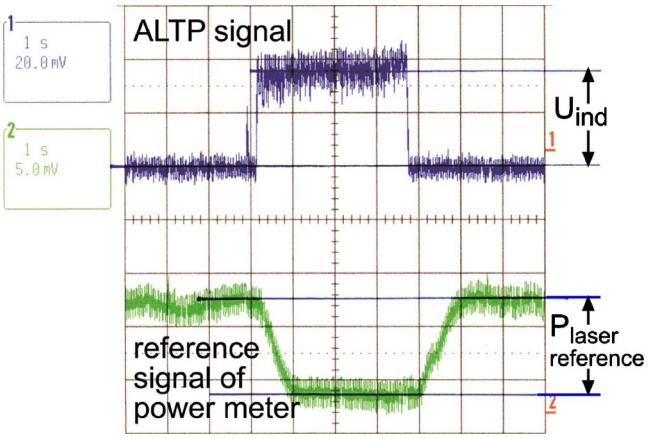

Fig. 4 Time signal of ALTP and reference detector

from the following, defining the sensitivity coefficient:

$$s = \frac{U_{\text{ind}}}{\alpha_a i} = \frac{U_{\text{ind}} a_{\text{ref}}}{\alpha_a P_{\text{laser}}} \tag{10}$$

where α_a is the absorption coefficient of the sensor surface. By differentiating this expression and adding the rms values of all single uncertainties listed in Table 2, leads to an overall uncertainty in the calibration of ~5.5%.

The measured heat flux can be determined from

$$q = \frac{U_m}{s} \tag{11}$$

The uncertainty in the measured signal U_m has to be taken, additionally, into account for a specific experiment to determine the total uncertainty.

Dynamic Calibration

The goal of the dynamic calibration is to obtain the amplitude-frequency response of the whole system of sensor and amplifier.

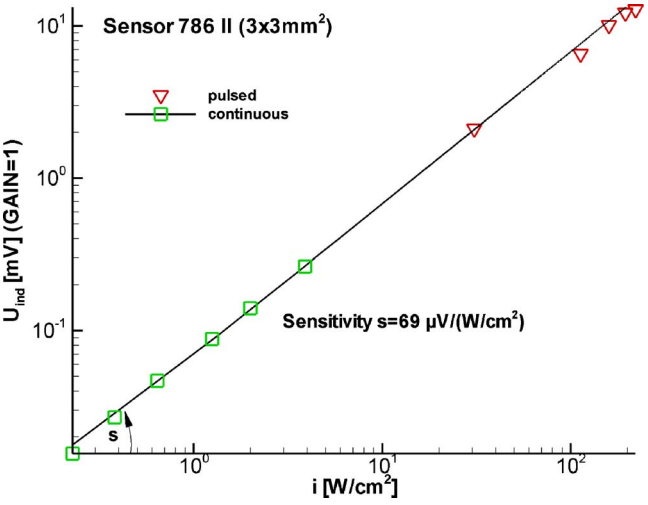

Fig. 5 Calibration curve for continuous and pulsed laser sources

Table 2 Uncertainty of measured values

$\Delta\alpha_a/\alpha_a$	$\Delta P_{\text{laser}}/P_{\text{laser}}$	$\Delta a_{\text{ref}}/a_{\text{ref}}$	$\Delta U_{\text{ind}}/U_{\text{ind}}$
5%	1%	0.01%	2%

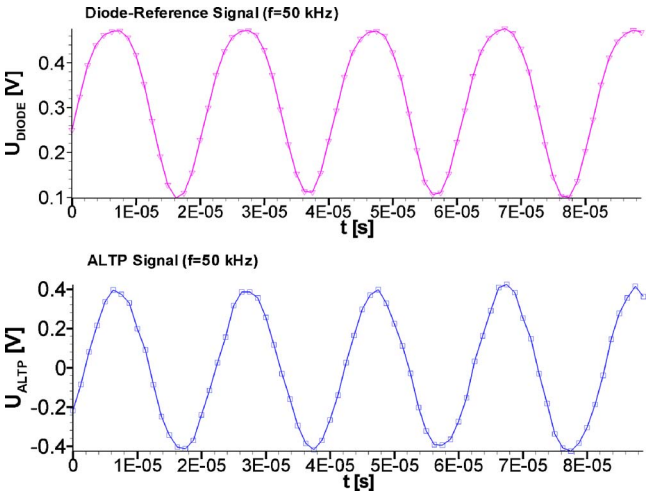

Fig. 6 ALTP signal and monitor diode reference for a 50 kHz modulated laser signal

The first investigation of the amplitude-frequency response by the exposure of the ALTP to a step function produced by a DC-excited CO_2 laser is described in [13]. The sine-wave calibration introduced for hot wires in [14] is expected to be a more precise and informative way to obtain the amplitude-frequency response of the ALTP. For the application of this calibration method, a 500 mW diode laser (Sony SLD 1332V) is used. The output of the laser can be modulated to sinusoidal waveforms in a frequency range between 1 kHz and 1 MHz and is monitored by a laser diode with a time constant of ~50 ns. Therefore, a reference signal with sufficient temporal resolution for such a high-frequency dynamic calibration is produced. In Fig. 6, the response of the diode and the ALTP are compared for a prescribed modulated laser beam of 50 kHz. The ALTP was fully covered by the broadened laser beam. The amplitude of the sinusoidal signal of the monitor diode (A_{diode}) and ALTP (A_{ALTP}) are registered and normalized. The resulting amplitude-frequency response for a uncoated sensor is plotted in Fig. 7. The amplitude-frequency response allows for the correction of measured time signals to obtain accurate amplitude spectra. A phase lag between the ALTP and the reference signal could not be observed.

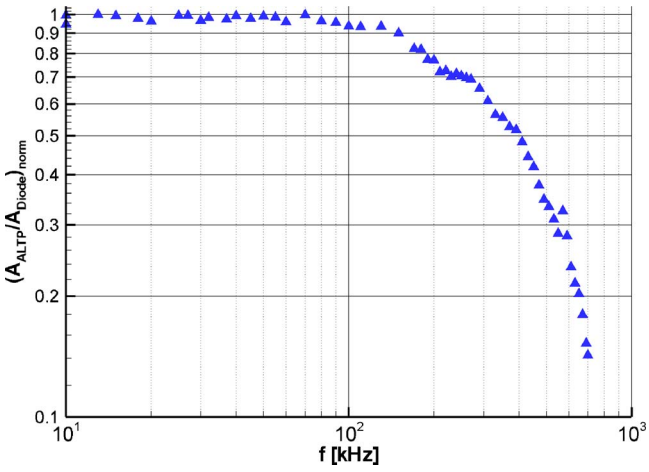

Fig. 7 Amplitude-frequency response for ALTP without protective coating

Downloaded 30 May 2010 to 128.113.26.88. Redistribution subject to ASME license or copyright; see http://www.asme.org/terms/Terms_Use.cfm

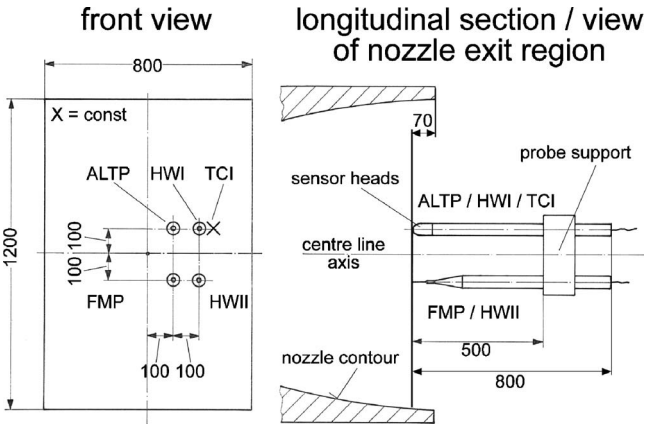

Fig. 8 Location of probes in SWK

Benchmark Experiments

In the following two sections, the capability of the ALTP is demonstrated in the subsonic and supersonic flow regimes. The results are compared to well-established measurement techniques and theoretical estimations to show the efficiency and limitations of the sensor.

Case 1: Comparative Stagnation Point Measurements of ALTP and FMP for $M=2.5$. The first performance demonstrations of the ALTP were carried out in the supersonic short duration wind tunnel (Stosswindkanal) of the IAG [15]. The goal of the experiments was the comparison of heat transfer rates at the stagnation point measured by the ALTP and a Dantec flush mounting probe (FMP). Furthermore, a comparison was made to theoretical estimates by Fay and Riddell [16] and to complete boundary layer computations.

An extensive discussion of the results can be found in [12]. The major results of these experiments are summarized in this section and demonstrate the performance of the ALTP in supersonic short duration test facilities.

The chosen flow conditions were $M=2.5$ and unit Reynolds number of $\mathrm{Re}_m=12.6\times10^6$ (for steady state I [Z1]) and 11.4×10^6 (for steady state II [Z2]). Both steady states allow a test sequence of 100 ms per run. Figure 8 shows the location of the probes in the test section of the tunnel. Two ALTP sensors were compared to a DANTEC FMP 55R45 operated by a DANTEC 56C20 temperature plug-in unit of a DANTEC 56C01 CTA system with a constant current of $I=1$ mA and an excitation of $U=0-12$ V. In addition to the FMP and the ALTP, two hot-wire probes (HW I and II) for defining the stagnation temperature as well as a thermocouple (TCI) to measure the initial temperature were mounted in the test section (see Fig. 8). Typical time signals of the FMP and the ALTP are shown in Figs. 9(*a*)–9(*c*), respectively. The time signals show the different flow phases in the test section. After the initial condition, the first steady state (Z1) establishes, followed by the transition phase, the second steady state (Z2), and the final flow breakdown.

From the measured temperature signal of the FMP, the heat transfer rates can be calculated using the Cook-Feldermann algorithm [2]. The results in Fig. 9(*b*) show a good quantitative agreement to the directly measured heat flux signal of the ALTP (Fig. 9(*c*)). The signals also demonstrate the significantly higher temporal resolution of the ALTP. The noise in the calculated heat flux of the FMP is caused by the integration procedure and A/D conversion. Overall, 16 runs with ALTP1 and 8 runs with ALTP2 were carried out and processed. Figure 10(*a*) shows the final results for the heat flux densities of all 24 runs and their comparison to theoretical estimations [16]. The difference of the heat flux values, measured by the individual sensors and normalized by

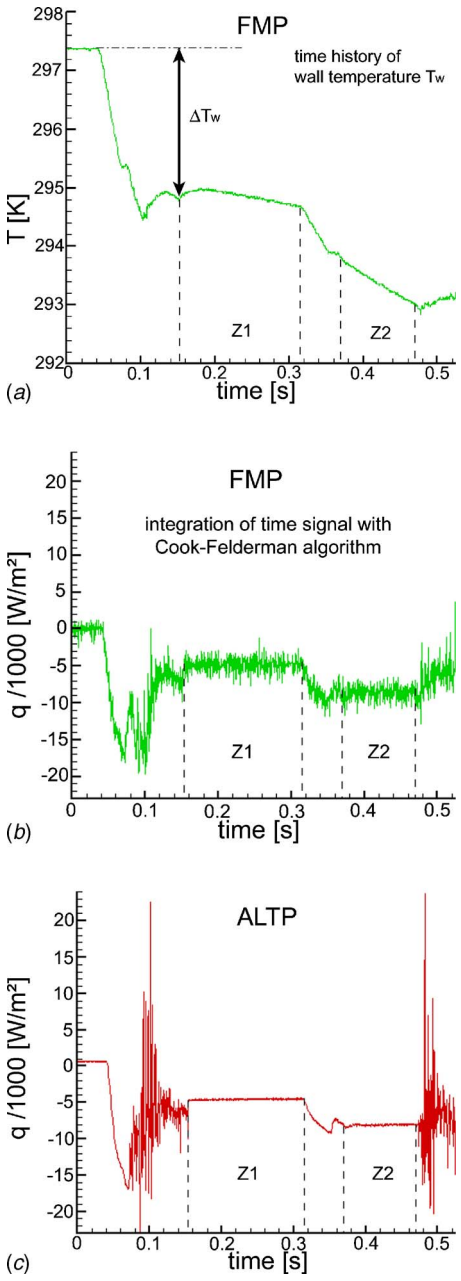

Fig. 9 (*a*) Time signal of FMP, (*b*) FMP signal after its integration, and (*c*) time signal of ALTP

their common mean values in Fig. 10(*b*), shows a fairly good agreement for the large amount of runs carried out (difference for most of the runs below 10%) and for the two different ALTPs. The major advantage of the ALTP in comparison to other heat flux gauges could be demonstrated in short duration wind tunnels due to its exceptionally low time constant. The discrepancy in reference to the theoretical heat flux densities can be deduced from uncertainties in the measured loading temperatures of the driver tube, which was used to define the theoretical stagnation conditions of the flow from the initial conditions.

Case 2: Comparison to Liquid Crystal Method on the Tip Wall of a Ribbed Channel. For the comparison to the liquid crystal method (TLC) the tip wall of a ribbed channel at the Institute of Aerospace Thermodynamics (ITLR) was used. Figure 11 shows a schematic of the channel. A more detailed description of the channel may be found in Part II [17]. The channel is 168 mm

Downloaded 30 May 2010 to 128.113.26.88. Redistribution subject to ASME license or copyright; see http://www.asme.org/terms/Terms_Use.cfm

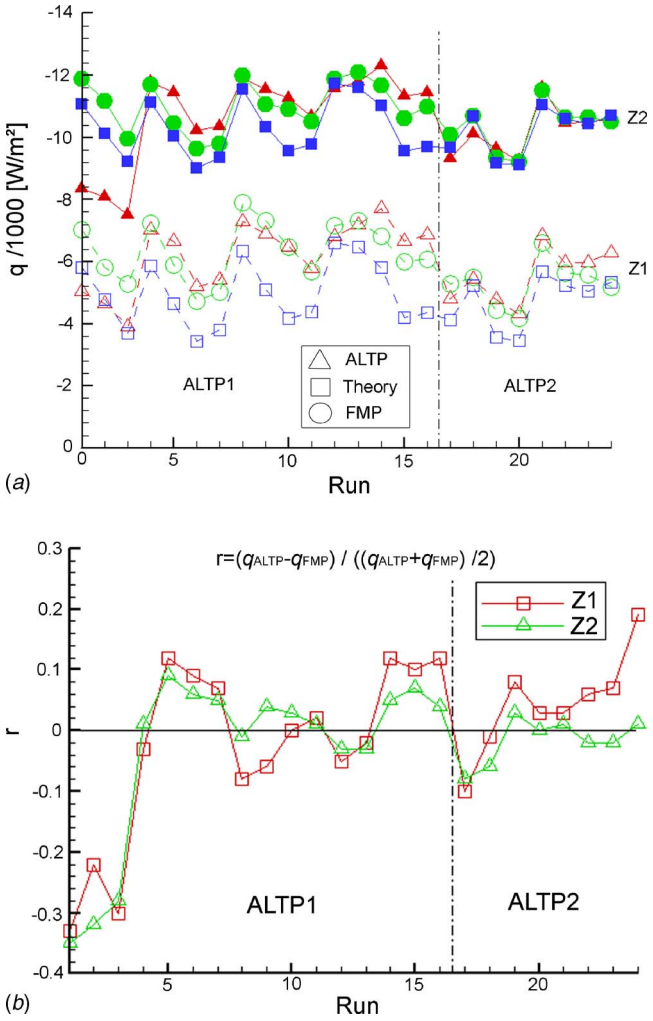

Fig. 10 (*a*) **Measured heat flux densities for ALTP1 and 2, FMP and theory versus runs,** (*b*) **ratio** $r=(q_{ALTP}-q_{FMP})/[(q_{ALTP}+q_{FMP})/2]$ **of measured heat flux densities by the different sensors**

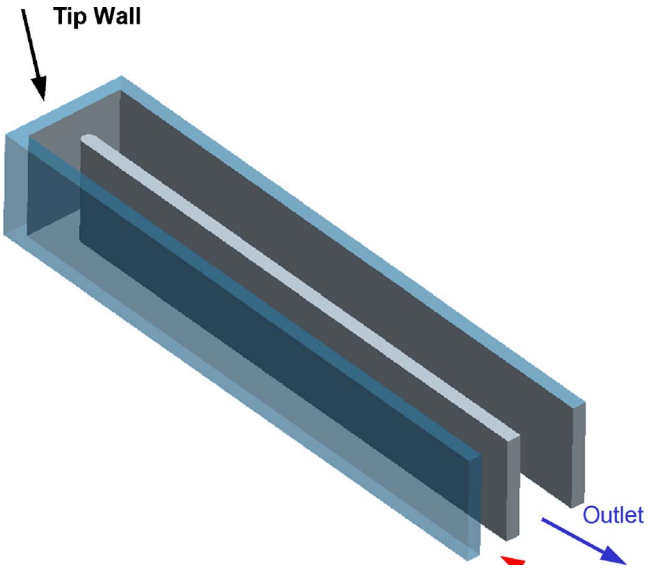

Fig. 11 Schematic working principle of the channel

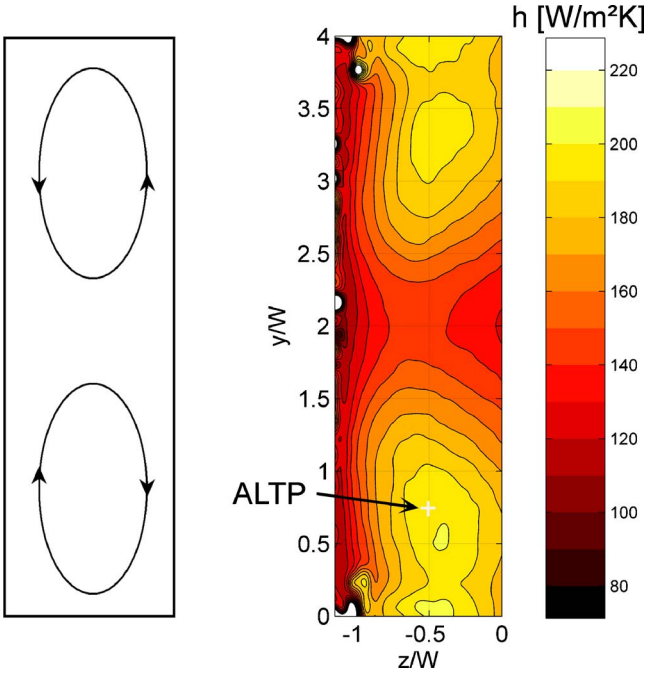

Fig. 12 Heat transfer coefficient distribution measured by TLC for Re=100,000

high and 42 mm wide (aspect ratio 4:1), resulting in a hydraulic diameter of $D_h=67.2$ mm. Rib turbulators are placed on the top and bottom walls in an angle of 60 deg to the flow direction. The turbulators cause rotation of heated fluid and the formation of two counterrotating vortices. These vortices impinge on the tip wall of the channel and cause a symmetric heat transfer distribution at this wall (see Fig. 12).

Simultaneous measurements of the TLC and the ALTP on the top and bottom halves of the wall allowed for quantitative comparisons of the measured heat transfer coefficients. The center of the impinging vortices was chosen because the maximum heat transfer coefficients are detectable in this location. Furthermore, it is fairly independent of the Reynolds number and also very easy to locate in the TLC results. In this site, the repeatability of the measurements for two different sensors was verified (see Table 3). The comparison of the TLC and the two ALTP exhibits a very good agreement.

As stated in the Static Calibration section, the total uncertainty of the measurement depends on the uncertainty of the calibration and the signal-to-noise ratio resulting for a specific experiment. For the present benchmark, the signal to noise ratio decreased due to the low heat fluxes measured. For the worst case, $(\Delta U_{rms}/U)_m$ was 5% and leads to a total value of uncertainty of 7.5%. The results lie well in the uncertainty limits of the TLC (7%) [17] and the ALTP (7.5%).

For a constant Reynolds number, the heat transfer coefficient should remain constant for different temperature jumps. In Table 4, the variation of the temperature from $\Delta T=(T_B-T_0)=9.6$ K to

Table 3 Repeatability of measurements and comparison of heat transfer coefficients for ALTP and TLC

Sensor	Re	u_∞ (m/s)	h_{ALTP} (W/m²K)	h_{TLC} (W/m²K)	Difference (%)
788 II	100,000	22.7	194.6	193.6	0.5
787 I	100,000	22.7	187.7	188.4	0.4

Downloaded 30 May 2010 to 128.113.26.88. Redistribution subject to ASME license or copyright; see http://www.asme.org/terms/Terms_Use.cfm

Table 4 Variation of temperature jump for Re=200,000

Sensor	Re	ΔT (K)	h_{ALTP} (W/m^2K)
788 II	200,000	9.6	297.6
788 II	200,000	22.5	295.4
		Difference	=1.0%

$\Delta T=22.5$ K demonstrates this characteristic for the ALTP.

The comparative study of the ALTP and the TLC showed very good results for internal channel flows. The two-dimensional distributions of the mean heat transfer coefficient created by the TLC were verified and expanded by the time-resolved but single point measurements of the ALTP. Therefore, the advantages of both techniques are combined in these measurements. The Reynolds number variation for this site and one additional location are presented in [17]. Furthermore, the time-resolved measurements and the spectral data are explained in this paper.

Suitability of the ALTP for Turbomachinery Studies. The benchmark cases presented in this paper show the capability of the ALTP for heat flux measurements in different environments and the fast frequency response of the sensor. Therefore, the ALTP sensor should be suitable for other short- or long-duration turbomachinery investigations as well, where other gauge-type sensors have been used in the past (see, e.g., Haldeman and Dunn [18–21]). Although the thermal stability of the sensor should be addressed for these applications in the case of larger temperature differences than given in the presented benchmarks, the heating of the sensor should be relatively small, at least in the first few milliseconds of a short-duration run since the sensor does not require active heating of the film. Because of the fast frequency response of the sensor, this relatively short data acquisition period should normally be sufficient. However, the disadvantages of most wall-mounted surface sensors, such as casing effects and conduction errors due to the insertion of a low conductivity substrate in a metallic surface, as well as durability in flows that are not entirely clean, would also apply for the ALTP sensor.

Conclusions

Time-resolved heat flux measurements are of interest for a wide range of applications in thermodynamics and fluid mechanics. Numerical simulations and turbulence models demand experimental validation and comparative measurements with high spectral resolution. The atomic layer thermopile (ALTP) has been introduced in this paper as a novel heat flux sensor with unique properties. It allows for highly time-resolved heat flux measurements up to 1 MHz and has a linear characteristic over 11 orders of magnitude.

Its working principle, the static and dynamic calibration, as well as its thermal properties were discussed. Furthermore, two benchmark experiments have been briefly described and the major results showed the capability of the ALTP for flow regimes from subsonic to supersonic flow speeds. The results have been compared to theoretical estimations and several established measurement techniques. The combination of two-dimensional optical measurement techniques are confirmed and expanded by pointwise, time-resolved heat flux measurements and lead to greater understanding of the influence of fluctuations in temperature fields and heat flux.

Acknowledgment

The authors gratefully acknowledge the funding of the Deutsche Forschungsgemeinschaft (DFG) within SPP 1147.

Nomenclature

A = amplitude
a_{ref} = reference area
α_c = tilt angle
α_a = absorption coefficient
h = heat transfer coefficient
c = specific heat
d = oxygen concentration
δ = thickness
$\vec{E}$ = thermoelectric field
$\vec{S}$ = Seebeck tensor
q = heat flux density
i = intensity
l = film length
k = thermal conductivity
M = Mach number
P_{laser} = laser power
Re = Reynolds number (based on hydraulic diameter)
D_h = hydraulic diameter
s = sensitivity coefficient
ρ = density
T = temperature
U = voltage
u_∞ = free stream velocity

Subscripts

F = ALTP film
S = ALTP substrate
t = total
0 = initial
B = bulk
ind = induced in calibration
m = measured
n = normal to surface
rms = root mean square

References

[1] Schultz, D. L., and Jones, T. V., 1973, "Heat Transfer Measurements in Short Duration Hypersonic Facilities," AGAR-Dograph No. 165.
[2] Cook, W. J., and Felderman, E. J., 1966, "Reduction of Data From Thin-Film Heat-Transfer Gages: A Concise Numerical Technique," AIAA J., **4**(3), pp. 561–562.
[3] Gardon, R., 1953, "An Instrument for the Direct Measurement of Intense Thermal Radiation," Rev. Sci. Instrum., **24**, pp. 366–370.
[4] Epstein, A. H., Guennette, G. R., Norton, R. J. G., and Cao, Y., 1986, "High-Frequency Response Heat-Flux Gauge," Rev. Sci. Instrum., **57**, pp. 639–649.
[5] Hayashi, M., Sakurai, A., and Aso, S., 1986, "Measurement of Heat-Transfer Coefficients in Shock Wave—Turbulent Boundary Layer Interaction Regions With a Multi-Layered Thin Film Heat Transfer Gauge," NASA TM - 77958.
[6] Godefray, J. C., Francois, D., Gageant, C., Miniere, F., and Portat, M., 1986, "Thin Film and High Temperature Thermal Sensors Deposited by RF Cathodic Sputtering," ONERA TP No. 1986-28.
[7] Hager, Jr., N. E., 1965, "Thin Foil Heat Meter," Rev. Sci. Instrum., **36**, pp. 1564–1570.
[8] Mee, D. J., 2002, "Boundary-Layer Transition Measurements in Hypervelocity Flows in a Shock Tunnel," AIAA J., **40**(8), pp. 1542–1548.
[9] Hager, J. M., Simmons, S., Smith, D., Onishi, S., Langley, L. W., and Diller, T. E., 1991, "Experimental Performance of a Heat Microsensor," ASME J. Eng. Gas Turbines Power, **113**, pp. 246–250.
[10] Renk, K. F., Betz, J., Zeuner, S., Lengenfellner, H., and Prettl, W., 1994, "Thermopile Effect due Laser Radiation Heating in Thin Films of High-T_c-Materials," Physica C, **37-40**, pp. 235–240.
[11] Zeuner, S., Lengfellner, H., and Prettl, W., 1995, "Thermal Boundary Resistance and Diffusility for $YBa_2Cu_3O_{7-\delta}$ Films," Phys. Rev. B, **51**(17), pp. 11903–11908.
[12] Knauss, H., Gaisbauer, U., Wagner, S., Buntin, D., Maslov, A., Smorodsky, B., and Betz, J., 2002, "Calibration Experiments of a New Active Fast Response Heat Flux Sensor to Measure Total Temperature Fluctuations—Part III," *Proc. of ICMAR 2002*, Novosibirsk, Russia, Vol. III, pp. 86–113.
[13] Maslov, A. A., Bountin, D. A., Shiplyuk, A. N., Smorodsky, B., Knauss, H., Gaisbauer, U., Wagner, S., and Betz, J., 2004, "ALTS-Sensor Application for Boundary Layer Measurements," *Proc. of ICMAR 2004*, Novosibirsk, Russia, Vol. II, pp. 137–146.
[14] Walker, D. A., and Walker, M. D., 1990, "Method for Fast Sine-Wave Cali-

Downloaded 30 May 2010 to 128.113.26.88. Redistribution subject to ASME license or copyright; see http://www.asme.org/terms/Terms_Use.cfm

bration of Hot-Wire Frequency Response," Rev. Sci. Instrum., **61**(3), pp. 1131–1135.
[15] Knauss, H., Riedel, R., and Wagner, S., 1999, "The Shock Wind Tunnel of Stuttgart University, A Facility for Testing Hypersonic Vehicles," Paper No. AIAA-99-4959.
[16] Fay, J. A., and Riddell, F. R., 1958, "Theory of Stagnation Point Heat Transfer in Dissociated Air," J. Aeronaut. Sci., **25**, pp. 73–85.
[17] Jenkins, S., von Wolfersdorf, J., Weigand, B., Roediger, T., Knauss, H., and Kraemer, E., 2008, "Time-Resolved Heat Transfer Measurements on the Tip Wall of a Ribbed Channel Using a Novel Heat Flux Sensor—Part II: Heat Transfer Results," ASME J. Turbomach., **130**, p. 011019.
[18] Haldeman, C. W., and Dunn, M. G., 2004, "Heat-Transfer Measurements and Predictions for the Vane and Blade of a Rotating High-Pressure Turbine Stage," ASME J. Turbomach., **126**, pp. 101–109.
[19] Iliopoulou, V., Denos, R., Billiard, N., and Arts, T., 2004, "Time-Averaged and Time-Resolved Heat Flux Measurements on a Turbine Stator Blade Using Two-Layered Thin-Film Gauges," ASME J. Turbomach., **126**, pp. 570–577.
[20] Holmberg, D. G., and Diller, T. E., 2005, Simultaneous Heat Flux and Velocity Measurements in Transonic Turbine Cascade," ASME J. Turbomach., **127**, pp. 502–506.
[21] Dunn, M. G., 2001, Convective Heat Transfer and Aerodynamics in Axial Flow Turbines," ASME J. Turbomach., **123**, pp. 637–686.
[22] Squire, H. B., 1938, *Modern Developments in Fluid Dynamics*, Vol. 2, Clarendon Press, Oxford.

Downloaded 30 May 2010 to 128.113.26.88. Redistribution subject to ASME license or copyright; see http://www.asme.org/terms/Terms_Use.cfm

Time-Resolved Heat Transfer Measurements on the Tip Wall of a Ribbed Channel Using a Novel Heat Flux Sensor—Part II: Heat Transfer Results

Sean Jenkins
e-mail: sean.jenkins@itlr.uni-stuttgart.de

Jens von Wolfersdorf

Bernhard Weigand

Institute of Aerospace Thermodynamics,
University of Stuttgart,
Pfaffenwaldring 31,
70569 Stuttgart, Germany

Tim Roediger

Helmut Knauss

Ewald Kraemer

Institute of Aerodynamics and Gas Dynamics,
University of Stuttgart,
Pfaffenwaldring 21,
70569 Stuttgart, Germany

Measurements using a novel heat flux sensor were performed in an internal ribbed channel representing the internal cooling passages of a gas turbine blade. These measurements allowed for the characterization of heat transfer turbulence levels and unsteadiness not previously available for internal cooling channels. In the study of heat transfer, often the fluctuations can be equally as important as the mean values for understanding the heat loads in a system. In this study, comparisons are made between the time-averaged values obtained using this sensor and detailed surface measurements using the transient thermal liquid crystal technique. The time-averaged heat flux sensor and transient TLC results showed very good agreement, validating both methods. Time-resolved measurements were also corroborated with hot film measurements at the wall at the location of the sensor to better clarify the influence of unsteadiness in the velocity field at the wall on fluctuations in the heat flux. These measurements resulted in turbulence intensities of the velocity and heat flux of 20%. *The velocity and heat flux integral length scales were about 60% and 35% of the channel width, respectively, resulting in a turbulent Prandtl number of* 1.7 *at the wall.* [DOI: 10.1115/1.2472417]

Keywords: internal cooling, ribs, turbulence, heat transfer

Introduction

Engine designers are continuously striving to increase the heat transfer levels in internal passages of turbine blades. This results in higher levels of cooling and thus permits higher turbine inlet temperatures, which lead to higher overall engine efficiency. It is clear that a greater understanding of the heat transfer processes in internal passages will assist in creating better designs.

It is with this goal in mind that experiments were undertaken to measure time-resolved heat fluxes at positions in an internally ribbed channel. To fully understand the heat loads in a system such as this, fluctuations in the heat flux can be equally or more important than the time-mean values. Identification of the range of frequencies present in the turbulence field and which of those frequencies are responsible for increasing heat transfer can also be helpful in improvement or validation of computational codes.

Many research groups have investigated heat transfer in internal passages; however, heat transfer turbulence spectra in gas turbine applications have been mainly investigated for external flows. A recent study by Nix and Diller [1] investigated the physical mechanism for heat transfer on a cylinder stagnation point by making simultaneous measurements of the velocity field and heat flux at the surface. They found a strong coherence between the signals at lower frequencies, indicating that the penetration of large-scale eddies through the boundary layer were responsible for augmentation of the heat transfer. They used a heat flux microsensor for the heat flux measurements, which was capable of resolving the range of frequencies in the low speed tunnel. They argued that the cylinder stagnation point is a good representation of the leading edge of a vane or blade, thus allowing the study of external blade heat transfer on a simplified model. Both velocity and heat flux spectra were reported, as well as turbulence intensities of both velocity and heat flux. An analytical model developed in a previous paper by Nix et al. [2], based on the turbulence length scale and turbulence intensity, showed good agreement with the augmentation of the heat flux by freestream turbulence.

In previous work by Holmberg and Diller [3] using the same sensor, measurements of external heat transfer were made at three positions on the pressure surface of a turbine blade. They investigated the effects of grid-generated turbulence conditions on the heat transfer and found that the mean heat transfer was higher for a smaller length scale given constant turbulence intensity.

Moss and Oldfield [4] made time-resolved measurements using thin-film gages and hot wires in a flat-plate boundary layer with high levels of freestream turbulence. They made simultaneous measurements of the velocity and heat flux and showed that turbulent eddies from the freestream penetrated the boundary layer, enhancing the heat transfer.

With respect to time mean results, data are very sparse for the tip wall of a two-pass high aspect ratio channel. A companion study [5] shows limited results on the tip wall for the same channel at one Reynolds number; however, the focus of that study is on heat transfer in the outlet channel. Hirota et al. [6] showed results on the tip wall for a low aspect ratio (1:2) channel using the sublimation method. They observed a high heat transfer area due to impingement of the flow in the turning region. However, the channel did not include ribs; thus, effects of rib-induced secondary flows were not investigated. Schnieder et al. [7] showed heat transfer distributions on the tip wall of a short rectangular (1:2) channel with 45 deg ribs and several flow-guide vane configurations in the bend region.

Contributed by the International Gas Turbine Institute of ASME for publication in the JOURNAL OF TURBOMACHINERY. Manuscript received July 24, 2006; final manuscript received September 26, 2006; published online January 28, 2008. Review conducted by David Wisler. Paper presented at the ASME Turbo Expo 2006: Land, Sea and Air (GT2006), Barcelona, Spain, May 8–11, 2006. Paper No. GT2006-91131.

 Copyright © 2008 by ASME

Downloaded 30 May 2010 to 128.113.26.88. Redistribution subject to ASME license or copyright; see http://www.asme.org/terms/Terms_Use.cfm

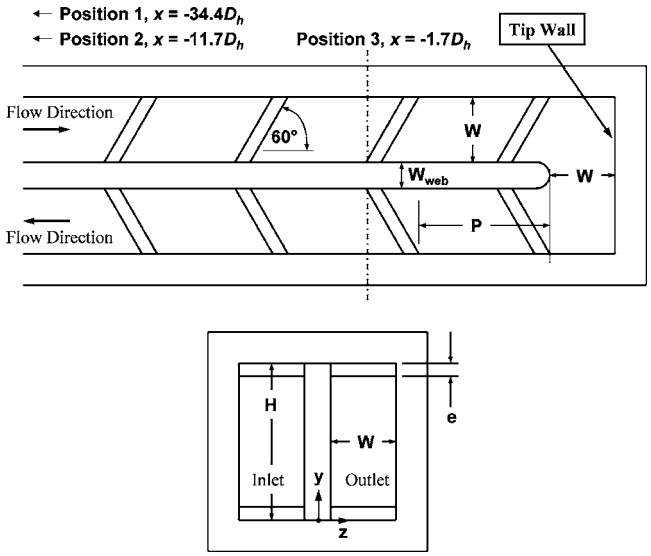

Fig. 1 Schematic top view and cross section of the test channel with 60 deg ribs

Although the secondary flows generated by angled ribs have been fairly well studied [8–10], the effects of these secondary flows on the tip-wall heat transfer have not. This critical region has been investigated in detail in the present study, both with respect to mean heat transfer distributions and time-resolved results.

The current study seeks to fill a gap in the literature by documenting the distribution of mean heat transfer on the tip wall of a high aspect ratio channel with angled ribs. Furthermore, it seeks to demonstrate the capability of a novel heat flux sensor to provide both mean and time-resolved heat flux information in such a channel. Measurements in this critical region of an internal passage should assist in the validation of computational codes, and shed light on the nature of the turbulence present at the tip wall.

Facility and Instrumentation

Measurements were made on the tip wall of a 4:1 aspect ratio, two-pass channel. The channel, shown in Fig. 1, was 2.4 m long and each pass had a width of $W=42$ mm and height of $H=168$ mm, resulting in a hydraulic diameter of $D_h=1.6W=67.2$ mm. The inlet channel had an entrance length of $L_e=1.524$ m to ensure hydrodynamically and thermally fully developed conditions preceding the measurement section with a length of $L_m=0.840$ m. This entrance length was required to accommodate a minimum of 15 ribs, which has been shown in several previous studies to provide fully developed heat transfer result in ribbed channels [11–13]. The inlet and outlet channels were connected by a sharp 180 deg bend. The divider wall had a thickness of $W_{web}=0.4W$ and the tip of the divider wall was radiused as shown in Fig. 1. The ribs had a square cross section and a height of $e/H=0.05$ (or $e/D_h=0.125$) and a spacing of $P/e=10$. They were arranged in a parallel fashion at an angle of $\alpha=60$ deg to the flow direction.

Transient Liquid Crystal Technique. The transient liquid-crystal technique (TLC) was used to determine the heat transfer coefficient distribution on the tip wall. The channel was constructed from 20 mm thick Plexiglas to offer good optical access and to fulfill the semi-infinite wall assumption required with this method. Inner surfaces of the channel were first coated with narrow band liquid crystals (Hallcrest BM/R31C1W/C17-10) and then black paint to provide high intensity in the colorplay of the liquid crystals. A CCD camera (Sony RBG Video Camera Module, Model XC-711P) was positioned to capture the color change

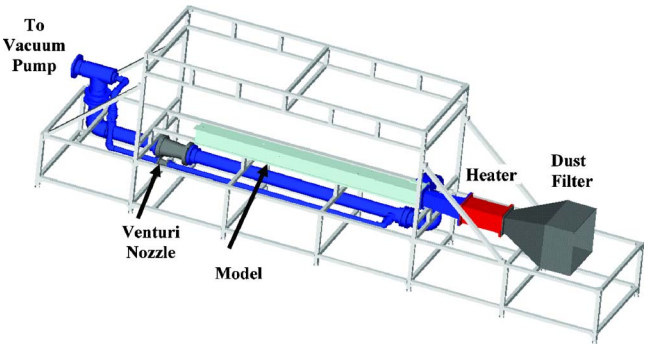

Fig. 2 Diagram of test rig

of the liquid crystal on the tip wall during the transient experiment, and this was recorded on digital video tape using a Sony digital video cassette recorder (Model GV-D900E PAL). The digital video was transferred to computer from the recorder for data analysis via FIREWIRE.

The temperature step for the transient liquid-crystal technique was provided by a mesh heater, which was square in cross section and was based on the design of Wang et al. [14] and Ireland et al. [15]. Airflow entered the test rig through a dust filter, as shown in Fig. 2, and after passing through the heater section, flowed through a contraction section, which reduced to the dimensions of the entrance of the inlet channel. The outlet of the channel was connected by a series of pipes to a vacuum pump system capable of flow rates up to 2.5 kg/s. As shown in Fig. 2, the piping system included a Venturi nozzle for measurements of the mass flow rate and also contained a valve for flow regulation.

In order to evaluate the experimental results, solution of the one-dimensional (1D) conduction equation with the assumption of a semi-infinite wall and convective boundary condition is required. The nondimensional temperature at the surface ($x=0$) is given by

$$\frac{T_W - T_0}{T_B - T_0} = 1 - \exp\left(\frac{h^2 \alpha_w t}{k_w^2}\right) \operatorname{erfc}\left(\frac{h\sqrt{\alpha_w t}}{k_w}\right) \tag{1}$$

with initial and boundary conditions of

$$t = 0: \; T = T_0$$

$$x = 0: \; -k\frac{\partial T}{\partial x} = h(T_W - T_B)$$

$$x \to \infty: \; T = T_0 \tag{2}$$

where T_0 is the initial fluid temperature, T_B is the bulk temperature, h is the heat transfer coefficient, and α_w and k_w are the thermal diffusivity and conductivity of the wall material, respectively. Since the bulk temperature at the measurement position was also a function of time, the time history of the temperature step must be incorporated into the solution of Eq. (1) with the help of Duhamel's superposition theorem [16]. This results in the following expression:

$$T_W - T_0 = \sum_{i=1}^{N} (T_{B,i} - T_{B,i-1}) \left[1 - \exp\left(\frac{h^2 \alpha_w (t - t_i)}{k_w^2}\right) \times \operatorname{erfc}\left(\frac{h\sqrt{\alpha_w (t - t_i)}}{k_w}\right) \right] \tag{3}$$

A transient heat transfer test was begun once constant flow rate and initial temperature conditions were obtained. Then power from a DC supply to the heater was switched on impulsively to provide the temperature step and the color change of the liquid crystals was recorded as the hot mainstream was imposed on the

Downloaded 30 May 2010 to 128.113.26.88. Redistribution subject to ASME license or copyright; see http://www.asme.org/terms/Terms_Use.cfm

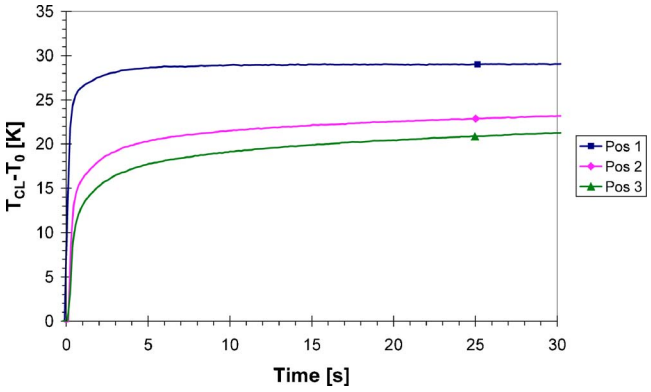

Fig. 3 Centerline temperature profiles for positions upstream of the bend

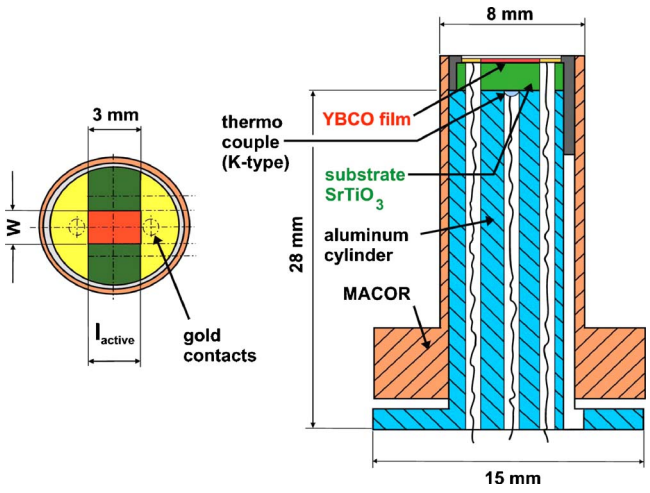

Fig. 4 Schematic cross section of the ALTP heat flux sensor module

cool surfaces. The thermal liquid-crystal color change was analyzed to determine the time point at which each pixel reached the calibrated green hue value (hue between 105 and 115 on 0–255 scale). Using the time of thermal liquid-crystal indication and a local time-resolved bulk temperature profile, Eq. (3) was solved for the heat transfer coefficient.

Measurements of the centerline temperature were made using Agilent 24307 data acquisition units with thermocouples placed at $34.4D_h$, $11.7D_h$, and $1.7D_h$ upstream of the bend in the inlet channel. This temperature data was used to account for the variation in bulk temperature both with position and time. As shown in Fig. 3, due to heat flux from the fluid to the wall, the time-dependent temperature history changed with position in the channel. Close to the heater, the profile was nearly a step change; however, further downstream the initial step was smoothed and the temperature was lower at each downstream position. To accurately calculate the local heat transfer coefficient, the local bulk temperature profile was calculated at the entrance to the bend using a model developed by von Wolfersdorf et al. [17] based on a mean heat balance along the inlet channel. The interpolation procedure is based on a 1D heat balance calculating the temperature drop over an infinitesimal short section using the heat flux into the walls assuming a mean heat transfer over the perimeter. This model was expanded with help from the Duhamel principle to account for a time-varying temperature profile as the starting point for the calculation. Thus, the bulk temperature history $[T_B(x,t)]$ was calculated for each axial position in the channel with the following:

$$\frac{T_B(x,t)-T_0}{T_E(t)-T_0} = 1 - \left[1 - \exp\left(\frac{-\bar{h}\mathcal{P}}{\dot{m}c_p}x\right)\right] \times \exp\left(\frac{\bar{h}^2\alpha_w t}{k_w^2}A^2\right)\operatorname{erfc}\left(\bar{h}A\sqrt{\frac{t\alpha_w}{k_w^2}}\right) \tag{4}$$

$$\text{with} \quad A = \frac{1-\exp\left(\frac{-\bar{h}\mathcal{P}}{\dot{m}c_p}x\right)}{\frac{\bar{h}\mathcal{P}}{\dot{m}c_p}x} \tag{5}$$

$$\bar{h}(x) = \frac{\int_{x'=0}^{x} hT_B\,dx'}{\int_{x'=0}^{x} T_B\,dx'} \tag{6}$$

where $\bar{h}$ is the average heat transfer coefficient, $\mathcal{P}$ is the perimeter of the cross section, $\dot{m}$ is the mass flow rate, c_p is the specific heat of the fluid at constant pressure, α_w and k_w are the thermal diffusivity and conductivity of the wall material, respectively, and $T_E(t)$ is the temperature history at the initial position in the calculation. This allowed for the calculation of the temperature history at the entrance to the bend region, which was used for the evaluation of the heat transfer for the inlet side of the tip wall. A second temperature history was computed at the midpoint of the bend at the beginning of the outlet for evaluation of results on the outlet side of the tip wall.

Measurements described fully in [5] showed that the centerline temperature agreed well with the mean temperature history. Using a numerical calculation of the velocity field from a preliminary study, comparisons between the mean temperature and a calculated bulk temperature were made and differences were found to be negligible. Therefore, the centerline temperature history was used in place of the bulk temperature history for all calculations of heat transfer coefficients.

Atomic Layer Thermopile (ALTP) Heat Flux Sensor. Time-resolved heat flux measurements were acquired using an atomic layer thermopile (ALTP) heat flux sensor, which was originally developed as a detector for optical radiation. It uses the thermopile effect created by a temperature gradient over a yttrium-barium-copper-oxide ($YBa_2Cu_3O_{3-d}$) crystal (later referred to as YBCO). Copper oxide layers and YBCO interlayers form atomic thermocouples connected in series. The thermopile works on the principle of the transverse Seebeck effect, caused by the anisotropy of the YBCO film in combination with a tilt angle of the crystal with respect to the film surface normal. A temperature gradient over the film creates a thermoelectric field E

$$E = \vec{S}\,\nabla\,\vec{T} \tag{7}$$

where $\vec{S}$ is the Seebeck tensor and $\nabla\vec{T}$ is the temperature gradient over the film.

It was shown that the signal of the ALTP is purely of thermoelectric origin, and laser calibration experiments showed a linear characteristic of the sensor over more than 11 orders of magnitude. Temperature gradients created by heat flux rates of a few milliwatts per square centimeter up to 20 kW/cm^2 (damage threshold for a 1 ms pulse) are detectable. It responds to radiation over a very large wavelength range from infrared to ultraviolet. For a detailed discussion of the characteristics of the sensor, the reader is referred to Part 1 [18].

A schematic of the ALTP heat flux sensor is shown in Fig. 4, detailing the construction and arrangement of components. The active area of the sensors used in these experiments was

Downloaded 30 May 2010 to 128.113.26.88. Redistribution subject to ASME license or copyright; see http://www.asme.org/terms/Terms_Use.cfm

3×3 mm. The housing of the module was made of a ceramic insulator (MACOR) to achieve mainly one dimensional heat flux through the substrate and the cylinder.

The sensor was attached to an amplifier and then to a low-pass filter. For data acquisition, a Dewetron transient recorder with an Insight A/D board (14 bit, 800 kHz) was used. All measurements were taken using a 10 kHz low-pass filter and amplified by 8500.

Hot-Film Gage-Dantec Flush Mounting Probe (FMP). For comparison to the heat flux fluctuations, a hot film gage (DANTEC Flush Mounting Probe 55R45) with an active length of 0.4 mm operated by a DANTEC 56C20 temperature plug-in unit in a DANTEC 56C01 CTA system was used to measure velocity fluctuations. Fluctuations in the hot film gage signal, were correlated with the velocity fluctuations u'.

Computation of Turbulence Quantities. Fluctuations in the velocity and heat flux were calculated from the integration of the power spectral density as follows:

$$u'^2 = \int_0^\infty E_u(f)df \quad q'^2 = \int_0^\infty E_q(f)df \tag{8}$$

With these quantities, the turbulence intensity and turbulent heat flux intensity were computed using the rms values divided by the mean

$$\mathrm{Tu} = \frac{\sqrt{u'^2}}{\bar{u}}, \quad \mathrm{Tu}_q = \frac{\sqrt{q'^2}}{\bar{q}} \tag{9}$$

The integral time scale was computed from an integration of the autocorrelation function from the time signal of the velocity or heat flux where the autocorrelation function was computed from the normalized data,

$$R_{xx} = \int_0^\infty \hat{q}(t)\hat{q}(t+\tau)dt, \quad \text{where} \quad \hat{q}(t) = \frac{q-\bar{q}}{q'} \tag{10}$$

and where $\bar{q}$ is the mean of the heat flux time signal and τ is the measurement interval. The autocorrelation function was integrated to determine the integral time scale as follows:

$$\mathrm{T}_f = \int_0^{\tau|R_{xx}=0} R_{xx}(\tau)d\tau \tag{11}$$

An integral length scale, Λ_f, can be derived from this quantity by the use of a representative bulk velocity as follows:

$$\Lambda_f = U_{\mathrm{bulk}}\mathrm{T}_f, \quad \Lambda_q = U_{\mathrm{bulk}}\mathrm{T}_q \tag{12}$$

The Kolmogorov scale was determined based on a point in the power density spectrum where the slope is approximately $m = -5/3$. This allows for calculation of the dissipation, ε, and thereby the Kolmogorov length scale, i.e. in the equilibrium range [19]:

$$E_u(k) = 0.5\varepsilon^{2/3}k^{-5/3} \tag{13}$$

and

$$\eta = \left(\frac{\upsilon^3}{\varepsilon}\right)^{1/4} \tag{14}$$

Uncertainty Analysis. Uncertainties related to the heat transfer measurements were estimated and are shown in Table 1. Uncertainties in the heat transfer measurements were based on temperature, time, and material property uncertainties. Temperature uncertainties were mainly bias errors as a result of the thermocouple calibration curve used and thus were not compounded in the use of a temperature evolution in the evaluation of heat transfer coefficients. The precision uncertainty in the temperature measurements was ~0.1 K. Uncertainties for the quantities presented in Table 1 are based on the precision uncertainty of the thermocouple measurements over the temperature range used (for $(T_B - T_0)$) and include uncertainties in the thermal liquid-crystal calibration (for $(T_W - T_0)$). Uncertainties in the material properties of the Plexiglas walls were estimated at 5%, resulting in a total uncertainty in the Nusselt number of ~8%.

Table 1 Uncertainties in measurement quantities

Quantity	ρ	Re	D_h	t	$T_B - T_0$	$T_W - T_0$
Uncertainty (%)	0.8	2.0	0.8	1.9	0.7	1.8

Uncertainties for the ALTP heat flux sensor were estimated based on the uncertainty of the reference detector used in the calibration of the sensor (2%), the uncertainty in the absorption rate of the ALTP (5%), and the uncertainty due to the signal-to-noise ratio (5%), to give an overall error of 7.5%.

Results and Discussion

Measurements of the heat transfer were made on the tip wall of a two-pass ribbed duct by the transient thermal liquid-crystal technique and with the atomic layer thermopile (ALTP) heat flux sensor for a range of Reynolds numbers. Comparisons are made between the mean value of the point-specific time-resolved heat flux measurements and a symmetric point within the spatially resolved mean Nusselt number distributions. Time-resolved results were available from the ALTP heat flux sensor, allowing for computation of spectral distributions of heat flux and other turbulence statistics. Measurements using the ALTP heat flux sensor were made in two locations, one on the inflow side at a position of high heat flux, and one position on the outflow side where the heat flux was lower. This allowed for a comparison of how turbulence spectra and statistics differed on the tip wall. In addition, a hot-film gage, operated in CTA mode, provided measurements of the turbulent velocity spectra at the same location as the heat flux sensor.

Time-Mean Results. The distribution of the heat transfer coefficient, shown in Fig. 5, is representative of the typical pattern for the tip wall in this high aspect ratio ribbed channel. The orientation of the figure is downstream towards the tip wall (see Fig. 1). Symmetric peaks in the heat transfer coefficient on the left side of the figure are due to the rib induced secondary flows. The ribs induce a flow along the ribbed walls from the divider wall to the outer wall, which then recirculates back to the divider wall at the midplane, giving two symmetric secondary flow structures, shown in the schematic in Fig. 5. The location of the heat flux sensor is shown with a white cross in the lower left corner, centered at roughly $y/W = 0.7$ and $z/W = -0.5$ and is referred to as Site 1. The sensor was placed in this position to take advantage of the symmetry of the results, thus allowing for a direct comparison between the heat flux sensor and thermal liquid-crystal results within the same experiment. This symmetry is shown in the schematic using results from a separate experiment without the heat flux sensor installed. In this example, agreement between the two symmetric positions was within 1%. The sensor was also placed in this location with relatively high heat flux and low gradients to reduce uncertainties in the heat flux sensor measurements. For the results shown at a Reynolds number of Re = 100,000, the maximum heat transfer occurred at about $y/W = 3.5$, $z/W = -0.4$, with a value of about Nu = 475. The heat transfer coefficient reached the lowest value of Nu = 275 at a point at midspan on the exit flow side of the tip wall ($z/W > 0$). The divider wall position is shown schematically on the figure with dashed lines to indicate the inlet and outlet sides. The peak heat transfer levels were driven by impingement of the secondary flow vortices, but these secondary flows were disrupted in the bend region, and on the outlet side of the tip wall, heat transfer levels were much lower.

A comparison between the ALTP heat flux sensor and the symmetric position in the TLC Nusselt number distribution showed good agreement with values of Nu = 467 and Nu = 469, respec-

Downloaded 30 May 2010 to 128.113.26.88. Redistribution subject to ASME license or copyright; see http://www.asme.org/terms/Terms_Use.cfm

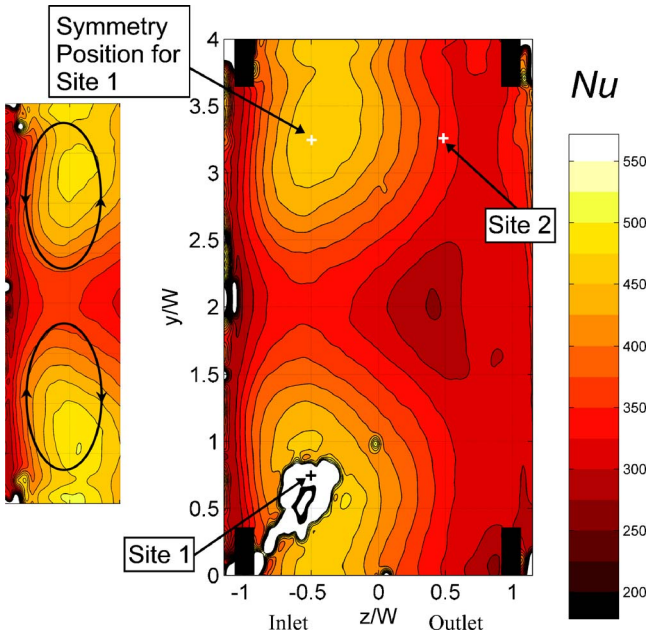

Fig. 5 Distribution of Nusselt number on the tip wall at Re =100,000 (with schematic of secondary flows)

tively, thus validating the procedure for determining the Nusselt number using the transient thermal liquid-crystal technique and also verifying the use of the ALTP heat flux sensor at these heat transfer levels and low Mach numbers. The heat flux was also measured for a second point positioned on the outflow side of the tip wall in the upper right corner (Site 2, in Fig. 5), where symmetry could also be used for comparisons. It should be noted that, due to the bulk fluid temperature rise during the test, the heat flux sensor recorded a slowly increasing heat flux, however, the heat transfer coefficient (or Nusselt number) was found to be constant.

Mean heat transfer coefficient distributions for a range of Reynolds numbers from Re=50,000 to 200,000 are shown in Fig. 6. In these figures, the scale is centered about a point determined by the average of the maximum and minimum Nusselt number. For all cases, the scale increment was $\Delta Nu=25$. It is immediately apparent from these figures that the pattern of the heat transfer was very similar in all cases, with symmetric islands of high heat transfer from the secondary flows on the inlet side and a lower level at midheight ($y/W=2.0$) on the outlet side. In contrast to these similarities, the gradient of the Nusselt number grew steadily with increasing Reynolds number, evident in the spacing of the contour levels. Less obvious was a shift in the position of the peak heat transfer, which moved downward with increasing Reynolds number, the most significant variation between Reynolds numbers of Re=50,000 and 100,000. The shape of the high heat transfer island also changed somewhat with Reynolds number. This was likely due to the higher momentum of the bulk flow at higher Reynolds numbers which constricted the secondary flow core.

In Fig. 7, a comparison for Site 1 between the heat transfer coefficients from the ALTP heat flux sensor and the symmetric point in the TLC distribution showed very good agreement. The data tracked very well over the entire Reynolds number range with a maximum difference of 6%.

Normally, the Nusselt number in a channel flow would be most appropriately normalized by the Dittus-Boelter equation [20]:

$$Nu_0 = 0.023\ Re^{4/5}\ Pr^{0.4} \tag{15}$$

However, as demonstrated in Fig. 8, this does not collapse the data. Instead, since the position of interest was on the tip wall, not on the channel wall, it experienced a flow condition much more like a jet stagnation point flow. Lee et al. [21] found that for high Reynolds numbers, the Nusselt number at the stagnation point of a jet varied according to $Nu \propto Re^m$, where the exponent was cited as $m=0.565$. In the current study, data were found to collapse using

$$Nu = 0.69\ Re^{0.565} \tag{16}$$

In this case, the Reynolds number was based on the channel hydraulic diameter. This normalization flattened out the results, thus demonstrating the applicability of this relation for the given flow conditions.

A comparison of measurements from the ALTP heat flux sensor and the symmetric point in the transient liquid-crystal distributions also showed good agreement for Site 2 on the outlet portion of the tip wall. Figure 9 shows the Nusselt number for both measurement techniques at both Sites 1 and 2 in a log-log scale. The difference in slopes for the two sites can be seen in this figure, and a least-squares fit resulted in an exponent of about $m=0.7$ for Site 2, closer to the value for turbulent channel or boundary layer flow compared with Site 1.

Time-Resolved Results and Spectra. Time-resolved results were analyzed from the ALTP heat flux sensor for both Sites 1 and 2 to obtain spectra of the turbulent heat flux and to obtain turbulent heat flux intensities and turbulence length scales. Heat flux results were corroborated by measurements of the velocity in identical experiments using a flush mounted hot-film probe at Site 1, with data taken for several Reynolds numbers.

A time trace of the heat flux and velocity is shown in Fig. 10, where high-frequency fluctuations and the influence of large-scale structures can be seen in both traces. Since the data were taken during separate experiments, no direct correspondence may be inferred from the time signals; however, the period of large-scale (low-frequency) fluctuations appears to be similar for the two traces.

Spectra for the hot-film probe are shown in Fig. 11 for channel Reynolds numbers of Re=50,000, 100,000, and 150,000 at Site 1. The increase in energy is evident with increasing Reynolds number, as is the extension of the inertial subrange to higher frequencies. With increasing Reynolds number, the slope of the power spectral density approached the universal $-5/3$ law expected for isotropic turbulence in the non-viscous inertial subrange. Steeper slopes in the spectral results for lower Reynolds numbers suggest larger degrees of anisotropy and viscous effects in the turbulence field at Site 1. In general, as the Reynolds number increases, the boundary layer becomes thinner, and viscous effects less influential. Therefore, damping of fluctuations near the wall becomes less significant at higher Reynolds numbers and the expected universal power law is approached [22].

Turbulence intensity of the velocity fluctuations was calculated at about Tu=20% for all Reynolds numbers. Autocorrelation of the time-resolved results provided integral time scales on the order of 1 ms using Eqs. (10) and (11). Since the flow at the measurement location was similar to a jet stagnation point flow, the bulk channel velocity was used to calculate an integral length scale based on a representative velocity (Eq. (12)). This resulted in an integral length scale of about $\Lambda_f=25$ mm$=0.60W$ at a channel Reynolds number of Re=100,000. This indicates that the energy containing eddies were of a size a little larger than half the width of the channel. An estimate of the frequency of the Kolmogorov scale was made using Eqs. (13) and (14), resulting in a frequency of about 3×10^4 Hz for a channel Reynolds number of Re=100,000. This frequency was just to the right of the range of frequencies shown in Fig. 11.

Frequency domain results for the heat flux showed similar trends. As seen in Fig. 12, the slope of the power spectral density also decreased with increasing Reynolds number, approaching a value of about $m=-2.4$ at a Reynolds number of Re=200,000. Nix and Diller [1] measured turbulence spectra using a heat flux

Downloaded 30 May 2010 to 128.113.26.88. Redistribution subject to ASME license or copyright; see http://www.asme.org/terms/Terms_Use.cfm

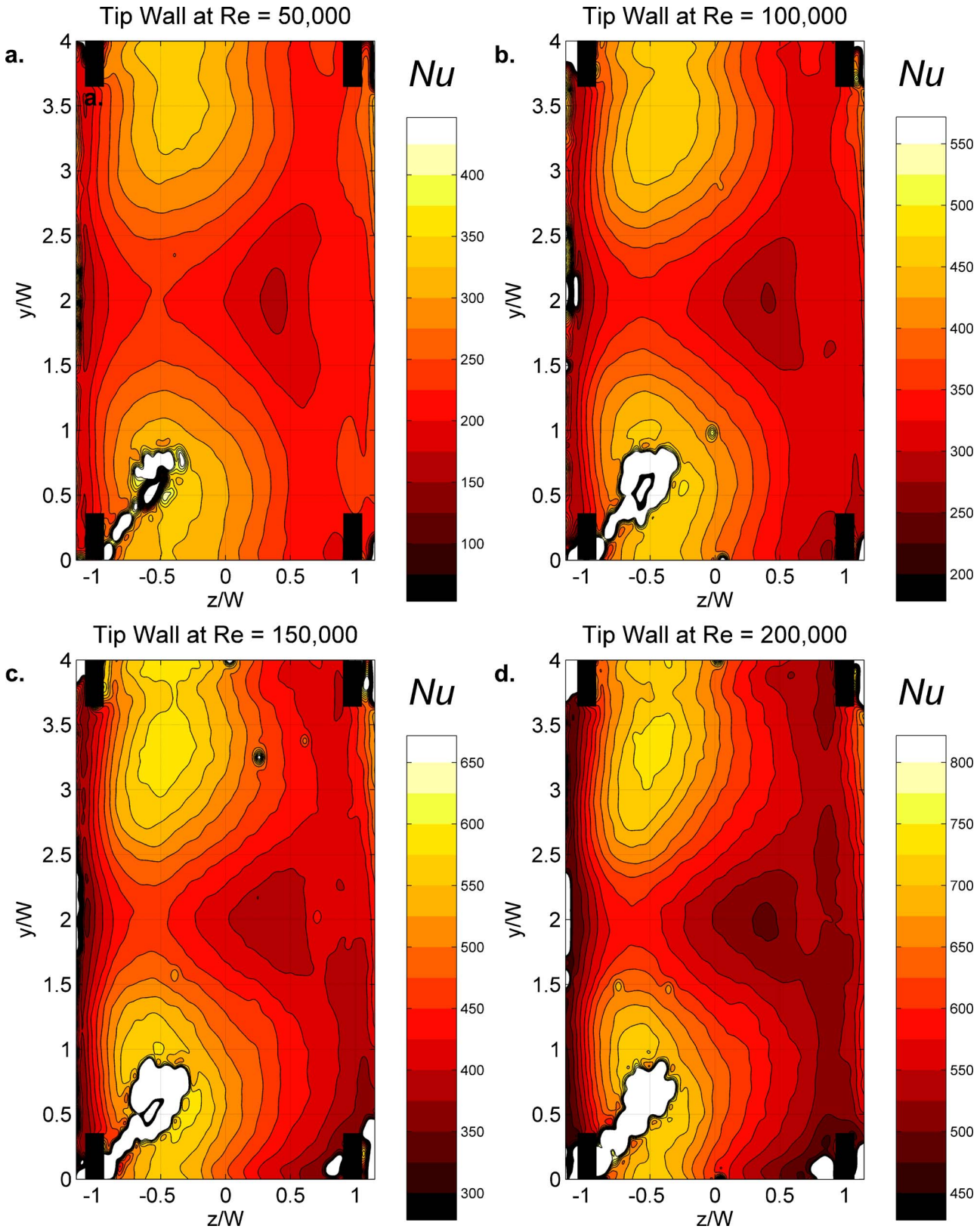

Fig. 6 Distribution of Nusselt number on the tip wall at Re=50,000 (*a*), 100,000, (*b*), 150,000 (*c*), and 200,000 (*d*)

gage positioned at the stagnation point on a cylinder and reported results in terms of the power spectral density of the heat flux. Examination of their results revealed a slope of the heat flux power spectral density of about $m=-2.3$, which compares well to the present work. Additionally, Lumley [23] suggested by dimensional analysis that the heat flux should follow a universal $-7/3$ law. The current results approach this suggested power law at the highest Reynolds numbers, thus reinforcing the evidence that a

Downloaded 30 May 2010 to 128.113.26.88. Redistribution subject to ASME license or copyright; see http://www.asme.org/terms/Terms_Use.cfm

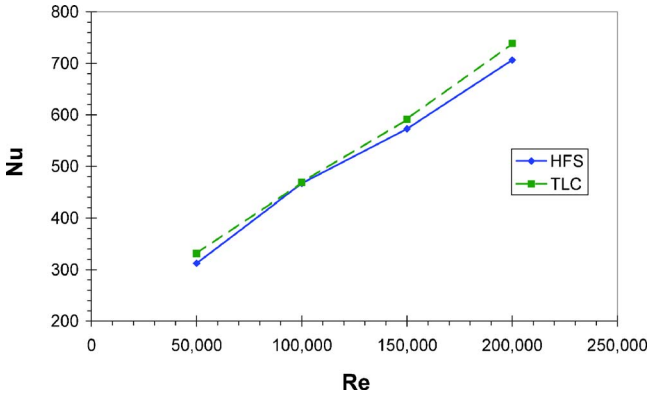

Fig. 7 Variation in the Nusselt number with Reynolds number for Site 1 of the heat flux sensor

power-law behavior is universal in the heat flux spectra as well. The heat flux spectra in the figure also show an increase in total energy in the flow with increasing Reynolds number and an increase in the extent of the inertial subrange.

The turbulent heat flux intensity Tu_q, which was found to be a little higher than $Tu_q=20\%$ for all Reynolds numbers. This relatively high value for the turbulent heat flux intensity indicates that turbulence played a large role in the augmentation on the mean heat flux at this location on the wall. Integral time scales on the order of 1 ms were calculated from the time signal, similar to the velocity signal. However, the integral length scale from the heat flux for a channel Reynolds number of Re=100,000 was calculated to be about $\Lambda_q=15$ mm, or 35% of the channel width. This

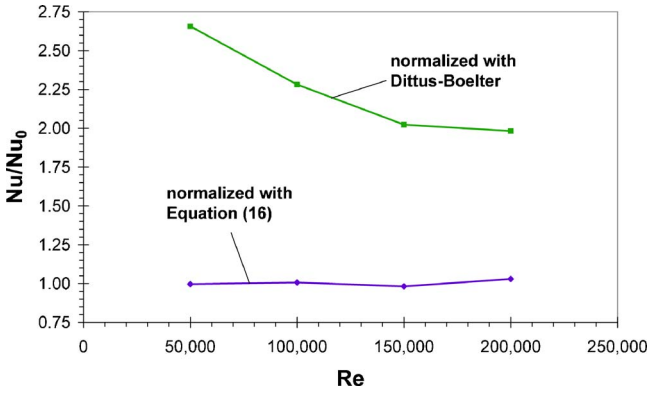

Fig. 8 Nusselt number for Site 1 normalized by the Dittus-Boelter equation and the relation given in Eq. (16)

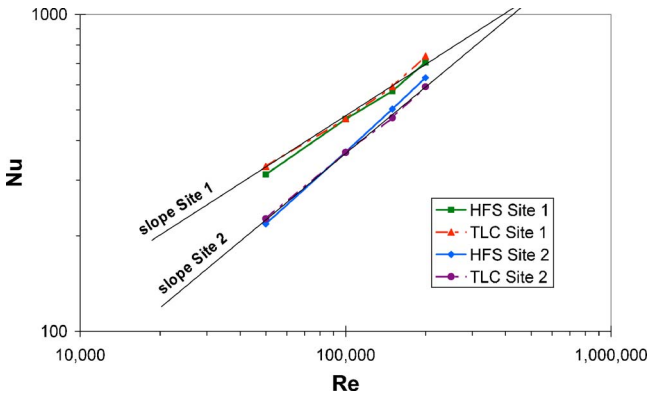

Fig. 9 Variation in the Nusselt number with Reynolds number for Sites 1 and 2 in log-log scale

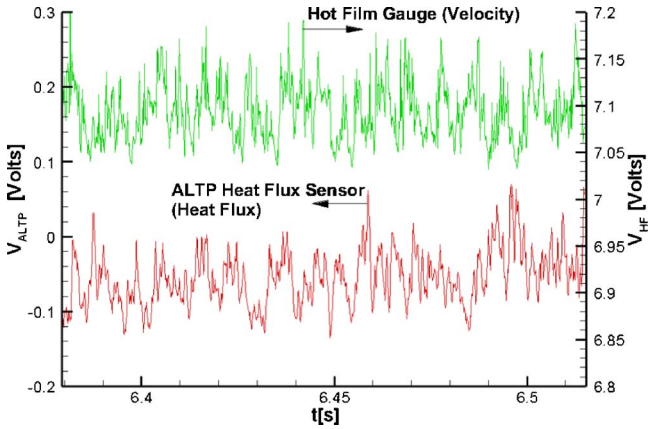

Fig. 10 Heat flux and velocity time signals at Site 1 for Re =100,000

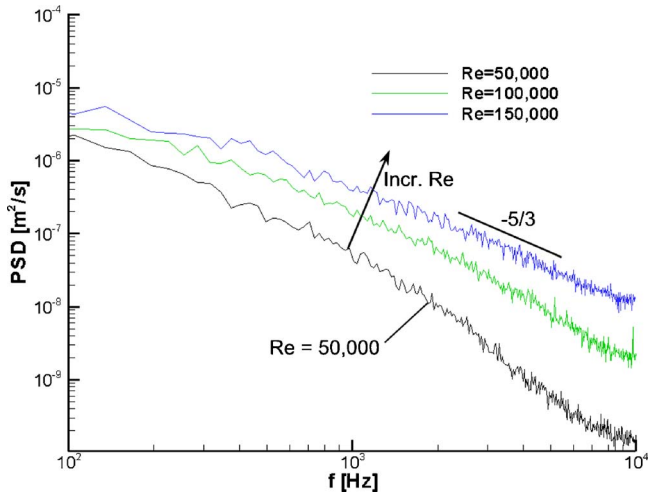

Fig. 11 Power spectral density of velocity versus frequency using a hot-film probe at Site 1

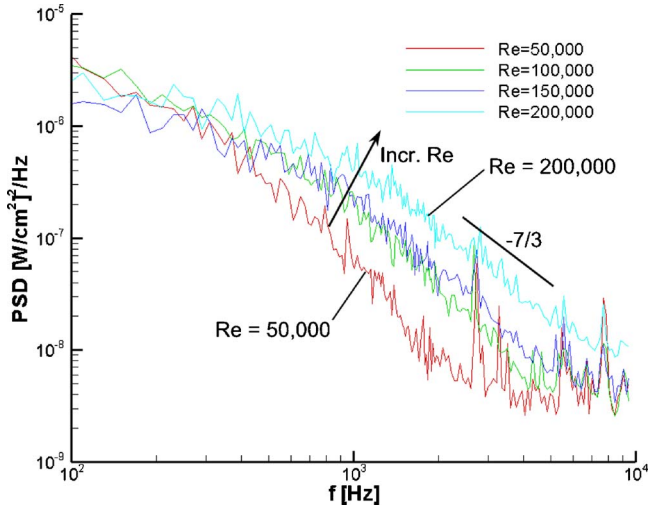

Fig. 12 Power spectral density of heat flux versus frequency using the ALTP heat flux sensor at Site 1

Downloaded 30 May 2010 to 128.113.26.88. Redistribution subject to ASME license or copyright; see http://www.asme.org/terms/Terms_Use.cfm

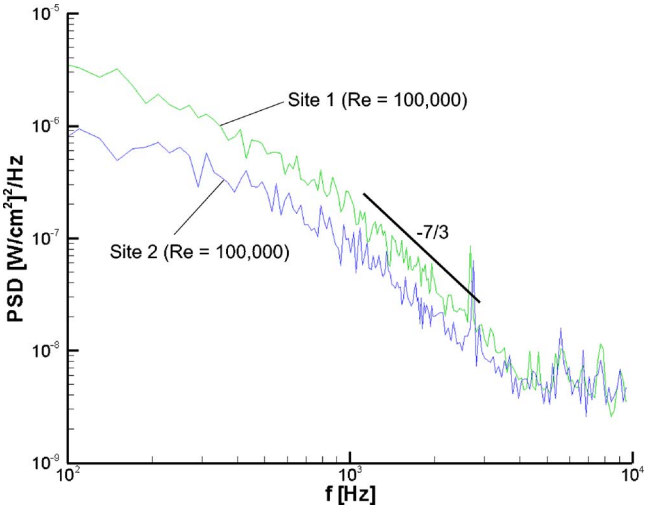

Fig. 13 Power spectral density of heat flux versus frequency using the ALTP heat flux sensor comparing Sites 1 and 2 at Re=100,000

indicates that the most energetic eddies related to the heat flux were somewhat smaller than those in the turbulent velocity field. Although the heat flux sensor was influenced most strongly by fluctuations in the channel axial direction, i.e., directed at the tip wall, it appeared that the large scale eddies affecting the heat flux were bound by the channel width and the region of circulation of the secondary flows. Examination of the results in Nix and Diller [1] and Nix et al. [2] also showed a trend of this type between velocity and heat flux.

The ratio of the velocity integral length scale to the heat flux integral length scale, which may be interpreted as the turbulent Prandtl number [24]

$$\mathrm{Pr}_t = \frac{\Lambda_f}{\Lambda_q} \tag{17}$$

had a value at the wall of 1.67 at Site 1 for a channel Reynolds number of Re=100,000, which is in the range of values measured close to the wall for boundary layers and obtained from simple models shown in [25].

Behavior of the spectra at Site 2 was similar to that at Site 1, but the spectra contained less energy at all Reynolds numbers. A comparison between spectra measured at Sites 1 and 2 for a Reynolds number of Re=100,000 is shown in Fig. 13. The difference in energy at lower frequencies can be clearly seen, while the spectra both trail off at the same higher frequency. The data also show that, even at this lower Reynolds number, the spectra approached the $-7/3$ law.

The spectra followed the same trends with Reynolds number for Site 2 as those shown in Fig. 12 for Site 1, but with lower energy at each Reynolds number. As for Site 1, the integral length scale was relatively large with a value of about $\Lambda_q = 15$ mm$=0.35W$ at a channel Reynolds number of Re=100,000. This would be expected since the flow was constrained in the same fashion approaching both positions. At Site 2, the turbulent heat flux intensity was found to be a little higher than $\mathrm{Tu}_q = 20\%$ for all Reynolds numbers.

Conclusions

Measurements of the mean heat flux on the tip wall of a two pass high aspect ratio (4:1) channel with angled ribs were made using a transient liquid-crystal technique. Concurrent measurements of both the mean and time-resolved heat flux were made with a novel heat flux sensor at two key locations on the tip wall to provide validation of both measurement methods and to provide additional information about the turbulence characteristics of the heat flux at these locations. Turbulence spectra for the velocity and heat flux at the wall were compared for a range of Reynolds numbers representative of heavy duty turbines.

Measurements of the mean Nusselt number on the tip wall demonstrated that the distribution of the mean heat transfer due to secondary flows was consistent over a range of Reynolds numbers. Comparisons between results from a transient liquid-crystal technique and a novel heat flux sensor showed very good agreement for two positions on the tip wall. Analysis of the variation in heat transfer with the Reynolds number demonstrated differences in the behavior of the flow field responsible for the heat flux at these locations. At the position of peak heat transfer on the inflow side of the tip wall (Site 1), the variation in Nusselt number with Reynolds number followed a trend more like that for jet stagnation point flow. At Site 2 on the outflow side of the tip wall, the trend was more similar to that found in turbulent channel or boundary layer flow.

Analysis of the time signal from a flush mounted hot film probe at Site 1 on the tip wall showed that the velocity spectrum approached the universal $-5/3$ power-law behavior for higher Reynolds numbers. Similar results for the same position for the heat flux showed that the spectra had a $-7/3$ slope in the nonviscous inertial subrange, consistent with dimensional analysis. Turbulence intensities of the velocity and heat flux were both $\sim 20\%$. Length scales were determined using the time signals and results showed the velocity integral length scale was $\sim 60\%$ of the channel width, while the heat flux integral length scale was $\sim 35\%$ of the channel width, resulting in a ratio of integral length scales (turbulent Prandtl number) at the wall of $\Lambda_f/\Lambda_q = 1.67$. These results show the importance of turbulence on the tip wall heat transfer in internal ribbed channels.

Acknowledgment

The authors gratefully acknowledge the financial support provided with the research and innovation initiative KW21 by the Ministry of Baden-Württemberg, Germany and ALSTOM Power. Additionally, the permission to publish this paper by ALSTOM Power is appreciated.

Nomenclature

c_p = specific heat (J/kg K)
D_h = hydraulic diameter, 67.2×10^{-3} m
e = rib height (m)
H = channel height, 0.168 m
h = heat transfer coefficient ($\mathrm{W/m^2\,K}$)
$\bar{h}$ = upstream averaged heat transfer parameter, ($\mathrm{W/m^2\,K}$)
k_w = thermal conductivity of the wall, (W/m K)
L_e = entrance length for the channel inlet, 1.524 m
L_m = measurement region in channel, 0.840 m
M = slope of power spectrum
$\dot{m}$ = mass flow rate (kg/s)
Nu = Nusselt number, (hD_h/k)
Nu_0 = Nusselt number from the Dittus-Boelter equation
P = pitch between ribs
$\mathcal{P}$ = channel perimeter, 0.420 m
Pr_t = turbulent Prandtl number
R_{xx} = autocorrelation function
Re = Reynolds number, ($U_{\mathrm{bulk}}D_h/\nu$)
T_0 = initial temperature (K)
T_B = bulk temperature (K)
T_{CL} = centerline temperature (K)
T_E = inlet temperature (K)
T_W = wall temperature (K)
t = time (s)

Downloaded 30 May 2010 to 128.113.26.88. Redistribution subject to ASME license or copyright; see http://www.asme.org/terms/Terms_Use.cfm

Tu = turbulence intensity, (u'/u_{mean})
Tu_q = turbulent heat flux intensity, (q'/q_{mean})
U_{bulk} = bulk channel velocity (m/s)
W = channel width, 0.042 m
x = axial channel coordinate
y = coordinate across channel width
z = coordinate across channel height
α_w = thermal diffusivity of the wall (m^2/s)
ε = dissipation (m^2/s^3)
Λ_f = turbulence integral length scale (m)
Λ_q = turbulence integral heat flux length scale (m)
ν = kinematic viscosity (m^2/s)
τ = measurement interval (s)
T_f = turbulence integral time scale (s)
T_q = turbulence integral time scale from heat flux (s)
ρ = density (kg/m^3)

References

[1] Nix, A. C., and Diller, T. E., 2005, "Experiments on the Physical Mechanism of Heat Transfer Augmentation by Freestream Turbulence at a Cylinder Stagnation Point," International Gas Turbine and Aeroengine Congress and Exposition, Reno-Tahoe, ASME Paper No. GT2005–68616.

[2] Nix, A. C., Diller, T. E., and Ng, W. F., 2004, "Experimental Measurements and Modeling of the Effects of Large-Scale Freestream Turbulence on Heat Transfer," International Gas Turbine and Aeroengine Congress and Exposition, Vienna, ASME Paper No. GT2004–53260.

[3] Holmberg, D. G., and Diller, T. E., 2005, "Simultaneous Heat Flux and Velocity Measurements in Transonic Turbine Cascade," ASME J. Turbomach., **127**, pp. 502–506.

[4] Moss, R. W., and Oldfield, M. L. G., 1996, "Effect of Free-Stream Turbulence on Flat-Plate Heat Flux Signals: Spectra and Eddy Transport Velocities," ASME J. Turbomach., **118**, pp. 461–467.

[5] Pape, D., Jenkins, S., von Wolfersdorf, J., Weigand, B., and Schnieder, M., 2006, "The Influence of Including a Partially Smooth Section in the 2nd Leg of an Internally Ribbed Two Pass Cooling Channel," International Gas Turbine and Aeroengine Congress and Exposition, Barcelona, ASME Paper No. GT2006–90802.

[6] Hirota, M., Fujita, H., Syuhada, A., Araki, S., Yoshida, T., and Tanaka, T., 1999, "Heat/Mass Transfer Characteristics in Two-Pass Smooth Channels With a Sharp 180-Deg Turn," Int. J. Heat Mass Transfer, **42**, pp. 3757–3770.

[7] Schnieder, M., Höcker, R., and von Wolfersdorf, J., 2001, "Heat Transfer and Pressure Loss in a 180 deg turn of a Rectangular, Rib-Roughened two Passage Channel," 5th World Conference on Experimental Heat Transfer, Fluid Mechanics and Thermodynamics, ExHFT5, Thessaloniki, Sep.

[8] Su, G., Chen, H. C., Han, J. C., and Heidmann, J. D., 2004, "Computation of Flow and Heat Transfer in Two-Pass Rotating Rectangular Channels (AR =1:1, AR=1:2, AR=1:4) with 45-Deg Angled Ribs by a Reynolds Stress Turbulence Model," International Gas Turbine and Aeroengine Congress and Exposition, Vienna, ASME Paper No. GT2004–53662.

[9] Abdel-Wahab, S., and Tafti, D. K., 2004, "Large Eddy Simulation of Flow and Heat Transfer in a Staggered 45° Ribbed Duct," International Gas Turbine and Aeroengine Congress and Exposition, Vienna, ASME Paper No. GT2004–53800.

[10] Viswanathan, A. K., and Tafti, D. K., 2005, "Detached Eddy Simulation of Flow and Heat Transfer in a Stationary Internal Cooling Duct With Skewed Ribs," International Gas Turbine and Aeroengine Congress and Exposition, Reno-Tahoe, ASME Paper No. GT2005–68118.

[11] Graham, A., Sewall, E., and Thole, K. A., 2004, "Flowfield Measurements in a Ribbed Channel Relevant to Internal Turbine Blade Cooling," International Gas Turbine and Aeroengine Congress and Exposition, Vienna, ASME Paper No. GT2004–53361.

[12] Han, J. C., and Park, J. S., 1988, "Developing Heat Transfer in Rectangular Channels With Rib Turbulators," Int. J. Heat Mass Transfer, **31**, pp. 183–195.

[13] Han, J. C., 1984, "Heat Transfer and Friction in Channels with Two Opposite Rib-Roughened Walls," ASME J. Heat Transfer, **106**, pp. 851–861.

[14] Wang, Z., Gillespie, D., and Ireland, P., 1996, "Advances in Heat Transfer Measurements Using Liquid Crystals," *Turbulent Heat Transfer (Engineering Foundation)*, San Diego, CA, pp. 1–25.

[15] Ireland, P., Neely, A., Gillespie, D., and Robertson, A., 1999, "Turbulent Heat Transfer Measurements Using Liquid Crystals," Int. J. Heat Fluid Flow **20**, pp. 355–367.

[16] Metzger, D. E., and Larson, D. E., 1986, "Use of Melting Point Surface Coatings for Local Convection Heat Transfer Measurements in Rectangular Channel Flows with 90-Deg Turns," ASME J. Heat Transfer, **108**, pp. 48–54.

[17] von Wolfersdorf, J., Hoecker, R., and Hirsch, C., 1998, "A Data Reduction Procedure for Transient Heat Transfer Measurements in Long Internal Cooling Channels," ASME J. Heat Transfer, **120**, pp. 314–321.

[18] Roediger, T., Knauss, H., Gaisbauer, U., Kraemer, E., Jenkins, S., and von Woldersdorf, J., 2008, "Time-Resolved Heat Transfer Measurements on the Tip Wall of a Ribbed Channel Using a Novel Heat Flux Sensor—Part I: Sensor and Benchmarks," ASME J. Turbomach., **130**, p. 011018.

[19] Pope, S. B., 2000, *Turbulent Flows*, Cambridge University Press, Cambridge, England.

[20] Incropera, F. P., and DeWitt, D. P., 1996, *Fundamentals of Heat and Mass Transfer*, 4th Ed., Wiley, New York.

[21] Lee, D., Greif, R., Lee, S. J., and Lee, J. H., 1995, "Heat Transfer From a Flat Plate to a Fully Developed Axisymmetric Impinging Jet," ASME J. Heat Transfer **117**, pp. 772–775.

[22] Bogard, D. G., and Thole, K. A., 1998, "Wall Bounded Turbulent Flows," *The Handbook of Fluid Dynamics*, CRC Press, Boca Raton, Sec. 13.5, pp. 13.50–13.63.

[23] Lumley, J. L., 1967, "Similarity and the Turbulent Energy Spectrum," Phys. Fluids, **10**(4), pp. 855–858.

[24] Schlichting, H., 1982, *Grenzschicht-Theorie*, Verlag G. Braun, Karlsruhe.

[25] Kays, W. M., Crawford, M. E., and Weigand, B., 2005, *Convective Heat and Mass Transfer*, 4th ed., McGraw-Hill, New York.

Downloaded 30 May 2010 to 128.113.26.88. Redistribution subject to ASME license or copyright; see http://www.asme.org/terms/Terms_Use.cfm

Vaneless Diffuser Advanced Model

Oleg Dubitsky

David Japikse

Concepts NREC,
217 Billings Farm Road,
White River Jct., VT 05001

A new vaneless diffuser model is presented. Upon thorough examination of the change in average total pressure, the average static pressure and the average flow angle through a vaneless diffuser, it was discovered that existing models fail to provide useful integrity. Consequently, a new model was built. It was learned that it was necessary to use a two-zone model of the flow entering the vaneless diffuser and to carefully model the two-zone degradation as the flow passes through the vaneless diffuser. The new model is presented with detailed testing. The impact upon future design is outlined, and the expectation is established that various future designs will require the integrity of the new model; old models can be used in limited cases with care. [DOI: 10.1115/1.2372781]

Introduction

This work is part of a four paper series. In the first part [1], we carefully reviewed how data matching could be scientifically conducted while utilizing both explicit and implicit knowledge. A large database of dependent modeling parameters and diverse potentially important independent controlling variables leads to modeling with minimal possible error. In the second paper [2], relationships between the dependent and independent variables were established in correlations and neural networks. The third paper [3] set out guiding principles, which govern work of this type, and in this fourth paper we present a new vaneless diffuser periodic performance model as used in the related studies.

History of Vaneless Diffuser Modeling

An understanding of the vaneless diffuser can be achieved if the conservation equations are solved by integrating through the vaneless diffuser. In a one-dimensional compressible flow analysis this is done as a succession of states through the vaneless diffuser. The full set of equations account for wall friction effects in both the meridional and angular momentum equations (adapted from Stanitz, 1952) [4]:

$$C_m \frac{dC_m}{dr} - \frac{C_\theta^2}{r} + C_f \frac{C^2 \cos\alpha}{b \sin\phi} + \frac{1}{\rho}\frac{dp}{dr} = 0 \tag{1}$$

$$C_m \frac{dC_\theta}{dr} + \frac{C_m C_\theta}{r} + C_f \frac{C^2 \sin\alpha}{b \sin\phi} = 0 \tag{2}$$

$$\frac{1}{\rho}\frac{d\rho}{dr} + \frac{1}{C_m}\frac{dC_m}{dr} + \frac{1}{b}\frac{db}{dr} + \frac{1}{r} = 0 \tag{3}$$

$$\frac{dh}{dr} + C_m \frac{dC_m}{dr} + C_\theta \frac{dC_\theta}{dr} = 0 \tag{4}$$

$$\rho = p/RT; \text{ or } \rho = f(p,T) \text{ for a real gas} \tag{5}$$

where ϕ is the diffuser inclination, such that $\phi = 90°$ is radial.

This set of equations can be solved directly by Runge-Kutta integration. However, it is important to specify an appropriate friction coefficient in order to get reasonable predictions. Since the flow in the vaneless diffuser is neither fully developed nor simply an inlet flow, the values of skin friction coefficient must be adjusted to obtain reasonable levels for the specific industrial application. Values of C_f can be used either as an average for the entire diffuser or as a function of local geometry and flow condition. The equation:

$$C_f = k\left(\frac{1.8 \times 10^5}{\mathrm{Re}}\right)^{0.2} \tag{6}$$

where k is a constant has been used [5]. A value of $k = 0.010$ is frequently used based on a review of different vaneless diffusers in industrial machines; however, applications exist where a value one-half this level or nearly twice this level has been necessary. An alternative approach to the average C_f is to use a skin friction coefficient as a function of Reynolds number based on the length from the inlet of the diffuser to the computational station. An example has been presented by Brown and Bradshaw [6] and is occasionally employed with the above set of equations. Such approaches have been discussed by individual designers, but have not been reported widely in the open literature. A further alternative based on the work of Traupel [7] is to add a dissipation coefficient. In Traupel's approach, this additional dissipation coefficient is added to Eq. (2).

The broad implications of the basic differential equations have been summarized in a study by Johnston and Dean [8]. Johnston and Dean parametrized equations similar to the preceding equations and deduced some of the basic fundamental trends for vaneless diffuser performance and presented them in summary graphs. They are of considerable value for education.

A significant contribution was made by Dean and Senoo [9] with an emphasis on the rotating wake behavior in the vaneless diffuser. Their theory predicted a significant, reversible work transfer between the primary (jet) and the secondary (wake) flows, leaving the impeller and entering the vaneless diffuser. They carefully explained the difference between diffusers with stationary inlet distortion patterns (no reversible work transfer) and the special case of the rotating distortion patterns. For their analysis, they assumed the flow to be incompressible, steady, and issuing from an impeller so that no circumferential variations in flow angle for either the primary or the secondary zone existed, although the flow angles were different for each. As the two zones enter the vaneless diffuser, they are not parallel to each other. However, they must have a common border in the relative coordinate system and, hence, there must be a force acting between the two zones to induce the velocity vectors to become parallel. This force causes changes in angular momentum and results in a pressure force between the primary and secondary zones. This force rotates at impeller speed in absolute space and leads to a fluctuating pressure at each point in the diffuser and consequently a reversible work transfer between the two zones. This force causes the rapid disappearance of secondary flows or wakes as the flow enters the

Contributed by the International Gas Turbine Institute (IGTI) of ASME for publication in the JOURNAL OF TURBOMACHINERY. Manuscript received October 1, 2004; final manuscript received February 1, 2005; published online January 28, 2008. IGTI Review chair: K. C. Hall. Paper presented at the ASME Turbo Expo 2005: Land, Sea and Air, Reno, NV, June 6–9, 2005, Paper No. GT2005-68130.

 Copyright © 2008 by Concepts ETI, Inc.

Downloaded 30 May 2010 to 128.113.26.88. Redistribution subject to ASME license or copyright; see http://www.asme.org/terms/Terms_Use.cfm

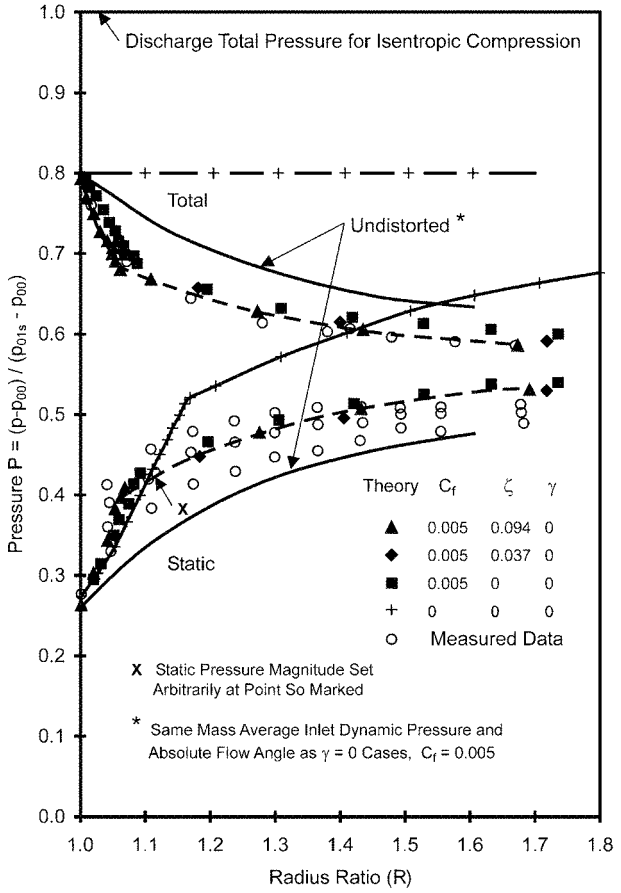

Fig. 1 The Dean and Senoo [9] comparison between theory and their pressure rise dataset for one operating point (replotted from the original)

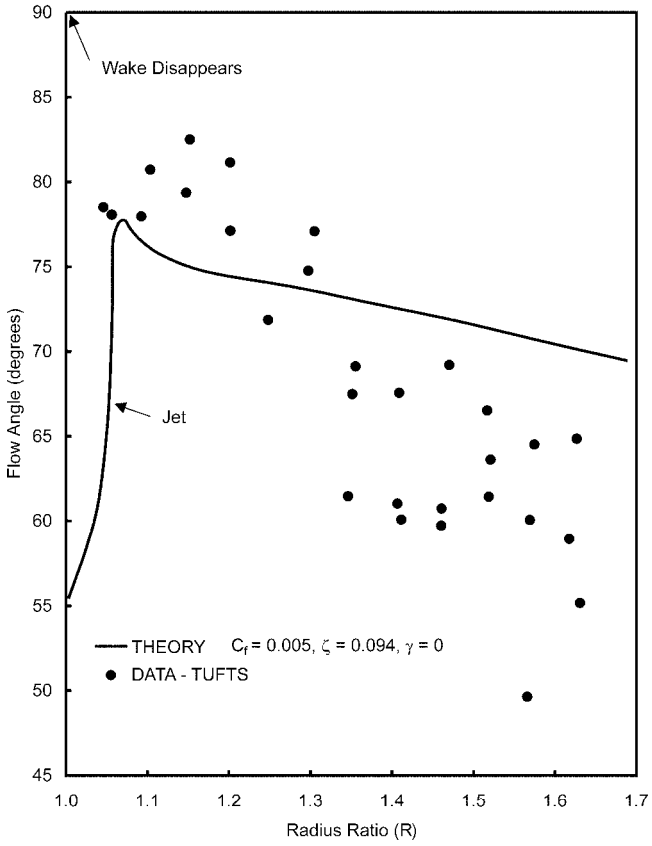

Fig. 2 The Dean and Senoo [9] comparison between theory and their estimated flow angle dataset for one operating point (replotted from the original)

diffuser from a rotating impeller. Consequently, the flow is unsteady with respect to the stationary system (or more accurately, it is periodic), but it is steady with respect to the rotating system.

Dean and Senoo recognized that the boundary between the primary and secondary zones is ill defined because of turbulent mixing; however, for their analysis they assumed that the velocity and direction of flow at a given radius are invariant across the primary (jet) region. The same was also assumed for the secondary (wake) region, but at different values from those for the primary zone. The ratio of secondary zone width to primary zone width varies with radius. As a consequence, the shape of the leading edge border of the primary zone cannot be identical to the shape of the trailing edge border, which implies that the direction of the primary zone should vary from the leading to trailing edge. The same is true for the secondary zone as well. The authors simplified their analysis by using the average direction for each flow and ignored the variations in angle across the zone. Additionally, the authors included the wall shear stress and recognized it should be different for both the primary and secondary zone; however, conventional flat plate shear stress correlations were employed.

In developing their analytical models, the authors further assumed that the primary zone does not mix with the secondary zone (no mass transfer). With the above assumptions, a set of conservation equations were written to describe the entire flow field and model the change in pressure through the diffuser. They did not compute an absolute or starting value (see Fig. 1 (x point)).

The authors were guided by one set of data using diverse types of instrumentation. Static pressure and total pressure were measured along the diffuser, but no mention was made of traversing across the flow field. It appears that these may be single point measurements, but this cannot be concluded rigorously from the information in the paper. Flow angles were obtained by observing tufts of wool on the sidewalls, which gave a rough indication, but the fluctuation of the tufts led to a wide range of possible observed angles. Additionally, hot-wire traces gave the investigators a fairly clear understanding of the comparative magnitudes of primary and secondary zone, as well as boundary regions between the two.

Figure 1 shows the change in total and static pressure measured for the Dean and Senoo blower application and the computed model. The solid curved lines show the model extreme for undistorted, or ideal, flow. Using a parametric study of skin friction and wake mixing coefficients, an array of computed values was achieved. Compared to the data shown as the open circles, good agreement was obtained on both the total pressure degradation and the static pressure rise for a skin friction coefficient of 0.005 and a wake mixing fraction of approximately 0.09. The authors felt that their theory was well established with this comparison to the set of data. Figure 2 shows the angle measurements for the same data and the computed result. This comparison is far less convincing.

The conclusions reached by the authors were indeed profound and are important even to this day. They noted the following:

1. Inlet distortions can have significant influences on vaneless diffuser flow behavior.
2. It is impossible to predict the behavior of a diffuser receiving distorted inlet flow from information on axisymmetric flow.
3. A rotating distorted flow in a vaneless diffuser leads to a significant pressure work transfer between high and low velocity regions.
4. The mixing shear stresses between jet and wake (primary

Downloaded 30 May 2010 to 128.113.26.88. Redistribution subject to ASME license or copyright; see http://www.asme.org/terms/Terms_Use.cfm

Table 1 Summary of available traverse datasets for pumps and compressors

Case	Description	# of radial traverse locations	β_{2b}	Speed lines
CCN5	Eckardt O	4	0	5
CCN6	Eckardt A	4	−30	4
CCN7	Eckardt B	4	−40	4
CCN103	Consortium	2	−25	3
CCN105	Consortium	2	0	3
CCN119	Consortium	2	−50	3
CCN120	Consortium	2	−50	3
CCN121	Consortium	2	−50	3
CCN122	Consortium	2	0	3
CCN123	Consortium	2	0	3
CCN124	Consortium	2	0	3
CCN30	pr=3.5 Consortium	1	−30	2
CCN31	pr=4	1	−45	2
CCN32	pr=2.8	1	−30	2
CCN33	pr=4.5	1	−40	2
CCN40	pr=3.5	1	−30	2
CCN42	pr=4	1	−42	2
CCN48	pr=5	1	−37.5	3
CCN57	pr=3.5	1	−30	3
CCN64	pr=4.5 Consortium	1	−42.5	1
CCN66	pr=3	1	−55	3
CCN6	Consortium pump	1	−75	1
CCN28	Consortium pump	1	−71	1
CCN54	Inducer pump	1	−60	2

and secondary) regions are less important than wall shear stresses in governing flow behavior.

Further conclusions were reached, but the above are the most important. Even though these ideas have been known for 45 years, the theory was rarely, if ever, put to practical application for industrial design and development. Indeed, the authors of this paper know of no case in which practical use was ever made of the Dean and Senoo theory. Eckardt in 1977 extended the Dean and Senoo work to compressible gas flow, improved on some of the limiting assumptions, and achieved better agreement to data. However, restrictive modeling assumptions still remained and a broad evaluation against data was still needed [10].

When attempting to use the theory directly for the present investigations, one reason for the lack of prior application became evident: the system of equations generally could not be solved. It is felt that this is due, in part, to the fact that the early work required great simplification in order to render practical computations of any type. The reader must recall that this work would have been done in the late 1950s, when computational power was exceedingly limited. Consequently, investigators at that time frequently made simplifications, which limited the results to very special cases for purposes of general investigation only. This appears to be the case for the Dean and Senoo investigation. In addition to the restrictions indicated above, which are drawn directly from comments in the paper, a careful analysis indicated that the fraction of secondary zone mass flow appears to be constant throughout the calculation, a fact that will not hold up well in a detailed analysis.

The prior technical literature for vaneless diffuser development has been based on limited data at best. Most of the vaneless diffuser investigations were based on static pressure data along the diffuser (alone). In a few cases, a total pressure traverse across the flow field was available. Rarely, however, have detailed traverses been made at various radial locations from which a careful examination of the change in total pressure and flow angle, with radius, can be deduced. All known available data have been collected and organized in Table 1. It will be observed that 37 speed line sets of multiple location traverse data have been identified, 26 speed line sets of single location traverse data have been collected and these comprise 24 different stages with in excess of 150 individual traverses. It is the multiple location data that are of the utmost importance for this investigation. Recognizing the importance of data of this type, a number of stages have been selected for further detailed laboratory traverse investigations, and these are underway at the present time. Reports on this information will be presented in the future.

Examples of the Stanitz method with a fully mixed impeller exit state to model the vaneless diffuser are shown in [1] and later. These examples illustrate the basic problem: there is no skin friction coefficient that can be used to model this flow field, using a steady flow assumption. Likewise, single zone models fail to correctly predict the difference between total and static parameters. This is tragic, because this is the system of modeling used by the turbomachinery industry for the past 50 years. Fortunately, there is one saving grace: for diffusers of sufficient length (arguably about 1.5 in radius ratio or greater) the end results turned out to be approximately correct when the simple skin friction coefficient is employed. It is the *distribution* of change of total pressure, static pressure, and flow angle in the inlet regions that fails. Thus, whenever careful consideration of the flow near the inlet of a vaneless diffuser is required, then the historical equations (1)–(4) should not be employed.

A new model has been developed that is inspired, in part, by the historical Dean and Senoo work, with the intent of remaining close to the modeling shown in the first set of equations (1)–(4). The objective is to extend the two-zone modeling approach used very successfully for the impeller well out into the vaneless diffuser. To do this, it is important to remove critical limitations from the Dean and Senoo model. Specifically, compressible flow using real gas or real liquid modeling with the full complement of continuity, momentum, and energy equations for each zone must be prepared. The built-in inconsistency of the Dean and Senoo model that froze the fraction of secondary zone mass flow must be removed. Consequently, several extra terms in the differential equations were lost in the original Dean and Senoo model and are given in the work later. Additionally, mass-averaged postprocessing for the flow results is necessary in order to compare with the data. Finally, it is important to take this model for the vaneless diffuser and connect it directly to the two-zone model for the impeller (a modeling system that is used by hundreds of companies and universities and available to all) so that one can now compute absolute levels of total and static pressures, as well as flow angles resulting directly from the impeller exit conditions through the vaneless diffuser. These impeller exit conditions (pressures, temperatures, and velocities) become the inlet conditions for the primary and secondary zones entering the diffuser.

Through the present work, the true wake from the blade surface (the base pressure problem) is treated as a sudden area change, with the thickness disappearing in the first spatial step of the flow integration (Borda-Carnot process). It is felt, based on the studies now conducted, that this should be removed in a further investigation by developing a three-zone model. Due to turbulent mixing at the primary/secondary zone interface, there is an interchange of mass, momentum, and energy. It is important to treat the primary and secondary zone separately with respect to wall shear and, as in the original Dean and Senoo work, the vaneless diffuser is considered to have stationary walls.

Model Description and Assumptions

The equations developed below are nearly identical to Eqs. (1)–(4) above. Their derivations are exactly like the original Stanitz [4] work, except applied to each zone separately and with boundary mixing terms added. The reader should find it easy to derive these equations guided by Appendix B and Fig. 6 of Stanitz. We will concentrate on the new terms.

Although Dean and Senoo found that wake-jet mixing was not a strong factor in comparison with wall friction, mass and energy

Downloaded 30 May 2010 to 128.113.26.88. Redistribution subject to ASME license or copyright; see http://www.asme.org/terms/Terms_Use.cfm

exchange effects are of significance in order to predict correctly the thermal state of the two zones (even after the alignment of the velocity fields is achieved).

Assuming the primary, secondary, and trailing edge blade-wake areas are preserved as the flow enters the vaneless diffuser:

Area fraction of primary zone wake

$$\varepsilon' = (1 - e) \tag{7}$$

Area fraction of secondary zone wake

$$\varepsilon'' = e \tag{8}$$

At the inlet station to the vaneless diffuser,

the flow area is assumed to be

$$A = 2\pi r b(1 - \Delta_{te}) \tag{9}$$

It is further assumed that the influence of trailing edge blade blockage disappears rapidly and, hence, provides a minor correction to the flow area and the geometrical derivative calculations during the first integration step only. No mass flow is assumed at the trailing edge blade wake zone, thus it does not carry mass, but provides flow blockage at the initial integration step and none at the next step.

General Models for Secondary and Primary Zone Mixing

The force per unit area due to mixing at the interface boundary is directed along the interface boundary (average relative flow angle between secondary and primary zones):

$$\tau_{\text{mix}} = \frac{\xi\bar{\rho}(\bar{W} - W)|\bar{W} - W|}{2} \tag{10}$$

where

$\bar{W} \sim 0.5(W' + W'')$—estimated velocity at secondary to primary interface boundary

$\bar{\rho} \sim 0.5(\rho' + \rho'')$—estimated density at secondary to primary interface boundary

Z—number of secondary-primary structures in vaneless diffuser space (number of passages/blades at impeller exit). Since the primary-secondary flow mixing is primarily due to turbulence, there is mass exchange between these entities, which can be deduced from turbulent flow theory (see the Appendix):

$$\gamma_{m,\text{mix}} \sim -\sqrt{\frac{\xi}{22}}\bar{\rho}(\bar{W} - W) \tag{11}$$

—the energy exchange due to mixing:

$$\gamma_{h,\text{mix}} = \gamma_{m,\text{mix}}(\bar{h}_{0,\text{rel}} - h_{0,\text{rel}}) \tag{12}$$

where

$$\bar{h}_{0,\text{rel}} = \begin{cases} h_0'' & \gamma'_{m,\text{mix}} > 0 \\ h_0' & \gamma'_{m,\text{mix}} < 0 \end{cases}$$

—average total relative enthalpy at the primary-secondary zone interface boundary. When W' or W'' is substituted for W in Eqs. (10)–(12), one obtains τ'_{mix}, $\gamma'_{m,\text{mix}}$, $\gamma'_{h,\text{mix}}$ or, respectively, τ''_{mix}, $\gamma''_{m,\text{mix}}$, $\gamma''_{h,\text{mix}}$.

Momentum Equations: Meridional,

$$C'_m\frac{dC'_m}{dr} - \frac{C'^2_\theta}{r} + C_f\frac{(C')^2\cos\alpha}{b\sin\phi} + \frac{1}{\rho'}\frac{dp}{dr} = \frac{\tau'_{\text{mix}}\cdot\cos\beta\cdot Z}{\pi r\varepsilon'\rho'\sin\phi} \tag{13}$$

$$C''_m\frac{dC''_m}{dr} - \frac{C''^2_\theta}{r} + C_f\frac{(C'')^2\cos\alpha}{b\sin\phi} + \frac{1}{\rho''}\frac{dp}{dr} = \frac{\tau''_{\text{mix}}\cdot\cos\beta\cdot Z}{\pi r\varepsilon''\rho''\sin\phi} \tag{14}$$

Tangential,

$$C'_m\frac{dC'_\theta}{dr} + \frac{C'_mC'_\theta}{r} + C_f\frac{(C')^2\sin\alpha}{b\sin\phi} = \frac{\tau'_{\text{mix}}\cdot\sin\beta\cdot Z}{\pi r\varepsilon'\rho'\sin\phi} \tag{15}$$

$$C''_m\frac{dC''_\theta}{dr} + \frac{C''_mC''_\theta}{r} + C_f\frac{(C'')^2\sin\alpha}{b\sin\phi} = \frac{\tau''_{\text{mix}}\cdot\sin\beta\cdot Z}{\pi r\varepsilon''\rho''\sin\phi} \tag{16}$$

Continuity Equations:

$$\frac{1}{\rho'}\left[\left(\frac{\partial\rho}{\partial p}\right)_h\frac{dp}{dr} + \left(\frac{\partial\rho}{\partial h}\right)_p\frac{dh'}{dr}\right] + \frac{1}{C'_m}\frac{dC'_m}{dr} + \frac{1}{b}\frac{db}{dr} + \frac{1}{r} + \frac{1}{\varepsilon'}\frac{d\varepsilon'}{dr} = \frac{\gamma'_{m,\text{mix}}Z}{\pi r\varepsilon'\rho'C'_m\sin\phi} \tag{17}$$

$$\frac{1}{\rho''}\left[\left(\frac{\partial\rho}{\partial p}\right)_h\frac{dp}{dr} + \left(\frac{\partial\rho}{\partial h}\right)_p\frac{dh''}{dr}\right] + \frac{1}{C''_m}\frac{dC''_m}{dr} + \frac{1}{b}\frac{db}{dr} + \frac{1}{r} + \frac{1}{\varepsilon''}\frac{d\varepsilon''}{dr} = \frac{\gamma''_{m,\text{mix}}Z}{\pi r\varepsilon''\rho''C''_m\sin\phi} \tag{18}$$

Energy Equations:

$$\frac{dh'}{dr} + C'_m\frac{dC'_m}{dr} + C'_\theta\frac{dC'_\theta}{dr} = \frac{\gamma'_{h,\text{mix}}Z}{\pi r\varepsilon'\rho'C'_m\sin\phi} \tag{19}$$

$$\frac{dh''}{dr} + C''_m\frac{dC''_m}{dr} + C''_\theta\frac{dC''_\theta}{dr} = \frac{\gamma''_{h,\text{mix}}Z}{\pi r\varepsilon''\rho''C''_m\sin\phi} \tag{20}$$

Supplementary Equations: A complementary equation of equality of static pressures and area fractions in the flow zones is used also:

$$p' - p'' = 0 \tag{21}$$

$$\varepsilon' + \varepsilon'' = 1 \tag{22}$$

The Unknowns: The above system of ten equations, complemented by thermodynamic functions and conversion relationships between absolute and rotating reference frames, is fully resolvable. The basic unknowns are $C'_m, C'_\theta, C''_m, C''_\theta, p, \varepsilon, \rho', \rho'', h', h''$.

Commentary

The equations are fully compressible and are modeled with real gas property models, with separate models for each zone. An inconsistency of the Dean-Senoo model, that the mass fraction of secondary zone is constant, has been removed, and this is useful for the model agreement shown in the next section. Hence, several extra terms have been added to the differential equations. For the present work, we have rigorously connected the two-zone vaneless diffuser model to the two-zone impeller model [11], but with the prior sudden expansion mixing loss suppressed. We have also added mass-average post-processing for flow results in each zone to report the propagating flow field and connect the model with downstream components. The output results are mass averaged for enthalpy and entropy. In the future we may treat the trailing edge blade wake as a distinct streamtube and also add wall blockage.

Downloaded 30 May 2010 to 128.113.26.88. Redistribution subject to ASME license or copyright; see http://www.asme.org/terms/Terms_Use.cfm

Of greatest interest is the prospect for computing the conditions up to a vaned diffuser throat on a periodic basis using this new approach (a later paper may be prepared).

The system of ten equations and ten unknowns is computed just as Eqs. (1)–(5) were solved with Runge-Kutta integration. In fact, the same algorithms were used, but with more equations.

Several examples (which show closure modeling, not blind prediction) of computations for the new model have been presented in the complementary studies, specifically [1,2]. We expand this now by showing additional cases. Figures 3–6 show summaries of the comparisons for the three Eckardt stages and for one of the Concepts NREC stages shown in Table 1. In these figures, the static pressure is automatically matched in our data processing procedure (a historical programming preference) with the deduced value of C_f resulting. Hence, the measured p values (shown as "x") fall exactly on the computed trend because p is used as input data and C_f is deduced for subsequent model building. [Note: due to the historical data modeling procedure, C_f is calculated from r_2 to the local r value for each match with a measured $p(r)$; hence, C_f is the local *cumulative* value from r_2 to r. This is essentially the drag coefficient.] The models (either Stanitz or the new model) then *predict* the resulting levels of mass-averaged total pressure and flow angle.

Figures 3–5 correspond to one case each from the three stages investigated by Eckardt and Trültzsch [12]. Excellent agreement has been obtained while all attempts to use the simpler Stanitz model have fallen short. Figure 6 has only an inlet and exit traverse, but this is enough data to establish a reasonable match. The variation in flow angle is very slight for this last case due to severe pinch, as used in the vaneless diffuser. Only by using *multiple* traverse location data is it possible to obtain a unique set of χ and δ_{2p} for a given flow point; a single traverse location does not contain enough information to obtain a unique solution (see paper [3] for more details).

The trend for C_f physically would be expected to start high and then drop down to some asymptotic value at large radius, or at a large value of a flow pathlength based Reynolds number. This is exactly what was found for Figs. 3 and 5, but not for Figs. 4 and 6. A sensitivity study revealed the answer: a very slight change (0.25% usually) in measured static pressure near the diffuser inlet is all that is necessary to flip the two questionable curves the correct way up.

Overall, it can be observed that excellent modeling has been achieved for this wide set of parameters. Some small defects can be found near the beginning of the vaneless diffuser and it is felt that these defects are sufficient to encourage us to expand the set of equations in the future to include further balance for the small wake immediately following the blade thickness and to include boundary layer displacement.

The collected sets of C_f data for all cases evaluated are shown in Fig. 7. The cumulative C_f values of Figs. 3–6 have been converted to local values and two trend lines have been added. A simple Reynolds number correlation, alone, is insufficient. We must obtain a correlation using other parameters in addition to Re, and this is discussed in [2]. Further, more processing of the current data is merited. The trend line of $\mathrm{Re}_x^{0.3}$ is closer to the data trend than the $\mathrm{Re}_x^{0.2}$ trend line, and this needs to be carefully considered. When the small changes mentioned above are included, a final correlation should be developed. Also, future tests are needed (and underway) to obtain more detailed data to expand this work. Both the company tests and the Eckardt tests would have been better if even more data had been logged: complete static pressure on both the front and rear walls (not done in any cases) and at least three full traverse sets (only Eckardt data).

A basic question must be asked: what is the impact of the revised modeling equations on future design? Recognizing that the early set of equations (1)–(4) has been sufficient for much industrial design and development work for the past 50 years, one would question whether the enhanced accuracy of the refined

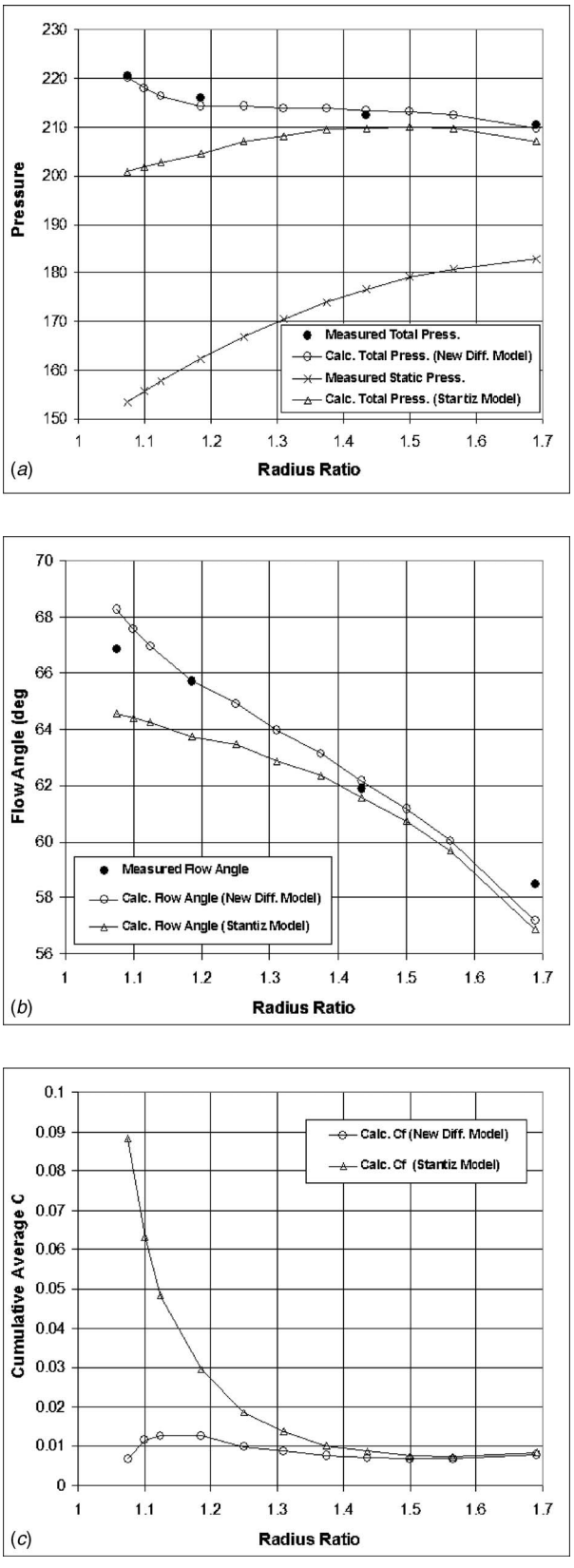

Fig. 3 A comparison of total pressure (*a*) and flow angle (*b*) data with a new periodic vaneless diffuser performance model and the Stanitz model. The resultant cumulative C_f coefficient is also shown (*c*). Static pressure (only) is a forced match to data for each model. The new model gives good $\bar{p}_0$ and $\bar{\alpha}$ agreement. An Eckardt rotor O case with traverse data at four different radii are shown. This matching permits a definitive evaluation of δ_{2p}–15.95°, δ_{2s}=12.4°; χ=0.13 and $C_f(r)$ (CCN5).

Downloaded 30 May 2010 to 128.113.26.88. Redistribution subject to ASME license or copyright; see http://www.asme.org/terms/Terms_Use.cfm

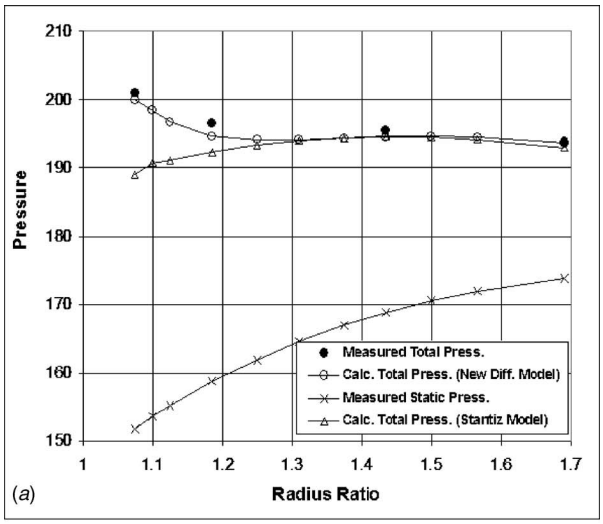

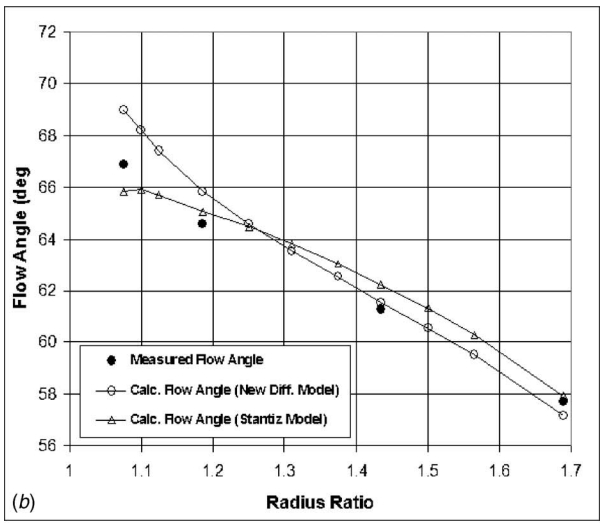

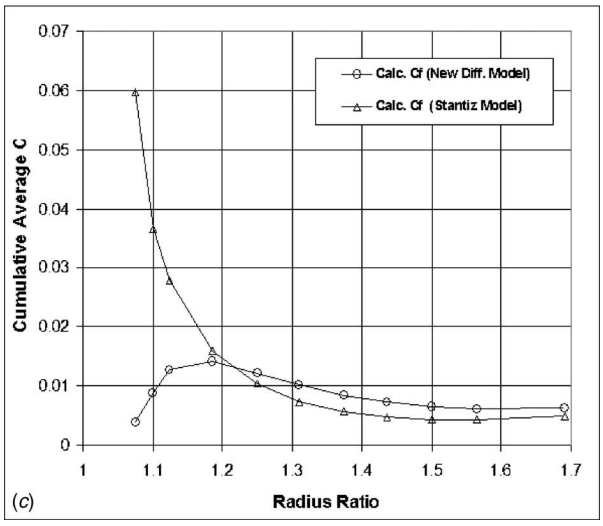

Fig. 4 A comparison of total pressure (*a*) and flow angle (*b*) data with a new periodic vaneless diffuser performance model. The resultant cumulative C_f coefficient is also shown (*c*). Static pressure (only) is a forced match to data for each model. The new model gives good $\bar{p}_0$ and $\bar{\alpha}$ agreement. The Eckardt rotor A case with traverse data at four different radii. This matching permits a definitive evaluation of δ_{2p}=−1.98°, δ_{2s}=15°, χ =0.227 and $C_f(r)$ (CCN6).

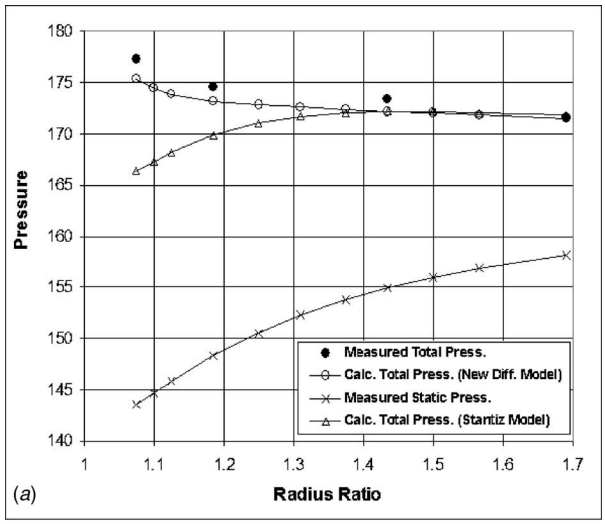

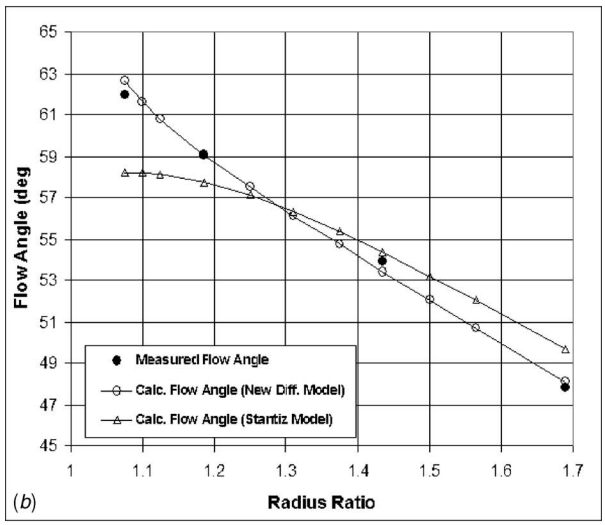

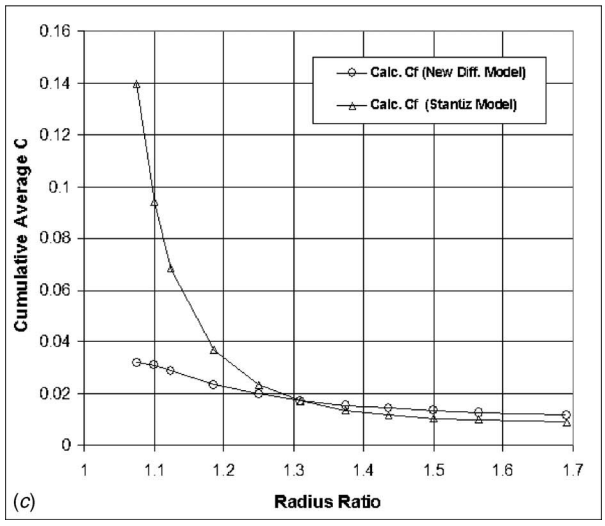

Fig. 5 A comparison of total pressure (*a*) and flow angle (*b*) data with a new periodic vaneless diffuser performance model. Resultant cumulative C_f coefficient is also shown (*c*). Static pressure (only) is a forced match to data for each model. New model gives good $\bar{p}_0$ and $\bar{\alpha}$ agreement. The Eckardt rotor B case with traverse data at four different radii. This matching permits a definitive evaluation of δ_{2p}=−1.98°, δ_{2s}=15°, χ =0.197 and $C_f(r)$ (CCN7).

Downloaded 30 May 2010 to 128.113.26.88. Redistribution subject to ASME license or copyright; see http://www.asme.org/terms/Terms_Use.cfm

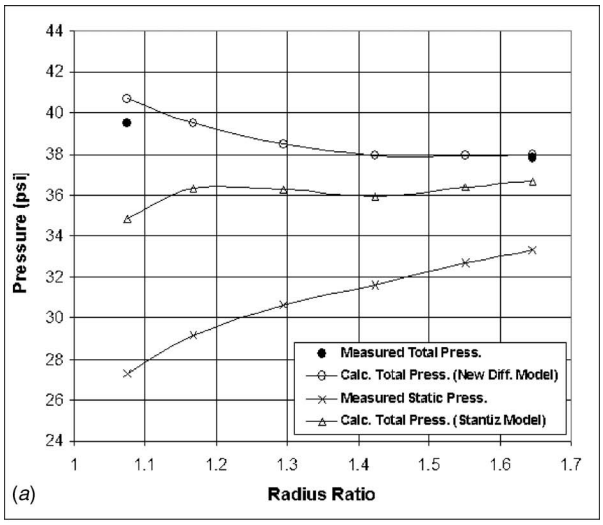

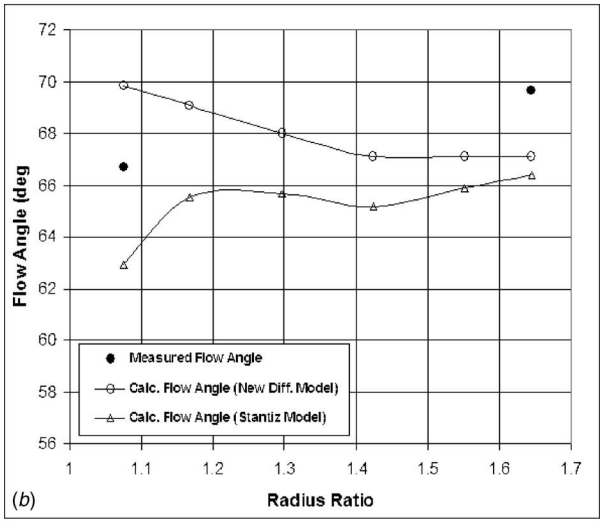

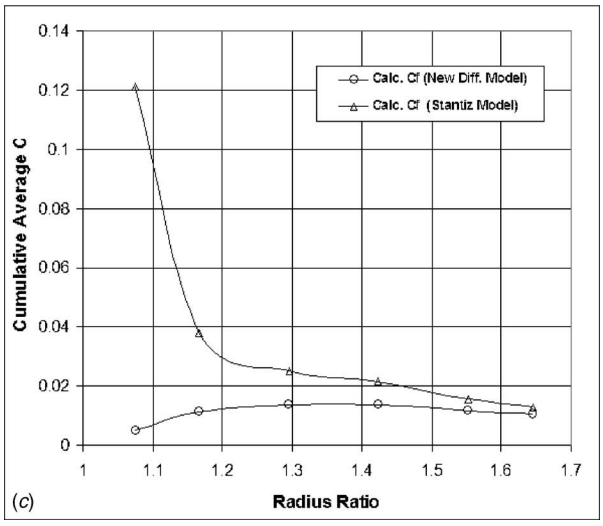

Fig. 6 A comparison of total pressure (*a*) and flow angle (*b*) data with a new periodic vaneless diffuser performance model. The resultant cumulative C_f coefficient is also shown (*c*). Static pressure (only) is a forced to data for each model. The new model gives good $\bar{p}_0$ and $\bar{\alpha}$ agreement. Concepts NREC case CCN103 with traverse data at two different radii. This matching permits a definitive evaluation of $\delta_{2p}=-5.93°$, $\delta_{2s}=17.4°$, $\chi=0.064$ and $C_f(r)$ (CCN103).

modeling is necessary. Nonetheless, when the comparison of the old and new models is taken under consideration, it is clear that there is a substantial improvement in modeling accuracy. Whenever short vaneless diffusers must be considered, the revised modeling is essential. Additionally, when inlet conditions for a vaneless diffuser must be studied in depth, then the revised model is also necessary (e.g., when studying inlet stability conditions). Even though the historical Stanitz model is approximately right at the diffuser exit, it is clear that the revised model is more accurate.

The authors' principal reason for pursuing this work, in fact, affords a further reason for using the revised model: it was necessary to obtain a good model of the vaneless diffuser performance in order to interpret historical datasets for which only a single vaneless diffuser, cross-channel, three-hole probe traverse was available, usually in the radius ratio range from 1.07 to 1.12. Desiring to use these data to back-calculate to the impeller tip, it is necessary to have a skin friction coefficient for the sidewalls, which would allow proper closure. A single traverse in this radius ratio range can only be interpreted back to the impeller tip by using the new model and with appropriate skin friction coefficients. Thus, the remaining data of Table 1 can now be interpreted in spite of the absence of subsequent traverse locations because a well-calibrated model is now available. Hence, improved impeller modeling is now possible.

A further use for this modeling will undoubtedly be available shortly. A parallel investigation is now being conducted to model, in great detail, stages with various types of downstream vaned systems, including channel diffusers, conical diffusers, airfoil diffusers, continuous crossovers, and return channels. To get this modeling to be precise, it will be necessary to use a time-dependent model from the impeller tip to the diffuser throat for many stages. It is believed that this model can be modified to allow the necessary calculations to be made. Consequently, the present work is a foundation for further development.

Conclusions

A new periodic vaneless diffuser model has been developed. It affords much improved modeling of both total pressure and flow angle along the diffuser radius. While the older models are approximately correct near the end of very long vaneless diffusers, the new model is necessary to understand the inlet and developing flow. It is necessary and appropriate to use the new periodic model only with two-zone impeller modeling. Improved impeller and diffuser models will result from this work. The very high integrity shown for the new model, when compared to measured data, provides a solid confirmation of the value of two-zone modeling and hints at the deficiencies of simpler approaches. Datasets shown herein are to be shared with other investigators.

Acknowledgments

The authors wish to acknowledge the concerted efforts of many who have greatly facilitated this work. Jean Wallace and Sharon Wight have carefully collected data for many years. Jane Waks has retrieved vast data from archives. Penny Palmer and Ellen Japikse have carefully revised text and aided the final paper form in countless ways. Many technicians and test engineers have contributed skilled resources over several decades to acquire the data employed herein. Special thanks go to Dr. Dietrich Eckardt for the use of his data for the past 25 years. The contributions of Dr. R. C. Dean and Dr. Y. Senoo over many decades are greatly appreciated. Finally, special thanks go to Rob Pelton who prepared many of the current figures.

Nomenclature

A = area; also a coefficient
b = passage depth
C = absolute velocity
C_f = skin friction coefficient

Downloaded 30 May 2010 to 128.113.26.88. Redistribution subject to ASME license or copyright; see http://www.asme.org/terms/Terms_Use.cfm

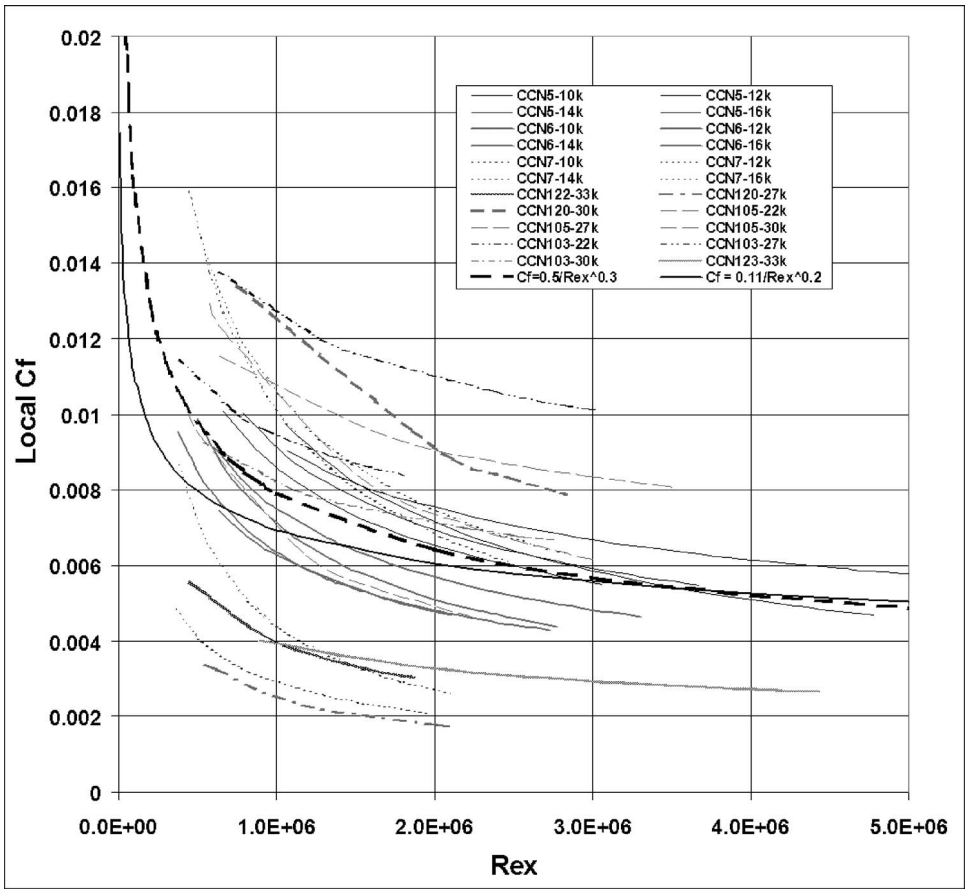

Fig. 7 Composite of all traverse based local C_f trends with diffuser length Re number, $Re_x = Cx/\nu$, where x is the flow pathlength based on a log spiral through the diffuser. The resultant model fit gives the cumulative value of C_f as $0.11/Re_x^{0.2}$ or $C_f = 0.5/Re_x^{0.3}$, where these values can only be used with the periodic model.

C_m = meridional velocity
C_θ = tangential velocity
CCN = centrifugal compressor database number
h = enthalpy
M = Mach number
m = mass flow rate
N = rotational speed
p = static pressure
pr = stage pressure ratio
r = radius
Re = Reynolds number
s = meridional streamwise coordinate
T = temperature
W = relative velocity
Z = blade number

Greek Symbols

α = absolute frame flow angle wrt stationary system; also, entrainment coefficient
β = relative flow angle
β_{2b} = exit blade angle
γ = mass or enthalpy flux per unit area, per subscripts
Δ_{te} = trailing edge thickness fraction
δ_{2p} = deviation of primary zone
δ_{2s} = deviation of secondary zone
ε, e = secondary flow area fraction
θ = tangential coordinate
ν = kinematic viscosity
ξ = turbulent mixing loss coefficient
Π = wetted perimeter
ρ = density
τ = shear stress
ϕ = diffuser inclination angle
χ = secondary zone mass flow fraction

Superscripts

$'$ = primary zone parameters
$''$ = secondary zone parameters

Subscripts

0 = stagnation state
h = enthalpy flux basis
m = mass flux basis
mix = mixed-out state
rel = relative state

Appendix: Detailed Derivations

The wall friction stress, force, and relevant perimeter are computed according to:

$$\tau_w = C_f \bar{\rho} \frac{C^2}{2}, \text{ applied for either the primary or secondary zone}$$

$$\hat{\tau} = \tau_w \Pi_w$$

$$\Pi_w = 2 \cdot (2\pi r) = \text{wetted perimeter, wake.}$$

Downloaded 30 May 2010 to 128.113.26.88. Redistribution subject to ASME license or copyright; see http://www.asme.org/terms/Terms_Use.cfm

The shear force, due to mixing at the interface boundary, is directed along the interface boundary. The initial correlation is assumed to be in the form, conventional for streamwise correlations for dissipation forces, similar to Dean and Senoo.

$$\tau_{\text{mix}} = \xi\bar{\rho}\frac{(W'' - W')|W'' - W'|}{2}$$

$$\hat{\tau}_{\text{mix}} = \tau_{\text{mix}}\Pi_{\text{mix}}$$

$$\Pi_{\text{mix}} = 2Zb$$

For the flows moving with higher velocity than the velocity at the boundary, the term is negative. The interaction between wakes and jets occurs in some boundary region, where flow properties can be different from the core parameters in the primary and secondary zones (jet and wake), due to velocity and thermal profiles and compressibility effects. We suggest defining an explicit boundary between primary and secondary domains and rewrite the correlation in the form, valid for a jet and wake:

$$\tau_{\text{mix}} = \xi\bar{\rho}\frac{(\bar{W} - W)|\bar{W} - W|}{2}$$

with

$\bar{W} \sim 0.5(W' + W'')$—estimated velocity at the secondary-primary interface boundary

ξ—turbulent mixing loss

$\bar{\rho} \sim 0.5(\rho' + \rho'')$—estimated density at the secondary-primary interface boundary

Z—number of secondary-primary structures in the vaneless diffuser space (number of passages/blades at the impeller exit). The mixing loss factor here is four times the mixing factor in the correlation used by Dean and Senoo.

The mixing process is the reason for entrainment, which increases the mass flow of the primary zone or jet. We shall use $\gamma_{m,\text{mix}}$ as the mass flow rate per unit area for this mixing process. Based on dimensional considerations, the entrainment velocity at the boundary can be related to the mixing friction force at the jet-wake boundary. Starting with the mass flux,

$$\gamma_{m,\text{mix}} \sim \bar{\rho}\left\{\frac{|\tau_{\text{mix}}|}{A_1\bar{\rho}}\right\}^{0.5}\text{sign}(W - \bar{W}) = \bar{\rho}\left(\frac{\xi}{2A_1}\right)^{0.5}(W - \bar{W})$$

where A_1, a simple empirical constant, can be estimated by comparing this relationship with an empirical correlation for entrainment rate. The sign of the entrainment flux is positive for jets, giving increased mass flow for jets at the expense of the wakes. Since there are no available correlations for entrainment rate for wake-jet structures in the vaneless space downstream of rotating impellers, an estimation can be made using the Prandtl correlation for turbulent shear stress and the entrainment coefficient for a planar undisturbed jet.

$$\nu_T = 0.037\frac{b}{2}|W - W_\infty| \sim 0.037\frac{2\pi r\varepsilon}{2Z}2|W - \bar{W}|$$

$$\tau_T = -\bar{\rho}\nu_T\frac{dW}{r\,d\theta} \sim \bar{\rho}\upsilon_T\frac{(\bar{W} - W)}{\frac{2\pi r\varepsilon}{2Z}}$$

$$\tau_T = \bar{\rho}0.037\frac{2\pi r\varepsilon}{2Z}2|\bar{W} - W|\frac{(\bar{W} - W)}{\frac{2\pi r\varepsilon}{2Z}} = \bar{\rho}0.037\cdot 4\frac{(\bar{W} - W)|\bar{W} - W|}{2}$$

$$\sim 0.15\bar{\rho}\frac{(\bar{W} - W)|\bar{W} - W|}{2}$$

The estimated mixing loss coefficient ~ 0.15 is below the one obtained by Dean and Senoo from test data $\sim(0.05\ldots0.09)*4 = 0.2\ldots0.4$, which is to be expected due to differences in the turbulence level and shear flow formation for undisturbed jets and real turbomachinery flows.

Thus, substituting the mixing loss factor for planar jets into the $\gamma_{m,\text{mix}}$ equation above:

$$\gamma_{m,\text{mix}} \sim \bar{\rho}\left(\frac{0.075}{A_1}\right)^{0.5}(W - \bar{W}).$$

From the other side, the entrainment mass flow can be obtained from an empirical correlation, with an entrainment coefficient $\alpha \sim 0.041$ for planar jets [13]:

$$\gamma_{m,\text{mix}} = \alpha\bar{\rho}(W - W_\infty) = 2\alpha\bar{\rho}(W - \bar{W}) = 0.082\cdot\bar{\rho}(W - \bar{W})$$

Equating both relationships for entrainment mass flow gives:

$$\left(\frac{0.075}{A_1}\right)^{0.5} \sim 0.082$$

$$A_1 \sim 11$$

With the above result, one can obtain the following estimation:

$$\gamma_{m,\text{mix}} \sim \sqrt{\frac{\xi}{22}}\bar{\rho}(W - \bar{W})$$

Thus, the mixing loss coefficient can be used in the model to control both mixing stresses and entrainment rate.

The energy equation deserves special comment, as it is not an obvious extension from Stanitz. Work by pressure forces is not needed, since there are no moving surfaces with pressure gradients. Work done by mixing forces on the moving boundary between the jet and wake is the product of the mixing force on the absolute velocity of the surface (which leads to the difference of the relative and absolute flow angles):

$$dE_{\text{mix}} = (\bar{\tau}_{\text{mix}}\cdot\vec{\bar{C}})\Pi_{\text{mix}}\,ds = \tau_{\text{mix}}\cdot\bar{C}\cdot\cos(\bar{\beta} - \bar{\alpha})\Pi_{\text{mix}}\,ds$$

$\bar{C}$—absolute velocity of the two-zone interface. Work done by wall friction forces is zero (stationary walls). Energy influx due to the relative total enthalpy exchange because of entrainment:

$$dE_e = \gamma_{m,\text{mix}}(\bar{h}_{0\text{rel}} - h_{0\text{rel}})\Pi_{\text{mix}}\,ds$$

$$\varepsilon\rho AC_m\frac{d}{ds}\left(h + \frac{C^2}{2}\right)ds = dE_{\text{mix}} + dE_e$$

$$\frac{d}{ds}\left(h + \frac{C^2}{2}\right) = \frac{\tau_{\text{mix}}\cdot\bar{C}\cdot\cos(\bar{\beta} - \bar{\alpha})\Pi_{\text{mix}}}{\varepsilon\rho AC_m} + \frac{\gamma_{m,\text{mix}}(\bar{h}_{0,\text{rel}} - h_{0,\text{rel}})\Pi_{\text{mix}}}{\varepsilon\rho AC_m}$$

$$\frac{d}{ds}\left(h + \frac{C^2}{2}\right) = \frac{\tau_{\text{mix}}\cdot\bar{C}\cdot\cos(\bar{\beta} - \bar{\alpha})2Zb}{\varepsilon\rho 2\pi rbC_m} + \frac{\gamma_{m,\text{mix}}(\bar{h}_{0,\text{rel}} - h_{0,\text{rel}})2Zb}{\varepsilon\rho 2\pi rbC_m}$$

$$\frac{d}{ds}\left(h + \frac{C^2}{2}\right) = \frac{\tau_{\text{mix}}\cdot\bar{C}\cdot\cos(\bar{\beta} - \bar{\alpha})Z}{\varepsilon\rho\pi rC_m} + \frac{\gamma_{m,\text{mix}}(\bar{h}_{0,\text{rel}} - h_{0,\text{rel}})Z}{\varepsilon\rho\pi rC_m}$$

$$\frac{dh}{ds} + C_m\frac{dC_m}{ds} + C_\theta\frac{dC_\theta}{ds} = \frac{\tau_{\text{mix}}\cdot\bar{C}\cdot\cos(\bar{\beta} - \bar{\alpha})Z}{\varepsilon\rho\pi rC_m} + \frac{\gamma_{m,\text{mix}}(\bar{h}_{0,\text{rel}} - h_{0,\text{rel}})Z}{\varepsilon\rho\pi rC_m}$$

If work by mixing surface is negligible:

$$\frac{dh}{ds} + C_m\frac{dC_m}{ds} + C_\theta\frac{dC_\theta}{ds} = \frac{\gamma_{m,\text{mix}}(\bar{h}_{0,\text{rel}} - h_{0,\text{rel}})Z}{\varepsilon\rho\pi rC_m}$$

or since $dr = \sin(\phi)ds$:

Downloaded 30 May 2010 to 128.113.26.88. Redistribution subject to ASME license or copyright; see http://www.asme.org/terms/Terms_Use.cfm

$$\frac{dh}{dr} + C_m \frac{dC_m}{dr} + C_\theta \frac{dC_\theta}{dr} = \frac{\gamma_{m,\mathrm{mix}}(\bar{h}_{0,\mathrm{rel}} - h_{0,\mathrm{rel}})Z}{\varepsilon \rho \pi r C_m \sin \phi}$$

The current experience of the authors indicates that the entrainment enthalpy exchange may well dominate over the work by interface mixing shear as suggested by the last equation.

References

[1] Japikse, D., and Oliphant, K. N., 2005 "Turbomachinery Modeling: Explicit and Implicit Knowledge Capturing," ASME Paper No. GT2005–68099.

[2] Pelton, R. J., Japikse, D., Maynes, D., and Oliphant, K. N., 2005, "Turbomachinery Performance Models," presented at ASME International Mechanical Engineering Congress & Exposition (IMECE), Orlando, FL, November 5–11, 2005.

[3] Japikse, D., 2005, "Multi-Variable, High Order, Performance Models," presented at ASME International Mechanical Engineering Congress & Exposition (IMECE), Orlando, FL, November 5–11, 2005.

[4] Stanitz, J. D., 1952, "One-Dimensional Compressible Flow in Vaneless Diffusers of Radial or Mixed-Flow Centrifugal Compressors, Including Effects of Friction, Heat Transfer and Area Change," NACA TN 2610.

[5] Japikse, D., 1996, *Centrifugal Compressor Design and Performance*, Concepts ETI, Inc., Wilder, VT.

[6] Brown, W. B., and Bradshaw, G. R., 1947, "Method of Designing Vaneless Diffusers and Experimental Investigation of Certain Undetermined Parameters," NACA TN 1426.

[7] Traupel, W., 1977, *Thermische Turbomaschinen*, Springer-Verlag, Berlin.

[8] Johnston, J. P., and Dean, R. C., 1966, "Losses in Vaneless Diffusers of Centrifugal Compressors and Pumps," ASME J. Eng. Power, **88**, pp. 49–62.

[9] Dean, R. C., and Senoo, Y., 1960, "Rotating Wakes in Vaneless Diffusers," ASME J. Basic Eng., **82**, pp. 563–570; (commentary on pp. 571–574).

[10] Eckardt, D., 1978, "Investigation of the Jet Wake Discharge Flow of a Heavily Loaded Centrifugal Compressor Impeller," ESA-TT-466, translation of DLR-FB 77-32 "Untersuchung der Strahl/Totwasser-Stroemung Hinter Einem Hochbelasteten Radialverdictherlaufrad."

[11] Japikse, D., 1985, "Assessment of Single- and Two-Zone Modeling of Centrifugal Compressors—Studies in Component Performance: Part 3," ASME Paper No. 85-GT-73.

[12] Eckardt, D., and Trültzsch, K-J., 1977, Vergleichende Strömungsuntersuchungen an drei Radialverdichter-Laufrädern mit konventionellen Meßverfahren, FVV Research Report (Forschungsberichte) #237.

[13] Agrawal, A., and Prasad, A., 2003, "Integral Solution for the Mean Flow Profiles of Turbulent Jets, Plumes and Wakes," J. Fluids Eng., **125**, pp. 813–822.

Downloaded 30 May 2010 to 128.113.26.88. Redistribution subject to ASME license or copyright; see http://www.asme.org/terms/Terms_Use.cfm

Investigation of Three-Dimensional Unsteady Flows in a Two-Stage Shrouded Axial Turbine Using Stereoscopic PIV—Kinematics of Shroud Cavity Flow

Yong Il Yun
School of Mechanical and Aerospace Engineering,
Seoul National University,
Seoul 151-742, Korea
e-mail: yongil.yun@samsung.com

Luca Porreca
e-mail: luca.porreca@ch.manturbo.com

Anestis I. Kalfas
e-mail: kalfas@lsm.iet.mavt.ethz.ch

Turbomachinery Laboratory,
Swiss Federal Institute of Technology Zurich,
Zurich CH-8092, Switzerland

Seung Jin Song
School of Mechanical and Aerospace Engineering,
Seoul National University,
Seoul 151-742, Korea
e-mail: sjsong@snu.ac.kr

Reza S. Abhari
Turbomachinery Laboratory,
Swiss Federal Institute of Technology Zurich,
Zurich CH-8092, Switzerland
e-mail: abhari@lsm.iet.mavt.ethz.ch

This paper presents an experimental study of the behavior of leakage flow across shrouded turbine blades. Stereoscopic particle image velocimetry and fast response aerodynamic probe measurements have been conducted in a low-speed two-stage axial turbine with a partial shroud. The dominant flow feature within the exit cavity is the radially outward motion of the main flow into the shroud cavity. The radial migration of the main flow is induced by flow separation at the trailing edge of the shroud due to a sudden area expansion. The radially outward motion is the strongest at midpitch as a result of interactions between vortices formed within the cavity. The main flow entering the exit cavity divides into two streams. One stream moves upstream toward the adjacent seal knife and reenters the main flow stream. The other stream moves downstream due to the interaction with the thin seal leakage flow layer. Closer to the casing wall, the flow interacts with the underturned seal leakage flow and gains swirl. Eventually, axial vorticity is generated due to these complex flow interactions. This vorticity is generated by a vortex tilting mechanism and gives rise to additional secondary flow. Because of these fluid motions combined with a contoured casing wall, three layers (the seal leakage layer, cavity flow layer, and main flow) are formed downstream of the shroud cavity. This result is different from the two-layer structure, which is found downstream of conventional shroud cavities. The seal leakage jet formed through the seal clearance still exists at 25.6% axial chord downstream of the second rotor. This delay of complete dissipation of the seal leakage jet and its mixing with the cavity flow layer is due to the contoured casing wall. Time-averaged flow downstream of the shroud cavity shows the upstream stator's influence on the cavity flow. The time-averaged main flow can be viewed as a wake flow induced by the upstream stator whose separation at the shroud trailing edge induces pitchwise nonuniformity of the cavity flow. [DOI: 10.1115/1.2720873]

Introduction

Shrouds are used to prevent pressure-driven leakage flow across the turbine blade tip. Nevertheless, there is still a gap between the stationary (casing wall or stator shroud) and rotating parts (rotor shroud or stator hub), and flow leaks through the gap. To reduce the leakage flow, labyrinth seals are often employed. Much work has been done to clarify how the labyrinth seal affects flow field not only within the seal cavity but also downstream of the blade passage. To quantify loss with a simple model, Denton [1] made a simplified description of the cavity flow that the meridional velocity of the leakage jet undergoes dissipation inside the shroud cavity while the swirl of the leakage flow remains unchanged. Thus, there is a mismatch of flow angle between the leakage and the main flows when the two flows interact. The mismatch causes a shear layer, which is a source of loss [1,2]. According to Wallis et al. [3], a strategy for reducing the losses associated with seal leakage flow is to minimize the entropy generated during the interaction between the seal leakage and the main flow. They added airfoil-shaped turning devices on top of the shroud surfaces to turn the leakage flow through the shroud cavity, but actually found performance degradation. Also, the seal leakage flow causes negative incidence on the subsequent stator, thus intensifying the passage vortex formed inside the subsequent stator [4–6]. Song and Song [7] developed an analytical model to predict flow response to labyrinth seals in an axial turbine stage with a shrouded rotor. In their control volume approach, they assumed that the leakage flow is radially inward at the exit of the cavity, and the leakage and the main flows remain separate downstream. Thus, downstream of the shroud cavity, there are two flow layers—the main flow and the leakage flow, which is retarded in the axial direction and tangentially underturned.

It was not until recently that the flow within the seal cavity was experimentally investigated in detail. Pfau et al. [8] made detailed measurements of the flow within the shroud cavity in an annular turbine cascade. They found a pitchwise variation in static pressure within the shroud cavity as well as radially outward and inward motions of fluid at the exit cavity. They inferred that the pitchwise nonuniformity of the flow within the cavity is attenuated as the leakage flow passes through three seal knives, presumably due to the mixing in the cavities. Also, they observed a radially stratified axial velocity distribution and a toroidal vortex within the exit cavity. Pfau et al. [9] investigated the flow field at

Contributed by the International Gas Turbine Institute of ASME for publication in the JOURNAL OF TURBOMACHINERY. Manuscript received June 3, 2006; final manuscript received October 9, 2006; published online January 28, 2008. Review conducted by David Wisler.

 Copyright © 2008 by ASME

Downloaded 30 May 2010 to 128.113.26.88. Redistribution subject to ASME license or copyright; see http://www.asme.org/terms/Terms_Use.cfm

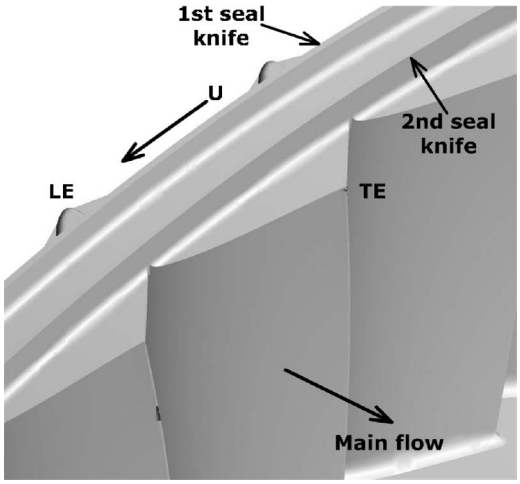

Fig. 1 Partially shrouded rotor

the inlet of the shroud cavity in a rotating turbine rig and found that the interaction between the main flow and cavity flow is mainly driven by a toroidal vortex moving at 83% of the rotor speed. Pfau et al. [10] also proposed nonaxisymmetric contouring on the shroud surface to reduce the leakage flow based on detailed flow measurements within the shroud cavity. Wolter et al. [11] conducted time-resolved flow-field measurements within three seal cavities formed by two seal knives attached to the shrouded turbine rotor blades. They observed, in the first cavity, a pitchwise nonuniformity due to the leading edge potential effect, which was also observed by Pfau et al. [8]. Furthermore, they found that the flow became tangentially uniform as it passed through the second cavity and then regained nonuniformity due to the interaction with the main flow in the exit cavity.

Conventional shroud covering the rotor blades extends beyond both the leading edge and trailing edge of the rotor blades in the axial direction. This type of full shroud increases the inertia near the rotor tip region, and consequently, rotor blades may suffer from structural problems. Porreca et al. [12] investigated the effects of partial shroud on turbine aerodynamics. The partial shroud covers $<40\%$ of the axial chord of the rotor and aims to reduce inertia as well as leakage. According to Porreca et al. [12], the underturned flow extends from the casing down to 60% and 80% span regions in the partial shroud case and full shroud case, respectively. They attributed the difference to the pressure-driven leakage flow through the tip clearance of the shroudless trailing-edge region of the partially shrouded blades.

Though researchers have shed light on the large-scale flow structure, such as the axial vorticity originating from the shear layer between the main flow and the underturned seal leakage flow in fully shrouded turbines [1–3,7], little is known about the finer structures of the cavity flow in partially shrouded turbines. This paper presents an experimental study of shroud cavity flow in a two-stage shrouded axial turbine test facility. The partial shroud geometry has been modified, as shown in Fig. 1. Shroud is added near the pressure side at the trailing edge to inhibit the pressure-driven leakage flow over the blade tip, which was observed by Porreca et al. [12]. The main focus of this paper is on the exit cavity flow behavior.

Stereoscopic particle image velocimetry (PIV) technology has primarily been used for this investigation. By using PIV, detailed flow field has been observed on several blade-to-blade measurement planes in the shroud exit of the second rotor. PIV is useful for this investigation because it is possible to observe not only the flow in the shroud cavity region but also the streamwise evolution of flow with fine spatial resolution. Also, unsteady pressure measurements have been carried out in an axial plane downstream of the second rotor by using fast response aerodynamic probe (FRAP) technology developed at the Swiss Federal Institute of Technology Zurich [13,14].

Table 1 Design parameters of the test turbine

Rotating speed	2625 rpm
Pressure ratio	1.38
Mass flow rate	10.65 kg/s
Number of blades (stator/rotor)	42/42
Aspect ratio	1.8
Tip diameter	800 mm
Mach number (stator/rotor)	0.35/0.1
Reynold number	2×10^5

The objective of this study is to address the following questions by observing the time-averaged as well as phase-locked averaged flow field in the partially shrouded turbine:

- How does the leakage flow behave within the partial shroud exit cavity?
- What are the finer structures of the cavity flow besides the large-scale axial vorticity due to the shear layer between the main flow and the underturned seal leakage flow?
- How does the seal leakage flow evolve downstream of the shroud cavity combined with a contoured casing wall?
- In the fixed frame downstream of the shroud cavity, how does each of the upstream stator and the rotor's geometry affect the shroud cavity flow?

Description of the Experiment

Test Turbine Rig. The present study has been conducted in a low-speed, quasi-closed-loop, two-stage axial turbine rig at the Swiss Federal Institute of Technology Zurich in Switzerland. All measurements have been carried out at the design condition. Table 1 summarizes the design parameters of this turbine facility. More detailed desciptions of the facility and its operation can be found in Porreca et al. [15].

Instrumentation. Two measurement techniques—stereoscopic PIV and FRAP—have been used for the present investigation. Since the flow in turbomachinery, particularly near the tip, is highly three-dimensional, stereoscopic PIV has been adopted for this study by using two cameras. The test turbine is equipped with a transparent optical window, which extends from −78% to 103% axial chord from the trailing edge of the second rotor and 1.2 blade pitch to facilitate an optical access to the shroud cavity region. The casing ring is rotatable for azimuthal traversing of aerodynamic probes, such as FRAP.

Figure 2 shows a schematic of the stereoscopic PIV setup used for this investigation. The digital images have been recorded with 1280×1024 pixel 12 bit charge coupled device (CCD) cameras (PCO SensiCam SVGA). For camera optics, Nikon AF MICRO NIKKOR lenses with a focal length of 60 mm have been used. A double-cavity Nd:YAG laser (Solo120PIV, New Wave Research) has been used as a light source. The laser generates a 120 mJ/pulse of 532 nm wavelength green visible light. The pulse width is 10 ns, and the repetition rate is 15 Hz. The bursts of laser light have been synchronized with cameras via a Dantec FlowMap system hub, and this synchronization has been triggered by an encoder installed near the rotor shaft. Thus, images in the same blade passage are captured. The time interval between two bursts has been set at 3 μs. The laser beam has been delivered to a laser endoscope (Intelligent Laser Application) through an articulated mirror arm. The laser endoscope not only generates laser sheet through a cylindrical lens but also bends the laser sheet by 90 deg with a prism at the tip. The outer diameter of the laser endoscope is 8 mm, and the divergence angle of the laser sheet is $\sim$16 deg. The cameras and laser endoscope have been mounted on a motor-controlled one-axis linear stage so that cameras and

Downloaded 30 May 2010 to 128.113.26.88. Redistribution subject to ASME license or copyright; see http://www.asme.org/terms/Terms_Use.cfm

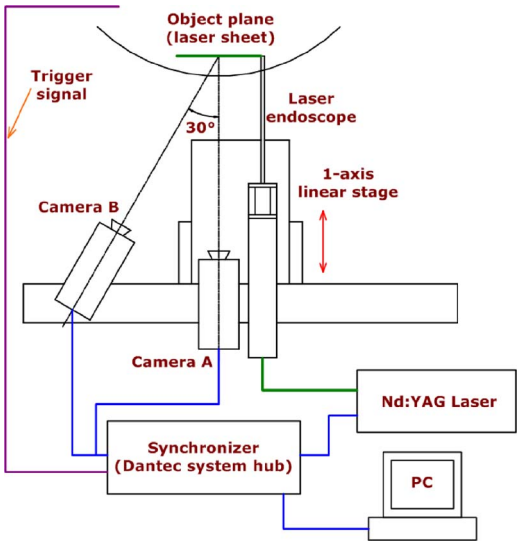

Fig. 2 Schematic of stereoscopic PIV setup

the light sheet move together in the radial direction. Inside the turbine rig, several blade-to-blade planes have been illuminated with the laser endoscope. As shown in Fig. 2, an angular displacement system (Scheimpflug condition) has been used for the stereoscopic cameras—camera A has been positioned such that its axis is perpendicular to the light-sheet plane to avoid interference with the laser endoscope, and camera B has been tilted by 30 deg. The image plane (CCD plane) of camera B has been further rotated by 5 deg to fulfill the Scheimpflug condition, which ensures that all particles in the object field are in good focus in the image plane. The flow has been seeded with 1 μm di-ethyl-hexyl-sebacat (DEHS) particles generated by a Laskin nozzle. The seeding port has been installed between the centrifugal compressor and the subsequent heat exchanger located upstream of the test section.

Each pair of images has been interrogated using cross-correlation analysis in 32×32 pixel subimages with an overlap of 50% between adjacent interrogations. An advanced interrogation method with window offset [16,17] has been used. Westerweel et al. [16] showed that the signal-to-noise ratio with window offset is approximately three times larger than that without window offset for flows with high turbulence intensity. Furthermore, the method of window offset effectively reduces the error due to loss of pairs. Spurious data are unavoidable in PIV, and, to filter out these spurious data, the local median test suggested by Westerweel [18] has been used.

For stereoscopic PIV in angular displacement configurations, as shown in Fig. 2, a perspective distortion of images occurs. Furthermore, there is the optical distortion of the image through the optical window. Thus, contrary to conventional two-dimensional PIV, a calibration procedure is necessary for stereoscopic PIV to compensate for these distortions. A three-dimensional calibration method [19,20] has been used for this investigation. The calibration procedure is to find a mapping function that maps the object coordinates onto the distorted image coordinates, and polynomial functions have been used for the current study. Once the polynomial coefficients are obtained through the calibration, one can reconstruct three-component true displacement values from cross-correlated nominal displacement values recorded with both cameras. More detailed descriptions of calibration and three-component reconstruction procedures can be found in Prasad [20] and Yun [21].

Figure 3 shows PIV and FRAP measurement planes within the cavity and downstream of the second rotor. Stereoscopic PIV has been conducted in three radial planes within the shroud cavity—

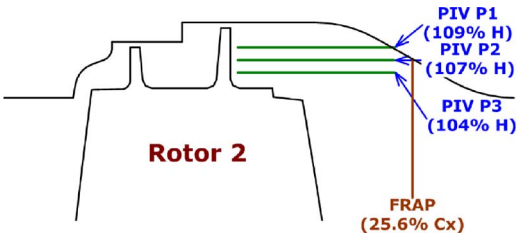

Fig. 3 Measurement planes within the cavity and downstream of the second rotor

P1, P2, and P3 at 109%, 107%, and 104% span, respectively. One blade-passing period has been divided into ten time steps, and 100 image pairs have been recorded in each plane at each time step. FRAP measurement has been made in an axial plane located at 25.6% axial chord from the trailing edge of the second rotor. The FRAP measurement grid comprises 1504 points distributed uniformly—32 points in the circumferential direction (3.5% pitch in 1.1 pitch) and 47 points in the radial direction. More detailed descriptions of both measurement techniques can be found in Porreca et al. [15].

The measurement uncertainty of stereoscopic PIV has been estimated by conducting a Monte Carlo simulation. Monte Carlo simulation has proven to be effective to evaluate PIV error because one can prescribe parameters, such as particle diameters, number of particles, displacement vectors, etc. [22]. To carry out the simulation, tracer particle images are artificially generated by assuming that the light intensity scattered from individual particles has a Gaussian profile. The initial location of each tracer particle is set by using a random number generator, and the locations of displaced particles in the second image frame are determined with predefined displacement vectors. After calculating cross-correlation with these images, one can obtain artificially generated PIV results, compare them against the predefined velocity values, and estimate PIV errors. Detailed descriptions of the simulation can be found in Yun [21].

Three-hundred image pairs have been generated for several points within the shroud cavity to carry out statistical evaluations. PIV error consists of *bias error* and *random error* [22]. Bias error is defined as the difference between the mean PIV value and the actual value. Random error is the standard deviation of the PIV values and is regarded as measurement uncertainty. Figure 4 shows PIV errors estimated at a typical point within the cavity for both one-hundred image pairs and three-hundred image pairs. The errors for each velocity component have been normalized by the actual values for each component. The errors from one-hundred image pairs are comparable to those from three-hundred image pairs. Therefore, one-hundred image pairs have been used. The

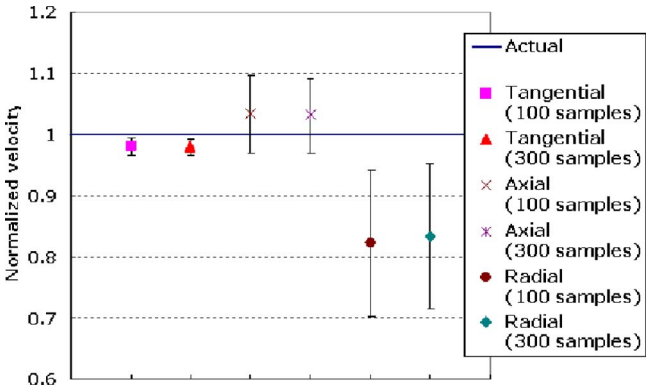

Fig. 4 PIV errors at a typical measurement point within the cavity

Downloaded 30 May 2010 to 128.113.26.88. Redistribution subject to ASME license or copyright; see http://www.asme.org/terms/Terms_Use.cfm

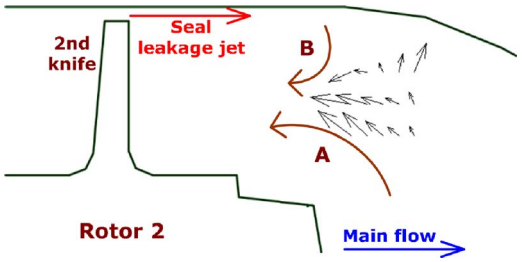

Fig. 5 Meridional view of time and pitchwise averaged velocity within the cavity

bias errors of tangential and axial velocities are about 2–3% while that of radial velocity is ~17%. The actual value of tangential velocity is slightly outside the uncertainty range, and that of axial velocity lies within the uncertainty range. The uncertainty levels of both velocities are about 2–6%. The actual value of radial velocity is outside the uncertainty range of ~12%. The error in radial velocity (or out-of-plane velocity) is larger than those of in-plane components (tangential and axial velocities), and this trend is consistent with the results reported in previous research [23]. Although the PIV error in radial velocity is larger than those of conventional probes, important flow features can still be captured.

Results and Discussion

The aim of this investigation is to clarify the kinematics of the flow within the shroud cavity of the second rotor. The flow features downstream of the second rotor are then examined.

Time- and Pitchwise-Averaged Features of the Cavity Flow. Figure 5 shows the meridional view of time- and pitchwise-averaged velocity field within the cavity. Signals could not be obtained above the shroud surface due to the reflection of the laser light. Therefore, time and pitchwise average has been taken in the region downstream of the trailing edge of the shroud. The most prominent feature found within the cavity is the radially outward and axially backward fluid motion. The fluid exiting the blade passage migrates radially outward into the shroud cavity and moves upstream toward the second seal knife (indicated as "A" in Fig. 5). At the upstream edge of the measured area near the casing, the fluid motion is radially inward and axially backward ("B" in Fig. 5). This motion originates from flow separation at the tip of the second seal knife. At the downstream edge of the measured area near the casing, the fluid resumes forward motion due to the interaction with the seal leakage flow. Though the seal leakage flow is not clearly captured because the measurement plane closest to the casing wall is 4 mm away from the wall, it can be hypothesized that there exists a thin-seal leakage layer above the measurement region adjacent to the casing wall.

Velocity triangles show time- and pitchwise-averaged azimuthal flow features. Figure 6(*a*) shows the axial evolution of velocity triangles in the uppermost measurement plane within the cavity (109% span). The flow gains positive axial momentum as it moves downstream. Absolute tangential velocities show underturned behavior, and the swirl level remains the same toward downstream. This underturning is due to the interaction of the cavity flow with the seal leakage flow.

Figure 6(*b*) shows velocity triangles of the cavity flow at three different spanwise locations at 0% axial chord from the trailing edge of the rotor. The flow closest to the main passage is still influenced by the radially outward and axially backward moving main flow with little swirl. However, the flow gains positive axial momentum and swirl due to the interaction with the seal leakage flow as it approaches the casing wall.

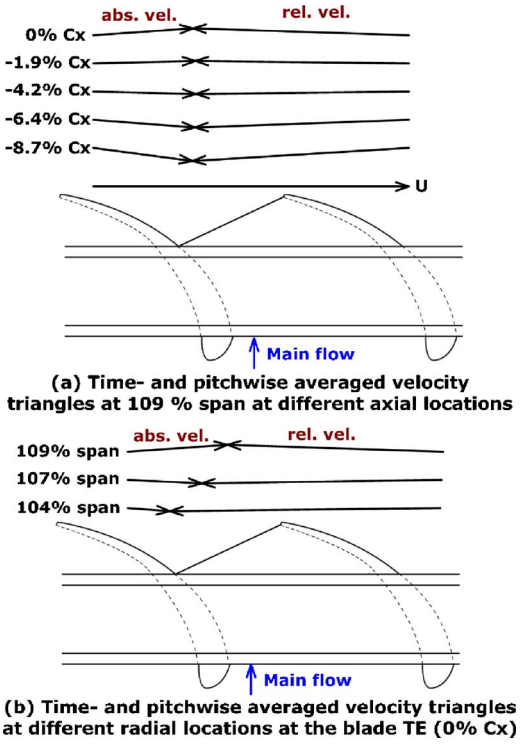

Fig. 6 Time and pitchwise averaged velocity triangles within the cavity

Upstream Stator Effect. Figure 7(*a*) shows the axial locations—–4% axial chord and 25.6% axial chord—where PIV and FRAP were respectively used to obtain time-averaged axial velocity fields. In the PIV measurement, the blade-passing period has been divided into ten time steps, and the time average has been taken with ten phase-locked averaged data sets. With FRAP, the time average has been taken with 109 phase-locked averaged data sets for a blade-passing period.

In the cavity (measured with PIV and shown in Fig. 7(*b*)), the reversed flow is still dominant. The seal leakage jet with positive axial velocity appears near the casing wall. Also, a pitchwise variation of the time-averaged axial velocity is visible, and the reversed flow is the strongest at midpitch. The pitchwise variation indicates the upstream stator's influence on the cavity flow for the following reason. The measurements of both PIV and FRAP have been done in the fixed frame, and time-averaging filters out the pitchwise variation due to the motion of the rotor. Thus, a pitchwise variation of parameters in the time-averaged results can be attributed only to fixed frame disturbances, such as the upstream stator.

At 25.6% axial chord downstream, no reversed flow is observed any more (Fig. 7(*c*)). Spanwise variation of axial velocity is similar to that within the cavity. The lowest axial velocity lies between 100% and 104% span. This indicates that the spanwise variation originates from the three layers near the shroud cavity—seal leakage jet, reversed cavity flow due to separation, and the main flow. Also, at 90% span, a pitchwise variation of the main flow is observed. The pitchwise location of the maximum velocity (0.5 pitch) of the main flow coincides with that of the minimum velocity of the cavity flow. The reason for this coincidence is explained later.

Effect of Partial Shroud Geometry. Figure 8 shows the pitchwise velocity profiles immediately downstream of the blade trailing edge within the cavity. The location where the data have been obtained is indicated in Fig. 8(*a*). The location has been selected because the data there show the most prominent pitchwise varia-

Downloaded 30 May 2010 to 128.113.26.88. Redistribution subject to ASME license or copyright; see http://www.asme.org/terms/Terms_Use.cfm

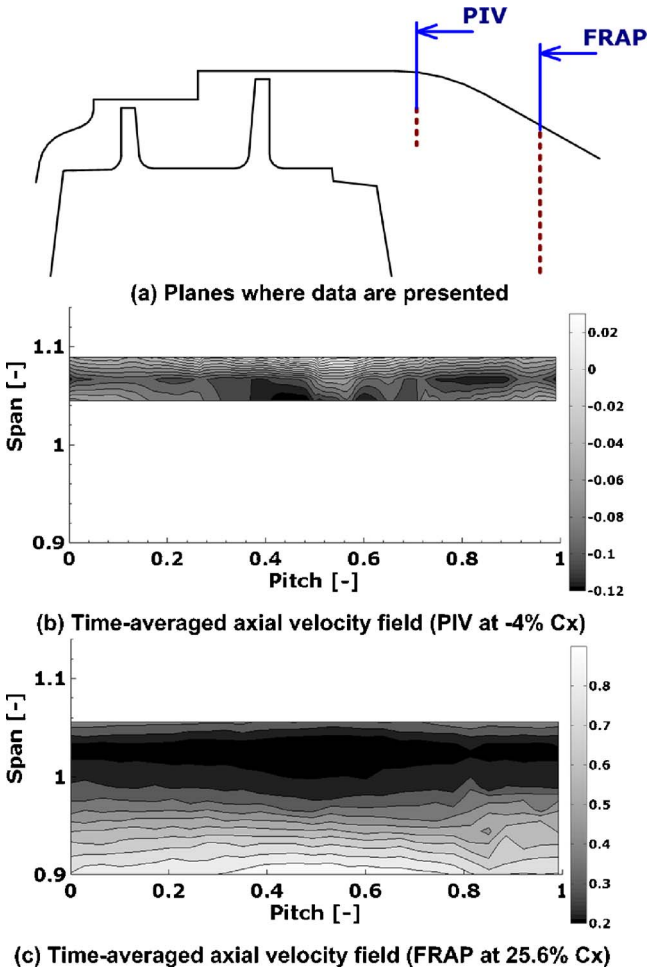

Fig. 7 Time-averaged axial velocity fields within and downstream of the cavity

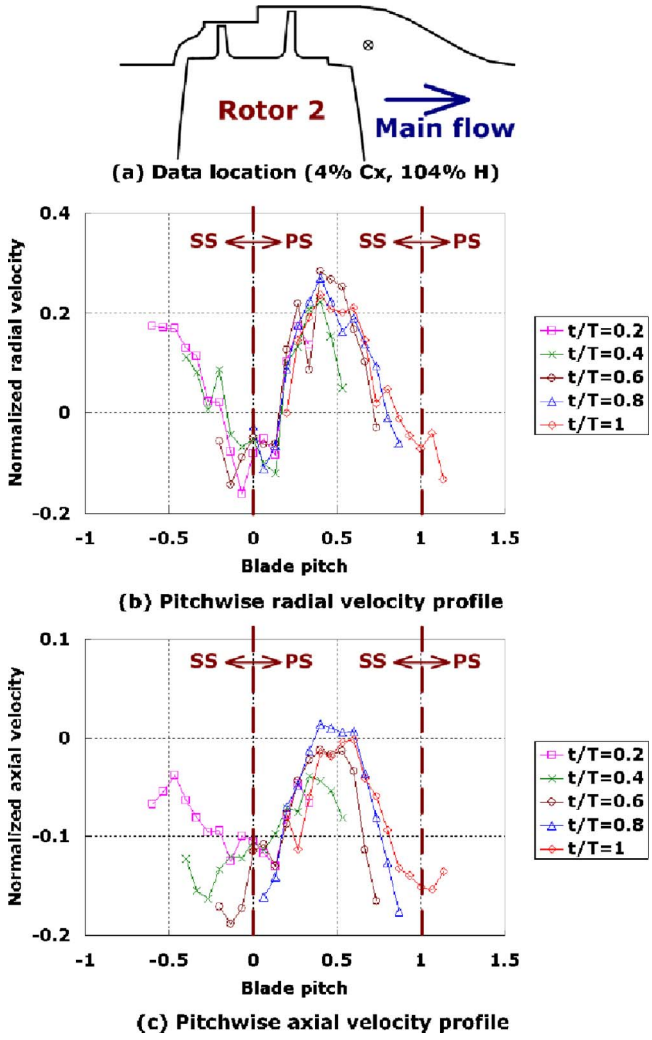

Fig. 8 Pitchwise velocity profiles downstream of the blade trailing edge within the cavity

tion. The data elsewhere show similar though weaker patterns. Pitchwise variations of normalized radial and axial velocities are plotted in Figs. 8(*b*) and 8(*c*), respectively. The velocities have been normalized by the axial velocity obtained by dividing the mass flow rate by the annulus area and density. Each velocity profile is a phase-locked average of 100 instantaneous data at each time step. In each plot, velocity profiles at five different time steps (t/T=0.2, 0.4, 0.6, 0.8, 1) have been plotted versus the rotor blade pitch. Because of relative motion between the optical window and the rotor, the location of measurement region relative to the rotor blade is different for each time step. Therefore, the velocity data in Fig. 8 have been adjusted so that their relative position to the rotor blade is the same. Overall, the velocity data collapse into one curve showing pitchwise variations of radial and axial velocities. These pitchwise variations are due to the shape of the partial shroud and rotate with the rotor.

In Fig. 8(*b*), the strongest radially outward motion of the main flow occurs at midpitch. The radially outward motion decays closer to the blades, and the flow becomes radially inward near the blades. Also the cavity flow has zero axial velocity at the midpitch location and negative axial velocity near the blades (Fig. 8(*c*)). The pitchwise profile of the axial velocity has the same phase as the radial velocity.

These flow patterns can be understood better by examining velocity field in meridional planes. Figure 9 shows the velocity fields in five meridional planes in one pitch within the cavity. Near the blades (Figs. 9(*b*) and 9(*f*)), the flow pattern is radially inward and axially backward. This pattern is nothing more than vortical

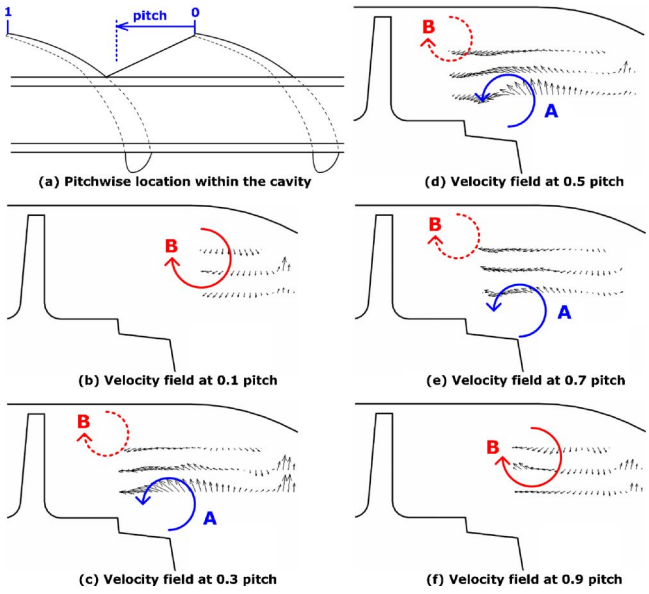

Fig. 9 Meridional velocity fields within the cavity

Downloaded 30 May 2010 to 128.113.26.88. Redistribution subject to ASME license or copyright; see http://www.asme.org/terms/Terms_Use.cfm

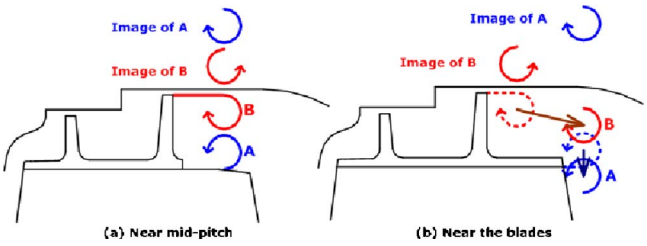

Fig. 10 Vortex interactions within the cavity

motion B (Fig. 5), which originates from flow separation at the tip of the seal knife. Near midpitch (Figs. 9(*c*)–9(*e*)), radially outward and axially backward motion (motion A in Fig. 5) is dominant within the cavity. Above the measured region, it can be hypothesized that motion B exists there but is located near the casing and the seal knife. Overall, motion B moves back and forth at a fixed tangential location while the blade rotates. Near the blades, motion A, which is weaker than the case at midpitch, does not appear. These motions of two vortical structures (motions A and B) can be explained in terms of vortex interactions shown in Fig. 10.

Below the inner surface of the shroud, the main flow exits the main passage while there is a dead flow zone above the outer surface of the shroud. Thus, the main flow is subject to a sudden area expansion and separates at the shroud trailing edge. The separated flow rolls up into vortex A. For a similar reason, the seal leakage flow separates at the tip of the seal knife and turns into vortex B. Both vortices affect each other (Fig. 10). Near midpitch (Fig. 10(*a*)), vortex B stays close to the adjacent seal knife due to the force induced by vortex A. The centers of each vortex are almost axially aligned so that a radial velocity on vortex A induced by other vortices is small. Near the blades (Fig. 10(*b*)), however, the axial extension of the shroud reaches the blade trailing edge. Thus, vortex A is located farther downstream than vortex B. In this case, the axially backward motion of B induced by A is much weaker than the axially forward motion induced by the image vortex of B. Therefore, vortex B moves farther downstream than at midpitch. Also, a radially inward velocity on A is induced by vortex B since the axial locations of both vortices are not aligned. Thus, vortex A is weakened or absent near the blades since vortex B suppresses the flow separation at the shroud trailing edge.

For this reason, the strongest radially outward motion of the flow takes place near midpitch (Fig. 8(*b*)). Also, near midpitch in Fig. 10(*a*), the radially outward motion with little axial motion due to vortex A is dominant. However, at the same location near the blades (Fig. 10(*b*)), the axially backward motion due to vortex B is prevalent. Thus, the pattern in Fig. 8(*c*) can be explained.

Generation of Axial Vorticity Within the Shroud Exit Cavity. In reality, fluid particles within the cavity do not move two-dimensionally (as shown in Fig. 9) but three-dimensionally. The path of fluid particles in A (Fig. 9) can be inferred by examining the absolute velocity fields in radial planes within the cavity (Fig. 11). Figures 11(*a*) and 11(*b*) show the phase-locked averaged velocity fields in the planes at 104% and 107% span, respectively, at a time step $t/T=0.8$. The data at $t/T=0.8$ have been chosen because the entire blade passage is visible through the optical window at this time step. Only the velocity data 4 mm apart from each other in the circumferential direction have been shown to enhance visibility. Fluid particles move radially outward and axially backward with little swirl in the plane at 104% span (encircled zone in Fig. 11(*a*)). Figure 11(*b*) shows that these particles gain swirl as they approach the casing wall by interacting with the underturned seal leakage flow and this motion corresponds to vortex A (Fig. 9). Downstream, fluid particles moving radially outward also gain swirl due to the interaction with the seal leakage

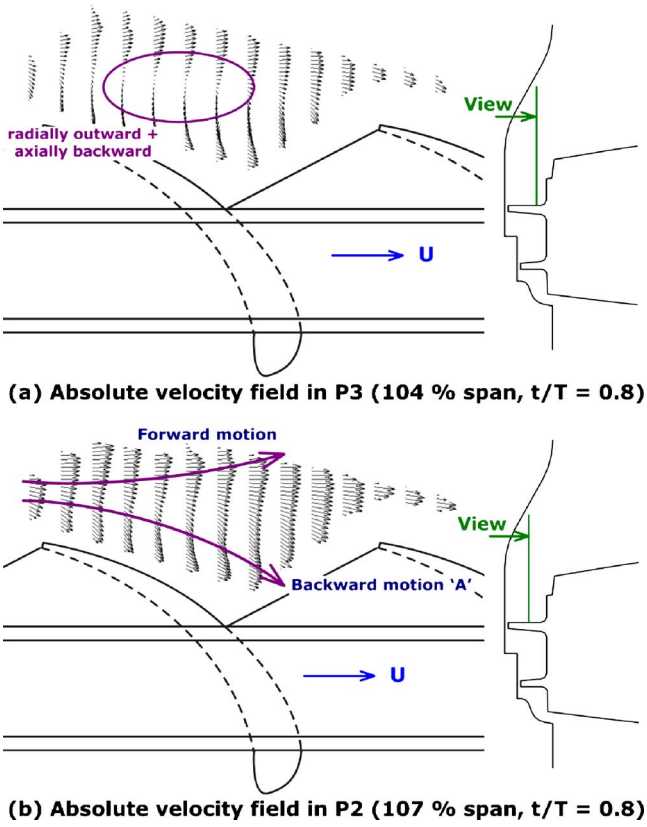

Fig. 11 Absolute velocity fields on blade-to-blade planes within the cavity

flow and then move downstream.

These three-dimensional flow features can be explained in terms of vorticity kinematics and an order of magnitude analysis. The axial, azimuthal, and radial directions are denoted by x_1, x_2, and x_3, respectively (Fig. 12). According to the PIV data in Fig. 11, the length scale along which the flow varies in the x_3 direction

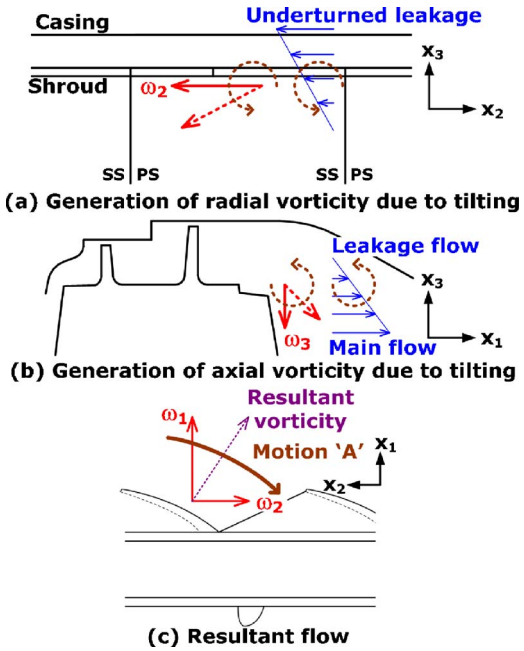

Fig. 12 Vorticity kinematics of the exit cavity flow

Downloaded 30 May 2010 to 128.113.26.88. Redistribution subject to ASME license or copyright; see http://www.asme.org/terms/Terms_Use.cfm

is much smaller than those in the x_1 and x_2 directions. The length scale in the x_1 and x_2 directions is approximately the blade pitch while that in the x_3 direction is the shear layer thickness, which is formed within the cavity as

$$x_1, x_2 \sim L \quad \text{where} \quad \delta \ll L \tag{1}$$

$$x_3 \sim \delta$$

Furthermore, the characteristic velocity in the x_1 and x_2 directions is the rotating speed,

$$u_1, u_2 \sim U \tag{2}$$

Thus, the orders of magnitude of each vorticity component can be estimated

$$\omega_1, \omega_2 \sim \frac{U}{\delta}$$

$$\omega_3 \sim \frac{U}{L} \tag{3}$$

The flows in the current investigation can be assumed to be incompressible because the Mach number at the exit of the rotor is 0.1 (Table 1). Thus, baroclinic effects can be neglected. Also, the flow has been observed in the fixed frame so that nonconservative forces, such as Coriolis force, can be neglected. Therefore, the vorticity equation is as follows:

$$\frac{D\omega_i}{Dt} = \omega_j \frac{\partial u_i}{\partial x_j} + \nu \frac{\partial^2 \omega_i}{\partial x_j \partial x_j} \tag{4}$$

where $i=1, 2, 3$.

With Eq. (3), the order of magnitude of each term of vorticity equation can be evaluated. Here, only the axial and tangential vorticity components $(i=1,2)$ are considered. The magnitude of the first term (tilting and stretching term) on the right hand side in Eq. (4) is approximately

$$\omega_j \frac{\partial u_i}{\partial x_j} \sim \frac{U^2}{\delta L} \tag{5}$$

The magnitude of the second term (viscous term) on the right hand side in Eq. (4) is

$$\nu \frac{\partial^2 \omega_i}{\partial x_1^2}, \quad \nu \frac{\partial^2 \omega_i}{\partial x_2^2} \sim \frac{1}{\mathrm{Re}} \frac{U^2}{\delta L} \tag{6}$$

$$\nu \frac{\partial^2 \omega_i}{\partial x_3^2} \sim \frac{1}{\mathrm{Re}} \frac{U^2}{\delta L} \left(\frac{L}{\delta} \right)^2 \tag{7}$$

The viscous terms in Eq. (6) are smaller than the tilting and stretching term Eq. (5) by a factor of 1/Re. In the current study, the Reynolds number is of an order of 10^5. Thus, Eq. (6) can be neglected compared to Eq. (5). The viscous term in Eq. (7) is larger than Eq. (6) by a factor of $(L/\delta)^2$. In the current case, $(L/\delta)^2 \sim 10^2$, and Eq. (7) is still three orders of magnitude smaller than Eq. (5). Thus, the viscous effects can be neglected and the vorticity field within the cavity is mainly dominated by tilting or stretching.

Figure 12 shows the main vortical features within the shroud cavity. As displayed in Fig. 10, flow separation due to a sudden area expansion gives rise to motion A near midpitch. This motion has a negative tangential vorticity component. As shown in Fig. 12(*a*), there is a radial gradient of tangential velocity between the underturned leakage flow and the main flow. If the vorticity is slightly tilted due to a perturbation such that it has a radial vorticity component, the radial vorticity becomes negative due to the tangential velocity gradient. In a meridional view (Fig. 12(*b*)), there is a radial gradient of axial velocity between the main flow and the axially retarded leakage flow. This velocity gradient tilts the negative radial vorticity such that a positive axial vorticity is generated. The resultant vorticity is shown in an azimuthal view (Fig. 12(*c*)). The vorticity has three components (the radial component is not shown in the figure), and the velocity field induced by this vorticity is consistent with motion A shown in Fig. 11. The generation of axial vorticity gives rise to additional secondary flow downstream of the rotor, and, eventually, increases loss.

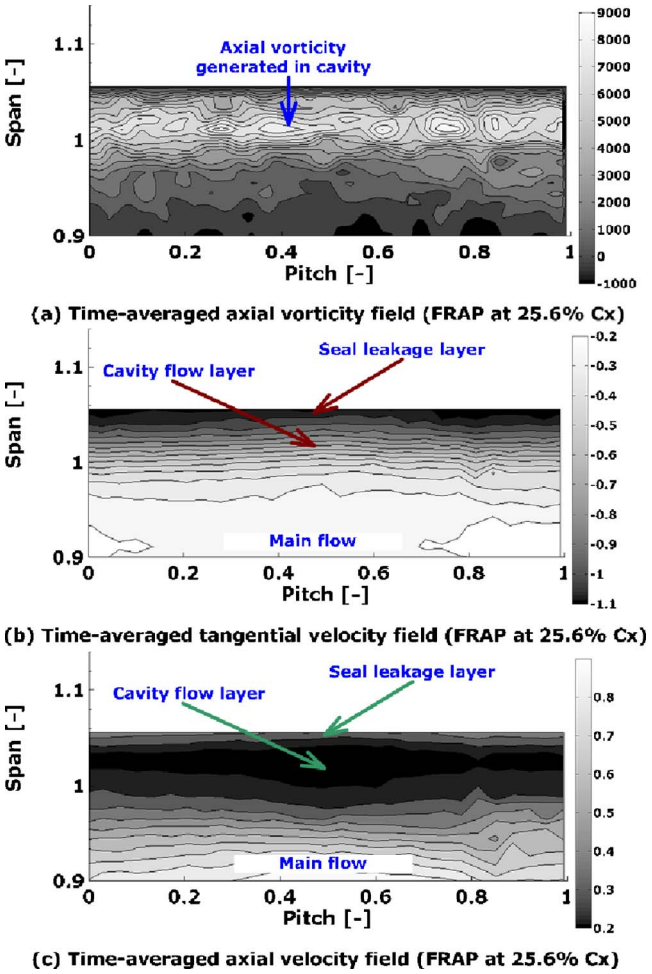

Fig. 13 Time-averaged flow velocities downstream of the shroud cavity

Downstream Flow Features. The axial vorticity discussed in the previous section can be observed farther downstream of the shroud cavity. Figure 13 shows time-averaged axial vorticity, axial and absolute tangential velocity fields at 25.6% axial chord downstream of the second rotor. The flow parameters have been obtained with FRAP. Between 100% and 102% span, there exists axial vorticity which originates from the flow within the cavity (Fig. 13(*a*)). Though this axial vorticity will eventually enhance mixing between the main flow and the seal leakage flow, there is still a clear division between the seal leakage layer and the main flow at this axial location. Between those two streams, there is a layer with different axial and tangential velocities from those of the leakage and main flows (termed cavity flow layer in Fig. 13). This feature is not clearly discernible in the tangential velocity field (Fig. 13(*b*)), where the seal leakage layer closest to the casing wall has the strongest swirl and the swirl gradually becomes weaker away from the casing wall. However, in the axial velocity field (Fig. 13(*c*)), the cavity flow layer, with the lowest axial velocity, between the main flow and the seal leakage layer is visible.

In classical shroud configurations (full shrouds and the casing wall recessed at 90 deg), the seal leakage jet is known to be dissipated inside the cavity before it exits the cavity [1]. Thus, it is

Downloaded 30 May 2010 to 128.113.26.88. Redistribution subject to ASME license or copyright; see http://www.asme.org/terms/Terms_Use.cfm

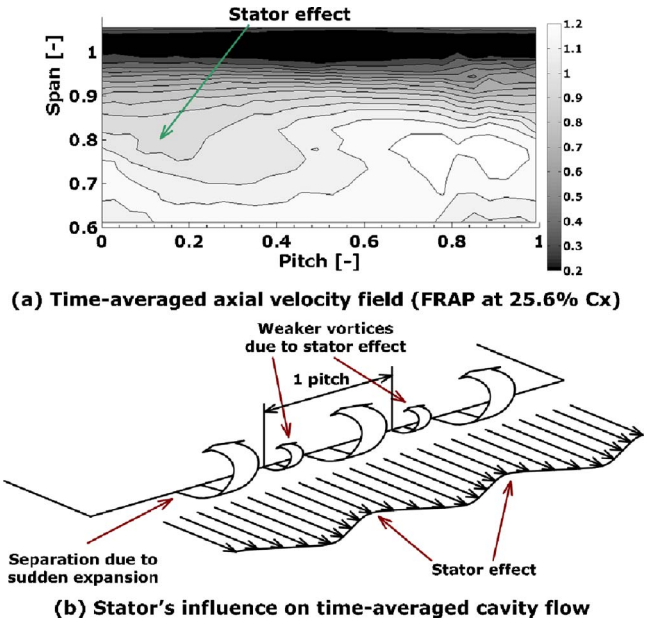

Fig. 14 Upstream stator effect on time-averaged cavity flow

commonly assumed that the flow downstream of such cavity has two layers—the seal leakage layer and main flow [7]. However, in the current investigation with a partial shroud and a contoured casing wall, the seal leakage jet remains at 25.6% axial chord downstream of the second rotor. The delay of dissipation is due to the contoured casing wall because it prevents direct impingement of the jet onto the cavity wall at the exit of the cavity and reduces the interaction of the leakage flow with the main flow [24].

Figure 14 presents an explanation for the coincidence between loci of the minimum axial velocity in the cavity layer and the maximum axial velocity of the main flow (Fig. 7). Figure 14(*a*) shows the time-averaged axial velocity field in the fixed frame in the same axial plane as that in Fig. 7(*c*) but covering a larger spanwise region. The axial momentum defect due to the upstream stator (wake and secondary flow) is visible at 80% span, and this can be simplified as a wake flow induced by the upstream stator. At the exit of the second rotor passage, the wake flow meets a sudden area expansion and separates. The flow with momentum defect rolls up into a weaker vortex, whereas that with higher momentum induces a stronger vortex (Fig. 14(*b*)). Thus, the pitchwise variation in the time-averaged cavity flow originates from the wake flow due to the upstream stator. The time-averaged flow field downstream of the second rotor can be simplified as a wake flow passing through a splitter plate (rotor shroud) above which no axial flow exists. Above the no axial flow zone closer to the casing wall, the seal leakage jet (not displayed in Fig. 14(*b*)) exists.

Conclusions

Detailed flow-field measurements have been carried out within and downstream of the exit shroud cavity in an axial, two-stage, partially shrouded turbine with a contoured casing wall. New conclusions from this investigation are as follows:

1. In the exit cavity, the radially outward motion of the main flow into the shroud cavity is the dominant flow feature. The radial migration of the main flow is induced by flow separation at the trailing edge of the shroud due to a sudden area increase.
2. The main flow entering the exit cavity divides into two streams. One stream moves upstream toward the adjacent seal knife and reenters the main flow stream. The other stream moves downstream due to the interaction with the thin-seal leakage flow layer. Fluid particles in both streams are entrained by the underturned seal leakage flow as they approach the casing wall, and thus gain swirl.
3. Because of the interaction between the vortex shed at the shroud trailing edge (A) and the vortex shed at the tip of the adjacent seal knife (B), the radially outward and axially backward motion is the strongest near midpitch while motion B is dominant within the cavity near the blades.
4. The vortical flow structures within the cavity are inviscid, and vorticity generation is mainly determined by vortex tilting. Because of this tilting mechanism, axial vorticity is generated within the cavity. The generation of axial vorticity gives rise to additional secondary flow downstream of the rotor, and, eventually, increases loss.
5. At 25.6% axial chord downstream of the second rotor, three layers—the seal leakage layer, cavity flow layer, and main flow—are distinctly visible. The seal leakage jet layer still exists at 25.6% axial chord downstream of the second rotor. The delay in the dissipation of the jet is due to the contoured casing wall.
6. The time-averaged flow feature downstream of the shroud cavity shows the upstream stator's influence on the cavity flow. The time-averaged main flow through the second rotor can be simplified as a wake flow that separates at the shroud trailing edge. This separation induces a pitchwise nonuniformity of the cavity flow layer.

Acknowledgment

The authors gratefully acknowledge Alstom Power Switzerland for their kind permission to publish the results. Y. I. Yun gratefully acknowledges support from the BK21 Project of the Korea Ministry of Education & Human Resources Development and Professor R. S. Abhari of the Swiss Federal Institute of Technology Zurich, Switzerland. He would also like to thank Dr. T. Kim at Xian Jiaotong University, China, for his helpful comments.

Nomenclature

C_x = axial chord length of the rotor blade
H = rotor blade span
L = blade pitch
LE = leading edge
PS = pressure side
Re = Reynolds number
SS = suction side
t = time
T = blade-passing period
TE = trailing edge
U = rotor speed
u = velocity
x = spatial variable
δ = shear layer thickness
ν = kinematic viscosity
ω = vorticity

Subscripts

1 = tangential direction
2 = axial direction
3 = radial direction

References

[1] Denton, J. D., 1993, "Loss Mechanisms in Turbomachines—The 1993 IGTI Scholar Lecture," ASME J. Turbomach., **115**(4), pp. 621–656.
[2] Hunter, S. D., and Manwaring, S. R., 2000, "Endwall Cavity Flow Effects on Gaspath Aerodynamics in an Axial Flow Turbine—Part I: Experimental and Numerical Investigation," ASME Paper No. 2001-GT-651.
[3] Wallis, A. M., Denton, J. D., and Demargne, A. A. J., 2001, "The Control of Shroud Leakage Flows to Reduce Aerodynamic Losses in a Low Aspect Ratio, Shrouded Axial Flow Turbine," ASME J. Turbomach., **123**(2), pp. 334–341.
[4] Peters, P., Breisig, V., Giboni, A., Lerner, C., and Pfost, H., 2000, "The Influence of the Clearance of Shrouded Rotor Blades on the Development of the

Downloaded 30 May 2010 to 128.113.26.88. Redistribution subject to ASME license or copyright; see http://www.asme.org/terms/Terms_Use.cfm

Flowfield and Losses in the Subsequent Stator," ASME Paper No. 2000-GT-478.
[5] Giboni, A., Menter, J. R., Peters, P., Wolter, K., Pfost, H., and Breisig, V., 2003, "Interaction of Labyrinth Seal Leakage Flow and Main Flow in an Axial Turbine," ASME Paper No. GT2003-38722.
[6] Giboni, A., Wolter, K., Menter, J. R., and Pfost, H., 2004, "Experimental and Numerical Investigation Into the Unsteady Interaction of Labyrinth Seal Leakage Flow and Main Flow in a 1.5-Stage Axial Turbine," ASME Paper No. GT2004-53024.
[7] Song, B. H., and Song, S. J., 2004, "Lateral Forces From Single Gland Rotor Labyrinth Seals in Turbines," ASME J. Eng. Gas Turbines Power, **126**(3), pp. 626–634.
[8] Pfau, A., Treiber, M., Sell, M., and Gyarmathy, G., 2001, "Flow Interaction From the Exit Cavity of an Axial Turbine Blade Row Labyrinth Seal," ASME J. Turbomach., **123**(2), pp. 342–352.
[9] Pfau, A., Schlienger, J., Rusch, D., Kalfas, A. I., and Abhari, R. S., 2005, "Unsteady Flow Interactions Within the Inlet Cavity of a Turbine Rotor Tip Labyrinth Seal," ASME J. Turbomach., **127**(4), pp. 679–688.
[10] Pfau, A., Kalfas, A. I., and Abhari, R. S., 2004, "Making Use of Labyrinth Interaction Flow," ASME Paper No. GT2004-53797.
[11] Wolter, K., Peters, P., Giboni, A., Menter, J. R., and Pfost, H., 2005, "Experimental and Numerical Investigation of the Unsteady Leakage Flow Through the Rotor Tip Labyrinth of a 1.5-Stage Axial Turbine," ASME Paper No. GT2005-68156.
[12] Porreca, L., Behr, T., Schlienger, J., Kalfas, A. I., Abhari, R. S., Ehrhard, J., and Janke, E., 2005, "Fluid Dynamics and Performance of Partially and Fully Shrouded Axial Turbines," ASME J. Turbomach., **127**(4), pp. 668–678.
[13] Porreca, L., Hollenstein, M., Kalfas, A. I., and Abhari, R. S., 2007, "Turbulence Measurements and Analysis in a Multi-Stage Axial Turbine," AIAA J. Propul. Power, **23**(1), pp. 227–234.
[14] Porreca, L., 2007, "Aerothermal Optimization of Partially Shrouded Axial Turbines," ETH Ph.D. dissertation N. 17138, Swiss Federal Institute of Technology, Zurich.
[15] Porreca, L., Yun, Y. I., Kalfas, A. I., Song, S. J., and Abhari, R. S., 2006, "Investigation of 3D Unsteady Flows in a Two-Stage Shrouded Axial Turbine Using Stereoscopic PIV and FRAP—Part I: Interstage Flow Interactions," ASME Paper No. GT2006-90752.
[16] Westerweel, J., Dabiri, D., and Gharib, M., 1997, "The Effect of a Discrete Window Offset on the Accuracy of Cross-Correlation Analysis of Digital PIV Recordings," Exp. Fluids, **23**(1), pp. 20–28.
[17] Scarano, F., and Riethmuller, M. L., 1999, "Iterative Multigrid Approach in PIV Image Processing With Discrete Window Offset," Exp. Fluids, **26**(6), pp. 513–523.
[18] Westerweel, J., 1994, "Efficient Detection of Spurious Vectors in Particle Image Velocimetry," Exp. Fluids, **16**(3-4), pp. 237–247.
[19] Soloff, S. M., Adrian, R. J., and Liu, Z-.C., 1997, "Distortion Compensation for Generalized Stereoscopic Particle Image Velocimetry," Meas. Sci. Technol., **8**(12), pp. 1441–1454.
[20] Prasad, A. K., 2000, "Stereoscopic Particle Image Velocimetry," Exp. Fluids, **29**(2), pp. 103–116.
[21] Yun, Y. I., 2006, "Axial Vorticity in the Cavity of a Partially Shrouded Axial Turbine," Ph.D. thesis, Seoul National University, Seoul.
[22] Raffel, M., Willert, C. E., and Kompenhans, J., 1998, *Particle Image Velocimetry—A Practical Guide*, Springer-Verlag, Berlin.
[23] Lawson, N. J., and Wu, J., 1997, "Three-Dimensional Particle Image Velocimetry: Error Analysis of Stereoscopic Techniques," Meas. Sci. Technol., **8**(8), pp. 894–900.
[24] Schlienger, J., Pfau, A., Kalfas, A. I., and Abhari, R. S., 2003, "Effects of Labyrinth Seal Variation on Multistage Axial Turbine Flow," ASME Paper No. GT2003-38270.

Downloaded 30 May 2010 to 128.113.26.88. Redistribution subject to ASME license or copyright; see http://www.asme.org/terms/Terms_Use.cfm

Experimental Validation of Quasisteady Assumption in Modeling of Unsteady Film-Cooling

Stefan Bernsdorf
MAN TURBO,
Hardstrasse 319,
CH-8023 Zürich, Switzerland

Martin G. Rose

Reza S. Abhari

Institute of Energy Technologies,
Department of Mechanical Engineering,
Swiss Federal Institute of Technology-ETHZ,
CH-8092 Zürich, Switzerland

This paper reports on the validation of the assumption of quasisteady behavior of pulsating cooling injection in the near hole flow region. The respective experimental data are taken in a flat plate wind tunnel at ETH Zürich. The facility simulates the film cooling row flow field on the pressure side of a turbine blade. Engine representative nondimensionals are achieved, providing a faithful model at a larger scale. Heating the free stream air and strongly cooling the coolant gives the required density ratio between coolant and free-stream. The coolant is injected with different frequency and amplitude. The three-dimensional velocities are recorded using nonintrusive PIV, and seeding is provided for both air streams. Two different cylindrical hole geometries are studied, with different angles. Blowing ratio is varied over a range to simulate pressure side film cooling. The general flow field, the jet trajectory, and the streamwise circulation are utilized in the validation of the quasisteady assumption. [DOI: 10.1115/1.2720878]

Keywords: film cooling, unsteady, modeling, density ratio, blowing ratio, PIV

Introduction

The main interest in the improvement of the film cooling, other than that of increased TET for better thermal efficiency, is better control of turbine blade lives. Blade life is an important economic parameter in the aero and industrial gas turbine business. The hot gas temperature and the cooling system principally determine the life of the turbine blades, resulting in a strong argument for the industry to engage in film cooling research.

A new experimental facility has been constructed at ETH Zürich. It has two main goals. First, to determine a better understanding of the physics involved in film cooling and the influence of the numerous flow parameters. Enhanced understanding will facilitate cooling development and design innovation. Second, the experimental results obtained with this facility are used to calibrate the novel *Burdet*-film-cooling model that has recently been implemented into the LSM-internal flow solver MULTI3, as presented in Burdet et al. and Burdet [1,2].

As designed, a large range of independent flow parameters can be adjusted in this unique facility. Geometrical, flow, and thermal conditions all cover the typical conditions of a turbine pressure side to a great extent.

The exchangeable cooling hole geometry is scaled up to a 5 mm diameter, while nondimensional spacing and length to diameter ratio are preserved. Arrangement of the holes in single and double arrays is possible. The holes can be cylindrical or shaped, with streamwise angle in the range from 20 to 90 deg and any lateral angle. This paper presents the results of two geometrical cases with a single array of 7 holes of constant diameter, length, and spacing. The variation is in the streamwise angle between 30 and 50 deg.

The governing flow conditions are Mach number M, density ratio DR, blowing ratio BR or momentum flux ratio IR. Additionally, the turbulence intensity Tu and the momentum thickness θ have a significant influence on the film cooling behavior. This paper presents the results of film cooling with variation in BR and DR.

Thermal management allows the independent adjustment of three temperature levels. The main flow is heated (120°C max), the secondary flow is cooled (−50°C min), and the test surface is temperature controlled (15–30°C) by internal cooling, effectively creating an isothermal boundary condition.

The importance of unsteady interaction between cooling jet and main flow has been reported previously by different researchers [2–15]. In recent publications the modeling of unsteady film cooling with CFD has used the assumption of quasisteady behavior of the near hole flow field (i.e., Burdet et al., Burdet [1,2]). A quasisteady behavior is defined here as the state where the steady flow equals the phase average and phase resolved flow with comparable flow condition present.

This facility offers the unique possibility to validate this assumption. The obtained steady and unsteady data sets with similar flow conditions are compared regarding different aspects of the respective flow field.

Previous Research

Extensive research was conducted in the field of steady film cooling, as outlined by Bernsdorf et al. [16]. It has been recognized, that unsteady effects do play a significant role in the film cooling performance, but the respective research is rather limited, as it is more expensive and time-consuming. Dunn and Dunn et al. [8,9] measured in a real turbine to capture the entire effect of unsteadiness on the film cooling effectiveness. Jung et al. [12,13] and Lee et al. [14] created a slow pulsation of the main flow with rotating vanes at the plenum exit and measured the heat transfer and film cooling effectiveness. Some flow visualization was performed as well [12]. Heidmann et al. [11] simulated the passing wakes and also presented a model. Phase averaged data were compared here. The suggestion for more detailed investigation of the flow was made. Bons [7] created pulsation of the injectant by means of a speaker. The averaged film cooling effectiveness was measured. Ligrani et al. [15] also pulsated the main flow with

Contributed by the International Gas Turnine Institute of ASME for publication in the JOURNAL OF TURBOMACHINERY. Manuscript received September 11, 2006; final manuscript received October 30, 2006; published online January 28, 2008. Review conducted by David Wisler. Paper presented at the ASME Turbo Expo 2006: Land, Sea and Air (GT2006), May 8–11, 2006, Barcelona, Spain, Paper No. GT2006-90166.

Downloaded 30 May 2010 to 128.113.26.88. Redistribution subject to ASME license or copyright; see http://www.asme.org/terms/Terms_Use.cfm

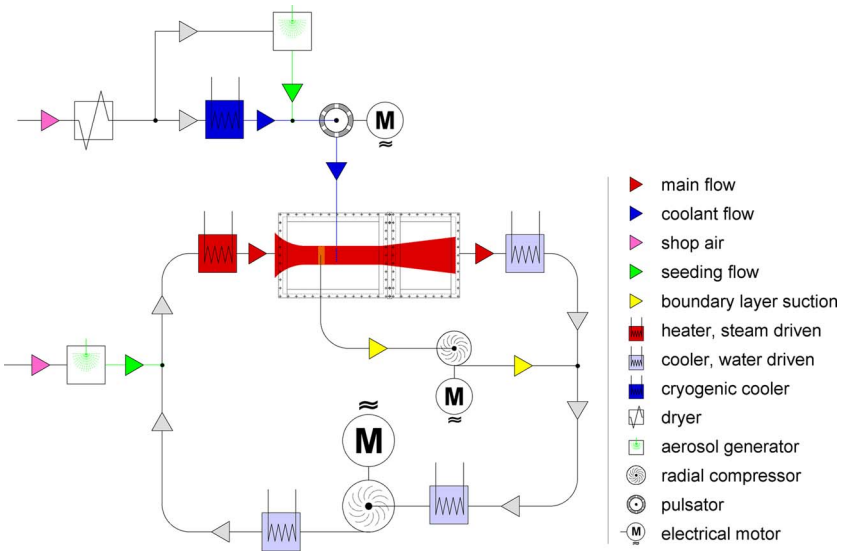

Fig. 1 Schematic of the test rig

rotating vanes. Film cooling effectiveness was measured and flow visualization was performed. Velocity traces got extracted from this data as well.

Altogether, these experiments looked into the thermal properties associated with unsteady film cooling. The data was mostly phase averaged while some provide time resolved information. No experiments to the best knowledge of the authors measure the detailed velocity field.

Modeling of unsteady film cooling was done. The models of Abhari [3,4] and Burdet [1,2] assume a quasisteady behavior of the periodic injection. This assumption has not been verified so far. The data presented here offer the unique opportunity to investigate that assumption regarding its validity.

Test Facility

The film cooling test rig, as shown in Fig. 1, is based on a former supersonic calibration facility. It consists of four major sections supported by a custom made monitoring system. The rig is designed to be operated with different measurement techniques. At present a stereoscopic PIV system is implemented.

The rig's operating range is given in Table 1 together with the respective range in real pressure side film cooling.

Mainflow. A centrifugal compressor of 297 mm diameter, driven by a 470 kW electrical motor, creates the main flow in the experimental closed loop facility. The impeller is taken from an ABB VTC 254 turbocharger. The gearbox and periphery are custom made for the application. The pressure in the system is self-adjusting by a small blowout valve. The resulting pressure level in the test section is around the ambient pressure level.

Temperature is controlled with a water-cooled heat exchanger downstream of the compressor, while a second cooler is installed just upstream of the impeller intake for its protection against overheating. That configuration allows a temperature range from 18°C to 40°C in the free stream. A steam-air heat exchanger is installed upstream of the test section to raise the main flow temperature up to 120°C. This 200 kW heat exchanger is fed by 7 bar saturated steam from the house heating system. The heater is controlled with a feedback control loop. The heat is extracted from the main flow downstream of the test section by a water-cooled heat exchanger.

Table 1 Capabilities of new test facility

	Typical conditions of pressure side film cooling	Capabilities of new test rig
DR	1–1.8	1–1.6
BR	0.8–4	0.5–3
IR	0.9–2	0.1–5
M	0.3–0.8	0.1–0.64
f_r	1–3	0–2.5

The pipe work containing the main flow is suspended from the ceiling to allow thermal expansion of the steel piping. Additionally, a compensator replaces a section of the pipe to allow angular and lateral displacement of the pipe without causing damage. The hot section of the test rig, between the steam heater and the water cooler, is wrapped in 30 mm thermal insulation sheets and the test section is thermally decoupled from the ambient by ceramic insulators.

The rotational speed of the impeller determines the pressure ratio and with that the resulting mass flow rate in the system. At its maximum speed of 30,000 rpm the compressor can deliver up to 4 kg/s. At present, the maximum mass-flowrate required is at about 1.5 kg/s, for a free stream Mach number of $M=0.5$.

The boundary layer thickness of the main flow is controlled by a suction arrangement, equivalent to starting the boundary layer at $L=0.49$ m upstream of the cooling hole center. A centrifugal blower drives the boundary layer suction, extracting through 327 discrete holes of 1.2 mm diameter stacked in 11 arrays over an area of 60×180 mm. The extracted air is fed back into the loop far downstream of the cooler. The maximum capacity of the suction is about 50 g/s and is adjusted with a hand valve.

Oil aerosol is blown from the seeding generator into the main flow upstream of the heater during PIV measurements.

Cooling Flow. The secondary flow is delivered by the shop air system with a maximum of 75 g/s. First a drier lowers the dew point of the air to −70°C. Two cylinders filled with water absorbing solid particles are alternately drying the air and recuperating inside that drier. Next in line is a fast acting self-controlling pressure control valve, followed by a mass flow measurement section. Downstream is a single cycle cooler, capable of reducing the temperature down to −63°C at the cooler exit. The 12 m piping connecting the cooler and the primary wind tunnel is wrapped in 40 mm insulation. A seeding generator containing 5 arrays of Laskin nozzles adds an oil aerosol 1.5 m upstream of the injection location.

Downloaded 30 May 2010 to 128.113.26.88. Redistribution subject to ASME license or copyright; see http://www.asme.org/terms/Terms_Use.cfm

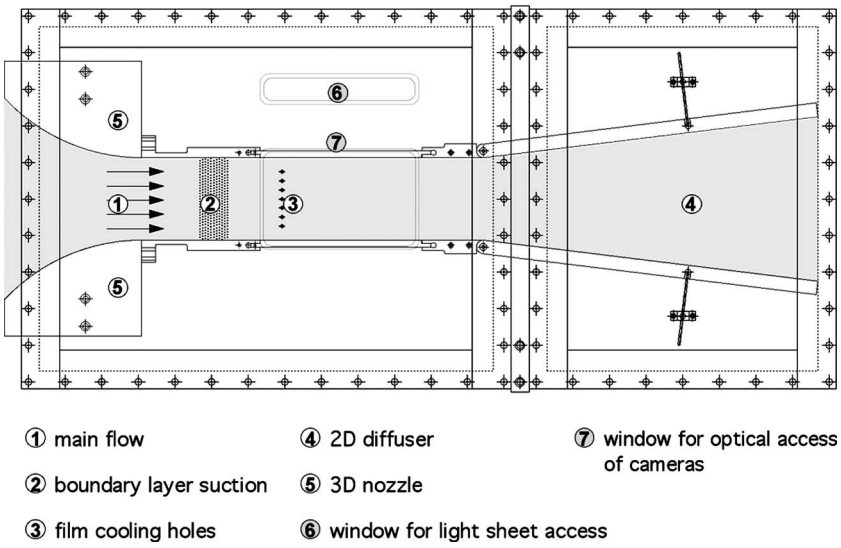

Fig. 2 Sketch of the test section

Test Section. The test section has a rectangular flow path of 40×181 mm cross section. A schematic is shown in Fig. 2. A 3D nozzle accelerates the flow coming from the settling chamber. The area of main interest is the injection site of the secondary flow in a range from $5d$ upstream to $35d$ downstream of the origin of coordinates (see Fig. 3). The injection is via a pulsator that modulates the coolant mass flow rate. This allows the variation of coolant pulsation frequency between 0 Hz and 1 kHz. A detailed description of this device can be found at Bernsdorf [6]. 15 mm glass walls on three sides provide optical access. The top and the bottom wall allow access of the light sheet. The light sheet is introduced to the system from the front, via the top window and a 45 deg mirror (see Fig. 4). The two cameras look into the test section through the front window. Downstream of the injection site is a 2D diffusor to recover some of the dynamic pressure.

The definition of the coordinate system and of the relevant geometrical parameters is illustrated in Fig. 3.

The origin of the coordinate system as used in all results presented is in the center of the middle hole, irrespective of geometry. The two different geometries presented in this paper are defined in Table 2.

PIV System. The PIV system utilized in this project is a commercially available stereoscopic system. 2 CCD cameras with a resolution of 1280×1024 pixel and a dynamic range of 12 bit are mounted on a 2-axis high accuracy traverse system, as shown in Fig. 5. The double pulsed Nd:YAG Laser with 120 mJ power per pulse and a maximum repetition rate of 10 Hz is mounted on an additional third traverse axis. The light sheet optics, which is connected directly with the laser, creates a light sheet in *XY*-orientation with variable thickness. The path of the light sheet inside the test section is illustrated in Fig. 4.

The cameras and the laser head are mounted on a massive cast iron table, as shown in relation to the test section in Fig. 5. Simultaneous traversing of the laser in vertical direction (Z_{laser} in Fig. 5) with traversing of the cameras in the horizontal direction

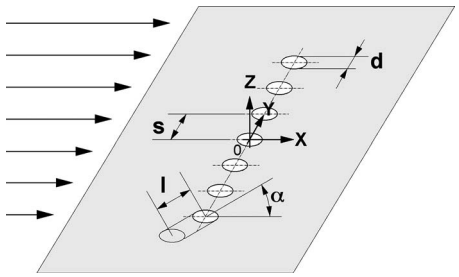

Fig. 3 Definition of the coordinates and dimensions

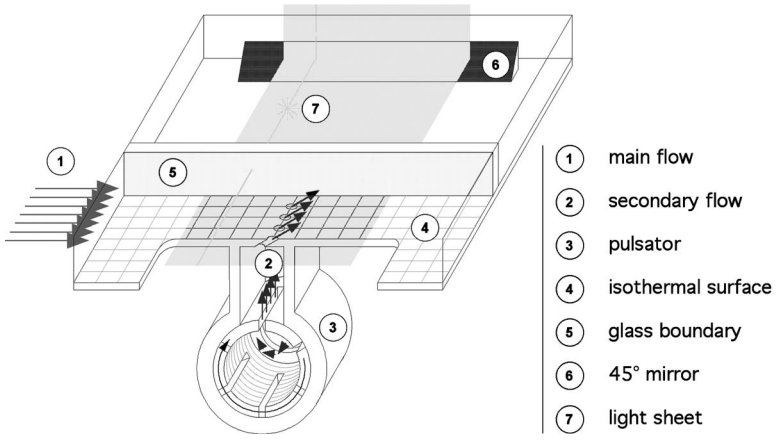

Fig. 4 Schematic of the injection arrangement

Downloaded 30 May 2010 to 128.113.26.88. Redistribution subject to ASME license or copyright; see http://www.asme.org/terms/Terms_Use.cfm

Table 2 Definition of geometry

geometry	d	No. f_{holes}	s/d	l/d	α
i	5 mm	7	4	2.8	30 deg
ii	5 mm	7	4	2.8	50 deg

($Z_{cameras}$ in Fig. 5) allows the scanning of the flow volume in the Z direction without the need of recalibration for every light sheet position.

The system also consists of two linked computers. The first computer is a specialized device containing the frame-grabber cards and the unit to synchronize the cameras, the laser and the trigger signal of the pulsator. It also functions as a data buffer between the second computer and the cameras. The second computer is a standard PC with 2TB of hard disk to store the results. This computer runs the PIV software package, which controls the first computer, organizes the data, and finally processes it.

Measurement Procedure

The conduction of a measurement series consists of two main parts. First, the flow parameters are adjusted with the aid of the real-time monitoring system. 40 primary data channels (pressure, temperature, frequency, and mass flow) are acquired directly from their corresponding sensors. These are written to file together with 10 derived flow parameters. The most relevant parameters like main flow Mach number, blowing ratio, and density ratio are shown online, thus allowing their fast and accurate adjustment. The warm up of the entire system can take up to 3 h, depending mainly on the density ratio chosen.

Secondly the flow velocities are measured using the PIV system. This includes a whole series of steps, starting with the setup of the cameras and the laser, going on to the calibration and error assessment, over to the actual measurement, and ends with the data processing.

The PIV system is used with two cameras at different angles to the test surface. Double pictures separated by a time step of 2.5 μs are taken throughout all experiments. The field of view of a camera is around 45 mm$\times$36 mm. The corresponding displacement between the two frames of a seeding particle travelling with the free stream main flow velocity of 110 m/s is close to 8 pixels.

The setup is the critical step in the PIV measurement, determining the quality and reliability of the final results. The cameras are adjusted so they look at the same area of the flow. Then they are focused and the light sheet is adjusted to be parallel to the XY-coordinates of the flow and to have a defined thickness of 1 mm. The three traverse axes are adjusted to be parallel to the X, Y, and Z-axis, respectively.

The calibration is performed with the aid of a single layer calibration target, consisting of a flat black plate with white points. The target is placed into the test section parallel to the XY-plane. The points are arranged in a 2D array of constant spacing and have three different sizes. The difference in size defines the centre of the target and the orientation. Both cameras take pictures of that target in 5 defined distances orthogonal to the target. The PIV software detects the points and determines a linear transformation matrix for each camera. This matrix allows the transformation of the pictures taken in the respective orientation of each camera into the flow coordinate system. Furthermore, the two matrices allow the transformation of the two 2D-vector fields, derived from each camera, into one vector field in the XY-plane with 3D-flow vectors.

Establishing the measurement accuracy (from raw picture to a 3D-vector field) is done with the aid of two simple experiments. Sandpaper is placed onto the test surface and lit in a diffuse way. The cameras are then traversed relative to the sandpaper while taking the double picture. The software is set in a way that the displacement between the double pictures corresponds to a velocity of 100 m/s in one direction and 0 m/s in the two other directions, thus creating a virtual and defined velocity field. The results show that the error for the U and the V-component is of the order of 1% of the virtual free stream velocity (U=100 m/s) while the error for the W component was about 5%.

In order to reduce the effect of reflection from the background 30 double frames are shot for each condition. A mean pixel value of those 30 double frames is determined after the measurement. The mean pixel is subtracted from every double frame, thus eliminating the background reflection.

The final cross-correlation on every single frame is performed with 32$\times$32 pixel interrogation windows to obtain a vector field. Further features used in the correlation are 50% overlap of the areas, a 1-step iterative refinement of the interrogation area with deforming windows, high accuracy subpixel refinement, and a peak validation with a ratio between the minimum peak height and the peak 2 of 1.1. A local moving average validation over 3$\times$3 vectors with an acceptance factor of 0.1 is chosen as local neighborhood validation. A Gaussian weighting function is applied to each interrogation area to deal with the particles at the border of the interrogation area. A detailed description of the options used can be found in the software manual [17].

The mean phase-resolved vector field over all 30 samples is determined for each camera in the next step. The 3D conversion is done with the two mean vector fields, thus giving a 2D plane in XY-orientation with averaged 3D velocity information.

The flow field is scanned in the Z-direction in increments of 1–3 mm. All resulting planes are combined in a flow volume containing the 3 component flow vectors as well as a number of derivatives like flow angle, vorticity, and shear stress. The flow volume consists of 10–12 planes with 79$\times$63 vectors, giving a total number of roughly 50,000–60,000 data points.

The pulsating cycle is resolved in 12 steps, triggered by a digital signal from the pulsator.

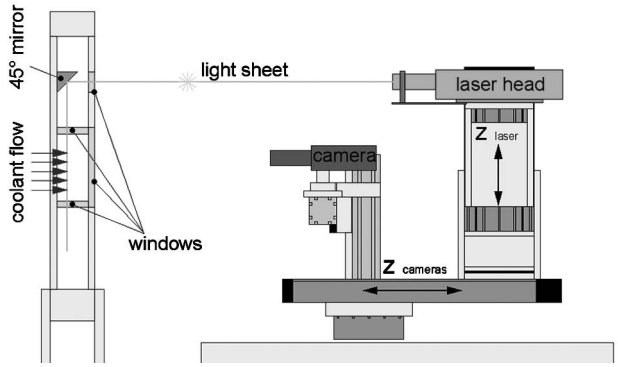

Fig. 5 Mounting of the PIV system

Flow Conditions

All results presented here are averaged over 20–30 double frames. The respective experiments were performed under steady flow conditions. The flow conditions of the different experiments are defined by the main flow Mach number M, the density ratio DR, the blowing ratio BR, the momentum flux ratio IR, the reduced frequency f_r based on the distance from the start of the boundary layer (or alternatively f_d based on the hole diameter) and the streamwise injection-angle α. The main flow boundary layer is defined by the momentum thickness θ and the shape factor H. An overview is given in Table 3.

The parameters are defined globally. The momentum thickness was quantified before the PIV measurement campaign with a 3 hole pneumatic probe at the location of the hole. The momentum thickness, nondimensionalized by the hole diameter, has a con-

Downloaded 30 May 2010 to 128.113.26.88. Redistribution subject to ASME license or copyright; see http://www.asme.org/terms/Terms_Use.cfm

Table 3 Parameters of experiments

Case	α	M	BR	DR	IR	f_r	f_d
1	30 deg	0.30	0.99	1.02	0.97	0	0
2	30 deg	0.30	0.99	1.53	0.65	0	0
3	30 deg	0.30	2.00	1.07	3.76	0	0
4	30 deg	0.30	2.04	1.66	2.51	0	0
5	30 deg	0.30	2.69	1.12	6.50	0	0
6	30 deg	0.30	2.69	1.73	4.19	0	0
7	50 deg	0.30	1.00	1.01	1.00	0	0
8	50 deg	0.30	2.00	1.06	3.78	0	0
9	50 deg	0.30	1.00	1.48	0.68	0	0
10	50 deg	0.31	2.01	1.60	2.56	0	0
11	30 deg	0.30	1.00	1.01	1.01	0.38	0.002
12	30 deg	0.30	2.00	1.06	3.78	0.38	0.002
13	30 deg	0.30	1.98	1.05	3.74	1.88	0.011
14	50 deg	0.30	1.00	1.01	1.00	1.88	0.011

stant value of $\theta=0.051$, with a shape factor of $H=2.3$. The velocity profiles show good correspondence to the 1/7-power approximation for turbulent boundary layers.

The density of the main flow is derived from the pressure and temperature taken just upstream of the cooling holes. The velocity of the main flow is derived from its directly measured mass flow rate, the cross section of the main flow area, and the aforementioned density. The density of the coolant flow is derived from the pressure and temperature taken in the plenum upstream of the cooling holes. The velocity of the coolant flow is derived from its directly measured mass flow rate, the total cross section of all cooling holes, and the aforementioned density. With that the above stated parameters BR, DR, and IR are defined. The main flow Mach number is derived from the velocity and the speed of sound, derived from the main flow temperature.

All parameters presented in the following analysis are nondimensionalized. The velocities are nondimensionalized with the respective free-stream velocity U_f and all length scales are nondimensionalized with the hole diameter d. All derived parameters are based on nondimensional values.

General Flow Field

The knowledge about the blowing ratio variation offers the opportunity to validate the thesis of a quasisteady near hole flow field. The static pressure variation in the plenum between pulsator and cooling hole is proportional to the variation of the blowing ratio, assuming a constant discharge coefficient and no loss of total pressure. The such obtained ensemble averaged BR variation for the two reduced frequencies investigated is shown in Fig. 6.

One phase (from 0 to 1) is resolved in 12 equal steps, indicated by the vertical lines in Fig. 6. The BR-shape of the BR-variation was subsequently confirmed by integration in the flow field [6]. The coupling of pulsation frequency and amplitude is clearly visible.

Comparisons between different measurements are made in two different ways in the following section. A visual comparison between the respective flowfields is achieved with respective figures, where the contours indicate the level of the axial velocity component and vectors indicate the in-plane velocity component V^*. The quality of this comparison is established with the correlation coefficient k, defined as

$$k = \frac{\sum \mathbf{u}_1 \cdot \mathbf{u}_2}{\sqrt{\sum |\mathbf{u}_1|^2 \sum |\mathbf{u}_2|^2}}$$

where the sum over all points in the displayed plane of scalar products of two measurements is normalized by the product of the sum of normed vectors. The subscript identifies the measurement the velocity vector $\mathbf{u}$ is taken from. k can take values between 0 and 1. The lowest value 0 indicates that the vectors do not match each other at all. The highest value 1 is reached when a perfect match between two flow fields is present.

The steady flow field for case 1 is compared to the corresponding phase resolved one in the pulsation cycle of case 11 with low pulsation frequency of $f_r=0.38$. The best match in blowing ratio occurs at phase 0.33 on the downward slope (see Fig. 6). The steady case 7 is compared to the unsteady case 14 with $f_r=1.88$ at phase 0 (see Fig. 6), which is at the end of the positive slope.

Additionally, a comparison between the steady case 3 with BR=2 and the phase 0.08 at $f_r=0.38$ (case 11) is performed, although the level of blowing ratio is about 0.2 lower.

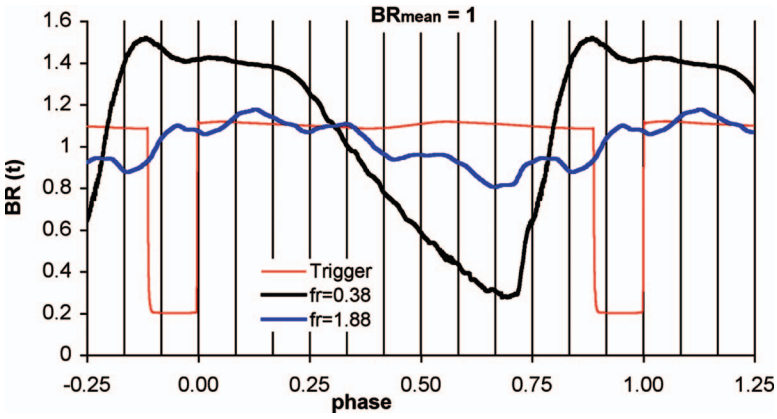

Fig. 6 BR variation for periodic cooling injection

Downloaded 30 May 2010 to 128.113.26.88. Redistribution subject to ASME license or copyright; see http://www.asme.org/terms/Terms_Use.cfm

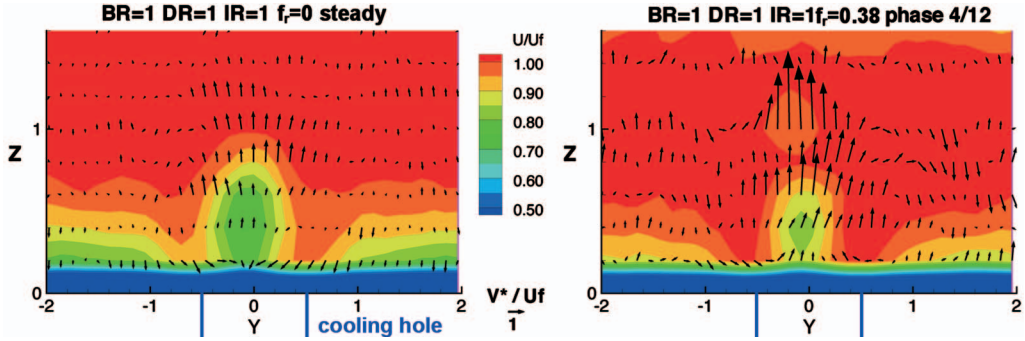

Fig. 7 Velocity field at $X=4$, case 1 and case 11, phase 4/12

First the steady case 1 with $\alpha=30$ deg, BR=1, DR=1 is compared to the pulsating case 11 with $\alpha=30$ deg, BR=1, DR=1 $f_r=0.38$ at phase 4/12, where a blowing ratio of about 0.95 is expected (Fig. 7).

The general shape as well as the magnitude of the jet differs visibly. The unsteady case has a more narrow low momentum core of the jet and a less pronounced boundary layer at both sides of the jet. It is also visible that the velocity data is rather noisy in this region of the flow volume, as was also observed when a small control volume was used to establish the blowing ratio. k takes the value of 0.33, supporting the observation of only partial correspondence of the two flow fields.

The comparison between this steady case 1 and the respective phase averaged case 11 is shown in Fig. 8.

The two pictures compare much better than the previous ones. For one the noise in the unsteady measurement seems to be averaged out due to the 12 times higher number of samples. Also the general shape and magnitude of the jet compares better. The unsteady case has slightly less low momentum fluid entrained into the jet and also a thinner boundary layer on both sides of the jet. This suggests that the entrainment is affected by the unsteadyness. k takes the value of 0.48, which is better than in the previous comparison. Still, the correspondence between the two flow fields is only partial.

Now the steady case 7 with $\alpha=50$ deg, BR=1, DR=1 is compared to the pulsating case 14 with $\alpha=50$ deg, BR=1, DR=1 $f_r=1.88$ at phase 0/12, where a blowing ratio of around BR=1 is expected (Fig. 9).

In this comparison, the general shape as well as the magnitude of the jets are very similar. The unsteady jet extends slightly higher and the drop of low momentum fluid on the outer sides of the kidney vortex pair is more pronounced. k has the value of 0.91, which supports the very good match of the two flow fields.

The comparison between this steady case and the respective phase averaged case is shown in Fig. 10.

In this comparison, the general shape, as well as the magnitude of the jets are very similar. The unsteady jet still extends slightly higher but the dip of low momentum fluid on the outer sides of the kidney vortex pair is less pronounced than in the previous comparison. k takes the value of 0.93, indicating an even better correspondence than in the phase resolved comparison.

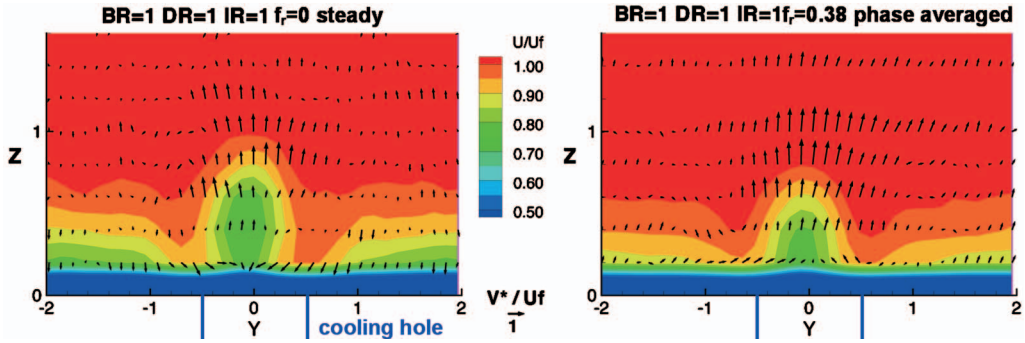

Fig. 8 Velocity field at $X=4$, case 1 and case 11, phase average

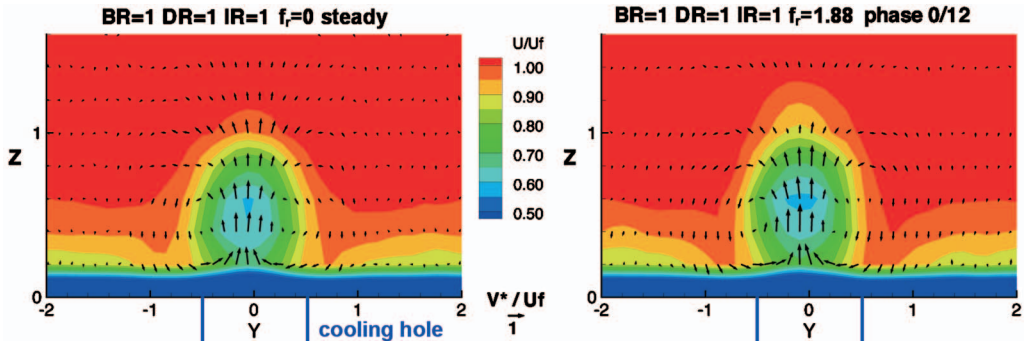

Fig. 9 Velocity field at $X=4$, case 7 and case 14-phase 0/12

Downloaded 30 May 2010 to 128.113.26.88. Redistribution subject to ASME license or copyright; see http://www.asme.org/terms/Terms_Use.cfm

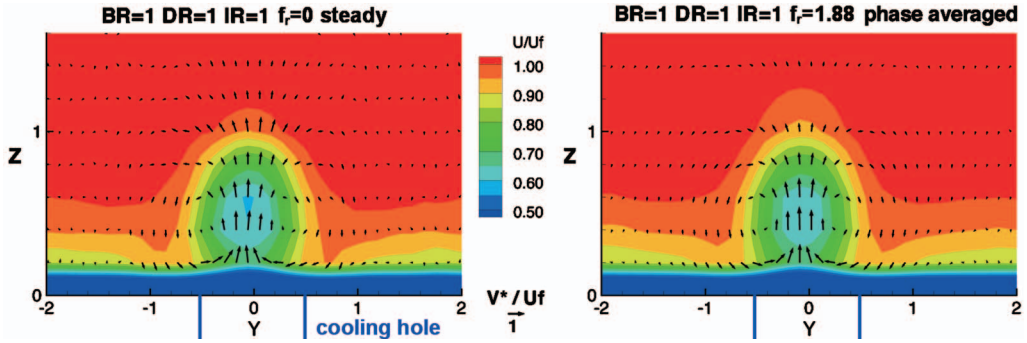

Fig. 10 Velocity field at $X=4$, case 7 and case 14-phase average

As a last comparison the steady case 3 with $\alpha=30$ deg, BR $=2$, DR$=1$ is shown with the pulsating case 11 with $\alpha=30$ deg, BR$=1$, DR$=1$ $f_r=0.38$ at phase 1/12, where a momentary blowing ratio of about BR$=1.7$ is expected (Fig. 11).

Although the blowing ratio and the momentum flux ratio are not very different the corresponding flow field clearly is. The unsteady jet is located closer to the wall, while the steady jet is lifted off. The steady jet is of greater strength and the boundary layer is thicker. The entrainment of low momentum fluid into the core of the jet is greater in the unsteady case. Additionally, the noisy data of the unsteady case makes the comparison look slightly worse. k takes the value of 0.57, indicating that the two cases do correspond only partly.

The illustration in Fig. 12 shows the phase resolved case 11 as isovelocity contours. This illustration indicates that periodic jet-lift off and reattachment is taking place. Phases 1–5 have a slightly lifted off jet, indicated by an almost undisturbed low-velocity plane ($U<U_f$ in light green) downstream of the hole. Phases 6–12 show some disturbance of the low velocity plane in the jet center. This indicates an attached jet.

Trajectory

The center line jet trajectory is defined by the streamline emerging from the center of the cooling hole. This definition allows an easy comparison with different sets of measured data or numerical results. It has to be stated, though, that this definition does not reflect the trajectory of the geometrical center of the jet and the disturbance it introduces into the main flow. The streamline will gradually move to the windward side of the jet, mainly due to the entrainment on the leeward side of the jet attributed to the kidney vortex pair.

Streamlines are inserted into the flow volume of each measurement case with the post processing tool Tecplot. The streamline path is integrated in three dimensions within the 3D volume field in flow direction with four steps between two data points. The injection site has to be at the lowest plane where measurements were taken, at $Z=0.2$. The streamline might not exit the boundary layer if it is inserted below that level as the velocity on the wall (at $Z=0$) is set to zero. This is done also in the region of the hole due to the lack of data in this region. The velocity between $Z=0$ and $Z=0.2$ is determined with linear interpolation.

The start point of the streamline in lateral direction is in the center of the hole at $Y=0$. The axial start point X_{start} is determined from the streamwise hole angle and the distance between the wall and the start of the stream line in the vertical direction $Z_{\text{start}}=0.2$ as

$$X_{\text{start}} = Z_{\text{start}} \cot \alpha$$

This is assuming that the jet emerges from the center of the hole with the stream wise hole angle and that the flow does not get deflected between $Z=0$ and $Z=0.2$. This assumption has been validated with a low blowing ratio case and a steep injection angle of 50 deg. This case 7 is considered to be affected most severely by the assumption taken. Validation shows, that the error is less than $0.15d$ or 11% of the axial hole extent, which is considered to be acceptable for the further analysis.

Comparison of the measured data with established trajectory models by Shandorov [18] and Abramovich [19] show, that the near hole trajectory defined with a streamline is not matched well with established models. It seems appropriate to create an empirical correlation based on the measured steady cases to facilitate further analysis based on the trajectory. A power function is used to match each of the 10 trajectories. The dependency on IR of the trajectory is modeled with another power function. The end result is a fit for each streamwise injection angle with six coefficients, that describe the near hole trajectory with high accuracy. A fit like this offers the opportunity of quick validation of numerical data, as the measurements are compressed in one equation.

The trajectories of the 10 steady filmcooling measurements are matched well with a Langmuir-power function,

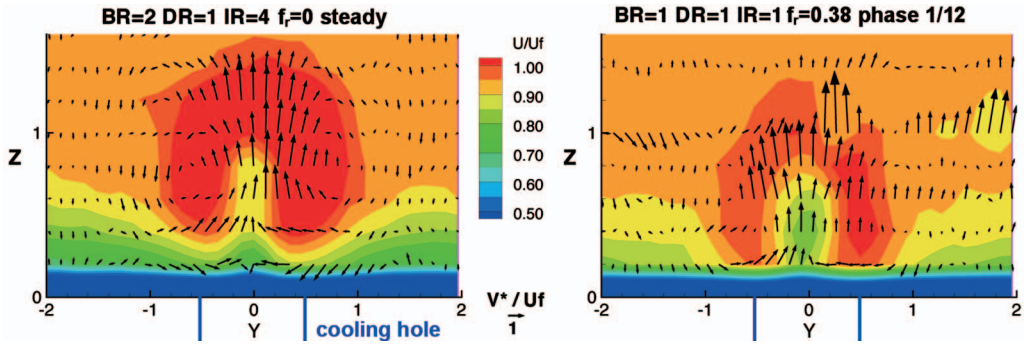

Fig. 11 Velocity field at $X=4$, case 3 and case 11-phase 1/12

Downloaded 30 May 2010 to 128.113.26.88. Redistribution subject to ASME license or copyright; see http://www.asme.org/terms/Terms_Use.cfm

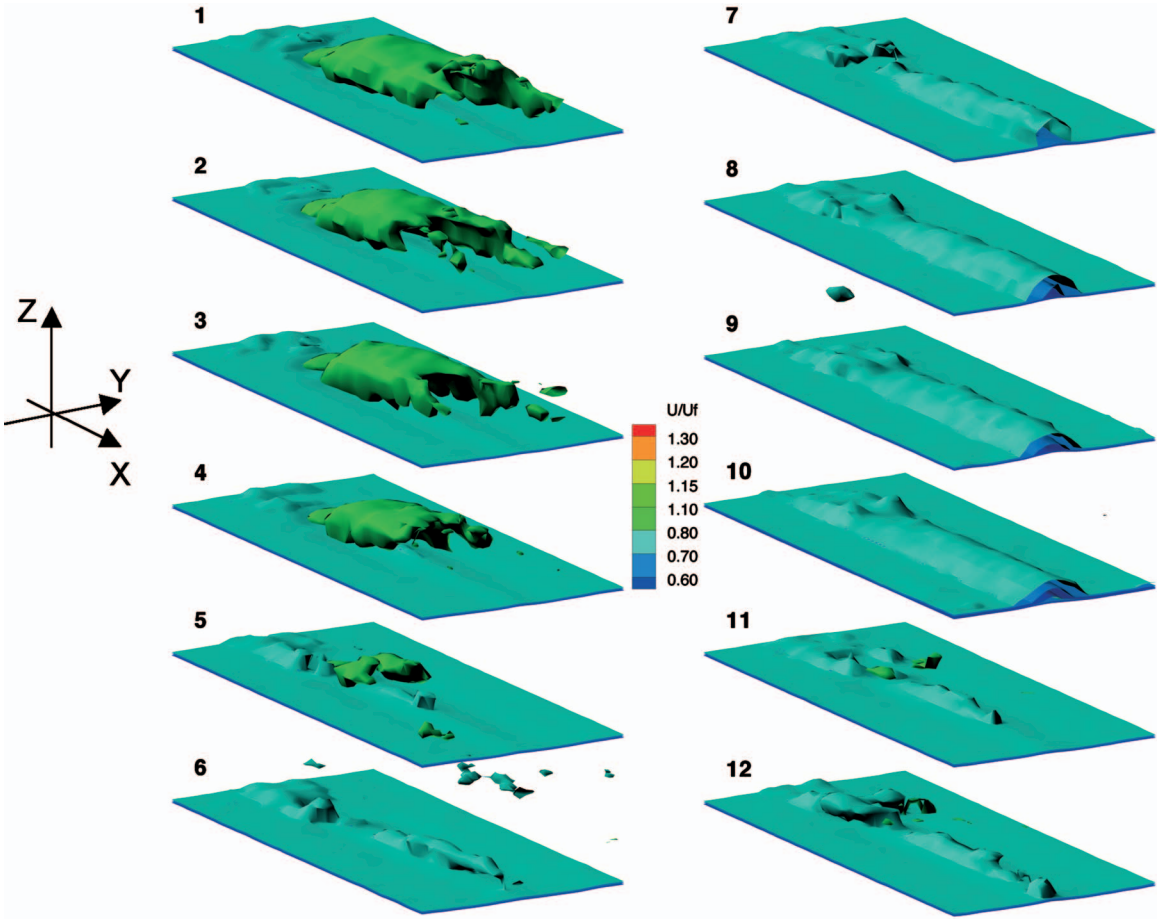

Fig. 12 Time resolved isovelocity contour for case 11

$$Z = \frac{a \cdot b \cdot X^{1-c}}{1 + b \cdot X^{1-c}}$$

and the three respective coefficients are matched with a simple power-fit as function of the momentum flux ratio

$$a = a_1 \cdot \mathrm{IR}^{a_2}$$

$$b = b_1 \cdot \mathrm{IR}^{b_2}$$

$$c = c_1 \cdot \mathrm{IR}^{c_2}$$

The center-line-trajectory is described with the above equations and six coefficients for each of the streamwise injection angles. The resulting maximum standard deviation between the correlation and the measured data is $0.03d$ with a maximum discrepancy of $0.13d$. The respective coefficients are summarized in Table 4.

The match is good for low momentum flux ratios, irrespective of density ratio and the streamwise injection angle. The highest measured momentum flux ratio of IR=6.5 shows the biggest discrepancy with a general underprediction of the trajectory of about 7%. The general curvature is reproduced well and at $X=1$ all trajectories are almost identical with the correlation. A blind test using data from this rig not used in the correlation showed an error in the order of the accuracy of the fit.

Table 4 Trajectory correlation coefficients

	a_1	a_2	b_1	b_2	c_1	c_2
30 deg	1.768	0.291	0.352	−0.251	0.042	0.647
50 deg	1.727	0.498	0.350	−0.305	0.405	−0.417

Results

Now the empirical trajectory fit is utilized to further investigate the quasisteady behavior of the near hole flow with pulsating coolant. For the unsteady case the trajectory constitutes a snapshot in time. A particle at $X=6$, as far as the investigated region extends, would have left the hole 0.3 ms earlier. This is assuming BR=1; this time would be shorter for higher BR. A cycle with $f_r=1.88$ resolved in 12 steps gives a similar time between the steps of $dt=0.3$ ms. The convection time is roughly equal to the time steps, meaning that a particle travels through the measurement domain in one time step.

First, case 11 with $\alpha=30$ deg, BR=1.0, DR=1.0 IR=1.0, and $f_r=0.38$ is investigated. The trajectory of the dataset with strong pulsation amplitude is compared to the correlation. The comparison is done with both, the part of the pulsation where a blowing ratio of BR=1 is expected as well as with the phase average, with a mean blowing ratio of also $\mathrm{BR}_{\mathrm{mean}}=1$. The comparison is shown in Fig. 13.

This comparison again shows the general character of the fit, as the match is in the order of the accuracy of the model with around 8%. Both trajectories, the phase averaged as well as the phase resolved case where a similar BR and IR as in the averaged case is expected are following similar paths. This confirms the thesis, that the near hole flow field behaves in a quasisteady manner with a pulsating cooling flow.

Downloaded 30 May 2010 to 128.113.26.88. Redistribution subject to ASME license or copyright; see http://www.asme.org/terms/Terms_Use.cfm

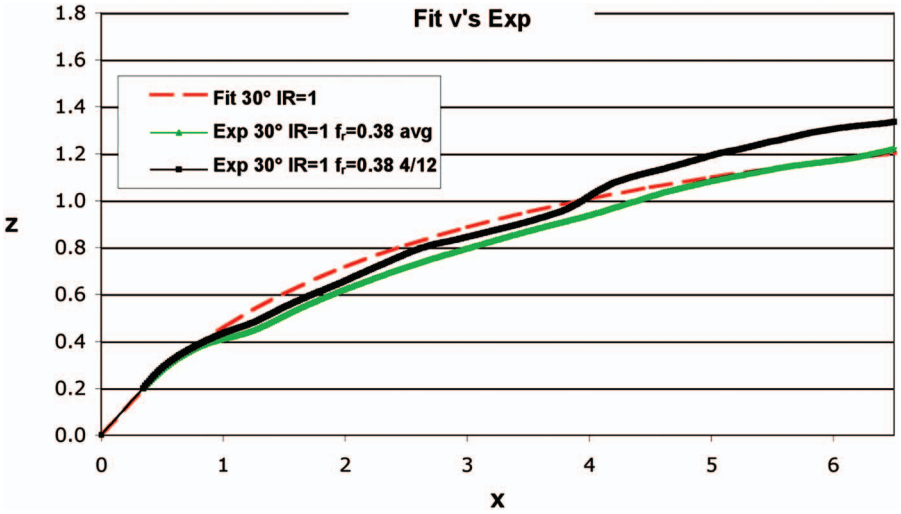

Fig. 13 Comparison between new correlation and unsteady experimental data

The most extreme trajectory of the respective phase with minimum and maximum blowing ratio is extracted to ensure the validity of the above comparison. The blowing ratio 2/12 shows a maximum and 10/12 shows the minimum. This case with low pulsating frequency is expected to have a strong variation of the trajectory, as the blowing ratio has strong variations. The trajectories are shown in Fig. 14.

It is clearly visible that the trajectory changes strongly over the pulsation phase. The match between the correlation and the measured trajectory is reasonably good for the high blowing part. The measured trajectory in the low blowing part falls after $X=2$. This is expected to be a convective effect, as a snapshot in time is displayed.

The comparison between the correlation and the measured trajectory is now made for the unsteady case 14 with low pulsating amplitude ($\alpha=50$ deg, BR=1.0, DR=1.0 IR=1.0, and $f_r=1.88$). The comparison again is done with part of the pulsation where a blowing ratio of BR=1 is expected and with the phase average, with a mean blowing ratio of also $BR_{mean}=1$. The comparison is shown in Fig. 15.

This comparison again shows the general character of the correlation, as the match is in the order of the accuracy of the model with around 8%. Both trajectories, the phase averaged as well as the phase resolved case where a similar BR and IR as in the averaged case is expected are following similar paths. This confirms the thesis, that the near hole flow field behaves in a quasi-steady manner with a pulsating cooling flow.

The trajectory of the respective phase with minimum and maximum blowing ratio is extracted to ensure the validity of the above comparison. This case with high pulsating frequency is expected to have less variation of the trajectory, as the blowing ratio has little strong variations. The extracted trajectories are shown in Fig. 16.

A clear change of the trajectory is visible also for this case with little variation of blowing ratio over the unsteady cycle. The phase resolved trajectories are matched well with the trajectory correlation. The quasisteady assumption is supported in this case.

Circulation

The circulation that is used in the following section compactly expresses the vortical information contained in the flow data in a single line. The axial circulation X of the coolant jet is calculated as a function of the axial coordinate X. In general the circulation of a vortex is expressed as the line integral of the velocity vector along a closed loop around this vortex,

$$\Gamma = \oint \boldsymbol{v} \cdot d\boldsymbol{r}$$

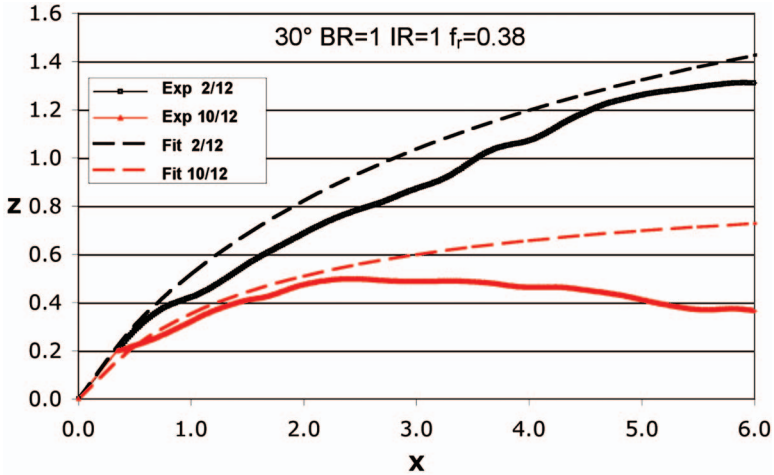

Fig. 14 Trajectory at maximum and minimum blowing ratio for $\alpha=30$ deg, BR=1, $f_r=0.38$

Downloaded 30 May 2010 to 128.113.26.88. Redistribution subject to ASME license or copyright; see http://www.asme.org/terms/Terms_Use.cfm

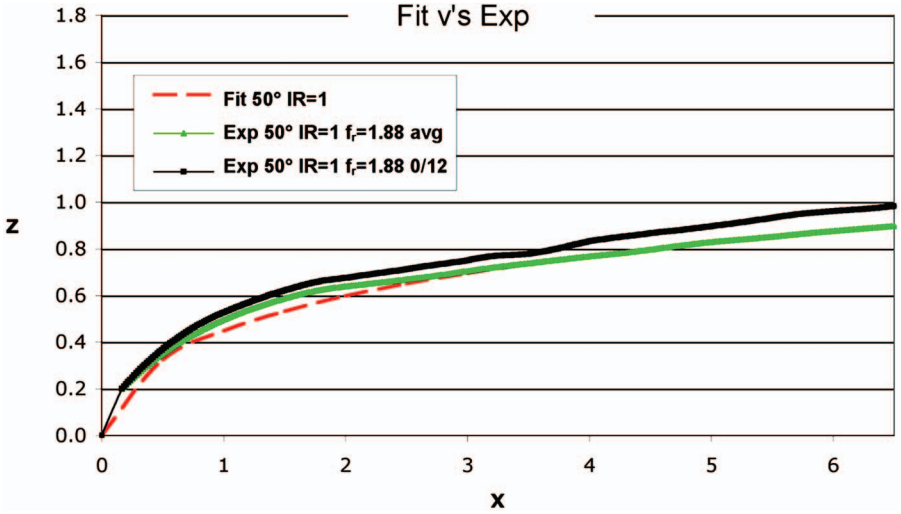

Fig. 15 Comparison between the new correlation and unsteady experimental data

This can be expressed as the integral of the vorticity vector over the area vector according to Stokes theorem. The area contains the vortex of interest,

$$\Gamma = \oiint \boldsymbol{\omega} \cdot d\boldsymbol{A}$$

This is the form used to derive the circulation from the vector field. The vorticity component normal on the area is integrated over the area. Since the circulation as a function of X is investigated, the area of integration is the YZ-plane. The vorticity component to be integrated is the streamwise vorticity ω_x. The vorticity is nondimensionalized with the cooling hole diameter d and the free stream velocity U_f. The equation applied to the data set now takes the form,

$$\Gamma_X = \oiint \boldsymbol{\omega}_X \cdot d\boldsymbol{A}_{YZ} = \oiint \left(\frac{\partial W}{\partial Y} - \frac{\partial V}{\partial Z} \right) \cdot d\boldsymbol{A}_{YZ}$$

The vortex of interest is the kidney vortex of the coolant jet. The sides of the kidney shape have an opposite sign of vorticity. Deriving the circulation for the entire kidney vortex should result in the value 0, given that the boundary layer does not contribute to the streamwise vorticity and the noise in the velocity field is isotropic.

The circulation used in the following sections is derived from the left-hand side (looking in stream wise direction) of the kidney vortex only, to gain information about dissipation of the vortical strength. The integration in the Y-direction is performed from the center of the cooling hole at $Y=0$ to the symmetry plane between the two holes at $Y=2$. The integration in the Z-direction is done over the full range of available data, from $Z=0$ to $Z=2.4$. The right-hand side should ideally give the same result with opposite sign. Figure 17 sketches the area of integration.

Typical plots of the entire kidney vortex, the left-hand side and the right-hand side for the circulation as a function of X are given in Fig. 18.

The plot in Fig. 18 confirms the theoretical considerations from before. Both sides have similar shaped circulation, mirrored at the abscissa. Circulation of the entire kidney vortex is about zero, indicating that the boundary layer does not contribute to the streamwise circulation and that the noise is isotropic.

Applying Kelvin's theorem to axial closed lines that surround

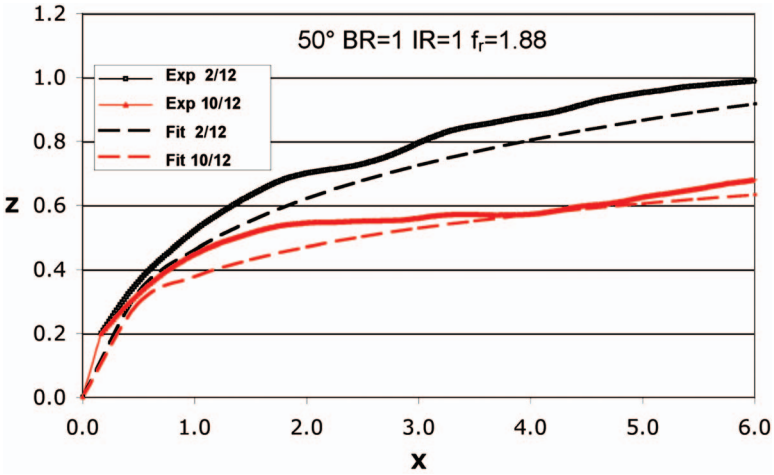

Fig. 16 Trajectory at the maximum and minimum blowing ratio for 50 deg, BR=1, f_r=1.88

Downloaded 30 May 2010 to 128.113.26.88. Redistribution subject to ASME license or copyright; see http://www.asme.org/terms/Terms_Use.cfm

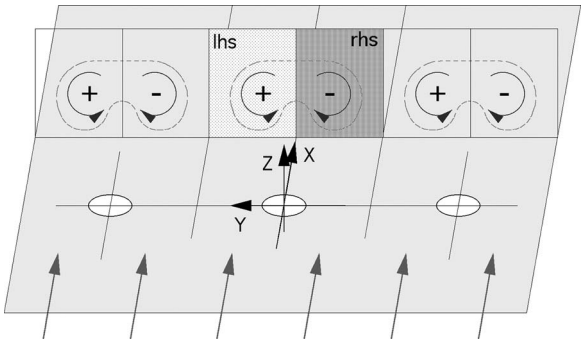

Fig. 17 Illustration of the area of circulation

both kidney vortices shows that the flow can be regarded as inviscid, incompressible, and with uniform density at any axial plane.

Comparing the circulation of a steady and a phase averaged case is done in Fig. 19. Cases 7 and 14 are used with mean flow conditions of $\alpha=50$ deg, BR=1, DR=1, and IR=1. Pulsation frequency is $f_r=1.88$. It is clearly visible, that the pulsation has little influence on the phase averaged circulation. The almost perfect match of this derivative of the velocity field further supports the thesis of quasisteady behavior in the case of small pulsation amplitude.

Summary

At $f_r=1.88$ pulsation (50 deg holes) a good match is observed, both with the phase average and the phase resolved; the flow is quasisteady. Therefore the flow at lower frequencies must also be quasisteady with the same pulsation amplitude.

The comparison to $f_r=0.38$ (30 deg) is different. The results suggest that the amplitude of the unsteady BR is the important factor. The strong amplitude must lead to some nonlinear events e.g., flow separations. This event could be attributed to film "lift off." The isosurface time histories shows unsteady lift of for this case (see Fig. 12). This would probably make a large difference, as it is intermittent, when compared to steady attached or lifted off jets.

The effect of hole angle could not be separated entirely from the effect of reduced frequency.

The quasisteady assumption is supported near the hole up to $f_r=1.88$ and with a pulsation amplitude ± 0.2 in BR. For ± 0.7 this is no longer well supported.

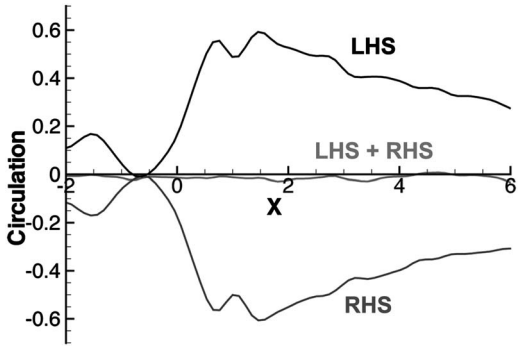

Fig. 18 Typical circulation of the kidney vortex

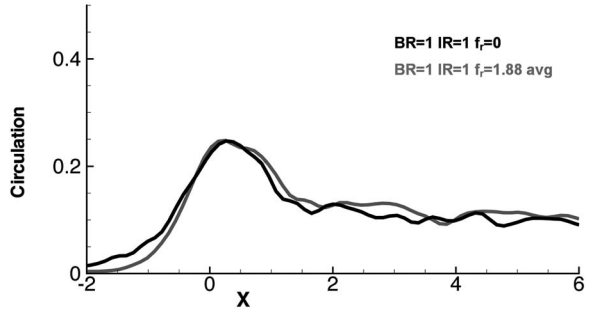

Fig. 19 Influence of pulsating on the axial circulation; α =50 deg, DR=1.0, BR=1.0

Conclusion

The assumption of quasisteady fashion of pulsating coolant injection has been investigated in detail. The final conclusion regarding the validity and limits of this assumption is based on results from the velocity field, the center-line trajectory of the coolant jet, and the streamwise circulation. It was found that the amplitude of the pulsation is the limiting parameter. This information is lacking in real turbines. It is, however, relevant for the numerical simulation of a turbine, where this information is present, either as a boundary condition or as a derivative.

For a low amplitude and frequencies below $f_r=1.88$ the pulsation of the injectant can be described as quasisteady with very good accuracy. This is valid for the investigated range between two hole diameters upstream and six diameters downstream of the cooling hole. The quasisteady postulate has limited validity for a high amplitude of pulsation. The phase average flow phenomena correspond reasonably well to the respective steady ones. The phase resolved flow displays unsteady effects that are not captured with quasisteady modeling. This is due to periodic lift-off and reattachment of the cooling jet.

Acknowledgment

The authors would like to acknowledge the support of this project by GE Aircraft Engines through their university strategic alliance program. Specifically the technical interaction with Dr. Robert Bergholz and Dr. Frederick Buck has been very helpful in the formulation of this project. The facility would not have been built without Hans Suter, Thomas Kuenzle, Peter Lehner, and Christoph Raeber.

Nomenclature

a,b,c = trajectory fit coefficients, subscripts 1 and 2
BR = blowing ratio $=\rho_c U_c/\rho_f U_f$
d = hole diameter
DR = density ratio $=\rho_c/\rho_f$
f = frequency of pulsation
f_d = alternative reduced frequency $=fd/U_f$
f_r = reduced frequency $=fL/U_f$
H = shape factor $=\delta^*/\theta$
IR = momentum flux ratio $=BR^2/DR$
k = correlation coefficient
L = distance boundary suction to hole center
l = length of the hole pipe
P = static pressure
s = pitch distance between two holes
T = total temperature
Tu = turbulence Intensity $=\sqrt{\overline{U'^2}}/U_f$
U,V,W = mean velocity components
V^* = velocity magnitude YZ plane $=(V^2+W^2)^{1/2}$
X = axial (streamwise) coordinate
Y = lateral coordinate
Z = vertical coordinate
α = streamwise injection angle
δ^* = displacement thickness $=\int(1-U/U_f)dx$
ρ = density
θ = momentum thickness $=\int U/U_f(1-U/U_f)dx$

Downloaded 30 May 2010 to 128.113.26.88. Redistribution subject to ASME license or copyright; see http://www.asme.org/terms/Terms_Use.cfm

ϖ = nondimensional vorticity = $\omega d / U_f$
ω_X = streamwise vorticity = $\partial W/\partial Y - \partial V/\partial Z$
ω_Y = crosswise vorticity = $\partial U/\partial Z - \partial W/\partial X$
ω_Z = normal vorticity = $\partial V/\partial X - \partial U/\partial Y$

Subscript

c = coolant fluid
f = free stream fluid

Superscript

$'$ = instantaneous value
∞ = time-averaged value

References

[1] Burdet, A., Abhari, R. S., and Rose, M. G., 2005, "The Modelling of Film Cooling—Part II: Model for use in 3D CFD," ASME Paper No. GT2005-68780.

[2] Burdet, A., 2005, "A Computationally Efficient Feature-Based Jet Model for Prediction of Film-Cooling Flows," Ph.D. thesis 16163, ETH Zurich.

[3] Abhari, R. S., 1996, "Impact of Rotor-Stator Interaction on Turbine Blade Film Cooling," ASME J. Turbomach., **118**, pp. 123–133.

[4] Abhari, R. S., Guenette, G. R., Epstein, A. H., and Giles, M. B., 1992, "Comparison of Time-Resolved Turbine Rotor Blade Heat Transfer Measurements and Numerical Calculations," ASME J. Turbomach., **114**, pp. 818–827.

[5] Bell, C. M., et al., 1999, "Film Cooling Subject to Bulk Flow Pulsations: Effects of Blowing Ratio, Freestream Velocity, and Pulsation Frequency," Int. J. Heat Mass Transfer, **42**(23), pp. 4333–4344.

[6] Bernsdorf, S., 2005, "Experimental Investigation of Film Cooling Flow Structure," Ph.D. thesis 16355, ETH Zurich.

[7] Bons, J. P., Rivir, R. B., MacArthur, C. D., and Pestian, D. J., 1995, "The Effect of Unsteadiness on Film Cooling Effectiveness," Paper No. AIAA-95-0306.

[8] Dunn, M. G., 1990, "Phase and Time Resolved Measurements of Unsteady Heat Transfer and Pressure in a Full-Stage Rotating Turbine," ASME J. Turbomach., **112**, pp. 531–538.

[9] Dunn, M. G., Seymour, P. J., Woodward, S. H., George, W. K., and Chupp, R. E., 1989, "Phase Resolved Heat-Flux Measurements on the Blade of a Full Scale Rotating Turbine," ASME J. Turbomach., **111**, pp. 8–19.

[10] Giang, T. T. L., 1999, "Effects of Unsteady Cooling Flow on Heat Transfer to a Film-Cooled Flat Plate," M.Sc. thesis, The Ohio State University, Columbus.

[11] Heidmann, J. D., Lucci, B. L., and Reshotko, E., 1997, "An Experimental Study of the Effect of Wake Passing on Turbine Blade Film Cooling," *Proceedings of the ASME Turbo Expo 1997*, Orlando, FL.

[12] Jung, I. S., Lee, J. S., and Ligrani, P. M., 2001, "Effects of Bulk Flow Pulsation on Film Cooling With Compound Angle Holes: Heat Transfer Coefficient Ratio and Heat Flux Ratio," ASME Paper No. 2001-GT-0129.

[13] Jung, I. S., and Lee, J. S., 1998, "Effect of Bulk Flow Pulsations on Film Cooling From Spanwise Oriented Holes," ASME Paper No. 96-GT-211.

[14] Lee, J. S., and Jung, I. S., 2002, "Effect of Bulk Flow Pulsations on Film Cooling With Compound Angle Holes," Int. J. Heat Mass Transfer, **45**, pp. 113–123.

[15] Ligrani, P. M., Subramanian, C. S., Coumes, T. M., Greco, F. J., Koth, H., and Longest, J. M., 1992, "Study of the Imposition of Bulk Flow Pulsations on Plane Channel Flow at Moderate Stokes Numbers," Exp. Therm. Fluid Sci., **5**, pp. 145–161.

[16] Bernsdorf, S., Rose, M. G., and Abhari, R. S., 2005, "Modelling of Film Cooling—Part I: Experimental Study of Flow Structure," ASME Paper No. GT2005-68783.

[17] 2002, "Flow Manager Software and Introduction to PIV Instrumentation," Dantec Dynamics A/S.

[18] Shandorov, G. S., 1957, "Flow From a Channel Into Stationary and Moving Media," Zh. Tekh. Fiz., **37**, p. 1.

[19] Abramovich, G. N., 1963, *The Theory of Turbulent Jets*, MIT Press, Cambridge, MA.

Downloaded 30 May 2010 to 128.113.26.88. Redistribution subject to ASME license or copyright; see http://www.asme.org/terms/Terms_Use.cfm

Huu Duc Vo
Department of Mechanical Engineering,
École Polytechnique de Montréal,
2900 boul. Edouard-Montpetit,
2500 ch. de Polytechnique,
Montreal, Quebec, H3T 1J4, Canada
e-mail: huu-duc.vo@polymtl.ca

Choon S. Tan
e-mail: choon@mit.edu

Edward M. Greitzer
e-mail: greitzer@mit.edu

Department of Aeronautics and Astronautics,
Massachusetts Institute of Technology,
77 Massachusetts Avenue,
Cambridge, MA 02139

Criteria for Spike Initiated Rotating Stall

A computational study to define the phenomena that lead to the onset of short length-scale (spike) rotating stall disturbances has been carried out. Based on unsteady simulations, we hypothesize there are two conditions necessary for the formation of spike disturbances, both of which are linked to the tip clearance flow. One is that the interface between the tip clearance and oncoming flows becomes parallel to the leading-edge plane. The second is the initiation of backflow, stemming from the fluid in adjacent passages, at the trailing-edge plane. The two criteria also imply a circumferential length scale for spike disturbances. The hypothesis and scenario developed are consistent with numerical simulations and experimental observations of axial compressor stall inception. A comparison of calculations for multiple blades with those for single passages also allows statements to be made about the utility of single passage computations as a descriptor of compressor stall. [DOI: 10.1115/1.2750674]

Keywords: compressor instability, rotating stall, spike stall inception, tip clearance flow

Introduction

There are two well-established routes to rotating stall, referred to as long length-scale or "modal" inception and short length-scale or "spike" inception, with the two routes distinguished by the type of initial perturbation in pressure/velocity. The former is characterized by the evolution, in tens of rotor revolutions, of a small amplitude disturbance with wavelength on the order of the annulus circumference, into a fully developed stall cell with approximately the same propagation speed. This type of stall inception is well described by so-called actuator disk models, which consider the overall effects of the blading, in essence smearing out the details of the flow on the blade scale. It has been shown both analytically [1,2] and experimentally [3] to occur at conditions at, or slightly beyond, the peak of the stagnation-to-static pressure rise of the compressor.

Many compressors, however, exhibit a short length-scale, or spike, stall inception. This phenomenon, which is less understood, was first described by Day [4]. It is characterized by the appearance of a disturbance (or "spike") two to three blade pitches in width at the rotor tip. The spike rotates at about 70% of the rotor speed and can grow into a two-dimensional stall cell more rapidly than in modal inception, within roughly three rotor revolutions. During this process, in contrast to modal stall inception, the propagation speed of the disturbance typically drops to below 50% of rotor speed. Also in contrast to modal stall, spike stall inception is observed to occur at flows where the stagnation-to-static pressure rise characteristic has a negative slope.

Unlike long length-scale stall inception, where the small amplitude of the modal disturbance lends itself to linear analysis, the velocity defect associated with the spike disturbance is comparable to the mean velocity through the compressor, and a nonlinear approach is required. Features of the evolution of an *input* spike disturbance into fully developed rotating stall have been captured using a nonlinear simulation that employed a three-dimensional distribution of body forces (again, smearing out the effects of discrete passages) by Gong et al. [5]. However, the more important process from the point of view of defining the conditions under which the process starts, in other words *the origin of the spike*, has not been resolved. These conditions are described in the present paper. They differ fundamentally from existing stall analyses in that the disturbance nature and scale is such that the structure of the flow within the passages, not just the integrated effects of the blade rows, must be addressed.

The experimental measurements of Day [4] show that the spikes are not only circumferentially localized, but are confined to the tip region of a rotor, leading to the possible association of their origin with the tip clearance flow. As such, the basic issue addressed in this paper is the causal link between tip clearance flow and spike stall inception, i.e., what is the mechanism (and the conditions) by which tip clearance flow leads to the formation of short length-scale rotating stall disturbances?

The paper is organized as follows. Rotor passage flow features common to compressors exhibiting spike stall inception are first identified. This allows focus on a particular rotor geometry while supporting the generic nature of the study. Time-accurate single blade passage computations are then used to define the criteria that set the single blade passage solution limit—referred to here as the *flow solution limit*—which is the lowest flow coefficient for which a steady solution exists. This is followed by a six blade passage flow simulation to clarify the link between tip clearance flow and spike disturbances and the utility of single blade passage solution limit as guideline for predicting compressor stall inception. The findings are then used to explain observed spike stall inception behavior.

Rotor Flow Features of Spike Stall

Single blade passage computations [6] on different compressor rotors that are known to exhibit spike stall inception indicate that the flow solution limit occurs when the interface between the incoming flow and tip clearance flow lines up with the rotor leading edge plane. Figure 1 shows the trajectory of the interface between the incoming and tip clearance flows [7]. The position of this interface results from a balance between the momentum of the incoming flow and that of the tip clearance flow. As the flow coefficient decreases, the axial momentum of the incoming flow reduces and the blade loading, which drives tip clearance flow and thus increases the momentum of the flow through the clearance [8], rises. The result is a movement of the interface toward the rotor leading edge plane, as observed from rotor casing oil flow pictures by Koch [9] and Saathoff and Stark [10]. The latter examined a low-speed compressor near the point of spike stall in-

Contributed by the International Gas Turbine Institute of ASME for publication in the JOURNAL OF TURBOMACHINERY. Manuscript received June 23, 2006; final manuscript received June 30, 2006; published on January 30, 2008. Review conducted by David Wisler. Paper presented at the ASME Turbo Expo 2005: Land, Sea and Air (GT2005), June 6–9, 2005, Reno, NV.

Downloaded 30 May 2010 to 128.113.26.88. Redistribution subject to ASME license or copyright; see http://www.asme.org/terms/Terms_Use.cfm

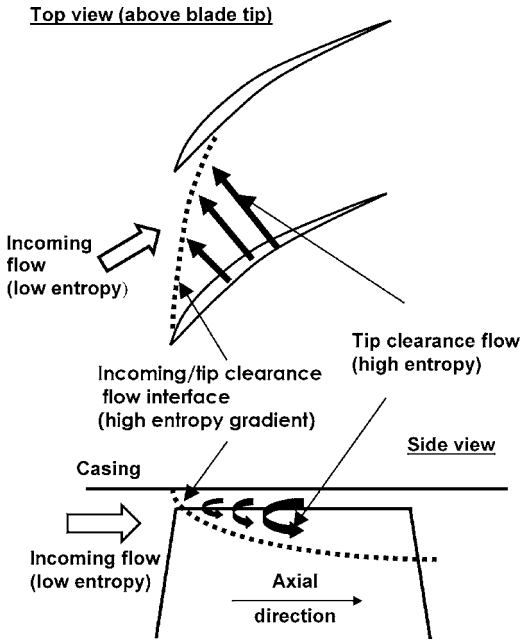

Fig. 1 Sketch of incoming/tip clearance flow interface

ception and found that the stall limit occurred when the interface was aligned with the leading edge. This will be seen to be a feature of the computations to be described.

In the computations, entropy/unit mass is used to track the interface. The tip clearance flow mixes after leaving the clearance, has higher entropy than the incoming flow, and the interface is a region of high entropy gradient. Contours of computed entropy/unit mass on the rotor blade tip radial plane at the flow solution limit, based on steady RANS computations, are shown in Figs. 2 and 3 for the low Mach number ($M_{tip} \approx 0.2$) E^3 rotor B and for the transonic rotor from NASA stage 35, respectively. Both of these are known to exhibit spike stall inception, the latter when subjected to inlet radial distortion [11,12]. The computations show that when the solution limit is reached the incoming/tip clearance flow interface is aligned with the rotor leading-edge plane at the blade tip. We cite these results to indicate that even with the large differences in design conditions a similar set of phenomena occur at the flow solution limit. The E^3 rotor B has the additional advantage of not exhibiting flow separation on the blade, allowing clearer isolation of the role of tip clearance flow on the flow solution limit. We thus focus on this rotor as a vehicle for establishing the context of the flow solution limit in relation to the onset of spike disturbances and in defining the role of tip clearance flow in the latter process.

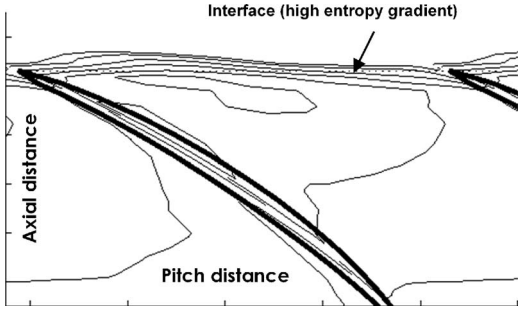

Fig. 2 Contours of entropy/unit mass at E^3 rotor blade tip at the flow solution limit

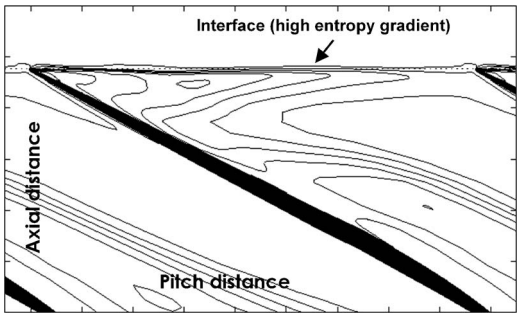

Fig. 3 Contours of entropy/unit mass at rotor 35 blade tip at flow solution limit/stall point

Features of Transients Beyond the Flow Solution Limit

Time-accurate single blade passage computations using UNSTREST [13], as described in the Appendix, were used to assess the behavior of the tip clearance flow beyond the flow solution limit and to identify the threshold flow events leading to spike stall inception. This involved incrementally increasing the exit tip pressure until the occurrence of a rapid transient, including a large drop in mass flow beyond the flow solution limit. The computed total-to-static pressure rise versus flow coefficient, seen in Fig. 4, shows both the steady-state flow regime (points 1–4) and the transient regime (points 5–8). The tip clearance was 1.8% chord. The corresponding variations of total blockage and the individual contributions (tip clearance blockage and passage-blade/hub-boundary layer blockage) [7] are also given. The flow solution limit (point 4) coincides with a rapid growth in blockage. This growth comes only from the tip blockage; blockage from blade and hub boundary layers does not grow as the flow coefficient drops below the flow solution limit.

One feature of the transient is the spillage of tip clearance flow to the adjacent blade passage ahead of the rotor leading edge and below (inboard of) the blade tip radius. This is sketched in Fig. 5, which shows the path of tip clearance flow fluid spilling into the next blade passage, a scenario suggested by Cumpsty [14]. Figure 6 shows the mass flow through the blade clearance (i.e., over the blade tip) and the mass flow spilling ahead of the blade leading edge below the blade tip. The operating points correspond to those in Fig. 4. The amount of spilled fluid increases while the amount flowing over the blade tip decreases, as the flow coefficient decreases below point 3. There is no leading-edge spillage below the blade tip at point 3, at a flow coefficient just above the flow

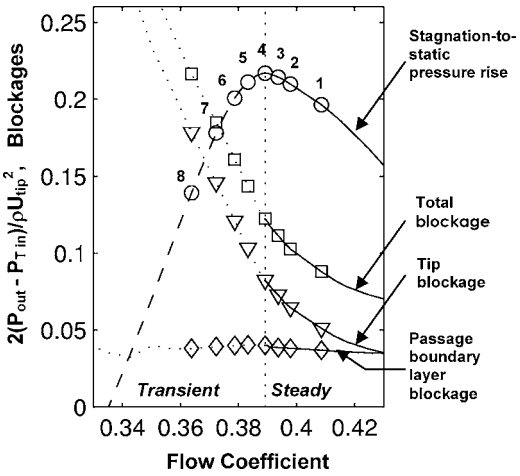

Fig. 4 Passage pressure rise and blockage as a function of flow coefficient for E^3 rotor B; 1.8% chord tip clearance

Downloaded 30 May 2010 to 128.113.26.88. Redistribution subject to ASME license or copyright; see http://www.asme.org/terms/Terms_Use.cfm

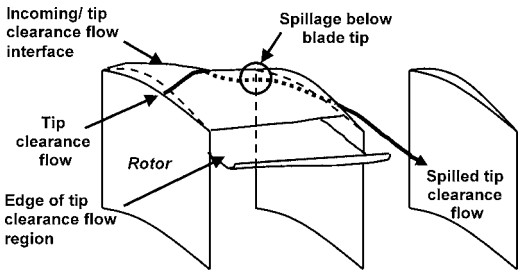

Fig. 5 Leading-edge tip clearance flow spillage below blade tip

solution limit (point 4). The onset of flow spillage below the blade tip means that the incoming/tip clearance flow interface crosses the blade leading edge. This is the common flow feature associated with compressors exhibiting spike stall inception identified in the previous section.

Figure 7 illustrates a second feature seen at flow coefficients below the flow solution limit. Fluid originating from the tip clearance moves (from an adjacent blade passage) into the blade passage *at the trailing edge*. The trajectory of this fluid is such that there is impingement on the pressure surface. This reversal of the tip clearance fluid from the adjacent blade passage (essentially an end-wall separation with a circumferential relative velocity component) will be referred to as "tip clearance backflow." The spanwise distribution of pitch-averaged mass flow (nondimensionalized by inlet stagnation density and blade tip speed) in Fig. 8 shows the onset of tip clearance backflow below the blade tip at the flow solution limit. The operating point numbers again correspond to those in Fig. 4. For steady-state solutions (points 1–3), Fig. 8 shows downstream (positive) mass flow below the blade tip. At the flow solution limit (point 4), the mass flow reaches zero at the blade tip. It then becomes negative for transient points at lower flow coefficients (points 5–8), signifying backflow below the blade tip.

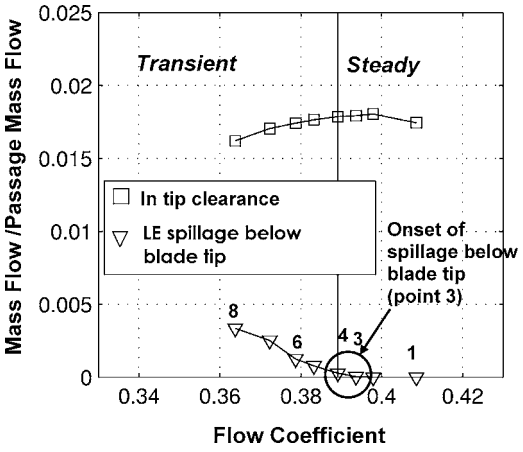

Fig. 6 Mass flow through tip clearance and mass flow spilled ahead of leading edge below blade tip

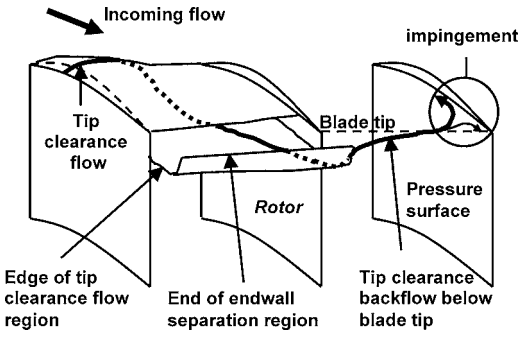

Fig. 7 Reversal ("backflow") of tip clearance fluid below the blade tip

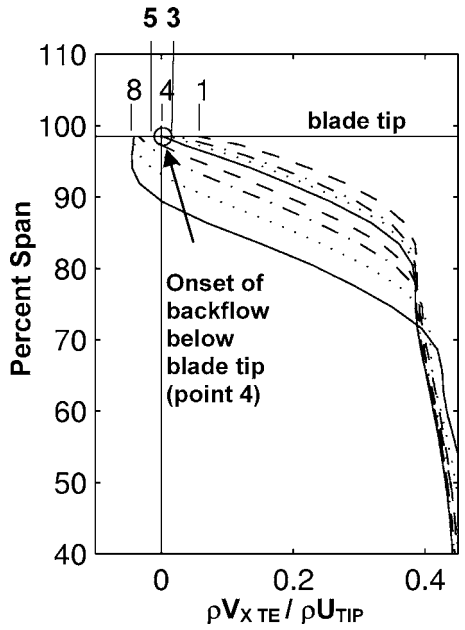

Fig. 8 Spanwise distribution of pitch-averaged mass flow at passage exit plane (1.8% chord tip clearance)

We can now consider how the above threshold flow events set the flow solution limit and contribute to the observed blockage growth. Figure 9 illustrates the connection between the impingement (sketched in Fig. 7) and the generation of higher blockage. The figure shows relative velocity vectors (Figs. 9(*a*) and 9(*c*)) and static pressure contours (Figs. 9(*b*) and 9(*d*)) at the blade tip radius, at two times corresponding to points 6 and 8 in Fig. 4. Features of interest are marked with circles. There is no pitch-average backflow below the blade tip at the trailing edge at the flow solution limit, but if the back pressure is increased, backflow occurs. Impingement of this backflow on the pressure surface increases the local pressure gradient at the rear of the blade passage, as shown by the more closely-spaced static pressure contours in Fig. 9(*d*) compared to Fig. 9(*b*). This drives the backflow upstream (Fig. 9(*c*) compared to Fig. 9(*a*)). The upstream movement of this fluid in turn leads to a further enhancement in backflow and additional local pressure rise from impingement, thus providing positive feedback and a conduit for further tip blockage increase.

We can also connect the tip clearance backflow to the observed increase in tip blockage beyond the flow solution limit. Figure 10 shows the variation with flow coefficient of the tip region blockage, evaluated at the trailing-edge plane, for the conditions of Fig. 4. The contributions from backflow (regions of negative axial velocity) and from local tip clearance fluid (tip blockage–backflow blockage) to the tip region blockage are also shown separately. For the transient flow regime (between points 4 and 8), the rate of increase in blockage associated with backflow accounts for most of the rate of increase in tip blockage.

Figure 11 illustrates the role of leading-edge spillage in setting the flow solution limit. The upper sketch (Fig. 11(*a*) depicts the tip clearance flow trajectory for a situation in which spillage has not occurred, and the lower sketch (Fig. 11(*b*)) the trajectory when there is leading-edge spillage. With the incoming/tip clearance flow interface inside the passage (no leading-edge spillage, as in Fig. 11(*a*)), the tip clearance fluid, as well as any backflow, either

Downloaded 30 May 2010 to 128.113.26.88. Redistribution subject to ASME license or copyright; see http://www.asme.org/terms/Terms_Use.cfm

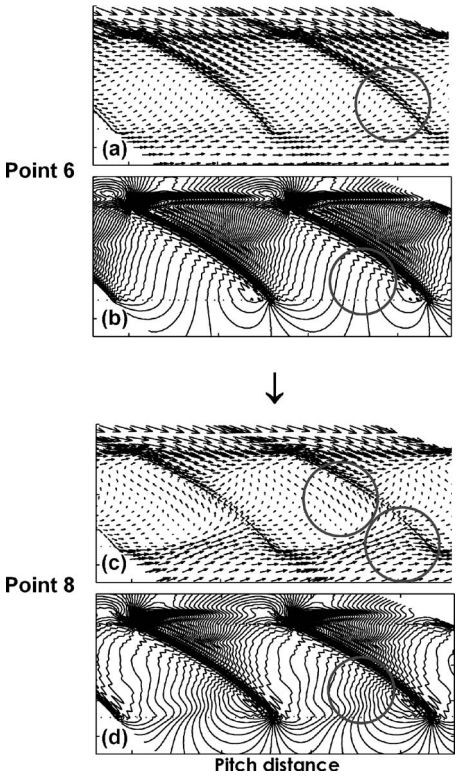

Fig. 9 Relative flow vectors and static pressure contour at rotor tip plane during transient beyond equilibrium solution limit. Figs. 9(*a*) and 9(*b*) correspond to point 6, and Figs. 9(*c*) and 9(*d*) to point 8, of Figs. 4, 6, and 8.

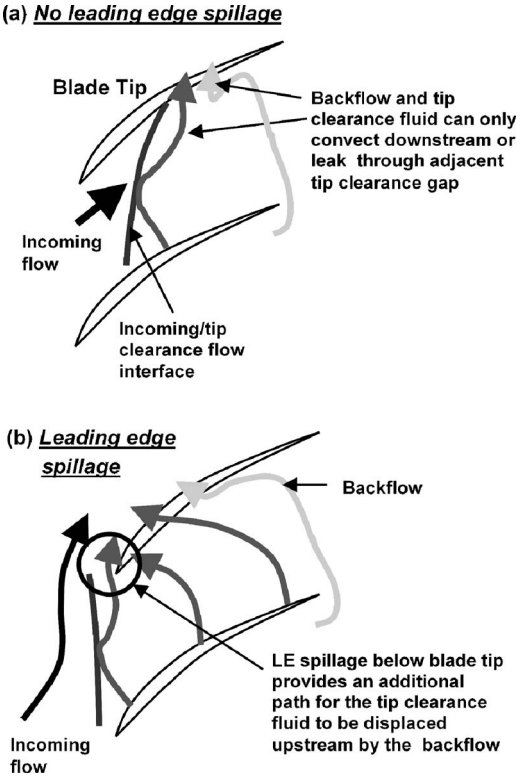

Fig. 11 Role of leading-edge spillage on upstream propagation of backflow

convects downstream or leaks through the adjacent tip clearance. However, leading-edge spillage below the blade tip (as in Fig. 11(*b*)) means that the tip clearance fluid has an additional path by which it can move upstream, especially when displaced by the backflow.

Although the two threshold flow events may start at different flow coefficients, the hypothesis of this paper is that both must be present (i.e., both criteria must be satisfied) for the flow solution limit to be reached. The flow solution limit will occur at the lower of the two flow coefficients at which the threshold flow events occur.

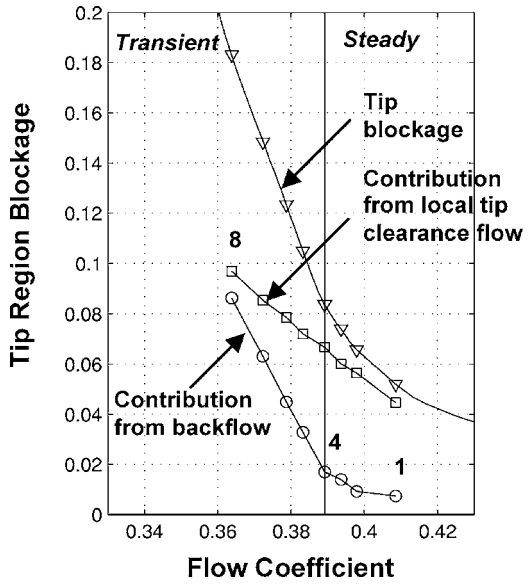

Fig. 10 Contribution of tip clearance backflow to overall tip region blockage

As an illustration of the above, tip clearance backflow can start at a higher flow coefficient than leading-edge spillage, but the flow solution limit will only occur when the latter appears. This is demonstrated by E^3 rotor B computations carried out at 3.0% chord tip clearance, where there is appreciable separation between the conditions for the occurrence of the two events and where the backflow occurs at a much higher flow coefficient than spillage. Figure 12 shows a time-averaged[1] pressure rise coefficient and pitch-averaged mass flow and spillage mass flow distributions. The symbols are the same as those in Figs. 4, 8, and 6, respectively.

Figure 12(*b*) shows the spanwise distribution of pitchwise average mass flow at the trailing edge. Backflow below the blade tip is seen at flow coefficients as high as point 1. However, the flow solution limit does not occur until the onset of leading edge spillage below the blade tip at point 4 (see Fig. 12(*c*)), where both conditions are satisfied.

In the converse situation, leading edge spillage can occur at a higher flow coefficient than the backflow, but again, the flow solution limit is reached only when backflow below the blade tip occurs. This situation is shown in Figs. 6 and 8 for the 1.8% chord tip clearance case. From Fig. 6, leading-edge spillage is seen to start at point 3. However, the flow solution limit for this case occurs at point 4, at the onset of trailing edge backflow (Fig. 8).

The link between the single passage flow solution limit and the tip clearance flow can thus be summarized as follows:

- The flow solution limit is characterized by the onset of rapid

[1]For large tip clearance sizes, as is the case here, steady oscillations in the tip clearance flow were found to occur near the flow solution limit. The values reported are thus time averaged. Similar oscillations were observed by Mailach et al. [15] and Marz et al. [16]

Downloaded 30 May 2010 to 128.113.26.88. Redistribution subject to ASME license or copyright; see http://www.asme.org/terms/Terms_Use.cfm

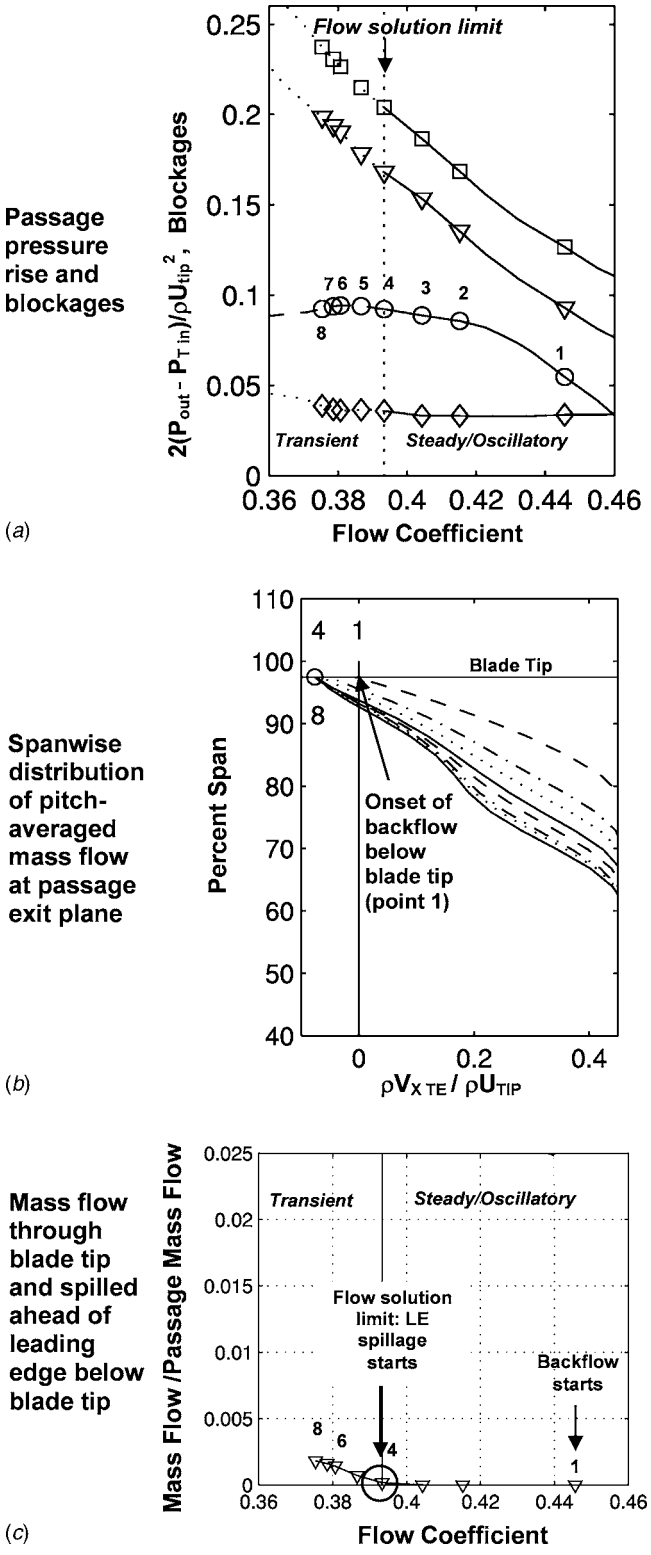

Fig. 12 Evaluation of passage flow solution limit criteria for 3.0% chord tip clearance: (*a*) passage pressure rise and blockages, (*b*) spanwise distribution of pitch-averaged mass flow at passage exit plane, and (*c*) mass flow through blade tip and spilled ahead of leading edge below blade tip

transient growth of the passage tip blockage until the tip blockage grows to the hub.

- The onset of the tip blockage growth is marked by two threshold flow events/criteria, which can start at different flow coefficients but must both be present:

1. Backflow of tip clearance fluid (zero pitch-averaged mass flow across the pitch) from adjacent blade passages at the trailing edge plane below the blade tip
2. Spillage of tip clearance fluid ahead of the blade leading edge below the blade tip into the next passage

In the next section, we connect this description of the blade passage flow solution limit with the formation of spike disturbances. We view four factors as underpinning this connection. First, is that the phenomena described occur in the tip region, where spike disturbances have been experimentally detected. Second, is that the spillage of tip clearance fluid to the adjacent blade passage ahead of the rotor leading edge is consistent with the generic flow features associated with spike stall inception, where the incoming/tip clearance flow interface lines up with the rotor leading-edge plane. Third, we have observed the impingement pattern of trailing-edge backflow in the stall computations by Hah et al. [17] on another low-speed rotor. Finally, the required presence of both threshold flow events for stall inception is observed in the study of rotating instabilities by Marz et al. [16]. Trailing-edge backflow can be seen in their multiple blade passage computations in the stable flow range, but they state that stall does not occur until the tip clearance flow leaks across the blade leading edge.

Link to Stall Inception

Multiple blade passage unsteady computations have been carried out to provide detailed comparison of the proposed criteria for single blade passage flow solution limit with the inception of rotating stall. In addition, the scenario for spike formation has been assessed against known experimental observations on stall inception. Both of these comparisons bear out both the scenario and the hypothesized criteria.

Six blade passages were used to simulate the formation of spike stall disturbances. While six passages are not ideal, two reasons can be put forward as an argument that the calculation demonstrates the central features of the spike waveform. First, the slope of the total-to-static pressure rise characteristics at the flow solution limit is negative and, thus, the only known route to rotating stall is via spike formation [3]. Second, spike disturbances have been experimentally measured to have a circumferential extent of two to three blade passages [4,11,18,19].

As described in the Appendix, the computational code, mesh, and procedure were the same as for the single blade passage computations. The single blade passage flow field corresponding to the flow solution limit was used for the initial condition. The equivalence between single and multiple blade passage flow solution limits is evidenced by the fact that, in the absence of any introduced asymmetry in the flow field, all blade passages stall simultaneously with the same transient beyond the flow solution limit as the single blade passage computation. To provide the circumferential nonuniformity associated with rotating stall, therefore, a small amplitude sinusoidal disturbance in stagnation pressure (velocity nonuniformity corresponding to ~1% of wheel speed and wavelength of six passages) was introduced upstream. The applied disturbance only existed during the first ten blade-pitch convection times, well before any spike disturbance formation and it extended over the full span. These initial disturbances, which favor modal stall inception rather than spikes at the tip, were chosen to ensure that the spikes would grow "naturally," rather than being forced by an initial disturbance.

Figure 13 shows results for the multiple blade passage stall simulation. There are five plots in Fig. 13. The uppermost one gives the time history of the mass flow during the stall transient. The lower four show the axial velocity deviation from the passage-averaged value, normalized by blade tip velocity, at the

Downloaded 30 May 2010 to 128.113.26.88. Redistribution subject to ASME license or copyright; see http://www.asme.org/terms/Terms_Use.cfm

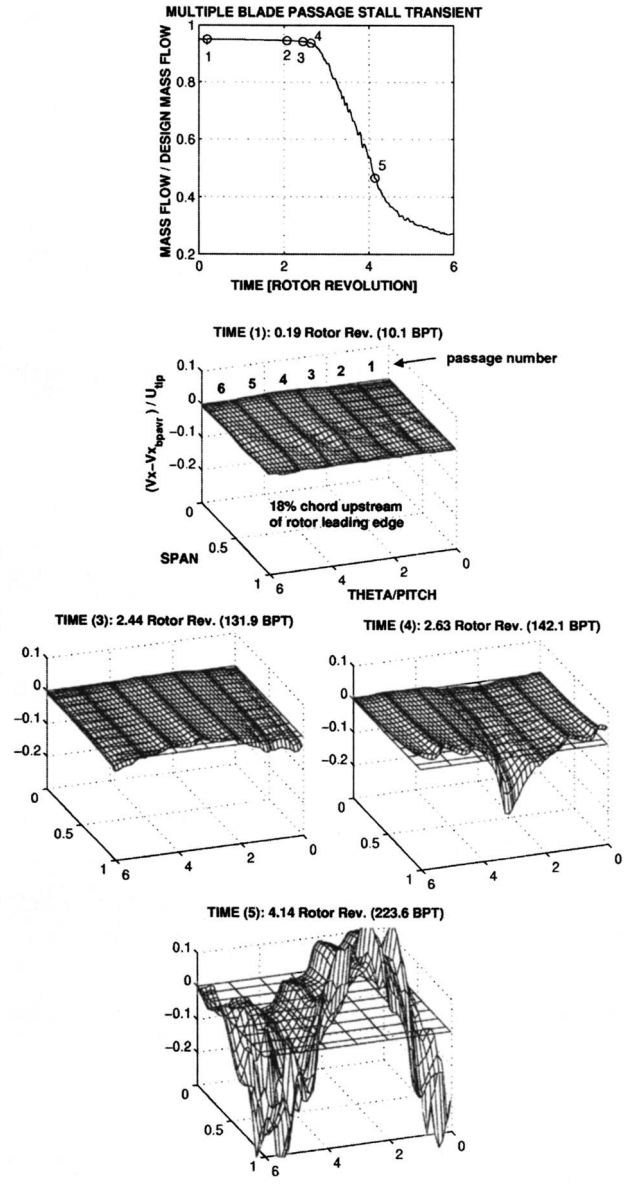

Fig. 13 Stall transient for multiple (six) blade passage configuration

different times marked in the mass flow time history. The three axes on the figure are axial velocity, span (going from 0 at the hub to 1.0 at the tip) and circumferential coordinate theta measured in blade pitches. The axial position of the plots is 18% chord upstream of the rotor leading edge, representative of hot-wire locations used in published measurements of spike disturbances (e.g., [4]).

At time instant (1), when the initially imposed disturbance is removed, no visible velocity defect at the blade tip is seen, implying the introduced flow asymmetry has not biased the results in favor of spikes. A short length-scale disturbance (in the form of an axial velocity deviation near the casing that is more pronounced at the crest) appears at time (3). At time (4), a velocity defect near the casing, which is localized over roughly two blade pitches becomes visible, accompanied by the start of a rapid drop in the mass flow. The disturbance grows rapidly in amplitude and also becomes more two-dimensional, as seen at time (5).

On the axial velocity deviation plots in Fig. 13, the direction of blade motion is from left to right along the *theta/pitch* axis. With respect to the blades the velocity defect (short length-scale disturbance) moves in the reverse direction because its speed is less than blade speed in the absolute frame of reference. The speed of the short length-scale disturbance can be estimated from the position of the maximum velocity deficit at different times, as in the experiments. The maximum velocity defect has moved by about three blade pitches between time steps (3) and (4), which are ten blade passing times (BPT) apart. The speed of the disturbance is thus ~70% of the rotor speed. The time scale of the growth to fully developed stall in the computations is essentially the time needed from inception (say time between (2) and (3)) until the disturbance extends across the entire span (roughly a revolution after time (5)), overall about three rotor revolutions.

Table 1 Comparison of measured [5] and computed spike disturbance for E^3 rotor B

Characteristics	Experiment	Computation
Circumferential extent	~2–3 blade pitch	~2–3 blade pitch
Radial extent	concentrated in tip region	last 10–20% span
Rotating speed	70–73% of rotor speed	~70% of rotor speed
Growth time to full stall cell	~3 rotor revolutions	~3 rotor revolutions

Table 1 compares the computed short length-scale disturbance to hot-wire measurements of spike disturbance in front of the E^3 rotor B [11] as summarized by Gong et al. [5]. The features of the disturbance obtained from the computations compares well to the measured features.

We also need to assess whether the criteria and scenario for spike disturbance formation are consistent with those for the single blade passage flow solution limit. To do this we examine: (i) tip clearance backflow at the trailing edge and (ii) leading edge tip clearance fluid spillage, for the blade passage behind the spike disturbance. Figure 14 displays the relative flow vectors at the blade tip radius at time (4). Figure 15 presents the relative flow vectors for the single blade passage calculation in the transient regime (beyond point 8 in Fig. 4) at a flow coefficient (0.343) near that (0.346) of passage 3 in Fig. 14. The two threshold events (flow spillage at leading edge and backflow at trailing edge) proposed as necessary for spike disturbance formation can be seen in both the multiple and single blade passage solutions.

Figure 16 shows the spanwise distribution of pitch-averaged mass flow and leading-edge tip clearance fluid spillage below the blade tip, for each blade passage at time (4). At this time, the velocity defect is in front of blade passages 3 and 4 and is moving toward blade passage 5. Figure 16 can be compared to Figs. 8 and 6 for the single blade calculations. In Figs. 14 and 16(*a*), passages 3 and 4 show trailing-edge backflow and impingement below the blade tip due to tip clearance fluid from adjacent blade passages. The other blade passages do not exhibit any trailing-edge backflow below the blade tip. Figures 14 and 16(*b*) also show leading-edge spillage of tip clearance fluid below the blade tip from blade passage (3) into passage (4). These two flow events are similar to those observed in the single blade passage flow transient past the flow solution limit.

Our inference from the multiple passage stall simulation is thus that the criteria, which set the single blade passage flow solution limit, also describe the conditions for the formation of spike stall disturbances. The flow solution limit is therefore viewed as a sufficient condition for spike formation although it is not a necessary one. A disturbance of sufficient amplitude introduced at a higher mass flow could trigger spike formation. However, even in this case, we expect the proposed spike formation scenario in terms of tip clearance backflow and spillage to apply.

The multiple blade passage stall simulation also provides in-

Downloaded 30 May 2010 to 128.113.26.88. Redistribution subject to ASME license or copyright; see http://www.asme.org/terms/Terms_Use.cfm

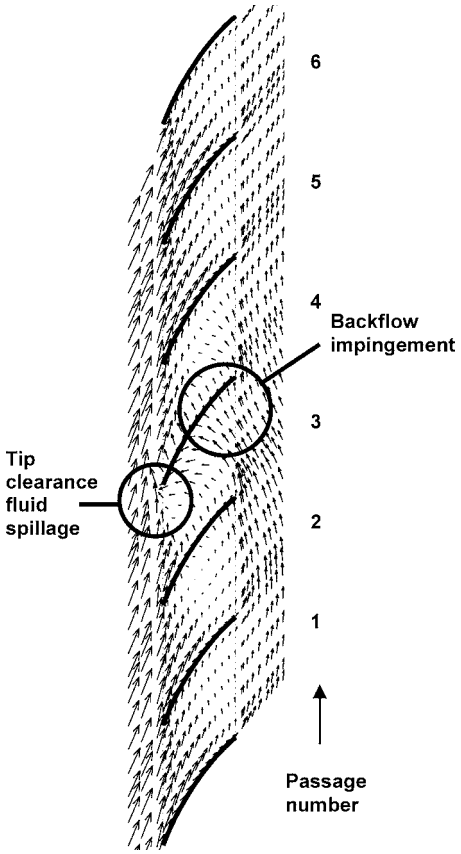

Fig. 14 Relative flow vectors at blade tip at time 4 of stall transient in Fig. 13

sight into the length scale of the spikes. The two criteria that set the single blade passage flow solution limit have a minimum of two passages as their circumferential extent and, at least as observed in all the calculations we have done, an extent of three passages for the maximum. In Fig. 14, all the leading-edge spillage fluid from the passage (3) flows into passage (4) such that the disturbance is most pronounced for these two passages. The backflow tip clearance fluid may come mainly from passage (2), but also from one or two passages beyond. Although quantitative scaling is yet to be done, the above extent relates well to the observed circumferential extent of the spikes.

Although not shown in this paper, we note that the computational results and criteria for spike formation are also in accord with the following experimental observations:

1. The blade loading at which both the backflow and spillage criteria occur corresponds to the critical tip incidence that Camp and Day [3] found for spike formation.
2. The best place to detect the spike disturbance on the E^3 compressor was at the trailing edge of the first rotor near the casing [20]. Details relating to items 1 and 2 are given by Vo [6].
3. Recent experiments by Deppe et al. [21] confirm the presence of both leading-edge spillage and trailing-edge backflow during spike formation on three different low-speed single-stage compressors.

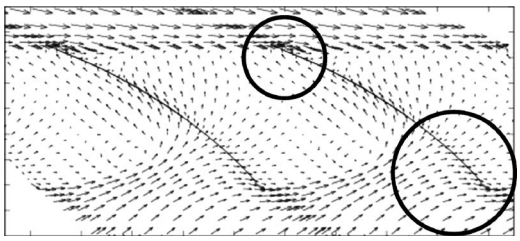

Fig. 15 Relative flow vectors at blade tip in single blade passage computation at a flow coefficient near that of passage 3 in Fig. 14

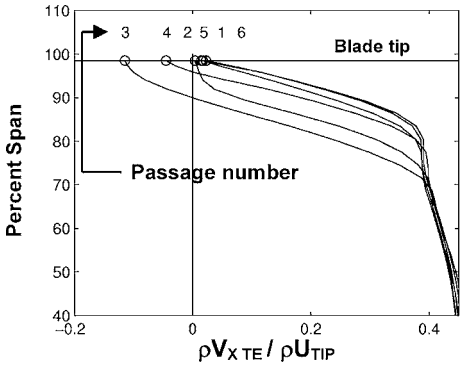

(*a*) **Spanwise distribution of pitch-averaged mass flow at passage exit plane**

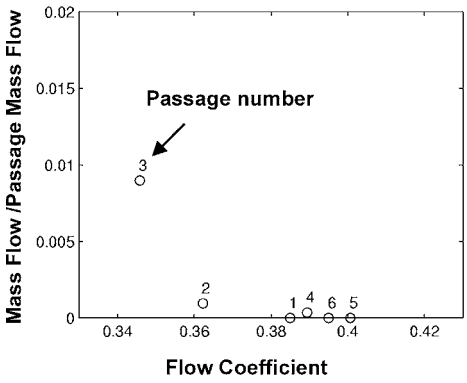

(*b*) **Leading edge spillage of tip clearance fluid below the blade tip**

Fig. 16 Tip clearance flow behavior in each blade passage at time (4): (*a*) spanwise distribution of pitch-averaged mass flow at passage exit plane and (*b*) leading-edge spillage of tip clearance fluid below the blade tip

The hypothesis presented concerning spike formation has practical implications for stall delay. Any technique that delays either of the two criteria that set the flow solution limit should result in a favorable movement of the stall point. Thus, both trailing-edge suction of the tip clearance backflow and leading-edge blowing, which would tend to delay the movement of the incoming/tip clearance flow interface to the leading-edge plane, should be effective in delaying the formation of spike disturbances and, thus, spike stall inception. One such example (although this is not the only explanation that can be given) is the observation by Lee and Greitzer [22] concerning the effect of end-wall suction and blowing on compressor stability. They reported that rear end-wall suction and/or leading-edge blowing were both effective in increasing the stall margin. Other examples (again with the above caveat) are the studies by Deppe et al. [21] and by Weigl et al. [23], which demonstrate the effectiveness of tip radially localized leading-edge blowing in delaying stall inception.

Summary and Conclusions

1. Net upstream (pitch- and time-averaged) mass flow at the trailing-edge blade tip, and (time-averaged) leading-edge tip

Downloaded 30 May 2010 to 128.113.26.88. Redistribution subject to ASME license or copyright; see http://www.asme.org/terms/Terms_Use.cfm

clearance flow spillage below the blade tip, are proposed as the two criteria that set the lowest flow coefficient at which a rotor blade passage can operate without the formation of spike disturbances.
2. These proposed criteria for the formation of spike disturbances are consistent with all published observations on axial compressor stall inception.
3. For compressors that exhibit short length-scale stall inception, techniques that delay either of the two proposed criteria for spike formation should be successful in extending the stable mass flow operating range.
4. The present work suggests that single blade passage computations may be used to predict stall inception if they contain:
   - exit flow boundary conditions that capture steady-state solutions past the peak pressure rise of a rotor blade (see the Appendix)
   - time-accurate computations so that the time-averaged flow field from oscillatory equilibrium solutions can be applied in the criteria for spike formation (Steady-state computations may not be suitable for cases with substantial unsteadiness from tip clearance flow oscillations, e.g., the large tip clearance case in Fig. 12, or interaction with adjacent blade rows.)
5. Based on the criteria presented, a conceptual framework that makes use of single blade passage computations for stall prediction in a compressor design system may be proposed:
   - Carry out single blade passage computations until the flow solution limit for all the blade rows in the compressor.
   - Find the flow solution limit with the highest mass flow and assess whether it occurs at a lower mass flow than the zero-slope peak of the (multistage) *compressor* stagnation-to-static pressure rise characteristic.
   - If yes, modal stall inception is predicted. If not, a spike disturbance is expected in the blade row that has its flow solution limit at the highest mass flow. The numerical approach by Gong et al. [5] then allows determination of whether the spike will grow to a fully developed rotating stall at this mass flow.

Acknowledgment

This work was funded by the U.S. Air Force Office of Scientific Research under Grant No. F49620-00-1-0014 monitored by Dr. T. J. Beutner, whose support is gratefully acknowledged. We would like to thank Prof. J. D. Denton and Dr. L. Xu for their help with setting up the code and computational mesh. The authors are also pleased to acknowledge Dr. J. J. Adamczyk, J. Bleeg, Dr. C. Hah, Dr. M. D. Hathaway, Dr. C. M. Rhie, Dr. H. Saathoff, and Dr. D. E. Van Zante, for providing useful information on features of the flow in other compressor geometries. Technical advice and insightful comments during the course of this work from Prof. E. E. Covert, Prof. N. A. Cumpsty, Dr. I. J. Day, Prof. J. J. Deyst, Dr. Y. Gong, Dr. T. P. Hynes, Prof. F. E. Marble, and Dr. J. P. Longley are also much appreciated. Finally, we would especially like to thank Dr. A. J. Strazisar for his thoughtful comments on the initial submission; the final version is better because of his input.

Appendix

UNSTREST [13] was used for time-accurate single and multiple blade passage computations. The mesh used for one passage was $106\times41\times45$ with a pinched blade tip and a tip clearance described by five radial grid points [6], which is standard for UNSTREST. As tip clearance flow is essentially a pressure-driven flow [8], the dominant effect of the pointed tip is to set an effective tip clearance size, rather than to alter the central features of the flow.

Because the same mesh is used for both the single and multiple (six) blade pitch computations, the upstream and downstream ducts are six blade pitches long. The length of the upstream and downstream ducts is set the same as the width of the multiple blade computational domain so that pressure disturbances with a wavelength equal to the domain width can decay to uniform conditions in the pitchwise direction at the boundaries. Consequently, the domain exit is far from the backflow region at the rotor trailing edge, thus avoiding reverse flow at the exit boundary.

The inlet boundary conditions consist of uniform stagnation pressure and temperature and axisymmetric radial distribution of swirl angle based on the spanwise distribution of the inlet guide vane exit angle in the E^3 compressor. A standard exit boundary condition, consisting of a specified axisymmetric tip static pressure with radial equilibrium, was implemented.

For single blade passage computations, the pressure rise versus flow curve in Fig. 4, points 1–4, was obtained by increasing the exit tip pressure until the flow solution limit (point 4) in increments of 0.005% of the dynamic pressure based on wheel speed. (For cases where the flow solution limit occurs at a flow coefficient lower than that of the peak exit static pressure—positively sloped part of the stagnation-to-static pressure-rise characteristic—a mass flow—throttle—exit boundary condition would be required. To initiate the stall flow transient (flow coefficients below point 4), the equilibrium flow limit is used as the initial solution, the back pressure is increased slightly, in this case by roughly 0.1% of the dynamic head based on blade tip speed.

For the multiple blade stall simulation, the single blade passage mesh and solution at the flow solution limit (point 4) are repeated six times pitchwise to provide the initial multiple blade flow solution limit. Circumferentially uniform inlet and exit conditions combined with the cylindrical coordinate system used in UNSTREST cause all the blade passages to stall simultaneously with the same transient.

Thus, a nonprejudicial (in terms of spike formation) inlet flow asymmetry was introduced through a full-span inlet stagnation pressure perturbation of six pitches in circumferential wavelength. The disturbance was applied only during ten blade passing times (about 1/20 of the development time of a spike). The total pressure inlet disturbance amplitude gave a rotor inlet velocity asymmetry of $\sim$1% of rotor tip speed; this was viewed as representative of asymmetries encountered in practice.

References

[1] Moore, F. K., and Greitzer, E. M., 1986, "A Theory of Post-Stall Transients in Axial Compressors—Part I: Development of Equations," ASME J. Eng. Gas Turbines Power, **108**, pp. 68–76.
[2] Longley, J., 1994, "A Review of Non-Steady Flow Models for Compressor Stability," ASME J. Turbomach., **117**, pp. 202–215.
[3] Camp, T. R., and Day, I. J., 1998, "A Study of Spike and Modal Stall Phenomena in a Low-Speed Axial Compressor," ASME J. Turbomach., **120**, pp. 393–401.
[4] Day, I. J., 1993, "Stall Inception in Axial Flow Compressors," ASME J. Turbomach., **115**, pp. 1–9.
[5] Gong, Y., Tan, C. S., Gordon, K. A., and Greitzer, E. M., 1999, "A Computational Model for Short Wavelength Stall Inception and Development in Multistage Compressors," ASME J. Turbomach., **121**, pp. 726–734.
[6] Vo, H. D., 2001, "Role of Tip Clearance Flow on Axial Compressor Stability," Ph.D. thesis, Massachusetts Institute of Technology, Cambridge, MA.
[7] Khalid, S. A., Khalsa, A. S., Waitz, I. A., Tan, C. S., Greitzer, E. M., Cumpsty, N. A., Adamczyk, J. J., and Marble, F. E., 1999, "Endwall Blockage in Axial Compressors," ASME J. Turbomach., **121**, pp. 499–509.
[8] Storer, J. A., and Cumpsty, N. A., 1991, "Tip Leakage Flow in Axial Compressors," ASME J. Turbomach., **113**, pp. 252–259.
[9] Koch, C. C., 1974, "Discussion of Benser W. A.: Transonic Compressor Technology Advancements," Fluid Mechanics, Acoustics, and Design of Turbomachinery, Part II, NASA SP-304.
[10] Saathoff, H., and Stark, U., 2000, "Tip Clearance Flow Induced Endwall Boundary Layer Separation in a Single-Stage Axial-Flow Low-Speed Compressor," ASME Paper No. 2000-GT-0501.
[11] Silkowski, P. D., 1995, "Measurements of Rotor Stalling in a Matched and Mismatched Multistage Compressor," GTL Report No. 221, Massachusetts Institute of Technology, Cambridge, MA.
[12] Spakovszky, Z. S., Weigl, H. J., Paduano, J. D., Van Schalkwyk, C. M., Suder, K. L., and Bright, M. M., 1999, "Rotating Stall Control in a High-Speed Stage

Downloaded 30 May 2010 to 128.113.26.88. Redistribution subject to ASME license or copyright; see http://www.asme.org/terms/Terms_Use.cfm

With Inlet Distortion—Part I: Radial Distortion," ASME J. Turbomach., **121**, pp. 510–516.
[13] Denton, J. D., 1986, "The Use of a Distributed Body Force to Simulate Viscous Effects in 3D Flow Calculations," ASME Paper No. 86-GT-144.
[14] Cumpsty, N. A., 1996, private communication.
[15] Mailach, R., Lehmann, I., and Vogeler, K., 2000, "Rotating Instabilities in an Axial Compressor Originating From the Fluctuating Blade Tip Vortex," ASME Paper No. 2000-GT-506.
[16] Marz, J., Hah, C., and Neise, W., 2001, "An Experimental and Numerical Investigation Into the Mechanisms of Rotating Instability," ASME Paper No. 2001-GT-536.
[17] Hah, C., Schulze, R., Wagner, S., and Hennecke, D. K., 1999, "Numerical and Experimental Study for Short Wavelength Stall Inception in a Low-Speed Axial Compressor," AIAA Paper No. 99-IS-033.
[18] Day, I. J., and Freeman, C., 1994, "The Unstable Behavior of Low and High Speed Compressors," ASME J. Turbomach., **116**, pp. 194–201.
[19] Dobat, A., Saathoff, H., and Wulff, D., 2001, "Experimentelle Untersuchungen zur Entstehung von Rotating Stall in Axialventilatoren," VDI-Ber., **1591**, pp. 345–360.
[20] Park, H. G., 1994, "Unsteady Disturbance Structures in Axial Flow Compressor Stall Inception," M.S. thesis, Massachusetts Institute of Technology, Cambridge, MA.
[21] Deppe, A., Saathoff, H., and Stark, U., 2005, "Spike-Type Stall Inception in Axial-Flow Compressors," *6th European Conference on Turbomachinery—Fluid Dynamics and Thermodynamics*, Lille, France, March, pp. 178–188.
[22] Lee, N. K. W., and Greitzer, E. M., 1990, "Effects of Endwall Suction and Blowing on Axial Compressor Stability Enhancement," ASME J. Turbomach., **112**, pp. 133–144.
[23] Weigl, H. J., Paduano, J. D., Frechette, L. G., Epstein, A. H., Greitzer, E. M., Bright, M. M., and Strazisar, A. J., 1998, "Active Stabilization of Rotating Stall and Surge in a Transonic Single Stage Compressor," ASME J. Turbomach., **120**, pp. 625–636.

Downloaded 30 May 2010 to 128.113.26.88. Redistribution subject to ASME license or copyright; see http://www.asme.org/terms/Terms_Use.cfm

Rain Ingestion in Axial Flow Compressors at Part Speed

Ivor Day
Whittle Laboratory,
University of Cambridge,
Cambridge, CB3 0DY, United Kingdom

John Williams[1]
Department of Engineering Science,
University of Oxford
Parks Road
Oxford, OX1 3PJ, United Kingdom

Christopher Freeman
Whittle Laboratory,
University of Cambridge,
Cambridge, CB3 0DY, United Kingdom

New experimental work is reported on the effects of water ingestion on the performance of an axial flow compressor. The background to the work is the effect that heavy rain has on an aeroengine compressor when operating in a "descent idle" mode, i.e., when the compressor is operating at part speed and when the aeromechanical effects of water ingestion are more important than the thermodynamic effects. Most of our existing knowledge in this field comes from whole engine tests. The current work provides the first known results from direct measurements on a stand-alone compressor. The influence of droplet size on path trajectory is considered both computationally and experimentally to show that most rain droplets will collide with the first row of rotor blades. The water on the blades is then centrifuged toward the casing where the normal airflow patterns in the vicinity of the rotor tips are disrupted. The result of this disruption is a reduction in compressor delivery pressure and an increase in the torque required to keep the compressor speed constant. Both effects reduce the efficiency of the machine. The behavior of the water in the blade rows is examined in detail, and simple models are proposed to explain the loss of pressure rise and the increase in torque. The measurements were obtained in a low speed compressor, making it possible to study the mechanical (increase in torque) and aerodynamic (reduction in pressure rise) effects of water ingestion without the added complication of thermodynamic effects. [DOI: 10.1115/1.2366511]

Introduction

During take-off and climb, aircraft engines operate at high power and are able to process large quantities of rain water without a significant loss in performance. Indeed, water injection is sometimes used in military engines to increase take-off power [1]. During the descent, however, the engines are usually operated at idle power, i.e., at a reduced rotational speed, and it is under these conditions that heavy rain poses a threat to stable operation [2]. In the past, incidences of compressor surge, loss of rotational speed, and combustor flameout have all been attributed to rain ingestion. To add to these problems, some engines have been found to be less tolerant of water ingestion than others [3]. Our understanding of how and why water has these adverse effects on engine behavior is very limited, and it is for this reason that the current project was initiated. The object of the work is not so much to simulate the behavior of an engine under wet conditions, but to study the fundamental physics of how liquid water behaves in a compressor and how it affects compressor performance.

Besides the aerodynamic and mechanical effects of water on compressor behavior, there are also thermodynamic effects to be considered, e.g. evaporation, temperature distortion, and changes in the gas properties. (See, for example, Davis [4] and Tomassetti [5].) In this context, evaporation is probably the principal factor, as is demonstrated by the practice of fog boosting to improve the cycle efficiency of industrial engines. For fog boosting, very fine droplets are used because fine droplets evaporate quickly and minimize the risk of water erosion during prolonged periods of operation. Rain ingestion, on the other hand, involves water droplets of larger dimensions and here the effects of evaporation are somewhat less important, particularly at reduced engine speeds.

During descent idle operation, at 20,000 ft, the Mach numbers in the HP compressor are low and the temperatures are not much above standard conditions at sea level. Evaporation is thus unlikely to be an important parameter under these conditions [6]. In the current tests, which have been conducted at atmospheric temperatures and at moderate rotational speeds, some evaporation is detected, but calculations suggest that the effect on compressor performance is negligible in comparison with aerodynamic and mechanical effects [7].

Certification tests of new engines are based on a maximum atmospheric water concentration of 20 g/m^3 [8]. However, Kissel [9] suggests that water levels may be significantly higher than this in severe rainstorms. In addition, the water concentration at the engine face is increased above the atmospheric level during descent idle, due to an effect known as "scoop." This effect is caused by the spillage of air around the engine at part-speed operation, and may lead to a doubling of the water concentration entering the engine. Due to inertia, water droplets above a certain micronic size are not able to follow the streamlines of the spilling air and thus continue straight into the engine inlet. The water capture stream tube is thus larger than the air capture stream tube [2].

As far as the core compression system is concerned, this increase in concentration due to the scoop effect is somewhat offset by the centrifugal action of the spinner and fan, which tend to divert water into the bypass duct. A significant amount of water does, however, enter the core, where, after further losses through bleed slots, it enters the HP compressor and can even reach the combustion chamber. The HP compressor thus experiences reduced water concentration compared to the front of the engine, but it is still this compressor that is most adversely affected by water ingestion.

As previously mentioned, droplets larger than a few microns in diameter are unable to follow the curvature of the gas streamlines and consequently deposit on the blade surfaces. CFD and particle tracking calculations have been used to produce Fig. 1, which shows the computed droplet trajectories for various droplet sizes entering the first rotor row of the test compressor [10]. Significant deviation from the gas streamlines occurs for all droplets with diameters greater than about 10 microns. This figure agrees with the maximum droplet size used in inlet fog boosting, where collisions with blade surfaces are avoided at all costs. In the current

[1]Formerly of the Whittle Laboratory, Cambridge.

Contributed by the International Gas Turbine Institute (IGTI) of ASME for publication in the JOURNAL OF TURBOMACHINERY. Manuscript received October 1, 2004; final manuscript received February 1, 2005; published online February 1, 2008. IGTI Review Chair: K. C. Hall. Paper presented at the ASME Turbo Expo 2005: Land, Sea and Air, Reno, NV, June 6–9, 2005, Paper No. GT2005-68582.

 Copyright © 2008 by ASME

Downloaded 30 May 2010 to 128.113.26.88. Redistribution subject to ASME license or copyright; see http://www.asme.org/terms/Terms_Use.cfm

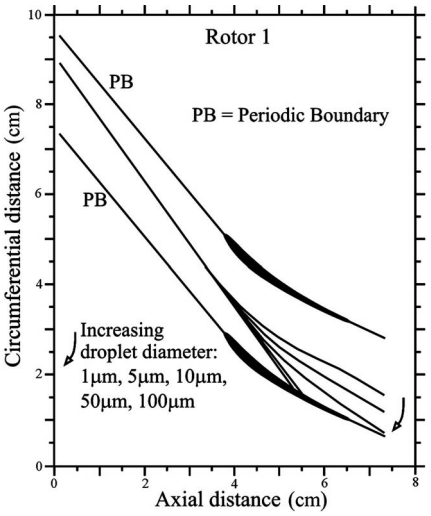

Fig. 1 Droplet trajectories through rotor 1 for various droplet diameters

experiments, where rain, rather than fog, is being considered, spray nozzles giving Sauter mean diameters in the range from 50 to 200 μm have been used.

During the descent, the spillage of air around the engine will cause the approaching air to decelerate as it nears the engine face. A droplet that is too large to respond to this change in speed will develop a slip velocity relative to the surrounding air. The drag force associated with this slip will cause the droplet to break up. Previous work suggests that all droplets with diameters around 600 μm and above will break up as they approach the engine [11]. A correlation proposed by Wolfe and Anderson [12] suggests that the volume mean diameter of the breakup products of a 600 μm diameter droplet will be an order of magnitude lower than the initial diameter. The droplet breakup process thus still produces droplets that are too large to follow the air path, i.e., about 60 microns. Raindrops, and their breakup products, are thus more likely to collide with the compressor blades than they are to pass through them.

In the past, experimental work has mainly consisted of whole engine tests where compressor performance is inferred from gross engine parameters such as fuel burn or changes in rotational speed [2]. In this type of testing, mechanical, aerodynamic, and thermodynamic effects are all present at the same time and all influence each other. It is thus difficult to separate one effect from another. In the work reported here, where thermodynamic effects have been kept to a minimum, it has been possible, for the first time, to separate the mechanical and aerodynamic effects of water ingestion. In addition, the use of a stand-alone compressor has provided a unique opportunity to acquire measurements from within a wet compressor.

Experimental Setup

The experiments were carried out in a four-stage laboratory compressor that was specially modified to cope with wet conditions. A schematic diagram of the test setup is given in Fig. 2. A venturi-type flow meter was added upstream of the compressor to provide a "dry" measurement of the air entering the compressor. (The bell-mouth inlet on the compressor itself could not be used for this purpose because of water contamination.) A water separator using commercial components was installed downstream of the compressor to remove the water from the discharge air. A short section of transparent casing was fitted downstream of the compressor through which the water leaving the compressor could be observed.

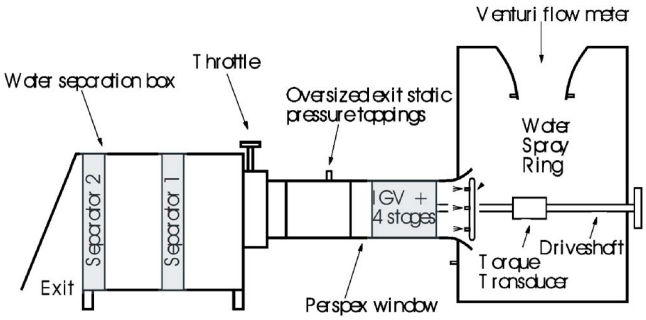

Fig. 2 Schematic of compressor test facility

The compressor itself consists of four stages preceded by a row of inlet guide vanes. The stagger settings of the stator rows, and the inlet guide vanes, are variable through the use of hand operated unison rings. The outer diameter of the compressor is 0.5 m, the hub/tip ratio 0.75 and the rotational speed is 3000 rpm. The blading (60 rotor and 58 stator blades per row) is of modern controlled diffusion design and the blade Reynolds Number is about 2.2×10^5 based on true chord.

The water spray system is positioned six chord lengths upstream of the IGVs. This system consists of a circular manifold, of mid-span diameter, fitted with a number of small industrial spray nozzles. Two high-pressure water pumps are used to supply the nozzles at pressures ranging from 5 to 40 bar, and rotameter-type flow meters are used to record the water flow rate.

Depending on the type of nozzles used, and the pressure of the water supplied, a range of spray patterns and droplet sizes can be produced. The manufacturers provided detailed calibration certificates for each nozzle type, and these were used throughout the experiments as a guide to the size of droplets being produced.

In the experiments, four types of nozzles were used:

(1) Impingement nozzles, producing a 90 deg spray cone of fine droplets between 51 and 97 μm Sauter mean diameters. (The word "impingement" arises because this type of nozzle shoots a high-pressure jet at an impingement pin attached to the nozzle body.)
(2) Whirl nozzles, producing a 30 deg cone of droplets between 116 and 174 μm diameter.
(3) Fan nozzles producing a flat spray of 15 deg spread with droplet sizes from 123 to 211 μm diameter.
(4) Straight jet nozzles producing a water pistol type jet of 1.5 mm diameter.

In the case of the impingement and whirl nozzles, the droplet size was determined by the water supply pressure. By varying the number of nozzles and the supply pressure, a range of droplet sizes at different water concentrations could be produced. The straight jet nozzles provide an unrealistic form of water supply, but this extreme case was useful in isolating certain aspects of water distribution at the compressor face. (Note: in all cases the nozzles were axisymmetrically distributed about the inlet.)

During testing, the following measurements were routinely acquired:

(1) Compressor rotational speed (averaged over five rotor revolutions).
(2) Temperature of injected water (measured by thermocouple in the supply line).
(3) Flow rate of injected water (rotameter reading).
(4) Temperature of incoming air (ambient air temperature in the laboratory).
(5) Flow rate of incoming air (calibrated venturi inlet).
(6) Inlet total pressure (measured in inlet plenum).

Downloaded 30 May 2010 to 128.113.26.88. Redistribution subject to ASME license or copyright; see http://www.asme.org/terms/Terms_Use.cfm

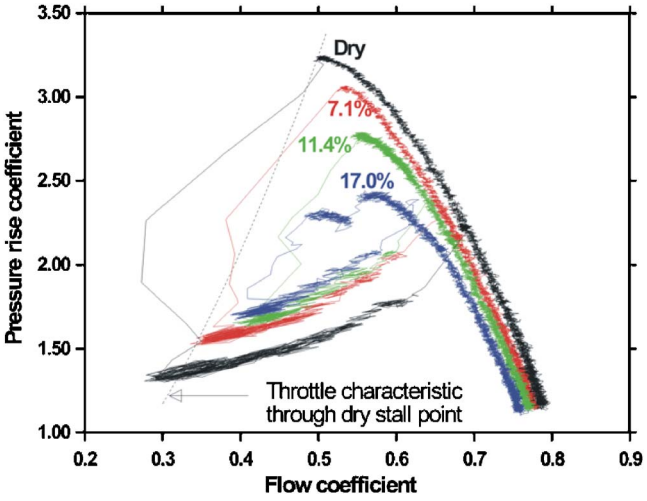

Fig. 3 Overall pressure rise characteristics for different amounts of water ingested

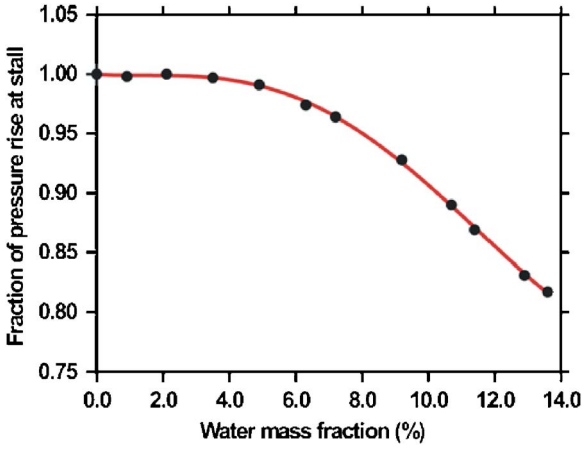

Fig. 4 Loss of pressure rise at stall as a function of the amount of water ingested

(7) Compressor outlet pressure. (Measured using the average pressure from a tight group of eight static pressure tappings in the exit duct just ahead of the throttle valve. The tappings were larger than normal in diameter and a long way downstream of the compressor at the top of the duct. This arrangement worked satisfactorily and trouble with water contamination was seldom experienced.)
(8) Compressor outlet temperature. (Measured by thermocouple in the exit plenum. The air at this point is saturated and therefore the wet and dry bulb temperatures are the same.)

More difficult to measure under wet conditions are the interstage pressure rise characteristics. For these measurement a specially designed purge system was used that employed a small choked orifice to continuously flush the static pressure tappings [10]. Other special measuring techniques are described at the appropriate place in the text.

Effect of Water Ingestion on Compressor Performance

In broad terms, the effect of spraying water into the compressor is to reduce the overall delivery pressure, and to increase the torque required to keep it spinning at the same speed.

In the "wet" performance measurements presented below, the nondimensional flow and pressure rise coefficients have been calculated, assuming that the water does not change the density or gas properties of the air [10]. This simplification is based on the idea that if the water is unevaporated, and locally concentrated in liquid form, it will occupy a negligible fraction of the annulus, and will have little effect on the thermodynamic properties of the air. (The volumetric fraction of the annulus occupied by water at a concentration of 15% mass is approximately 0.0002.) The nondimensional quantities are defined thus: flow coefficient $=v_x/U$, pressure rise coefficient $=\Delta p_{ts}/0.5\rho U^2$, corrected torque=torque/(ρ/ρ_0), where v_x is the mean air axial velocity; U is the mean blade speed; Δp_{ts} is the total-to-static pressure rise across the compressor; ρ is the actual air density and ρ_0 is a reference air density (1.225 kg/m^3).

The Effect on Pressure Rise. The effect of water on the performance of the compressor is a complicated matter, because small amounts of water appear to have little or no effect and larger amounts have a very pronounced effect.

Figure 3 is a good example of the dramatic effect that water can have on the overall total-to-static pressure rise characteristic. It can be seen that, for non-trivial amounts of water, the loss of pressure rise is significant. In this particular case, a large change in the flow coefficient at peak pressure rise is also observed. This indicates a clear loss of surge margin under wet conditions. (Note: such a large loss of surge margin is not always observed. This will be discussed in a later section.)

As previously mentioned, "small" amounts of water have little effect on the overall pressure rise characteristic; as is demonstrated in Fig. 4 where a loss of peak pressure rise is plotted against the water mass fraction. The first part of the graph, from 0% to 4%, is relatively flat, but after that the trend changes and the pressure falls steadily as the water concentration is increased.

The shape of the curve in Fig. 4 is generally true for all the tests conducted, but it is not possible to fix 4% as the point at which water starts to have an effect on pressure rise. Under different test conditions, and using different spray nozzles, the changeover point has been found to lie anywhere between 3% and 7%. (It is conceivable that the changeover point represents the water concentration at which the rotor tip clearance gap, particularly of the first stage, is affected by the water. This idea requires further study.)

The Effect of Droplet Size. An investigation into the effect of droplet size on the compressor performance was conducted using the impingement nozzles. By altering the driving pressure and the number of nozzles used, the mean droplet size can be changed from 51 to 97 μm without changing the amount of water delivered to the compressor. It was found that a change in droplet size over this range has no detectable effect on the behavior of the compressor. Even droplets of a much larger diameter, produced by plastic garden spray nozzles, produced the same basic effect on the pressure rise and stall margin.

The fan nozzles, which also generate a fine spray, had the same effect on compressor behavior as the impingement nozzles. The straight jet nozzles, on the other hand, had surprisingly little effect on the stalling flow coefficient, but produced a similar loss of pressure rise [10].

The Effect on Drive Torque. In terms of power input, the overall effect of injecting water into the compressor is to increase the torque required to keep it turning at the same speed. Figure 5 shows the torque characteristics for dry operation and for 11.4% water ingestion. The increase in torque when water is present is quite dramatic. For a wider range of water concentrations, Fig. 6 shows that the increase in torque is directly proportional to the amount of water ingested.

The linearity of the torque graph in Fig. 6 is in sharp contrast with the pressure rise curve in Fig. 4. For small quantities of

Downloaded 30 May 2010 to 128.113.26.88. Redistribution subject to ASME license or copyright; see http://www.asme.org/terms/Terms_Use.cfm

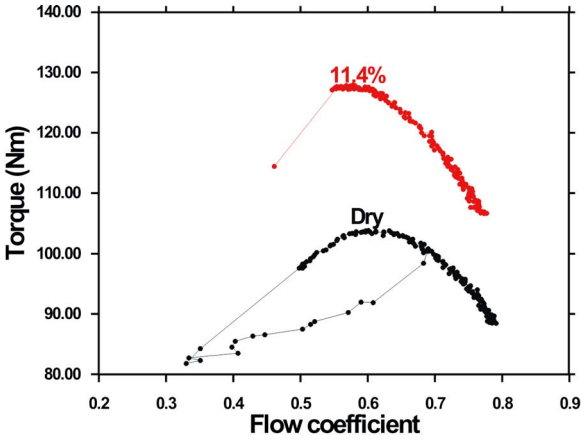

Fig. 5 Characteristics showing the increase in corrected torque brought about by 11.4% water ingested

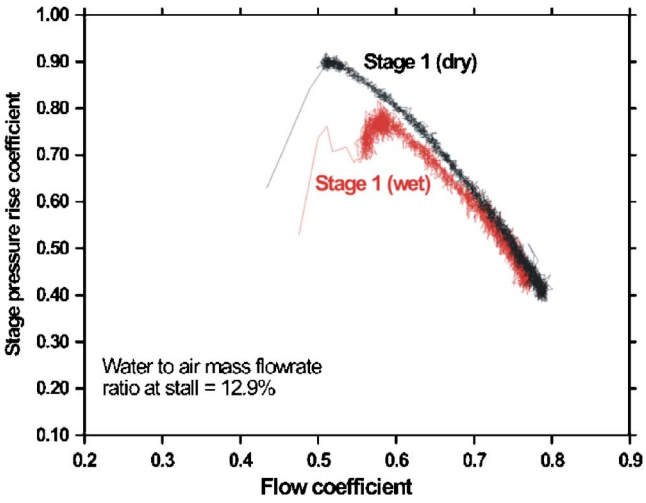

Fig. 7 Static-to-static pressure rise characteristics for stage 1

water, the pressure rise is independent of the amount of water added, whereas the torque plot shows direct proportionality right from the start. This can be interpreted as saying that, in the absence of evaporation, the increase in torque is due purely to the mechanical processing of the water by the blades.

Other experiments with different spray nozzles show that the increase in torque is always a linear function of the amount of water added, but that the gradient might be slightly different [10]. As discussed in the next section, the straight jet nozzles have a reduced effect on the first stage of the compressor, and thus the rate of torque increase is slightly less than that shown in Fig. 6. (Figure 6 was obtained by using the fine-spray nozzles that affect all four stages equally.)

The Effect on Stall Margin. Stall inception in the test compressor has been studied on previous occasions, e.g., Camp and Day [13], and it is known that stall in this compressor initiates in the first rotor—even though all the rotors are physically identical. Figure 7 shows the first stage characteristics for wet and dry operation. It can be seen that the wet characteristic turns over very sharply, and because of this the compressor is forced into stall prematurely. The presence of water thus makes the first stage, which is always the first to fail under dry conditions, even more susceptible to stalling.

In other tests reported by Williams [10], the straight jet nozzles produced some results that, at first sight, appear to be anomalous. With the straight jet nozzles, the drop in pressure rise, and the increase in torque, are slightly less dramatic, and the stall margin is hardly affected at all. Further tests show, however, that because of the high velocity of the jets (higher than air speed), and the concentrated nature of the flow, the water passes through the first rotor without experiencing much centrifugal action. In simplistic terms, we can thus think of the straight jets as having more influence on the latter stages of the compressor than on the first. In this way the lack of effect on the stall margin, and the reduced effect on pressure rise and torque, can be explained.

Stall inception is a complicated problem, especially when stage-matching issues are involved. The situation is made even more complex by the presence of water, and it is thus not surprising that the literature contains differing reports on the effect of water ingestion on surge margin.

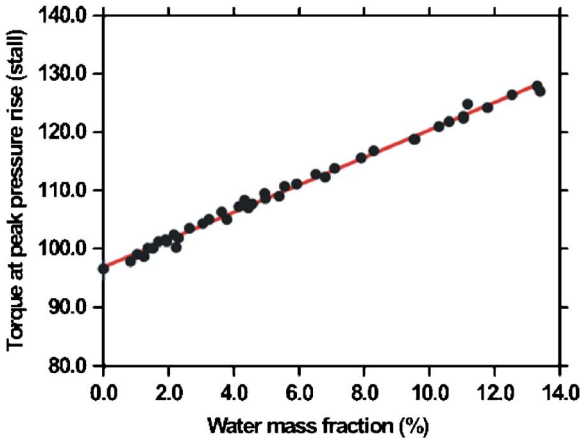

Fig. 6 Variation in corrected torque at stall point for various quantities of water ingested

Water Distribution Within the Compressor

We have considered the overall effects of water on compressor performance, but what happens to the water after its initial interaction with the first stage, i.e., how does the water make its way through the remaining stages of the machine? In the end it emerges that the flow pattern is so simple one might be tempted to say that it was obvious from the beginning.

The first point to note about the behavior of the water in the heart of the compressor is that 90% of the annulus is virtually dry. This conclusion comes from water extraction tests and borescope observations, where, in locations away from the outer casing, the lens of the scope remains dry and quite clear vision is possible. The second point is that, although some fine airborne droplets are produced by splashing and impact, most of the water makes its way through the compressor in sheet-water form. (Remember, these observations apply to reduced speed operation.)

In detail, downstream of the rotor rows, the water is concentrated in a sheet on the outer casing and is propelled in a predominantly tangential direction by the moving blades. As the water moves rearward, this sheet is "peeled off" by the stator blades, where it rides up the pressure side of each blade and leaves the trailing edge in a narrow sheet of coarse droplets. These droplets then strike the blades of the following rotor and the resulting surface water is again centrifuged toward the casing. This idea is illustrated in the following sketch.

Downloaded 30 May 2010 to 128.113.26.88. Redistribution subject to ASME license or copyright; see http://www.asme.org/terms/Terms_Use.cfm

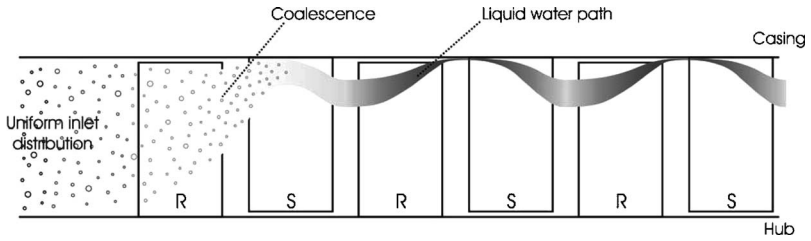

This description of the water moving through the compressor is equally valid for both small and large concentrations of water. It is, however, easier to measure and observe the behavior of the water if the concentration is high, and for this reason, most of the following discussion is based on water levels between 10% and 15% by mass.

Water Distribution Measurements Downstream of the Rotor Rows. The water flow on the casing wall just downstream of a rotor row is not easy to observe with a borescope because it is moving very fast and the film is very thin. Instead, experiments were conducted with a water extraction probe to determine the concentration of water at all radii between hub and casing. The water extraction probe consisted of a 3 mm hypodermic tube with a pick-up hole, 1.5 mm in diameter, drilled into the tube near the sealed end. A vacuum system, always set at a constant pressure difference to the prevailing pressure in the compressor, was used to extract a timed sample of air and water from the compressor. A cyclonic separation system was used and the mass of water was obtained by weighing—giving data in the form of milliliters per minute.

Figure 8 shows a graph of the water concentration plotted against the radial position from hub to casing downstream of rotor 3. The concentration of water near the casing is obvious, as is the comparative dryness near the hub. It should be noted, however, that the measurements taken near the casing suggest a thicker water film than is actually the case. This comes about because the fast moving water on the casing tends to ride up the stem of the probe, by as much as a diameter and more, and so gives a misleading impression of the film thickness. As the probe is aspirated, there is also a certain amount of "scooping" to be considered.

To get an idea of what the actual film thickness might be, it is useful to do a simple calculation. The assumption is made that all the water entering the compressor is concentrated on the casing wall, i.e., there is no splashing or evaporation. A rough estimate of the axial component of the film velocity can be obtained by timing how long it takes for colored die, injected suddenly, to move through the compressor and appear on the downstream casing window. A velocity of about 1 m/s was obtained, and from this a surface film thickness of 0.4 mm can be derived—based on a water mass fraction of 15%. This figure is only slightly less than the 0.6 mm film thickness derived from tests with a small boundary-layer probe. (Note: the rotor tip clearance is about 0.35 mm.)

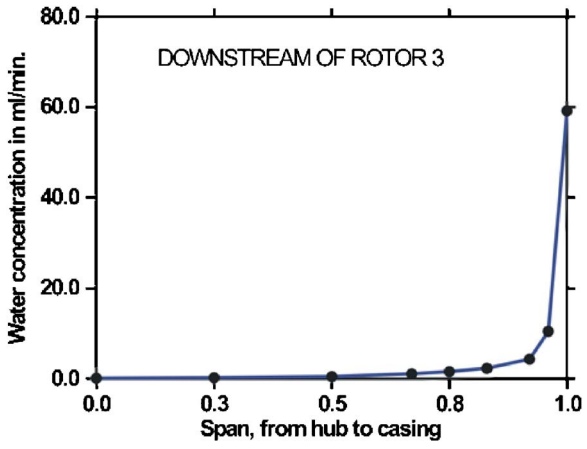

Fig. 8 Water extraction measurements taken downstream of rotor 3 for 17.1% water ingested

By rotating the water extraction probes, both cylindrical and cobra type, it is possible by repeated sampling to measure the flow direction of the water on the casing. The measurements show a clearly defined peak at about 82 deg swirl, i.e. 8 deg off pure tangential flow in the positive swirl direction. Using the cobra probe, but pushed slightly inward to avoid water contamination, shows that the airflow angle in this region, under wet conditions, takes a more axially inclined path of about 57 deg. The air and the water near the casing thus move in different directions.

Water Distribution Measurements Downstream of the Stator Rows. On the casing, the water leaves the rotor at an oblique angle and is received by the stator blades. Each blade "peels off" a thin stream of water, which, under its own momentum, rides up the pressure side of the blade and leaves the passage in a sheet of coarse droplets covering about a third of the outer span of the blade. The basic idea is illustrated in the sketch below. Note that most of the stator exit flow area will be dry.

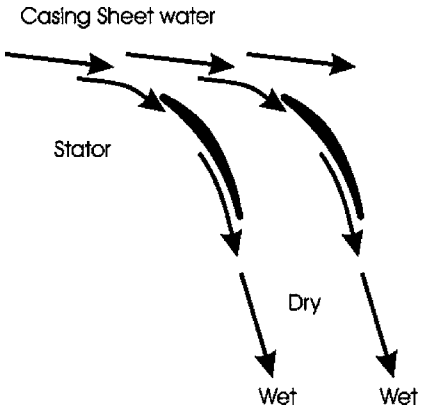

A small cascade experiment was set up to help visualize the movement of the water through the blades. With air flowing through the cascade, a tangentially directed film of water was injected onto the cascade end wall just upstream of the blades. The photograph of the resulting water pattern is shown in Fig. 9. It can be seen that the water leaves the cascade in a localised sheet covering about a third of the blade height.

It remains to be shown that the behavior of the water observed in the cascade experiment is a realistic picture of what actually happens in the compressor. To do this, an area traverse was set up downstream of stator 3 to measure the water concentration over 14 radial traverses covering an area of about one and one half-blade pitches. The cylindrical water extraction probe was used and after two weeks work, and the consumption of eight thousand gallons of water, the contour plot in Fig. 10 was obtained.

Figure 10 unfortunately only covers one complete blade pitch, but it does show quite clearly that the water is concentrated over the outer third of the span and is localized in the wake region of the blades. It may thus be concluded that the water in the compressor behaves in a similar way to that illustrated by the cascade experiment.

Downloaded 30 May 2010 to 128.113.26.88. Redistribution subject to ASME license or copyright; see http://www.asme.org/terms/Terms_Use.cfm

Fig. 9 Photograph of cascade experiment showing sheets of water coming off the pressure side of the stator blades

At the end of this section on the distribution of water in the compressor, we are left with a picture of a swirling sheet of water on the casing downstream of a rotor row, and a localized stream of water coming of each stator blade. Apart from odd airborne droplets, the remainder of the annulus is virtually dry.

The Loss of Delivery Pressure Under Wet Conditions

Borescope Observations. The suction surface of the stator blades is most easily observed with the borescope, because the water movement on this surface is relatively slow. The most striking features here are the rivulets crossing the blade surface, and the accumulation of water in the separation zones.

The sketch in Fig. 11 shows how most of the suction surface, except near the hub, is covered by narrow water tracks along which fine droplets can be seen to move slowly from the leading to trailing edge. Between the tracks, the blade surface appears to be dry. The fact that the wet tracks do not move about suggests that they are fed by water spilling around the leading edge from the pressure side of the blade, and this water simply follows the wet path of the previous droplets. In the suction side corner of the stator passage near the casing, water accumulates in the suction-side-corner-separation. At the trailing edge, a water bead can also be seen filling the trailing-edge-separation line.

The above picture of the water patterns on the suction side of

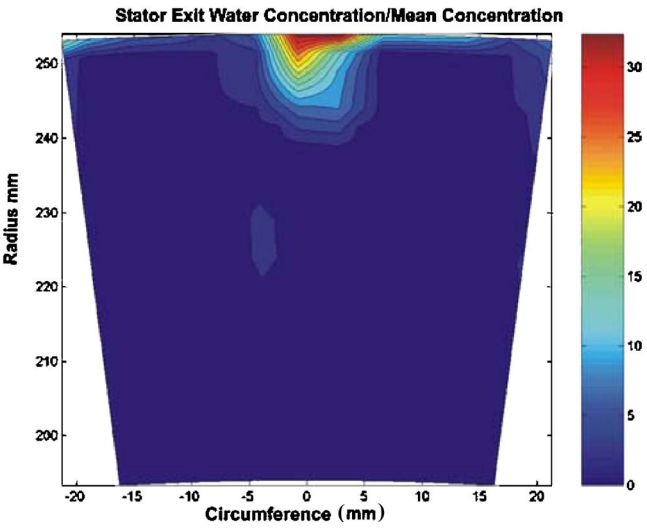

Fig. 10 Water concentration measurements obtained from area traverse downstream of stator 3

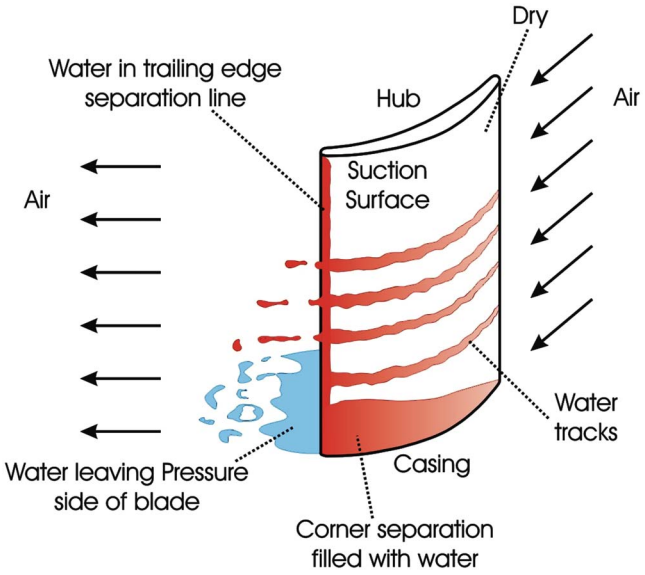

Fig. 11 Sketch of water distribution on suction side of stator blades

the stator blades suggests that the blade performance might be aerodynamically altered by the presence of the water. Perhaps this could partly explain the loss of pressure rise that accompanies water ingestion. Further borescope observations show, however, that this is not the case. If the water supply to the compressor is suddenly switched off, the compressor performance returns to the dry level in less than a second, as demonstrated in Fig. 12.

Continued borescope observation shows that the water tracks on the suction side of the stator blades remain visible for half a minute or more and only disappear through evaporation. The alteration of the stator blade profile by the water is thus not thought to have a big effect on the compressor delivery pressure.

Support for the above point also comes from an experiment in which a "dishwashing liquid" was used to reduce the surface tension of the water. A liquid soap dispenser was fitted to the high-pressure water supply system, and in spite of careful measurement, no change in delivery pressure could be detected. The only observable effect of the soap was a marvelous display of bubbles growing from every chink and leak in the system.

Detailed Aerodynamic Measurements. Because most of the compressor annulus remains relatively dry during water ingestion,

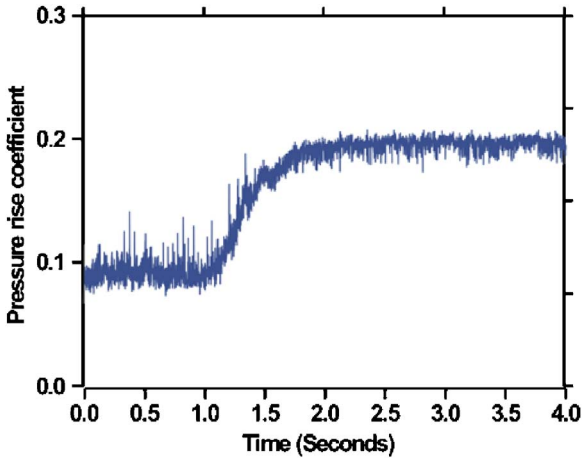

Fig. 12 Local pressure recovery in compressor after sudden termination of water supply

Downloaded 30 May 2010 to 128.113.26.88. Redistribution subject to ASME license or copyright; see http://www.asme.org/terms/Terms_Use.cfm

Table 1 Volumetric flow rates obtained under wet and dry conditions with throttle position adjusted for nominal inlet flow in all tests

	Dry	Wet m^3/s
Rotor 2 Exit	3.36	3.25
Rotor 3 Exit	3.33	3.34
Stator 3 Exit	3.39	3.60
Rotor 4 Exit	3.22	3.22

it is possible, with some care, to obtain aerodynamic measurements between the blade rows. A standard cylindrical three-hole probe measuring total pressure, static pressure, and flow direction can be used in the dryer parts of the annulus, but, due to the odd passing droplet, this type of probe with small diameter holes is likely to get blocked. It has been found, however, that a single-hole probe, much like the water extraction probe mentioned earlier, can be used successfully with only occasional blockage problems.

The single-hole probe used here was 3 mm in diameter with a transverse hole of 1 mm diameter drilled into the tube near the sealed end. This probe was slowly rotated about its longitudinal axis while continuously recording the pressure and the angular displacement. From prior calibration it is possible to obtain measurements of total pressure, static pressure, and flow direction from the recorded data. The pressure signal from the probe as it is rotated about its axis gives a bell-shaped curve of which the rising and falling sides should be perfectly symmetrical. The symmetry of this curve when measuring under wet conditions can be used as a check for water contamination. Any asymmetrical results can be rejected and a fresh attempt made to obtain a reliable reading. An automatic purge system was connected to the probe to make sure it was free of water before the start of each measuring rotation.

(In the data reported below, the last measurement near the casing wall often shows a sudden change in direction. This is not surprising in view of the amount of water present in this region and these outlying measurements near the casing should be regarded with caution.)

The results from the rotating single-hole probe were remarkably consistent, and under dry conditions agreed well with the design intent of the compressor. The general reliability of the rotating probe measurements can be assessed by traversing from hub to casing and then deriving the volumetric flow rate through the compressor. Measurements were obtained downstream of all the rotor rows, and downstream of stator 3. In the latter case, downstream of a stationary blade row, an area traverse would normally be required, but this was not possible with so much water concentrated on the pressure side of the passage, and so measurements from a single pitchwise location had to suffice.

Table 1 shows the volumetric flow rates obtained under wet and dry conditions with the throttle position adjusted to give the same nominal inlet flow for all the tests. Downstream of the rotor rows the wet and dry measurements agree fairly well. The deviation downstream of the stator row is somewhat larger, but this is probably the result of measuring at a single pitchwise location. The conclusion to be drawn from these measurements is that reliable aerodynamic data can be obtained from inside a wet compressor.

The detailed flow measurements show that the compressor stages all produce roughly the same pressure rise under dry conditions. When water is present, the first stage sometimes behaves oddly, but the second, third, and fourth stages all behave in a similar way, approaching the condition of a "repeating stage" [14]. By considering the measurements from rotor 3 and stator 3, observations can thus be made about the performance of a typical wet stage:

(1) The presence of water in the compressor changes the velocity distribution across the span, particularly near stall, in such a way as to reduce the axial velocity in the outer part of the annulus and increase the velocity in the inner part; see Fig. 13 for measurements taken downstream of rotor 3. (The measurements downstream of stator 3 exhibit a similar shift of flow toward the hub.)
(2) When wet, the exit flow angles in the rotor relative frame indicate an increase in flow deviation in the outer region of the annulus, and a reduction in deviation nearer to the hub. Figure 14 shows the measurements at rotor 3 exit at near stall conditions. The change in deviation in this figure is consistent with the change in axial velocity distribution, i.e., when the axial velocity is reduced the deviation increases, and visa versa.
(3) The absolute exit flow angles from stator 3 are relatively unaffected by the presence of water, see Fig. 15, which is for an operating point near the stall. These measurements support the earlier borescope observations that the presence of water on the stator suction surface does not appear to have a big effect on the blade performance.

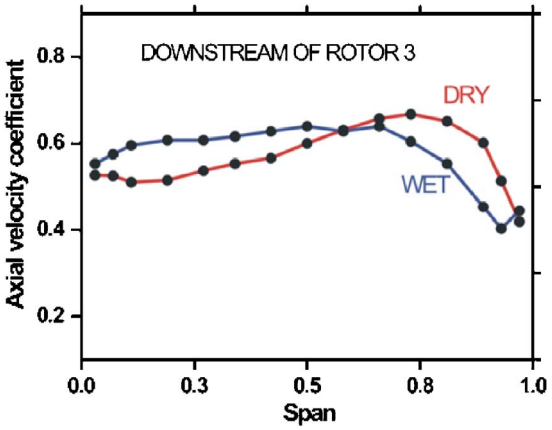

Fig. 13 Shift in axial velocity distribution near stall due to 17.1% water ingestion

From the stage 3 measurements, using the basic quantities of total pressure, static pressure, and flow direction, it is possible to derive the isentropic pressure rise across the stage at each radial location using the relationship

$$\Delta p = \rho U \, \Delta V_\theta.$$

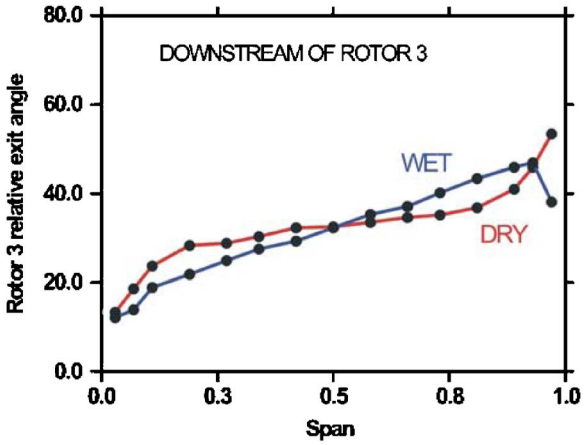

Fig. 14 Shift in rotor relative exit angle near stall due to 17.1% water ingestion

Downloaded 30 May 2010 to 128.113.26.88. Redistribution subject to ASME license or copyright; see http://www.asme.org/terms/Terms_Use.cfm

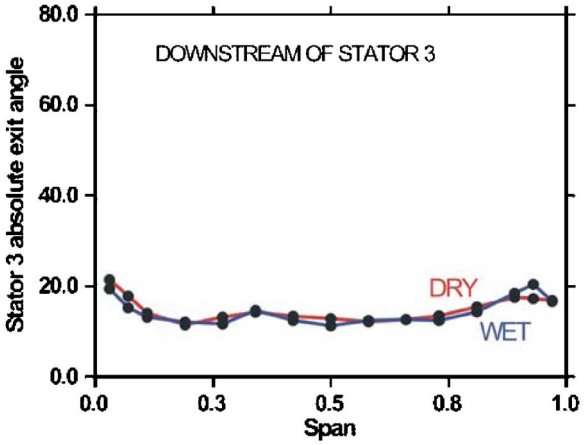

Fig. 15 Stator exit angles near stall for wet and dry operation

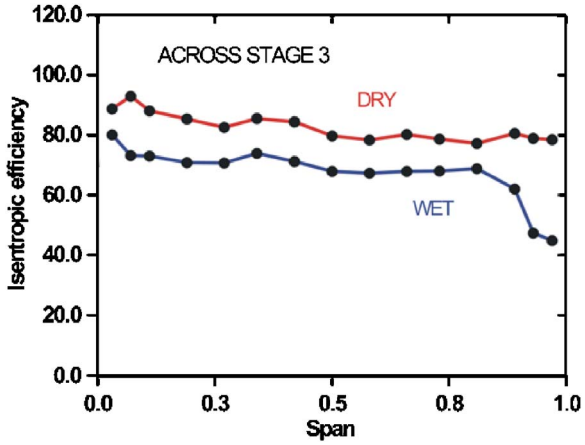

Fig. 17 Efficiency estimates for wet and dry conditions near stall, for stage 3

This ideal pressure rise is compared with the actual stage pressure rise for both wet and dry conditions in Fig. 16. From the isentropic lines it can be seen that the work input to the stage is much the same under wet and dry conditions for most of the span, but rises steeply near the casing when water is present.

The difference between the actual and ideal pressure rise can be used to derive the isentropic efficiency at each measuring location along the span. The results are presented in Fig. 17 for both wet and dry conditions. It can be seen that the aerodynamic efficiency of the compression process is everywhere reduced under wet conditions, particularly in the outer region of the annulus.

Discussion

The Loss of Delivery Pressure. In the last section it was shown that water ingestion changes the velocity distribution and flow direction across the span, and also reduces the aerodynamic efficiency. What remains to be established is the physical mechanisms by which these changes come about, and how they relate to the overall performance of the compressor.

In simplistic terms, the compressor can be divided into three flow regions: the inner annulus that is virtually dry, the outer annulus that is dry but may contain some airborne droplets, and a casing region where most of the water is concentrated in liquid form. The latter region occupies such a small volume that it can be ignored for the present. (As previously mentioned, the volumetric fraction of water at 15% mass is only 0.0002.)

A parallel annulus model can now be applied to the inner and outer parts of the annulus—with the usual requirement that the discharge pressure from both parts is the same. In Fig. 18 a dry operating point, A, is shown on a typical fixed speed compressor characteristic. When a significant amount of water is added to the flow, the compressor discharge pressure will fall and the overall operating point will move down the throttle characteristic to settle out at some point B. When water is added, we know from Fig. 13 that the flow velocity in the inner part of the annulus will increase and that in the outer part will decrease. We can therefore separately depict the operating points of these two parts as points C and D in Fig. 18. Point C, representing the flow in the inner annulus, must lie on the dry characteristic-because the local flow rate in this region has increased, the pressure rise has dropped, and the air is comparatively dry. The operating point for the outer part of the annulus, on the other hand, does not move up the dry characteristic as the local flow coefficient is reduced, but rather moves to a new lower pressure level at point D. This reduced pressure level for the outer annulus indicates an increase in aerodynamic losses in this region, as is known to occur from Fig. 16.

The increase in the losses in the outer part of the annulus can possibly be attributed to the drag imposed on the air as it tries to accelerate water droplets that become entrained in the flow—this includes the coarse droplets leaving the pressure side of the stator blades. Estimates suggest that accelerating just 10% of the water up to air speed will be sufficient to explain the additional losses in the outer region of the annulus.

As can be seen in Fig. 18, C and D, and their combined average B, are all on the same pressure level. This is a necessary require-

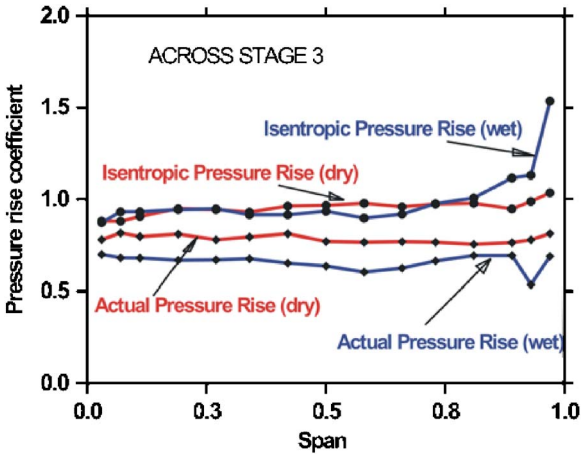

Fig. 16 Isentropic pressure rise compared with actual pressure rise near stall for wet and dry conditions, for stage 3

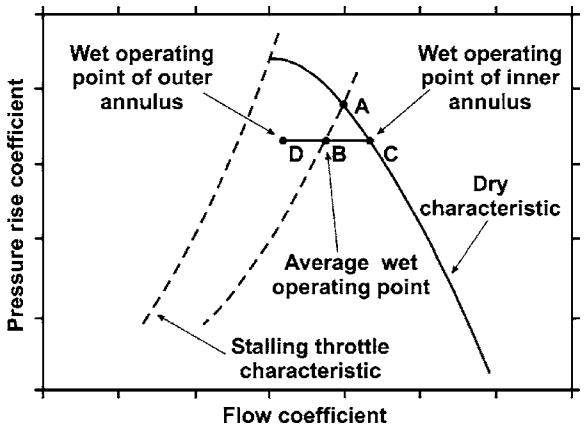

Fig. 18 Parallel annulus model showing the wet operating points of the inner (C) and outer (D) parts of the annulus

Downloaded 30 May 2010 to 128.113.26.88. Redistribution subject to ASME license or copyright; see http://www.asme.org/terms/Terms_Use.cfm

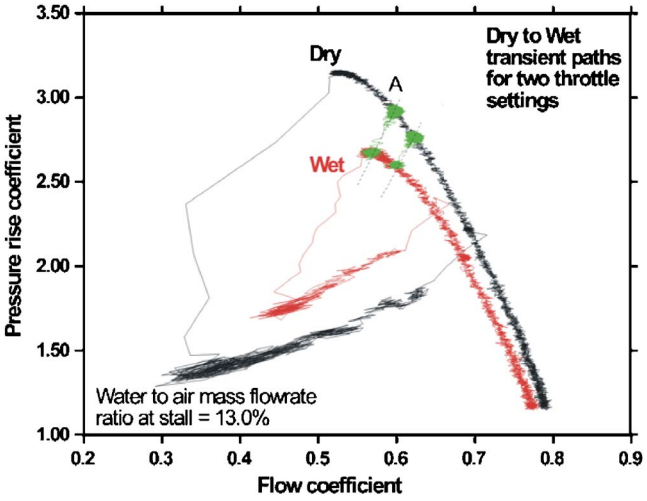

Fig. 19 Movement of operating points on overall total-to-static characteristic for sudden water injection

ment of radial equilibrium in the nonswirling flow downstream of the stator rows. (The measured static pressure downstream of stator 3, wet or dry, is perfectly uniform from hub to casing.) Note that the flow coefficient applicable to point D will be fixed by the requirement that the area average of the flow coefficients for points C and D must add up to the mean flow coefficient at point B.

Thus, by dividing the compressor into two annular regions, by increasing the losses in the outer region and by redistributing the flow toward the hub, we end up with a new operating point for the wet compressor at point B. This new point, which lies at a lower pressure level and a lower flow rate, is one of many points defining the wet characteristic of the compressor. Measurements supporting this shift in operating point are presented in Fig. 19 for sudden water ingestion at a fixed throttle setting.

It should be noted that the flow in the outer part of the annulus, point D in Fig. 18, operates at a lower flow coefficient than the average for the whole span and the flow in this region is thus most likely to trigger stall. The parallel compressor model thus suggests a possible reason why the stall margin of a compressor might be reduced under wet conditions. (In Fig. 19, water addition at any dry operating point to the left of point A will result in rotating stall.)

The Increase in Drive Torque. It will be recalled from Figs. 5 and 6 that the torque increases dramatically as water is ingested and that the increase is proportional to the amount of water added.

In addition, the behavior of the water in the compressor was previously described as leaving the rotor at high speed in the tangential direction and then being brought back to the near axial direction by the stator blades. The torque required to achieve this stage-by-stage change in tangential momentum can be estimated very simply by assuming that all the water passing through the stage is accelerated up to blade speed by the rotors and then decelerated again by the stators:

$$\Delta T = \dot{m}\Delta(RV_\theta) \times \text{number of stages}.$$

Thus, for 13% of water by mass, the calculated torque increase is 40 Nm. The measured value is 32 Nm—which is reasonable considering that no slip factor has been included, and that the water flow is never fully tangential and never fully axial. (A requirement of this simple model is that the torque should increase linearly with the mass of water added—which is certainly true according to Fig. 6.)

If evaporation levels are low, we can therefore conclude that the mechanical processing of water is responsible for the greater part of the increased torque required to keep the wet compressor spinning at a constant speed. It has in any case already been shown that the isentropic work input to the air is not greatly altered by the presence of water, and therefore any additional torque must be absorbed by the water itself.

Conclusions

(1) Most of the existing information on water ingestion in axial flow compressors has come from whole engine tests. In such tests, the influence of water can be divided into three parts: thermodynamic (evaporation, change in gas properties, etc.), aerodynamic (loss of pressure rise, efficiency, and stall margin) and mechanical (an increase in torque). By testing in a system where the thermodynamic effects are minimal, and by obtaining direct measurement from a standalone compressor, it has been possible, for the first time, to quantify the aerodynamic and mechanical effects of water ingestion.

(2) The effect of water ingestion on compressor delivery pressure depends on the amount of water ingested. In the current tests, water mass fractions of less than 3% or 4% had little effect on pressure rise. Larger quantities produced increasingly significant performance losses. It is thought that the changeover point is linked to the amount of water necessary to fill the rotor tip clearance gap.

(3) The effect of water ingestion on drive torque is immediately effective right from the smallest quantity of water ingested. The torque has been shown to increase linearly with the amount of water added.

(4) The influence of water ingestion on compressor stability is difficult to quantify. In most cases premature stalling was observed, but in some configurations little or no change in stall margin was detected. No reliable trends can be reported.

(5) Inside the compressor, water concentration measurements show that 90% of the annulus is virtually dry. Useful aerodynamic measurements can thus be obtained from within a compressor operating under wet conditions.

(6) Particle tracking calculations, and experimental results, show that most droplets of more than a few microns in size will collide with the first rotor row. After this initial collision, the droplets coalesce and the water moves through the rest of the compressor in liquid form.

(7) Once inside the compressor, water depositing on the rotor blades is centrifuged onto the casing where it moves tangentially in sheet form until it strikes the stator blades. Here it is turned in the axial direction and moves radially inward before leaving in streams of coarse droplets from the pressure side of the blades. This flow pattern is repeated stage by stage through the compressor.

(8) Borescope observations, and reduced surface tension experiments, suggest that compressor performance under wet conditions is not greatly influenced by blade surface effects, changes in boundary layer or alterations in separation patterns. Tip clearance effects and droplet drag in the outer regions of the annulus appear to have a far greater influence on compressor performance.

(9) When water is ingested, the effect on the compressor is to alter the radial distribution of the flow. The velocity in the outer part of the annulus is reduced and that in the inner part is increased. In keeping with this velocity shift toward the hub, the deviation angles downstream of the rotors increase in the outer part of the annulus and decrease in the inner part. The flow deviation downstream of the stator rows is not altered by the presence of water.

(10) From detailed flow measurements, estimates of the isentropic work input to a stage have been obtained for wet and dry conditions. The results show that the work input is unchanged by the presence of water, except in the outer

Downloaded 30 May 2010 to 128.113.26.88. Redistribution subject to ASME license or copyright; see http://www.asme.org/terms/Terms_Use.cfm

region of the annulus, where it ramps up near the casing. The pressure rise across the stage is everywhere reduced when a large amount of water is present, and thus the overall aerodynamic efficiency of the stage is reduced.

(11) Measurements of the torque required to drive the compressor show that the torque increases linearly with the amount of water ingested. In view of the fact that the isentropic work input to the air does not increase significantly under wet conditions, the greater part of this additional torque is absorbed in the mechanical processing of the water–thermodynamic effect being excluded.

(12) Having established that the water in the compressor moves tangentially in the rotors and axially in the stators, a simple momentum calculation can be used to estimate the additional torque required to drive the compressor. The estimates agree well with the experimental results.

(13) A simple parallel annulus model has been proposed to explain the loss of pressure rise when a large amount of water is ingested. The model covers the observed increase in losses near the casing and the overall shift of the flow toward the hub. It also explains why a loss of stall margin might occur when water is present.

Acknowledgment

The authors would like to express their gratitude to Rolls-Royce plc for their interest in the work, and particularly to Dr. Simon Gallimore, who first proposed the project, and who has maintained a guiding influence over the past six years. Thanks also to Arthur Rowe at Rolls-Royce, and to Ashley Peterson and Lorraine Baker at the Whittle Laboratory for their helpful input to the paper. Grateful thanks are also extended to the British Civil Aviation Authority, and especially to Dr Steve Griffin, for the financial support of the project.

References

[1] Rolls-Royce plc, 1996, *The Jet Engine*, 5th ed. Rolls-Royce plc.
[2] AGARD, 1995, "Recommended Practices For the Assessment of the Effects of Atmospheric Water Ingestion on the Performance and Operability of Gas Turbine Engines," AGARD Advisory Report No. 332.
[3] Riley, S., 1997, "Whole Engine Water/Ice Ingestion Strategy—Final Report," Technical report, Rolls-Royce plc.
[4] Davis, M., 2004, "A Numerical Investigation of the Effects of Steam Ingestion on Compression System Performance," ASME Paper No. GT2004-54190.
[5] Tomassetti, N. R., 1967, "Steam Ingestion in Aircraft Gas Turbine Engines," *Proceedings 7th National Conference on Environmental Effects on Aircraft and Propulsion Systems*, September, Princeton, NJ.
[6] Rowe, A. L., 2003, private communication.
[7] Young, J. B., and White, A. J., 2004, private communication, University of Cambridge.
[8] JAA, 1997, "Ingestion of Rain and Hail, Harmonised Changes to JAR-E and FAR. Part 33," Joint Aviation Authorities, Technical Report.
[9] Kissel, G. J., 1980, "Rain and Hail Extremes at Altitude," J. Aircr., **17**, pp. 464–467.
[10] Williams, J. C., 2003, Ph.D. thesis, Department of Engineering, Cambridge University.
[11] Kennedy, J. B., and Roberts, J., 1990, "Rain Ingestion in a Gas Turbine Engine," in *Proceedings of 4th ILASS Meeting*, Hartford, CT.
[12] Wolfe, H. E., and Anderson, W. H., 1964, "Kinetics Mechanism and Resultant Droplet Sizes for the Aerodynamic Breakup of Liquid Drops," Aerojet-General Corporation, Technical Report 0395-04(18)SP.
[13] Camp, T. R., and Day, I. J., 1998, "A Study of Spike and Modal Stall Phenomena in a Lowspeed Axial Compressor," J. Turbomach., **120**, pp. 393–401.
[14] Horlock, J. H., 2004, "Flow Through a Repeating Stage in an Axial Compressor—A Reconsideration," ASME J. Turbomach., **126**, pp. 677–679.

Downloaded 30 May 2010 to 128.113.26.88. Redistribution subject to ASME license or copyright; see http://www.asme.org/terms/Terms_Use.cfm

Discussion: "Criteria for Spike Initiated Rotating Stall" (Vo, H. D., Tan, C. S., Greitzer, E. M., 2008, ASME J. Turbomach., 130, p. 011023)

A. Deppe

H. Saathoff
e-mail: h.saathoff@tu-braunschweig.de

U. Stark

Institut für Strömungsmechanik
TU Braunschweig,
Braunschweig 38106, Germany

*The paper "Criteria for Spike Initiated Rotating Stall" by Vo et al. (2008, ASME J. Turbomach., **130**, p. 011023) provides a very important contribution to the understanding of spike-type stall inception in axial-flow compressors by demonstrating that spike-type disturbances are directly linked to the tip leakage flow of the rotor. The computational study of Vo et al. leads to the conclusion that two conditions have to be fulfilled simultaneously for the formation of spike-type stall: (i) axial backflow at the leading edge plane and (ii) axial backflow at the trailing edge plane. The objective of the present technical brief is to support these findings by corresponding experimental results.*
[DOI: 10.1115/1.2750673]

Introduction

The material in this technical brief was obtained from an experimental investigation of three different single-stage axial-flow low-speed compressors [1]. The characteristics of the compressors measured for a tip clearance-to-chord ratio of $s/l=0.015$, are presented in Fig. 1, showing the nondimensional inlet-stagnation to outlet-static (total-to-static) pressure rise ψ_{ts}.

Experimental Setup and Instrumentation

At the last stable operating point of each compressor, the slope of the total-to-static pressure characteristic is clearly negative. Therefore, following Camp and Day [2], spike-type stall inception has to be considered for all stages. Four pressure probes were used to detect the circumferential as well as the radial evolution of the initial disturbance. The unsteady pressure traces were measured simultaneously upstream (probes 1 and 2) and downstream (probes 3 and 4) of the rotor. Probes 1 and 2, two pitches apart and 2 mm or 45 mm immersed, respectively, are two 90 deg cranked total pressure probes facing the rotor at an angle of 60 deg. Probes 3 and 4, also two pitches apart but only 2 mm immersed, are two calibrated cylindrical pressure probes with a 45 deg downstream directed axis angle of the measuring holes. For further details concerning the setup, the reader is referred to [1].

The accuracy of the Kulite™ XCS-062-5D sensors used as the probe's heads is sufficient in order to resolve the given pressure magnitudes as well as the fluctuations in time (see [3]). Some thoughts have to be given to the time-dependent aerodynamic characteristics of a fast response pressure probe. Since the probe head, which is placed into the flow, represents a solid boundary, the surface pressure at a given point always contains contributions from the inertial effects in the flow around the body. The effect was investigated on a small sphere in a periodically pulsating jet by Kovasznay et al. [4]. According to the theory developed in [4], the contribution of the inertial term was estimated to be less than 3% of the steady term within the present investigation. This is due mainly to the small size of the probes. Even though different types of probes were used in the present setup upstream and downstream of the rotor (see [1]), the contributions from the inertial term would effect all probes in the same way, reducing the error concerning temporal and quantitative resolution even further. Therefore, the accuracy of the described instrumentation is considered to be sufficient for the following qualitative signal analysis.

Rotor Flow During Stall Inception

A selected result of the instantaneous pressure measurements for probes 1 and 3 is shown in Fig. 2 for stage 2 with a tip clearance-to-chord ratio $s/l=0.015$. The starting point for the following analysis and discussion is the total pressure trace of probe 1 (close to the casing, upstream of the rotor). During stable compressor operation, the total pressure trace is formed by the upstream effect of the corresponding rotor blades. A first disturbance of the total pressure upstream of the rotor is shaped like a spike and represents a distinct pressure and suction peak of small circumferential extension (Saathoff et al. [5]). Proceeding from the initial spike, the disturbance grows in circumferential as well as radial direction until, after less than ten rotor revolutions, again a steady state, fully developed stall, is reached.

In order to gain insight into the corresponding tip clearance flow field phase-locked, ensemble-averaged casing, wall pressure distributions were measured (see [1]). An analysis of the associated pressure fluctuations reveals high values in a band-like area slightly upstream of the tip clearance vortex due to the interaction of the incoming flow and the axially backward directed tip clearance flow. For a near stall flow rate, this upstream interaction zone is aligned with the rotor inlet plane while the pressure fluctuations reach a maximum. This is a common result for all three compressors. This situation turns out to be the critical condition for spike-type stall inception because further throttling of the compressor leads to an unsteady spillage of tip clearance flow ahead of the rotor blade leading edge. In this regard, the outcome of the present analysis of the measured casing wall pressure distributions agrees

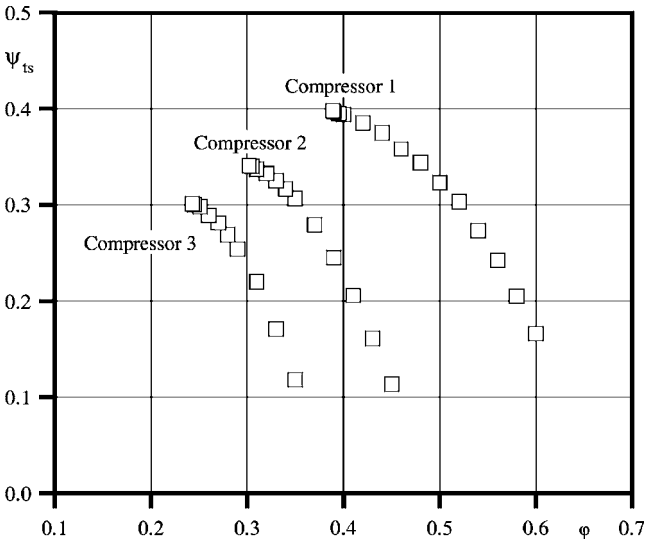

Fig. 1 Single-stage compressor characteristics

Contributed by the Turbomachinery Division of ASME for publication in the JOURNAL OF TURBOMACHINERY. Manuscript received June 21, 2006; final manuscript received March 19, 2007; published online January 30, 2008. Review conducted by Zoltan Spakovszky.

Downloaded 30 May 2010 to 128.113.26.88. Redistribution subject to ASME license or copyright; see http://www.asme.org/terms/Terms_Use.cfm

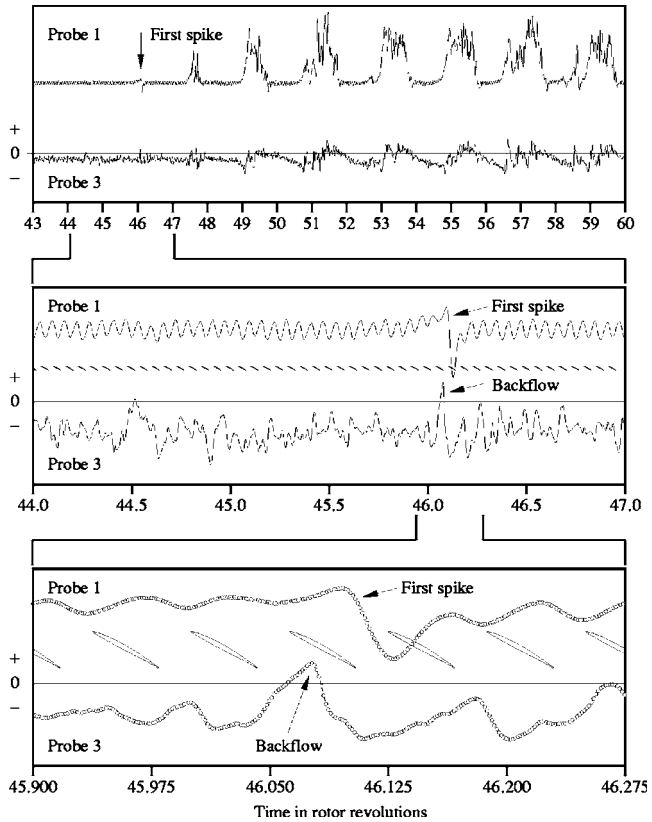

Fig. 2 Unsteady pressure distributions up- and downstream of the rotor (Compressor 2)

well with the findings of Vo et al. [6]. Both investigations do not show any blade stall (severe blade boundary layer separation) in the tip region.

According to Vo et al. [6], there is a second condition for spike-type stall inception to occur. This second condition, the appearance of locally confined, unsteady backflow at the rotor outlet close to the casing wall, must be fulfilled simultaneously with the first condition. This numerical result was the reason to additionally investigate the rotor outlet flow during the inception process parallel to the rotor inlet flow utilizing two downstream probes as described above. The specially calibrated probes indicate a change from axial downstream to axial upstream flow by a change of sign of the measured pressure coefficient.

The second pressure trace obtained from probe 3 for compressor 2 is given in Fig. 2, top frame. During data reduction, trace 3 was shifted in the rotor direction to compensate for the circumferential distance (exactly one pitch) between the two probes. Trace 1 shows the evolution of an initial spike into a fully developed stall cell as has been explained before. The corresponding signal of probe 3 shows axially backward directed flow exactly at the position of the first spike in trace 1. This means that the critical point is found, where the conditions described by Vo et al. [6] are fulfilled for the first time during stall inception. The simultaneity of the occurrence of spikes in the leading and trailing edge pressure traces was observed every time compressor 2 was taken into stall. Identical results were found for compressors 1 and 3.

A close-up of the traces is shown in the middle frame of Fig. 2, demonstrating more clearly that the first spike in trace 1 directly links up with a backflow-indicating spike in trace 3. Spikes of this type occur several times, irregularly distributed along the circumference before the first spike in trace 1 can be detected. Figure 2, bottom frame, represents a still closer view of the pressure signals together with the rotor tip cascade. The arrangement of the cascade and the pressure signals indicates that backflow occurs near the trailing edge and spills forward near the leading edge of the same blade. From these results, it was concluded that spike-type stall inception starts with local spots of backflow at the rotor outlet next to the casing. For the three-stage configurations investigated, this result was found and could be repeated. These findings are, furthermore, confirmed by a corresponding experimental low-speed model investigation of a high-pressure compressor stage (see [7]).

References

[1] Deppe, A., Saathoff, H., and Stark, U., 2001, "Spike-Type Stall Inception in Axial Compressors," *6th European Conference on Turbomachinery—Fluid Dynamics and Thermodynamics*, Lille, France, pp. 178–188.

[2] Camp, T. R., and Day, I. J., 1998, "A Study of Spike and Modal Stall Phenomena in a Low-Speed Axial Compressor," ASME J. Turbomach., **120**, pp. 393–401.

[3] Brodersen, S., and Wulff, D., 1992, "Measurements of the Pressure and Velocity Distribution in Low-Speed Turbomachinery by Means of High-Frequency Pressure Transducers," ASME J. Turbomach., **114**, pp. 100–107.

[4] Kovasznay, L. S. G., Tani, I., Kawamura, M., and Fujita, H., 1981, "Instantaneous Pressure Distribution Around a Sphere in Unsteady Flow," ASME J. Fluids Eng., **103**, pp. 497–502.

[5] Saathoff, H., Deppe, A., Stark, U., Rohdenburg, M., Rohkamm, H., Wulff, D., and Kosyna, G., 2003, "Steady and Unsteady Casing Wall Flow Phenomena in a Single-Stage Low-Speed Compressor at Part-Load Conditions," Int. J. Rotating Mach., **9**, pp. 327–335.

[6] Vo, H. D., Tan, C. S., and Greitzer, E. M., 2007, "Criteria for Spike Initiated Rotating Stall," ASME J. Turbomach., **130**, p. 011023.

[7] Dobrzynski, B., Saathoff, H., and Kosyna, G., 2006, "Stall Inception in Axial-Flow Compressors With and Without an Inlet Guide Vane," *13th International Conference on Modelling Fluid Flow Technologies (CMMF'06)*, Budapest, Hungary, pp. 1147–1154.

Downloaded 30 May 2010 to 128.113.26.88. Redistribution subject to ASME license or copyright; see http://www.asme.org/terms/Terms_Use.cfm